Seismic Vulnerability Assessment of Existing URM Structures through a Simplified Analytical Method

Sapienza University of Rome,
Department of Geotechnical and Structural Engineering

Eng. Claudia Sansoni

Supervisor
Prof. Eng. Stefano Pampanin

April 2021

Abstract

Existing UnReinforced Masonry (URM) buildings are characterized by a high seismic vulnerability, as seen from the consequences of past earthquakes. These damages can be essentially interpreted on the basis of two collapse mechanisms: Out-Of-Plane and In-Plane (when the “box-behaviour” is guaranteed), according to the structural details of the buildings and the direction of the seismic action.

Several numerical tools have been developed for the seismic analysis of URM structures but most of them are very computationally demanding and too complex for the daily use of practicing engineers.

This Thesis proposes a simplified analytical (“by-hand”) procedure for the seismic vulnerability assessment of existing URM structures, from an analogy with the SLaMA (Simplified Lateral Mechanism Analysis) method, developed and extensively validated for reinforced concrete structures. This mechanism-based methodology provides a first approximation of the global seismic behaviour of a building starting from the sub-system level.

Key features of the SLaMA procedure are the evaluation of: a) the moment-curvature/rotation capacity curves at component level; b) the hierarchy of strength at subassembly level and c) the capacity curve of the global mechanism. When dealing with URM structures, the building geometry is defined by means of an Equivalent Frame model and to assess the analytical elements bending capacity a peculiar section analysis, the Monolithic Beam Analogy approach, is implemented.

Experimental in-plane tests on panels, one-storey substructure and two-storey wall, available in literature, are used to validate the SLaMA-URM procedure against macro-mechanical finite element and equivalent frame modelling.

Through a parametric analysis, prototype buildings with different geometric configurations are analyzed by the SLaMA-URM method, where the interaction between the In-Plane and the Out-Of-Plane performances of walls is taken into account, thus obtaining the global structural performance.

Some retrofit strategies are then applied and their effect is evaluated through the procedure, in order to achieve a higher capacity, both in terms of the ultimate performance (%NBS) and the expected economic losses (EAL). To further investigate the different

response of the structures, two seismic intensities (high and medium) of the construction site are considered.

At the end, a cost-benefit analysis is performed to facilitate the selection of the most appropriate retrofit strategy, not only through the total intervention costs but also through a useful parameter that defines the cost of one percentage point of NBS (1%NBS cost).

In conclusion, the SLaMA-URM method, being totally implemented by simple spreadsheets, wants to be an effort in the process to put the designer at the center of the seismic performance assessment and of the design of retrofit interventions, allowing him to acquire a greater sensitivity towards the obtained results.

Acknowledgements

At the end of this long and important experience, some acknowledgments are certainly due.

Special thanks go to my Supervisor, Stefano Pampanin, for his support and his invaluable advice. His technical guidance allows me to carry out this Thesis with perseverance and conviction. Without any doubt, if I hadn't met him, I never would have thought to embark on this amazing road.

I want to thank Professor Paulo B. Lourenço for the kind welcome and for allowing me to be part of his research group during the period at the University of Minho. Thanks to him, Luis and Rui I have spent there amazing months during which I really grew professionally and personally.

I would like to thanks my friends (in particular Alberto and Mary) that, especially during the difficult periods, had sustained me and tried, successfully, to make lighter the burdens of this work. Special thanks go also to my colleagues (Simona, Jonathan, Carlos, Mohsen, Murilo and Mario) that have been and are definitely more than this. I hope we will meet soon to celebrate together again.

I would like to thank my family for the support and to allow me to get this far today. Last but not least, I would like to thank Simone without whom this achievement probably would not have been possible.

Table of contents

4. Performance assessment and seismic retrofit of URM structures

5. The SLaMA-URM method

6. Applications of the SLaMA-URM method: In-Plane performance

7. Seismic assessment and retrofit of URM prototype structures through the SLaMA-URM method

1. Introduction

1.1 Background and research motivation

The masonry structures are the oldest buildings present in every part of the world and often represent the cultural heritage of each country. Their simple construction, adaptability and durability have justified their wide use in the building industry, in the past as well as nowadays. These considerations are particularly relevant in the Italian territory, where the masonry buildings, according to the ISTAT report (2011) are 57% of all the Italian building structures (Figure 1.1a). Moreover, most of them, around 74%, were built before any seismic code was available (Figure 1.1b), i.e. before the approval of the technical standards for construction in seismic areas in 1974 (L. 64/1974) and the following Ministry Decrees. Despite these considerations, the conservation state of these constructions was defined approximately as good even if their capability to sustain a seismic event is unknown.

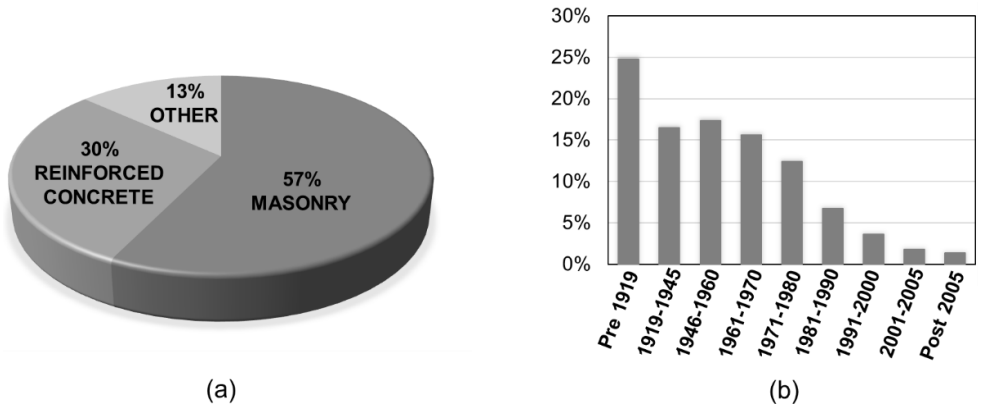

Figure 1.1. ISTAT (2011) data: (a) construction materials of the Italian building heritage and (b) age of construction of the masonry buildings.

Although the simplicity of these constructions represents a major advantage, the analysis of their mechanical behaviour represents a true challenge. This is principally due to the intrinsic characteristics of the masonry material, heterogeneous and anisotropic, that grant the structures a complex and non-linear mechanical behaviour.

Moreover, past and recent earthquakes (i.e. Friuli - 1976, Athens - 1999, Central Italy - 2017), have shown the significant structural vulnerability of the UnReinforced Masonry (URM) buildings, as highlighted by the severe observed damages (Figure 1.2). This high vulnerability can be addressed to several causes, among them the most important are: the design according to old code provisions (which did not consider seismic aspects); the age of the constructions (that frequently did not undergo proper restoration); the properties of the masonry material (often of poor quality) and the structural details of the buildings (such as the level of the connections between masonry walls and between walls and diaphragms). All of these considerations need to be properly taken into account when evaluating the seismic performances of masonry buildings.

Figure 1.2. Several and different types of damages observed in URM structures after Central Italy earthquake of 2016 (adapted from Menna et al., 2016).

According to the characteristics of the masonry structures, it is possible to distinguish a hierarchy of the failure mechanisms (Giuffrè, 1993) that are: the crumbling of the masonry, the Out-Of-Plane modes and the In-Plane modes, as shown in Figure 1.3. Each of them needs to be evaluated and prevented at the best. It should be noted that this hierarchy of failure mechanisms means that if the masonry is prone to crumble, this mechanism will damage the structure well before the onset of Out-Of-Plane modes. The same happens for the In-Plane ones that do not occur in presence of Out-Of-Plane modes, which will damage the structure in advance.

(a) (b) (c)

Figure 1.3. Damages from past Italian earthquakes to URM structures: (a) crumbling of the masonry, (b) Out-Of-Plane modes and (c) In-Plane modes (adapted from Fragomeli et al., 2018; Santarsiero et al., 2016).

Often it is possible to identify serious structural deficiencies of existing URM buildings that lead to a high seismic vulnerability. These deficiencies are associated with:

- the absence or ineffectiveness of elements and/or systems that guarantee a good "box-like" behavior of the structure;
- low strength offered by walls subjected to actions orthogonal to their plane;
- low strength of the individual structural elements (ability to resist to the In-Plane seismic actions of the wall);
- bad global seismic response of the building.

In order to deal with the safety assessment of masonry structures, several studies have shown a significant interest in the development of reliable modelling and analysis methods. The complex masonry structural response has been investigated by different computational strategies in literature, such as, for example, advanced modelling approaches based on the finite element (FE) method. Although this kind of modelling strategy is capable to provide accurate results, it may also be computationally demanding and, therefore, of limited application within seismic vulnerability assessment studies. Moreover, it is a common thought that more sophisticated analyses always provide a more accurate response, resulting in a more efficient design and a better assessment for existing buildings. However, this is not always true. Complex and advanced models need, and are highly dependent on, a

great number of input parameters, each subjected to judgement, probabilistic outcomes and potential errors. Moreover, it is important to highlight that most of these input parameters are difficult to obtain with precision in existing URM structures since often the knowledge about the construction material is scarce and/or difficult to obtain. As mentioned in New Zealand guidelines (NZSEE, 2017), there is a fine balance between accuracy, reliability (or precision), cost and complexity in structural analysis (see Figure 1.4). Due to these reasons, simplified models are usually preferred as they allow a good compromise in balancing efficiency with accuracy, in terms of usability, computational burden and reliability of results, when performing analysis of existing URM structures. Among simplified models, the structural component-based ones, such as the Equivalent Frame (EF) method, are the most used in seismic assessment studies and are typically preferred by the engineers in daily professional practice.

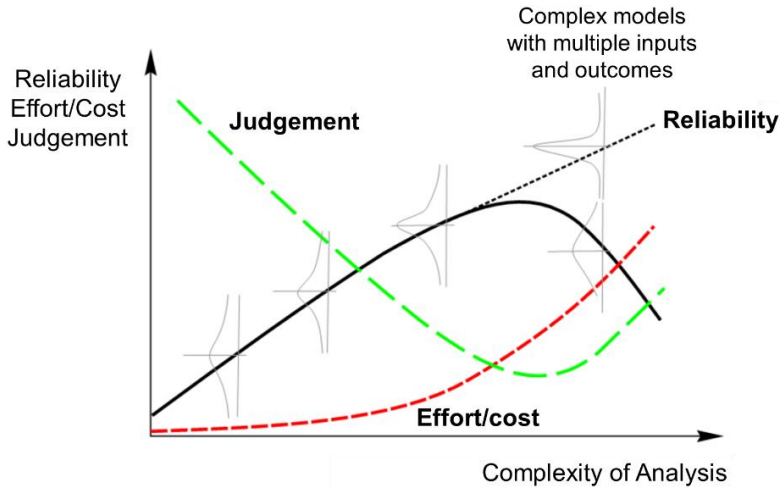

Figure 1.4. Trade-off between reliability, engineering judgement, cost and complexity of structural analysis (adapted from NZSEE, 2017).

Furthermore, nowadays in the field of earthquake engineering, the characterization of the behaviour of a structure has become increasingly important and moves from the prescriptive design approaches towards performance approaches. In these latter, the economic evaluation of the structure has become increasingly important. It means that nowadays the structural behaviour can be described by the expected level of damage (economic point of view) as well as the ultimate performance observed in seismic events. This economic consideration can be taken into account to identify the best retrofit intervention that enhances the seismic performance of a building.

In this context, the trend has too often and unfortunately moved towards a “black-box” approach, with computer modelling becoming the objective of the design instead of support to the design itself. This is particularly true for practicing engineers that, due to the short amount of time available to perform a seismic assessment, usually use the “default” set of parameters that available software presents. This approach leads to reliable results in the vast majority of the cases for new building design, but this can be less reliable in the case of assessment of existing structures, in which the “default” model might be unable to catch all the structural weaknesses.

Due to these reasons, a simplified procedure that puts the designer at the centre of the seismic assessment process of existing URM structures and that can help the daily practitioners engineers in the decision-making process of the best retrofit intervention, is still missing.

1.2 Objectives

This Thesis relies on the above considerations and it is focused on the numerical and analytical approaches for URM structures and the analysis of the possible failure mechanisms of the URM structural components, towards the development of a new analytical method to assess the seismic vulnerability of existing and reinforced masonry buildings. The main objectives can be summarized as follows:

- development of a new analytical procedure for achieving in first approximation the capacity of URM structures, starting from the hierarchy of strength of the structural components. This method originates from the Simplified Lateral Mechanism Analysis (SLaMA) for reinforced concrete structures and it is herein developed and adapted to masonry structures;
- investigation of the structural response of URM buildings through numerical modelling and validation of these results against experimental campaigns available in literature;
- validation of the new implemented analytical SLaMA-URM procedure through a comparison with the numerical and the experimental outcomes;
- investigation of the response of URM structures by varying their geometry, in order to further validate the proposed procedure and highlight its range of application;

- consider the interaction between the In-Plane and the Out-Of-Plane performance of URM structures to define the structural global performance of URM structures;
- use the SLaMA-URM method to evaluate the seismic performance of prototype buildings in order to evaluate alternative retrofit solutions and perform the corresponding losses assessment;
- identification of the best retrofit solution by comparing the ultimate performance, the expected economic losses (EAL) and the intervention costs.

1.3 Organization of the Thesis

The Thesis is organized as follows:

- **Chapter 2** describes the main properties of the masonry material, providing a description of its uniaxial and biaxial behaviour. A brief description of the different idealizations of the structural behaviour of masonry structures is shown. At last, the different micro and macro-modelling strategies for the study of the masonry are discussed, together with their advantages and drawbacks.

- **Chapter 3** contains an overview of the state-of-the-art on the Out-Of-Plane and In-Plane failure mechanisms of URM structures, outlining the several formulations used to assess the strength of piers and spandrels in a simplified way, available in literature and adopted by codes. Due to the topic of this Thesis, more detail is given to the In-Plane failure mechanisms, thus providing an extended overview of the existing structural components analytical models.

- **Chapter 4** describes the evolution of the performance design of structures and highlights the main methods to define the seismic performance in terms of ultimate strength. Furthermore, the fundamental concepts underlying the estimate of the expected economic losses for construction are discussed. At last, are described the main retrofit intervention strategies and techniques that can be adopted in existing URM structures.

- **Chapter 5** presents the new simplified analytical procedure, named SLaMA-URM, proposed in this Thesis. At first, the main steps of the SLaMA procedure for reinforced concrete structures are shown. Then the extension and the no-

trivial adaptation to the case of URM structures are presented. This new method takes into account both the In-Plane and the Out-Of-Plane possible failure mechanisms of the URM structures, to identify their global ultimate performance. Since the procedure to define the In-Plane seismic performance represents the focus of this Thesis, a comprehensive view on it is reported. At last, the limitations and a summary of the role of the SLaMA-URM method are discussed.

- **Chapter 6** reports the application of the SLaMA-URM method to some URM cases study subjected to In-Plane loads, available from experimental tests reported in literature. Different walls have been investigated, from simple panels to a one-storey substructure and a two-storey wall. For each case study, numerical simulations based on macro-mechanical Finite Element Model (FEM) and Equivalent Frame Model (EFM) were performed. Different modelling approaches have been adopted to investigate aspects related to the computational burden and hence to the complexity of the analysis. At last, the SLaMA-URM procedure was applied to a set of frame structure case studies that differ in the number of bays and levels. The resulting non-linear capacity curves were compared with the performed EF numerical Pushover analyses, in order to validate and evaluate the accuracy of the SLaMA-URM method.

- **Chapter 7** presents the application of the SLaMA-URM method to URM prototype buildings, in which the interaction between the In-Plane and the Out-Of-Plane responses is taken into account. The global capacity curves were derived by considering both mechanisms and the global performance level is identified. Some retrofit strategies are then proposed and their effect on the capacity is evaluated, both in terms of the ultimate performance (%NBS) and the expected economic losses (EAL). At last, a cost-benefit analysis was carried out in order to identify the best retrofit solution.

- **Chapter 8** summarizes the main conclusions of the Thesis and proposes some future developments.

1.4 References

Fragomeli, A., Galasco, A., Graziotti, F., Guerrini, G., Kallioras, S., Magenes, G., ... & Marchesi, B. (2018). Comportamento degli edifici in muratura nella sequenza sismica dell'Italia centrale del 2016-Parte 2: Esempi di centri colpiti. Progettazione sismica, 3, 75-104.

Giuffrè A. (1993). Sicurezza e conservazione dei centri storici in area sismica, il caso Ortigia. Laterza, Bari, Italy.

ISTAT. (2011). 154° Censimento della Popolazione e delle Abitazioni. http://www.istat.it/it/censimento popolazione/censimento-popolazione-2011).

L. 64/1974. (1974). Legge 2 febbraio 1974, n. 64. Provvedimenti per le costruzioni con particolari prescrizioni per zone sismiche, Gazzetta Ufficiale, (076), (in Italian).

Menna, C., Frascadore, R., Moroni, C., Lignola, G. P., De Martino, G., Salzano, A., ... & Cosenza, E. (2016). Rapporto fotografico relativo ai danni subiti da alcuni edifici a seguito del sisma del centro Italia del 2016.

NZSEE (New Zealand Society for Earthquake Engineering). (2017). The Seismic Assessment of Existing Buildings: Part C2, Technical Guidelines for Engineering Assessments. Wellington: NZSEE.

Santarsiero, G., Chiauzzi, L., & Masi, A. (2016). Analisi del danneggiamento di edifici situati nella zona Sud del comune di Amatrice: confronto pre e post sisma del 24/08/2016 (V2). Report fotografico, Versione, 2.

2. Masonry: material properties and modelling

2.1 Introduction

This Chapter describes, initially, the main properties of the masonry material, providing a description of its uniaxial and biaxial behaviour. Afterward, a brief description of the different idealizations of the structural behaviour that can be adopted when analysing masonry structures is shown. Finally, the different micro and macro-modelling strategies for the study of the masonry are presented, as well as their corresponding advantages and drawbacks.

2.2 Masonry properties

Masonry is a heterogeneous material composed of units, of natural or artificial origin, jointed by dry or mortar joints. The units are represented by irregular stones, ashlars, adobes, bricks and blocks, and can be joined together using mortar (commonly clay, lime or cement-based mortar) or just by simple superimposition. From different combinations of units and joints, several arrangements can be defined. In Figures 2.1 and 2.2 are shown some possible classifications and arrangements of stone and brick masonry.

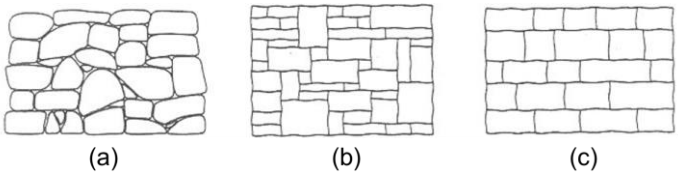

Figure 2.1. Classification of stone masonry: (a) ribble masonry, (b) ashlar masonry and (c) coursed ashlar masonry (Lourenço, 1998).

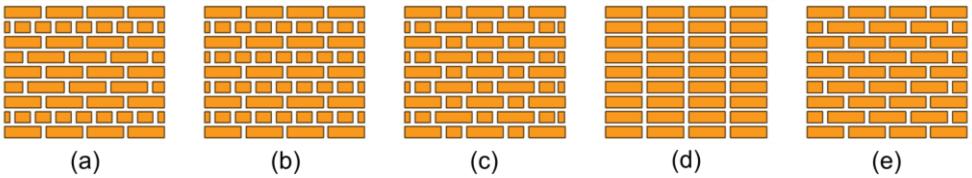

Figure 2.2. Possible arrangements for brick masonry: (a) American (or common) bond, (b) English (or cross) bond, (c) Flemish bond, (d) stack bond, (e) stretcher bond (adapted from Lourenço, 1998).

Due to the presence of the bed and the head joints, that identify the planes of weakness, the masonry can be defined as a discontinuous material, with an anisotropic behaviour in elastic and plastic domains. Given its complex behaviour the study of the masonry has been an important challenge in the last century with studies that focused on both its uniaxial and biaxial behaviour. Moreover, some experimental tests to observe the corresponding failure (uniaxial compressive, tensile and shear failure) were performed on ancient structures and materials (Page, 1981, 1983; Mann, 1982; Dhanasekar *et al*., 1985; Atkinson *et al*., 1989; Vonk, 1992; Neville, 1995; Binda *et al*., 1996b; Vermeltfoort, 1997; Van der Pluijm, 1993, 1997; Jefferson and Mills, 1998; Jukes and Riddinton, 1998; Roca *et al*., 2001).

The uniaxial behaviour is defined when the stress-displacement relation of the specimen is identified. This consists of defining all the “trends” of the representative curve, from the pre-peak branch to the more important post-peak one. Indeed, as all the frictional materials, also the masonry is characterized by the peculiar softening in the branch after the peak, in which continuous imposed displacements correspond to a progressive decrease of the mechanical strength. The softening behaviour is a salient feature of quasi-brittle materials (i.e. clay brick, mortar, ceramics, rock or concrete) which fail due to the progressive internal crack growth, due to the heterogeneity of the material itself, for the presence of different phases and defects (flaws and voids). Indeed, as stated in Lourenço (2010), the mortar, even prior to loading, contains microcracks due to shrinkage experienced during curing. Inclusions and microcracks are also present in clay bricks and are due to the shrinkage, caused by the burning process. As the deformation increases, these initial cracks grow, until the peak load is reached. At that point the cracks become macrocracks, hence it is necessary to reduce the load in order to avoid an uncontrolled growth of cracks. In a deformation-controlled test the macrocrack growth results in softening and localization of cracking in a small zone while the rest of the specimen unloads.

Details on the softening behaviour in the tensile failure are outlined in Hordijk (1991). For the shear failure, a softening process is observed as the cohesion degradation in Coulomb friction models. Instead in Van Mier (1984) and in Vonk (1992) it is stated that, for the compressive failure, the softening behaviour is highly dependent upon the boundary conditions adopted in the experiments and the size of the specimen.

The typical stress-displacement diagrams of quasi-brittle materials under uniaxial tension, compression and shear are shown in Figure 2.3. More in detail, in tension and compression the inelastic behaviour can be described by the corresponding fracture

energies, tensile $G_{f\,I}$ and compressive G_c, defined as the integral of the corresponding stress-displacement diagram. Regarding the shear failure mechanism (generally identified as mode II), it corresponds to the slip of the unit-mortar interface under shear loading, and the shear inelastic behaviour can be described by the mode II fracture energy $G_{f\,II}$, defined by the integral of the τ – δ diagram, in absence of a normal confining load.

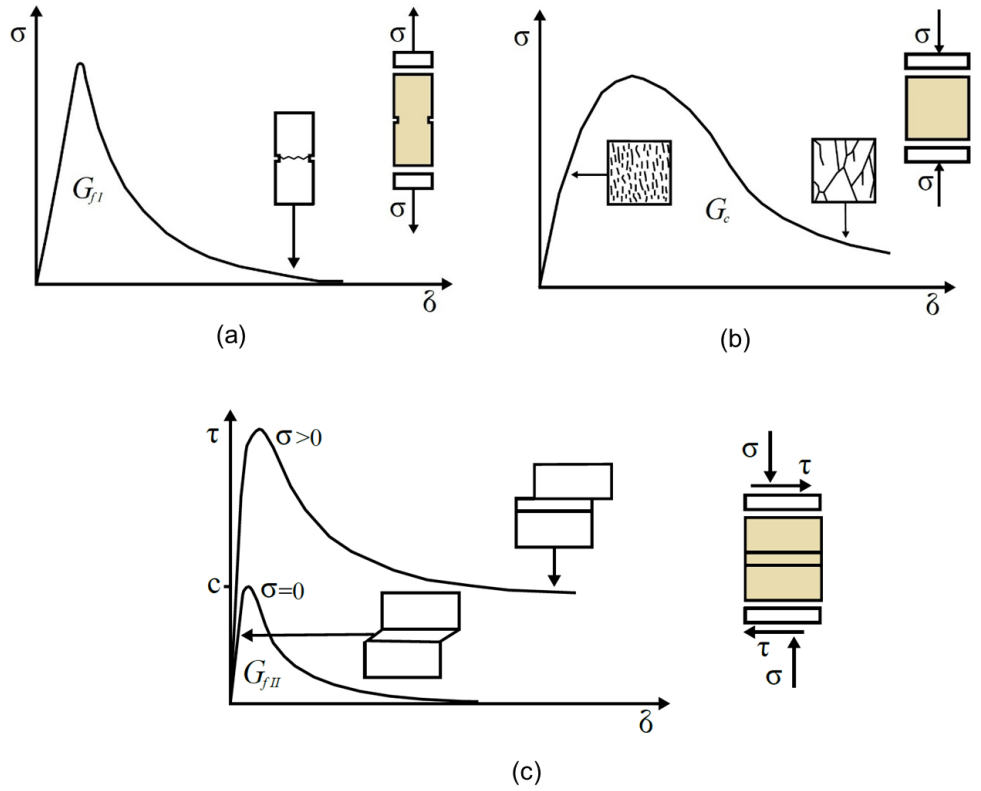

Figure 2.3. Typical behaviour of quasi-brittle materials under uniaxial (a) tensile and (b) compressive loading, and (c) behaviour of masonry under shear (Lourenço, 1996).

The uniaxial compressive loading leads to a state of triaxial compression in the mortar and of compression/biaxial tension in the unit. As stated in Mann and Betzler (1994), the failure in this loading condition, is reached when, increasing the deformation, after the development of the vertical cracks in the units along the specimen middle line, more cracks appear and lead to the split of the prism. Instead, regarding the uniaxial tensile behaviour, the failure is caused by the relatively low tensile bond strength between the bed joint and the unit. Furthermore, two types of failure can develop with respect to the relative strength of joints and units (Backes, 1985): i) stepped cracks through head and bed joints and ii) vertical

cracks through the units and head joints. In the first case, in the post-peak stress-displacement diagram, a residual plateau can be observed, and this behaviour is governed by the fracture energy of the head joints and the post-peak shear trend of bed joints. In the second case, in the stress-displacement diagram, a progressive softening that reaches zero is observed, and the post-peak trend is governed by the fracture energy of the units and head joints.

With regard to the biaxial behaviour, it is strongly dependent on the anisotropic nature of the masonry, i.e. the presence and the orientation of the bed and head joints. These joints, identifying the material axes, influence the orientation of the principal stresses and hence the definition of the strength of the masonry. Due to the masonry anisotropic nature, the biaxial strength envelope can be described by a three-dimensional surface, in terms of the full stress vector in a fixed set of material axes, or in terms of principal stresses and rotation angle between the principal stresses and the material axes.

The main experimental tests carried out to investigate the biaxial behaviour of masonry were performed by Page (1981, 1983), where half-scale brickwork panels, made of solid clay units, were subjected to proportional biaxial loading (Figure 2.4). From these studies, it was defined that the principal stresses orientation relative to the material axes and the principal stress ratio play a fundamental role in the strength and failure modes definition.

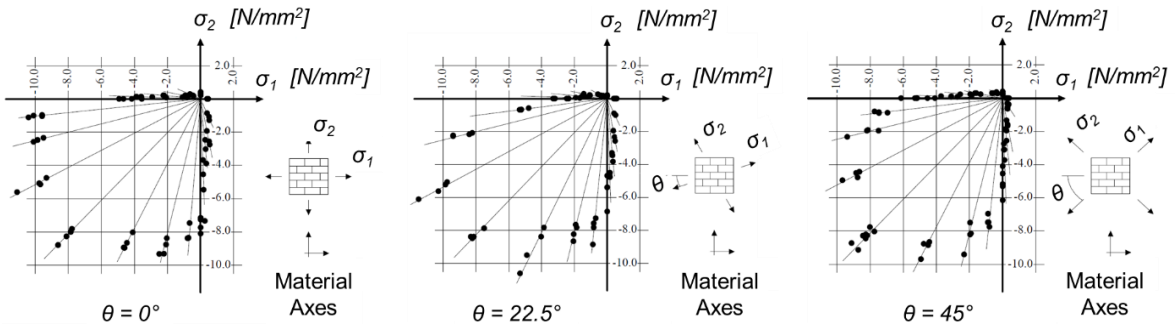

Figure 2.4. Biaxial strength of solid clay brickwork panels (Page, 1981).

The properties of masonry are strongly dependent on the properties of its components. Several are the experimental tests carried out to investigate the unit, mortar and the unit mortar interface behaviour. More details on them can be found for uniaxial compressive displacement-controlled tests in Vermeltfoort (1997) and Roca *et al*. (2001); for uniaxial tensile tests in Jukes and Riddinton (1998) and Van der Pluijm (1997) and for the shear tests in Van der Pluijm (1997), Binda *et al*. (1996b) and Jukes and Riddinton (1997).

2.3 Structural behaviour of masonry

Among the different possibilities to describe the masonry behaviour associated with the given structural problem, the most commonly adopted are the elastic, plastic and non-linear behaviours, each defined by its peculiar load-displacement diagram, shown in Figure 2.5. According to the selected model, different degrees of complexity are generated as well as different analysis costs, in terms of required input data and experience/knowledge of the "user". For example, a non-linear analysis can give a more complete and reliable structural response than a linear one (elastic or plastic), but in return requires a higher level of complexity that results in higher costs.

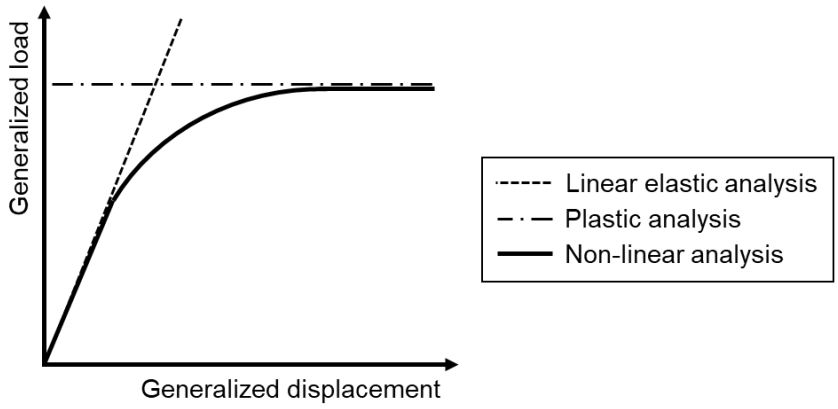

Figure 2.5. General load-displacement diagrams of linear elastic, plastic and non-linear structural analyses (adapted from Lourenço, 2002).

In Oliveira (2003) the main characteristics of the three aforementioned masonry behaviours are outlined. The main associated issues are also highlighted.

More in detail, the assumption of linear elastic behaviour (i.e. a compressive and tensile infinite linear elastic behaviour), is a valid procedure only in the case of materials with tensile strength, in a which higher level of stresses can be reached. Otherwise, it represents an excessive approximation that brings to a not reasonable analysis to describe the behaviour of masonry. This consideration is especially true for ancient structures, as highlighted in Macchi (1997).

A different analysis approach that can be adopted for masonry structures is the plastic analysis, or limit analysis. It consists of evaluating the maximum, or limit, load that a structure

can sustain before reaching the failure, assuming a ductile behaviour of the masonry (with zero tensile strength). It is generally based on two methods (the static, i.e. lower bound method, or the kinematic, i.e. upper bound method) and aims to define a load multiplier that leads to the failure of the structure. In the first method, a lower bound of the limit load is obtained, through equilibrium equations, while in the second one the formation of plastic hinges in the structure identifies a mechanism and an upper bound of the limit load is obtained.

The more reliable behaviour that can be assumed for the masonry is the non-linear one since it is able to describe the complete structural response of a structure, from the elastic branch up to the failure. Of course, as stated previously, this adequacy is paid for with a higher demand for input data and increased complexity of the analysis. To use the non-linear analysis, non-linear constitutive models have to be adopted. The main theories at the base of these models are based on phenomenological approach (i.e. based on experimental tests), and can be classified as:

- *The theory of plasticity*. The pioneering work on the plasticity is the Tresca's one (1964). It consists of replicating the dislocations of the material, being the plastic material behaviour characterized by the occurrence of permanent deformations. Different are the non-linear models, based on the plasticity theory, developed for the study of masonry structures (Dhanasekar *et al*., 1985; Stankowski *et al*., 1993; Lofti and Shing, 1994; Pegon and Pinto, 1996; Lourenço and Rots, 1997; Lourenço *et al*., 1998). Most of these constitutive models were further improved, to be able to deal not only with the monotonic loading conditions but also with the cyclic ones. Important components, such as the stiffness degradation and hysteretic energy dissipation, were introduced in the classical theory of plasticity;
- The *continuum damage mechanics*. In this theory, the central issue is the concept of damage itself. Damage is represented by the decrease in the elastic property (i.e. of the elasticity modulus, as stated in Maugin, 1992) due to the decrease of the area that transmits internal forces, that occurs when microcracks appear and propagate. The continuum damage mechanics was introduced firstly by Kachanov (1958) for creep-related problems and then it was modified by different groups (Lemaitre and Caboche, 1985; Kachanov, 1986; Mazars and Pijaudier-Cabot, 1989). Several damage models have been proposed to analyse the masonry structures (Papa, 1996; Gambarotta and Lagomarsino, 1997; Berto *et al*., 2002).

2.4 Modelling approaches for URM structures

The mechanical behaviour of masonry structures has been investigated by several studies presented in literature. As a consequence, there are different modelling approaches, from those more complex, with more time required and hence more expensive, to those simpler and easily applicable by users in daily professional practice. The choice of the best modelling strategy is not necessarily identified by the more complex one but depends on several aspects as: the availability of the information on the material and the building (accurate modelling requires an exhaustive material experimental description), the scale of the analyses to be carried out (hence if it is investigated the structure at a local or global scale) and the availability of financial resources and time to complete the analyses. Complex computational methods require more detailed information on the properties of the masonry components (units, mortar and bricks) and although can potentially provide very accurate results, but they are much computationally demanding and, therefore, of limited application in ordinary seismic vulnerability assessment studies. On the other side, simpler methods reside on important simplified assumptions on the masonry material (i.e. assuming it as a homogeneous continuum) and hence can lead to a less accurate but more efficient solution.

Depending on the accuracy level and required simplicity, two main different modelling strategies can be considered (Lourenço, 2002):

(i) the micro-modelling is distinguished in “detailed” (Figure 2.6a) if the units and the mortar in the joints are modelled with continuum elements and the unit-mortar interface is modelled with discontinuum elements; or in “simplified” (Figure 2.6b), if the mortar joints and the unit-mortar interface are modelled with discontinuum line interface elements and only the expanded units are modelled with continuum elements;

(ii) the macro-modelling (Figure 2.6c) in which the components of the masonry (units, mortar joints and unit-mortar interface) are smeared out in a homogeneous anisotropic continuum.

Both these strategies can be adopted using different approaches (according to the aim of the analysis) as Finite Element method, Discrete Element Method (DEM) and the limit analysis for the micro-modelling, while continuum finite elements and structural component models for the macro-modelling. Therefore, the micro- and macro-modelling can be used for structures analysis at a different scale: the micro-modelling is typically used to investigate the

local behaviour of masonry structures, instead macro-models are generally used for large structures in which a uniform distribution of stresses can be assumed in each macro-length.

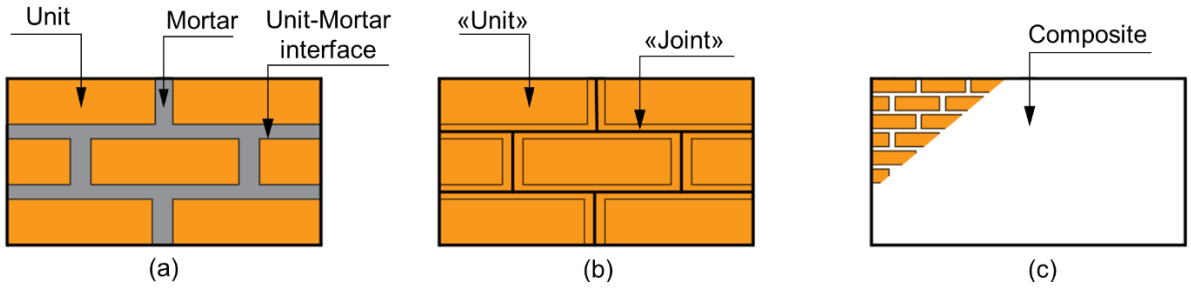

Figure 2.6. Main modelling strategies for masonry structures: (a) detailed micro-modelling; (b) simplified micro-modelling; (c) macro-modelling (adapted from Lourenço 2002).

In the context of FE analysis, based on the description of the material (and the formulated nonlinear constitutive laws), in addition to the choice of the scale, it is possible to make a distinction between two approaches: discrete and continuous. The former refers to the micro-modelling, where the material is described through the geometric and mechanical characteristics of its constituents (blocks, mortar joints and the blocks-joints interface, if considered), assumed as distinct units, while the latter refers to the macro-modelling, where the masonry is assumed as a homogeneous continuum. Of course, since there are different interpretations of the masonry material, the obtained results might be different, and the choice depends on the analysis to consider. Usually, simplified models are oriented towards achieving an adequate compromise between computational burden, complexity, cost, accuracy and reliability (or precision) of the results when performing nonlinear analysis for existing URM structures. Within this context, the macro-element method, classified as a structural component model in the macro-modelling approach, is typically used to analyse complex real structures, giving a fair compromise between accuracy and computational efforts. Indeed, the macro-element strategy allows to obtain information on both damage progression and limit conditions of masonry structures with a very low computational burden. It discretizes the wall by a set of masonry panels defined as “piers”, (the vertical resistant elements), “spandrels” (the horizontal elements, coupling the piers under seismic loads) and “joints” (connections between piers and spandrels), see Figure 2.7b. Among this approach, the Equivalent Frame (EF) method is frequently adopted in seismic assessment analysis by engineers practitioner for its practice-oriented, reduced time and cost. In this method, piers and spandrels are considered according to an effective height and length, respectively, while

their connections are modelled as rigid offsets (Figure 2.7c). The national and international codes (i.e. NTC 2018; EN1998 2005), understanding the advantages that derive from this schematization for the seismic assessment through a non-linear static analysis, suggested adopting this method in the analyses.

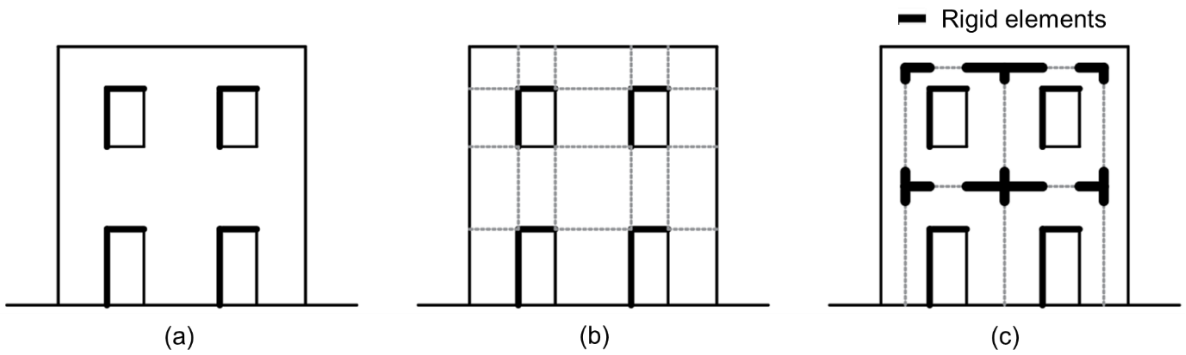

Figure 2.7. Example of structural component models of the structure (a) in: (b) macro-element modelling and (c) Equivalent Frame method (adapted from Lourenço, 2002).

In the following Sections, a brief revision on the two main strategies for the numerical modelling (detailed and simplified micro- and macro-modelling) of the masonry structures is discussed. Particular attention is given to the macro-modelling, i.e. the approach used in this Thesis.

2.4.1 Micro-modelling

The micro-scale modelling is the most accurate approach to analyse URM structures because it models each masonry component (units and joints mortar) with its specific mechanical properties and appropriate constitutive laws. Regarding the geometry, it is discretized following the actual arrangement.

In the masonry assemblages, the nonlinear response of the joints is fundamental and it depends on the interface between units and joints mortar, that is considered as the weakest link, where tensile or shear failure typically occurs, as highlighted by different experimental tests (Jukes and Riddington, 1997; Smith and Carter, 1977; Drysdale *et al*., 1979; Hofmann and Stöckl, 1986; Atkinson *et al*., 1989; Schubert and Hetzemacher, 1992). If the model, besides unit and joints mortar, takes into account the unit-mortar interface as a discontinuum element with initial fictitious stiffness (to avoid interpenetration of the continuum too), the

micro-modelling is defined as detailed. Contrarily, if the interface is neglected and, in order to represent the actual geometry, units are modelled as expanded, the micro-modelling is defined as simplified (also because the mortar Poisson's effect is neglected).

In micro-scale modelling, different methods can be distinguished to represent URM walls: the Finite Element (FE) method, the Discrete Element Method (DEM) and the limit analysis.

The FE method, with interface elements, was at first considered by Page (1978), reproducing the nonlinearity of the masonry (modelled with continuum elements representing the elastic bricks) and the failure of the joints (modelled as "linkage elements" with high compressive strength and low tensile and shear strength). This model aimed to study the in-plane behaviour of masonry walls, describing the progress of the material damage through a progressive degradation of the interface elements stiffness. The explicit reference to the problem of the seismic forces is found in Lofti and Shing (1994)'s work, which studied the behaviour of masonry walls under shear forces and axial load through interfaces models. Other important literature studies that adopted an analogue modelling approach are e.g. Rots (1991), Baggio and Trovalusci (1993) and Lourenço and Rots (1997). In this latter work, for the first time, in addition to the failure mechanisms involving the mortar joints (i.e. cracking in the joints and bed or head joint sliding) and the block failures are also considered (i.e. cracking of the masonry units and crushing of the masonry). For its typology, the micro-modelling FE method is used mostly to reproduce the behaviour of walls characterized by limited dimensions (Pegon and Pinto, 1996; Lourenço and Rots, 1997; Giambanco and Gati, 1997; Giambanco *et al*., 2001; Formica *et al*., 2002; Pelissou and Lebon, 2009; Senthivel and Lourenço, 2009; Rekik and Lebon, 2010). Two examples of the finite element model (with interface elements) are shown in Figures 2.8 and 2.9.

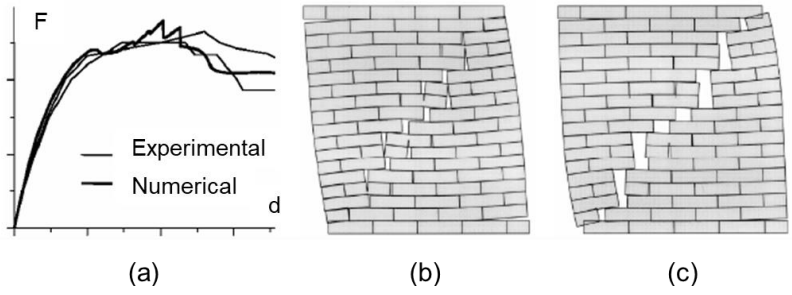

Figure 2.8 Micro-modelling of a shear wall: (a) force-displacement diagram; (b) deformed mesh at peak load; (c) deformed mesh at ultimate load (Lourenço, 1996).

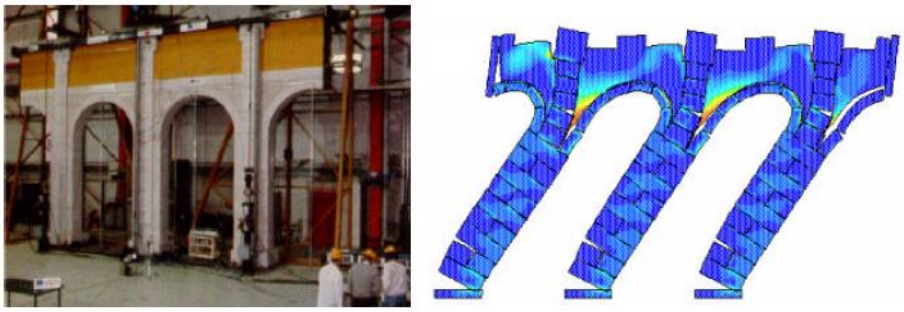

Figure 2.9 Discontinuum finite element model of the monastery of S. Vicente de Fora, in Lisbon (Pegon and Pinto, 1996).

The DEM was developed by Cundall (1971) for a blocky rocks system and then adapted to masonry structures to reproduce the discontinuity of the masonry material. It consists of: (i) the schematization of the system by an assembly of blocks connected together through contact points, (ii) the integration of the equations of blocks motion, which allows large displacements, rotations, cracks or complete detachment between the single elements (contrarily to what happens in FE method), (iii) sequential updating of blocks position. This method differs from the continuous one for the compatibility conditions on displacements, because in the latter the compatibility must be imposed between internal elements, instead of in the former it is replaced by the constitutive contact models between adjacent units. In the DEM the representation of the contacts and the interaction between the blocks are represented by a set of contact points. Each contact force depends on the relative displacement of the block at that point. Adjacent blocks can be touched along a common edge segment or in discrete points. This hypothesis makes it easier to manage the movements between system blocks and grants an important computational efficiency. The simplest model of mechanical interaction between blocks is to assume that blocks are connected by normal and shear elastic springs, i.e. the interaction forces are proportional to the relative displacement between the two blocks. In this method, the position of the contact points is updated automatically when the blocks move and the process of cracking is defined with the simplest technique with respect to the FE modelling. A disadvantage is that the crack propagation depends mainly on the element shape, size and arrangement, as highlighted in Meguro and Tagel-Din (2000). Two examples of the application of the DEM to masonry structures are shown in Figure 2.10.

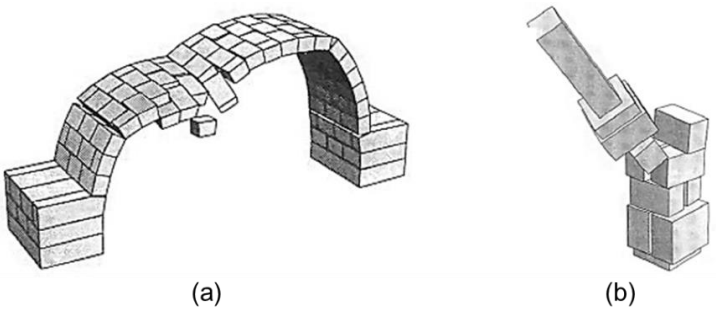

Figure 2.10 Examples of application of the Discrete Element Method (DEM) to analyze: (a) masonry arch bridge (Lemos, 1995); (b) dry stone masonry pedestal sustaining a statue (Sincraian, 2001).

In the micro-modelling field, the Kooharian (1952) and Heyman (1966) works introduce the limit analysis to investigate the masonry block structures. This is a structural analysis method to estimate the collapse load of a structure and the related mechanism. It is based on a set of limit theorems, based on the conservation of energy and it is essentially referred to the study of balances and kinematics of rigid bodies, tracing the masonry wall to one kinematic chain, starting from the hypotheses of no-tensile strength and, in general, of infinite compressive strength (i.e. no deformability is considered). Assuming the kinematics, the system has a unique equivalent degree of freedom, giving the possibility to calculate the static multiplier of loads at the mechanism activation threshold: this multiplier would represent, under the hypothesis of perfectly rigid behaviour up to the activation, the value of the horizontal collapse acceleration associated with that particular collapse mechanism. In the past years, several researches aimed to the analytical and correct formulation of the limit analysis of URM structures to develop a unilateral model for the material, assumed as rigid (Como, 1992) or elastic (Giaquinta and Giusti, 1985; Del Piero, 1989; Di Pasquale, 1992; Angelillo, 1993; Angelillo *et al*., 2010; Fortunato, 2010; Fraternali, 2011; Angelillo *et al*., 2013; Angelillo *et al*., 2018; Angelillo, 2019). From an application point of view, many models based on FE analysis have been reported in literature and it is possible to distinguish continuum (Como and Grimaldi, 1985; De Buhan and De Felice, 1997; Milani *et al*., 2006) from discrete approaches (Livesley, 1978, 1992; Baggio and Trovalusci, 1993; Sutcliffe *et al*., 2001).

Micro-modelling, thanks to its fidelity to the actual geometry and arrangement of the masonry material, has the advantage to be extremely accurate and for this reason, it is currently considered the most advanced modelling in the field of scientific research. On the other hand, it requires a computational burden extremely high that, in many cases, cannot be afforded for simulating the nonlinear response of entire buildings. However, micro-modelling

plays an important role in the comparison, verification and calibration of the masonry mechanical parameters.

2.4.2 Macro-modelling

To limit the computational burden derived from sophisticated modelling approaches (i.e. micro-modelling) and to reduce the intrinsic complexity of masonry material, the macro-scale modelling has been introduced. In this approach, the masonry material is considered as a continuum anisotropic whose mechanical behaviour is derived from phenomenological observations or through appropriate homogenization procedures.

The continuum behaviour is defined through mean macroscopic quantities derived from the mechanical and geometric properties of masonry constituents (units and joints mortar). The difficulty in these kinds of approaches is given by the identification of a nonlinear anisotropic law for the continuum material, but once it is formulated, this modelling allows to reproduce, describe and analyse, in a sufficiently accurate way, the behaviour of small, large and complex structures until collapse.

While phenomenological approaches have found wide use in limit analysis, micromechanical approaches are the main reference for the study of the response of the material to damage. Many models actually propose a mixed approach where micromechanical theory is employed in the homogenization of the material elastic properties, while phenomenological considerations are adopted to describe the inelastic damage laws. One of the first important contributions to the continuous modelling of masonry was proposed by Pietruszczak and Niu (1992), where the aim of obtaining the three-dimensional modelling of the masonry was pursued through a purely micromechanical approach. The procedure homogenization is carried out in two steps: (i) at first a continuum consisting in a matrix of blocks and secondary (or head) mortar joints is homogenized (assuming an elastic-brittle behaviour); (ii) the second phase of homogenization of the continuum is carried out adding the principal (or bed) mortar joints (assuming an elastic-plastic behaviour and interface with perfect cohesion). Then, in addition, determining the average elastic parameters of the homogenized continuum, an evolution law for damage, from the inelastic phase to collapse, is defined.

A similar procedure, from the two steps homogenization to the description of the damage, is schematized in Maier *et al*. (1991). In this study, for the first time in masonry modelling, the principles of fracture mechanics and damage to micro-cracked solids, processed in previous years in the field of concrete structures, were introduced.

Homogenization of mechanical properties in recent decades has attracted growing interests and led to the definition of different homogenization procedures for in-plane 2D cases, such as (Lee *et al*., 1996; Alpa and Monetto, 1994; Andreas, 1996; De Buhan and De Felice, 1997; Luciano and Sacco, 1997; Lourenço *et al*., 1997; Gambarotta and Lagomarsino, 1997; Berto *et al*., 2002; Uva and Salerno, 2006; Calderini and Lagomarsino, 2008; Sacco, 2009). The extension to 3D cases, subjected also to out-of-plane forces, was investigated by different studies in the past years (Cecchi and Sab, 2002b; Cecchi *et al*., 2005; Chengqing and Hong, 2006).

In macro-scale modelling, Finite Element (FE) and structural component models can be distinguished to reproduce and simulate the behaviour of URM structures.

The continuum FE method was developed in several studies (Pegon and Anthoine, 1997; Lourenço *et al*., 1998; Macchi, 2001; Lourenço, 2000, 2002; Silva *et al*., 2018).

The simplest adopted approach to model URM structures is highlighted by the structural component models (Marques and Lourenço, 2011; 2014). These approaches aimed to the substantial reduction of the computational burden (for an important reduction of the number of degrees of freedom) being based on discrete modeling of the entire structure in the assembling of the macro-elements as structural components. They are a priori identified, on the basis of earthquake-damage observations, from which it was observed that the damage and crisis are generally focused in some regions of the URM walls (piers and spandrels), while in their connections zones no systematic damage phenomena occur. Piers panels are the vertical structural elements, responsible for resisting vertical and horizontal loads, while the spandrel panels are the horizontal elements, between two aligned openings, that have a coupling role for adjacent pier panels when the structure is subjected to horizontal loads. All the parameters that characterize the macro-elements are average quantities, and the information of what happens locally within the portion of the structure represents generalized values. The main difference between the structural components models and the finite element models is the adopted constitutive law. In the first case, it attempts to reproduce the mechanical response of panel-scale structural components, while the constitutive law of the

FE models tries to reproduce the mechanical behavior of the masonry material. The reliability of these models is obviously linked to the ability to describe the damage phenomena that occur: a single macro-element has to be able to describe the fundamental modalities of masonry collapse, such as flexural and shear failure and has also to match the correct level of degradation.

In the models of the structural components, it is possible to distinguish between one-dimensional modelling of the URM components (idealized as a beam with nonlinear behaviour or as strut-elements) and models based on two-dimensional modelling of piers, spandrel and joint (the connection between pier and spandrel).

In the one-dimensional strut modelling of URM components, the model proposed by Calderoni *et al*. (1987, 1989), shown in Figure 2.11, schematizes the wall in equivalent struts (with an inclination and stiffness that reproduce the wall behavior), considering the reagent portion of the structure. The model is characterized by a “variable geometry” since it considers the variations of dimensions and inclination of the struts according to the increase of the reagent portion of masonry. When the equilibrium limit configuration is reached (or when the strut reaches its compressive strength), the crisis of the panel occurs.

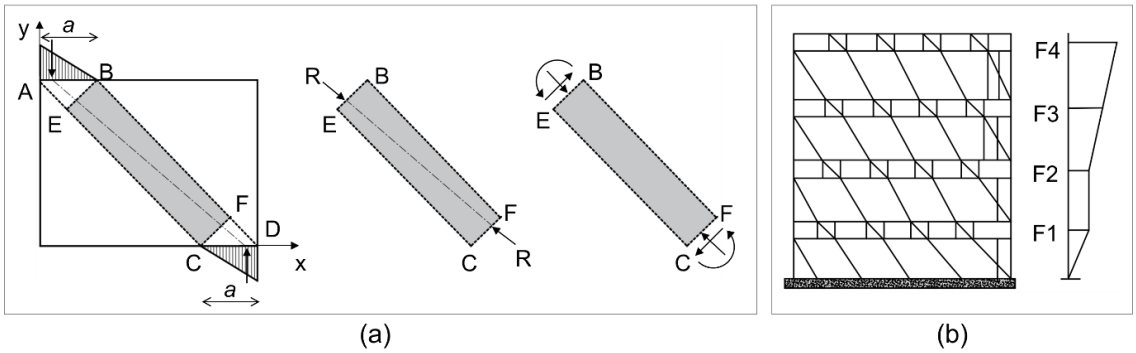

Figure 2.11. Modelling of walls through equivalent struts: (a) identification of the strut element; (b) wall modelled with equivalent struts (adapted from Calderoni et al., 1987, 1989).

In the context of the one-dimensional modelling of URM components, an important role is assumed by the equivalent frame models, in which the structure is idealized by means of linear elements as beam type with shear and flexural deformations. Among these, the POR method proposed by Tomaževič (1978) is considered the pioneering one. It consists of a schematization of the URM structures in shear-type frames carrying out analyses on each floor. The scheme of the URM walls resulted in a “weak pier-strong spandrel” approach,

where the pier panels are modelled with an elastic-plastic relationship to describe the beam nonlinearity, with a limit strength value based on the diagonal cracking failure mechanism, while the spandrel panels and the nodal region are considered rigid. Since the dramatic consequences of the Irpinia earthquake in the 1980s for at least 30 years, this method, for its easy applicability in the nonlinear seismic analysis, was widely used by practitioners and suggested by the past national codes. Nowadays this approach is outdated for its excessive approximations, related to the assumption that the piers are the only panels subjected to crisis and the spandrels are considered infinitely rigid. If this approach can lead to acceptable results in the case of squat pier panels subjected to high axial loads and spandrel panels sufficiently rigid, in all other cases, it overestimates the response of URM walls and leads to wrong expected failure mechanisms, that does not match the damage observed after earthquake events.

Successive upgrades of this method were developed. In order to consider the flexibility and limited strength of spandrel panels, the PORFLEX method was developed by Braga and Dolce (1982). It considers both the flexure and shear mechanisms for pier panels and only the shear mechanism for the spandrel panels (moving from the shear-type assumption to the plastic hinge development), still neglecting the axial load variation on the pier panels.

Another modification was made by the POR 90 method proposed by Dolce (1991). As in the POR method, the pier panels are characterized by an elastic-plastic law, with shear and flexural failure mechanisms, but the definition of the pier panels stiffness was derived from the equivalent height of them, based on the spandrel panels geometric dimensions. Not taking into account the variation of the axial force to which the pier panels are subjected, all of the POR methods do not satisfy the global equilibrium of the wall, not balancing the overturning moment induced by horizontal actions. Furthermore, these methods, considering the nonlinear analysis distinctly at each floor, lead to the implicit assumption of boundary condition for piers, which in reality depends on the stiffness and strength of spandrel panels. To correctly taking into account these aspects, a global analysis of the structure is requested.

To overcome some of the important limitations of the POR methods, the so-called macro-element models can be adopted. These approaches idealize the URM wall as an equivalent frame in which deformable components (pier and spandrel panels) are linked by rigid joint panels.

Among the applications of equivalent frame models, the SAM method, developed by Magenes and Calvi (1996), is one of the first proposed. This method overcomes the issue of

the POR ones in satisfying the wall global equilibrium, by considering the analysis of the whole multi-storey structure. It models the pier and the spandrel panels with truss elements and the pier-spandrel panels connections as rigid elements (see Figure 2.12a). To consider approximately the joint panel deformability, the effective height of the piers panel is taken from Dolce (1991)'s formulation while the length of the spandrel is set equal to the length of the openings. To each pier panel is associated an elastic-plastic shear-horizontal displacement relationship (see Figure 2.12b), and the ultimate shear value is identified by the minimum between flexural, sliding shear and diagonal cracking shear strength. This method takes into account the axial load variation on the piers during the analysis, hence considering the possible variation on the piers shear strength. Regarding the spandrel panels, it is assumed an elastic-brittle relationship and the ultimate strength value is limited by the minimum between sliding and diagonal cracking shear, neglecting the flexural behaviour. The main hypotheses of the SAM method are: (i) the spandrel panels are characterized by a finite strength; (ii) the pier panels change their constraint conditions by increasing the load, going from a shear-type model to a cantilevered model; (iii) the acting loads are distributed based on the linear elastic stiffness of panels. The crisis of the components is reached in terms of drift. Indeed, in Magenes and Calvi (1997)'s study, it was highlighted that the ultimate displacement can be assumed equal to the ultimate distortion, assumed as drift, given by the ratio between horizontal displacement and the height of the panel. This assumption resides in the observations that walls with different aspect ratios tend to present a very limited dispersion of the ultimate angular deformation values, compared with that found for the displacement ultimate ductility values.

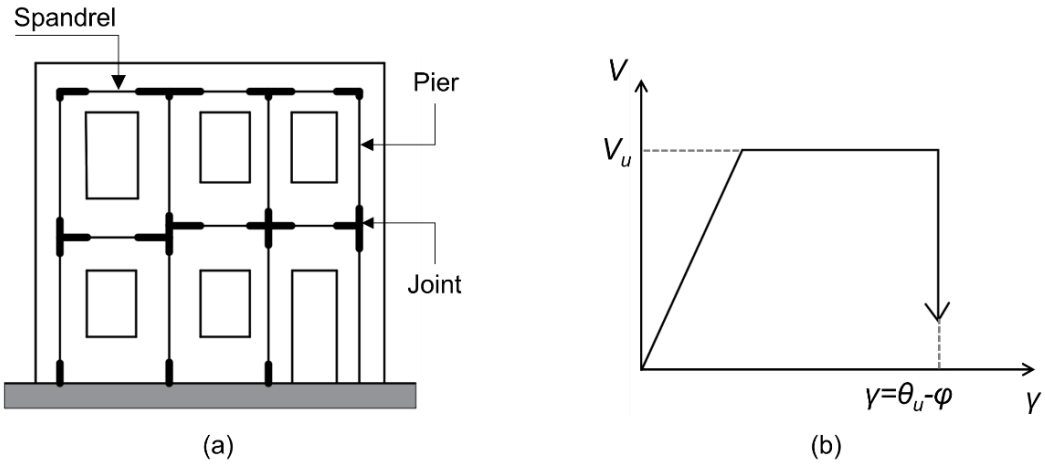

Figure 2.12. SAM method: (a) equivalent frame model and (b) bilinear relationship assumed for piers (adapted from Magenes, 2000).

In addition to the several comparisons and validations both with experimental tests (Magenes *et al*., 1995) and with others modeling strategies (including FEM methods), successive improvements of the SAM method were developed by Magenes and Della Fontana (1998), where multi-mode dynamic analysis and static pushover of URM structures were performed.

According to the equivalent frame approach, a model based on the use of multi-springs nonlinear zero-length elements connected by rigid links was presented by Rinaldin *et al*. (2016), as schematically shown in Figure 2.13. Nonlinear springs were placed at the two ends of the URM components (piers and spandrels) for describing the flexural (rocking) behavior and in the middle for representing the shear (sliding and diagonal cracking) response. The pier-spandrel connection is modelled as rigid links. Specific hysteretic rules were used for reproducing the stiffness and strength degradation as well as the actual energy dissipation capacity under cyclic loading.

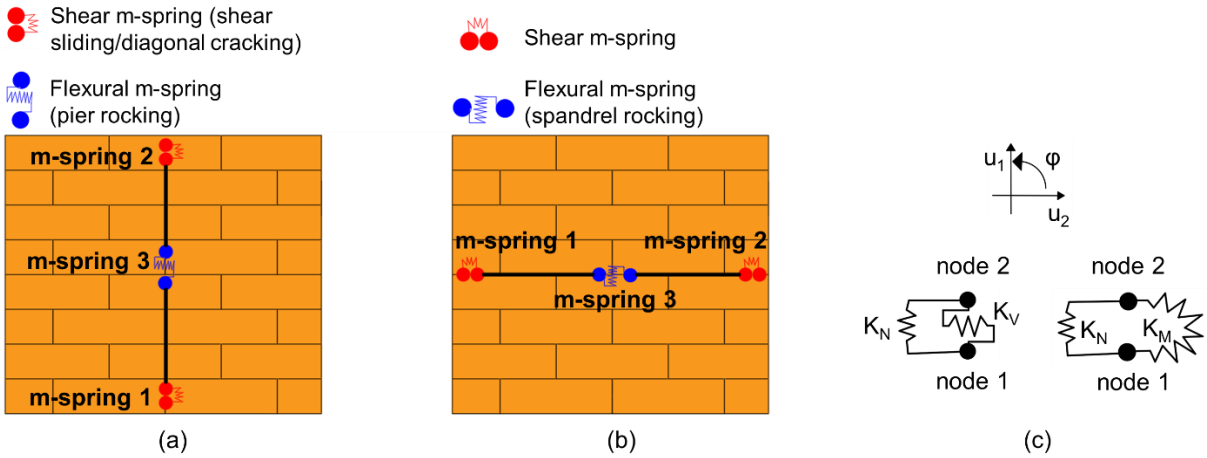

Figure 2.13. Macro-elements with nonlinear springs for (a) piers and (b) spandrels; (c) shear (on the left) and flexural (on the right) multi-spring elements (adapted from Rinaldin et al., 2016).

Among the macro-element bi-dimensional models, it is possible to insert the RAN method, developed by Augenti *et al*. (1984a-g). In its first definition, it allowed to perform linear static analysis of URM structures and, in a more recent version with some improvements, the method was extended to a nonlinear incremental static analysis by means of a distributed plasticity modelling of masonry components (Augenti and Parisi, 2009a). Through the idealization of URM wall with openings using an equivalent frame composed of

two-dimensional elements panels (spandrel, pier and joint) with axial, flexural and shear flexibilities (schematically shown in Figure 2.14), the global seismic performance is assessed. The modelling consists of considering: (i) joint panels as infinitely rigid; (ii) the mechanical properties of vertical (piers panel) and horizontal (spandrel panels) macro-elements through limit strength domains and force-displacement curves dependent on geometrical and mechanical non-linearity phenomena; (iii) masonry as a homogeneous no-tensile resistant elastic-plastic material in uniaxial compression. If the box behaviour is guaranteed by the presence of rigid floor diaphragms and/or tie-elements (e.g. RC ring beams or steel ties), the global response of the structure can be considered. If this is not the case, each masonry wall can be analyzed separately from the others through linear or nonlinear seismic analysis.

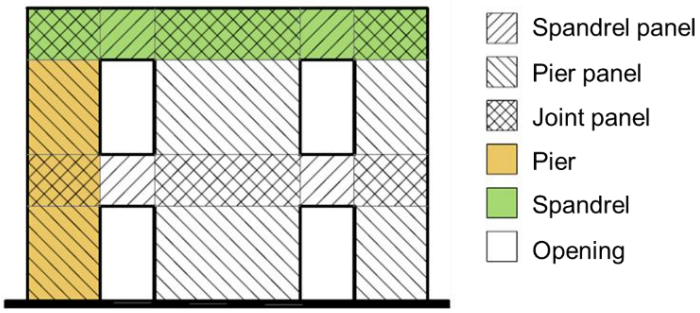

Figure 2.14. Macro-elements within a regular masonry wall with openings (Augenti et al., 2011).

Both the models developed by Braga and Liberatore (1990) and D'Asdia and Viskovic (1994) are two-dimensional macro-element models. In these, the unilateral no-tension behaviour of the masonry is assumed. The first consists of a series of elementary triangular compressed panels and assumed a stress state with the null tensile strength of the masonry (Figure 2.15a). From several applications, it was found that this model overestimates the ultimate strength of the structure probably because it neglects the shear failure mechanism of URM walls. Contrarily, the second model adopts techniques to modify the geometry of the panels during the analysis, in order to exclude the portion of masonry in whose tensile stresses exceed the strength value and hence to reproduce the progressive partialisation of the transversal section and the degradation of the global stiffness. The model is based on the introduction of macro-elements consisting of a limited number of triangular elastic-linear finite elements (Figure 2.15b). These finite elements have constant deformation, i.e. are characterized by a displacement field that depends linearly on the vertices displacements.

Two different macro-elements are adopted: one to model piers and spandrels while another to model the linked panels between piers and spandrels. With increasing section partialisation, the shape and the behavior of the panel become similar to those of a strut, capable of identifying the real trend of the masonry in resisting loads by assuming equilibrium configurations with the development of only compression stresses.

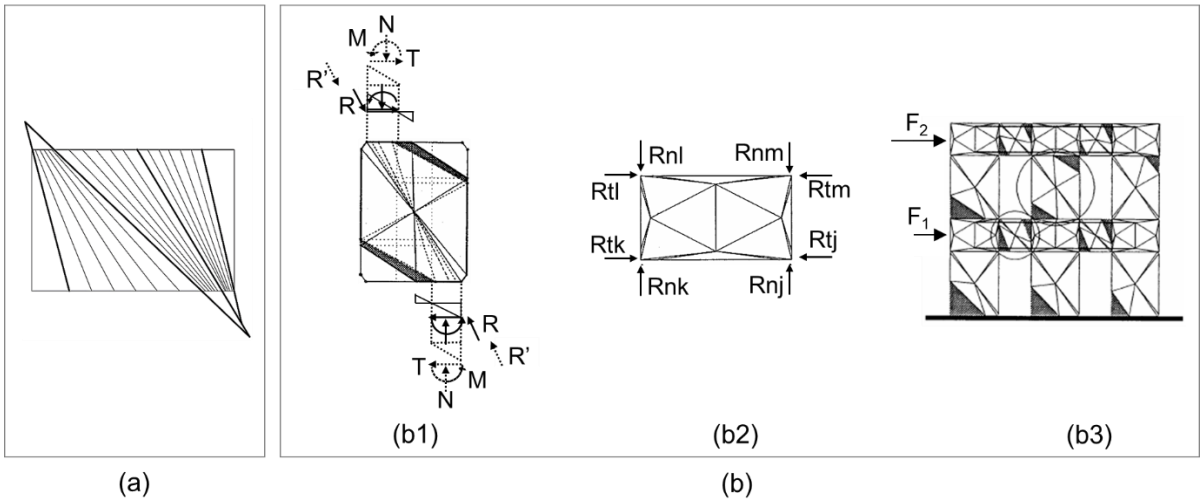

Figure 2.15. Two macro-element models: (a) Braga and Liberatore's model (adapted from Braga and Liberatore, 1990); (b) D'Asdia and Viskovic (1994)'s model: (b1) pier; (b2) connection zone; (b3) wall (adapted from D'Asdia and Viskovic, 1994).

Another important method that belongs to the two-dimensional macro-element classification, is that developed by Brencich and Lagomarsino (1998). It is based on the modelling of URM structures with an assemblage of frame-equivalent wall models, to reproduce pier and spandrel panels, connected by rigid offsets at the end sections (pier-spandrel joints). The macro-element is composed of a central rigid part and two extreme parts with bending flexibility and neglected dimensions (Figure 2.16a). At first, each of the extreme parts was characterized by two translational and rotational kinematic DOFs. With successive model improvements, two additional DOFs were associated with the central part to account for shear mechanisms and rocking, resulting in a macro-element with eight DOFs (Figure 2.16b). A refinement of this method, and the subsequent validation with experimental results, was performed by Penna (2002). In detail, the author modifies the compression behavior with the implementation of a phenomenological model with limited strength at the edges of the panel while bending-overturning, in order to take into account also the condition of crushing and compression damage of the reduced sections.

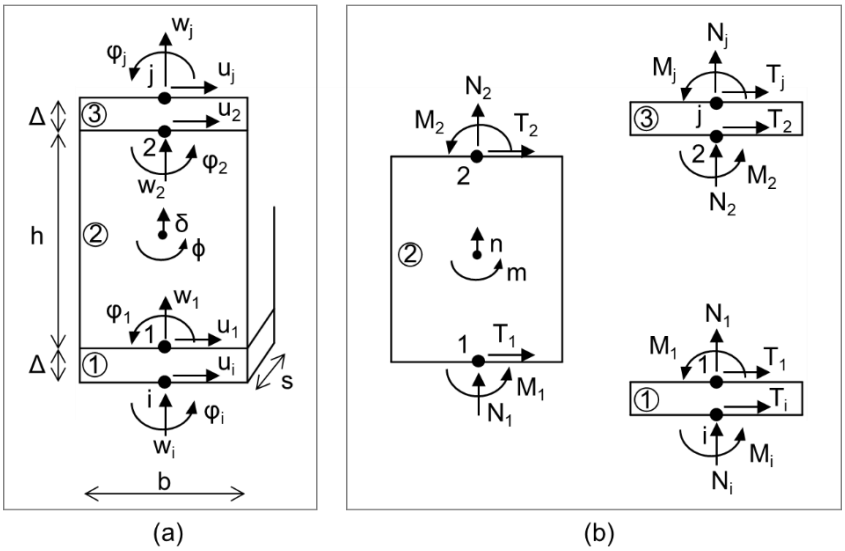

Figure 2.16. Kinematic model of the macro-element: (a) of the whole panel and (b) of the individual substructures (adapted from Lagomarsino et al., 2013).

This method was implemented in the software TREMURI (Lagomarsino *et al*., 2013) and its validation and calibration were carried out also by Cattari *et al*. (2004), through quasi-static lateral loading tests performed on a URM building model in displacement control. An important novelty, with respect to the SAM method, is the possibility to consider in the global capacity the in-plane flexibility of floor diaphragms, in order to adopt the wooden, metallic or vaulted diaphragms that are commonly found in existing URM buildings.

Another two-dimensional model was developed by Caliò *et al*. (2005, 2008, 2012). It can be considered somewhere between the discrete and macro-element model as it is conceived. At first, the 2D model was developed. The piers and spandrels are idealized through equivalent discrete elements made of nonlinear springs to simulate the in-plane nonlinear response of masonry walls. An articulated quadrilateral constituted by four rigid edges connected by four hinges and two diagonal nonlinear springs represents the basic panel element (see Figure 2.17a). The panel can interact along each side with other panels by means of an arbitrary number of nonlinear springs (defining interface elements). This kind of modelling leads to consider the interaction effect between masonry and other elements (e.g. RC ring beams or steel ties). This approach can be adopted also in structures with irregular or complex geometry (as not aligned openings), thanks to the possibility to increase the mesh density for each structural component, as shown in Figure 2.17b. The model is able to identify the in-plane failure mechanism of URM walls (i.e. toe-crushing/rocking,

diagonal cracking and sliding) and the possible combined one. To extend this modelling to 3D structures, it is possible to consider the assembling of 2D walls, if the global “box behaviour” is guaranteed by effective connections between orthogonal walls and/or rigid floor diaphragm. Otherwise, the simulation of the out-of-plane failure mechanisms is provided. In addition to the 2D macro-element model, also the 3D model was developed by the authors. In Caliò *et al*. (2012), the reliability of the approach was evaluated by means of experimental nonlinear incremental static analyses performed on masonry structures, and such a modeling approach was used to represent piers and spandrels through basic panel elements. This modeling strategy was used in Pantò *et al*. (2016, 2018) to simulate also the masonry material response in addition to the structural components one.

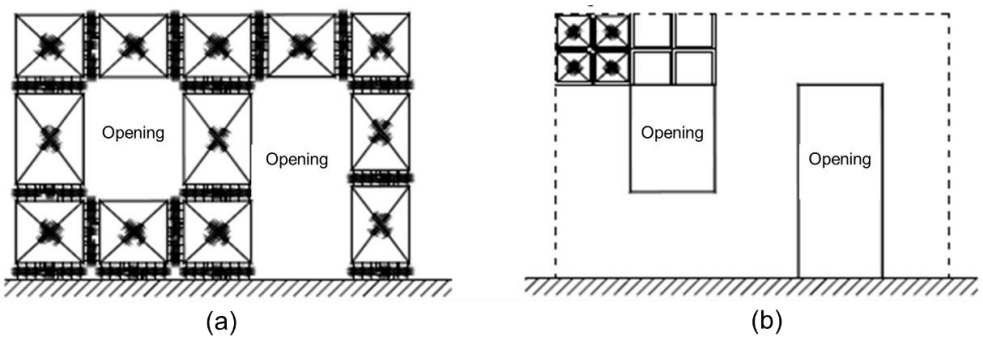

Figure 2.17. Modelling of a wall through two different meshes: (a) a macro-model for each wall panel and (b) 4-macro-elements mesh for each wall panel (adapted from Caliò et al., 2012).

From the brief overview of the main modelling approaches employed in the analysis of URM structures, it can be said that the alternative discontinuous finite or discrete element models appear possible, although expensive, and advantageous only in the research field. On the contrary continuous simplified models, thanks to their limited computational burden and their balance between accuracy and efficiency of the solution they are the most widely diffused for the seismic assessment of URM structures in daily practices. This is true especially in the case of engineering practitioners, thanks to their usually easy and fast definition of model and mechanical characterization. Nevertheless, most of these simplified approaches, as they are conceived, do not allow to consider aspects related to structural details (such as the effective connections between orthogonal walls) and consider an a priori schematization of the geometry and mechanical properties that could also be far from the real one.

2.5 References

Alpa, G., Monetto, I. (1994). Microstructural model for dry block masonry walls with in-plane loading, Journal of the mechanics and physics of solids, vol. 42, No. 7, 1159-1175.

Andreas, U. (1996). Failure Criteria for Masonry Panels under In-plane Loading. Journal of structural engineering ASCE 122(1). p. 37–46.

Angelillo, M. (1993). Constitutive relations for no-tension materials. Meccanica, 28(2), 195–202.

Angelillo, M., L. Cardamone, A. Fortunato. (2010). A numerical model for masonry-like structures, Journal of Mechanics of Materials and Structures, 5, 583–615.

Angelillo, M., E. Babilio, A. Fortunato. (2013). Singular stress fields for masonry-like vaults. Continuum Mechanics and Thermodynamics, 25:423–441.

Angelillo, M. (Ed.). (2014). Mechanics of masonry structures. London, UK: Springer.

Angelillo, M., Fortunato, A., Gesualdo, A., Iannuzzo, A., & Zuccaro, G. (2018). Rigid block models for masonry structures. International Journal of Masonry Research and Innovation, 3(4), 349-368.

Angelillo, M. (2019). The model of Heyman and the statical and kinematical problems for masonry structures. International Journal of Masonry Research and Innovation, 4(1-2), 14-31.

Atkinson RH, Amadei BP, Saeb S & Sture S. (1989). Response of masonry bed joints in direct shear. Journal of Structural Engineering: 115(9): 2276–2296.

Augenti, N., et al. (1984a). La verifica dei pannelli murari. Proceedings of the 2nd Italian National Conference ASS.I.R.C.CO., Ferrara, Italy (in Italian).

Augenti, N., et al. (1984b). La deformazione dei pannelli murari. Proceedings of the 2nd Italian National Conference ASS.I.R.C.CO., Ferrara, Italy (in Italian).

Augenti, N., et al. (1984c). Il pannello murario pesante. Proceedings of the 2nd Italian National Conference ASS.I.R.C.CO., Ferrara, Italy (in Italian).

Augenti, N., et al. (1984d). Il pannello murario vincolato. Proceedings of the 2nd Italian National Conference ASS.I.R.C.CO., Ferrara, Italy (in Italian).

Augenti, N., et al. (1984e). Il pannello murario armato o contornato. Proceedings of the 2nd Italian National Conference ASS.I.R.C.CO., Ferrara, Italy (in Italian).

Augenti, N., et al. (1984f). Classificazione e tipologia delle pareti murarie. Proceedings of the 2nd Italian National Conference ASS.I.R.C.CO., Ferrara, Italy (in Italian).

Augenti, N., et al. (1984g). Introduzione al calcolo delle pareti murarie. Proceedings of the 2nd Italian National Conference ASS.I.R.C.CO., Ferrara, Italy (in Italian).

Augenti, N. and Parisi, F. (2009a). Non-linear static analysis of masonry structures. Thirteenth Italian National Conference on Earthquake Engineering. Paper No. S4-01.

Augenti, N., Parisi, F., Prota, A., Manfredi, G. (2011). In-plane lateral response of a full-scale masonry sub-assemblage with and without an inorganic matrix-grid strengthening system. Journal of Composites for Construction 15:4, 578-590.

Backes, H. P. (1985). On the behavior of masonry under tension in the direction of the bed joints. Dissertation, Aachen University of Technology, Aachen, Germany.

Baggio, C., and P. Trovalusci. (1993). Discrete models for jointed block masonry walls. The Sixth North American Masonry Conference. Vol. 2.

Berto, L., Saetta, A., Scotta, R., Vitaliani, R. (2002). An orthotropic damage model for masonry structures, International Journal for Numerical Methods in Engineering, 55, 127-157.

Binda, L, Tiraboschi, C., Mirabella Roberti, G., Baronio, G., Cardani, G. (1996b). Measuring masonry material properties: detailed results from an extensive experimental research, Part II: Tests on masonry specimens. Report 5.1, Politecnico di Milano.

Braga F. e Dolce M. (1982). Un metodo per l'analisi di edifici multipiano in muratura antisismici, Proc. of the 6 th I.B.Ma.C., Roma, pp.1088-1099.

Braga, F. e Liberatore, D. (1990). A finite element for the analysis of the response of masonry buildings, Proc. 5th North American Masonry Conference, 201-212, Urbana.

Brencich A & Lagomarsino S. (1998). A macroelement dynamic model for masonry shear walls. In: Pande G et al. (eds.). Computer Methods in Structural Masonry 4. London: E&FN Spon.: 67–75.

Calderini C, Lagomarsino S. (2008). A continuum model for in-plane anisotropic inelastic behaviour of masonry. ASCE Journal of Structural Engineering; 134(2):209–220.

Calderoni B., Marone P., Pagano M. (1987), Modelli per la verifica statica degli edifici in muratura in zona sismica, Ingegneria sismica, n. 3, pp.19-27.

Calderoni B., Lenza P., Pagano M. (1989). Attuali prospettive per l'analisi sismica non lineare di edifici in muratura, Atti del 4° Congresso Nazionale ANIDIS, Milano.

Caliò, I., Marletta, M., Pantò, B. (2005). A simplified model for the evaluation of the seismic behaviour of masonry buildings, 10th International Conference on Civil, Structural and Environmental Engineering Computing, August 30 – September 2, Rome, Italy.

Caliò, I., Marletta, M., Pantò, B. (2008). A discrete element approach for the evaluation of the seismic response of masonry buildings, 14th World Conference of Earthquake, Beijing, China.

Caliò I, Marletta M, Pantò B. (2012). A new discrete element model for the evaluation of the seismic behaviour of unreinforced masonry buildings. Eng Struct 40:327–338.

Cecchi, A., Sab, K. (2002b). Out of plane model for heterogeneous periodic materials: the case of masonry, European J. Mech. A. Solids 21, 715–746.

Cecchi, A., Milani, G., Tralli, A. (2005). Validation of Analytical Multiparameter Homogenization Models for Out-of-Plane Loaded Masonry Walls by Means of the Finite Element Method, Journal of

Engineering Mechanics, Vol. 131, No. 2, 185-198, DOI: 10.1061/(ASCE)0733-9399(2005)131:2(185).

Chengqing, W., Hong, H. (2006). Derivation of 3D masonry properties using numerical homogenization technique, Numerical Methods in Engineering 66(11), 1717-1737, DOI: 10.1002/nme.1537.

Como, M., & Grimaldi, A. (1985). A unilateral model for the limit analysis of masonry walls. In Unilateral Problems in Structural Analysis (pp. 25-45). Springer, Vienna.

Como, M. (1992). Equilibrium and collapse of masonry bodies. Meccanica, 27(3), 185–194.

Cundall P. A. (1971). A Computer Model for Simulating Progressive, Large-scale Movement in Blocky Rock System – Proc. Symp. Int. Soc. Rock Mech. Nancy.

D'Asdia, P. e Viskovic, A. (1994). L'analisi sismica degli edifici in muratura. Ingegneria Antisismica, Anno XI, n.1.

De Buhan, P., & De Felice, G. (1997). A homogenization approach to the ultimate strength of brick masonry. Journal of the Mechanics and Physics of Solids, 45(7), 1085-1104.

De Castro Oliveira, Daniel Vitorino. (2003). Experimental and numerical analysis of blocky masonry structures under cyclic loading. PhD Thesis. doktorski rad, Universidade do Minho.

Del Piero, G. (1989). Constitutive equation and compatibility of the external loads for linear elastic masonry-like materials. Meccanica, 24(3), 150-162.

Dhanasekar, M., Page, A.W., Kleeman, P.W. (1985). The failure of brick masonry under biaxial stresses. Proc. Instn. Civ. Engrs., Part 2, 79, pp. 295-313.

Di Pasquale, S. (1992). New trends in the analysis of masonry structures. Meccanica, 27(3), 173-184.

Dolce, M. (1991). Schematizzazione e modellazione degli edifici in muratura soggetti ad azioni sismiche. L'Industria delle Costruzioni, 25:44-57 (in Italian).

Drysdale RG, Hamid AA & Heidebrecht AC. (1979). Tensile strength of concrete masonry. Journal of the Structural Division (ASCE): 105(7): 1261–1276.

EN 1998 (European Committee for Standardization). (2005). Design of structures for earthquake resistance - Part 3: Assessment and retrofitting of buildings. Eurocode 8, Brussels, Belgium: EN.

Formica, G., Sansalone, V., Casciaro, R. (2002). A mixed solution strategy for the nonlinear analysis of brick masonry walls, Comput. Methods Apll. Mech. Engrg. 191, 5847-5876.

Fortunato, A. (2010). Elastic solutions for masonry-like panels. Journal of Elasticity, 98, 87–110.

Fraternali, F. (2011). A Mixed Lumped Stress–Displacement Approach to the Elastic Problem of Masonry Walls. Mechanics Research Communications, 38, 176–180.

Gambarotta, L., Lagomarsino, S. (1997). Damage models for the seismic response of brick masonry shear walls. Part I: the mortar joint model and its application, Earthquake engineering and structural dynamics, vol. 26, 423-439.

Giambanco, G., Di Gati, L. (1997). A cohesive interface model for the structural mechanics of block masonry, Mechanica Research Communications 24(5), 503-512.

Giambanco, G., Rizzo, S., Spallino, R. (2001). Numerical analysis of masonry structures via interface models, Comput. Methods Appl. Mech. Engrg. 190, 6493-3511.

Giaquinta, M., E. Giusti. (1985). Researches on the equilibrium of masonry structures. Archive for Rational Mechanics and Analysis, 88, 359–392.

Heyman J. (1966). The stone skeleton. Int. Journal of Solids and Structures 2: 249-279.

Hofmann P & Stöckl S. (1986). Tests on the shear-bond behaviour in the bedjoints of masonry. Masonry International: 9: 1–15.

Hordijk, D.A. (1991). Local approach to fatigue of concrete. Dissertation, Delft University of Technology, Delft, The Netherlands.

Jefferson, A. D., & Mills, N. R. (1998). Fracture and shear properties of concrete construction joints from core samples. Materials and structures, 31(9), 595-601.

Jukes, P., Riddington, J.R. (1997). A review of masonry joint shear strength test methods. Masonry International, 11(2), pp. 37-41.

Jukes, P., & Riddington, J. R. (1998). Review of masonry tensile bond strength test methods. Masonry International, 12(2), 51-57.

Kachanov, L. M. (1958). Rupture time under creep conditions (in Russian). Izvestia Akademii Nauk, Otd Tech Nauk, USSR, 8, pp. 26-31.

Kachanov, L. (1986). Introduction to continuum damage mechanics (Vol. 10). Springer Science & Business Media.

Kooharian A. (1952). Limit analysis of voussoir (segmental) and concrete arches. Journal Amer. Conc. Inst. 24(4): 317-328.

Lagomarsino, S., Penna, A., Galasco, A. and Cattari, S. (2013). TREMURI program: an equivalent frame model for the nonlinear seismic analysis of masonry buildings. Eng. Struct. 56:1787–1799.

Lee, J.S., Pande, G.N., Middleton, J., Kralj, B. (1996). Numerical modelling of brick masonry panels subject to lateral loadings, Computer & Structures, vol. 61, No. 4, 735-745.

Lemaitre J. and Caboche, J.L. (1985). Mècanique des materiaux solides. Dunod, Paris.

Lemos, J. V. (1995). Computational topics in discrete element modeling. In International Journal of Rock Mechanics and Mining Sciences and Geomechanics Abstracts (Vol. 3, No. 32, p. 118A).

Livesley, R. K. (1978). Limit analysis of structures formed from rigid blocks. International Journal for Numerical Methods in Engineering, 12(12), 1853-1871.

Livesley, R. K. (1992). A computational model for the limit analysis of three-dimensional masonry structures. Meccanica, 27(3), 161-172.

Lofti, H.R., Shing, P.B. (1994). Interface model applied to fracture of masonry structures, Journal of Structural Engineering, ASCE, vol. 120, No. 1, 63-81.

Lourenço, P.B. (1996). Computational strategies for masonry structures. Ph.D. Dissertation, Delft University of Technology, Delft, The Netherlands.

Lourenço, P.B., Borst, R., Rots, J.G. (1997). A plane stress softening plasticity model for orthotropic materials, International Journal for Numerical Methods in Engineering, 40, 4033-4057.

Lourenço P.B. & Rots J.G. (1997). A multi-surface interface model for the analysis of masonry structures. Journal of Engineering Mechanics: 123(7): 660–668.

Lourenço, P.B. (1998). Experimental and numerical issues in the modelling of the mechanical behaviour of masonry.

Lourenço, P. B., Rots, J. G., & Blaauwendraad, J. (1998). Continuum model for masonry: parameter estimation and validation. Journal of structural engineering, 124(6), 642-652.

Lourenço PB. (2000). Anisotropic softening model for masonry plates and shells. Journal of Structural Engineering: 126(9): 1008–1016.

Lourenço, P.B. (2002). Computations on historic masonry structures. Progr. Struct. Eng. Mater. 4:301–319.

Lourenço, P. B. (2010). Recent advances in masonry modelling: micromodelling and homogenisation. In Multiscale modeling in solid mechanics: computational approaches (pp. 251-294).

Luciano, R., Sacco, E. (1997). Homogenization technique and damage model for old masonry material, International Journal of Solids and Structures, vol. 34, No. 24, 3191-3208.

Macchi G. (1997). General methodology. The combined use of experimental and numerical techniques inside a single study. P. Roca et al. (eds.). Structural Analysis of Historical Constructions. CIMNE, Barcelona, pp. 10-23.

Macchi G. (2001). Diagnosis of the facade of St. Peter's Basilica in Rome. In: Lourenço PB & Roca P (eds.). Historical Constructions. Guimaraes: Universidade do Minho: 309–317.

Magenes, G., Calvi, G.M. and Kingsley, G.R. (1995). Seismic testing of a full-scale, two-story masonry building: test procedure and measured experimental response, in Experimental and Numerical Investigation on a Brick Masonry Building Prototype – Numerical Prediction of the Experiment, GNDT Report 3.0, Pavia, Italy.

Magenes, G., and Calvi, G.M. (1996). Prospettive per la calibrazione di metodi semplificati per l'analisi sismica di pareti murarie. Proceedings of the Italian National Conference "La Meccanica delle Murature tra Teoria e Progetto", Pitagora, Bologna, Italy (in Italian).

Magenes, G and Calvi, G.M. (1997). In-plane Seismic Response of Brick Masonry Walls. Earthquake engineering and structural dynamics 26. p. 1091-1112.

Magenes G., Della Fontana A. (1998). Simplified non-linear seismic analysis of masonry buildings, 5 th International Masonry Conference, Proc. of the British Masonry Society, 8, 190-195.

Magenes, Guido. (2000). A method for pushover analysis in seismic assessment of masonry buildings. Proceedings of the12th world conference on earthquake engineering. Vol. 42.

Maier, G., Nappi, A., & Papa, E. (1991). Damage models for masonry as a composite material: a numerical and experimental analysis. Constitutive Laws for Engineering Materials, 427-432.

Mann, W., & Betzler, M. (1994). Investigations on the effect of different forms of test samples to test the compressive strength of masonry. In Proc. 10th. Brick and block Masonry Conf., eds. NG Shrive and A. Huizer, University of Calgary, Calgary, Alberta, Canada (pp. 1305-1313).

Mann, W. (1982). Failure of shear-stressed masonry: an enlarged theory, tests and application to shear walls.

Marques, R. and Lourenço, P.B. (2011). Possibilities and comparison of structural component models for the seismic assessment of modern unreinforced masonry buildings. Comput. Struct. 89:2079–2091.

Marques, R. and Lourenço, P.B. (2014). Unreinforced and confined masonry buildings in seismic regions: Validation of macro-element models and cost analysis. Eng. Struct. 64:52–67.

Maugin, G. A. (1992). The thermomechanics of plasticity and fracture (Vol. 7). Cambridge University Press.

Mazars, J., & Pijaudier-Cabot, G. (1989). Continuum damage theory—application to concrete. Journal of engineering mechanics, 115(2), 345-365.

Meguro, K. and H. Tagel-Din. (2000). Applied element method for structural analysis: Theory and application for linear materials, Structural Engineering, JSCE, 17(1),21-35.

Milani, G., Lourenço, P. B., & Tralli, A. (2006). Homogenised limit analysis of masonry walls, Part I: Failure surfaces. Computers & structures, 84(3-4), 166-180.

Milani G, Lourenço PB, Tralli A. (2006). Homogenised limit analysis of masonry walls. Part II: structural examples. Comput Struct 84:181–195.

Milani G, Lourenço PB, Tralli A. (2006). Homogenization approach for the limit analysis of out-of-plane loaded masonry walls. ASCE J Struct Eng 132(10):1650–1663.

Neville, A. M. (1995). Properties of concrete (Vol. 4). London: Longman.

NTC (Norme Tecniche per le Costruzioni). (2008). Decreto ministeriale del 14 gennaio 2008. Rome: Ministero delle Infrastrutture e dei Trasporti. (in Italian).

NTC (Norme Tecniche per le Costruzioni). (2018). Aggiornamento delle Norme Tecniche per le Costruzioni. Decreto ministeriale del 17 gennaio 2018. Rome: Ministero delle Infrastrutture e dei Trasporti. (in Italian).

Page AW. (1978). Finite element model for masonry. Journal of the Structural Division (ASCE): 104(8): 1267–1285.

Page AW. (1981). The biaxial compressive strength of brick masonry. Proc. Instn. Engrs., Part 2, 71, pp. 893-906.

Page AW. (1983). The strength of brick masonry under biaxial compression-tension. Int. J. Masonry Constr., 3(1), pp. 26-31.

Pantò B, Cannizzaro F, Caddemi S, Caliò I. (2016). 3d macroelement modelling approach for seismic assessment of historical masonry churches. Adv Eng Softw 97:40–59.

Pantò B, Caliò I, Lourenço P. (2018) A 3D discrete microelement for modelling the out-of-plane behaviour of infilled frame structures. Eng Struct 175:371–385.

Papa, E. (1996). A unilateral damage model for masonry based on a homogenisation procedure. Mechanics of Cohesive-frictional Materials: An International Journal on Experiments, Modelling and Computation of Materials and Structures, 1(4), 349-366.

Pegon, P., & Pinto, A. V. (1996). Seismic Study of Monumental Structures: Structural Analysis, Modelling and Definition of Experimental Model. European Commission Joint Research Centre Institute for Systems, Informatics and Safety.

Pegon, P., & Anthoine, A. (1997). Numerical strategies for solving continuum damage problems with softening: application to the homogenization of masonry. Comp. & struct., 64(1-4), 623-642.

Pelissou, C., Lebon, F. (2009). Asymptotic modeling of quasi-brittle interfaces, Computers and Structures 87, 1216-1223.

Penna, A. (2002). Una procedura a macro-elementi per l'analisi dinamica non lineare di edifici in muratura. PhD Thesis, Polytechnic of Milan, Milan, Italy (in Italian).

Pfeifer, G., Pfeifer, G., Achtziger, J., Ramcke, R., & Zilch, K. (2001). Masonry construction manual. Birkhauser.

Pietruszczak, S., & Niu, X. (1992). A mathematical description of macroscopic behaviour of brick masonry. International journal of solids and structures, 29(5), 531-546.

Rekik, A., Lebon, F. (2010). Identification of the representative crack length evolution in a multi-level interface model for quasi-brittle masonry. International Journal of Solids and Structures 47, 3011-3021.

Rinaldin G, Amadio C, Macorini L. (2016). A macro-model with nonlinear springs for seismic analysis of urm buildings. Earthq Eng Struct Dyn 45(14):2261–2281.

Roca, P., Oliveira. D., Lourenço, P., Carol, I. (2001). Mechanical response of dry joint masonry. G. Arun and N. Seçkin (eds): 2nd International Congress on Studies in Ancient Structures, Yildiz Technical University, Istanbul, pp. 571-579.

Rots, J.G. (1991). Numerical simulation of cracking in structural masonry, Heron, 36(2), 49-63.

Sacco, E. (2009). A nonlinear homogenization procedure for periodic masonry, European Journal of Mechanics A/Solids 28, 209-222.

Schubert P and Hetzemacher P. (1992). On the flexural strength of masonry. Masonry International: 6(1): 21–28.

Senthivel, R., Lourenço, P. B. (2009). Finite element modeling of deformation characteristics of historical stone masonry shear walls, Engineering Structures 31, 1930-1943.

Silva, L.C., Lourenço, P.B. and Milani, G. (2018). Derivation of the out-of-plane behaviour of masonry through homogenization strategies: Micro-scale level. Comput. Struct. 209:30–43.

Silva, L.C., Mendes, N., Lourenço, P.B. and Ingham, J. (2018). Seismic structural assessment of the Christchurch Catholic Basilica, New Zealand. Structures 15:115–130.

Sincraian, G. E. (2001). Seismic behaviour of blocky masonry structures. A discrete element method approach. Civil Engineering PhD Thesis.

Smith BS & Carter C. (1977). Hypothesis for shear failure of brickwork. Journal of the Structural Division (ASCE): 97(4): 1055–1062.

Stankowski, T., Runesson, K., & Sture, S. (1993). Fracture and slip of interfaces in cementitious composites. I: Characteristics. Journal of engineering mechanics, 119(2), 292-314.

Sutcliffe, D. J., Yu, H. S., & Page, A. W. (2001). Lower bound limit analysis of unreinforced masonry shear walls. Computers & Structures, 79(14), 1295-1312.

Tomaževič M. (1978). The computer program POR, Report ZRMK, 1978 (in Slovene).

Uva, G., Salerno, G. (2006). Towards a multiscale analysis of periodic masonry brickwork: a FEM algorithm with damage and friction, International Journal of Solids and Structures 43, 3739-3769.

Van der Pluijm, R. (1993). Shear behaviour of bed joints. A.A. Hamid and H.G. Harris (eds): Proc. 6th North American Masonry Conference. Vol. 1, pp. 125-136.

Van der Pluijm, R. (1997). Non-linear behaviour of masonry under tension. Heron, 42(1), pp. 25-54.

Van Mier, J.G.M. (1984). Strain-softening of concrete under multiaxial loading conditions. Dissertation, Eindhoven University of Technology, Eindhoven, The Netherlands.

Vermeltfoort, A.T. (1997). Effects of the width and boundary conditions on the mechanical properties of masonry prisms under compression. Proc.11th Int. Brick/Block Mas. Conf., pp.181-190.

Vonk, R.A. (1992). Softening of concrete loaded in compression. Dissertation, Eindhoven Univ. of Technology, Eindhoven, The Netherlands.

3. Seismic performance of existing URM structures

3.1 Introduction

The seismic response of URM structures subjected to lateral load is characterized by a defined hierarchy of failure modes (Figure 3.1). In detail, if the quality of the mortar is poor, the first failure mechanism expected to occur is the crumbling of the masonry. If the mortar has an adequate characterization but the orthogonal walls are not sufficiently connected to each other and/or the wall-to-diaphragm connections are not guaranteed, the out-of-plane mechanisms (or first mode) occur in the structure. Instead, if the “box-like” (or monolithic) behaviour is guaranteed, the in-plane mechanisms (or second mode) are activated.

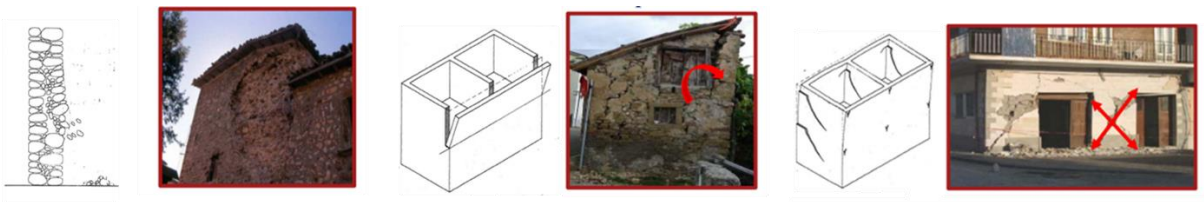

Figure 3.1. Hierarchy of failure mechanisms: (a) masonry crumbling; (b) out-of-plane failure; (c) in-plane failure (adapted from Giuffrè, 1993).

Moreover, the stiffness (or vice versa flexibility) of floor diaphragms plays an important role in the overall response of URM structures. The horizontal diaphragms have the task of redistributing the seismic force between the vertical resistant elements and this capacity depends greatly on the type of floor present in the building. Two macro-categories of the floor can define according to their plane or orthogonal stiffness: rigid and flexible floors. The presence of a rigid diaphragm (i.e. with concrete slab) allows, if the adequate connections between vertical elements are guaranteed, the "box-like" behaviour of the structure, redistributing the horizontal seismic force in a way proportional to the stiffness of the resistant elements. This consequently implies that the stiffer vertical element absorbs a greater rate of horizontal effort than the others. On the other hand, a flexible diaphragm (i.e. a simple timber

floor) no longer guarantees the overall response of the structure to the seismic action, showing behaviour similar to that of a supported beam characterized by flexural and shear deformation, causing out-of-plane local mechanisms.

The analysis of the overall response of a building can be carried out when local out-of-plane collapse mechanisms are prevented (i.e. in presence of tie rods or spreader-beam) and consequently the structure behaviour is governed by the in-plane resistance of the walls. Contrarily, when the construction does not manifest a clear global behaviour, but reacts to the earthquake as a set of isolated subsystems (or macro-elements) it is necessary to carry out a comprehensive set of local analyses.

For the purpose of this Thesis, the behaviour of the URM structural components under lateral loads has to be investigated. This Chapter is dedicated to an overview of the state-of-the-art on the Out-Of-Plane and In-Plane failure mechanisms of URM structures, outlining the several formulations, available in literature and adopted by national and international codes, to assess the strength in a simplified way. Due to the topic of this Thesis, more detail is given to the in-plane failure mechanisms, to provide a wide overview of the existing structural elements analytical models.

3.2 Out-Of-Plane failure mechanisms

The damage observation from past earthquakes has shown that the most recurrent failure mechanism in URM structures is the overturning of entire walls or, most commonly, of a portion of them (D'Ayala, 1999b; Karantoni and Bouckovalas, 1997; Tomaževič *et al*., 1999; D'Ayala and Speranza, 2003a).

Among the factors that contribute to the overturning vulnerability of URM structures, the degree of connection between orthogonal walls and the in-plane stiffness of floor diaphragms greatly affect the seismic response of the structures (Rota *et al*., 2011). Indeed, in the case of poor wall-to-floor connection, the only restraint to overturning is the friction of the contact surface exerted by other elements to a wall. Hence different types of failure due to the overturning of the walls orthogonal to the seismic load is expected to occur, leading to severe damage at any intensity of shaking. In Figure 3.2 are shown some examples of the typical mechanisms for overturning failures.

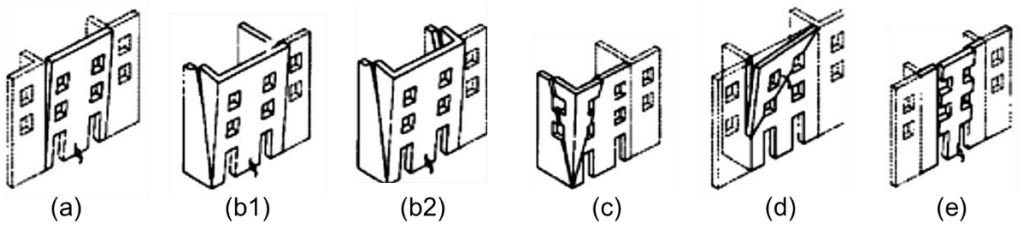

Figure 3.2. Mechanisms of overturning failures (adapted from D'Ayala and Speranza, 2003a).

Contrarily, the simple overturning failure can be avoided improving the connection between walls and horizontal diaphragms through the introduction of, for example, ties or ring beams, leading to the appearance of mechanisms based on the arch effect (see Figure 3.3).

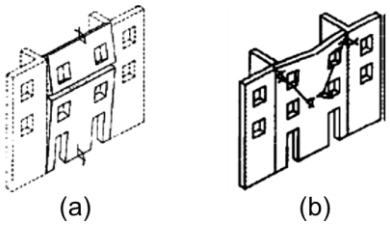

Figure 3.3. Mechanisms based on the arch effect (adapted from D'Ayala and Speranza, 2003a).

From the '80s, some methodologies were proposed in literature to identify the seismic vulnerability of URM existing buildings (Benedetti and Petrini, 1984; Bernardini *et al.*, 1990; Giuffrè, 1993; Giuffrè and Carocci, 1997; Brun *et al*., 1999; D'Ayala and Speranza, 1999a; de Felice and Giannini, 2001; D'Ayala and Speranza, 2003a; Modena *et al*., 2004a; Munari *et al.*, 2009), aiming to a strengthening program, based on priorities. These methodologies proposed to identify the horizontal static-equivalent forces that activate specific local failure mechanisms, or overturning of some structural portions of the building. At first, these structural portions, or macro-elements, with an autonomous behaviour with respect to that of the entire building, should be identified. These macro-elements, based on the load and on the masonry properties, could be defined by single or combined structural components, and they are characterized by loss of equilibrium, or kinematic mechanisms (caused by the absence of effective wall-to-wall and/or wall-to-horizontal structures connections). Through the limit analysis of equilibrium, as suggested by the Italian Code (NTC 2018), the possible collapse kinematic mechanisms of each identified macro-element have to be considered. To this aim, the following (on the safe side) assumptions are usually made: limited deformability

(hypothesis acceptable for masonry); null tensile strength of masonry; neglected sliding between blocks; infinite compressive strength of masonry (considering concentrated hinges). For a more realistic simulation, some approximations can also be modified, considering the sliding of the blocks (in presence of friction), the walls connection and a limited masonry compressive strength (considering the plastic hinge adequately set back from the edge of the section). Finally, the multiplier of the horizontal loads which leads to a loss of equilibrium of the system (that activated the kinematic mechanism), or collapse multiplier, can be identified. The mechanism connected to the lowest value of collapse multiplier is the weakest one and, consequently, the most probable to occur. The choice of the macro-elements to analyse in a given building can be facilitated by referring to abaci of the typical damages occurring in constructive typologies (i.e. buildings, churches, palaces) obtained from the observation of the past earthquakes damage. An example of the abacus of the possible collapse mechanisms for row buildings is shown in Figure 3.4.

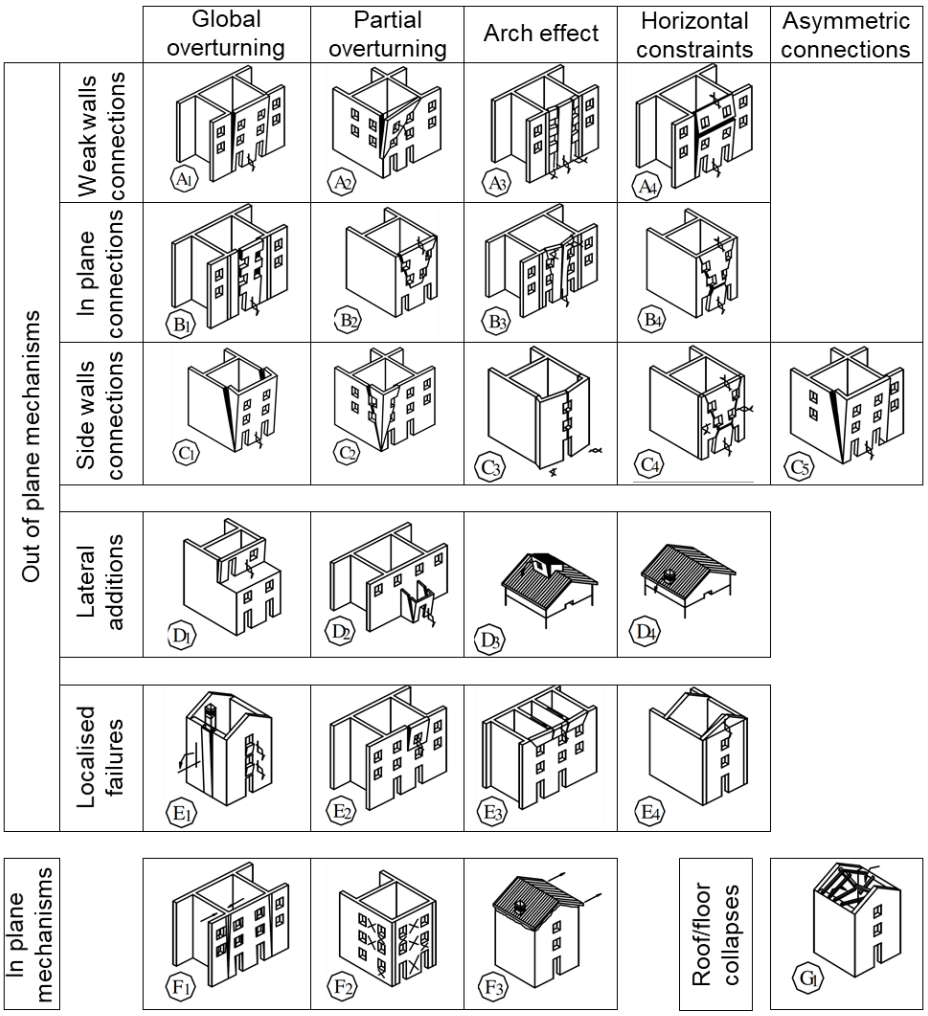

Figure 3.4. Abacus of the collapse mechanisms for row buildings (D'Ayala and Speranza, 1999a).

As aforementioned, the analysis of local collapse mechanisms is necessary only if the building does not show a monolithic (or “box-like”) behaviour. Indeed, the experience from the past earthquakes has shown that the prevention of the out-of-plane collapse mechanisms can be provided by an effective connection between orthogonal walls and between walls and horizontal diaphragms.

3.3 In-Plane failure mechanisms

The II mode mechanisms are activated when the “box-like” behaviour of the structure is guaranteed, more in detail when the orthogonal walls and wall-to-diaphragm connections are adequate. Among these mechanisms, the flexural and shear behaviour can be recognized. More details are given in the following Sections.

3.3.1 Structural components analytical models

In the following Sections, the flexural and shear mechanisms are extensively presented, providing an overview on the main rules and formulations given in literature or code provisions to assess the corresponding strength for the structural URM components (pier and spandrel). Regarding the pier-spandrel joints, the evidence of no damage in URM walls during earthquakes has led to assume them as rigid, in the Equivalent Frame (EF) modelling approach, and furthermore different studies have been developed to estimate the effective deformable height and length of piers and spandrels, respectively (e.g. Dolce, 1991; Lagomarsino *et al*., 2013).

3.3.2 Pier behaviour

As observed from damage after earthquakes, the masonry piers when subjected to in-plane loading can typically show two typologies of failure mechanisms and crack patterns (Magenes and Calvi, 1997): (i) a flexural failure mode, in terms of toe-crushing failure, if the compression strength is low when compared to the compression stress, or in terms of rocking failure if the piers are expected to rotate; and (ii) a shear response, in terms of diagonal cracking, if diagonal cracks are developed in a step-wise manner through the

mortar joints or in a straight diagonal line through the bricks, or in terms of sliding failure if horizontal cracks define sliding planes in the bed-joints. In Figure 3.5 are shown the possible in-plane failure mechanisms of a URM pier subjected to lateral load.

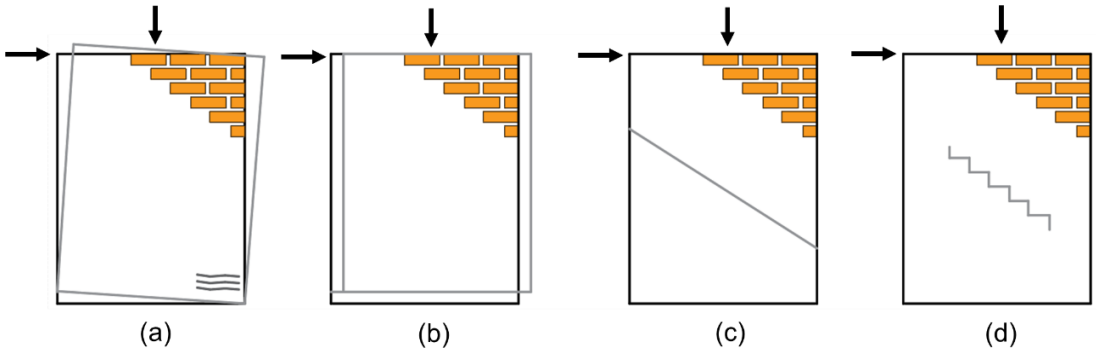

Figure 3.5. In-plane behaviour modes for laterally loaded URM piers: (a) rocking/toe crushing; (b) shear sliding; (c) diagonal cracking through the bricks; (d) stair stepped diagonal cracking (adapted from Marzahn, 1998).

The failure mode is strongly dependent on the geometric aspect ratio, on the boundary conditions, on the material properties and on the applied axial load, as highlighted in several experimental campaigns (Magenes and Calvi, 1992; Vasconcelos, 1995; Vasconcelos and Lourenço, 2006; Calderini *et al*., 2009). In general, it can be observed that: the rocking behaviour characterizes the slender piers subjected to low vertical compression levels; the crushing occurs for high levels of vertical compression (related to the masonry compressive strength); the bed-joint sliding behaviour takes place in very squat piers (Abrams, 1992; Magenes and Calvi, 1992; Anthoine *et al.*, 1994; Magenes and Calvi, 1997) or in moderately slender piers for a high level of vertical compression (Mayes and Clough, 1975a; Bosiljkov *et al.*, 2003; Vasconcelos and Lourenço, 2006); the diagonal cracking behaviour is expected to occur in moderately slender piers with high axial load (Vasconcelos and Lourenço, 2009) and in detail, the diagonal cracking through the bricks tends to prevail over the stair-stepped one for increasing levels of vertical compression (Lourenço *et al*., 2005) and for increasing ratio between mortar and brick strengths (Mayes and Clough, 1975b; Bosiljkov *et al.*, 2003). Furthermore, from Vasconcelos and Lourenço (2006) and Giuffrè (1993), it was stated that by increasing the interlocking of the bricks, the stair-stepped diagonal cracking strength becomes higher, leading to the development of one of the other failure mechanisms.

Regarding the displacement capacity, few are the indications from experimental campaigns. Italian and European codes suggest limit values, based on the flexural or shear

expected failure mode, with reference to Magenes (2010) experimental results. More in detail, in that study it was found that for a pier with height equal to h and displacement capacity equal to δ_u, the ultimate drift (assumed as $\theta_u = \delta_u/h$) can be defined for flexural failure mode as $\theta_u > 0.8\%$ and for shear failure mode as $\theta_u \leq 0.4\%$. Although the international recommendations are very useful for the practicing engineers giving an important value for the analyses, nowadays it is clear how these values are the magnitude of the displacement capacity which depends not only on the typology of the expected failure mode but also on the geometric aspect ratio, on the applied vertical axial load (Frumento *et al*., 2009) and on the boundary conditions of the piers.

3.3.2.1 Flexural (rocking) failure

The rocking response of walls was firstly identified by Housner, with his Simple Rocking Model (SRM) (Housner, 1963), in which rocking motion is investigated for structures of inverted pendulum type and expressed in function of the size and slenderness of the blocks, of the coefficient of restitution and of the ground motion properties.

In the following years, several studies in literature aimed to describe the rocking failure mode of URM piers in an analytical way, to be of daily use by engineering practitioners. Most of these formulations have been derived from the equilibrium of the forces, assuming a behavior of the masonry similar to the one of concrete under uniaxial compression. In detail, it was considered that this failure mode is characterized by horizontal cracks along mortar joints that generate a localized damage mechanism on one side, reduce the resisting section and concentrate the compressive stresses on the opposite side. To analyse the flexural behaviour of URM piers is generally adopted the sectional analysis, assuming no-tensile strength and limited compressive strength. In the following are outlined the main formulations available in literature and in national and international codes to define the rocking failure strength, which generally governs piers with a high aspect ratio and low vertical axial stress.

Magenes and Calvi (1997) presented a procedure to assess the response of brick masonry walls, using refined numerical simulations and laboratory tests to validate their analytical prediction in terms of strength, failure modes and in general in terms of the non-linear response of masonry walls. As shown in Figure 3.6, the formulation of the rocking strength V_r is defined assuming an idealized rectangular distribution of compressive stress in

the pier toe, with the coefficient k, assumed equal to 0.85, to reduce the ultimate compressive strength of the masonry f_u (Equation 3.1):

$$V_r = \frac{Dtp}{2\alpha_v}\left(1 - \frac{p}{kf_u}\right) \tag{3.1}$$

where D and t are the length and the thickness of the pier, respectively; p is the mean compressive stress (due to the axial load P); α_v is the shear ratio defined as the ratio of the effective height to the width of the pier as $\alpha_v = \psi' H/D$, with ψ' taken as 1 if the pier is fixed-free pier (cantilevered condition) or 0.5 if it is fixed-fixed pier. As highlighted in this study, the rocking strength results strongly dependent on the value of α_v and just a little on the parameters k and f_u.

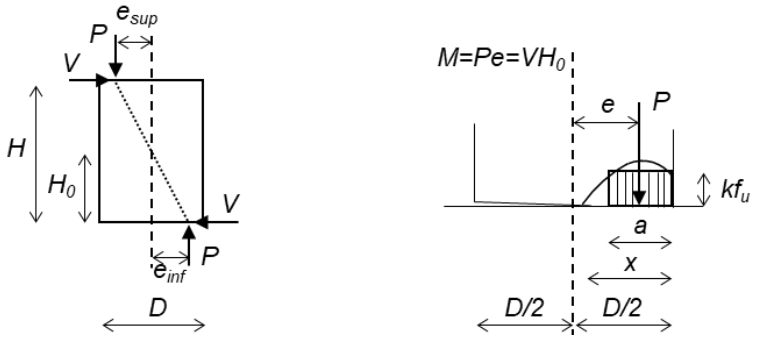

Figure 3.6. Assumptions adopted for assessing the rocking strength of a wall (adapted from Magenes and Calvi, 1997).

A similar formulation for the design lateral resistance in rocking mode $H_{f,w}$ is assumed in Tomaževič (1999). In his study, it is considered a characteristic compressive strength of the masonry f_k, instead of the ultimate compressive strength, and a partial safety factor for masonry γ_m is adopted (Equation 3.2):

$$H_{f,w} = \frac{Dtp}{2\alpha_v}\left(1 - \frac{\gamma_m p}{f_k}\right) \tag{3.2}$$

Regarding national and international codes, in the Italian code (NTC 2018) and in New Zealand guidelines (NZSEE 2017b) the flexural strength related to the rocking mechanism is typically defined assuming an equivalent rectangular compressive stress block.

International codes give different but similar expressions for the ultimate flexural strength and the corresponding ultimate drift of piers. The formulations adopted by Eurocode 8 (EN1998 2005), ASCE 41, New Zealand guidelines (NZSEE 2017b) and Italian code (NTC 2018) are detailed in the following.

Eurocode 8 (EC8) defines the shear strength V_f of a pier under an axial load N corresponding to the rocking behaviour due to combined bending and axial load as (Equation 3.3):

$$V_f = \frac{DN}{2H_0}(1 - 1.15\nu_d) \tag{3.3}$$

where D and H_0 are the depth of the pier and the distance between the section where the flexural capacity is attained and the contra flexure point, respectively; N is the acting axial load; ν_d is the normalized axial load assumed as N/Dtf_d, where t is the thickness of the pier and f_d is the design compressive strength, defined as $f_d = f_m/CF_m$ (where f_m is the mean compressive strength and CF_m is the confidence factor for masonry). The ultimate drift corresponding to the failure under combined bending and axial force is assumed as 0.008 H_0/D.

In ASCE 41 the shear strength V_r is defined as (Equation 3.4):

$$V_r = 0.9(\alpha P_D + 0.5P_w)\frac{L}{h_{eff}} \tag{3.4}$$

where α is a factor equal to 0.5 for cantilevered pier or 1.0 for fixed-fixed pier; h_{eff} is the height of the pier; P_D and P_w are the superimposed and the dead load on the top of the pier the self-weight of the pier, respectively; L and h_{eff} are the length and the height of the pier, respectively.

In New Zealand guidelines (NZSEE 2017b) the maximum probable rocking strength of the pier V_r is calculated as (Equation 3.5):

$$V_r = 0.9(\alpha P + 0.5P_w)\frac{L_w}{h_{eff}} \tag{3.5}$$

where α is a factor equal to 0.5 for fixed-free pier and equal to 1.0 for fixed-fixed pier; P and P_w are the superimposed and the dead load on the top of the pier, respectively; L_w is the

length of the pier; h_{eff} is the height to the resultant of the seismic force. It Is recommended to limit the ultimate lateral drift for a rocking pier to the lower of 0.003 h_{eff}/L_w or 0.011.

Italian code (NTC 2018) considers the same failure mode assumed in EN1998 (2005) for the rocking behaviour of piers. More in detail, the combined bending and axial force define the ultimate moment strength M_u corresponding to (Equation 3.6):

$$M_u = \left(l^2 t \frac{\sigma_0}{2}\right)\left(1 - \frac{\sigma_0}{0.85 f_m}\right) \tag{3.6}$$

where l and t are the length and the thickness of the pier, respectively; σ_0 is the axial compressive stress due to the gravity loads; f_m is the mean compressive strength of the masonry. The ultimate drift at Collapse Limit State (CLS) corresponding to the failure under combined bending and axial force is assumed as 0.01. In the case of static non-linear analysis, the ultimate displacement at Ultimate Limit State (ULS) can be assumed as ¾ of the displacement at CLS.

3.3.2.2 Shear failure

For the shear strength, several formulations exist that consider the different mechanisms of bed-joint sliding and diagonal cracking, distinguishing the diagonal cracks that develop predominantly along mortar joints, from those that affect also masonry bricks. It is observed that the behaviour under shear loads is more complex than the flexural one since weak planes along the horizontal and vertical mortar joints occur.

For the definition of the shear failure, the Mann and Müller (1973) model represents an undisputed milestone. In this model, the masonry is assumed as a composite and anisotropic material, composed of bricks and mortar and characterized by different failure modes. The fracture criteria are based on the analysis of a single isolated brick subjected to vertical axial stresses σ_y, to uniformly distributed shear stresses τ, and with no-horizontal compressive stress and consequently no-transferred shear stresses through the vertical mortar joints. For a generic masonry element (Figure 3.7a) it is possible to consider the axial stress in the vertical direction (Figure 3.7b) and the shear stress, that produces a vertical force couple in each brick (see Figure 3.7c, expressed as $\pm\varphi\tau$, in terms of the interlocking parameter

$\varphi = 2\Delta_y/\Delta_x$, where Δ_y and Δ_x are the height and the width of the bricks). The resulting altered vertical stresses $\sigma_{1,2}$ on the bed joints (Figure 3.7d) are defined as (Equation 3.7):

$$\sigma_{1,2} = \sigma_y \pm \tau \frac{2\Delta_y}{\Delta_x} \tag{3.7}$$

From this consideration, it is clear that the part of the bricks with the reduced vertical stress σ_2 will show at first the shear failure in the bed joint. According to this formulation, in the Mann and Müller (1973) theory the generally used Mohr-Coulomb formulation for the sliding shear failure of horizontal bed joint, which considers the shear strength τ from the two contributions of cohesion c and friction $\mu\sigma_y$, was modified considering the reduction of vertical stress from σ_y to σ_2. More in detail the reduced sliding shear strength τ (Equation 3.8) can be defined from the reduced cohesion $\bar{c}$ (Equation 3.9) and the reduced friction coefficient $\bar{\mu}$ (Equation 3.10), as:

$$\tau = \bar{c} + \bar{\mu}\sigma_y \tag{3.8}$$

$$\bar{c} = c\frac{1}{1 + \mu\frac{2\Delta_y}{\Delta_x}} \tag{3.9}$$

$$\bar{\mu} = \mu\frac{1}{1 + \mu\frac{2\Delta_y}{\Delta_x}} \tag{3.10}$$

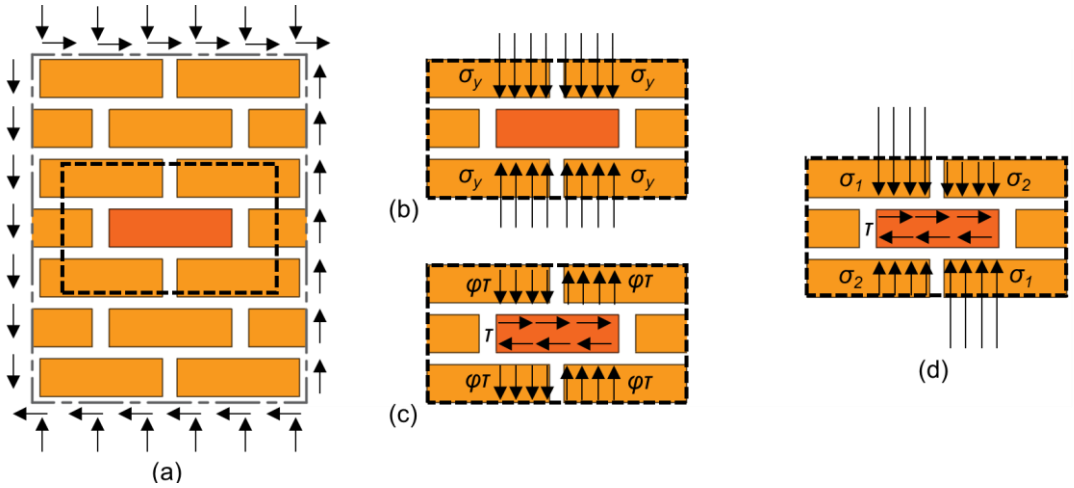

Figure 3.7. Schematization of: (a) masonry element subjected to shear and compression loads; (b) brick subjected to vertical axial stress; (c) brick subjected to shear stress and vertical force couple; (d) resulting vertical and horizontal stresses on the brick (adapted from Calderini et al., 2010).

To define the diagonal cracking shear failure, in Mann and Müller (1973) it is adopted the same theory and it is assumed that the brittle failure occurs when the tensile principal stress of the brick $\sigma_{1,b}$ reaches the bricks tensile strength f_{bt}. From more detailed investigations, it results that in these conditions, in the middle of the bricks, the horizontal stress σ_x is null and the shear stress is equal to $2.3\,\tau$ (see Equations 3.11 and 3.12).

$$\sigma_{1,b} = f_{bt} = \frac{\sigma_y}{2} - \sqrt{\left(\frac{\sigma_y}{2}\right)^2 + (2.3\tau)^2} \tag{3.11}$$

$$\tau = \frac{f_{bt}}{2.3}\sqrt{1 + \frac{\sigma_y}{f_{bt}}} \tag{3.12}$$

The previous formulations of shear failure by sliding along horizontal bed-joints and by diagonal cracking through the bricks are reported in an envelope of the failure criteria in the vertical stress-shear stress domain, presented in Mann and Müller (1973). They are represented by the “line c” and “line d”, in Figure 3.8.

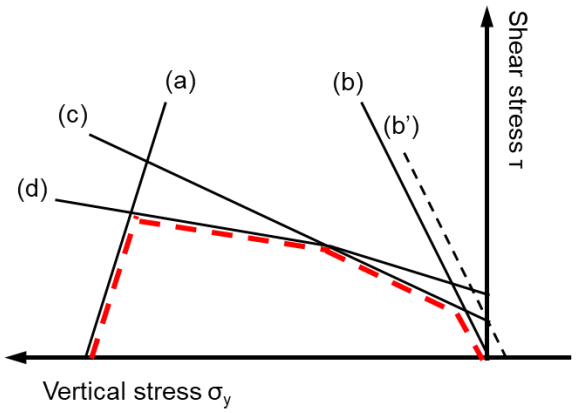

Figure 3.8. Envelope curve of the failure stresses in the vertical stress-shear stress domain (adapted from Mann and Müller, 1979).

Regarding the other lines of the envelope, the “line a” refers to the compression failure of the masonry, which is assumed to develop when the ultimate compressive strength of the masonry f_u is reached (see Equation 3.13), instead of the “lines b-b’” refers to the failure of the horizontal joint, in case the tensile strength of the bed-joint $f_{t,bj}$ is neglected (see Equation 3.14) or considered (see Equation 3.15).

$$\tau = \left(f_u - \sigma_y\right)\frac{\Delta_x}{2\Delta_y} \tag{3.13}$$

$$\tau = \sigma_y\frac{\Delta_x}{2\Delta_y} \tag{3.14}$$

$$\tau = \left(\sigma_y + f_{t,bj}\right)\frac{\Delta_x}{2\Delta_y} \tag{3.15}$$

Another important work from which the following researches usually start is the Turnšek and Čačovič (1971) approach, in which the masonry is schematized by an equivalent isotropic homogeneous continuum, assuming a high strength of the mortar. This model defines the shear strength from the pier aspect ratio and from the non-linear stress distribution. It is assumed that the diagonal cracking failure occurs when the diagonal tensile strength of the masonry f_{dt} (defined via experimental tests) is reached at the centre of the pier (Equation 3.16):

$$V_d = \frac{f_{dt}Dt}{\xi}\sqrt{1 + \frac{f_a}{f_{dt}}} \tag{3.16}$$

where D and t are the width and the thickness of the pier, respectively; f_a is the average vertical compressive stress; ξ is a parameter defined equal to 1.5.

As observed in the following, the parameter ξ has been considered differently by other studies, as by Benedetti and Tomaževič (1984) that assumes $\xi = 1$ for $H/D \leq 1$; $\xi = H/D$ for $1 < H/D < 1.5$ and $\xi = 1.5$ for $H/D \geq 1.5$, where H and D are the height and the length of the considered pier. Then, ξ was further modified from Magenes and Calvi (1997), after numerical simulations, and substituted by $1 + \alpha_v$ where α_v is the shear ratio, to take into account also the effect of the boundary conditions in the definition of the shear diagonal cracking strength.

The Mann and Müller (1973) and Turnšek and Čačovič (1971) works are based on two different descriptions of the masonry but laid the basis for all the researches that will be discussed in the following sections. The first is more realistic, considering a composite and non-homogeneous material instead the second one idealizes the masonry in an equivalent isotropic material.

In Sections 3.3.2.2.1 and 3.3.2.2.2, some of the main formulations of shear diagonal cracking and bed-joint sliding failure, derived from the previously mentioned theories, are reported. More in detail, for the former, two kinds of failure mechanisms are considered: the failure only along mortar joints and that also through the bricks.

3.3.2.2.1 Diagonal cracking failure

The diagonal cracking mode is a typical brittle failure of squatter piers with a high vertical compression stress and low tensile masonry strength, that shows an X-type cracking, only along the mortar joints (in case of weak mortar-brick adhesion) or also through the bricks (in case of good mortar-brick adhesion), see Figure 3.9.

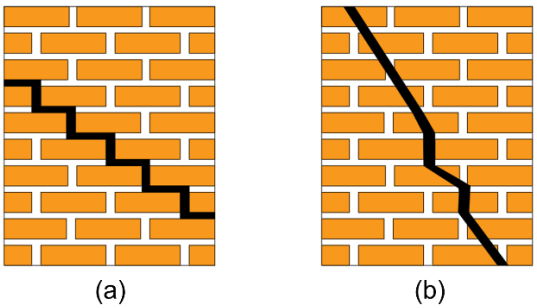

Figure 3.9. Diagonal shear modes of failure: (a) along mortar joints and (b) through the bricks.

Some formulations to describe both these mechanisms are discussed in the following.

Failure only along mortar joints

The failure only along mortar joints occurs when the brick units are stronger than the mortar joints and the main formulae are based on the Mohr-Coulomb's linear friction model. In the following, some formulations about the shear failure governed by joint failures are reported.

In Magenes and Calvi (1997) the ultimate shear strength V_d (Equations 3.17) is defined from the local cohesion c and from the coefficient of bed-joints friction μ (obtained by experimental tests). More in detail, V_d is defined from the minimum shear stress defined for the cracked τ_{cs} (Equation 3.18) or for the whole τ_{ws} section (Equations 3.19):

$$V_d = Dt\tau_u \qquad \text{with } \tau_u = \min(\tau_{cs}; \tau_{ws}) \tag{3.17}$$

$$\tau_{cs} = \left(\frac{1.5c' + \mu' p}{1 + \frac{3\, c' \alpha_v}{p}} \right) \tag{3.18}$$

$$\tau_{ws} = \left(\frac{c' + \mu' p}{1 + \alpha_v} \right) \tag{3.19}$$

where D and t are the width and the thickness of the pier, respectively; p is the value of the compressive stress; α_v is the shear ratio, defined as the ratio of the effective height to the width of the pier as $\alpha_v = \psi' H/D$, where ψ' is taken as 1 if the pier is fixed-free pier (cantilevered condition) or as 0.5 if it is fixed-fixed pier; c' and μ' are defined as $c' = kc$ and $\mu' = k\mu$, with $\kappa = \frac{1}{1+\left(\frac{2\mu\Delta_y}{\Delta_x}\right)}$ (considering the influence of the head joints, as suggested by Mann and Müller, 1973); Δ_x and Δ_y are the length and the height of the brick unit, respectively.

Tomaževič (1999) defines a formulation, adopted also in Eurocode 8 (EN1998 2005), for the design shear resistance of masonry $H_{sd,w}$. This expression (Equation 3.20) is defined from the shear strength under zero compression stress f_{v0}, from the constant μ_c defining the contribution of compression stresses, from the design compression stress (perpendicular to shear) σ_d and from the masonry partial safety factor γ_M:

$$H_{sd,w} = l_c t \frac{(f_{v0} + \mu_c \sigma_d)}{\gamma_M} \tag{3.20}$$

where l_c and t are the length of the compressed part of the pier and its thickness, respectively. It is observed that the parameters f_{v0} and μ_c are global strength parameters of masonry, unlike the corresponding local ones adopted in Magenes and Calvi (1997).

Regarding the diagonal cracking shear failure mode, Andreas (1996) highlights as the Mohr-Coulomb friction criteria, used in the previous formulations, can be used just for piers with medium-high compression stresses.

Failure also through bricks

The failure initiated by shear-tensile cracking of bricks occurs when mortar joints are stronger than the brick units, or when their values are comparable or in presence of high axial loads. In the following, some formulations that analytically explain this behaviour are reported.

Magenes and Calvi (1997) suggested an interpretation of the pier global lateral strength $V_{d,b}$ based on the shear strength criterion proposed by Mann and Müller (1973), see Equation 3.21. It takes into account the brick tensile strength f_{bt} and the effects of the boundary conditions and the aspect ratio through a corrective factor of the shear ratio $(1 + \alpha_v)$. This last considers also the effects of the stress distribution, of the propagation of the cracking and of the shear-flexure interaction.

$$V_{d,b} = Dt \frac{f_{bt}}{2.3(1 + \alpha_v)} \sqrt{1 + \frac{p}{f_{bt}}} \tag{3.21}$$

where D and t are the width and the thickness of the pier, respectively, and p is the compressive stress.

In Tomaževič (1999), the effect of the boundary conditions is not considered, and the shear capacity $H_{sd,w}$ (Equation 3.22) is defined just from the geometrical aspect ratio *b*, that is assumed as $b = 1$ for $h/l \leq 1$; $b = h/l$ for $1 < h/l < 1.5$ and $b = 1.5$ for $h/l \leq 1.5$ (where h and l are the height and the length of the pier).

$$H_{sd,w} = A_w \frac{f_{tk}}{\gamma_M b} \sqrt{\frac{\sigma_d \gamma_M}{f_{tk}} + 1} \tag{3.22}$$

where A_w is the horizontal cross-section area of the pier; f_{tk} is the characteristic tensile strength of masonry brick; γ_M is the partial safety factor for the masonry; σ_d is the design compression stress (perpendicular to shear).

Abrams (2001), according to the FEMA 273 recommendations, adopts the following formulation (Equation 3.23):

$$V_{dt} = f'_{dt} A_n \frac{L}{h_{eff}} \sqrt{1 + \frac{f_a}{f'_{dt}}} \tag{3.23}$$

where f'_{dt} is the lower bound of the masonry diagonal tension strength; f_a is the lower bound of the vertical compressive strength; A_n is the net area of the section; L is the length of the pier and h_{eff} is the height of the resultant lateral force. In the study, it is observed that in the previous expression, the aspect ratio defined as L/h_{eff} has to be in the range of values as 0.67-1.0.

International codes (as ASCE 41, NZSEE 2017b and NTC 2018) give different indications and formulations about the piers diagonal cracking shear strength.

In ASCE 41 the diagonal tensile cracking shear strength is given by (Equation 3.24):

$$V_{dt} = f'_{dt} A_n \beta \sqrt{1 + \frac{f_a}{f'_{dt}}} \tag{3.24}$$

where f'_{dt} is the diagonal tension strength of the masonry; f_a is the axial compressive stress due to the gravity loads; β is a factor defined as $\beta = 0.67$ for $L/h_{eff} < 0.67$; $\beta = L/h_{eff}$ for $L/h_{eff} = [0.67 - 1.0]$ and $\beta = 1.0$ for $L/h_{eff} > 1.0$, where L and h_{eff} are the length and the height of the pier, respectively.

New Zealand guidelines (NZSEE 2017b) defines the maximum pier diagonal tensile strength V_{dt} as (Equation 3.25):

$$V_{dt} = f_{dt} A_n \beta \sqrt{1 + \frac{f_a}{f_{dt}}} \tag{3.25}$$

where f_{dt} is the masonry diagonal tension strength; f_a is axial compression stress due to gravity loads; A_n is the net area of the section; β is a factor to correct non-linear stress distribution and it is defined as $\beta = 0.67$ if $h_{eff}/l > 1.5$ (slender piers); $\beta = 1.0$ if $h_{eff}/l < 1.0$ (squat piers), where h_{eff} is the height to resultant force and l is the length of the pier.

The Commentary to the Italian Technical Standard for buildings (CNTC19, 2019) distinguishes two typologies of masonry when analysing the diagonal cracking shear mode:

(i) with irregular texture, for which the diagonal cracking failure is governed by the reference shear strength τ_0, as (Equation 3.26):

$$V_{t,dc} = lt\frac{f_{td}}{b}\sqrt{1+\frac{\sigma_0}{f_{td}}} \tag{3.26}$$

where l and t are the length and the thickness of the pier, respectively; f_{td} is the design tensile diagonal cracking strength, defined as $f_{td} = 1.5\tau_0$; σ_0 is the axial compressive stress; b is a coefficient that considers the stresses distribution on the section, defined as $b = h/l$ that has to vary in the range [1-1.5], where h is the pier height.

(ii) with regular texture, for which the cracking can develop in a diagonal pattern through the mortar joints (governed by the masonry shear strength in absence of axial load f_{v0}, ideally associated with the joint crisis) or in a diagonal pattern through bricks (governed by the limit strength parameter f_{vlim}), and is defined as (Equation 3.27):

$$V_t = \frac{lt}{b}\left(\frac{f_{v0d}}{1+\mu\varphi}+\frac{\mu}{1+\mu\varphi}\sigma_0\right) \leq V_{t,lim} \tag{3.27}$$

where f_{v0d} is the design masonry shear strength in absence of vertical load; μ is the friction coefficient; φ is the interlocking coefficient defined as the ratio between the height of the brick and the minimum overlap length of the bricks of two successive courses; $V_{t,lim}$ is a limit value that can be defined in function of the tensile bricks strength f_{btd}, according to Equation 3.28:

$$V_{t,lim} = \frac{lt}{b}\frac{f_{btd}}{2.3}\sqrt{1+\frac{\sigma_0}{f_{btd}}} \tag{3.28}$$

The ultimate displacement at Collapse Limit State (CLS) corresponding to the diagonal cracking shear failure is assumed as 0.005. In the case of static non-linear analysis, the ultimate displacement at Ultimate Limit State (ULS) can be assumed as ¾ of the displacement at CLS.

3.3.2.2.2 Bed-joint sliding failure

The bed-joint sliding mode is a typical brittle failure of squat piers with a low vertical compression stress and it appears as a horizontal crack along the bed-joints, see Figure 3.10.

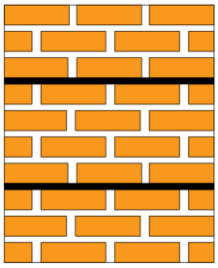

Figure 3.10. Sliding shear mode of failure.

Some formulations to describe this mechanism are shown in the following.

Magenes and Calvi (1997), Tomaževič (1999) and Eurocode 8 (EN1998 2005) define the bed-joint sliding shear capacity V_s, neglecting the cohesion contribution from assuming the joint already cracked in tension due to flexure, as (Equation 3.29):

$$V_s = \mu P \tag{3.29}$$

where μ is the sliding coefficient of the masonry joint and P is the vertical compressive force.

A different formulation for the bed-joint sliding strength is defined by Abrams (2001), that, according to the FEMA 273, adopts the following expression (Equation 3.30):

$$V_{bjs} = \nu_{me} A_n \tag{3.30}$$

where ν_{me} is the expected bed joint sliding shear strength and A_n is the net area of the section.

Regarding the International codes (EN1998 2005; ASCE 41; NZSEE 2017b; NTC 2018) the following formulations are adopted for the piers sliding shear strength.

Eurocode 8 (EN1998 2005) considers a shear sliding strength V_f as (Equation 3.31):

$$V_f = D' t f_{vd} \tag{3.31}$$

where f_{vd} is the masonry shear strength, defined as $f_{vd} = f_{vm0} + 0.4N/D't \leq 0.065f_m$, where f_{vm0} is the mean shear strength in absence of vertical load; N is the applied axial load; D' and t are the depth of the compressed area and the thickness of the pier, respectively; f_m is the mean compressive strength. The ultimate drift corresponding to the shear is assumed as 0.004 H_0/D (where D and H_0 are the depth of the pier and the distance between the section where the flexural capacity is attained and the contra flexure point).

In ASCE 41 the ultimate bed-joint sliding strength V_{bjs} (Equation 3.33) is given by the expected bed-joint sliding shear stress v_{me} (Equation 3.32):

$$v_{me} = \frac{0.75\left(0.75v_{te} + \frac{P_{CE}}{A_n}\right)}{1.5} \tag{3.32}$$

$$V_{bjs} = v_{me}A_n \tag{3.33}$$

where v_{te} is the mean shear strength of mortar joints, from the in-place testing, and P_{CE} and A_n are the expected vertical axial compressive force and the section net area of the pier. The piers ultimate horizontal displacement for shear sliding is assumed as $\delta_u = 0.0075h_{eff}$.

New Zealand guidelines (NZSEE 2017b) define the maximum probable sliding shear strength V_s as (Equation 3.34):

$$V_s = 0.7\left(t_{nom}L_w c + \mu_f(P + P_w)\right) \tag{3.34}$$

where t_{nom} and L_w are the nominal thickness and the length of the pier, respectively; c is the masonry bed-joint cohesion; μ_f is the masonry coefficient of friction; P and P_w are the superimposed and the dead load on the top of the pier and its self-weight on the sliding plane considered. It is recommended to limit the lateral drift in case of shear sliding crisis at 0.003.

Italian code (NTC 2018) and Eurocode 8 (EN1998 2005) consider, for new buildings, a friction sliding shear strength V_t defined by (Equation 3.35):

$$V_t = l't f_{vd} \tag{3.35}$$

where l' and t are the depth of the compressed area and the thickness of the pier, respectively; f_{vd} is the masonry shear strength defined as $f_{vd} = f_{vm0} + 0.4\sigma_n$, where f_{vm0} is the mean shear strength in absence of vertical load and σ_n is the axial compressive stress.

The ultimate displacement at Collapse Limit State (CLS) corresponding to the sliding shear failure is assumed as 0.005. In the case of static non-linear analysis, the ultimate displacement at Ultimate Limit State (ULS) can be assumed as ¾ of the displacement at CLS.

3.3.3 Spandrel behaviour

With respect to the several theories and experimental investigations developed for the masonry piers, for URM spandrels there is a lack of knowledge and the experimental studies are rather few and recent (Gattesco *et al*., 2008; Dazio and Beyer, 2010; Augenti *et al*., 2011; Beyer and Dazio, 2012; Graziotti *et al*., 2012; Parisi *et al*., 2014; Knox *et al*., 2017). Despite the recognized fundamental importance of the spandrel region in the global response of URM structures, as evidenced by the earthquakes damage, little has been done to investigate and understand their non-linear behaviour under lateral actions (Augenti, 2007; Cattari and Lagomarsino, 2008).

Nonetheless, given that the URM existing buildings are typically characterized by a lack of coupled tensile resistant elements (as floor tie beam/rods and lintels) and that if present, the coupling action is difficult to include in simplified structural models, it was common practice to neglect masonry spandrels while modelling the structure. It leads to a severe underestimation of the global strength thus highlighting a rocking failure mode, that results in an unrealistic condition, based on earthquake damage evidences.

Until about a decade ago, it was considered satisfactory to define the capacity of URM structures with reference to simplified approaches that allowed to define an upper and lower bound of global strength, without spandrel modelling (i.e. in NZSEE 2006 and in FEMA 356). More in detail, it was referred to the two following approaches: the “strong spandrel-weak pier” approach, in which the spandrels are assumed as elements with infinite stiffness and strength and the collapse is reached for piers failure and the “weak spandrel-strong pier” approach, where the contribution of the spandrels, in terms of stiffness and strength, is completely neglected, and the piers are considered completely uncoupled. The first approach can be assumed acceptable when resistant elements, as reinforced concrete lintels, tie-beams or reinforced concrete slab, are coupled with spandrels (i.e. in new buildings), guaranteeing a coupling effect between piers. Instead, the second one refers to historical

buildings, typically characterized by flexible (timber) diaphragms, by masonry or timber lintels, hence without any resistant elements coupled to the spandrel.

Furthermore, based on the selected approach ("strong spandrel-weak pier" or weak spandrel-strong pier" one), different boundary conditions on the piers have to be considered, and therefore different strength of the structure will be obtained. In the case of "strong spandrel-weak pier" approach the piers are assumed with fixed-fixed boundary conditions (i.e. their height is the height of the adjacent opening) and the structural strength increases (Cattari and Lagomarsino, 2009); on the contrary, in the "weak spandrel-strong pier" approach the piers assumed the cantilevered condition (i.e. their height is the entire wall height) and the structural strength results as an overestimation of the actual wall strength (Bruneau, 1994).

Both these approaches, although easy to apply, are inappropriate to represent the behaviour of existing URM structures, because the actual response is usually positioned in an intermediate condition between them.

In Figure 3.11, a schematization of the responses of a URM structure subjected to lateral loads, considering different levels of coupling provided by spandrels, is shown.

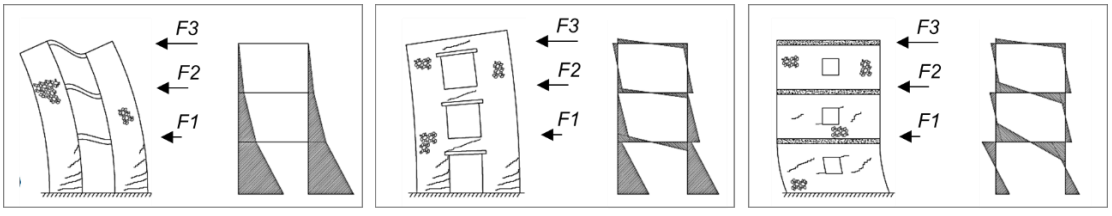

Figure 3.11. Effect of the different degree of coupling provided on moment distribution by the: (a) weak spandrels; (b) intermediate spandrels; (c) strong spandrels (adapted from Tomaževič, 1999).

Other inconsistent approach consists in considering the experimental results of piers to model spandrels as piers rotated to 90 degrees, with the same failure criteria. This assumption was for example adopted by the previous Italian code (NTC 08), in which the spandrels contribution to the global response depends on the fact that the acting axial load was known or not. In detail, if it was known, the spandrel behaviour was assimilated to the piers behaviour. If the axial load was unknown, the coupling of the spandrel with any tensile resistant element was taken into account. In particular, if the spandrel was coupled with tie-

rods or reinforced concrete beam, an equivalent strut response can be assumed, if not, the strength associated with the rocking mechanism is zero. Considering that generally the spandrel axial load is unknown, and when it is known it is typically low, it was stated that the rocking failure occurs generally first than the diagonal cracking failure, contrarily to what is highlighted by the seismic damage evidences.

Therefore, to fill this important lack of knowledge, thus understanding the spandrel influence on the global response of buildings, analysing their behaviour and their coupling role, some recent researches have been developed and some experimental campaigns have been carried out (Benedetti and Magenes, 2001; Yi *et al*., 2006; Gattesco *et al*., 2008; Dazio and Beyer 2010; Dizhur *et al*., 2010; Augenti *et al*., 2011; Beyer and Dazio, 2012; Graziotti *et al*., 2012; Parisi *et al*., 2014; Knox *et al*., 2017).

From seismic damage observations and experimental investigations, it has been stressed that the possible failure mechanisms of the spandrels are the flexural and the shear modes (Figure 3.12). In detail, for the first typology of failure, the rocking mode is the most observed (in particular on the top floor in the buildings), instead, the toe-crushing is very rare to find. For the second typology of failure, the diagonal cracking mode is expected to occur in the spandrels subjected to medium-high axial load (at mid-storeys), instead, the bed-joint sliding failure is avoided thanks to the interlocking phenomena at the interface between spandrels end-sections and the contiguous masonry (Cattari and Lagomarsino, 2008).

Figure 3.12. Some examples of earthquake damage in existing unreinforced masonry buildings (Cattari and Lagomarsino, 2008).

As aforementioned, in the common practice, for many years, the capacity strength of the spandrels has been defined as the one of the piers, hence the rocking failure was reached when the failure at compressed corners was reached and it was defined neglecting the

masonry tensile strength. Instead, the diagonal cracking failure was defined according to Mann and Müller (1973) or Turnšek and Čačovič (1971).

Regarding the flexural response, a strength approach finalized to the definition of this behaviour has been proposed in the FEMA 306 and then refined in a more recent research study (Cattari and Lagomarsino, 2008). It is based on the bricks interlocking phenomena at the end-sections with the contiguous masonry, thanks to which a response as “equivalent strut” has been shown by the spandrel that results characterized by an “equivalent” tensile strength.

As research studies move forward, national and international building codes are trying to accordingly update. In detail, in the Italian code (NTC 2018) and Eurocode 8 (EN1998 2005) it is specified that if a spandrel is coupled by an effective lintel or by tie-rods, it can be assumed as a pier rotated by 90 degrees. This, in particular, is specified in NTC 2018 in case the horizontal axial load is known; otherwise, an equivalent strut is assumed (if a coupled tensile resistant element is present), and the shear strength depends on the cohesion. In absence of any resistant element coupled to the spandrel, the bricks interlocking phenomena at the end-sections with the contiguous masonry can be considered (FEMA 306; Cattari and Lagomarsino, 2008) to avoid an excessive underestimation of the flexural capacity.

In the following Sections 3.3.3.1 and 3.3.3.2 are outlined the main formulations of flexural (rocking) and shear (diagonal cracking) strength of the spandrel, derived by research studies and adopted by international codes.

3.3.3.1 Flexural (rocking) failure

The flexural behaviour of the spandrels, due to the generally low values of axial load which usually characterize these elements (in absence of resistant elements), can be described only by the rocking mechanism, considering a very rare occurrence of the crushing one.

FEMA 306, departing from the common practice of assimilating the spandrel to a rotated pier, proposes an evaluation procedure for the analytical definition of the expected moment capacity of the spandrel, assuming the interlocking between the bed joints and the collar joints at the pier-spandrel interface. Adopting an elastic stress distribution across the end of the spandrel and considering the neutral axis located at the mid-height of the spandrel, the

moment capacity is defined from the tension and the compression resultants derived from the mortar shear strength (see Figure 3.13).

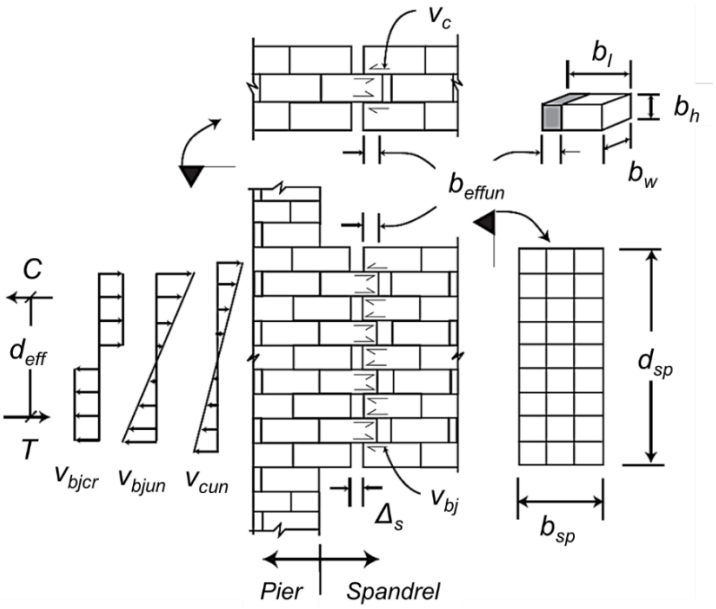

Figure 3.13. Spandrel joint sliding (adapted from FEMA 306).

More in detail, the tensile resulting force T (Equation 3.37) (as well as the corresponding moment M_{spun}, see Equation 3.38) is derived from the bed-joint v_{bjun} and the collar joint shear stresses v_{cun}, obtained by the shear stress v_{un}, reported in Equation 3.36:

$$v_{un} = \frac{0.75\left(0.75v_{te} + \frac{\gamma P_{CE}}{A_n}\right)}{1.5} \tag{3.36}$$

where v_{te} is the mean shear strength of the mortar joints, from in-place testing; P_{CE} and A_n are the expected vertical axial compressive force and the section net area of the adjacent pier, respectively; γ is a coefficient assumed equal to 0.5, if the vertical axial stress on the spandrel is assumed as half of that of adjacent piers, or equal to 0 (if the axial stress on the spandrel collar joints at the end of the spandrel can be neglected).

$$T = \left[v_{bjun} b_w b_{effun} + v_{cun} b_h b_{effun}(NB - 1)\right]\eta \tag{3.37}$$

$$M_{spun} = d_{effun} T \tag{3.38}$$

where b_w and b_h are the width and the height of the brick unit plus the bed joint thickness, respectively; b_{effun} is the effective length of the interface defined as the half-length of the brick unit ($b_l/2$); NB is the number of brick wythes; η is defined as $NR/2$, where NR is the number of bed-joints rows assumed as 0.5 d_{sp}/b_h, with d_{sp} is the depth of the spandrel; d_{effun} is the distance between the tensile and compressive resultant forces assumed as 2/3 d_{sp}.

Although the approach used by FEMA 306 is an innovative approach with respect to the practice of the time, also in this case, the use of simplified models as “strong spandrel-weak pier” type or “weak spandrel-strong pier” type is suggested.

Successively, in Cattari and Lagomarsino (2008) are given the first important indications on the definition of spandrel flexural behaviour. A strength criterion based on the blocks (or bricks) interlocking phenomena at the end-sections with the contiguous masonry is proposed, assuming the development of an “equivalent strut” response by the spandrel and consequently the presence of an “equivalent” tensile strength, that characterized the spandrel element and not the masonry material. Considering a uniform distribution of the tensile and shear stresses (respectively perpendicular to the head joints and on the bed joints) and neglecting the head joints mechanical properties, the “equivalent” tensile strength f_{tu} can be obtained by the minimum values of the strength obtained from the two failure mechanisms described in Figure 3.14:

a') the *(brittle) tensile failure of the block*. It occurs when, in a reference volume at the end-sections interface, the horizontal stress σ_x reaches the tensile strength of the block f_{bt} (Equation 3.39):

$$f_{tu,a'} = \sigma_x = \frac{f_{bt}}{2} \tag{3.39}$$

b') the *(ductile) shear failure of the horizontal mortar joints*. Assuming no-stresses developed in the head joints and a Mohr-Coulomb approach, in which the cohesion of the bed joints is neglected, the shear strength (see Equation 3.40) is strongly dependent on: the compressive stress σ_y acting at the spandrel end-section (assumed as 65% of the mean compression stress acting on the adjacent pier section), the friction coefficient μ and the interlocking parameter $\varphi = \Delta_x/2\Delta_y$ (where Δ_x and Δ_y are the width and the height of the block):

$$f_{tu,b'} = \frac{\Delta_x}{2\Delta_y}\mu\sigma_y \tag{3.40}$$

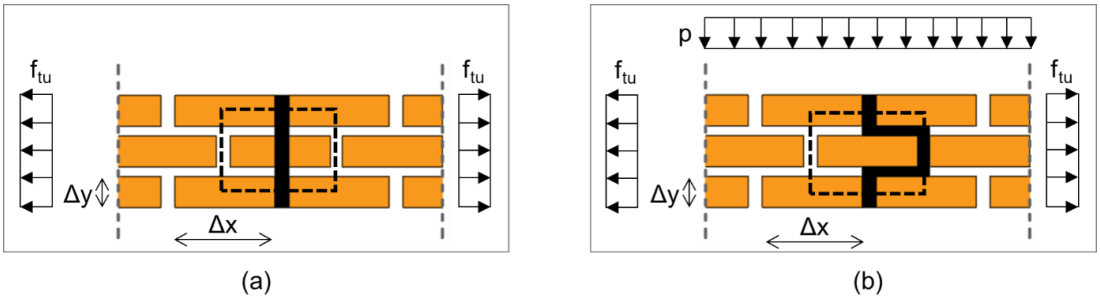

Figure 3.14. Spandrel failure mechanism: (a) tensile failure of the block and (b) shear failure of the horizontal mortar joints (adapted from Cattari and Lagomarsino, 2008).

As highlighted in Cattari and Lagomarsino (2008), the failure of the joints is generally the first failure to occur, principally due to the higher strength of the blocks.

Adopting the aforementioned equivalent tensile strength and the compressive strength of the masonry, and assuming an elastic-perfectly plastic (with limited ductility in tension and compression) constitutive law, the flexural behaviour can be obtained (Cattari, 2007).

To confirm the theoretical basis of the proposed formulation, in Cattari and Lagomarsino (2008) some numerical FE models were performed. It was found that in spandrels with an aspect ratio of $\lambda = 1.35$, at first, the head joints open in tense corners and the damage mechanism activates; only subsequently the "equivalent strut" behaviour, with its typical diagonal cracks from the centre to the corners of the element, has developed. Contrarily, in spandrels with an aspect ratio of $\lambda = 2$, the rocking behaviour occurs, without the formation of any diagonal crack. Furthermore, from parametric analyses, it was found that the adoption of low values of tension ductility or, vice versa, of infinite tension ductility, does not affect significantly the results in terms of the failure domains. For more details refer to Cattari (2007).

Calderoni *et al*. (2011) carried out an experimental campaign to investigate the seismic URM spandrels capacity and studied the failure mechanism for different geometrical aspect ratios. The authors also developed (and validated) an analytical model to define the spandrel capacity, assuming the formation of an "arched strut" along the spandrel diagonal, when it is subjected to lateral loads. Two typologies of spandrel failure are distinguished: i) crushing of

the edges of the panel and ii) tension cracking at the centre of the strut. The corresponding strength (V_{comp} and V_{tens}) are reported in Equations 3.41 and 3.42:

$$V_{comp} = \frac{f'_{mx} b_s c 2e}{L_s} \tag{3.41}$$

$$V_{tens} = \frac{f_{td} b_s sin\alpha 2 L_s^2}{8 f cos^2 \alpha} \tag{3.42}$$

where f'_{mx} is the compressive strength of the masonry in the horizontal direction; c is the effective zone; e is the eccentricity of the axial compressive force; f_{td} is the tensile strength of the masonry along the diagonal direction; α is the angle of inclination of the strut; f is the height of the arched strut. It should be noticed that the spandrel shear capacity adopted in this study is independent of the external forces applied, but is only a function of the geometry of the strut.

Beyer (2012) developed simple analytical mechanical models to estimate the peak and the residual strength of the brick masonry spandrels (supported by a timber lintel or a shallow arch), and then validated them against experimental tests. The flexural peak moment strength $M_{p,fl}$ is estimated from the tensile strength of the head joints (following the Mohr-Coulomb relationship) and from the interlock of the bed joints, assuming a linear stress distribution over the height of the spandrel, see Equation 3.43.

$$M_{p,fl} = \left(f_t + p_{sp}\right) \frac{h_{sp}^2 t_{sp}}{6} \tag{3.43}$$

where f_t is the total equivalent tensile strength of the uncracked masonry spandrel; p_{sp} is the horizontal mean axial stress; h_{sp} and t_{sp} are the height and the thickness of the spandrel. The peak shear strength associated with the formation of cracks through joints $V_{p,s1}$ or through the bricks $V_{p,s2}$ are given respectively by Equations 3.44 and 3.45:

$$V_{p,s1} = \frac{2}{3}\left(c_p + \mu_p p_{sp}\right) h_{sp} t_{sp} \tag{3.44}$$

$$V_{p,s2} = h_{sp} t_{sp} \frac{f'_{bt}}{2.3(1+\alpha_v)} \sqrt{1 + \frac{p_{sp}}{f'_{bt}}} \tag{3.45}$$

where c_p is the cohesion; μ_p is the friction coefficient; f'_{bt} is the tensile strength of the bricks; α_v is the spandrel shear ratio defined as $l_{sp}/2h_{sp}$, where l_{sp} is the length of the spandrel.

The residual strength $V_{p,s2}$ after flexural cracking is considered governed by a diagonal compressed strut in the masonry spandrel, and it is given by Equation 3.46, in which a compressive stress-block distribution is assumed (with a constant stress of 0.85 f_{hm}, where f_{hm} is the horizontal masonry compressive strength).

$$V_{p,s2} = \frac{P_{sp} h_{sp}}{l_{sp}} \left(1 - \frac{p_{sp}}{0.85 f_{hm}}\right) \tag{3.46}$$

The residual strength after shear cracking was not considered when the contribution of a timber lintel or masonry arch is neglected. In this work a FE numerical parametric study for spandrels with different aspect ratios was developed and from this it was stated that the assumptions made by FEMA 306 and Cattari and Lagomarsino (2008) on the mean axial stress at the end of the spandrel as 50% and 65%, respectively, of the vertical compressive stress of the adjacent pier, are consistent with the obtained numerical stress.

Italian code (NTC 2018) defines the maximum spandrel moment M_u, and the corresponding shear strength V_p, associated to the rocking mechanism, in presence of resistant tensile elements coupled to the spandrel, as (Equations 3.47 and 3.48):

$$M_u = H_p \frac{h}{2} \left(1 - \frac{H_p}{0.85 f_{hd} h t}\right) \tag{3.47}$$

$$V_p = \frac{2M_u}{l} \tag{3.48}$$

where h and t are the height and the thickness of the spandrel, respectively; f_{hd} is the design horizontal compressive strength; H_p is the minimum of the tension strength between the tensile resistant element and $0.4 f_{hd} h t$; l is the length of the spandrel. In absence of any resistant element coupled to the spandrel, the bricks interlocking phenomena at the end-sections with the contiguous masonry can be considered (FEMA 306; Cattari and Lagomarsino, 2008).

3.3.3.2 Shear (diagonal cracking) failure

Regarding the shear behaviour of the spandrel, the only mechanism that can occur is the diagonal cracking mechanism, as bed-joint sliding mechanism is prevented by the interlocking phenomena that originated at the spandrel end-sections-contiguous masonry interface.

FEMA 306 identified shear capacity formulation for the spandrel as the diagonal tensile capacity expression for the piers. According to this, the expression for the adopted diagonal tension strength of the spandrel is (Equations 3.49):

$$V_{sps} = f'_{dt} d_{sp} b_{sp} \beta \sqrt{1 + \frac{f_{ae}}{f'_{dt}}} \tag{3.49}$$

where f'_{dt} is the diagonal tension strength; d_{sp} and b_{sp} are the depth and the width of the spandrel, respectively; f_{ae} is the horizontal axial stress in the pier (assumed as 0 if it is unknown); β is a coefficient dependent by the spandrel aspect ratio and in detail it is assumed $\beta = 0.67$ for $L_{sp}/d_{sp} \leq 0.67$; $\beta = L_{sp}/d_{sp}$ for $0.67 \leq L_{sp}/d_{sp} \leq 1.0$ and $\beta = 1.0$ for $L_{sp}/d_{sp} > 1.0$, where L_{sp} is the length of the spandrel.

In Italian code (NTC 2018) the spandrel shear strength in absence of any resistant element can be calculated according to Equation 3.50:

$$V_t = h t f_{vd0} \tag{3.50}$$

where f_{vd0} is the design masonry shear strength in absence of vertical load.

Parisi *et al*. (2011) investigate the in-plane response of URM walls with openings, before and after the strengthening of the spandrels with an inorganic matrix-grid. In this study, the numerical results were compared with the experimental ones and an analytical model was presented. More in detail, for analysing the strengthened walls, the study started from the unreinforced configurations, and the nominal lateral strength corresponding to the toe-crushing mode V_p was evaluated, according to the stress-block criterion, according to Equation 3.51:

$$V_p = \frac{h}{l}(1 - \overline{N_d})N_d \tag{3.51}$$

where h and l are the length and the height of the spandrel, respectively; N_d is the applied axial force; $\overline{N_d}$ is the same value normalized to the ultimate axial force N_u (assumed as $N_u = f_{d,m} h t_m$, where $f_{d,m}$ is the masonry compressive strength and t_m is the spandrel thickness). The nominal lateral strength corresponding to the diagonal tension cracking mode V_t was evaluated according to the Turnšek and Čačovič (1971) yield criterion, as (Equation 3.52):

$$V_t = \beta N_u \sqrt{1 + \frac{\overline{N_d}}{p\beta}} \tag{3.52}$$

where β is the ratio between the diagonal tensile strength at zero compression and the masonry uniaxial compressive strength; p is the shear stress distribution factor related to the aspect ratio of the panel. The nominal lateral strength corresponding to the stair-stepped diagonal sliding mode V_{sd} was evaluated according to the Mohr-Coulomb friction law, following Equation 3.53:

$$V_{sd} = \frac{1}{p}(\gamma + \mu_a \overline{N_d}) N_u \tag{3.53}$$

where γ is the ratio between the shear sliding strength at zero confining stress and the masonry uniaxial compressive strength; μ_a is the masonry fictitious friction coefficient (assumed as 0.4 in Eurocode 6 (EN1996 2006) and NTC 2008).

3.4 References

Abrams, D. P. (1992). Strength and behavior of unreinforced masonry elements. Proceedings of Tenth World Conference on Earthquake Engineering.

Abrams, D.P. (2001). Performance-based Engineering Concepts for Unreinforced Masonry Building Structures. Progress in Structural Engineering and Materials 3. p. 48–56.

Andreas, U. (1996). Failure Criteria for Masonry Panels under In-plane Loading. Journal of structural engineering ASCE 122(1). p. 37–46.

Anthoine, A., G. Magonette and G. Magenes. (1994). Shear compression testing and analysis of brick masonry walls, Proceedings of the 10th European Conference on Earthquake Engineering, Vienna, Austria.

ASCE/SEI 41-06. (2000). Pre-standard and Commentary for the Seismic Rehabilitation of Buildings, FEMA 356, American Society of Civil Engineers, Washington D.C, United States.

Augenti, N. (2007). Resistenza delle fasce di piano di edifici in muratura sollecitate da azioni sismiche. Proceedings of the 12th Italian National Conference on Earthquake Engineering, Pisa, Italy, Paper No. 7 (in Italian).

Augenti, N., Parisi, F., Prota, A., Manfredi, G. (2011). In-plane lateral response of a full-scale masonry sub-assemblage with and without an inorganic matrix-grid strengthening system. Journal of Composites for Construction 15:4, 578-590.

Benedetti D. and Petrini V. (1984). On the seismic vulnerability of masonry buildings: Proposal of an evaluation procedure. L'Industria Italiana delle Costruzioni, No. 149, pp. 66-78.

Benedetti, D. and G. Magenes. (2001). Correlazione tra tipo di danno ed energia dissipata negli edifici in muratura, Ingegneria Sismica, 2(In Italian),53-62.

Benedetti, D. and M. Tomaževič. (1984). Sulla verifica sismica di costruzioni in muratura (on the seismic assessment of masonry structures), Ingegneria Sismica, 1(0),9-16 (In Italian).

Bernardini A., Gori R., Modena C. (1990). Application of Coupled Analytical Models and Experiential Knowledge to Seismic Vulnerability Analyses of Masonry Buildings. Earthquake Damage Evaluation and Vulnerability Analysis of Buildings Structures.

Beyer, K. (2012). Peak and residual strengths of brick masonry spandrels. Eng. Struct., 41, 533-547.

Beyer, K. and Dazio, A. (2012). Quasi-static cyclic tests on masonry spandrels. Earthq. Spectra 28:907–929.

Bosiljkov, V., Page, A., Bokan-Bosiljkov, V., & Žarnić, R. (2003). Performance based studies of in-plane loaded unreinforced masonry walls. British Masonry Society.

Brun S., Giovinazzi S., Idri C., Lagomarsino S., Penna A., Podestà S., Resemini S., Rossi B. (1999). Models for the assessment of seismic retrofit of churches. IX Convegno Nazionale "L'ingegneria Sismica in Italia", ANIDIS, Torino, Italy, September.

Bruneau, M. (1994). Seismic evaluation of unreinforced masonry buildings - a state-of-the-art report, Canadian Journal of Civil Engineering, 21(3),512539.

Calderini, C., Cattari, S., and Lagomarsino, S. (2009). In-plane strength of unreinforced masonry piers. Earthquake engineering & structural dynamics, 38(2), 243-267.

Calderini, C., Cattari S., and Lagomarsino S. (2010). The use of the diagonal compression test to identify the shear mechanical parameters of masonry. Constr. and build. Mater. 24.5: 677-685.

Calderoni, B., E.A. Cordasco, P. Lenza and G. Pacella. (2011). A simplified theoretical model for the evaluation of structural behaviour of masonry spandrels, International journal of Structural Integrity, 5(2/3),192-214.

Cattari S. (2007). Modellazione a telaio equivalente di strutture esistenti in muratura e miste muratura-c.a.: formulazione di modelli sintetici. Ph.D. Dissertation (in Italian), University of Genoa, Italy.

Cattari, S. and S. Lagomarsino. (2008). A Strength criterion for the flexural behaviour of spandrels in unreinforced masonry walls, The 14th World Conference on Earthquake Engineering, Beijing.

Cattari, S. and S. Lagomarsino. (2009). Modelling the seismic response of unreinforced existing masonry buildings: A critical review of some models proposed by codes, 11th Canadian Masonry Symposium, Toronto, Canada.

CNTC19 (2019). Circolare applicativa delle Norme Tecniche delle Costruzioni di cui al DM 17/01/2018. (NTC 2018). Italy: Gazzetta Ufficiale N.42 del 20/02/218. Ministero delle Infrastrutture e dei Trasporti. (in Italian).

Dazio, A., Beyer, K. (2010). Seismic behaviour of different types of masonry spandrles, 14th European Conference on Eathquake Engineering, Ohrid, FYROM, 30 August - 3 September 2010.

D'Ayala D., Speranza E. (1999a). Identificazione dei meccanismi di collasso per la stima della vulnerabilità sismica di edifici nei centri storici. IX Convegno ANIDIS, Torino, Italy.

D'Ayala D. (1999b). Correlation of seismic vulnerability and damages between classes of buildings: Churches and houses, in Seismic Damage to Masonry Buildings. Balkema, Rotterdam, pp. 41-58.

D'Ayala D., Speranza E. (2003a). Definition of collapse mechanisms and seismic vulnerability of historic masonry buildings. Earthquake Spectra, No. 19, pp. 479-509.

de Felice, G., & Giannini, R. (2001). Out-of-plane seismic resistance of masonry walls. Journal of earthquake engineering, 5(02), 253-271.

Dizhur, D., N. Ismail, C. Knox, R. Lumantarna and J.M. Ingham. (2010). Performance of Unreinforced and Retrofitted Masonry Buildings During the 2010 Darfield Earthquake, New Zealand Society for Earthquake Engineering Bulletin, 43(4),321-339.

Dolce, M. (1991). Schematizzazione e modellazione degli edifici in muratura soggetti ad azioni sismiche. L'Industria delle Costruzioni, 25:44-57 (in Italian).

EN 1996 (European Committee for Standardization). (2006). Design of masonry structures - Part 1-1: General rules for reinforced and unreinforced masonry structures. Eurocode 6: EN.

EN 1998 (European Committee for Standardization). (2005). Design of structures for earthquake resistance - Part 3: Assessment and retrofitting of buildings. Eurocode 8, Brussels, Belgium: EN.

FEMA 273 (Federal Emergency Management Agency). (1997). NEHRP Guidelines for the Seismic Rehabilitation of Buildings. Washington DC, US:FEMA.

FEMA 306 (Federal Emergency Management Agency). (1998). Evaluation of earthquake damaged concrete and masonry wall buildings: Basic procedures manual. Washington DC, US:FEMA.

Frumento S, Magenes G, Morandi P, Calvi GM (2009). Interpretation of experimental shear test on clay brick masonry walls and evaluation of q-factors for seismic design. Eucentre Research Repor 2009/02. IUSS Press, Pavia, Italy.

Gattesco, N., Clemente I., Macorini L., Noè S. (2008). Experimental investigation of the behaviour of spandrels in ancient masonry buildings, Proc. of the 14th WCEE, Beijing, China.

Giuffrè A. (1993). Sicurezza e conservazione dei centri storici in area sismica, il caso Ortigia. Laterza, Bari, Italy.

Giuffrè A., Carocci C. (1997). Codice di Pratica per la sicurezza e la conservazione dei Sassi di Matera. La Bautta, Matera, Italy.

Graziotti, F., Magenes, G. and Penna, A. (2012). Experimental cyclic behaviour of stone masonry spandrels. Proc. of the 15th WCEE 24–28.

Housner G.W. (1963). The Behavior of inverted Pendulum Structures during Earthquakes. Bulletin of the Seismological Society of America, 53(2):403–417.

Karantoni F., Bouckovalas G. (1997). Description and analysis of building damage due to Pyrgos, Greece earthquake. Soil Dynamics. Earthquake Engineering., No. 16, pp. 141-150.

Knox, C.L., Dizhur, D. and Ingham, J.M. (2017). Experimental cyclic testing of URM pier-spandrel substructures. J. Struct. Eng. 143:04016177.

Lagomarsino, S., Penna, A., Galasco, A. and Cattari, S. (2013). TREMURI program: an equivalent frame model for the nonlinear seismic analysis of masonry buildings. Eng. Struct. 56:1787–1799.

Lourenço, P. B., Oliveira, D. V., Roca, P., & Orduña, A. (2005). Dry joint stone masonry walls subjected to in-plane combined loading. Journal of Structural Engineering, 131(11), 1665-1673.

Magenes, G. (2010). Earthquake resistant design of masonry structures: rules, backgrounds, latest findings. In 8th International Masonry Conference (pp. 1-15).

Magenes, G., & Calvi, G. M. (1992). Cyclic behaviour of brick masonry walls. In Proceedings of the 10th world conference on earthquake engineering (pp. 3517-3522).

Magenes, G and Calvi, G.M. (1997). In-plane Seismic Response of Brick Masonry Walls. Earthquake engineering and structural dynamics 26. p. 1091-1112.

Mann, W. and R. Müller. (1973). Bruchkriterien fur querkraftbeanspruchtes Mauerwerk und ihre Anwendung auf gemauerte Windscheiben, Die Bautechnik, 50, pp421-425.

Mann, Ing W., and Ing H. Müller. (1979). IV-3. Cracking Characteristics of Transversely Loaded Brick Masonry in Theory and Practice.

Marzahn, G. (1998). The Shear Strength of Dry-Stacked Masonry Walls. Leipzig Annual Civil Engineering Report, Institut f¨ur Massivbau und Baustofftechnologie, Wirtschaftswissenschaftliche Fakultät, Universität Leipzig.

Mayes, R. L., and Clough, R. W. (1975a). State-of-the-art in seismic shear strength of masonry - An evaluation and review. Dept. No. EERC 75-21, Univ. of California, Berkeley, Calif., Oct.

Mayes, R. L., and Clough, R. W. (1975b). A literature survey—Compressive, tensile, bond and shear strength of masonry. Rept. No. EERC 75-13, Univ. of California, Berkeley, Calif., June.

Modena C., Valluzzi M.R., Binda L., Cardani G., Saisi A. (2004a). Vulnerability of historical centres in seismic area: reliability of assessment methods for different building typologies. XIII International Brick and Block Masonry Conference, Amsterdam, Netherland, 4-7July.

Munari M., Valluzzi M.R., Saisi A., Cardani G., Modena C., Binda L. (2009). The limit analysis of macro-elements in masonry aggregate buildings as a methodology for the seismic vulnerability study: an application to umbrian city centers. XI Canadian Mas. Symposium., Toronto, pp. 1-10.

NTC (Norme Tecniche per le Costruzioni). (2008). Norme Tecniche per le Costruzioni. Decreto ministeriale del 14 gennaio 2008. Rome: Ministero delle Infrastrutture e dei Trasporti. (in Italian).

NTC (Norme Tecniche per le Costruzioni). (2018). Aggiornamento delle Norme Tecniche per le Costruzioni. Decreto ministeriale del 17 gennaio 2018. Rome: Ministero delle Infrastrutture e dei Trasporti. (in Italian).

NZSEE (New Zealand Society for Earthquake Engineering). (2017b). The Seismic Assessment of Existing Buildings: Part C8, Unreinforced Masonry Buildings, Technical Guidelines for Engineering Assessments. Wellington: NZSEE.

Parisi, F., G.P. Lignola, N. Augenti, A. Prota and G. Manfredi. (2011). Nonlinear behaviour of a masonry sub-assemblage before and after strengthening with inorganic matrix-grid composites, ASCE Journal of Composites for Construction, 15(5),821-832.

Parisi, F., Augenti, N. and Prota, A. (2014). Implications of the spandrel type on the lateral behavior of unreinforced masonry walls. Earthq. Eng. Struct. Dyn. 43:1867–1887.

Rota, M., Penna, A., Strobbia, C., and Magenes, G. (2011). Typological seismic risk maps for Italy. Earthq. Spect. 27(3):907–926

Tomaževič, M. (1999). Earthquake-Resistant Design of Masonry Buildings. Imperial College Press.

Tomaževič M., Klemenc I., Lutman M. (1999). Seismic behavior of masonry buildings. Lesson from the Bovec earthquake of April 12, 1998. VIII Canadian Conf. of Earthq. Eng., Vancouver, Canada.

Turnšek, V. and F. Čačovič (1971). Some experimental results on the strength of brick masonry walls, Proceedings of the 2nd International Brick Masonry Conference, Stoke-on-Trent.

Vasconcelos G (1995). Experimental investigations on the mechanics of stone masonry: characterization of granites and behaviour of ancient masonry shear walls. Ph.D. Thesis, University of Minho, Portugal.

Vasconcelos G, Lourenço PB. (2006). Assessment of the in-plane shear strength of stone masonry walls by simplified models. V International Seminar on SAHC06, New Delhi, India, pp. 843-850.

Vasconcelos, G., & Lourenço, P. B. (2009). Experimental characterization of stone masonry in shear and compression. Construction and Building materials, 23(11), 3337-3345.

Yi, T., F.L. Moon, R.T. Leon and L.F. Kahn. (2006). Analyses of a two-storey unreinforced masonry building, J. Struct. Eng., ASCE, 132(5),653-661.

Yi, T., F.L. Moon, R.T. Leon and L.F. Kahn. (2006). Lateral Load Tests on a Two-Storey Unreinforced Masonry Building, Journal of Structural Engineering, 132(5),643-652.

4. Performance assessment and seismic retrofit of URM structures

4.1 Introduction

In recent decades, in the field of earthquake engineering, the characterization of the behaviour of a structure has become increasingly important. More in detail, from prescriptive design approaches we have progressively moved towards performance approaches. The former are based mainly on the structure safety check against the design actions while the latter aim to a broader and articulated estimate not only of the structure demand but also of its capacity, in order to consider all the critical situations that may affect it. Furthermore, in these new strategies, an additional criterion has become increasingly important in recent years, i.e. the economic evaluation of the structure expected performance. More in detail, the characterization of the structural behaviour towards the various considered seismic intensities, allows to correlate from an economic point of view the performance of the building to the expected seismic events and to the expected level of damage.

The same criteria can be adopted in the decision-making process to establish the more suitable and effective retrofit preventive intervention. Indeed, damage evidence after past earthquakes, showed that many existing buildings do not withstand seismic load without collapse or with moderate damage and hence most of them need preventive intervention. When dealing with the retrofitting of structures, the choice of the best solution is crucial, and several criteria have to be considered.

In the following Sections, after a brief discussion of the performance design evolution of the structures (Section 4.2), the main methods to define the seismic performance in terms of ultimate strength are reported (Section 4.3). Then, the fundamental concepts underlying the estimate of the expected economic losses for constructions are discussed (Section 4.4). Finally, the main retrofit intervention strategies and techniques that can be adopted in the existing URM structures are described (Section 4.5).

4.2 Seismic risk assessment of existing structures

Seismicity indicates the frequency and strength with which earthquakes occur, and it represents a physical feature of the site. By knowing the frequency and energy associated with the earthquakes that characterize a site, and by attributing a value of probability to the occurrence of a seismic event of a given magnitude in a certain time interval, it is possible to define the seismic hazard. The higher this value is, the more likely it is that an earthquake of that magnitude will occur in the same time interval. The consequences of an earthquake depend on the characteristics of a building in terms of resistance to the actions of a seismic shock. The predisposition of a building to be damaged is defined as vulnerability. The more a building is vulnerable (by type, inadequate design, poor quality of materials and methods of construction, poor maintenance), the greater the consequences. At last, another important definition is the exposure and it regards the greater or lesser presence of assets exposed to risk, the possibility to suffer economic damage, to cultural assets, the loss of human life.

The seismic risk is determined by the combination of these three components: hazard, vulnerability and exposure. It is a measure of the expected damage in a given time interval, according to the type of seismicity, of buildings resistance and of nature, quality and quantity of the involved assets.

After the strong and important earthquakes of the past, the need for an effective method of estimating and predicting the response of the buildings, when subjected to seismic force, has become evident under the essential requirements of life safety. An important support was given by research studies developed in earthquake-risk areas in the world, like USA, New Zealand, Japan and Europe. Hence, the best seismic assessment standards or guidelines, like FEMA 356, ATC 40, ASCE/SEI 41-06, EN 1998 (2005), NZSEE 2017 and NTC 2018 have been written in that high seismic risk regions.

From that moment, the importance to evaluate the seismic risk of the existing building heritage, mostly designed with codes prior to the seismic ones, played a fundamental role, aiming especially to obtain a territorial-scale seismic prevention plan.

The development of innovative design techniques was starting by the American FEMA 273 and FEMA 356 and within the Vision 2000 project (SEAOC, 1995). Generally speaking, these new strategies have introduced the evaluation of a building behavior through the

analysis of its performance by varying the considered input, in such a way to be able to design the structure according to the level of needed global performance.

In order to characterize these aspects in a more synthetic and meaningful way, levels of significant damage of the structure have been defined, i.e. the Limit States. In particular have been identified Exercise Limit States (ELS), which refer to the most frequent conditions for the structure, both in terms of seismic action and of allowed damage, and Ultimate Limit States (ULS), which instead concern the performance of the structure near the collapse.

In the context of seismic design, for example, in Italian Code (NTC 2018) among the ELS are identified the Operation Limit State (OLS) and the Damage Limit State (DLS), while the Ultimate Limit States are divided into Life Safety Limit State (VLS) and Collapse Prevention Limit State (CLS). Similarly in other codes, for example in FEMA 274, are set states of Immediate Occupancy (IO), Life Safety (LS) and Collapse Prevention (CP). Even if the DLS is not considered in FEMA 274, it is specified that in the initial part of a structural behavior the design must be carried out under damage control conditions. While starting from LS state, the construction must be designed within the view of human life safety.

Practically, design becomes an iterative process that needs to verify that the performance associated with the aforementioned Limit States are achieved after seismic events with a fixed occurrence frequency, thus relating the probability of reaching a Limit State by the structure with the probability exceeding the corresponding intensity of the considered seismic action.

This methodology is defined Performance-Based Earthquake Engineering (PBEE). The Vision 2000 document (SEAOC, 1995) identifies and schematizes in a simple matrix the performance objectives (Figure 4.1). More in detail, the fully operational, operational, life safety and near collapse performance states, are expressed in terms of expected structural and non-structural damage as well as post-event effects in terms of operability and repairs as well as four intensity levels defined in terms of their return period: frequent (50% in 30 years), occasional (50% in 50 years), rare (10% in 50 years), and very rare (10% in 100 years). It is observed that the different performance levels are coupled with earthquake intensities with respect to the building occupancy. Indeed, improved performance is required for facilities that have a critical function for the community, while the level of acceptable damage increases (or performance reduces) as the seismic intensity increases.

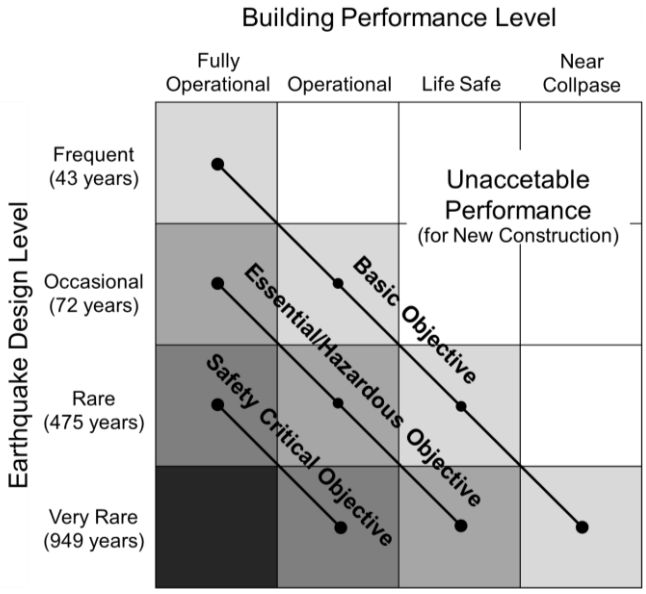

Figure 4.1. Vision 2000 recommended seismic performance objectives (adapted from SEAOC, 1995).

After the Vision 2000 document (SEAOC, 1995), the Federal Emergency Management Agency (FEMA) published the FEMA 273 (1997), FEMA 274 (1997) and FEMA 356 (2000) in which a similar matrix was proposed, but with the focus on the rehabilitation of existing structures rather than on new constructions. Finally, the ASCE/SEI 41-06 was published with quantitative rules and more comprehensive acceptance criteria for both structural and non-structural components. Later, a global performance matrix was proposed by Kam *et al*. (2010). With respect to the original one, this matrix incorporates three measures of performance with both structural and non-structural damage, namely peak inter-storey drift ratio, residual inter-storey drift ratio and peak floor acceleration.

Once recognized the importance of evaluating the seismic risk of existing building heritage, the essential task became to “quantify” the problem, in order to enable owners of earthquake-prone buildings and other stakeholders to decide if a retrofit intervention is required and then to select the most appropriate solution to reduce the seismic vulnerability and consequently the seismic risk to an explicit acceptable level.

To this aim, in New Zealand the seismic performance of existing buildings is assessed using a performance measure that indicates the level of shaking intensity, relative to the design level of a new structure, that would cause the building to reach its Ultimate Limit State (i.e. Life Safety). This measure is termed %NBS, or ‘‘Percentage of New Building Standard’’,

in accordance to NZSEE 2017 and represents the performance indicator to establish whether or not an existing structure has to be retrofitted.

This approach has recently been incorporated into the Italian Code (Ministry Decree n.65 7/03/2017). More in detail, as for the %NBS, the ISV is defined as an indicator of seismic performance and it is given by the relationship between the capacity and the demand, i.e. the performance of an existing building against the standard required for a new one.

According to the %NBS, buildings can be classified as ‘‘earthquake prone’’ (EPB) or high risk (%NBS lower than 33%), moderate risk (%NBS in the range 34-67%) or low risk (%NBS higher than 67%). Hence, on the buildings that cannot withstand (at ULS level) a seismic intensity of one-third of the design one (referred to as ‘‘moderate’’ earthquake, i.e. %NBS < 33%) owners have to intervene. On the contrary, if the %NBS is greater than 33%, no building upgrade is mandatory.

This approach is a simple and clear way to quantify and classify existing building heritage with respect to the seismic vulnerability, however, it could be misleading, as well described in Ligabue *et al*. (2018). Indeed, due to the fact that the %NBS indicator addresses only the shaking intensity associated with the reaching of the Ultimate Limit State (ULS) or Life Safety (LS) Limit State, with the same %NBS can be associated structures with different probabilities of collapse that might undergo different levels of damage, thus leading to different repairing costs when subjected to the same seismic event. Moreover, it is recognized that the level of safety of an existing building retrofitted up to 100%NBS is different from that of a new construction designed according to the current code. This is due to the partial safety coefficients that have to be used in the new building design, to increase the external loads and reduce the mechanical strength.

Another important evidence regards the correlation between the seismic risk and the %NBS. As suggested by NZSEE 2006, this indicator is not linearly correlated to the seismic risk of the building, but an increase of the targeted %NBS would result in a more than proportional reduction of risk (see Figure 4.2a). More in detail, it can be deduced that 33%NBS corresponds to approximately twenty times the risk of the building reaching a similar condition to which a new building would reach in a full design earthquake, and 67%NBS corresponds to a risk of three times.

A peculiar relationship correlates the cost of the retrofit intervention with the performance (%NBS), as shown in Figure 4.2b. More in detail, the cost of the retrofit interventions follows

a step function with the targeted %NBS, so that alternative retrofit techniques can be combined and integrated in order to reach the next level of performance.

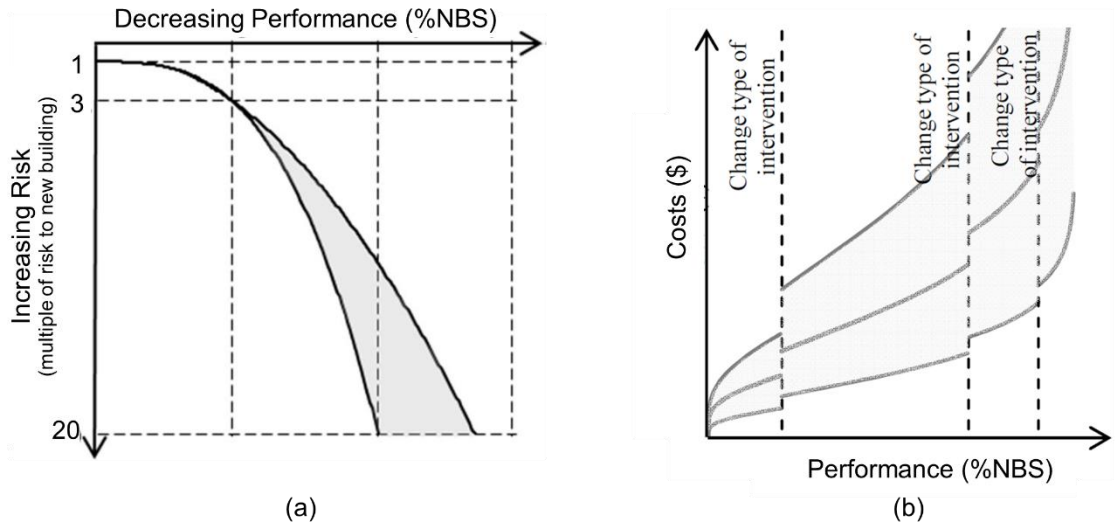

Figure 4.2. (a) Performance (as %NBS) and risk correlation (adapted from NZSEE 2006) and (b) expected retrofit intervention cost as performance function (adapted from Beetham, 2013).

According to the aforementioned reasons, an evaluation of the building performance that relies only on the %NBS is not widely recommended. For more reliable results in terms of the entire seismic performance of existing structures and informed decisions on whether apply an appropriate retrofit solution, another important parameter needs to be considered. The expected direct and indirect losses, hence the expected annual loss (EAL), can be considered an effective addictive parameter of structural performance and could be explicitly included to support the decision-making process of the retrofit intervention. For more details refer to Section 4.4.

4.3 Seismic performance of existing structures

Among the various analysis techniques that can be used to investigate the response of existing structures, such as the linear static, the linear dynamic, the non-linear static and the non-linear dynamic methods, herein the pushover, or non-linear static, analysis is treated. In this method, two different loads are simultaneously applied to the structure: a vertical constant one (due to the gravity) and a varying horizontal one (that defines the seismic

action), which is applied by monotonically increasing the displacement of a specific node (called control node) of the structure. The horizontal forces are modelled as acting on the centre of mass of each floor and their distribution does not change while the displacement increases (Figure 4.3). The application of the lateral forces induces inelastic deformation in the building components and this non-linear response needs to be taken into account while mathematically modelling the Pushover analysis. As a result, the Pushover analysis is translated in the capacity curve which combines the total base shear experienced by the structure with the displacement of the control node.

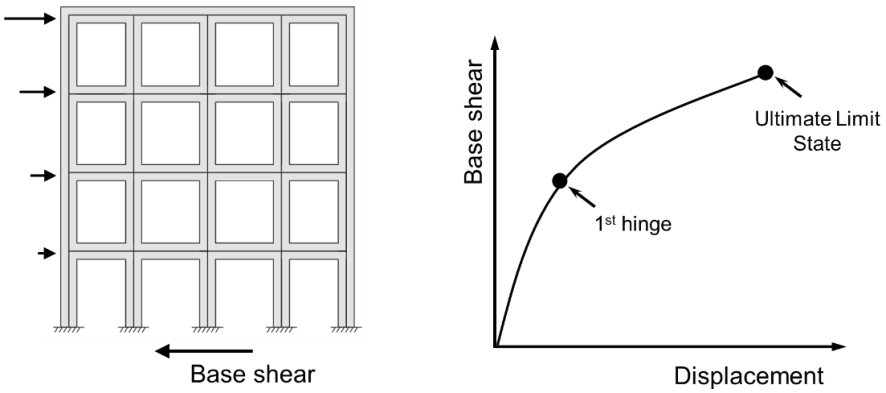

Figure 4.3. Non-linear static (or Pushover) analysis.

The main limitations of the Pushover analysis are summarized in the following:

- the distribution of the lateral forces often depends only on the first mode of the building, thus it is improbable to correctly identify the collapse mechanism due to higher modes;
- the distribution of the lateral forces applied does not vary with the displacement, hence the changes in inertial forces cannot be considered. These changes arise from damages in the structural elements that induce modification in the local stiffness.

This first limitation can be faced in two different ways: by implementing the Modal Response Spectrum Analysis of the building as a force that is proportional to the storey shear distribution, or by using a sequential Pushover analysis for the different modes of the building and then combining the results as suggested by Goel and Chopra (2004). Both these methods, however, are based on elastic modal properties and do not allow to evaluate in a proper way the effects of the higher modes. As a consequence, they give misleading results in the non-linear range of building response. The second limitation can be overcome

by using modified procedures available in literature, such as the one proposed by Antoniou and Pinho (2004), that allows changing the force vector, in an adaptive way, with respect to the damage-induced redistribution of loadings in the structure.

Following the nonlinear static procedures, once the nonlinear static pushover analysis of the multiple-degree-of-freedom (MDOF) structural system has been performed, the pushover curve is transformed into the capacity curve of an equivalent single-degree-of-freedom (SDOF) oscillator. Then, the seismic performance of the building can be defined within an ADRS (Acceleration-Displacement Response Spectrum) diagram. These steps are generally done with specific methods and among them, the most commonly used are: the Capacity Spectrum method (proposed in ASCE 41-13), the N2 method (presented in EN1998 2005) and the Displacement-Based method (proposed in NZSEE 2017). In the following is reported a brief comparison between them. For more details on these methods refer to Gentile (2017).

Capacity Spectrum Method (CSM) – ASCE 41-13

The capacity spectrum obtained through this method consists of a bi-linear curve with an initial linear part that is inelastic and with stiffness ratio, followed by an elastic linear part that is tangent to the refined curve at the origin. By imposing the equality between the area beneath the obtained curve and the refined one, an equivalent yield displacement can be obtained. This idealization, however, can lead to an under-prediction of the real equivalent yield displacement if the first cracking of the element is explicitly inserted in the characterization. For this reason the main concept on which the CSM relies on is that the SDOF oscillator is characterized starting from the secant stiffness through the performance point in place of the tangent one. Moreover this procedure is capable to deal with three different hysteretic behaviours that refer to: structures which have full hysteresis cycles, structures with pronounced degradation in strength and stiffness or an intermediate condition.

N2 method – EN 1998 (2005)

The N2 method was developed by Fajfar and Fischinger (1988). It starts by defining the SDOF system response with respect to the first modal shape in the chosen direction of the analysis. The basic requirement of this procedure is an elastic-perfectly plastic bi-linear idealization of the capacity curve. The procedure considers the two possible responses of the system: elastic and inelastic. This latter is solved by means of equal-displacement or equal-energy rule, with respect to the period of the structure. Safety verifications can be conducted

by using the local deformation demand of the structural elements which corresponds to the global displacement.

Displacement-Based Assessment - NZSEE 2017

The Displacement-Based Assessment (Priestley, 1997) is the Pushover analysis method implemented in NZSEE 2017. This procedure deals with the characterization of the secant properties of the equivalent SDOF system by giving a certain global displacement. The final result of the procedure is the evaluation of the Percentage of New Building Standard (%NBS): a value that compares the expected building capacity with the minimum required for a new structure according to the Building Code. In this procedure, the Pushover analysis is carried out and the capacity curve is cut off at the Ultimate Limit State (ULS) point that is reached when some structural elements collapse, thus provoking a life safety issue.

In Figure 4.4 a qualitative comparison among the seismic assessment results with the three methods discussed so far (CSM, N2 and DBA) is reported. Generally speaking, the outcome may considerably vary with respect to the adopted procedure.

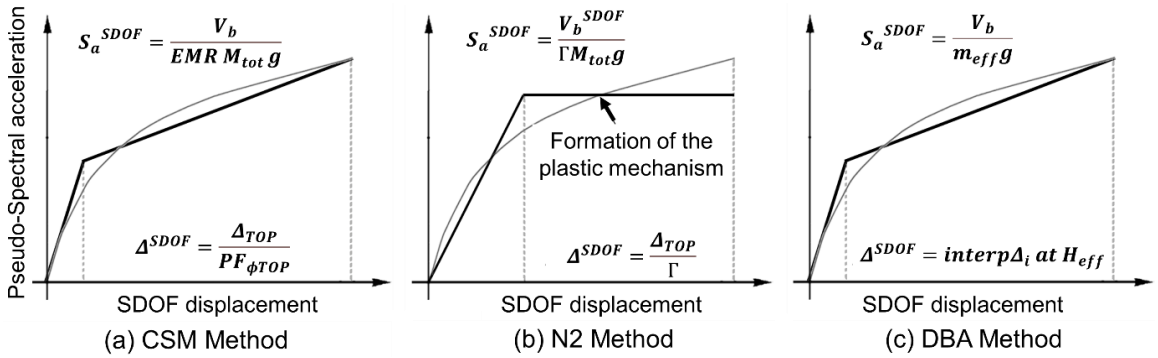

Figure 4.4. Characterization of the SDOF response in the (a) CSM, (b) N2 and (c) DBA methods (adapted from Gentile, 2017).

The CSM and the DBA methods suggest the same methodology: to define an elastic curve with hardening that ends at the ULS point. On the contrary, the N2 method uses a bi-linearization methodology that yields an elastic-perfectly plastic curve more focused on the base shear plastic mechanism, i.e. the initial stiffness. Moreover, the N2 method is the only one that really needs a bi-linearization procedure, while the others can be applied also to the original refined curve.

More in detail, in the CSM and the DBA methods the equivalent SDOF system is generated with respect to the secant to the ULS stiffness and the equivalent viscous damping (EVD) which is related to the actual ductility demand. Therefore the seismic demand, with respect to the elastic one, is proportionally reduced through the EVD of the system. A difference among CSM and DBA methods resides in the adopted parameters which are calibrated in different ways. In the N2 method, instead, the same SDOF system is characterized starting from the initial elastic stiffness and the displacement demand is calculated from the 5%-damped spectrum. Therefore an equal-displacement rule (that depends on the assumed behaviour factor) is used to obtain the expected inelastic demand. In the choice among the equal-displacement or equal-energy rules resides the major weakness of the N2 method since these approximations are valid only for a limited number of hysteresis cycles. As a consequence, the CSM and DBA methods are more rational with respect to the N2 method, since the use of the secant properties to characterize the SDOF system allows to better capture the overall structural behaviour. In Guerrini *et al.* (2017) are highlighted the limits of the aforementioned methods (N2 in particular) for structures with a low vibration period and some possible corrections are provided.

4.4 Losses assessment

Among the performance-based earthquake engineering (PBEE) methodologies, a risk assessment framework was proposed by the Pacific Earthquake Engineering Research (PEER) Centre and it is summarized in Porter (2003). In this approach, it is suggested to consider some aspects correlated with economic losses, that were never considered before in the analysis of a structure subjected to an earthquake event. Among them, three broad categories can be identified: i) the losses of human lives (“Deaths”), ii) direct economic losses (“Dollars”) due to building damage and any repairs/demolitions needed afterword, and iii) the losses due to periods of inactivity, and therefore to lost earnings, that follow seismic events (“Downtime”).

Briefly, the procedure consists of four steps (Figure 4.5): 1) the definition of the seismic hazard of the construction site, 2) the identification of the structure response to the seismic demand, 3) the correlation between the response of the structure and the consequent damage and finally 4) the analysis of the expected economic losses for the estimated

damage level. The aim is to obtain an economic evaluation of the expected performance of the structure, to facilitate the decision-making process during the design phase.

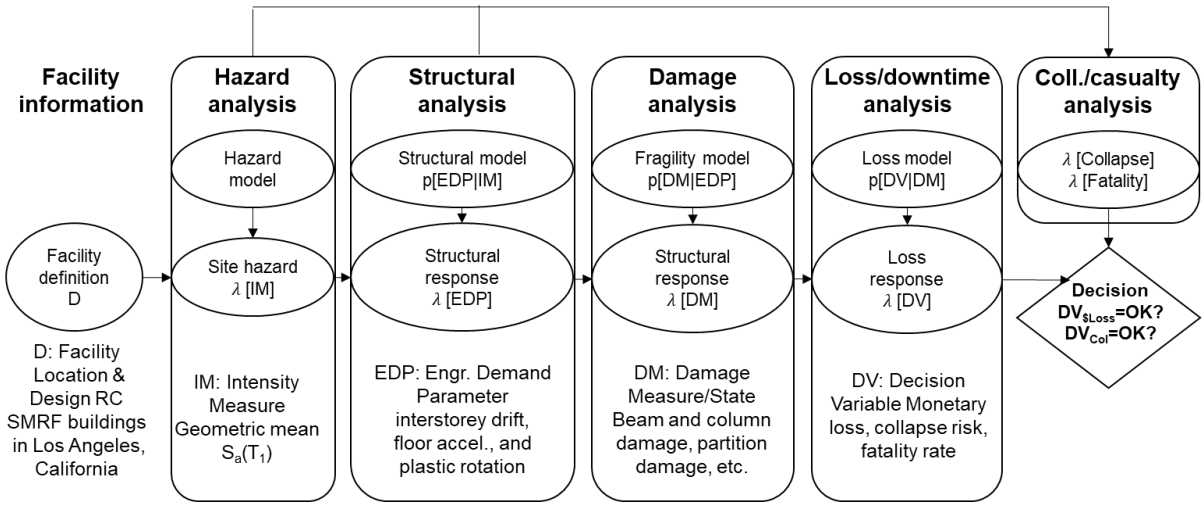

Figure 4.5. PEER PBEE methodology (adapted from Goulet et al., 2007).

Due to the fact that the PEER framework is comprehensive and based on fully probabilistic analysis, it is generally considered too onerous for implementation by design professionals. For this reason, numerous research studies proposed simplified procedure for the loss evaluation of buildings, facilitating the use of this methodology in the context of daily professional practice (Porter *et al*., 2004; Solberg *et al*., 2008; Sullivan and Calvi, 2011; Zareian and Krawinkler, 2012; Welch *et al*., 2012). These procedures maintain the probabilistic nature of the seismic input (modelled using design spectra provided by the return time variation, according to the associated construction site), but use simplified cost models or otherwise known relationships between the damage of the structure and the expected economic losses.

Among the simplified procedures, the Welch *et al*. (2012)'s one is herein considered. This started from the proposal of Sullivan and Calvi (2011) to incorporate the direct loss estimation in the Direct DBA procedure, to provide simplified probabilistic loss estimation.

At first, it is important to highlight that the most significant parameter for decision-makers is the Expected Annual Loss (EAL), as it quantifies losses on the basis of a time period rather than an assumed intensity scenario. It is the average annual value of the expected economic losses expressed as a percentage of the rebuilding cost of the structure and hence

it is a representative measure of the earthquake performance of the building. As outlined in Welch *et al*. (2012), the calculation of the EAL is typically carried out by performing single intensity-based loss estimates over an intensities interval that ranges from the initial accumulation of loss to an intensity that captures the upper bound of probabilistically significant events. Generally speaking, the EAL parameter can be calculated by integrating the total loss curve, in the mean annual frequency versus expected loss diagram.

In Welch *et al*. (2012) a simplified tri-linear loss model is defined (see Figure 4.6). More in detail, the total loss curve is approximated by defining four limit states: zero loss, operational, damage control, and near collapse. The substantial difference with the refined EAL curve (obtained through the more complex PEER methodology) is, as can be seen from Figure 4.6, that the relation frequency-cost is built in a discrete way, through an analysis by scenario and the points of this curve correspond to the Limit States identified by the modern performance design. For each of these remarkable points, a seismic demand is set, depending on pre-established probabilities of exceedance in the reference period. Moreover, these inputs are compared with the corresponding levels of structure capacity, evaluated differently according to the considered Limit State, and hence in relation to the type of damage that is desired, associated with the specific seismic intensity. Typically, the capacity levels at ELS are evaluated on the performance of non-structural components and therefore related to the functional characteristics of the building. While at the ULS the behaviour of the structural systems near the collapse and consequently to the life-safety is considered.

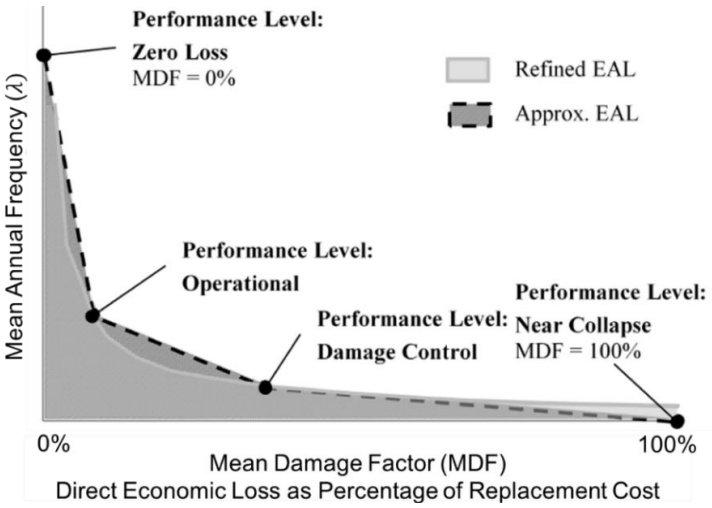

Figure 4.6. Approximated Expected Annual Loss (EAL) obtained by the proposed Direct DBA loss model in Welch et al. (2012) and the refined one (adapted from Beetham, 2013).

In the Italian guidelines (Ministry Decree n.65 7/03/2017) a very useful procedure for the classification of buildings is presented. More in detail, it introduces operational tools for the seismic risk classification of existing buildings based on two parameters: an economic one, called Expected Annual Loss (EAL, or PAM in Italian), and a structural one, associated with the seismic safety index (%NBS, or ISV). The first parameter takes into account economic losses due to structural and non-structural damage and refers to the cost of reconstruction (RC) of the building. While the second parameter is defined as the ratio between the capacity, expressed in terms of maximum peak ground acceleration (PGA) compatible with the achievement of the Life Safety Limit State (VLS), and the expected demand (i.e. the design PGA at the VLS, indicated in NTC 2018 based on the construction site).

Regarding the EAL parameter, it is considered as the cost of repairing the damages produced by seismic events during the life of the construction, broken down annually and expressed as a percentage of the reconstruction cost. The area under the curve represents the direct economic losses, function of the mean annual frequency of exceedance of the seismic action for various intensities (equal to the inverse of the average return period) and the losses associated with such actions (in terms of RC %). The simplification of that curve is made through the assumption of the mean annual frequency of exceedance of the limit states for the structure and the losses associated with them. In particular, it is proposed a relationship between the various Limit States and the associated economic losses (Figure 4.7), expressed as a percentage of the reconstruction cost (RC %), starting from the real costs incurred for the repair of buildings in L'Aquila city after the earthquake of 2009 (Dolce and Manfredi, 2015).

To define this curve, in addition to the known ultimate (CLS and VLS) and operational (DLS and OLS) limit states, two border limit states are identified:

- *Start Damage Limit State (SDLS)*. No economic loss and a conventional period return equal to $T_R = 10$ years (i.e. $\lambda = 0.1$) is associated to this LS;
- *Reconstruction Limit State (RLS)*. An economic loss of 100% and a conventional period return equal to that of the CLS are assumed. More in detail, this LS suggests the complete demolition and reconstruction of the structure rather than any retrofit interventions.

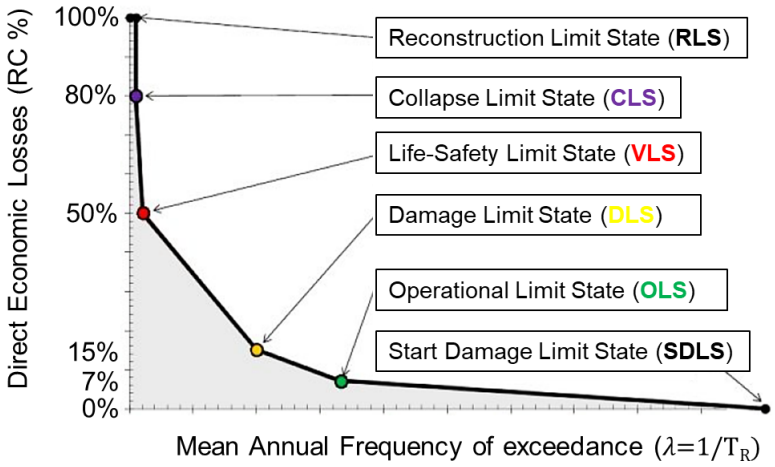

Figure 4.7. Expected Annual Loss (EAL) curve (adapted from Ministry Decree n.65 7/03/2017).

To define the Risk Class, the EAL class and the ISV class (or %NBS) of the building (Table 4.1) are evaluated and consequently the minimum of these classes identified the Risk Class.

Table 4.1. EAL and IS-V (or %NBS) classes attribution (adapted from Ministry Decree n.65 7/3/2017).

EAL	EAL Class
EAL ≤ 0.50%	A^+_{EAL}
0.5% < EAL ≤ 1.0%	A_{EAL}
1.0% < EAL ≤ 1.5%	B_{EAL}
1.5% < EAL ≤ 2.5%	C_{EAL}
2.5% < EAL ≤ 3.5%	D_{EAL}
3.5% < EAL ≤ 4.5%	E_{EAL}
4.5% < EAL ≤ 7.5%	F_{EAL}
7.5% ≤ EAL	G_{EAL}

IS-V (or %NBS)	IS-V Class
100% < IS-V	A^+_{IS-V}
80% ≤ IS-V < 100%	A_{IS-V}
60% ≤ IS-V < 80%	B_{IS-V}
45% ≤ IS-V < 60%	C_{IS-V}
30% ≤ IS-V < 45%	D_{IS-V}
15% ≤ IS-V < 30%	E_{IS-V}
IS-V ≤ 15%	F_{IS-V}

Ottonelli *et al*. (2020) presented an important work on the evaluation of the EAL, focused on existing masonry buildings. In that study, it was proposed an analytical approach based on a cost function that is directly dependent on the damage level associated with different structural elements and identified by specific engineering demand parameters. Starting from O'Reilly and Calvi (2019), this study aims to highlight the importance of the cost-benefit evaluations in order to move towards the EAL design from the Performance-Based Design

(i.e. the approach currently adopted in almost all national and international codes) that is essentially based on the correlation of the structural response, to specific Performance Levels (or the Limit States - LS). To this aim, the criterion for the attainment of the severe damage Performance Level is explicitly based on a cost function, aimed to quantify the economic losses. More in detail, assuming that the most advisable approach to define loss estimations is the analytical one, the paper proposes a loss estimation analytical model, that can be applied to any building, according to the component-based approach (Mitrani-Reiser and Beck, 2007) and then the direct loss is calculated by summing the losses overall damageable components in the building. An explicit use of nonlinear dynamic analyzes on a detailed 3D model of the structure is requested.

This proposed procedure is an important and complete tool to describe the seismic response of masonry buildings, in terms of direct economic losses. Its importance resides in the literature gap on the quantification of this aspect. Indeed, this topic is less detailed in literature with respect to the other two risk analysis components (hazard and vulnerability), since the main studies in this field come from the American environment (as the FEMA P-58-1) where the URM is not widespread as in Europe.

As a result, from Ottonelli *et al*. (2020) emerged that, in masonry structures, the structural losses represent the main contribution in the global EAL. But among these, the disaggregation between the in-plane and the out-of-plane contributions cannot be inferred, because the paper refers to a specific case study. More information should be investigated to this aim. Defining the EAL (together with the %NBS) makes it possible to highlight the critical conditions of the structure and then choose the best retrofit solution.

4.5 Seismic retrofit strategies and techniques

In the recent past, the catastrophic effects due to the seismic events that occurred in the various countries of the world have made it necessary to focus the attention on the seismic vulnerability assessment of the buildings heritage as well as on the retrofitting of it, to safeguard in case of a new seismic event. Many existing buildings have been designed with inadequate construction details, and to ensure that they withstand seismic load without collapse or with moderate damage a preventive intervention is needed.

In a strengthening or repair intervention, two concepts are important: techniques and strategies. The techniques refer to the practical way to apply the retrofit solution, while the strategy is the effect that the intervention is expected to have. Another important concept to clarify regards the strengthening and repair meanings. Strengthening means the intervention that is required when the available geometry or section, even after strengthening, cannot offer the required strength. In all other cases, the repair interventions are considered.

When dealing with the retrofitting of structures, the choice of the best solution represents a key point. The best solution means designing both efficient and respectful interventions consistent with conservation principles. Several criteria can be outlined to help this choice by recognizing that the engineering judgement plays a fundamental role in the definition of the priority interventions and needed strengthening.

For defining the retrofit interventions to apply to existing buildings it is needed at first to investigate the capacity of the structure and its seismic vulnerability. To this aim, several assessment methods, analytical or numerical, can be adopted. Once the expected failure mechanisms of the structure are identified, it is possible to develop a strategy of retrofit interventions based on a priorities scale (i.e. the expected brittle failures are resolved before those ductile). When the strategy is clear, it is possible to identify the best techniques to apply, in order to achieve the intended purpose.

In Section 4.5.1 the main seismic retrofit strategies are described and in Section 4.5.2 the main traditional techniques to strengthen or repair existing structures are reported.

4.5.1 Retrofit strategies

In literature, the main strategies for strengthening an existing structure can be summarized and schematized as in Sugano (1996). In detail, with reference to Figure 4.8, the performance of an existing building can be improved, in order to reach the required one, by increasing the strength (a) or the ductility (c) or, alternatively, by increasing simultaneously both of them (b).

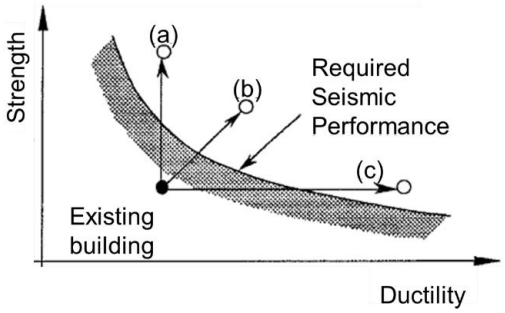

Figure 4.8. Possible seismic retrofit strategies (adapted from Sugano, 1996).

To reach the required seismic performance it is possible to intervene on several aspects at the local and/or at the global structural level, at first in a qualitative way, identifying the best retrofit strategy and then in a quantitative way, adopting the best reliable strengthening or repair technique.

More in detail, the possible strategies that can be adopted in the strengthening of existing structures aim to act on the following aspects:

- *Confinement*. This condition, which refers to the limitation of the deformation, can be related to a local or global condition. When acting locally, a structural element can be strengthened increasing the mechanical properties while at the global level the confinement effect can be modified aiming to the generation of a box-behavior, thus avoiding out-of-plane mechanisms.
- *Reinforcement*. New material, with higher mechanical properties, can be added to the element resisting section. This added part has to be well connected to the element to guaranteed its increase of strength and stiffness.
- *Enlargement*. The section of structural elements can be increased with new material, with mechanical properties similar to the existing one. An increase of strength can be reached thanks to the higher resisting area. An adequate connection or interlocking between the existing element and the new material has to be provided in order to get the expected improvements.
- *Material substitution*. The damaged parts of the structure can be removed and replaced with new materials, similar to the existing ones, or better.
- *Structural substitution*. Creation of new load-bearing structure with modern materials, without the dismantling of the old one. It is used to maintain the

external features of an existing building with insufficient capacity, and improve the behaviour and mechanical properties of the structural element.

- *Tying*. Steel bars anchored to the structure with plates (or other devices) can be adopted to adequately connect structural elements or parts of the existing structures. Tie bars are non-invasive and can be easily removed. This solution has been widely used in Italy and in Northern Europe since after earthquakes it showed a great improvement in building seismic performance, due to their mechanical compliance and compatibility with masonry structures.
- *Propping.* It consists of supporting/sustaining a structural part by adding elements. It can be applied to damaged or intact structures in order to increase their strength or stiffness. It is commonly divided into lateral (strutting) and vertical propping.
- *Anchoring or fastening*. To improve the stability of a structure, it can be fastened to rock and soil. Moreover, to tie together parts with poor connection or interlocking, avoiding local failures, it is possible to use stiff devices (pins, cramps or short ties) and guarantee micro-continuity in the structure and hence increase its strength.
- *Buttressing.* To laterally prop a structure the addition of concrete or masonry massive elements can be used. Through their self-weight, the buttresses can resist lateral forces and deformations.
- *Prestressing*. External loads or pre-compression can be used in a structural element to change the stress field.
- *Isolation*. External devices can be placed at the foundation- structure interface to absorb the seismic force and vibrations.

As aforementioned, the decision of the retrofit strategy to adopt derives from a particular process that consists of: i) identifying the expected failure mechanisms, ii) adopting an adequate interventions strategy to improve the response with respect to the failure mode defined before, iii) defining the practical way to perform the chosen retrofit strategy. The first step of the procedure is carried out by an assessment vulnerability method, that aims to define the capacity of the existing structure. Regarding the second step, a strategy to improve the local and/or global behaviour of the structure is defined. In detail, it is possible to hypothesize to improve the mechanical performance of masonry or the capacity of the

elements to prevent brittle mechanisms. Otherwise, a “box-behaviour” could be desired. Alternatively, an increase of the dissipative capacity of the structure is recommended. Finally, the third step (discussed in detail in Section 4.5.2) consists of defining the practical actions to do for realizing the defined strengthening strategy, by identifying also the more suitable technique. For example to improve the ductility grout injection can be used; to guarantee effective wall-to-wall connections steel ties can be inserted; to enhance the energy dissipation of the structure anchors or anchor plates can be adopted.

In Table 4.2 are resumed some practical actions corresponding to the main possible intervention strategies.

Table 4.2. Practical intervention actions to be performed according to selected strategy (adapted from NIKER 2012).

INTERVENTION STRATEGY	PRACTICAL ACTION
Improve the quality of masonry and the capacity of elements	Improvement of strength or stiffness of vertical elements
Improve the capacity of elements and the box-behaviour	Improvement of strength or stiffness of horizontal elements
	Improvement of connection between walls
	Improvement of connection between floor slabs (or roofs) and walls
Increase of the dissipative capacity of existing structural elements	Enhancement of energy dissipation capacity by means of specific dissipative devices

When selecting the repair or strengthening solutions, with the aim to support end-users in the decision process, it is also essential to consider the following criteria:

- *Minimal intervention*. A reduced impact (or minimal alteration) of the intervention on the existing structure is favored if the same required safety level is reached.
- *Compatibility*. If new materials or technical devices are used for strengthening, they have to be compatible with the existing ones, not leading to undesirable side-effects such as chemical, physical, mechanical, thermal and rheological incompatibility phenomena.

- *Durability*. The designed strengthening intervention should be durable as well as the new materials and devices used.
- *Non-invasiveness*. The least invasive techniques should be selected in the strengthening of structures if alternative solutions are possible.
- *Non-obtrusiveness.* The strengthening of existing structures should be harmonious with the entire system and also recognizable from the existing part to avoid distortion in historical evidence.
- *Removability*. The strengthening intervention should be, if possible, reversible or removable to be replaced with other solutions if requested. It represents a severe criterion, usually too demanding and unrealistic.

The *easy-to-implement* criterion, as well as the *low cost,* should be considered also if they are not within the criteria. By considering these criteria, the best strengthening solution is found, among a set of alternative possibilities and combinations of different techniques.

4.5.2 Retrofit techniques for URM buildings

The purpose of this Section is to give a general understanding of the principal techniques to employ to enhance the seismic behavior of UnReinforced Masonry (URM) buildings.

In Table 4.3 some possible techniques that can be applied according to the practical action, and consequently to the established intervention strategy (see also Table 4.2), are summarised and classified.

In the following, a brief description of the main traditional retrofit techniques is reported. For the purpose of this Thesis, attention was given to those aiming at an improvement of the in-plane and out-of-plane behaviour of structural elements and of the structure in its complexity. For this reason, the techniques to improve the seismic behaviour of horizontal elements, such as the floors and the roofs are not reported.

The techniques described below are: tie-rods, jacketing by R.C. plaster, grout injections, reinforced injections (or stitching), repointing and reinforced repointing, FRP, discrete confinement, “scuci-cuci” (i.e. “unstitch-stitch”), enlargement and buttresses.

Table 4.3. Intervention techniques corresponding to practical intervention actions (adapted from NIKER 2012).

PRACTICAL ACTION	INTERVENTION TECHNIQUE
Improvement of strength or stiffness of vertical elements	Grout injection
	Reinforcement with steel wires
	Reinforcement usin geo-nets
	Reinforcement with belts
Improvement of strength or stiffness of horizontal elements	Composite strengthening of vaults extrados and intrados
	Strengthening by substitution of single planking (90°) for double planking (45°)
Improvement of connection between walls	Strengthening of traditional timber connections using bolts
	Steel plates
	Steel flat bars (NSM technique)
	Grouted metallic anchor
	Anchor pins
	Grouted metallic anchors
Improvement of connection between floor slabs (or roofs) and walls	Metallic tie + steel angle
Enhancement of energy dissipation capacity by means of specific dissipative devices	Hysteretic/frictional anchoring devices

Tie-Rods

One of the most efficient and widely used retrofit techniques in existing buildings is the application of tie rods. This strategy brings important improvements to the structures, as the strong increase of the wall-to-wall and wall-to-floor connections. Consequently, it leads to a reduction of the out-of-plane mechanism of walls and to an increase in the in-plane strength.

It is also adopted to bear the static thrust of arches, vaults and roofs. It is a technique characterized by low cost and easy application. Its use was known since Byzantine times and continued up to our days, especially for the seismic areas (Milizia, 1785; Rondelet, 1832; Archivio Storico, 1861; Giuffrè and Carocci, 1999; Carocci, 2001). Since the beginning, they were adopted as a seismic protection and their usual position in the buildings was at the roof/floor level, to improve the connections between orthogonal walls and between walls and diaphragms. With respect to the tie tension and the masonry quality, it is possible to identify the more effective anchoring system. It should be noted that if not correctly designed, this technique could lead to unexpected and irreversible consequences. More in detail, in case of

excessive high tension in the ties, during an earthquake, severe damages can be caused to the masonry at the anchoring level, due to the high generated stiffness.

Practically speaking, the rods are commonly composed of three elements: a metal tie, an external anchor and link plates; their characteristics are briefly described below (Figure 4.9).

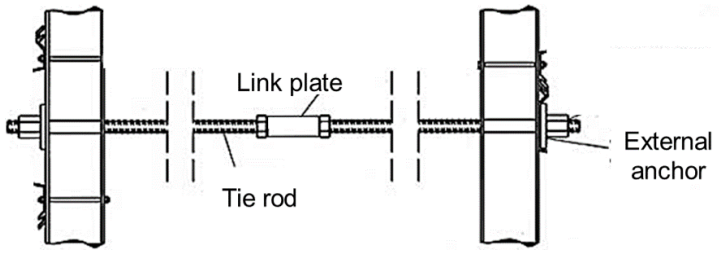

Figure 4.9. Schematic representation of a tie rod.

The metal tie can be realized in several ways and among them, the most commonly used are with a reinforcement bar, with rectangular section plates or with strands of harmonic steel. As a common rule, the cylindrical shaped rods are inserted directly in the masonry while the ones with the rectangular section plates are used at the floor extrados or beneath the flooring. The rods are generally made of steel and, in order to protect them from atmospheric degradation, are embedded in a sheath filled with cement mortar.

In literature, several different types of external anchor, with changing shapes and usages are described and reported. A brief overview of the most commonly used is summarized as follows:

- *Round-shaped*. It is essentially a round-shaped steel plate (see Figure 4.10a), with a diameter that generally varies in the range of 20-50 cm. Frequently the plate is reinforced by a diagonal rib design that enhances the strength. This kind of anchor can be fixed by means of a single or several bolts or by the insertion of wedges at the interface between the rod and the anchor;

- *Rectangular-shaped with a single or double rod*. It is a rectangular or squared steel plate (see Figure 4.10b), with dimensions that range from 20 up to 50 cm and, as for the round-shaped ones, also these plates are frequently reinforced by ribs and can be fixed by bolts or by wedges at the rod-anchor interface. This geometrical shape can be adopted also in the case of a double tie rod inside the wall. In this case, it is referred to as double rod configuration;

- *Bar-shaped simple or Y-shaped*. It is composed of one (see Figure 4.10c) or more bars that can have a simple cylindrical shape or different shape according to the esthetics requirements of the building (i.e. S-shape, symbols, star). The length of each bar generally varies in the range 60-120 cm and with different heights. In the case of a single anchor, it has to be inserted with an angle of 45° with respect to the flooring, in such a way that the bottom part interacts with the orthogonal wall while the upper part interacts with the floor. In case the 45° positioning is not feasible, it is commonly used a Y-shaped anchor. The closing of the rod-end can be done with a single bolt, but more frequently it is used an eyelet;

- *With two UNP channels*. It consists of two UNP profiles connected through rigid metal plates, with respect to the single bar configuration. This option grants a higher strength and a higher area of contact. The tensioning of the rod, also in this case, is done with a bolt at the end of the rod;

- *L-shaped*. It is used when the rods are inserted into two orthogonal walls. In this way, a single L-shaped metal plate with reinforced ribs at the extremities is positioned at the edge. The tensioning of the rods, also in this case, is made through bolts.

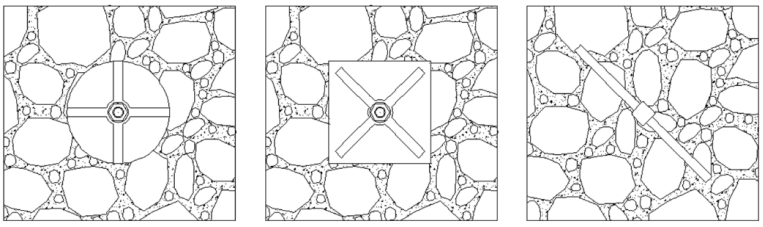

Figure 4.10. Schematization of the main typologies of external anchor: (a) round-shaped, (b) rectangular-shaped and (c) simple bar-shaped.

The link plates are the third component of a tie rod and are used in two cases: if the rods are not long enough or when the rods have to be pre-tensioned from the inside (in absence of any tensioning external bolt). The three link plates most used, available in literature, are: the fork connector, the tensioning sleeves and the hinge with bolt and nut.

Jacketing by Reinforced Concrete plaster

This consolidation technique acts by adding concrete layers on both sides of a masonry wall. These layers have a typical thickness of 3-5 cm, are armed through a metallic net and are fixed to the wall through transversal connectors. With this procedure, both the strength

and stiffness of the wall are enhanced. Recently it was demonstrated that this result can be assumed true only if the layers are used on both sides of the wall, and are well connected to it by transversal connectors (Baloević *et al*., 2016). In detail, a thicker section of the wall can be obtained and an appreciated increase of compressive, tensile and shear strength of it as well as the ductility can be observed (Binda *et al*., 1994).

This approach is strongly recommended in case of masonry strongly damaged, incoherently assembled, on which other techniques cannot be applied. Moreover, it is effective also for walls constructed with solid bricks or made by stones and can be useful in the case of strongly compressed walls in which the double layer of concrete performs high confinement. Nevertheless, the execution on site of this intervention on inhomogeneous walls could lead to some problems in connecting the two sides of the wall (Figure 4.11).

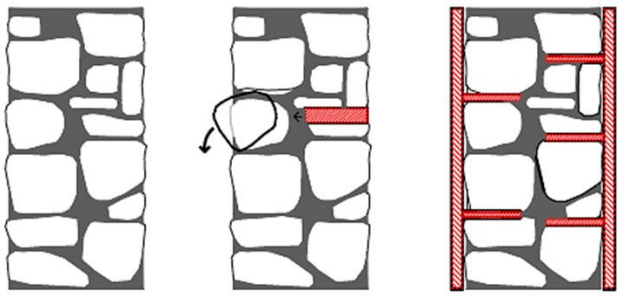

Figure 4.11. Schematization of the application of the R.C. plaster (Binda et al., 2003a).

Practically speaking this technique presents several advantages such as: it is easy and cheap; it grants an increase of strength for both in-plane and out-of-plane mechanisms; it can remove the effect arising from localized lesions and does not alter the masonry tensional state. The main disadvantage is its invasiveness from the architectonical point of view, since it practically covers the wall, for this reason, it cannot be used for historically relevant building. Moreover, some technical issues need to be taken into account. From simple ones, such as changes induced in the thermal behavior of the masonry and its breathability, to more dangerous such as a consistent increment in the weight of the structure that can alter the building mass center and creates uneven distribution of loads, in case of seismic action. It is important to highlight that this latter can be avoided by performing interventions in a symmetrical manner. Another issue refers to the great increase in stiffness of the wall that thus reducing its capability to deform under lateral load. Furthermore, steel corrosion can be

developed in case the steel cover thickness is insufficient, leading to low durability of the intervention.

As a safety rule, in case the intervention needs to be done on the intermediate floor, it is suggested to perform the intervention also at the levels below, down to the ground level. This suggestion aims to avoid any discontinuity or irregularity in terms of stiffness and/or strength on the overall behaviour of the building (Figure 4.12).

From a technical point of view the reinforced plaster is applied as follows:

1) the original plaster is removed and each hole or lesion in the naked masonry is filled with grout injection, in order to obtain a perfectly smooth surface (see Figure 4.12a);
2) the wall is drilled to create the holes necessary for the transversal connectors (see Figure 4.12b). These holes need to be uniformly distributed;
3) standard deformed steel bars with a diameter of 4-8 mm are generally used as connectors. They are inserted into the holes and blocked in place by grout injections (see Figure 4.12c). It is recommended to use at least 4 bars per m^2;
4) the steel net is inserted on both sides of the wall and, with a distance of around 2 cm from the wall, linked to the bars (see Figure 4.12d). The most common steel net used is the electro-welded mesh panel (with a diameter in the range of 4-8 mm and mesh size of 10x10 cm or 15x15 cm);
5) the concrete is sprayed directly on the wall in order to obtain a final wall thickness of 3-5 cm (see Figure 4.12e).

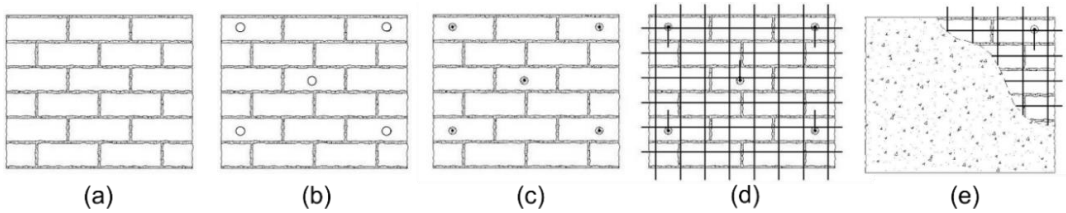

Figure 4.12. Practical procedure to apply the reinforced plaster: (a) remove the original plaster, (b) create the holes, (c) insert deformed steel bars in the holes, (d) apply the steel net on wall sides and (e) spray the concrete on the wall (Vinci, 2019).

Some typical failures (see Figure 4.13) can occur in case of wrong execution of this intervention, such as: the insufficient steel mesh overlapping; the insufficient transversal ties confining action (Modena and Bettio, 1994; Modena *et al*., 1997b); the lack of connection between the nets in orthogonal walls and in correspondence to the floors; the absence of steel transversal connectors; the use of too short connectors; the lack of uniformity of distribution of the repaired areas in the structure (can cause torsion stresses due to non-uniform distribution of the stiffness).

Figure 4.13. Some possible failure due to: (a) insufficient steel mesh overlapping, (b) insufficient transversal ties confining action, (c) lack of connection between nets and (d) absence of connectors (adapted from Binda et al., 2003a).

Grout injection

This consolidation technique consists of injecting a grout material inside the void in the masonry that can be native (such as in the case of walls made by stones with a high ratio of voids) or due to lesions. Through this intervention, the mechanical parameters (strength and stiffness) of the masonry are increased. The grout may be of different composition, i.e. cement, resinous or chemical mixtures and the rationale is not only to fulfill the voids but also to tightly bound the different parts of the masonry.

Strengthening by grout injections of masonry walls has been largely applied in Italy, after the past earthquakes, nevertheless, only few research focused and investigated the effectiveness of this technique (Tomaževič and Turnšek, 1982; Tomaževič, 1992; Binda *et al*., 1993a,b; Binda *et al*., 1994; Modena and Bettio, 1994; Bettio *et al*., 1996; Laefer *et al*., 1996; Valluzzi *et al*., 2004). Past researches focused especially on the response to this strengthening intervention in terms of strength increase rather than on chemical, physical and mechanical compatibility with the original masonry (Modena *et al*., 1997a,b,c; Binda *et*

al., 1997). Due to the scarce knowledge about the effectiveness of this intervention, important attention has to be given to the masonry characteristics, since some types of walls could be not injectable and ineffectiveness of the consolidations can be observed.

The grout can be injected into the wall in two different modalities: by gravity or by pressure. The grout injection with high pressure is by far the best way to execute this intervention because the grout can rapidly and efficiently seal the voids. It is important to highlight that applying high pressure to a strongly damaged wall, will further damage the wall itself.

It is a low cost intervention that adds strength to the masonry without altering its tensional state and can remove effects due to diffuse lesions. The major advantage of this technique is that it does not alter the original external appearance of the structures, so it has been widely used to strengthen historically relevant buildings. On the other side, this intervention presents two major issues that need to be considered while choosing the best consolidation strategy: induces an increase in the structural stiffness and does not improve the connection between orthogonal walls.

The major issues of the grout injections intervention are: (i) the lack of information on the real size distribution of the voids in the wall, (ii) the grout difficulty in filling thin cracks (2-3 mm); (iii) segregation phenomena that can be induced by a high rate of absorption of the material inside the wall to be consolidated; (iv) the presence of silty or clayey materials that makes difficult an optimal grout penetration; (v) the need for sufficiently low injection pressure to avoid not only air trapping within the cracks but also fine voids or even wall disruption.

From a technical point of view, the procedure requires trained workers since all the procedure is quite complex. Prior to the injection phase, there is a preparation procedure that is described as follows:

1) At first the plaster is removed and the surface is well cleaned in such a way to highlight the presence of lesions;
2) Then the lesions and the voids are sealed off, using the mortar most possible similar to the existing one (in terms of deformation characteristics, i.e. Elastic Modulus and Poisson's Ratio);
3) To select the density of the holes (i.e. the mean distance that the grout can travel inside the masonry), it is performed a first hole at the top of the wall and a series

of holes beneath it. The grout is pumped in the first hole and it is checked what is the last hole in which the grout arrives. Twice the distance between this hole and the initial one is taken as holes distance (2-3 injections point per m^2 could be effective), see Figure 4.14;

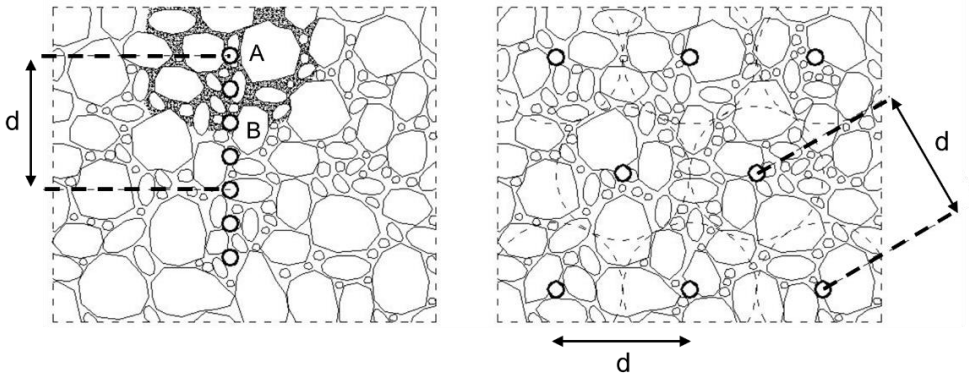

Figure 4.14. Optimal selection of holes density (adapted from Vinci, 2019).

4) The holes are realized on a triangular mesh according to the distance previously evaluated. Each hole reaches a depth that ranges from 2/3 to 4/5 of the wall thickness and is drilled not perfectly horizontal, but with a slight downslope in order to favor the grout intercalation;

5) In these holes are inserted the pipes that will deliver the grout. The interface between the pipe and the holes is then sealed off with mortar in such a way to prevent grout leaking;

6) Then through the pipes, the masonry is washed, in order to remove the drilling debris and to highlight the presence of un-noticed lesions;

7) At this stage the wall is ready for the injections that, according to the masonry degradations state and to the type of selected grout, can be done in three different ways: by positive pressure, by negative pressure or by gravity.

The injection by positive pressure (see Figure 4.15a) consists of injecting the grout mixture by means of a hydraulic pump. The choice of the correct pressure level has to be calibrated with respect to the degree of damage in the structure and it is reached by starting with 1 atm and growing further up to 4-5 atm. The injections are performed from bottom to top, and for each level are performed from the edges toward the center of the structure.

The injection by negative pressure (see Figure 4.15b) can be used only in presence of particularly liquid grout, such as the synthetic one. In this method, the intervention is made on two lines of pipes each time, from bottom to top. For each line, the bottom pipes are connected to the grout reservoir while at the upper pipes it is applied negative pressure. The intervention proceeds until the grout reaches the upper pipes and until the wall is fully injected.

The injection by gravity (see Figure 4.15c) is the only choice in the case of heavily damaged masonry. It consists of inserting the grout in each pipe and let it flow inside the masonry under the action of gravity. This method is not capable of completely fill the voids in the structure but only covering the bigger ones.

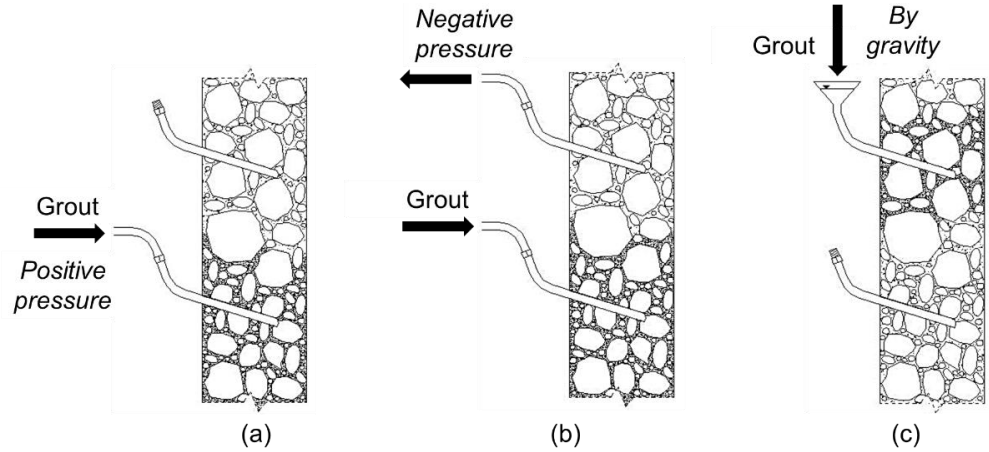

Figure 4.15. Injection grout by: (a) positive pressure, (b) negative pressure and (c) gravity (adapted from Vinci, 2019).

A practical example of the grout injection application is shown in Figure 4.16.

Figure 4.16. Injection grout procedure: (a) holes drilling, (b) plastic pipes sealing and (c) grout injection (adapted from NIKER 2012).

The material to be injected needs to comply with some requirements in terms of mechanical properties (strength and elastic modulus must be the most possible similar to the masonry ones), penetration capacity (homogeneous and composed of small grains), hardening time (not too short in order to avoid the hardening during the intervention), chemical characteristics (stable over time and tightly bonding with the masonry). The two more commonly used materials for the grout injection are: (i) cement-based (in case it is necessary to achieve a high compression strength) and (ii) mortar-based (its mechanical properties are very close to the masonry one even if does not allow to achieve a high increase in strength).

Reinforced injection (or stitching)

This technique is similar to the previous one (grout injections), but it consists of inserting a reinforced bar in the injections. The holes are drilled and filled with bars and mortar to guarantee a higher cohesion and mechanical properties of the strengthened structural element. It is able to increase also ductility and sometimes also to tie different parts together.

The bars can be made of steel or FRP. The holes are then injected with fluid mortar or grout. It should be highlighted that epoxy resin can generate some severe compatibility problems.

In Figure 4.17a a schematization of the intervention technique is shown.

If it could represent a valid solution for strengthening structural elements, from experience it was observed that this technique is ineffective in stone masonry because the perfect anchoring of the metal tie inserted into the holes cannot be guaranteed (Figure 4.17b). Due to the fact that the reinforced injections cannot be removed, it constitutes an invasive and irreversible technique.

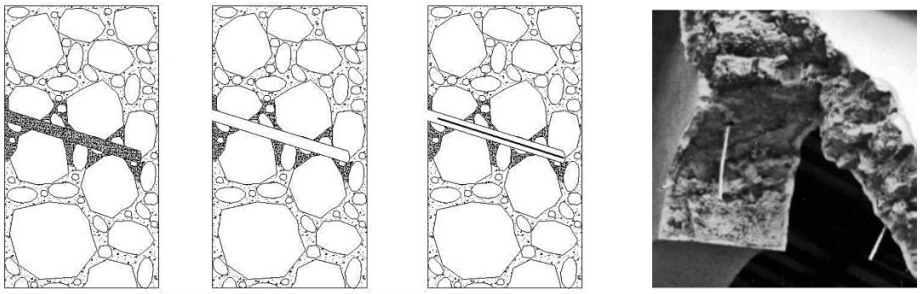

(a) (b)

Figure 4.17. Reinforced injection: (a), schematization of the intervention technique (adapted from Vinci, 2019) and (b) ineffective stitching (adapted from NIKER 2012).

Repointing and reinforced repointing

This technique consists of the partial but deep removal of original deteriorate mortar in joints and subsequent substitution with new mortar. It is used when the masonry walls are visibly deteriorated at joints or mortar level. To observe an appreciable increase in structural behaviour, the new mortar needs to have better mechanical properties and durability. Due to the fact that the new mortar can be still removed, the technique is considered reversible. A practical example of the application is shown in Figure 4.18.

(a) (b) (c)

Figure 4.18. Structural repointing: (a) cleaning the joints, (b) first layer of repointing and (c) final result (adapted from Binda et al., 2005).

If the joints are regularly horizontal, then reinforced repointing can be provided. It consists of combining the aforementioned repointing with the inclusion and the laying of reinforced bars (steel or FRP) in the mortar matrix. This technique increases the compressive and shear strength in small thickness masonry. Moreover, it is able to provide additional ductility and to improve the connection between different parts of the structure.

In Figure 4.19 it is shown the procedure of this intervention technique.

(a) (b) (c) (d)

Figure 4.19. Reinforced repointing: (a) make holes drilling, (b) positioning of the transversal steel tie, (c) detail of the transversal steel tie (d) finishing of the intervention (adapted from Valluzzi et al., 2004).

FRP

This consolidation technique consists of the application of strips, sheets or plates of composite materials to vertical or horizontal structural elements. The FRP materials are constituted by fiber-reinforced polymeric matrix, hence they are inhomogeneous and anisotropic materials. The anisotropy of the FRP arises from the structure of the fibers themselves since they are parallel to one another thus creating a preferential direction in which there is an increase in the tensile strength (Figure 4.20). At the same time, the FRP does not alter the compression and flexural behavior of the structure, with the advantages of adding a really reduced mass, which is fundamental in presence of a mass issue.

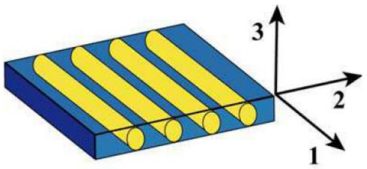

Figure 4.20. Unidirectional FRP material (CNR-DT 200/2004).

The typical behaviour of FRP materials is linear-elastic up to the failure. For this reason, these materials are considered brittle ones. The ultimate deformation (failure) of the material depends on the debonding of FRP, which can occur for:

- tearing of the fiber to reach the ultimate strength;
- laceration of the fibers due to cracking of the element material;
- delamination at the interface between the FRP and the element.

This intervention grants several advantages, such as the reduced weight, the great resistance capacities and the high resistance to the corrosion and to the fatigue. The FRP materials can be applied also in the historical relevance buildings since they do not alter the external appearance. Moreover, they can increase both the in-plane and the out-of-plane strength. Their flexibility and easy application allow a wide range of interventions for existing structures.

Among the different shapes, the FRP sheets represent the most commonly adopted solution in the case of building reinforcement. The FRP is composed during the intervention, i.e. at first the adhesive matrix adheres to the element and then, during the gluing stage, the fibers are applied to the matrix. Generally speaking, the FRP materials are made of two different “phases” that are macroscopically distinguishable, such as fibers and the polymeric

matrix. These two different materials bring different mechanical characteristics to the structure: if the polymeric matrix binds the fibers to the structural elements on which they are applied, the fibers give higher strength and stiffness to the element. This fact grants an additional tuning factor to the intervention.

Although the FRP materials for existing masonry buildings are taken into account in daily practice, at present, the local mechanisms involved in the failure of these structures strengthened by FRP laminates (such as delamination) still need to be experimentally and numerically deepened. On the contrary, the contribution of the FRP strengthening on the shear behaviour was investigated in Valluzzi *et al*. (2002), through an experimental campaign conducted on brick masonry panels, subjected to diagonal compression tests, considering different reinforcement configurations and different kinds of fibers (carbon, glass and polyvinyl alcohol), see Figure 4.21. The experimental campaign outlined that FRP reinforcement applied only at one side of the panels does not significantly modify the shear collapse mechanisms of URM. The double-side configurations, instead, can provide a more ductile failure and an increase of the ultimate capacity. Moreover, the diagonal configuration results more efficient in terms of shear capacity than the grid set up, although this latter offers a better stress redistribution that causes a crack spreading and a less brittle failure. Furthermore, less stiff FRP material appeared to be more effective both in terms of ultimate strength and stiffness increase of the panels. That was due to the particular design criterion used (weaker material has a larger adhesion area), and also to the fact that stiffer material is more prone to debonding, especially when the number of layers increases.

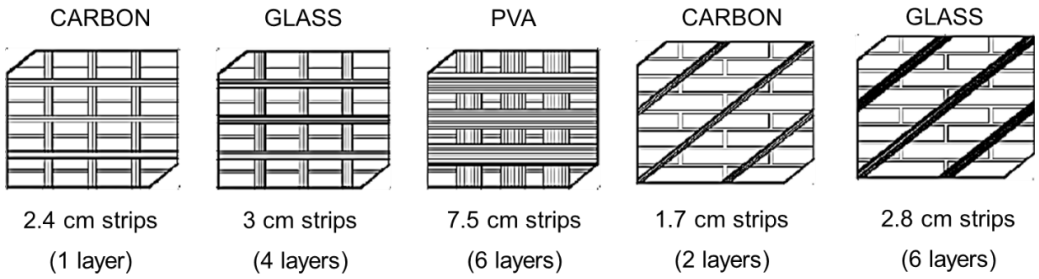

Figure 4.21. Some strengthening solutions: single and double-side strengthening patterns (adapted from Valluzzi et al., 2002).

The execution of this strengthening intervention requires the following steps:

1) remove the existing plaster;
2) apply the primer resin, organic or polymeric;
3) apply an epoxy (or other) mortar layer to smooth and regularize the surface;

4) apply the first layer of epoxy resin;
5) apply the first layer of laminate, the second layer of epoxy resin, and the second laminate layer according to the selected layout;
6) apply the eventual coating.

Examples of FRP applications on existing buildings are shown in Figure 4.22.

(a) (b)

Figure 4.22. FRP application examples: (a) grid pattern (Sika Limited, 2003) and (b) shear strengthening on one side (Motavalli, 2005).

Discrete confinement

This technique can be applied both to piers and to walls. Regarding the piers, the technique consists of the application of steel rings in critical sections, to give local confinement that increases compressive strength where it is needed. This kind of intervention can be adopted when the piers are subjected to an excessive compressive force, to avoid the crushing of masonry. In Figure 4.23a an example of an application is reported.

(a) (b)

Figure 4.23. Discrete confinement of a: (a) pier and (b) multi-layer wall (adapted from EU-India cross program, 2006).

Regarding the walls, to guarantee adequate connections between different layers of multiple leaf masonry, transversal steel bars anchored to plates, or R.C. elements cast in transversal holes drilled through the whole thickness of the wall, can be used (Figure 4.23b). This intervention, in addition to avoiding the separation of layers, can lead to an increase in the mechanical properties of the wall. Nevertheless, it is considered rather invasive and to be effective requires the introduction of several different reinforcements.

"Scuci-Cuci" (i.e. "Unstitch-Stitch")

This technique consists of local dismantling and rebuilding to regain the structural continuity along cracks and preserve the wall mechanical efficiency. The substitution material to be used has to be the most similar to the original one, not only for shape and dimensions but also for strength and stiffness, in order to avoid the expulsion of the intervention. Of course, the new material has to be adequately connected to the existing structure, to guarantee a monolithic behaviour. This technique can be adopted in the case of walls with severe but localized cracks or with highly deteriorated parts and particular attention should be given to the compatibility of the new portion with the remaining wall structure.

Practically speaking, the existing masonry pattern is locally removed where major deterioration has occurred. By manually "pull" or by hydraulic jacks welded to steel sections (in case of high wall thickness), the scrapping of the joints can be done and the removal of the units does not have to cause percussion or vibration. Simultaneously the introduction of new materials, from the bottom up, is provided. At this step, no coaction states should be generated. In the end, the area between the new and old masonry is sealed, using supports in order to avoid possible issues related to the inevitable settling of the new masonry due to mortar shrinkage. To this aim, small thickness joints are suggested, to limit the reductions in the volume of the mortar itself and to gradually load the rebuilt portions of masonry. Figure 4.24 shows the procedure.

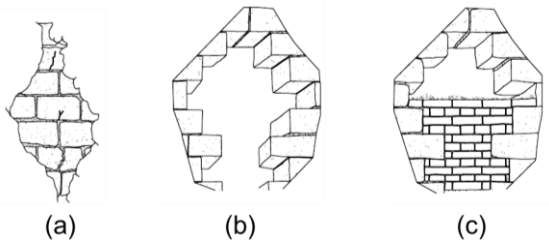

Figure 4.24. "Scuci-Cuci" procedure: (a) damaged portion of masonry wall, (b) removal of damaged stones and (c) filling with new masonry (adapted from EU-India cross program, 2006).

Enlargement

This strengthening technique consists in adding new material (i.e. an additional leaf of masonry) compatible with the original one (to respect the mechanical compatibility) to enlarge the structural element sections (Figure 4.25). For the effectiveness of the intervention, a correct and adequate connection has to be provided. The aims of this technique are: an increase of the strength of the element as well as of the overall shear capacity of the structure, an increase of the stability and, in the case of a too high stress field, a better distribution of load on a larger resisting section.

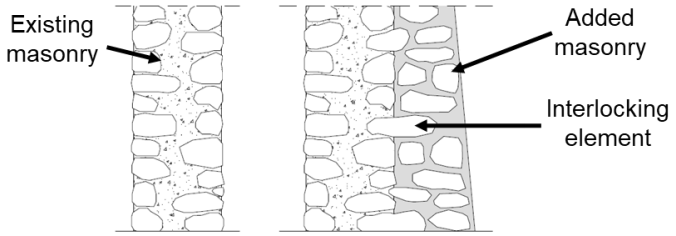

Figure 4.25. Schematization of the enlargement of a wall.

Buttresses

The introduction of massive concrete or masonry elements to prop a structure on a side can represent an effective technique to increase the capacity of the structure against lateral loads. Through its weight, a buttress can contrast the lateral deformation of a structure and avoid the related failure mechanisms. Originally the buttresses were built as part of the entire original construction, resulting in very efficient, thanks to the fact that are characterized by the same type of masonry, are part of the same foundation and are adequately connect to the rest of the structure. However, different is the usage of the buttresses as a later strengthening device. Due to the less interlocking with the structure, their efficiency has to be assumed reduced. This fact can be neglected by adopting plying arches in between the structure and the new buttresses. It represents a removable and non-invasive solution because it is constructed as an external solution.

In Table 4.4 is provided a summary of the objectives that the techniques described above can reach and their range of application.

Table 4.4. Strengthening intervention techniques and their effect, applicability, advantages and limits.

INTERVENTION TECHNIQUE	EFFECT	APPLICABILITY	ADVANTAGES	LIMITS
TIE-RODS	1. Improve box-behaviour 2. Improve in-plane wall strength 3. Reduce out-of-plane mechanisms 4. Improve othogonal walls connection	1. Not suggested for very low quality masonry	1. Really effective 2. Reversible 3. Not too invasive	1. May lead to irreversible consequences
JACKETING BY R.C. PLASTER	1. Increase in-plane and out-of-plane wall strength, stiffness and ductility 2. Improve structure global behaviour	1. Elements suffering too high compressive force 2. Not adapted for historical structures	1. Remove effect of isolated cracks 2. Easy to apply 3. Does not alter masonry tensional state 4. Limited cost	1. Highly invasive and irreversible 2. High increase of wall stiffness and mass 3. May lead to bars corrosion 4. Alters the masonry breathability 5. May lead eccentricity under dynamic load
GROUT INJECTION	1. Increase of in-plane wall strength	1. Thick walls 2. Walls with high percentage of voids 3. Walls with many smeared cracks	1. Restore uniformity of wall strength 2. Impair water penetration 3. Restore continuity in multi-leaf wall 4. Not alter masonry tensional state 5. Does not alter appearence 6. Limited cost	1. Irreversible 2. Increase of wall stiffness 3. May cause segregation and skrinkage 4. May not be effective 5. Requires trained workers
REINFORCED INJECTION (STITCHING)	1. Increase the in-plane and out-of-plane wall strength 2. Improve connection of adjacent walls 3. Increase strength and ductility	1. Needing higher cohesion and mechanical characteristics	1. Does not alter the masonry tensional state 2. Does not alter the appearence 3. Can control crack propagation	1. Can be obstrusive 2. May need intense intervention
REPOINTING AND REINFORCED REPOINTING	1. Increase compressive and shear strength	1. Deterioreted joints 2. Mortar in poor conditions	1. Impair water penetration 2. Confining effect 3. Reversible	1. May accelerate masonry decay 2. Not effective in irregular masonry 3. May lead to corrosion
FRP	1. Increase wall in-plane flexural and shear strength and out-of-plane strength 2. Increase wall ductility	1. Limited work space	1. Very low weight 2. High mechanical properties 3. Anti-corrosion properties 4. Does not alter the appearence	1. May lead to delamination failure
DISCRETE CONFINEMENT	1. Punctual confinement 2. Increase wall strength, stability and stiffness	1. Pier suffering too high compressive force 2. Multi-leaf masonry walls with no sufficient connections	1. Reversible	1. May weak wall during drilling procedure
«SCUCI-CUCI»	1. Preserve and regain mechanical efficiency	1. Walls with severe but localized cracks	1. Restore original structure behaviour	1. Useless to apply to walls with low quality masonry 2. Should be used in combination with other techniques
ENLARGEMENT	1. Distributing load to a larger section	1. Elements in good condition with too high stress 2. Too slender walls	1. Increase of resistant sections	1. Increase of wall mass 2. May lead to foundation problems
BUTTRESSES	1. Increase structure stiffness and integrity 2. Improve structure global behaviour 3. Confine the stucture horizontally	1. Structures with low resistance to lateral forces	1. Relieve stresses in certain places	1. Alter the appearence 2. Might be irreversible

4.6 References

Antoniou, S. & Pinho, R. (2004). Advantages and limitations of adaptive and non-adaptive force-based pushover procedures, Journal of Earthquake Engineering 8(4), 497–522.

Archivio Storico Comunale di Norcia. (1861). Consigli e Riformanze reg. 151, cc 65-70. Consigli dal 1858 al 22 gennaio 1861.

ASCE/SEI 41-06 (2000). Pre-standard and Commentary for the Seismic Rehabilitation of Buildings, FEMA 356, American Society of Civil Engineers, Washington D.C, United States.

ASCE 41-13 (2014). Seismic Evaluation and Retrofit of Existing Buildings, American Society of Civil Engineer and Structural Engineering Institute, Reston, Virginia, USA.

ATC (1996). ATC-40: Seismic evaluation and retrofit of concrete buildings, Applied Technology Council, Redwood City.

Baloević, G., Radnić, J., Grgić, N., & Matešan, D. (2016). The application of a reinforced plaster mortar for seismic strengthening of masonry structures. Composites Part B: Engineering, 93, 190-202.

Beetham T. (2013). Simplified displacement based performance assessment of retrofit alternatives for decision making. Master Thesis, University of Pavia.

Bettio C., Modena C., Riva, G. (1996). The efficacy of consolidating historical masonry by means of injections. VII North American Masonry Conference - NAMC, Notre Dame, U.S.A., pp. 458-471.

Binda L., Baronio G., Tiraboschi C. (1993a). Repair of brick-masonries by injection of grouts: experimental research. Journal of Structural Engineering, Madras, India, Vol. 20, No.1, pp. 29-44.

Binda L. Modena C., Baronio G. (1993b). Strengthening of masonries by injection technique. VI North American Masonry Conference - NAMC, Philadelphia, Vol. 1, pp. 1-14.

Binda L., Modena C., Baronio G., Gelmi A. (1994). Experimental qualification of injection admixtures used for repair and strengthening of stone masonry walls. X International Brick and Block Masonry Conference – I2BMC, Calgary, Canada, Vol.2, pp. 539-548.

Binda L., Modena C., Baronio G., Abbaneo S. (1997). Repair and investigation techniques for stone masonry walls, Construction and Building Materials, Vol. 11, N. 3, pp. 133-142.

Binda L., Cardani G., Penazzi D., Saisi A., (2003a). Performance of some repair and strengthening techniques applied to historical stone masonries is seismic areas. ICPCM a New Era of Building, Cairo, Egypt, 18-20 February, Vol. 2, pp. 1195-1204.

Binda L., Borri A., Corradi M., Tedeschi C. (2005). Experimental evaluation of shear and compression strength of masonry wall before and after reinforcement: deep re-pointing. I Canadian Conference on Effectiveness Design of Structures, Hamilton, Ontario 10-13 July, pp. 293-304.

Carocci C. (2001). Guidelines for the safety and preservation of historical centres in seismic area. III International Seminar on Structural Analysis of Historical Constructions - SAHC, Guimarães, Portugal, 7-9 November, pp. 145-165.

CNR-DT 200-2004. (2004). Guide for the Design and Construction of Externally Bonded FRP Systems for Strengthening Existing Structures.

Cornell, C. A., F. Jaylayer, R. O. Hamburger, and D. A. Foutch. (2002). Probabilistic basis for 2000 SAC federal emergency management agency steel moment frame guidelines. Journal of Structural Engineering 128 (4): 526–53. doi: 10.1061/(ASCE)0733-9445(2002)128:4(526).

Dolce M., Manfredi G. (2015). Libro Bianco sulla ricostruzione privata fuori dai centri storici nei comuni colpiti dal sisma dell'Abruzzo del 6 Aprile 2009. (in Italian) Doppiavoce: 210.ISBN 978-88-89972-50-2.

EN 1998 (European Committee for Standardization). (2005). Design of structures for earthquake resistance - Part 3: Assessment and retrofitting of buildings. Eurocode 8, Brussels, Belgium: EN.

EU-India economic cross cultural programme. (2006). Identification of strengthening strategies. Project Contract No: ALA/95/23/2003/077-122. Project Beneficiary: Universidade do Minho, Portugal.

Fajfar, P. & Fischinger, M. (1988). N2 - A method for non-linear seismic analysis of regular buildings, Ninth world conference on earthquake engineering.

FEMA 273 (Federal Emergency Management Agency). (1997). NEHRP Guidelines for the Seismic Rehabilitation of Buildings. Washington DC, US:FEMA.

FEMA 274 (Federal Emergency Management Agency). (1997). NEHRP Commentary on the Guidelines for the Seismic Rehabilitation of Buildings. Washington DC, US:FEMA.

FEMA 356 (Federal Emergency Management Agency). (2000). FEMA-356: Prestandard and commentary for the seismic rehabilitation of buildings. Washington DC, US:FEMA.

FEMA P58-1. (2012). Seismic performance assessment of buildings: Volume 1 – Methodology, FEMA P-58-1. Prepared by the Applied Technology Council for the Federal Emergency Management Agency, Washington, DC.

Gentile, R. (2017). Extension, refinement and validation of the simple lateral mechanism analysis (SLaMA) for the seismic assessment of RC structures (Doctoral dissertation, PhD thesis, Department of Civil, Environmental and Landscape, Building Engineering and Chemistry, Polytechnic University of Bari, Bari, Italy).

Giuffrè A., Carocci C. (1999). Codice di Pratica per la sicurezza e la conservazione del centro storico di Palermo, Laterza, Bari.

Goel, R. K. & Chopra, A. K. (2004). Evaluation of Modal and FEMA Pushover Analyses: SAC Buildings, Earthquake Spectra 20(1), 225–254.

Goulet, C. A., Haselton, C. B., Mitrani-Reiser, J., Beck, J. L., Deierlein, G. G., Porter, K. A., and Stewart, J. P. (2007). Evaluation of the seismic performance of a code-conforming reinforced-

concrete frame building-from seismic hazard to collapse safety and economic losses. Earthquake Engineering and Structural Dynamics, 36(13):1973–1997.

Guerrini, G., Graziotti, F., Penna, A., & Magenes, G. (2017). Improved evaluation of inelastic displacement demands for short-period masonry structures. Earthquake Engineering & Structural Dynamics, 46(9), 1411-1430.

Kam, W.Y., Pampanin, S., Palermo, A. and Carr, A.J. (2010). Self-centering structural systems with combination of hysteretic and viscous energy dissipations. Earthquake Engineering & Structural Dynamics. 39:10, 1083–1108.

Laefer D., Baronio G., Anzani A., Binda L. (1996). Measurement of grouts injection efficacy for stone masonry wall. VII North American Masonry Conference - NAMC, Notre Dame, USA, Vol.1, pp. 484-496.

Ligabue, V., Pampanin, S., & Savoia, M. (2018). Seismic performance of alternative risk-reduction retrofit strategies to support decision making. Bulletin of Earthquake Engineering, 16(7), 3001-3030.

Milizia F. (1785). Principi di architettura, Venezia.

Ministry Decree n.65 7/3/2017. (2017). Ministerial Decree n.65 of 27 February 2017, integrated with the changes of n.58 of 7 March 2017. Guidelines for the seismic risk classification of constructions. Rome, Italy: Italian Ministry of Infrastructures and Transport. (In Italian).

Mitrani-Reiser, J., and J. Beck. (2007). An ounce of prevention: Probabilistic loss estimation for performance-based earthquake engineering, PhD Thesis, CalTech, USA.

Modena C., Bettio C. (1994). Experimental characterization and modelling of injected and jacketed masonry walls. Italian-French Symposium Strengthening and Repair of Structures in Seismic Area, Nizza, pp. 273-282.

Modena, Binda L., Anzani A. (1997a). Investigation for the Design and Control of the Repair Intervention on Historical Stone Masonry Wall. VII International Conference and Exhibition, Structural Faults and Repair, Edinburgh, Vol. 3, pp. 233-242.

Modena C., Zavarise G., Valluzzi M.R. (1997b). Modelling of stone masonry walls strengthened by r.c. jackets. IV International Symposium On Computer Methods in Structural Masonry - STRUMAS, Florence, Italy, pp. 285-292.

Modena C., Tempesta F., Tempesta P. (1997c). Una tecnica a secco basata sull'uso del legno per l'adeguamento statico di solai in legno. L'Edilizia, No. 11-12.

Motavalli M. (2005). Seismic Assessment and Retrofitting of Shariati Museum in Tehran, FRP Strengthening of Masonry, Fibre Composites, FS07, Empa Switzerland, University of Tehran. Iran.

NIKER Project. (2012). New integrated knowledge based approaches to the protection of cultural heritage from Earthquake-induced Risk. European research project

NZSEE (New Zealand Society for Earthquake Engineering). (2006). Assessment and improvement of the structural performance of buildings in earthquakes recommendations of a NZSEE study group on earthquake risk buildings. NZSEE, New Zealand.

NZSEE (New Zealand Society for Earthquake Engineering). (2017). The seismic assessment of existing buildings - technical guidelines for engineering assessments. Wellington, New Zealand.

NTC (Norme Tecniche per le Costruzioni). (2018). Aggiornamento delle Norme Tecniche per le Costruzioni. Decreto ministeriale del 17 gennaio 2018. Rome: Ministero delle Infrastrutture e dei Trasporti. (in Italian).

O'Reilly, G. J., and G. M. Calvi. (2019). Conceptual seismic design in performance-based earthquake engineering. Earthquake Engineering & Structural Dynamics 48 (4): 389–411. doi: 10.1002/ eqe.3141.

Ottonelli, D., Cattari, S., & Lagomarsino, S. (2020). Displacement-Based Simplified Seismic Loss Assessment of Masonry Buildings. Journal of Earthquake Engineering, 24(sup1), 23-59.

Porter, K. A. (2003). An overview of PEER's performance-based earthquake engineering methodology. Proceedings of 9th International Conference on Applications of Statistics and Probability in Civil Engineering (ICASP9) San Francisco, CA.

Porter, K. A. and Beck, J. L. (2004). Simplified PBEE to estimate economic seismic risk for buildings. Proceedings of Performance-Based Seismic Design [PBSD] - Concepts and Implementation, Bled, Slovenia.

Porter, K. A., Beck, J. L., and Shaikhutdinov, R. (2004a). Simplified estimation of economic seismic risk for buildings. Earthquake Spectra, 20(4):1239–1263.

Priestley, M. (1997). Displacement-based seismic assessment of reinforced concrete buildings, Journal of Earthquake Engineering 1(1), 157–192.

Rondelet G. (1832). Trattato teorico e pratico dell'arte di edificare, Libro VII.

SEAOC (1995). Vision 2000 Report: Performance Based Seismic Engineering of Buildings.

Sika CarboDur FRP Composites for Repair & Strengthening of Structures. (2003). Sika Poland Sp. z o.o. ul. Karczunkowska 89 02-871 Warszawa Polska, www.sika.pl.

Solberg, K. M., Dhakal, R. P., Mander, J. B., and Bradley, B. A. (2008). Computational and rapid expected annual loss methodologies for structures. Earthquake Engineering and Structural Dynamics, 37(1):81–101.

Sullivan, T. J. and Calvi, G. M. (2011). Considerations for the seismic assessment of buildings using direct displacement-based assessment approach. Proceedings of the 2011 ANIDIS Conference, Bari, Italy.

Sugano S. (1996). State-of-the-art in techniques for rehabilitation of buildings, 11th World Conference on Earthquake Engineering, Paper N° 2175.

Tomaževič M., Turnšek V. (1982). Verification of the seismic resistance of masonry buildings. British Ceramic Society: Loadbearing Brickwork, No. 30, pp. 360-369.

Tomaževič M. (1992). Laboratory and in situ tests of the efficacy of grouting and tying of stone masonry walls. International Workshop on Effectiveness of Injection Techniques and Retrofitting of Stone and Brick Masonry Walls in Seismic Area, pp. 95-116.

Valluzzi MR, Tinazzi D, Modena C. (2002). Shear behaviour of masonry panels strengthened by FRP laminates. Construction and Building Materials 2002;16(7):409–16.

Valluzzi M.R., da Porto F., Modena C. (2004). Behavior and modeling of strengthened three-leaf stone masonry walls. Materials and Structures, MS 267, Vol. 37, April, pp. 184-192.

Valluzzi M.R., Binda L., Modena C. (2004). Mechanical behavior of historic masonry structures strengthened by bed joints structural repointing, Construction and Building Materials, Elsevier Science Ltd., July 2004, Vol 19/1 pp 63-73.

Vinci, M. (2014). I tiranti in acciaio nel calcolo delle costruzioni in muratura (in Italian). Flaccovio Dario editore.

Vinci, M. (2019). Metodi di calcolo e tecniche di consolidamento per edifici in muratura (in Italian). Dario Flaccovio.

Welch, D., Sullivan, T. J., and Calvi, G. M. (2012). Towards a direct displacement-based loss assessment methodology for RC frame buildings. Proceedings of 15thWorld Conference on Earthquake Engineering, Lisbon, Portugal.

Zareian, F. and Krawinkler, H. (2012). Conceptual performance-based seismic design using building-level and story-level decision support system. Earthquake Engineering and Structural Dynamics, 41(11):1439–1453.

5. The SLaMA-URM method

5.1 Introduction

In this Chapter, the simplified analytical procedure, based on the EF discretization, is proposed for the seismic vulnerability assessment of existing URM buildings. This procedure follows an analogy with the SLaMA method reported in the New Zealand guidelines (NZSEE 2017a), developed for Reinforced Concrete (RC) structures, that is an analytical (performed "by hand") non-linear analysis technique that provides a first estimation of the global capacity of buildings, starting from the local behaviour of the structural components.

Masonry buildings show a different response under seismic actions with respect to the RC ones. For these latter typologies, the In-Plane response of the walls parallel to seismic forces represents the global capacity of the structure, while URM buildings, according to their structural details, can show both In-Plane and Out-Of-Plane mechanisms, with respect to the direction of the forces and according to the structural details. Also for this reason, the adaptation of the SLaMA method to URM buildings was not that trivial.

In this Chapter, at first, the main steps of the procedure for RC structures are shown (Section 5.2), and then the way to extend and apply it to the case of URM buildings is presented (Sections 5.3 and 5.4). The limitations and a summary of the role of the SLaMA-URM are then discussed (Section 5.5).

5.2 The SLaMA method for RC structures

The SLaMA method originates from studies on the assessment of RC buildings, among which one of the more important is that proposed by Priestley and Calvi (1991). In this work a capacity design-based assessment procedure focused on the global behaviour of buildings was proposed. The effect of the detailing of single components was taken into account and the global response of the building was measured by the pseudo-spectral acceleration, corresponding to the structure natural period. Starting from this research, in Park (1995) a

focus was given on the individuation of the probable plastic mechanism of the frame from the characteristics of the single components. The flexural and shear behaviours of these components were defined and the global response resulted as a ratio between the base shear capacity and the demand. An improvement was given by Priestley (1997), that changed the general point of view. In order to define the performance of the structure and the expected damage level in terms of displacements (more appropriate, as suggested in Priestley *et al*., 2007), the author focused on a displacement-based assessment procedure. Consequently, the result was expressed in terms of displacement capacity-demand ratio, derived from calculations on an equivalent SDOF system.

Both the procedures, the force-based proposed by Park (1995) and the displacement-based proposed by Priestley (1997), were introduced in the New Zealand guidelines NZSEE (2006), and named Simple Lateral Mechanism Analysis (SLaMA), as an alternative to the non-linear analyses. This procedure was extensively applied to real and ideal cases study buildings in New Zealand and through these applications, it was possible to identify the procedure gaps and improve it.

The SLaMA method is now prescribed in the new version of the seismic assessment guidelines of the New Zealand Society for Earthquake Engineering (NZSEE 2017a) for seismic assessment of existing buildings, and its use is suggested before the implementation of a more complex computational model. The SLaMA method is based on an analytical nonlinear approach to obtain the capacity curve of a given frame-like RC structure through simple “by hand” (i.e. implemented in an electronic spreadsheet) calculations: since simplified assumptions are made, no numerical computer model is needed.

The global seismic behaviour of the building is estimated from the evaluation of the local capacity (i.e. of the components) by considering a chain of failure mechanisms among the structural subassemblies, and finally estimating the probable capacity curve of the structure (base shear vs horizontal displacement). More in detail, the methodology consists of some consequential steps (see Figure 5.1): 1) obtain the building data (geometry, material properties, and structural details) and the information on the seismic hazard; 2) evaluate the flexural and shear capacities at the component level; 3) define the hierarchy of strength among column, beam and joint at subassembly level; 4) evaluate the overturning moment capacity of the structure and the global force-displacement response (corresponding to different types of mechanisms as Beam Sidesway, Mixed Sidesway and Column Sidesway), from the equilibrium of the internal moment capacities at global structure level; 5) plot the

capacity curves in the “Acceleration-Displacement Response Spectra” (ADRS) domain to define the performance point and the %NBS (as suggested in NZSEE 2017a) or the ISV index (as suggested in Ministry Decree n.65 7/03/2017) of the building.

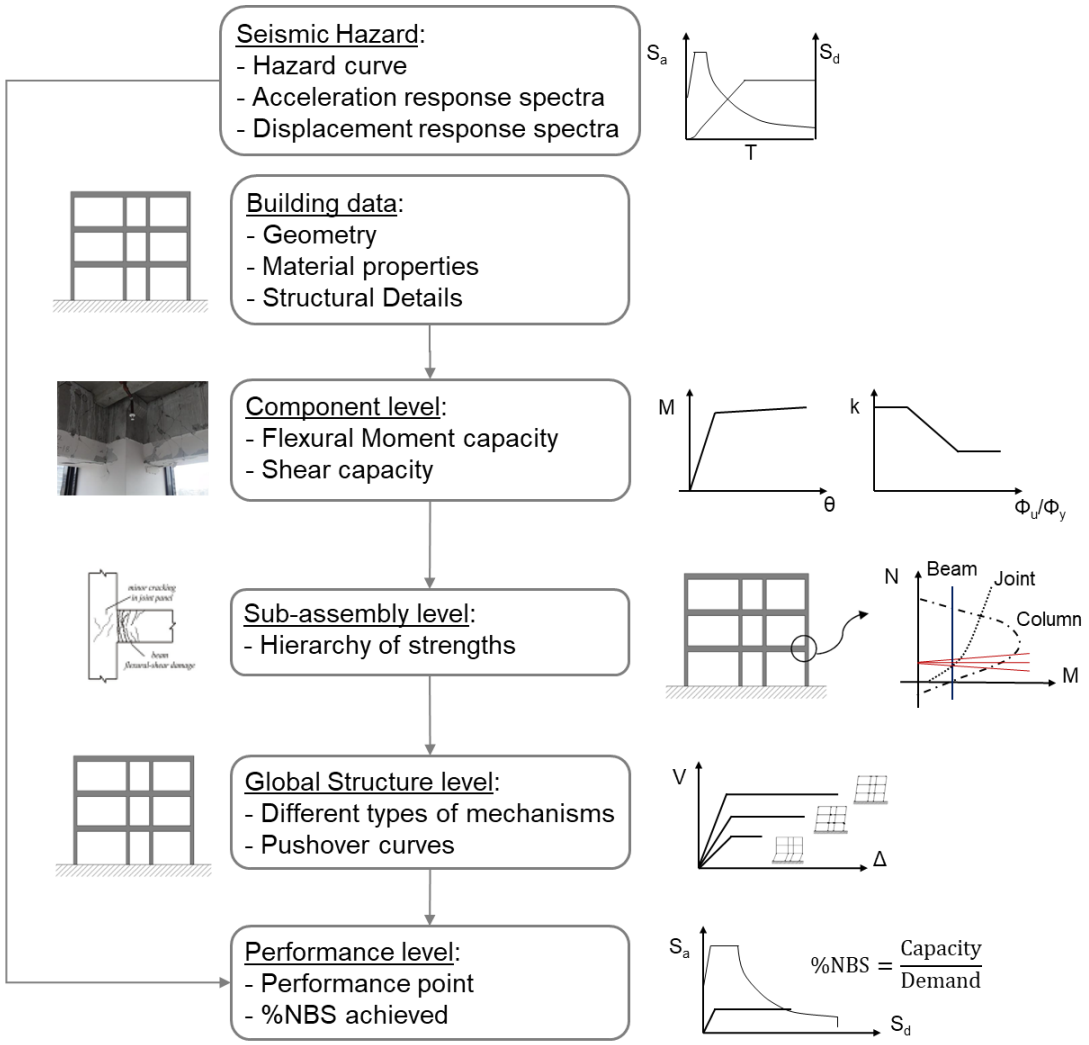

Figure 5.1. Flowchart of the SLaMA method for R.C. structures.

The SLaMA method can be useful also to define the performance of retrofit alternatives in terms of %NBS of the retrofitted structures.

The procedure has been extensively validated and improved for Reinforced Concrete (RC) structures in Gentile *et al*., 2019.

5.3 From SLaMA to SLaMA-URM method

In this Thesis, the SLaMA method is extended, adapted and applied to the case of URM structures, relying on the hypothesis of regular and frame-like buildings. The proposed procedure is called the SLaMA-URM method.

To apply SLaMA method to URM buildings, some specific considerations need to be taken into account. Post-earthquake damage observations have shown that the Out-Of-Plane (OOP) mechanisms generally represent a greater risk than the In-Plane ones. Hence, since the SLaMA method considers only the global behaviour of the buildings, some additional precautions should be taken in such a way to integrate the analyses on the OOP response of the structure in the SLaMA-URM method.

As stated in Section 3.1, the masonry walls are characterized by a hierarchy of collapse mechanisms. The first is the crumbling of the masonry that can occur when the quality of the material texture has poor characteristics. In this case, walls collapse before any mechanism with higher resistance occurs. This aspect should be considered at first in the analysis of an existing structure, hence, in case of probable masonry crumbling, the designer should intervene with appropriate techniques (see Section 4.5.2) to satisfy the required monolithic behaviour. On this basis, it is possible to approach the analysis of the subsequent possible collapse mechanisms. According to the hierarchy of the collapse mechanisms, the following possible modes to occur are the Out-Of-Plane ones (or the first mode mechanisms). These correspond to the Out-Of-Plane kinematics of single walls or portions of the structure. These are phenomena of overturning (rocking) that lead to the collapse of the structure due to loss of balance. OOP mechanisms occur in buildings when the absence (or poor effectiveness) of the walls-to-walls and/or the walls-to-diaphragms connections do not guarantee the establishment of global behaviour of the structure. It is evident that in such cases, the global verification of the structure (pushover or other) has no correspondence with its actual seismic behavior, if the necessary protections to prevent these mechanisms are not adopted in advance.

Among the OOP mechanisms, the simple overturning of external walls under the action of an earthquake represents one of the most frequent and dangerous damage situations. It can be developed in various ways, on one or more floors of the building, depending on the actual walls to diaphragms connection at the various levels of the structure. In presence of ring beams or tie rods, this type of mechanism is unlikely to manifest, as these elements

prevent its activation. Another possible OOP mechanism is the vertical bending, which can occur when the wall is well connected at the ends, slightly connected at the sides and free in the central part. While, if there is a good wall-to-wall connection and the wall is free to rotate on the top, or in presence of a pushing roof, the expected mechanism is the horizontal bending.

To obtain a global response that is defined by the In-Plane mechanisms, and hence characterized by higher strength and ductility, it is needed to intervene on the building structure impairing the OOP mechanisms. The probable In-Plane mechanisms of a masonry wall are the flexural and the shear failure crises, widely described in Chapter 3.

The SLaMA-URM method herein proposed is a seismic assessment procedure of URM buildings, which considers both the Out-Of-Plane and the In-Plane behavior within the displacement-based approach. More in detail, with reference to Figure 5.2, the procedure consists of collecting the seismic hazard of the construction site and the building data and then making considerations on the response of the structure. At first, the masonry material quality is assessed: if it is poor, the masonry crumbling failure mode is expected to occur. In the case of good masonry quality, instead, it is carried out the evaluation of the connections between walls, in order to understand if the “box-behaviour” of the structure is guaranteed. If this is the case, the eventual OOP mechanisms are prevented and the only IP mechanisms of the walls (parallel to the seismic actions) are considered. In this case, the %NBS of the structure corresponds directly to the %NBS calculated for the IP mechanisms (Figure 5.3a). If the “box-behaviour” is not guaranteed, also the seismic performance of the probable OOP mechanisms of the walls orthogonal to the forces has to be calculated. Consequently, the %NBS of the structure corresponds to the minimum of the values calculated from the OOP and the IP mechanisms (Figure 5.3b).

It is worth noting that the walls-to-diaphragms connections (poor or adequate), as well as the stiffness or flexibility of the existing diaphragms, can influence the OOP mechanisms. They lead to different failure modes than the simple overturning of external walls, such as vertical and horizontal bending, or can increase the possibility that they appear at earlier stages, strongly limiting the global ductility of the structure. In this Thesis, the applications of the SLaMA-URM method (see Chapter 7) refer to rigid diaphragms, for sake of simplicity.

The strength related to the probable OOP mechanisms, with reference to the description in Section 3.2, is calculated based on the geometry of the wall and on the strength of the

materials. More in detail, due to the negligible tensile strength of the masonry and the slenderness of masonry walls they can lose static equilibrium for very low values of Peak Ground Acceleration (PGA). According to the displacement-based approach (DBA), the assessment of rocking masonry structures can be performed and the static multiplier that induces the onset of rocking is obtained by evaluating the work done by the equilibrated forces on a set of compatible generalized virtual displacements (through the Theorem of Virtual Works). DBA requires evaluating the seismic multiplier under an incremental kinematic analysis, i.e. increasing step-by-step the rotation of blocks till loss of static equilibrium is reached. The obtained curve (horizontal multiplier versus displacement of a control point) is a sort of pushover curve, which can be transformed into a capacity curve (spectral acceleration versus displacement) of the substitute structure (nonlinear equivalent Single Degree of Freedom System, SDOF). The %NBS can be calculated as the ratio between the displacement capacity and demand. Due to the fact that the calculations of the OOP performance do not represent the innovation of this Thesis, for more details on it refer to Section 3.2, where some literature is reported, or to Section 7, where they are considered in the analysed cases study structures.

On the contrary, due to the fact that the In-Plane seismic performance represents the main proposal of this Thesis, a comprehensive view is reported in the following Sections. Due to the fact that the SLaMA-URM method can be easily applied to frame-like buildings, it is clear that the discretization into an Equivalent Frame idealization (i.e. deformable piers and spandrels connected by rigid nodes) of the In-Plane walls is a suitable choice.

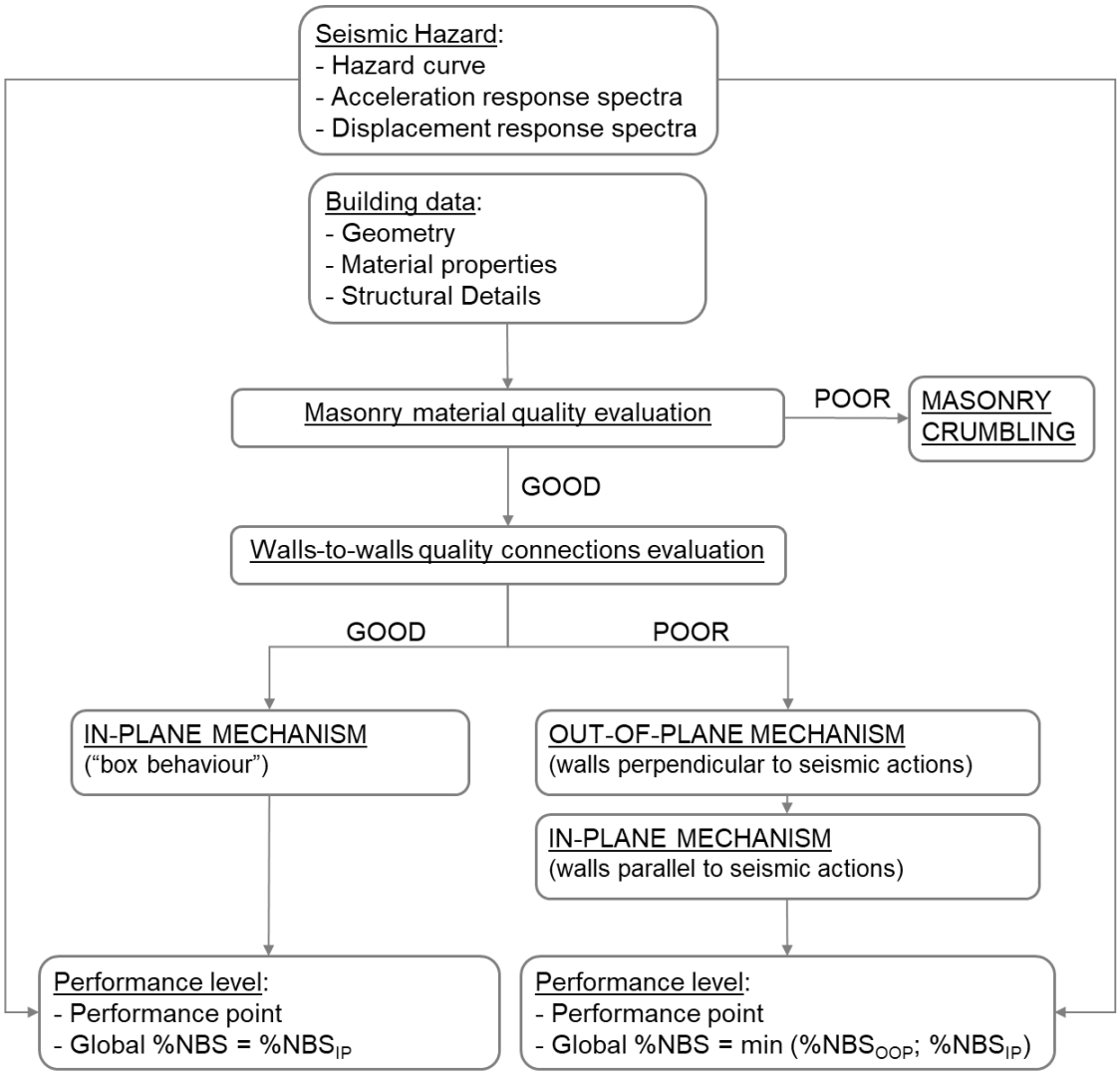

Figure 5.2. Flowchart of the SLaMA-URM method.

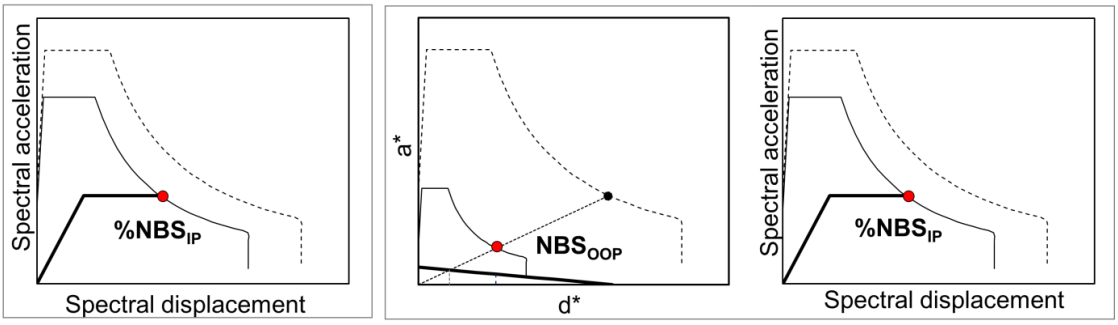

Figure 5.3. Seismic performance level of: (a) "box-like" structure and (b) structure with probable OOP and IP mechanisms.

5.4 In-Plane mechanisms performance level

The key steps to define the In-Plane seismic performance of a wall, according to SLaMA-URM method, are briefly listed below, summarized in Figure 5.4 and extensively discussed in the next subsections:

- Collection of the *building data* and identification of the site *seismic hazard* (see Section 5.4.1);
- *Analysis at component level*: the strength and deformation of each structural component are calculated. The In-Plane flexural and shear capacities are defined according to the rules given in literature and/or code provisions and the possibility that the shear failure anticipates the flexural failure is investigated. As a result, moment-rotation curves and moment-axial load (M-N) interaction domains for piers and spandrels are defined. Different considerations can be made for pier-spandrel joints, as outlined in Section 5.4.2;
- *Analysis at subassembly level*: the interaction and comparison between components capacity are assessed in each subassembly, to identify the sequence of the failure mechanisms and hence the hierarchy of strength. This comparison is expressed in terms of a common parameter, i.e. the Equivalent Pier Moment, in the Moment-Axial load (M-N) performance domain. The probable inelastic mechanism of the frame-like building is assessed. More details are given in Section 5.4.3;
- *Analysis at global structure level*: according to the assumptions of deformed shape profiles and imposing global equilibrium conditions, a bi-linear global capacity curve is calculated. Each lateral resisting system is referred to an equivalent SDOF system and, in each principal direction of the building, the capacity curves of the parallel systems are summed up and the seismic performance of the building is assessed in the Acceleration Displacement Response Spectrum (ADRS). For more details refer to Section 5.4.4;
- Identification of the *In-Plane Performance level* of the structure through the comparison between the capacity and the ADRS curve (Section 5.4.5).

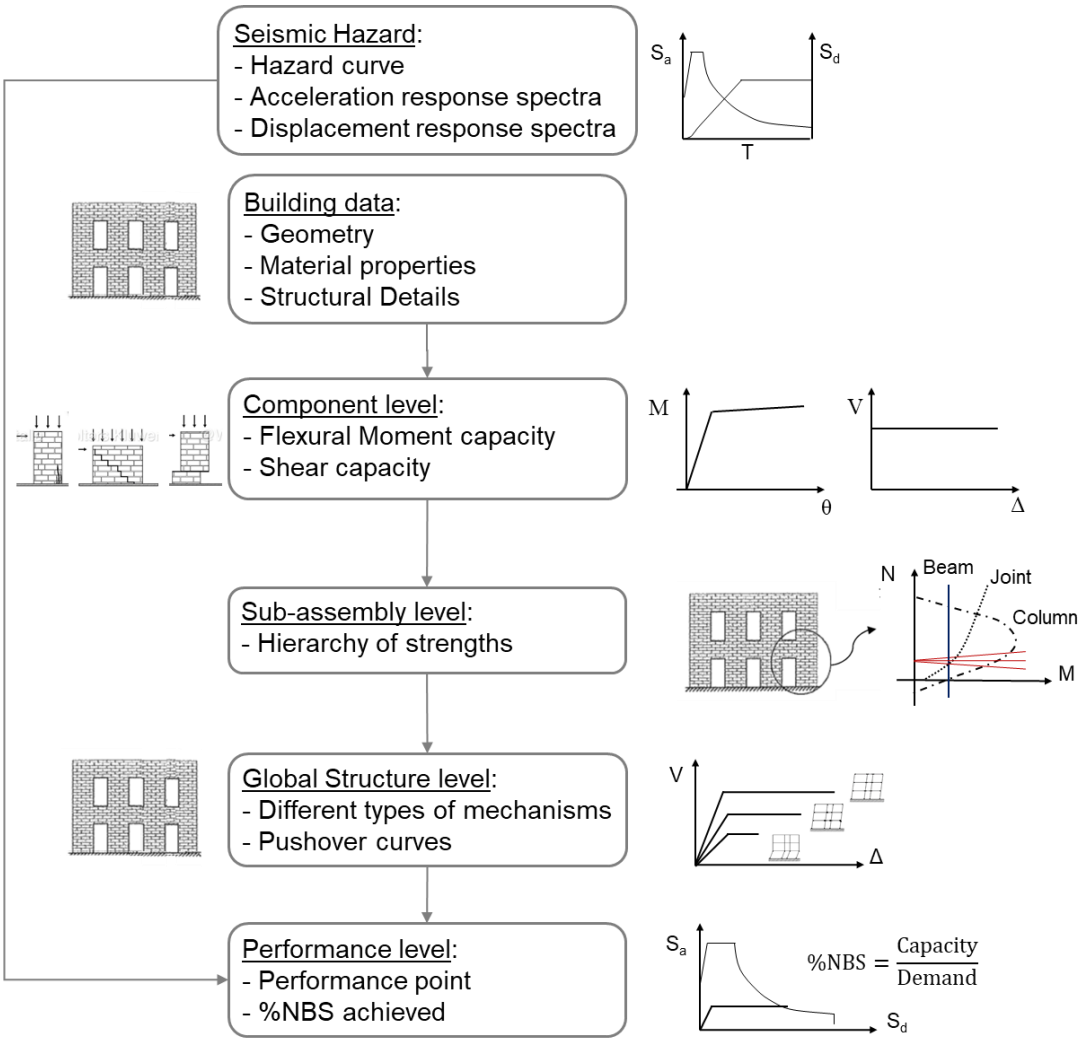

Figure 5.4. Flowchart to define the In-Plane performance level of a wall according to the SLaMA-URM method.

5.4.1 Building data and seismic hazard

The seismic hazard and the collection of the building data are the two fundamental input data for the SLaMA-URM method.

The collection of the building data consists of defining geometry, material properties and structural details of the building under examination. They can be found from construction drawings and documents, on-site investigation, in situ or laboratory tests, in codes and standards.

The seismic hazard represents the severity of the earthquakes expected in a specific site and following Cornell's Method (1968) it is possible to construct the hazard curve for a fixed period or peak acceleration, correlating the spectral ordinate with an exceeding probability in a period of 50 years. From this, the acceleration and displacement spectra, representing the demand in the ADRS, has to be compared with the capacity curve of the structure.

5.4.2 Analysis at component level

The first analysis of the SLaMA-URM method is at the component level. In this Section, the procedure to define the probable strength and deformation capacity of the pier, spandrels and (if considered) pier-spandrel joint is described.

To determine the capacity models for structural components, such as flexural and shear strength for piers and spandrels, each seismic code or guideline provides different formulations, derived from literature (see Section 3.3).

In the SLaMA-URM method, although the aforementioned formulations are widely recognised and commonly adopted in the professional practice (see Section 3.3.2.1), to define the flexural capacity of the URM components a peculiar sectional analysis, named Monolithic Beam Analogy (MBA), is adopted (Section 5.4.2.1). It consists of estimating "by hand" the moment capacity of piers and spandrels to define the moment-rotation curves and the moment-axial load (M-N) domains, adopting simple and more complex stress-strain relationships.

For the shear strength of piers and spandrels the SLaMA-URM method lends itself to adopt the main formulations existing in literature, reported in Sections 3.3.2.2 and 3.3.3.2, respectively.

The pier-spandrel joints are assumed as rigid elements, thus neglecting their capacity contribution. Nevertheless, in Section 5.4.2.4 a preliminary analytical approach to derive their strength capacity is considered, with the aim to assess their effect on the hierarchy of strength at the subassembly level.

In the next Sections the tools to perform analysis at the component level are discussed, with regard to the formulations adopted in the SLaMA-URM applications, presented in Chapter 6.

5.4.2.1 Monolithic Beam Analogy (MBA)

In order to define the moment capacity of the URM structural components, a peculiar sectional analysis, named Monolithic Beam Analogy (MBA) is proposed in this Thesis.

The MBA approach, introduced in Pampanin *et al*. (2001) for controlled rocking systems, is based on the concept of ductile jointed connections, where the inelastic demand is concentrated at the critical section through opening and closing of an existing gap at the interface (rocking motion of the beam or wall panel) (Pampanin, 2003). Due to the gap-opening/closing, the strain compatibility of the section is violated, and the traditional section analysis cannot be adopted. The MBA was founded on an alternative compatibility condition at the global level to overcome this issue, for the partially unbonded or debonded reinforcement connections. The member compatibility condition is provided by imposing equal global (member) displacement between a system with ductile connections and an equivalent reinforced concrete (or monolithic) system (Figure 5.5).

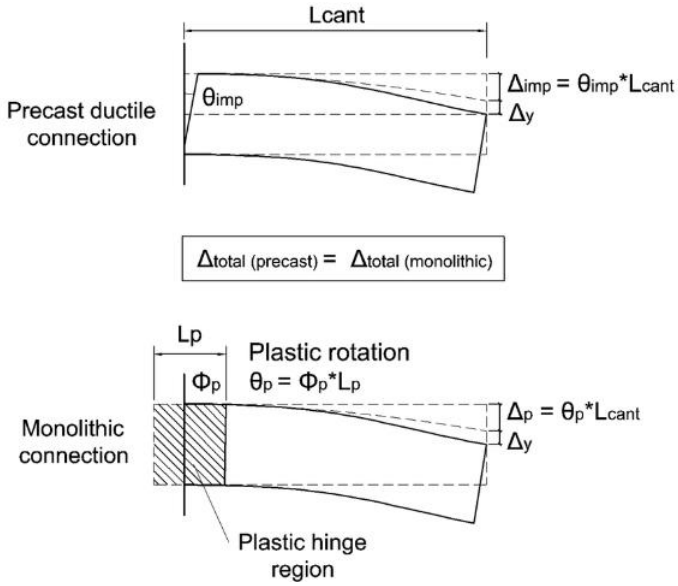

Figure 5.5. Monolithic Beam Analogy (MBA) concept (Pampanin et al., 2001).

In a monolithic cantilever, the total displacement is given by the sum of the elastic and plastic (at the plastic hinges region) contributions. For a precast concrete cantilever, the total displacement is given, basically, by the sum of the elastic and the opening gap (at the beam-column interface) contributions. Assuming that both the systems in Figure 5.5 have the same

displacement, Equations 5.1 - 5.3 lead to Equation 5.4, where the plastic displacement Δ_p is expressed in terms of the imposed gap opening θ_{imp} and the cantilever length L_{cant} (or distance to the contra flexure point).

$$\Delta_{tot(precast)} = \Delta_{tot(monolithic)} \tag{5.1}$$

$$\Delta_{imp} + \Delta_{el} = \Delta_p + \Delta_{el} \tag{5.2}$$

$$\Delta_{imp} = \Delta_p \tag{5.3}$$

$$\theta_{imp} L_{cant} = \Delta_p \tag{5.4}$$

The MBA is an iterative approach defined by some important steps: 1) fix the rotation θ_{imp}, 2) guess the neutral axis depth c; 3) evaluate the deformation in the post-tension tendons; 4) calculate the mild steel reinforcement and the concrete strains. Regarding the concrete, to overcome the difficulty to identify its strain, the member compatibility between the precast and the equivalent monolithic connection is introduced.

In the monolithic case, using the yielding ϕ_y and the ultimate ϕ_u curvatures concepts, introduced in Paulay and Priestley (1992), the concrete strain can be obtained by Equations 5.5 - 5.9.

$$\Delta_p = \theta_p \left(L_{cant} - \frac{L_p}{2} \right) = (\phi_u - \phi_y) L_p \left(L_{cant} - \frac{L_p}{2} \right) \tag{5.5}$$

$$\theta_{imp} L_{cant} = (\phi_u - \phi_y) L_p \left(L_{cant} - \frac{L_p}{2} \right) \tag{5.6}$$

$$(\phi_u - \phi_y) = \frac{\theta_{imp} L_{cant}}{L_p \left(L_{cant} - \frac{L_p}{2} \right)} \tag{5.7}$$

$$\phi_u = \frac{\varepsilon_c}{c} = \frac{\theta_{imp} L_{cant}}{L_p \left(L_{cant} - \frac{L_p}{2} \right)} + \phi_y \tag{5.8}$$

$$\varepsilon_c = \left[\frac{\theta_{imp} L_{cant}}{\left(L_{cant} - \frac{L_p}{2} \right) L_p} + \phi_y \right] c \tag{5.9}$$

where L_p is the plastic hinge length, defined as $L_p = 0.08L_{cant} + l_{sp}$, where l_{sp} is the strain penetration length.

At this step, an expression of the concrete strain in terms of neutral axis depth, as $\varepsilon_c = f(c)$, is obtained: each obtained ε_c satisfies the section equilibrium. For each position of neutral axis c, Equation 5.9 provides a compatible concrete strain.

Once the section equilibrium is satisfied, it is possible to calculate the moment capacity. The whole MBA procedure is summarized in Figure 5.6.

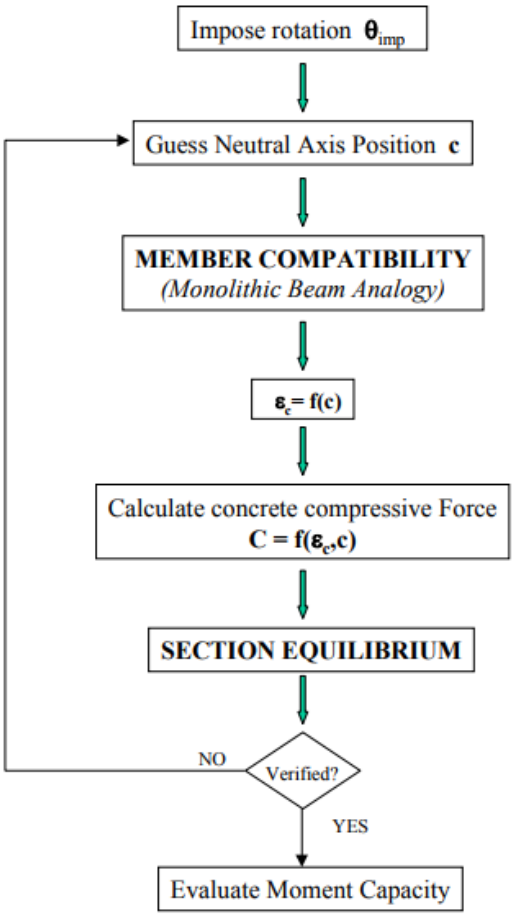

Figure 5.6. Flowchart of the Monolithic Beam Analogy (MBA) approach (Pampanin et al., 2001).

Since masonry walls subjected to horizontal loads are characterized by a typical rocking behaviour, the MBA approach is herein applied to them. More in detail, as a system defined by ductile jointed connections, the inelastic deformations demand is assumed to be concentrated at the critical sections (at the ends of piers and spandrels) where the opening

of a gap is expected to occur, and the components are assumed as rigid elements. According to the MBA approach, to define the moment capacity of URM components (piers and spandrels) a moment-rotation relationship is adopted instead of a traditional moment-curvature relationship when defining the section behaviour.

Equation 5.10 can be derived, as shown previously, from an analogy in terms of displacement between the URM cantilever element and an equivalent monolithic RC element:

$$\varepsilon_{c,i} = \left[\frac{\theta_i L_{cant}}{\left(L_{cant} - \frac{L_p}{2} \right) L_p} + \phi_y \right] c_i \tag{5.10}$$

where $\varepsilon_{c,i}$ is the strain value at the corresponding neutral axis depth c_i; ϕ_y is the elastic curvature, assumed as $\phi_y = 2\,\varepsilon_{yc}/B$, where ε_{yc} is the elastic compressive strain, B is taken as the length B_p for the piers and the height h_{sp} for the spandrels; L_{cant} is the distance from the element-end and the point of contra flexure and L_p is the assumed depth of the cracking (theoretical equivalent plastic hinge length) at the element-end, which is taken approximately as $0.1L_{cant}$. The cantilever length L_{cant}, in case of fixed-fixed boundary conditions, is assumed as half of the effective height $h_{p,eff}/2$ for piers and as half of the clear span $L_{sp}/2$ for the spandrels; in case of cantilevered boundary condition, it is equal to the effective height $h_{p,eff}$ for piers and the clear span L_{sp} for the spandrels. In Figure 5.7 are shown the geometric parameters adopted for piers and spandrels to define the strain value, at a defined rotation, according to the MBA approach.

Structural component	L_{cant}	L_p	ϕ_y
PIER	$h_p/2$ (for fixed-fixed piers) h_p (for cantilevered piers)	$\sim 0.1L_{cant}$	$2\,\varepsilon_y/B_p$
SPANDREL	$L_{sp}/2$	$\sim 0.1L_{cant}$	$2\,\varepsilon_y/h_{sp}$

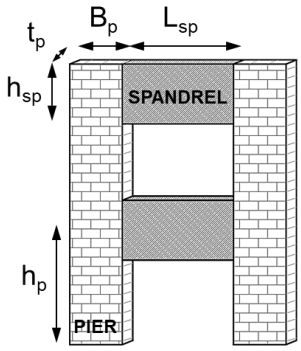

Figure 5.7. Geometric parameters of piers and spandrel used in the MBA formulation.

In Figure 5.8 the steps to define the moment capacity of the piers through the MBA approach are shown.

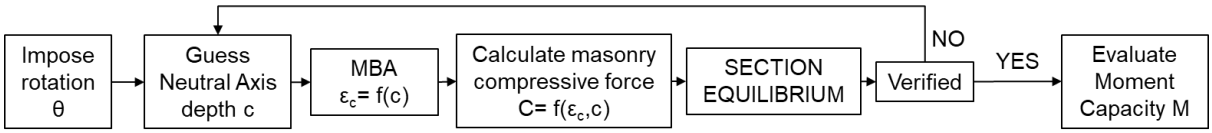

Figure 5.8. Flowchart to calculate the moment capacity of URM components through the MBA approach.

The adoption of the MBA approach for masonry walls lets to assume more reliable stress-strain constitutive laws for masonry with respect to those proposed by codes (i.e. by NTC 2018 or NZSEE 2017). Moreover, it calculates the rotation capacity of components, which hence is not assumed a priori (as in NTC 2018 and in other codes).

5.4.2.2 Pier

The moment capacity of URM piers can be obtained by hand calculations through the sectional analysis by MBA approach (see Section 5.4.2.1). The flexural response is taken into account when the moment-rotation analysis (considering the gravity axial load) is performed. The corresponding moment-rotation curve can be simplified in a tri-linear curve, defined by the elastic (θ_y, M_y), the peak (θ_p, M_p) and the ultimate (θ_u, M_u) points. In addition, the moment-axial load (M-N) interaction domain is calculated.

Different stress-strain relationships can be adopted for masonry material to represent its compression behaviour. Italian code (NTC 2018) and New Zealand guidelines (NZSEE 2017b) suggest to assume an equivalent rectangular compressive stress-block to define the flexural capacity related to the rocking mechanism, according to the closed-form in Equation 5.11:

$$M_u = \left(l^2 t \frac{\sigma_0}{2}\right)\left(1 - \frac{\sigma_0}{0.85 f_m}\right) \tag{5.11}$$

To go beyond the simplification related to the stress-block assumption, more reliable constitutive laws for masonry material can be adopted, from simple to more accurate. The

MBA approach lends itself to this aim. From literature, it is known that the masonry material can be assumed as homogeneous material with no-tensile resistant (NTR) capacity, and different stress-strain relationship can be assumed: from the elastic-perfectly plastic EPP model (Augenti and Parisi, 2010; Brencich and De Francesco, 2004; Cattari, 2007) to the strain-softening models in the post-peak range (Cavaleri *et al*., 2005; Brencich and de Felice, 2009). An EPP relationship can be used to capture the elastic trend and the subsequent plastic plateau. It represents a crude simplification of the URM behaviour, but it is widely used in the professional practice and research studies when the stress-block simplification is considered too approximated. As an alternative, a parabola-rectangle (PR) diagram (as suggested by EN 1996 - 2006) can be assumed. This relationship allows to capture the non-linear initial trend of the masonry in compression and the plastic plateau after the peak stress. To catch the strain softening behaviour after the peak, a more reliable stress-strain relationship can be adopted. Among these, the Kaushik *et al*. (2007) model can be considered. It is derived from the Kent and Park (1971) model, proposed for reinforced concrete material, and then adapted to masonry material. It is characterized by an initial parabolic variation, followed by post-peak softening and a linear decreasing variation, until a constant stress. The ultimate strain is defined based on the ductility of the mortar. From some adjustments to the Kaushik *et al*. (2007) model, Lumantarna (2012) derived a stress-strain relationship for New Zealand URM. These refinements, taken into account from extensive experimental tests made on the URM material after the February 2011 Christchurch earthquake, concern the expression of the effective yield strain.

For EPP-NTR and PR-NTR models, the compressive “yield” (or elastic limit) (ε_{yc}) and ultimate (ε_{uc}) strains can be assumed a priori (i.e. they can be assumed as for the concrete material, equal to 0.02 and 0.0035, respectively). For Lumantarna and Kaushik stress-strain relationships, the yield strain depends on the material properties of masonry, and the ultimate strain is based on the mortar ductility.

In Figures 5.9 - 5.11 are shown the aforementioned analytical stress-strain relationships (EPP, PR, Kaushik and Lumantarna’s models) that can be assumed for the URM piers in compression.

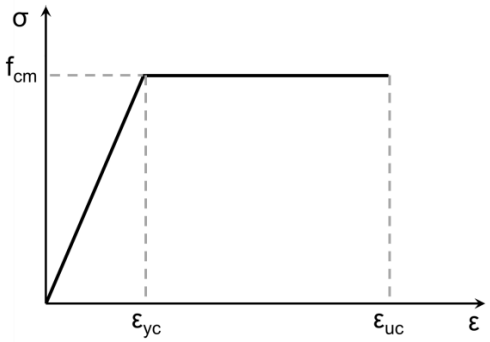

Analytical stress-strain model	$\sigma = E_m \varepsilon$	for $0 \le \varepsilon \le \varepsilon_{yc}$
	$\frac{\sigma}{f_{cm}} = 1$	for $\varepsilon_{yc} \le \varepsilon \le \varepsilon_{uc}$

Figure 5.9. Elastic-perfectly plastic (EPP) stress-strain model.

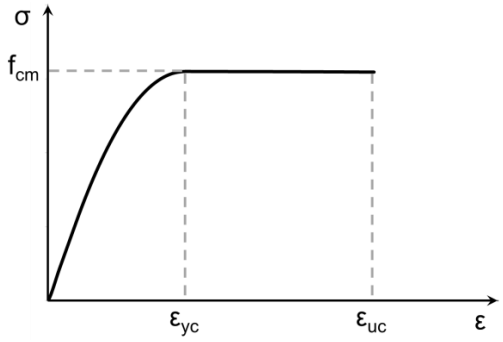

Analytical stress-strain model	$\frac{\sigma}{f_{cm}} = 2\frac{\varepsilon}{\varepsilon_{yc}} - \left(\frac{\varepsilon}{\varepsilon_{yc}}\right)^2$	for $0 \le \varepsilon \le \varepsilon_{yc}$
	$\frac{\sigma}{f_{cm}} = 1$	for $\varepsilon_{yc} \le \varepsilon \le \varepsilon_{uc}$

Figure 5.10. Parable-rectangle (PR) stress-strain model.

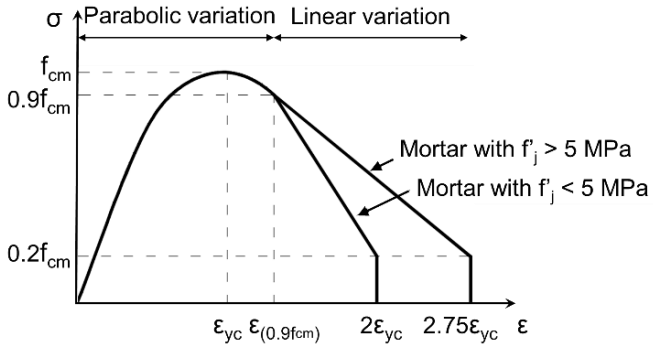

Analytical stress-strain model	$\frac{\sigma}{f_{cm}} = 2\frac{\varepsilon}{\varepsilon_{yc}} - \left(\frac{\varepsilon}{\varepsilon_{yc}}\right)^2$		
Yield strain	$\varepsilon_{yc} = \frac{a f_{cm}}{f'^{b}_{j} E^{c}_{m}}$		
MODEL	**a**	**b**	**c**
Kaushik et al. (2007)	0.27	0.25	0.7
Lumantarna (2012)	0.21	0.25	0.7

Figure 5.11. Analytical stress-strain model proposed by Kaushik et al. (2007) and adapted by Lumantarna (2012).

In Appendix A.1 are reported the formulations to define the moment capacity by the traditional sectional analysis, for the EPP and the Lumantarna models, developed, i.e. by Cattari (2007) and Knox (2012), in function of the compression ductility. For more details about the comparisons of the results obtained adopting both the approaches (i.e. the

traditional sectional analysis and the MBA approach) refer to Section 6.2.3.1, 6.2.3.2, 6.3.3.1, 6.3.3.2.

It should be noted that piers capacity and resulting failure mechanisms are dependent on the acting axial load, given by the gravity load N and the effect of the axial load variation $\pm\Delta N$, due to the coupling effect of the spandrel during the lateral sway (Figure 5.12). The variation of the axial load ΔN can be obtained from the spandrel shear resistance V_{sp} (see Section 5.4.2.3), given by the minimum of the spandrel flexural and shear strength capacity.

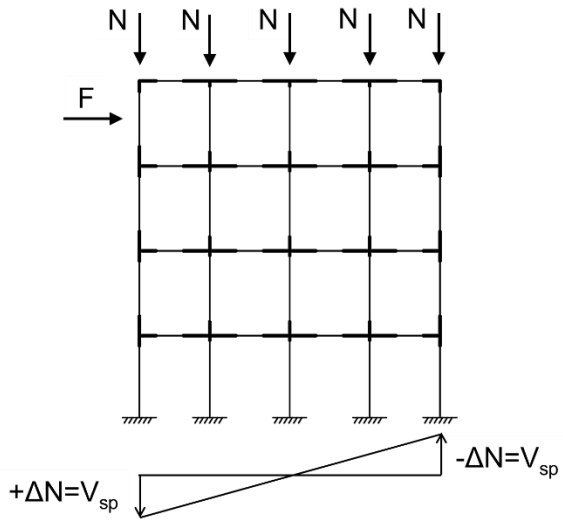

Figure 5.12. Frame subjected to horizontal load and gravity load with axial load variation.

The sectional analysis developed by the MBA approach identifies the moment-rotation behaviour of the section of the piers. To obtain the total rotation of the masonry element, its elastic contribution has to be added. To this aim, the initial stiffness K_{el} can be calculated according to the ASCE (2007), following Equation 5.12, and then the elastic contribution in terms of rotation can be defined by calculating the elastic shear from the elastic moment, through the pier cantilever length.

$$K_{el}=\left(\frac{{h_{eff}}^3}{nE_mI}+1.2\frac{h_{eff}}{B_pt_pG_m}\right)^{-1} \tag{5.12}$$

where h_{eff} corresponds to the effective height $h_{p,eff}$, that can be derived i.e. by the Dolce's rule (Dolce, 1991); B_p and t_p are the length and the thickness of the pier, respectively; E_m

and G_m are the Young's and shear modulus, respectively; I is the moment of inertia; n is a coefficient that takes into account the boundary conditions of the elements, that is equal to 12 in the case of the fixed-fixed condition and equal to 3 in the case of the cantilevered condition.

In accordance with the fixed-fixed condition, the pier contra-flexure point is assumed as located at mid-effective height ($h_{p,eff}/2$, considering the bending moment distribution), contrarily, the cantilever length can be assumed equal to pier effective height ($h_{p,eff}$). The limit elastic shear, displacement and rotation are calculated as follows: $V_y = M_y/L_{cant}$, $\Delta_y = V_y/K_{el}$, $\theta_y = \Delta_y/L_{cant}$.

In Figure 5.13 it is shown an example of moment-rotation curves obtained with the MBA approach by the NTR model.

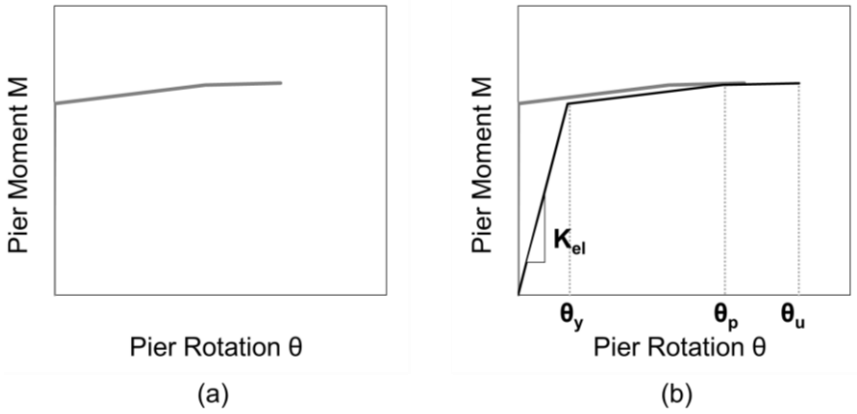

Figure 5.13. (a) Example of pier moment-rotation curve with NTR model, according to the MBA approach and (b) the resultant curve adding the component elastic rotation contribution.

To catch the expected failure of URM piers, the shear capacity has to be investigated and compared with the flexural one. Several formulations exist to consider the different mechanisms of diagonal cracking and bed-joint sliding, as reported in Section 3.3.2.2. For the diagonal cracking, in codes two are the most common approaches: i) the Turnšek and Cačovic criterion (Turnšek and Cačovic, 1971), in which the strength $V_{s,dc}$ is defined based on the masonry tensile strength (see Equation 5.13) and ii) the Mann and Müller model (Mann and Müller, 1982), that assumes the shear strength $V_{s,bdj}$ based on the cohesion and the friction coefficient (Equation 5.14).

$$V_{s,dc}=\frac{B_p t_p f_t}{b}\sqrt{1+\frac{\sigma}{f_t}} \tag{5.13}$$

$$V_{s,bdj} = l' t_p (f_{v0} + \mu\sigma) \tag{5.14}$$

where B_p and t_p are the length and the thickness of the pier, respectively; $b = h_{p,eff}/B_p$ is the pier aspect ratio that varies in the range [1-1.5]; f_t is the tensile strength of the masonry; σ is the mean compressive stress (induced by the axial load N on the pier, with B_p and t_p dimensions of the pier cross-section); l' is the compressive length; f_{v0} is the initial shear strength at zero compressive stress, estimated as $f_t/1.5$ (NTC 2018); μ is the friction coefficient of the masonry.

The piers strength thresholds are expressed in terms of moment capacity calculated from the pier shear strength ($V_{s,dc}$ and $V_{s,bdj}$) and the pier cantilever length L_{cant} as $M = V_{s,dc}(or\ V_{s,bdj})L_{cant}$. Since this parameter is considered not affected by the pier rotation, it is represented by a horizontal line in the moment-rotation curve.

Once both the flexural and the shear mechanisms are defined in a moment-rotation domain, a comparison between the corresponding curves identifies the expected failure mechanism of the URM pier (see Figure 5.14): if there is an intersection between the two curves then it is expected to occur the shear failure mechanism; on the contrary, a flexural failure mechanism defines the response of the URM pier.

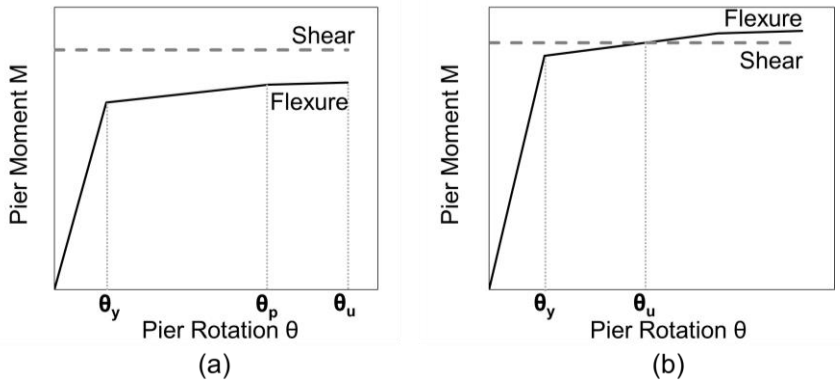

Figure 5.14. Pier moment-rotation curve: (a) expected flexural failure and (b) expected shear failure.

At the component level, in addition to the moment-rotation domain, the moment-axial load (M-N) pier interaction domain is defined. To this aim, the MBA approach can be adopted and the stress-strain relationships previously mentioned can be used. According to this approach, it is possible to describe the moment capacity in function of the compressive strain ductility $\mu_{\varepsilon c}$ and understand the over- or under- estimation in the definition of the M-N domains made by Italian code (NTC 2018) and New Zealand guidelines (NZSEE 2017b), which assumed the closed-form, reported in Equation 5.11. An example of a pier M-N domain is shown in Figure 5.15.

For more details refer to Sections 6.2.3.2, 6.3.3.2 and 6.4.4.2. It is evident that the adoption of different stress-strain models leads to different M-N limit domains, and these differences depend especially on the own characteristics of the adopted model.

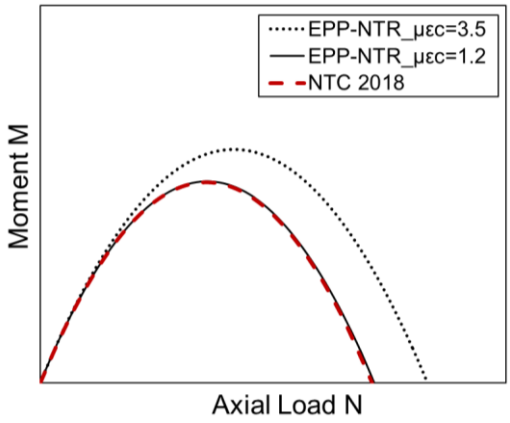

Figure 5.15. Example of pier M-N limit domains adopting different values of $\mu_{\varepsilon c}$ and the Italian Code (NTC 2018) closed-formulation with the EPP-NTR model.

5.4.2.3 Spandrel

The capacity of the URM spandrels, in accordance with literature and code formulations (see Section 3.3.2.2), depends on the possible coupling with tensile resistant elements, as effective lintel or tie rods. If the URM spandrels are coupled or if they are uncoupled but the horizontal axial load is known, they are considered as piers rotated by 90 degrees (NTC 2018; EN 1998 2005). This assumption means that for spandrels the same formulations used for the piers to define the flexural capacity can be adopted, with the addition of the component tensile contribution. More in detail, the moment-capacity is defined through the

MBA approach, considering the compression capacity given by the masonry material and the tension capacity given by the resistant elements (if present). In absence of any resistant element coupled to the spandrel, the bricks interlocking effect at the end-sections with the contiguous masonry can be taken into account (FEMA 306, 1998; Cattari and Lagomarsino, 2008) to avoid an excessive underestimation of the flexural capacity. In this case, an equivalent tensile strength is considered in the MBA approach to define the moment capacity.

The assessment of the flexural capacity of URM spandrels consists of the calculation of the moment-rotation and the moment-axial load diagrams through the MBA approach (see Section 5.4.2.1).

The stress-strain relationships that can be adopted for masonry material, in compression and tension (if bricks interlocking effect is considered), are several. In compression, it is possible to refer to the stress-strain relationships assumed for the URM piers (see Section 5.4.2.2).

Regarding the analysis of the URM spandrels, characterized by a compression stress-strain relationship and a resistant in tension (TR) model the moment-capacity curves can be defined in two different ways, characterized by: 1) limited ductility in tension ($\mu_{\varepsilon t} = \varepsilon_{ut}/\varepsilon_{yt}$), i.e. tension governed failure (TR-TF), and 2) limited ductility in compression ($\mu_{\varepsilon c} = \varepsilon_{uc}/\varepsilon_{yc}$) and unlimited ductility in tension, i.e. compression governed failure (TR-CF). In the latter, the moment capacity is reached when the extreme compression fibre reaches the ultimate compression strain ε_{uc}, while in the former the moment capacity is reached when the extreme tension fibre reaches the ultimate tension strain ε_{ut}.

In Appendix A.1 are reported the formulations to define the moment capacity by the traditional sectional analysis, for the EPP-TR and the Lumantarna-TR models, following the formulations developed i.e. by Cattari (2007) and Knox (2012).

In Figures 5.16 - 5.18 are reported some stress-strain relationships in compression (EPP, PR, Kaushik's and Lumantarna's models) and in tension (EPP model) that can be assumed for the URM spandrels.

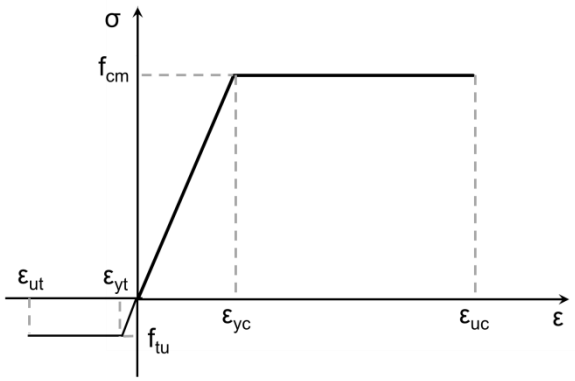

Analytical stress-strain model	*Compression*	$\sigma = E_m \varepsilon$	for $0 \le \varepsilon \le \varepsilon_{yc}$
		$\frac{\sigma}{f_{cm}} = 1$	for $\varepsilon_{yc} \le \varepsilon \le \varepsilon_{uc}$
	Tension	$\sigma = E_m \varepsilon$	for $\varepsilon_{yt} \le \varepsilon \le 0$
		$\frac{\sigma}{f_{tu}} = 1$	for $\varepsilon_{ut} \le \varepsilon \le \varepsilon_{yt}$

Figure 5.16. Elastic-perfectly plastic (EPP) stress-strain model in compression and tension.

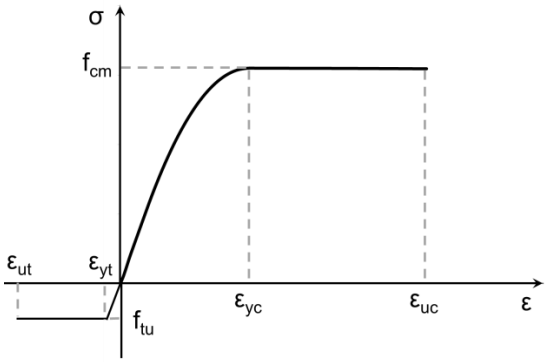

Analytical stress-strain model	*Compression*	$\frac{\sigma}{f_{cm}} = 2\frac{\varepsilon}{\varepsilon_{yc}} - \left(\frac{\varepsilon}{\varepsilon_{yc}}\right)^2$	for $0 \le \varepsilon \le \varepsilon_{yc}$
		$\frac{\sigma}{f_{cm}} = 1$	for $\varepsilon_{yc} \le \varepsilon \le \varepsilon_{uc}$
	Tension	$\sigma = E_m \varepsilon$	for $\varepsilon_{yt} \le \varepsilon \le 0$
		$\frac{\sigma}{f_{tu}} = 1$	for $\varepsilon_{ut} \le \varepsilon \le \varepsilon_{yt}$

Figure 5.17. Parable-rectangle (PR) stress-strain model in compression and elastic-perfectly plastic (EPP) model in tension.

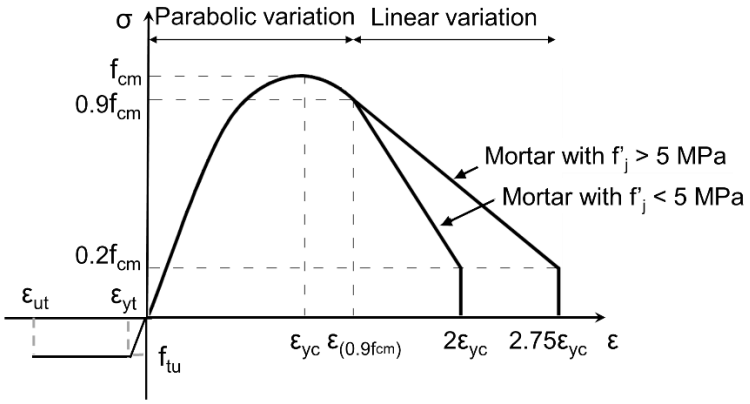

Analytical stress-strain model	*Compression*	$\frac{\sigma}{f_{cm}} = 2\frac{\varepsilon}{\varepsilon_{yc}} - \left(\frac{\varepsilon}{\varepsilon_{yc}}\right)^2$				
		$\varepsilon_{yc} = \frac{a f_{cm}}{f'^{b}_{j} E^{c}_{m}}$		a	b	c
			Kaushik et al. (2007)	0.27	0.25	0.7
			Lumantarna (2012)	0.21	0.25	0.7
	Tension	$\sigma = E_m \varepsilon$	for $\varepsilon_{yt} \le \varepsilon \le 0$			
		$\frac{\sigma}{f_{tu}} = 1$	for $\varepsilon_{ut} \le \varepsilon \le \varepsilon_{yt}$			

Figure 5.18. Analytical stress-strain model proposed by Kaushik et al. (2007), and adapted by Lumantarna (2012), in compression and elastic-perfectly plastic (EPP) model in tension.

As for the piers, once the moment-rotation curve of the spandrel section is identified through the MBA approach, the elastic contribution of the element can be added. In the same way, the initial stiffness K_{el} can be calculated according to Equation 5.15, (directly derived by Equation 5.12):

$$K_{el} = \left(\frac{{h_{eff}}^3}{nE_m I} + 1.2\frac{h_{eff}}{h_{sp} t_p G_m}\right)^{-1} \tag{5.15}$$

where h_{eff} corresponds to the spandrel clear span L_{sp}; h_{sp} and t_p are the height and the thickness, respectively; E_m and G_m are the Young's and shear modulus, respectively; I is the moment of inertia; n is a coefficient that takes into account the boundary conditions of the elements, that is equal to 12 in the case of the fixed-fixed condition and equal to 3 in the case of the cantilevered condition.

The elastic shear, displacement and rotation can be calculated as: $V_{el} = M_{el}/L_{cant}$; $\Delta_{el} = V_{el}/K_{el}$; $\theta_{el} = \Delta_{el}/L_{cant}$, respectively, where L_{cant} is the spandrel cantilever length,

assumed as mid-span ($L_{span}/2$) if the fixed-fixed condition is assumed and equal to the length of the spandrel (L_{span}) in the case of the cantilevered condition.

In Figure 5.19 an example of spandrel moment-rotation curves obtained with MBA approach for the TR-TF and TR-CF models is shown.

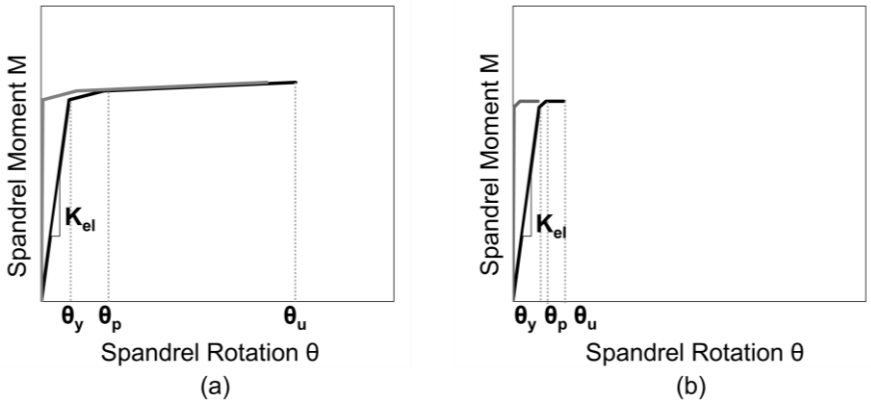

Figure 5.19. Example of spandrel moment-rotation curve according to the MBA approach (without and with elastic stiffness contribution): (a) TR-TF governed model and (b) TR-CF governed model.

Once the flexural capacity is defined in terms of the moment-rotation curve, the possibility of occurrence of the shear failure has to be checked. To this purpose, the shear strength can be calculated, considering if the horizontal axial load is known or unknown. In the first case, the piers shear strength formulations can be adopted. More in detail, Equations 5.13 and 5.14 are used to define the diagonal cracking and sliding shear strength, respectively. Instead, in the case of unknown spandrel axial load, the shear strength $V_{s,dc}$ can be calculated (as suggested in NTC 2018), following Equation 5.16:

$$V_{s,dc} = h_{sp} t_p f_{v0} \tag{5.16}$$

where h_{sp} and t_p are the height and the thickness of the spandrel, respectively and f_{v0} is the initial shear strength at zero compressive stress, estimated as $f_t/1.5$ (NTC 2018).

In the case in which the URM spandrel is coupled with any tensile resistant element, the shear strength can be defined from the transverse steel reinforcement contribution (if present).

The moment capacity is calculated from the spandrel shear resistance $V_{s,dc}$ and the spandrel cantilever length (L_{cant}) as $M = V_{s,dc}L_{cant}$. Since this parameter is considered not affected by the spandrel rotation, it is represented by a horizontal line in the moment-rotation curve.

An intersection of the shear strength curve with the flexural moment-rotation curve of the spandrel indicates a shear failure and the corresponding rotation can be assumed as the ultimate rotation of the spandrel. An example is reported in Figure 5.20.

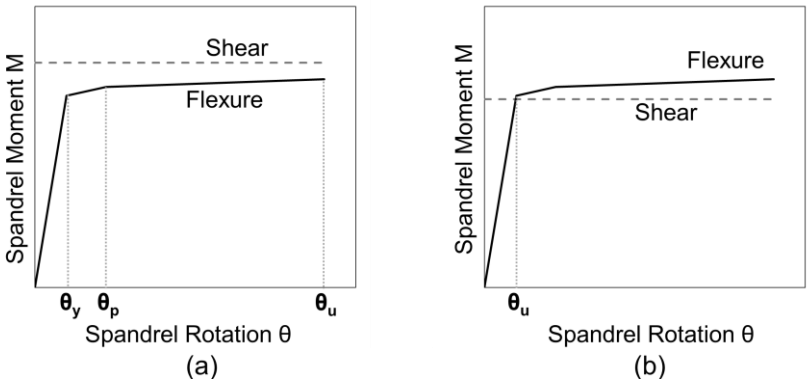

Figure 5.20. Spandrel moment-rotation curve: (a) expected flexural failure and (b) expected shear failure.

Also the moment-axial load (M-N) spandrel interaction domains can be defined through the MBA approach, adopting the aforementioned stress-strain relationships. Different moment capacity domains can be obtained varying the compressive $\mu_{\varepsilon c}$ and tensile $\mu_{\varepsilon t}$ strain ductility and considering their effect on the flexural response of the URM spandrels.

In Figure 5.21a are shown examples of M-N limit domains of a spandrel with rectangular cross-section, obtained with the EPP stress-strain relationship, for the case of no-tensile-resistance (NTR) and tensile-resistance (TR). This comparison highlights that the contribution of the equivalent tensile strength makes a marked difference in the moment capacity in the low axial load region (typical condition of the URM spandrels).

Examples of spandrel M-N limit domains considering the cases of compression (CF), tension (TF) governed failure and different compressive and tensile strain ductility, are shown in Figure 5.21b. For the EPP-TR-CF model, compressive strain ductility values of $\mu_{\varepsilon c} = 1.2$ and $\mu_{\varepsilon c} = 3.5$, are adopted. For the EPP-TR-TF model, a tension strain ductility of $\mu_{\varepsilon t} = 50$ is

considered. As it is observed, the M-N domains expand for an increase of $\mu_{\varepsilon c}$. Moreover, both the EPP-TR-CF model, with $\mu_{\varepsilon c} = 3.5$, and the EPP-TR-TF model give the same M-N limit domains. For more detail refer to Section 6.3.3.2.

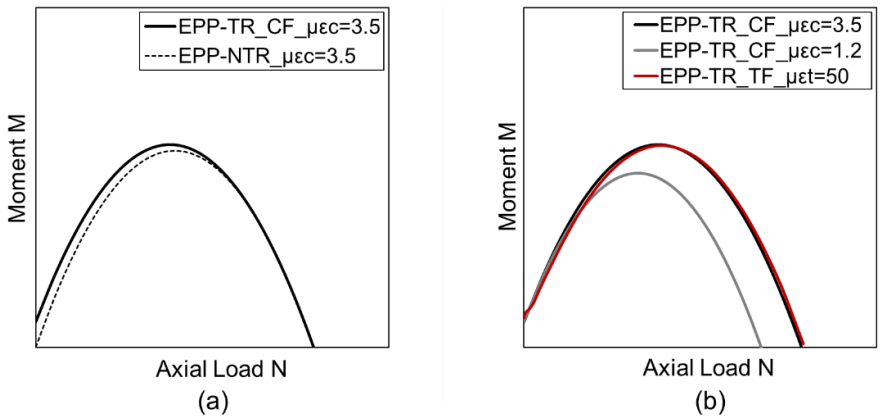

Figure 5.21. Spandrel M-N limit domains: (a) adopting EPP-NTR and EPP-TR models and (b) adopting EPP-TR model with different values of $\mu_{\varepsilon c}$ (CF model) and $\mu_{\varepsilon t}$ (TF model).

5.4.2.4 Pier-spandrel joint

The evidence of no (or limited) damage to pier-spandrel joints in URM walls during earthquakes has led to assume them as rigid joints in the EF modelling approach. Moreover, different studies have been developed to estimate the effective deformable height and length of piers and spandrels, respectively (e.g. Dolce, 1991; FEMA 306, 1998).

In this Thesis, the influence of the URM pier-spandrel joints on the global capacity of the structure is mostly neglected since these components are assumed as rigid, according to the conventional approach. In this Section, a preliminary analytical approach to derive the strength capacity of pier-spandrel joints is considered aiming to assess their effect on the pier M-N performance domain. Four potential failure mechanisms of URM pier-spandrel joints are addressed: diagonal compression, toe crushing, sliding shear, and diagonal shear (tension). An equivalent diagonal strut mechanism within the pier-spandrel joint is assumed, following the analogy of a RC frame-infill wall combined behaviour (Bertoldi *et al.*, 1993). According to this hypothesis, the expected failure mechanism of the pier-spandrel joint is defined by the minimum strength, i.e. first strength limit to be reached amongst different

failure mechanisms, and so the corresponding lateral resistance of the equivalent strut is calculated.

There are many research studies (Polyakov, 1960; Holmes, 1961; Smith, 1966; Mainstone, 1971, 1974; Liuaw and Kwan, 1984; Paulay and Priestley, 1992; Flanagan and Bennett, 2001) that improved the diagonal equivalent strut model, that nowadays is a simple and rational way to represent the combined frame-infill response under the seismic actions. In these systems, with the increasing of the horizontal loads, a gap between the panel and the frame at the nodes opens, coupled with sliding along the horizontal and vertical contact surfaces, with increased stress in the panel. In this condition the axial stress in the corners, still in contact with the frame, becomes relevant. It is, therefore, reasonable to model the infill wall in the frame, as a system reinforced by equivalent diagonal struts that simulate the axial behavior of the infill. An extensive literature review on the details of the different formulations adopted can be found in Asteris *et al*. (2011). Among them, it is worth noting the formulations proposed in Bertoldi *et al*. (1993), that allow to calculate the axial stiffness and strength of the strut, taking into account the different possible failure mechanisms that might affect the masonry panel. More in detail, in the strut-based modelling proposed in Bertoldi *et al*. (1993), an infill panel surrounded by a portion of RC frame is considered and a rectangular cross-section is associated to each equivalent strut, with thickness t_w (equal to the thickness of the masonry infill), diagonal length d_w and width b_w. This latter parameter is dependent on the parameter λh (function of the properties of the equivalent strut, see Equation 5.17), defined from the relative stiffness λ of the frame to the masonry panel and the height h of the column (or the inter-storey height).

$$\lambda h = \sqrt[4]{\frac{E_{w\theta} t_w \, sen(2\theta)}{4 E_c I_c h_w}}\, h \tag{5.17}$$

where E_c is the modulus of elasticity of the column; I_c is the moment of inertia of the column; t_w is the thickness of the masonry panel; θ is the slope of the infill diagonal strut to the horizontal; h_w is the height of the masonry panel (between beam axes) and $E_{w\theta}$ is the modulus of elasticity of the masonry panel, in function of the slope of the strut to the horizontal axis (Equation 5.18).

$$E_{w\theta} = \left[\frac{cos^4\theta}{E_{wh}} + \frac{sin^4\theta}{E_{wv}} + cos^2\theta sin^2\theta \left(\frac{1}{G} - 2\frac{\nu}{E_{wv}}\right)\right]^{-1} \tag{5.18}$$

where E_{wh} and E_{wv} are the elastic modules of the masonry in the vertical and horizontal direction, respectively; G is the shear modulus and ν is the Poisson's coefficient.

In Figure 5.22 are shown the geometric parameters involved in the equivalent diagonal strut model for infilled R.C. frames.

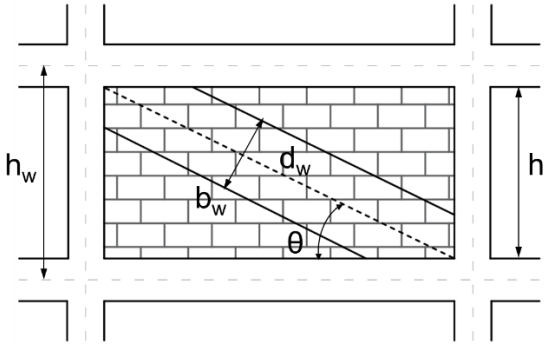

Figure 5.22. Diagonal strut-model for infilled R.C. frames.

From the parameter λh and two constants K_1 and K_2 (Table 5.1), calibrated on experimental tests and FEM models of fully-cracked infills, the width of the strut b_w can be calculated, as suggested in Bertoldi *et al*. (1993), following Equation 5.19:

$$\frac{b_w}{d_w} = \frac{K_1}{\lambda h} + K_2 \tag{5.19}$$

Table 5.1. Calibration parameters for the equivalent strut (Bertoldi et al., 1993).

	$\boldsymbol{\lambda h < 3.14}$	$\boldsymbol{3.14 < \lambda h < 7.85}$	$\boldsymbol{\lambda h > 7.85}$
$\boldsymbol{K_1}$	1.3	0.707	0.47
$\boldsymbol{K_2}$	-0.178	0.01	0.04

The infill panels can be affected by different collapse mechanisms and these are schematized in four potential failure mechanisms: the compression failure at the centre of the panel, the compression failure at the corner edges, the sliding shear failure and the diagonal tension failure. The formulations of the strength associated with these mechanisms are

reported in Table 5.2. The strength of the equivalent strut can be defined as the minimum of those strength of each mechanism ($f_{strut} = min(\sigma_{w,i})$). The corresponding maximum axial load P_{max} of the equivalent strut can be calculated with Equation 5.20.

$$P_{max} = f_{strut} b_w t_w \tag{5.20}$$

Table 5.2. Formulation of strength associated to the infill panels failure mechanisms.

Compression failure at the center of the panel	$\sigma_w = \frac{1.16 f'_w tan\theta}{K_1 + K_2 \lambda h}$
Compression failure at the corner edges	$\sigma_w = \frac{1.12 f'_w \, sin\theta \, cos\theta}{K_1 (\lambda h)^{-0.12} + K_2 (\lambda h)^{0.88}}$
Sliding shear failure	$\sigma_w = \frac{(1.2 sin\theta + 0.45 cos\theta) f_{wu} + 0.3\sigma_v}{b_w / d_w}$
Diagonal tension failure	$\sigma_w = \frac{0.6 f_{ws} + 0.3\sigma_v}{b_w / d_w}$

σ_w is the failure stress of the equivalent strut; f'_w is the compression strength; θ is the slope of the equivalent diagonal strut; f_{wu} is the shear sliding strength in the joints; f_{ws} is the shear resistance of the diagonal compression; σ_v is the vertical compression stress due to gravity loads.

Also in URM cases, the role of the pier-spandrel joints is to transfer the shear actions from the piers, and this is possible through the development of a strut mechanism. Assuming this, an "equivalent strut" strength mechanism is adopted, and the aforementioned strut-based modelling (Bertoldi *et al*., 1993) is adapted to the URM pier-spandrel joints. The first clear difference is the geometric configuration of the system, since, in the URM frames, the masonry material characterizes piers, spandrels and pier-spandrel joints. For this reason, Equation 5.17, which defines the parameter λh in the RC case, can be modified following Equation 5.21. More in detail, the moment of inertia of the column I_c is substituted by that of the joint panel I_j ($I_j = t_j b_j^3/12$, where t_j and b_j are the thickness and the width of the joint panel, respectively) and the modulus of elasticity of the column E_c is substituted by the masonry modulus of elasticity $E_{j\theta}$.

$$\lambda h = \sqrt[4]{\frac{E_{j\theta} t_j sen(2\theta)}{4 E_p I_j h_j}}\, h \tag{5.21}$$

If the horizontal E_{jh} and the vertical E_{jv} modulus of elasticity of the masonry are the same (see Equation 5.18), these parameters are simplified with the pier elastic modulus E_p, as a consequence, the parameter λh no longer depends on the stiffness of the material (Equation 5.22).

$$\lambda h = \sqrt[4]{\frac{t_j sen(2\theta)}{4 I_j h_j}}\, h \tag{5.22}$$

where h is the height of the masonry joint panel, assumed equal to h_j.

In Figure 5.23 are shown the geometric parameters involved in the equivalent diagonal strut model for an interior URM pier-spandrel joint panel.

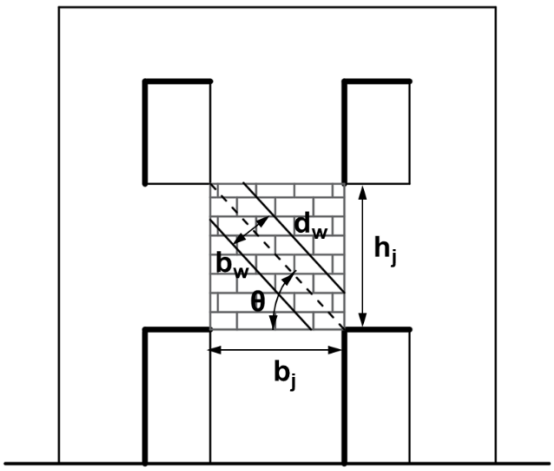

Figure 5.23. Diagonal strut-model for an interior URM pier-spandrel joint panel.

The formulations shown in Table 5.2 are adopted to define the strength $\sigma_{w,i}$ corresponding to the four possible failure mechanisms and consequently the preliminary analytical strength capacity of the URM pier-spandrel joints, as the minimum of the calculated strength ($f_{strut} = min(\sigma_{w,i})$). The corresponding horizontal shear force V_{jh} can be calculated through Equation 5.23.

$$V_{jh} = f_{strut} b_w t_j cos\theta \tag{5.23}$$

The shear deformation γ associated with the minimum strength f_{strut} can be calculated through Equation 5.24.

$$\gamma = \frac{f_{strut}}{G_m} \tag{5.24}$$

5.4.3 Analysis at subassembly level

The evaluation of the hierarchy of strength is carried out through the interaction between the strength of the structural components. At each pier-spandrel subassembly of a frame, the strength of the assessed components are compared following a force-based approach, identifying the expected failure mechanism and hence the corresponding capacity. To this aim, a reference common parameter is required to express and compare the strength of each mechanism. The selected parameter for the SLaMA-URM procedure is the Equivalent Pier Moment (EPM), following the suggestion of the SLaMA method in Pampanin *et al*. (2007). The pier moment-axial load (M-N) interaction domain, or performance domain, is adopted to identify the sequence of failure mechanisms in each pier-spandrel subassembly. In this diagram, the lower EPM, associated to each possible pier, spandrel or joint (if considered) mechanism, individuates the first crisis expected to occur.

In the pier M-N performance domain, the capacity of the URM components identifies the seismic performance (see Sections 5.4.3.1 and 5.4.3.2). The seismic demand is defined as the axial load variation $\pm \Delta N$ (see Section 5.4.3.3), due to the lateral load on the frame, and it can be expressed in terms of the EPM, by equilibrium conditions to each floor of the frame.

The comparison of the strength of the structural components is made according to the NZSEE guidelines (NZSEE 2017a), hence the interactions between the URM component capacity (related to the possible mechanisms) and the seismic demand ($\pm \Delta N$) identify the sequence of events in each subassembly of the frame, i.e. the hierarchy of strength.

The direction of the seismic action (i.e. from the left to right direction or from right to left direction, named “push” or “pull” directions, respectively, see Figure 5.24) influences the results of the analysis. This is due to the consequent increase or decrease of the axial load in the piers, due to the coupling effect of the spandrel during the lateral sway.

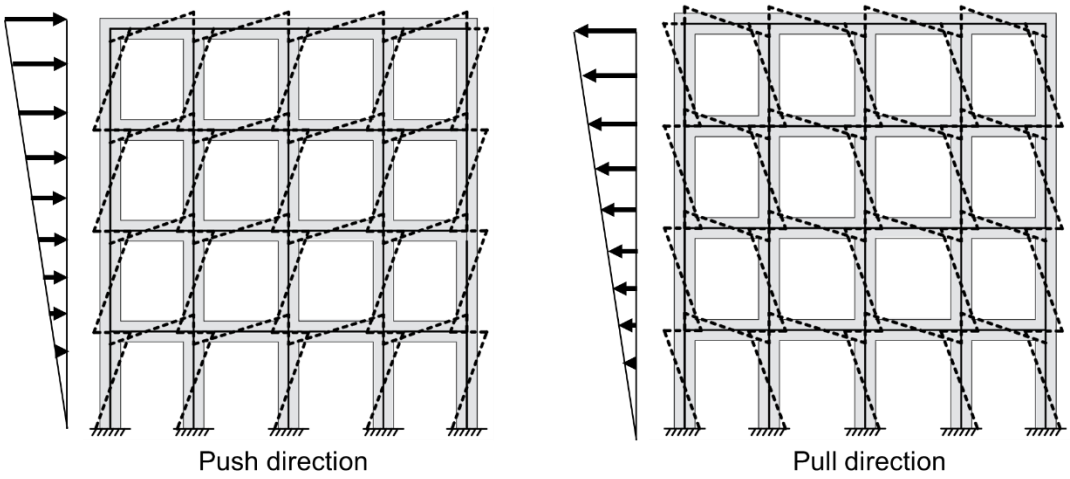

Figure 5.24. Push and pull direction of the analysis.

In Figure 5.25 is shown an example of the typical M-N performance domain for an exterior pier-spandrel joint subassembly.

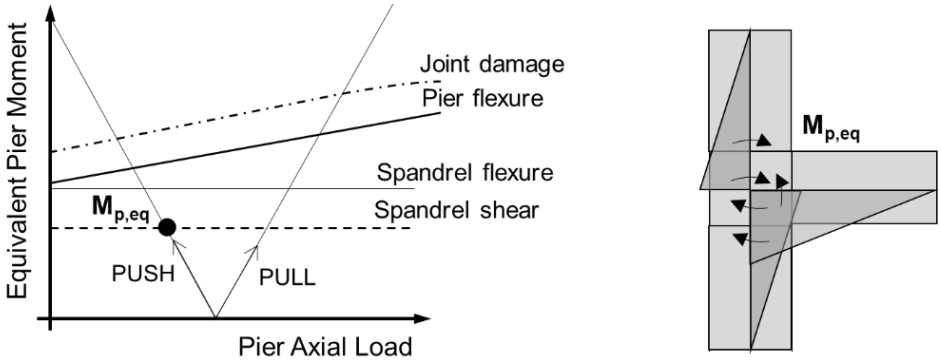

Figure 5.25. M-N performance domain for a generic exterior pier-spandrel joint subassembly.

It should be noted that different cases have to be considered if the joints panels are assumed as rigid elements or not. Indeed, this assumption leads to define an effective height of the piers (i.e. from Dolce, 1991; $h_{p,eff}$ in Figure 5.26b), instead of their clear height (to the interface with spandrels; h_p in Figure 5.26c), to consider the non-deformable joint panels region. Since the choice to consider the joints panel involves a modification of the assumed structural components geometry, a distinction at this level of analysis is necessary.

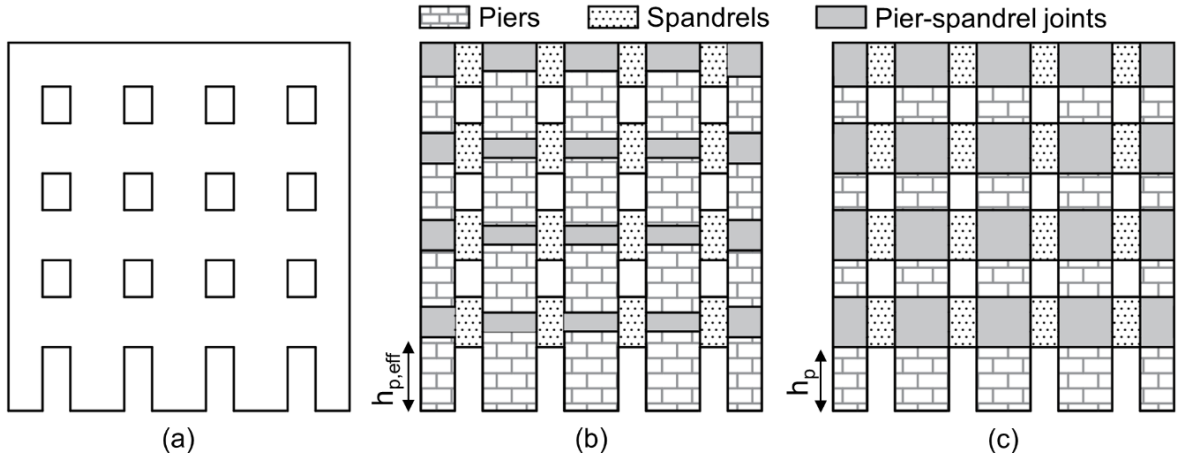

Figure 5.26. Schematization of (a) a multi-storey URM wall in case of rigid (b) or deformable (c) joint panels.

In the following Section 5.4.3.1, the formulations to define the EPM for piers and spandrels when the pier-spandrel joints are assumed as rigid, are shown. If the contribution of the joints panel is considered in the analysis, the formulations to define the EPM for the joint mechanisms are outlined in Section 5.4.3.2.

In Section 5.4.3.3 are shown the calculations for the seismic demand in terms of axial load variation and finally in Section 5.4.3.4 is reported an example of pier M-N performance domain.

5.4.3.1 The Equivalent Pier Moment (EPM) for URM piers and spandrels

From the assumption of rigid joints, the hierarchy of strength has to be assessed between the pier and the spandrel involved in the considered subassembly and to this aim the Equivalent Pier Moment (EPM) should be defined for their different possible failure mechanisms. EPM means to identify the needed pier moment to reach a specific condition in the other structural components (such as, for example, the development of the plastic hinge in the spandrel).

From the capacity of the possible failure mechanisms of the URM structural components (outlined in Sections 5.4.2.2 - 5.4.2.4), it is possible to calculate the EPM by rotational equilibrium at the top pier-joint panel interface, considering the typology of the pier-spandrel subassembly (Figure 5.27) and its geometry.

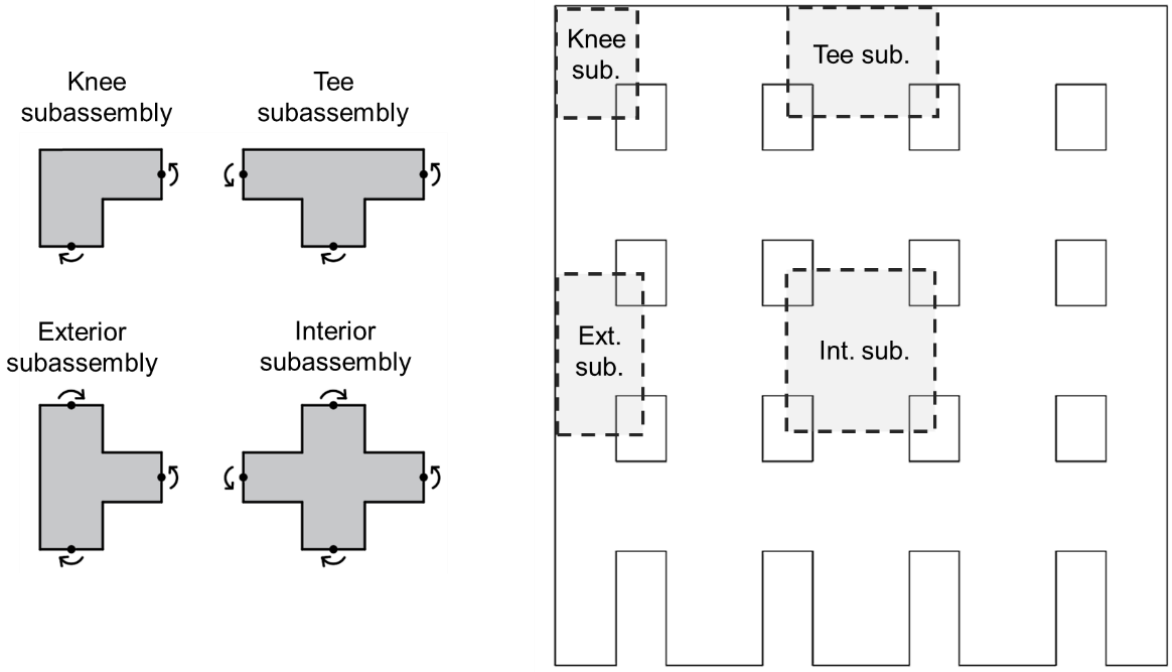

Figure 5.27. Pier-spandrel subassembly typologies in a frame lateral resisting system.

It is worth noting that for the piers, the EPM can be obtained in a direct way, once the analysis at component level is performed. To consider the non-deformable region at the pier-spandrel joints, the height of the piers is defined, i.e. from Dolce 1991, as an effective height ($h_{p,eff}$ in Figure 5.27b). Hence, the factor used to convert the pier shear force in the EPM refers to the cantilever length, identified as the distance to the point of contraflexure. In the following, this parameter is defined as l'_p for the different typologies of pier-spandrel subassembly: exterior (Figure 5.28a), interior (Figure 5.28b), knee (Figure 5.28c) and tee (Figure 5.28d) .

The geometric parameters involved in the procedure are shown in Figure 5.28 and are defined as: l'_p is the clear height of the piers to the joint panel interface ($l'_{p,top}$ for the top pier and $l'_{p,bot}$ for the bottom pier); l_p is the distance between the contraflexure points of piers, in case of the exterior and interior subassemblies (Figure 5.28a-b) or the distance between the pier contraflexure point and the horizontal axis of the spandrel, in case of the knee and tee subassemblies (Figure 5.28c-d); l'_{sp} is the clear span of the spandrel ($l'_{sp,l}$ for the left spandrel and $l'_{sp,r}$ for the right one) and l_{sp} is the distance between the contraflexure point of the spandrel and the vertical axis of the pier ($l_{sp,l}$ for the left spandrel and $l_{sp,r}$ for the right one).

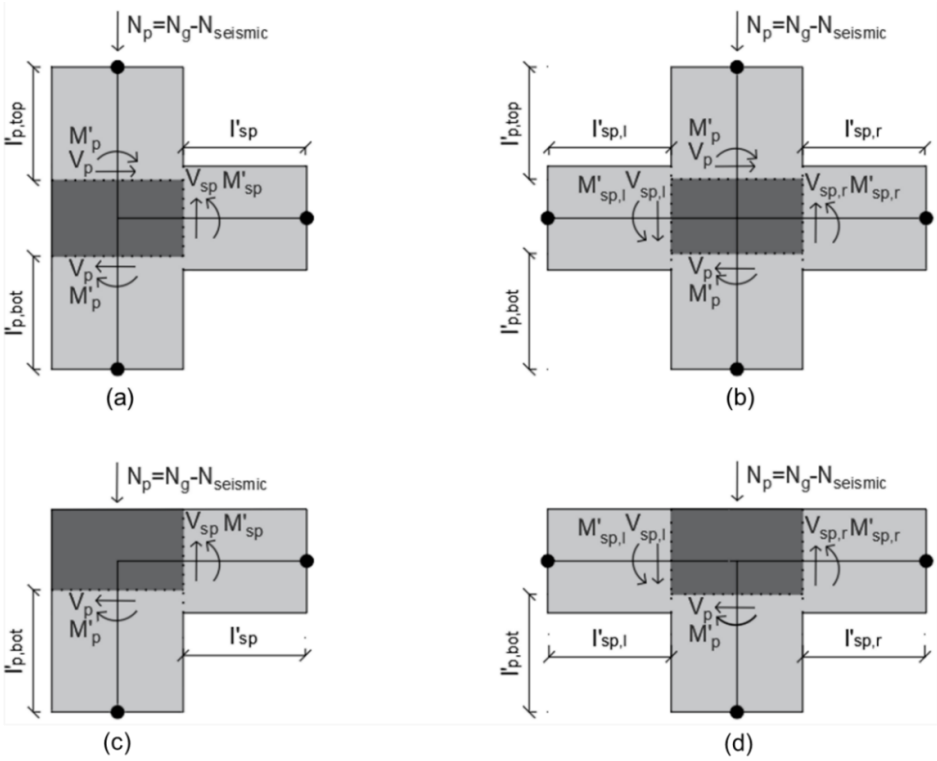

Figure 5.28. Schematization of the four typologies of subassembly: (a) exterior, (b) interior, (c) knee, (d) tee.

It is worth noting that the effective height of the piers, which in the following refers to Dolce (1991), can be calculated according to other proposals in literature (Augenti, 2006; Moon *et al*. 2006; Lagomarsino *et al*., 2013).

With reference to the typologies of the subassembly in Figure 5.28, the calculations to define the EPM corresponding to the formation of the plastic hinge and the shear failure of the piers and the spandrels, from the rotational equilibrium of the pier-spandrel subassembly (considering the different typologies) are shown in Tables 5.3 - 5.6, while a summary of the EPM formulations is reported in Tables 5.7 - 5.8.

It is worth noting that the parameters with an apex are referred to the internal actions calculated at the joint panel interface, while those without apex are calculated at the joint centroid. Furthermore, the directions of the internal actions refer to the push direction seismic load.

Due to the fact that to compute the capacity of the frame, it is necessary to know the Equivalent Spandrel Moment (ESM), the formulations to define this parameter are reported in

Tables 5.9 - 5.10, for the exterior/knee and for the interior/tee subassemblies, respectively. This parameter is calculated by the rotational equilibrium imposed about the joint centroid, following the same approach adopted to define the EPM.

It is observed that the derived EPM and ESM formulations for the exterior and for the knee subassemblies are equal. The same can be observed for the interior and the tee subassemblies, with the only distinction made on the definition of the pier length l_p.

Table 5.3. Equivalent Pier Moment (EPM) calculations for exterior joints.

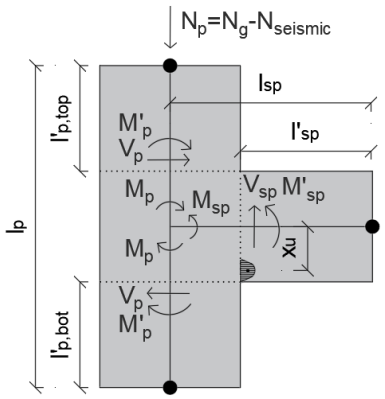

Rotational equilibrium	$V_p l_p = V_{sp} l_{sp}$	(5.25)
Spandrel shear	$V_{sp} = \frac{V_p l_p}{l_{sp}}$	(5.26)
Pier moment at the joint panel interface	$M'_p = V_p l'_p$	(5.27)
Spandrel moment at the joint panel interface	$M'_{sp} = V_{sp} l'_{sp} = \frac{V_p l_p}{l_{sp}} l'_{sp}$	(5.28)
EPM for spandrel flexural capacity	$M'_{p,spf} = \frac{l'_p l_{sp}}{l_p l'_{sp}} M'_{y,sp}$	(5.29)
EPM for spandrel shear capacity	$M'_{p,sps} = l_{sp} \frac{l'_p}{l_p} V_{sp}$	(5.30)

l'_p, for simplicity, is assumed as $l'_p = avg(l'_{p,top}, l'_{p,bot})$; $M'_{y,sp}$ is the yielding moment of the spandrel, that substitutes the spandrel moment M'_{sp}, to reach the EPM ($M'_{p,spf}$); V_{sp} is the shear strength of the spandrel.

Table 5.4. Equivalent Pier Moment (EPM) calculations for interior joints.

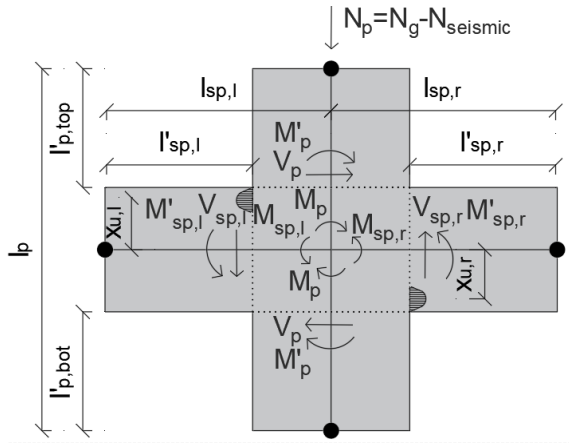

Rotational equilibrium	$V_p l_p = V_{sp,l} l_{sp,l} + V_{sp,r} l_{sp,r}$	(5.31)
Left spandrel shear	$V_{sp,l} = \frac{V_p l_p - V_{sp,r} l_{sp,r}}{l_{sp,l}}$	(5.32)
Right spandrel shear	$V_{sp,r} = \frac{V_p l_p - V_{sp,l} l_{sp,l}}{l_{sp,r}}$	(5.33)
Pier moment at the joint panel interface	$M'_p = V_p l'_p$	(5.34)
Left spandrel moment at the joint panel interface	$M'_{sp,l} = V_{sp,l} l'_{sp,l}$	(5.35)
Right spandrel moment at the joint panel interface	$M'_{sp,r} = V_{sp,r} l'_{sp,r}$	(5.36)
Relationship between pier and spandrel moments	$M'_p = \frac{l'_p}{l_p}\left(M'_{sp,l}\frac{l_{sp,l}}{l'_{sp,l}} + M'_{sp,r}\frac{l_{sp,r}}{l'_{sp,r}}\right)$	(5.37)
EPM for spandrel flexural capacity (1st spandrel is yielding)	$M'_{p,spf\ 1st} = \frac{l'_p}{l_p}\left(\frac{l_{sp,l}}{l'_{sp,l}} + \frac{l_{sp,r}}{l'_{sp,r}}\right) M'_{y,sp\ 1st}$	(5.38)
EPM for spandrel flexural capacity (both spandrels are yielding)	$M'_{p,spf\ both} = \frac{l'_p}{l_p}\left(M'_{y,sp,l}\frac{l_{sp,l}}{l'_{sp,l}} + M'_{y,sp,r}\frac{l_{sp,r}}{l'_{sp,r}}\right)$	(5.39)
Spandrel shear capacity in terms of the EPM	$M'_p = \frac{l'_p}{l_p}\left(V_{sp,l}\, l_{sp,l} + V_{sp,r}\, l_{sp,r}\right)$	(5.40)
EPM for spandrel shear capacity	$M'_{p,sps} = \left(l_{sp,l} + l_{sp,r}\right)\frac{l'_p}{l_p} V_{sp\ 1st}$	(5.41)

**l'_p, for simplicity, is assumed as $l'_p = avg(l'_{p,top}, l'_{p,bot})$; $M'_{p,spf\ 1st}$ is the EPM corresponding to the first beam yields; $M'_{y,sp\ 1st}$ is the lowest yielding moment of the left or the right spandrel; $M'_{p,spf\ both}$ is the EPM corresponding to the formation of both spandrel plastic hinges; $M'_{y,sp,l}$ and $M'_{y,sp,r}$ are the yielding moments of the left and the right spandrels, respectively; $M'_{p,sps}$ is the EPM corresponding to the shear failure of the spandrels; $V_{sp\ 1st}$ is the lowest shear strength between that of the left and the right spandrel.*

Table 5.5. Equivalent Pier Moment (EPM) calculations for knee joints.

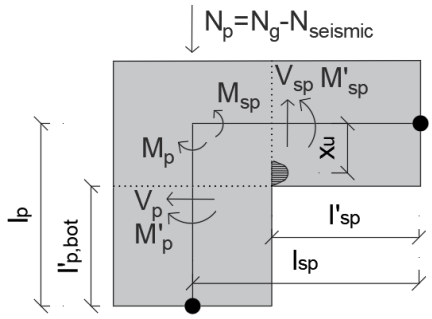

Rotational equilibrium	$V_p l_p = V_{sp} l_{sp}$	(5.42)
Spandrel shear	$V_{sp} = \frac{V_p l_p}{l_{sp}}$	(5.43)
Pier moment at the joint panel interface	$M'_p = V_p l'_p$	(5.44)
Spandrel moment at the joint panel interface	$M'_{sp} = V_{sp} l'_{sp} = \frac{V_p l_p}{l_{sp}} l'_{sp}$	(5.45)
EPM for spandrel flexural capacity	$M'_{p,spf} = \frac{l'_p l_{sp}}{l_p l'_{sp}} M'_{y,sp}$	(5.46)
EPM for spandrel shear capacity	$M'_{p,sps} = l_{sp} \frac{l'_p}{l_p} V_{sp}$	(5.47)

**$M'_{y,sp}$ is the yielding moment of the spandrel, that substitutes the spandrel moment M'_{sp}, to reach the EPM ($M'_{p,spf}$); V_{sp} is the shear strength of the spandrel.*

Table 5.6. Equivalent Pier Moment (EPM) calculations for tee joints.

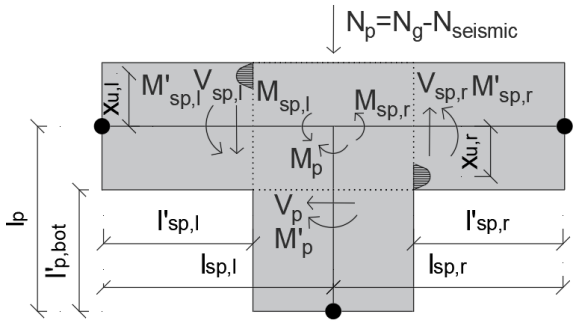

Rotational equilibrium	$V_p l_p = V_{sp,l} l_{sp,l} + V_{sp,r} l_{sp,r}$	(5.48)
Left spandrel shear	$V_{sp,l} = \frac{V_p l_p - V_{sp,r} l_{sp,r}}{l_{sp,l}}$	(5.49)
Right spandrel shear	$V_{sp,r} = \frac{V_p l_p - V_{sp,l} l_{sp,l}}{l_{sp,r}}$	(5.50)
Pier moment at the joint panel interface	$M'_p = V_p l'_p$	(5.51)
Left spandrel moment at the joint panel interface	$M'_{sp,l} = V_{sp,l} l'_{sp,l}$	(5.52)
Right spandrel moment at the joint panel interface	$M'_{sp,r} = V_{sp,r} l'_{sp,r}$	(5.53)
Relationship between pier and spandrel moments	$M'_p = \frac{l'_p}{l_p}\left(M'_{sp,l}\frac{l_{sp,l}}{l'_{sp,l}} + M'_{sp,r}\frac{l_{sp,r}}{l'_{sp,r}}\right)$	(5.54)
EPM for spandrel flexural capacity (1st spandrel is yielding)	$M'_{p,spf\ 1st} = \frac{l'_p}{l_p}\left(\frac{l_{sp,l}}{l'_{sp,l}} + \frac{l_{sp,r}}{l'_{sp,r}}\right) M'_{y,sp\ 1st}$	(5.55)
EPM for spandrel flexural capacity (both spandrels are yielding)	$M'_{p,spf\ both} = \frac{l'_p}{l_p}\left(M'_{y,sp,l}\frac{l_{sp,l}}{l'_{sp,l}} + M'_{y,sp,r}\frac{l_{sp,r}}{l'_{sp,r}}\right)$	(5.56)
Spandrel shear capacity in terms of the EPM	$M'_p = \frac{l'_p}{l_p}\left(V_{sp,l}\, l_{sp,l} + V_{sp,r}\, l_{sp,r}\right)$	(5.57)
EPM for spandrel shear capacity	$M'_{p,sps} = \left(l_{sp,l} + l_{sp,r}\right)\frac{l'_p}{l_p} V_{sp\ 1st}$	(5.58)

$M'_{p,spf\ 1st}$ is the EPM corresponding to the first beam yields; $M'_{y,sp\ 1st}$ is the lowest yielding moment of the left or the right spandrel; $M'_{p,spf\ both}$ is the EPM corresponding to the formation of both spandrel plastic hinges; $M'_{y,sp,l}$ and $M'_{y,sp,r}$ are the yielding moments of the left and the right spandrels, respectively; $M'_{p,sps}$ is the EPM corresponding to the shear failure of the spandrels; $V_{sp\ 1st}$ is the lowest shear strength between that of the left and the right spandrel.

Table 5.7. Summary of the Equivalent Pier Moment (EPM) formulations for exterior and knee joints.

	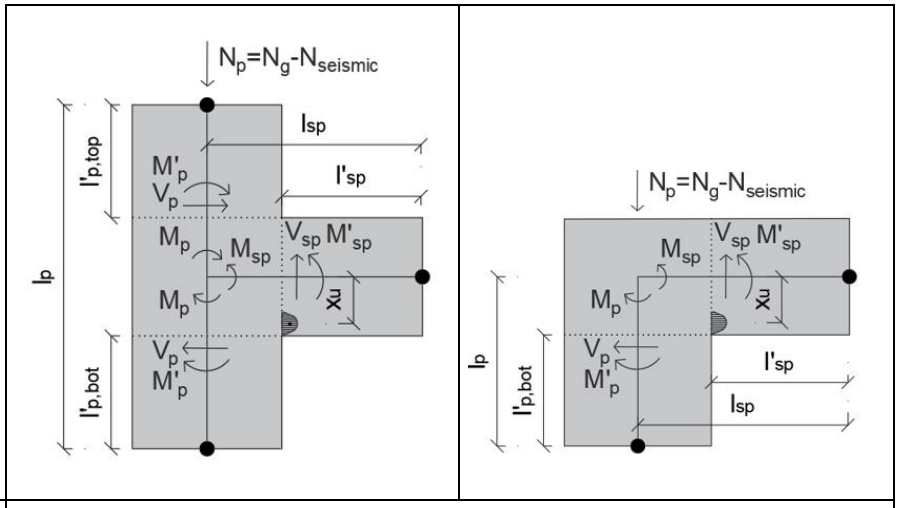
Top pier flexure	$M'_{y,p\ top}$
Bottom pier flexure	$M'_{y,p\ bot}$
Pier shear	$l'_{p,top}V_{p\ top}$ *(or bot)*
Spandrel flexure	$\frac{l'_p l_{sp}}{l_p l'_{sp}} M'_{y,sp}$
Spandrel shear	$l_{sp}\frac{l'_p}{l_p}V_{sp}$

l'_p, for simplicity, is assumed as $l'_p = avg(l'_{p,top}, l'_{p,bot})$; $M'_{y,p\ top}$ and $M'_{y,p\ bot}$ are the yielding moments of the top and the bottom piers; $M'_{y,sp}$ is the yielding moment of the spandrel; $V_{p\ top}$ is the shear strength of the top pier; V_{sp} is the shear strength of the spandrel; V_{jh} is the shear strength of the joint.

Table 5.8. Summary of the Equivalent Pier Moment (EPM) formulations for interior and tee joints.

	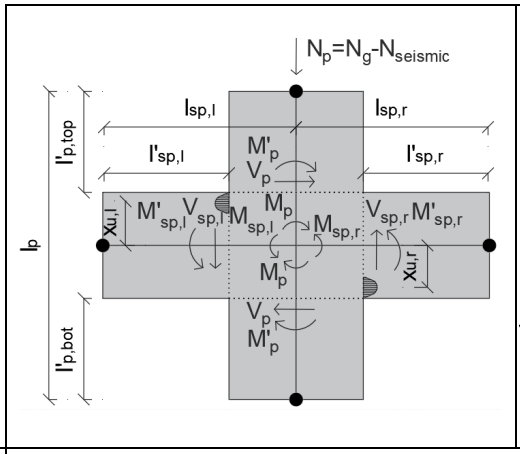	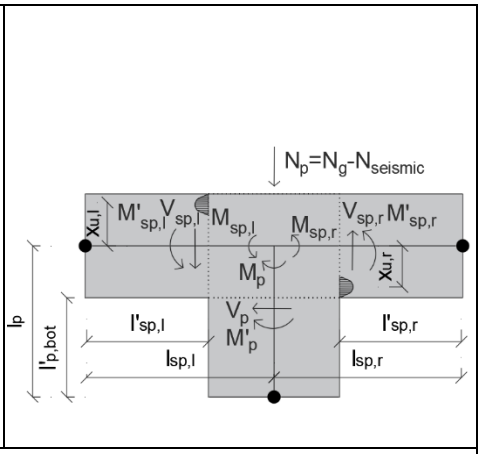
Top pier flexure	$M'_{y,p\ top}$	
Bottom pier flexure	$M'_{y,p\ bot}$	
Pier shear	$l'_{p,top}V_{p\ top}$ *(or bot)*	
Left spandrel flexure	$\frac{l'_p}{l_p}\left(\frac{l_{sp,l}}{l'_{sp,l}}+\frac{l_{sp,r}}{l'_{sp,r}}\right)M'_{y,sp,l}$	
Right spandrel flexure	$\frac{l'_p}{l_p}\left(\frac{l_{sp,l}}{l'_{sp,l}}+\frac{l_{sp,r}}{l'_{sp,r}}\right)M'_{y,sp,r}$	
Both spandrels flexure	$\frac{l'_p}{l_p}\left(M'_{y,sp,l}\frac{l_{sp,l}}{l'_{sp,l}}+M'_{y,sp,r}\frac{l_{sp,r}}{l'_{sp,r}}\right)$	
Spandrel shear	$l_{sp}\frac{l'_p}{l_p}V_{sp\ 1st}$	

**l'_p, for simplicity, is assumed as $l'_p = avg(l'_{p,top}, l'_{p,bot})$; l_{sp} is assumed as $l_{sp} = avg(l_{sp,l}, l_{sp,r})$;); $M'_{y,p\ top}$ and $M'_{y,p\ bot}$ are the yielding moments of the top and bottom piers; $M'_{y,sp,l}$ and $M'_{y,sp,r}$ are the yielding moments of the left and the right spandrels, respectively; $V_{p\ top}$ is the shear strength of the top pier; $V_{sp\ 1st}$ is the lowest shear strength between that of the left and the right spandrel.*

Table 5.9. Summary of the Equivalent Spandrel Moment (ESM) formulations for exterior and knee joints.

	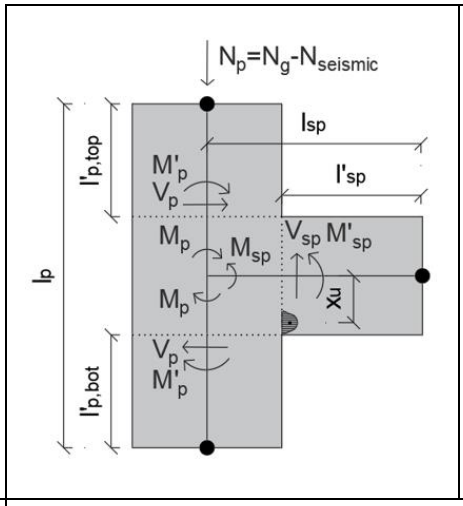	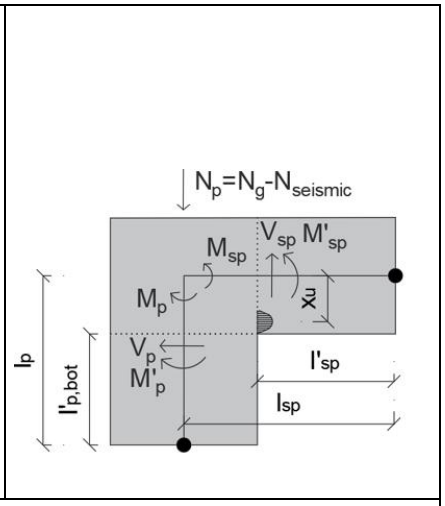
Top pier flexure	$\frac{l_p l'_{sp}}{l'_{p,top} l_{sp}} M_{y,p\ top}$	
Bottom pier flexure	$\frac{l_p l'_{sp}}{l'_{p,bot} l_{sp}} M_{y,p\ bot}$	
Pier shear	$l_{p,top} V_{p\ top}$ *(or bot)*	
Spandrel flexure	$\frac{l_{sp}}{l'_{sp}} M'_{y,sp}$	
Spandrel shear	$l_{sp} V_{sp}$	

l'_p, for simplicity, is assumed as $l'_p = avg(l'_{p,top}, l'_{p,bot})$; $M'_{y,p}$ is the yielding moment of the top pier; $M'_{y,sp}$ is the yielding moment of the spandrel; V_p is the shear strength of the top pier; V_{sp} is the shear strength of the spandrel; V_{jh} is the shear strength of the joint.

Table 5.10. Summary of the Equivalent Spandrel Moment (ESM) formulations for interior and tee joints.

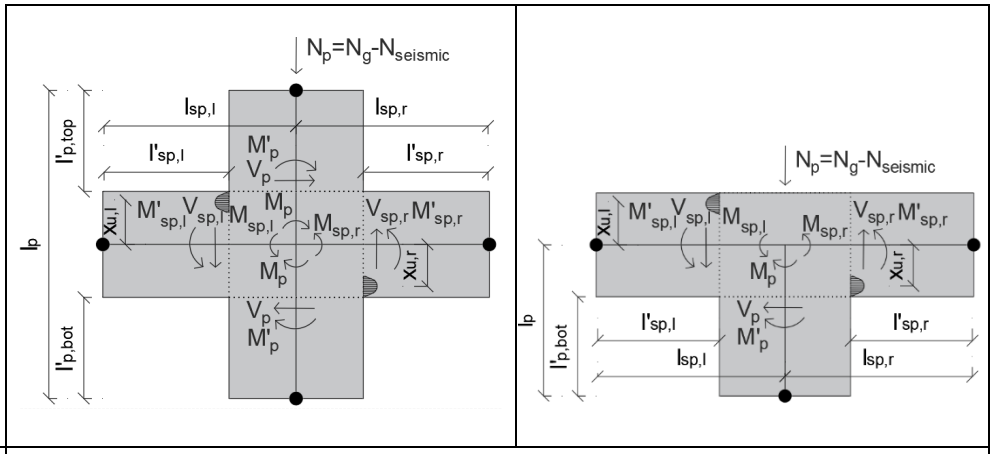

Top pier flexure	$\frac{l_p l'_{sp}}{2l'_{p,top} l_{sp}} M_{y,p\ top}$
Bottom pier flexure	$\frac{l_p l'_{sp}}{2l'_{p,bot} l_{sp}} M_{y,p\ bot}$
Pier shear	$\frac{l_p}{2} V_{p\ top}$ *(or bot)*
Left spandrel flexure	$\frac{l_{sp,l}}{l'_{sp,l}} M'_{y,sp,l}$
Right spandrel flexure	$\frac{l_{sp,r}}{l'_{sp,r}} M'_{y,sp,r}$
Both spandrels flexure	$avg\left(M'_{y,sp,l} \frac{l_{sp,l}}{l'_{sp,l}} + M'_{y,sp,r} \frac{l_{sp,r}}{l'_{sp,r}}\right)$
Spandrel shear	$l_{sp} V_{sp\ 1st}$

l'_p, for simplicity, is assumed as $l'_p = avg(l'_{p,top}, l'_{p,bot})$; l_{sp} is assumed as $l_{sp} = avg(l_{sp,l}, l_{sp,r})$; $M'_{y,sp,l}$ and $M'_{y,sp,r}$ are the yielding moments of the left and the right spandrels, respectively; $V_{sp\ 1st}$ is the lowest shear strength between that of the left and the right spandrel.

According to a simplified equilibrium approach, the EPM, corresponding to the spandrel flexural and shear failure, can be defined assuming that the piers above and below a floor level have similar stiffness, considering the typology of the subassembly and then referring to a local (rotational) equilibrium at pier-spandrel joints. As schematized in Figure 5.29, assuming the top pier moment equal to the bottom one, the EPM can be defined approximately as: half of the spandrel moment ($M_p \approx M_{sp}/2$) in the exterior subassemblies (Figure 5.29a); the average of the left and right spandrel moments ($M_p \approx (M_{sp,left} + M_{sp,right})/2$) in the interior subassemblies (Figure 5.29b); the spandrel moment ($M_p \approx M_{sp}$) in the knee subassemblies (Figure 5.29c); the sum of the left and right spandrel moments ($M_p \approx M_{sp,left} + M_{sp,right}$) in the tee subassemblies (Figure 5.29d).

It is worth mentioning that the directions of the moments in Figure 5.29 refer to the push load direction, from left to right. In the case of pull load (from right to left) the moments are in the opposite direction.

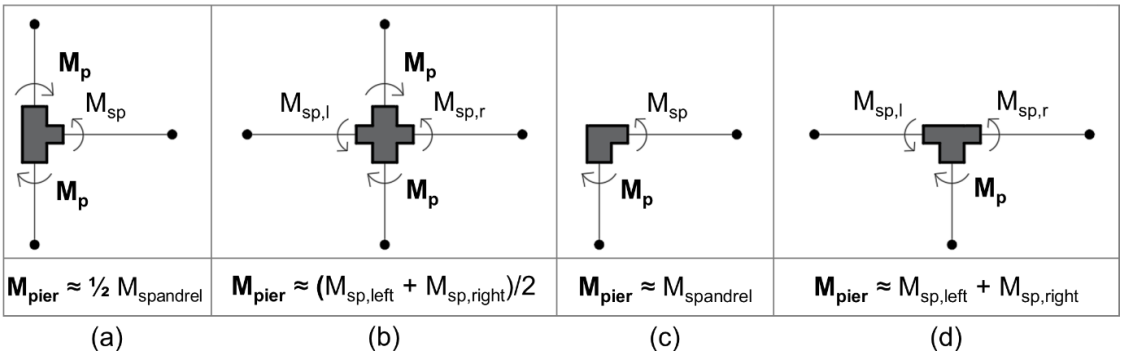

Figure 5.29. Schematization of the simplified equilibrium of the: (a) exterior, (b) interior, (c) knee and (d) tee subassemblies.

According to this approach, in Tables 5.11 - 5.14 are reported the EPM and ESM formulations, for the piers and spandrels possible failure mechanisms, for the four different typologies of the subassembly.

Table 5.11. Summary of the Equivalent Pier Moment (EPM) formulations for exterior and knee subassemblies.

	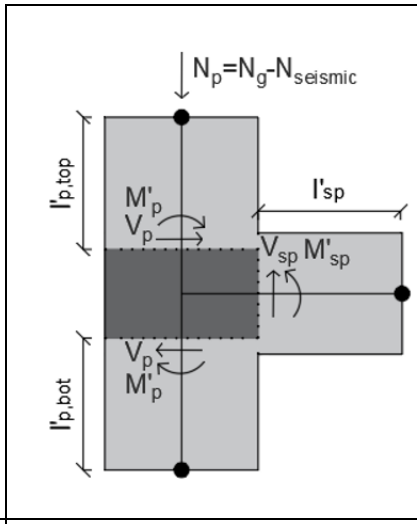	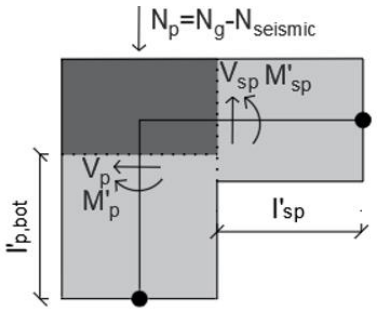
Pier flexure	$M'_{y,p}$	$M'_{y,p}$
Pier shear	$l'_p V_p$	$l'_p V_p$
Spandrel flexure	$M'_{y,sp}/2$	$M'_{y,sp}$
Spandrel shear	$l'_{sp} V_{sp}/2$	$l'_{sp} V_{sp}$

l'_p, for simplicity, is assumed as $l'_p = avg(l'_{p,top}, l'_{p,bot})$; $M'_{y,p}$ is the yielding moment of the top pier; $M'_{y,sp}$ is the yielding moment of the spandrel; V_p is the shear strength of the pier; V_{sp} is the shear strength of the spandrel.

Table 5.12. Summary of the Equivalent Pier Moment (EPM) formulations for interior and tee subassemblies.

	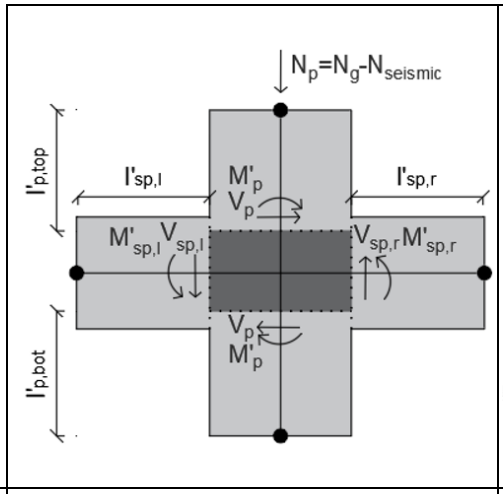	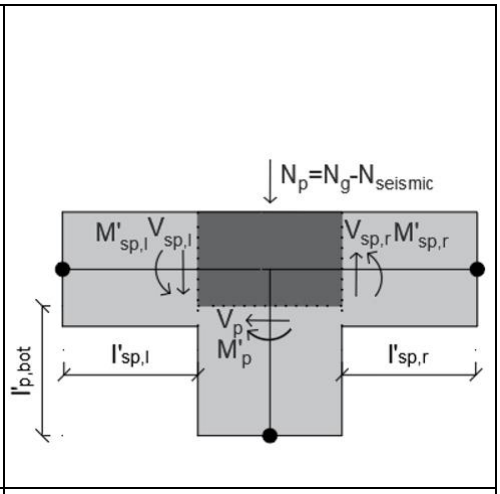
Pier flexure	$M'_{y,p}$	$M'_{y,p}$
Pier shear	$l'_p V_p$	$l'_p V_p$
Both spandrels flexure	$\frac{M'_{y,sp,l} + M'_{y,sp,r}}{2}$	$M'_{y,sp,l} + M'_{y,sp,r}$
Spandrel shear	$\frac{l'_{sp,l} V_{sp,l} + l'_{sp,r} V_{sp,r}}{2}$	$l'_{sp,l} V_{sp,l} + l'_{sp,r} V_{sp,r}$

**l'_p, for simplicity, is assumed as $l'_p = avg(l'_{p,top}, l'_{p,bot})$; $M'_{y,sp,l}$ and $M'_{y,sp,r}$ are the yielding moments of the left and the right spandrels, respectively; $V_{sp,l}$ and $V_{sp,r}$ are the shear strength of the left and the right spandrel, respectively.*

Table 5.13. Summary of the Equivalent Spandrel Moment (ESM) formulations for exterior and knee subassemblies.

	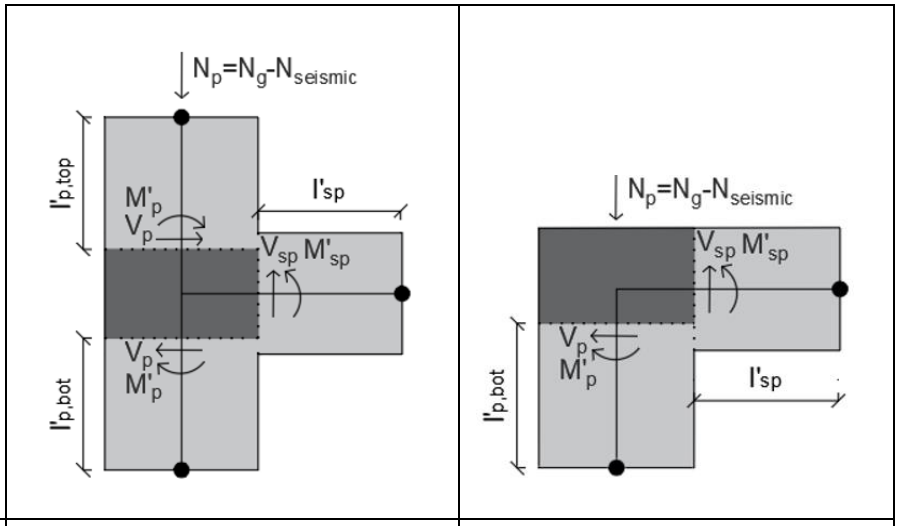	
Pier flexure	$2M'_{y,p}$	$M'_{y,p}$
Pier shear	$2l'_pV_p$	l'_pV_p
Spandrel flexure	$M'_{y,sp}$	$M'_{y,sp}$
Spandrel shear	$l'_{sp}V_{sp}$	$l'_{sp}V_{sp}$

**l'_p, for simplicity, is assumed as $l'_p = avg(l'_{p,top}, l'_{p,bot})$; $M'_{y,p}$ is the yielding moment of the top pier; $M'_{y,sp}$ is the yielding moment of the spandrel; V_p is the shear strength of the pier; V_{sp} is the shear strength of the spandrel.*

Table 5.14. Summary of the Equivalent Spandrel Moment (ESM) formulations for interior and tee subassemblies.

	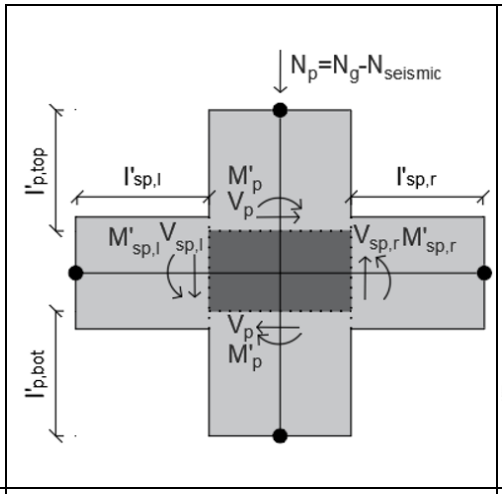	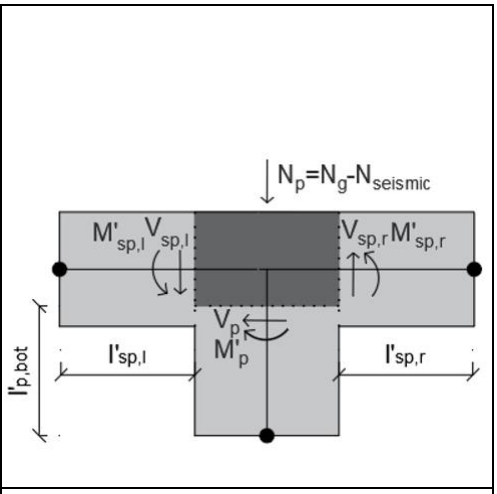
Pier flexure	$M'_{y,p}$	$M'_{y,p}/2$
Pier shear	$l'_p V_p$	$l'_p V_p/2$
Both spandrels flexure	$\frac{M'_{y,sp,l}+M'_{y,sp,r}}{2}$	$M'_{y,sp,l}+M'_{y,sp,r}$
Spandrel shear	$\frac{l'_{sp,l}V_{sp,l}+l'_{sp,r}V_{sp,r}}{2}$	$l'_{sp,l}V_{sp,l}+l'_{sp,r}V_{sp,r}$

**l'_p, for simplicity, is assumed as $l'_p = avg(l'_{p,top}, l'_{p,bot})$; $M'_{y,sp,l}$ and $M'_{y,sp,r}$ are the yielding moments of the left and the right spandrels, respectively; $V_{sp,l}$ and $V_{sp,r}$ are the shear strength of the left and the right spandrel, respectively.*

5.4.3.2 The Equivalent Pier Moment (EPM) for URM pier-spandrel joints

The contribution of the pier-spandrel joints in the M-N performance domain can be taken into account, starting from the actual geometry of the URM components, and in particular on the height of the piers. Indeed, in this case, the clear height of the piers, to the interface with the spandrels, has to be considered (h_p in Figure 5.26c), and the dimensions of the pier-spandrel joints are assumed as shown in Figure 5.30, where b_j and h_j are the width and the height of the joint panel, corresponding to the width of the piers B_p and the height of the

spandrel h_{sp}, respectively. Since the choice to consider the joints panel changes the assumed structural components geometry, a distinction at the component and at the subassembly level of analysis should be made.

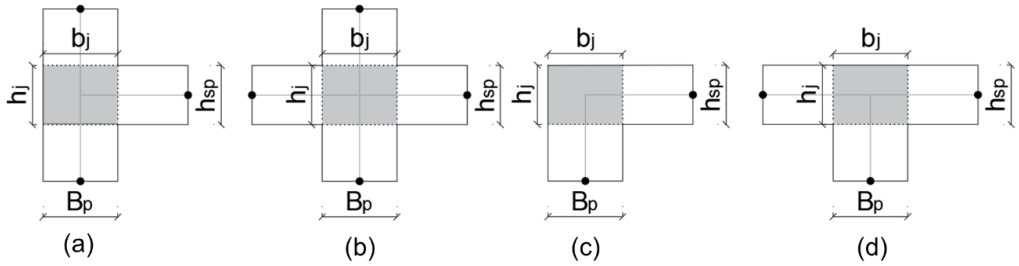

Figure 5.30. Geometric dimensions of the joint panel of the: (a) exterior, (b) interior, (c) knee and (d) tee subassemblies.

From the assumption of deformable pier-spandrel joints, once the actual geometry of the components is defined, the hierarchy of strength has to be assessed between the joint, pier and spandrel involved in the subassembly and to this aim the Equivalent Pier Moment (EPM) should be defined for their different possible failure mechanisms.

For the piers and the spandrels the same considerations outlined in Section 5.4.3.1 are assumed, with the difference that the rotational equilibrium is calculated at the centroid of the subassembly and that the parameter l'_p refers to half of the clear height of the piers (h_p in Figure 5.26c). The calculations of the EPM for the different typologies of pier-spandrel subassembly (exterior, interior, knee, tee) are shown in Tables 5.15 - 5.18, and summarized in Tables 5.19 - 5.20.

According to a more simplified equilibrium approach, the EPM for the spandrel flexural and shear failure can be defined as shown in Figure 5.29, considering first the typology of the subassembly, and then calculating the local (rotational) equilibrium between pier and spandrel, with no considerations for the geometry of the URM components.

Regarding the pier-spandrel joints, the capacity in terms of the equivalent bending moment of the pier needs to be calculated. To this aim, starting from simplified equilibrium equations, the pier equivalent shear force V_p and, consequently, the Equivalent Pier Moment (EPM) can be obtained. V_p can be defined from the lateral resistance of the equivalent strut V_{jh} (calculated in Section 5.4.2.4), as a function of typology/geometry of the subassembly

and on translational equilibrium considerations. More in detail, the shear demand of the joint panel (V_{jh}) is calculated from the pier shear (V_p) and the tension-compression action (C_{sp} or T_{sp}) of the spandrel(s) cross-section (as $V_{jh} = C_{sp} - V_p$ for exterior pier-spandrel joints and $V_{jh} = C_{sp} + T_{sp} - V_p$ for the interior pier-spandrel joints), as suggested in Paulay and Priestley (1992). The EPM is then calculated multiplying V_p by the corresponding pier cantilever height l'_p of the considered subassembly (see Figure 5.31).

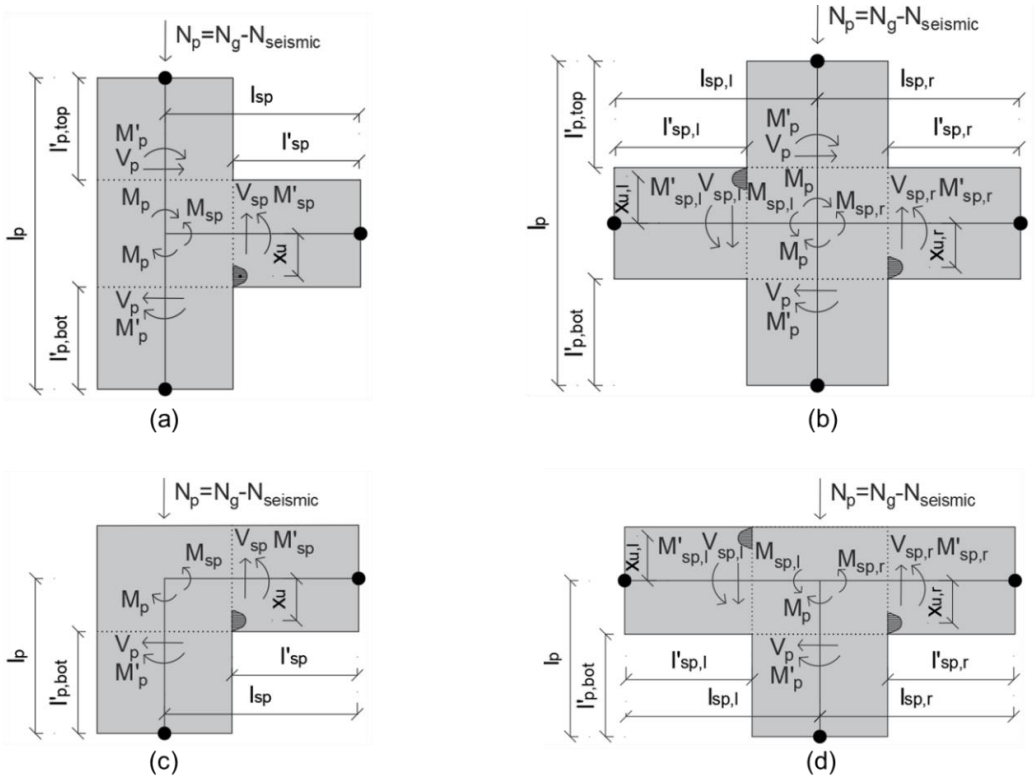

Figure 5.31. Schematization of the typologies of subassembly: (a) exterior, (b) interior, (c) knee, (d) tee subassemblies.

It is noted that all the parameters with an apex are referred to the internal actions calculated at the joint panel interface, while those without apex are calculated at the joint centroid. The geometric parameters that are involved in the procedure are shown in Figure 5.31 and are defined as: l'_p is the clear height of the piers to the joint panel interface ($l'_{p,top}$ for the top pier and $l'_{p,bot}$ for the bottom pier); l_p is the distance between the contra flexure points of piers, in case of the exterior and interior subassemblies (Figure 5.31a-b) or the distance between the pier contra flexure point and the horizontal axis of the spandrel, in case

of the knee and tee subassemblies (Figure 5.31c-d); l'_{sp} is the clear span of the spandrel ($l'_{sp,l}$ for the left spandrel and $l'_{sp,r}$ for the right spandrel) and l_{sp} is the distance between the contra flexure point of the spandrel and the vertical axis of the pier ($l_{sp,l}$ for the left spandrel and $l_{sp,r}$ for the right spandrel).

In Tables 5.15 - 5.18 are reported the detailed formulations to define the EPM of the pier, spandrel and joint from rotational equilibrium considerations, for the four pier-spandrel subassemblies (exterior, interior, knee and tee). The adopted approach follows the one used for the beam-column RC subassembly presented in Gentile (2017). A summary of the EPM formulations is reported in Tables 5.19 - 5.20. It is worth noting that the directions of the moments in figures and tables refer to a hypothesized push load, i.e. that acts from left to right.

For all the typologies of pier-spandrel joints, it is assumed that the moment of the spandrel at the joint interface can be expressed as $M'_{sp} = C_{sp}x_u$, where C_{sp} is the resultant of the masonry compression forces and x_u is the internal lever arm between the centroid of the resultant of the forces in the compression zone and the horizontal axis of the spandrel, at the ultimate condition. In the interior joints, the EPM corresponding to the joint shear capacity is calculated assuming that the left and right spandrel yielding moments are equal to their average ($M'_{sp,av} = M'_{sp,l} + M'_{sp,r}/2$). From this assumption, the tension and compression forces of the spandrels result equal ($C_{sp,r} = T_{sp,l}$) and the value of the joint shear strength can be obtained as $V_{jh} = 2C_{sp,r} - V_p$.

Furthermore, for the interior and tee subassemblies, a distinction on the development of the plastic hinge on an individual or both spandrels is made. More in detail, the EPM corresponding to the formation of the plastic hinges in the spandrel is defined: i) when the first spandrel (between the left and right one) yields, resulting in that the bending moment of the two spandrels is equal by equilibrium (Equation 5.80 and 5.108) or ii) when both the spandrels (left and right) yield at the same time (Equation 5.81 and 5.109). Regarding the shear failure of the spandrel, the EPM is given by the lowest spandrels shear strength, which results, from equilibrium, the same for both spandrels (Equation 5.83 and 5.111).

To compute the capacity of the frame it is necessary to know the Equivalent Spandrel Moment (ESM). The formulations to define this parameter are reported in Tables 5.21 - 5.22, for the exterior/knee and for the interior/tee subassemblies, respectively. This parameter is calculated by the rotational equilibrium imposed about the joint centroid, following the same

approach adopted to define the EPM. The derived EPM and ESM formulations for the exterior and the knee subassemblies are equal. The same is obtained for the interior and the tee subassemblies, with the only distinction made on the definition of the pier length l_p.

Table 5.15. Equivalent Pier Moment (EPM) calculations for exterior joints.

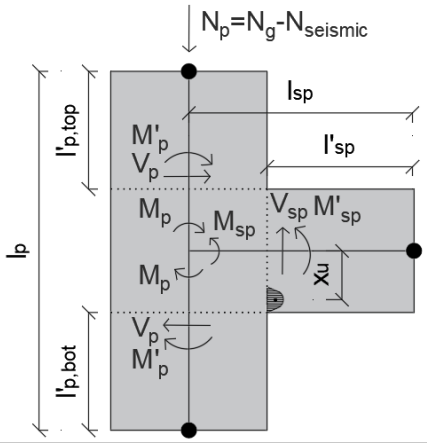

Horizontal shear force on the joint panel	$V_{jh} = C_{sp} - V_p$	(5.59)
Rotational equilibrium	$V_p l_p = V_{sp} l_{sp}$	(5.60)
Spandrel shear	$V_{sp} = \frac{V_p l_p}{l_{sp}}$	(5.61)
Pier moment at the joint panel interface	$M'_p = V_p l'_p$	(5.62)
Spandrel moment at the joint panel interface	$M'_{sp} = V_{sp} l'_{sp} = C_{sp} x_u$	(5.63)
Spandrel masonry compression	$C_{sp} = \frac{M'_{sp}}{x_u} = \frac{V_{sp} l'_{sp}}{x_u} = \frac{V_p l_p l'_{sp}}{l_{sp} x_u}$	(5.64)
EPM for spandrel flexural capacity	$M'_{p,spf} = \frac{l'_p l_{sp}}{l_p l'_{sp}} M'_{y,sp}$	(5.65)
EPM for spandrel shear capacity	$M'_{p,sps} = l_{sp} \frac{l'_p}{l_p} V_{sp}$	(5.66)
Joint shear capacity	$V_{jh} = C_{sp} - V_p = \frac{V_p l_p l'_{sp}}{l_{sp} x_u} - V_p = V_p \left[\frac{l_p l'_{sp}}{l_{sp} x_u} - 1\right]$	(5.67)
Pier shear capacity	$V_p = \frac{V_{jh}}{\left[\frac{l_p l'_{sp}}{l_{sp} x_u} - 1\right]}$	(5.68)
EPM for joint shear capacity	$M'_{p,js} = V_p l'_p = \frac{V_{jh} l'_p}{\left[\frac{l_p l'_{sp}}{l_{sp} x_u} - 1\right]}$	(5.69)

Table 5.16. Equivalent Pier Moment (EPM) calculations for interior joints.

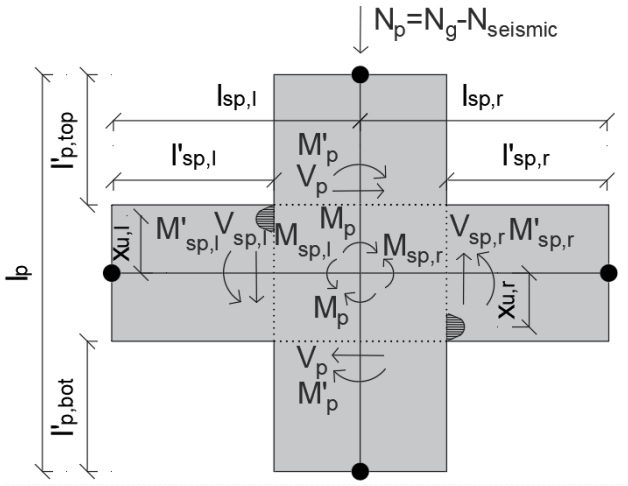

Horizontal shear force on the joint panel	$V_{jh} = C_{sp,r} + T_{sp,l} - V_p$	(5.70)
Rotational equilibrium	$V_p l_p = V_{sp,l} l_{sp,l} + V_{sp,r} l_{sp,r}$	(5.71)
Left spandrel shear	$V_{sp,l} = \frac{V_p l_p - V_{sp,r} l_{sp,r}}{l_{sp,l}}$	(5.72)
Right spandrel shear	$V_{sp,r} = \frac{V_p l_p - V_{sp,l} l_{sp,l}}{l_{sp,r}}$	(5.73)
Pier moment at the joint panel interface	$M'_p = V_p l'_p$	(5.74)
Left spandrel moment at the joint panel interface	$M'_{sp,l} = V_{sp,l} l'_{sp,l} = T_{sp,l} x_{u,l}$	(5.75)
Right spandrel moment at the joint panel interface	$M'_{sp,r} = V_{sp,r} l'_{sp,r} = C_{sp,r} x_{u,r}$	(5.76)
Average right and left spandrel moments at the joint panel interface	$M'_{sp,av} = \frac{M'_{sp,l} + M'_{sp,r}}{2}$	(5.77)
Spandrel masonry compression	$C_{sp,r} = T_{sp,l} = \frac{M'_{sp,av}}{x_u} = \frac{V_{sp,r} l'_{sp,r}}{x_u}$	(5.78)
Relationship between pier and spandrel moments	$M'_p = \frac{l'_p}{l_p}\left(M'_{sp,l}\frac{l_{sp,l}}{l'_{sp,l}} + M'_{sp,r}\frac{l_{sp,r}}{l'_{sp,r}}\right)$	(5.79)
EPM for spandrel flexural capacity (1st spandrel is yielding)	$M'_{p,spf\ 1st} = \frac{l'_p}{l_p}\left(\frac{l_{sp,l}}{l'_{sp,l}} + \frac{l_{sp,r}}{l'_{sp,r}}\right) M'_{y,sp\ 1st}$	(5.80)
EPM for spandrel flexural capacity (both spandrels are yielding)	$M'_{p,spf\ both} = \frac{l'_p}{l_p}\left(M'_{y,sp,l}\frac{l_{sp,l}}{l'_{sp,l}} + M'_{y,sp,r}\frac{l_{sp,r}}{l'_{sp,r}}\right)$	(5.81)

Spandrel shear capacity in terms of the EPM	$M'_p = \frac{l'_p}{l_p}\left(V_{sp,l}\, l_{sp,l} + V_{sp,r}\, l_{sp,r}\right)$	(5.82)
EPM for spandrel shear capacity	$M'_{p,sps} = \left(l_{sp,l} + l_{sp,r}\right)\frac{l'_p}{l_p} V_{sp\ 1st}$	(5.83)
Joint shear capacity	$V_{jh} = 2C_{sp,r} - V_p = \frac{2l_p V_p}{\left(\frac{l_{sp,l}}{l'_{sp,l}} + \frac{l_{sp,r}}{l'_{sp,r}}\right)x_u} - V_p$	(5.84)
Pier shear capacity	$V_p = \frac{V_{jh}}{\left[\frac{2l_p}{\left(\frac{l_{sp,l}}{l'_{sp,l}} + \frac{l_{sp,r}}{l'_{sp,r}}\right)x_u} - 1\right]}$	(5.85)
EPM for joint shear capacity	$M'_{p,js} = V_p l'_p = \frac{V_{jh} l'_p}{\frac{2l_p}{\left(\frac{l_{sp,l}}{l'_{sp,l}} + \frac{l_{sp,r}}{l'_{sp,r}}\right)x_u} - 1}$	(5.86)

**l'_p, for simplicity, is assumed as $l'_p = avg(l'_{p,top}, l'_{p,bot})$; $M'_{p,spf\ 1st}$ is the EPM corresponding to the first beam yields; $M'_{y,sp\ 1st}$ is the lowest yielding moment of the left or the right spandrel; $M'_{p,spf\ both}$ is the EPM corresponding to the formation of both spandrel plastic hinges; $M'_{y,sp,l}$ and $M'_{y,sp,r}$ are the yielding moments of the left and the right spandrels, respectively; $M'_{p,sps}$ is the EPM corresponding to the shear failure of the spandrels; $V_{sp\ 1st}$ is the lowest shear strength between that of the left and the right spandrel.*

Table 5.17. Equivalent Pier Moment (EPM) calculations for knee joints.

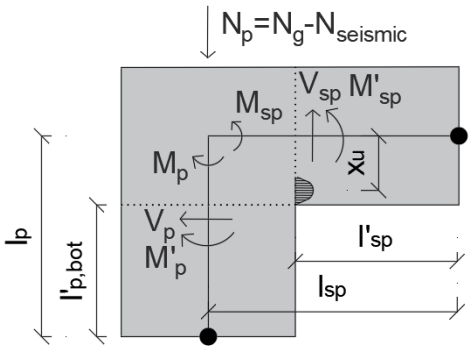

Horizontal shear force on the joint panel	$V_{jh} = C_{sp} - V_p$	(5.87)
Rotational equilibrium	$V_p l_p = V_{sp} l_{sp}$	(5.88)
Spandrel shear	$V_{sp} = \frac{V_p l_p}{l_{sp}}$	(5.89)
Pier moment at the joint panel interface	$M'_p = V_p l'_p$	(5.90)
Spandrel moment at the joint panel interface	$M'_{sp} = V_{sp} l'_{sp} = C_{sp} x_u$	(5.91)
Spandrel masonry compression	$C_{sp} = \frac{M'_{sp}}{x_u} = \frac{V_{sp} l'_{sp}}{x_u} = \frac{V_p l_p l'_{sp}}{l_{sp} x_u}$	(5.92)
EPM for spandrel flexural capacity	$M'_{p,spf} = \frac{l'_p l_{sp}}{l_p l'_{sp}} M'_{y,sp}$	(5.93)
EPM for spandrel shear capacity	$M'_{p,sps} = l_{sp} \frac{l'_p}{l_p} V_{sp}$	(5.94)
Joint shear capacity	$V_{jh} = C_{sp} - V_p = \frac{V_p l_p l'_{sp}}{l_{sp} x_u} - V_p = V_p \left[\frac{l_p l'_{sp}}{l_{sp} x_u} - 1\right]$	(5.95)
Pier shear capacity	$V_p = \frac{V_{jh}}{\left[\frac{l_p l'_{sp}}{l_{sp} x_u} - 1\right]}$	(5.96)
EPM for joint shear capacity	$M'_{p,js} = V_p l'_p = \frac{V_{jh} l'_p}{\left[\frac{l_p l'_{sp}}{l_{sp} x_u} - 1\right]}$	(5.97)

**$M'_{y,sp}$ is the yielding moment of the spandrel, that substitutes the spandrel moment M'_{sp}, to reach the EPM ($M'_{p,spf}$); V_{sp} is the shear strength of the spandrel.*

Table 5.18. Equivalent Pier Moment (EPM) calculations for tee joints.

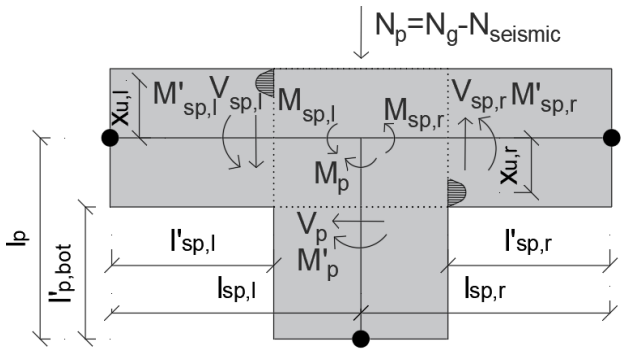

Horizontal shear force on the joint panel	$V_{jh} = C_{sp,r} + T_{sp,l} - V_p$ (5.98)
Rotational equilibrium	$V_p l_p = V_{sp,l} l_{sp,l} + V_{sp,r} l_{sp,r}$ (5.99)
Left spandrel shear	$V_{sp,l} = \frac{V_p l_p - V_{sp,r} l_{sp,r}}{l_{sp,l}}$ (5.100)
Right spandrel shear	$V_{sp,r} = \frac{V_p l_p - V_{sp,l} l_{sp,l}}{l_{sp,r}}$ (5.101)
Pier moment at the joint panel interface	$M'_p = V_p l'_p$ (5.102)
Left spandrel moment at the joint panel interface	$M'_{sp,l} = V_{sp,l} l'_{sp,l} = T_{sp,l} x_{u,l}$ (5.103)
Right spandrel moment at the joint panel interface	$M'_{sp,r} = V_{sp,r} l'_{sp,r} = C_{sp,r} x_{u,r}$ (5.104)
Average right and left spandrel moments at the joint panel interface	$M'_{sp,av} = \frac{M'_{sp,l} + M'_{sp,r}}{2}$ (5.105)
Spandrel masonry compression	$C_{sp,r} = T_{sp,l} = \frac{M'_{sp,av}}{x_u} = \frac{V_{sp,r} l'_{sp,r}}{x_u}$ (5.106)
Relationship between pier and spandrel moments	$M'_p = \frac{l'_p}{l_p}\left(M'_{sp,l}\frac{l_{sp,l}}{l'_{sp,l}} + M'_{sp,r}\frac{l_{sp,r}}{l'_{sp,r}}\right)$ (5.107)
EPM for spandrel flexural capacity (1st spandrel is yielding)	$M'_{p,spf\ 1st} = \frac{l'_p}{l_p}\left(\frac{l_{sp,l}}{l'_{sp,l}} + \frac{l_{sp,r}}{l'_{sp,r}}\right) M'_{y,sp\ 1st}$ (5.108)
EPM for spandrel flexural capacity (both spandrels are yielding)	$M'_{p,spf\ both} = \frac{l'_p}{l_p}\left(M'_{y,sp,l}\frac{l_{sp,l}}{l'_{sp,l}} + M'_{y,sp,r}\frac{l_{sp,r}}{l'_{sp,r}}\right)$ (5.109)
Spandrel shear capacity in terms of the EPM	$M'_p = \frac{l'_p}{l_p}\left(V_{sp,l}\, l_{sp,l} + V_{sp,r}\, l_{sp,r}\right)$ (5.110)

EPM for spandrel shear capacity	$M'_{p,sps} = \left(l_{sp,l} + l_{sp,r}\right)\frac{l'_p}{l_p}V_{sp\,1st}$	(5.111)
Joint shear capacity	$V_{jh} = 2C_{sp,r} - V_p = \frac{2l_pV_p}{\left(\frac{l_{sp,l}}{l'_{sp,l}}+\frac{l_{sp,r}}{l'_{sp,r}}\right)x_u} - V_p$	(5.112)
Pier shear capacity	$V_p = \frac{V_{jh}}{\left[\frac{2l_p}{\left(\frac{l_{sp,l}}{l'_{sp,l}}+\frac{l_{sp,r}}{l'_{sp,r}}\right)x_u}-1\right]}$	(5.113)
EPM for joint shear capacity	$M'_{p,js} = V_p l'_p = \frac{V_{jh}l'_p}{\frac{2l_p}{\left(\frac{l_{sp,l}}{l'_{sp,l}}+\frac{l_{sp,r}}{l'_{sp,r}}\right)x_u}-1}$	(5.114)

**$M'_{p,spf\,1st}$ is the EPM corresponding to the first beam yields; $M'_{y,sp\,1st}$ is the lowest yielding moment of the left or the right spandrel; $M'_{p,spf\,both}$ is the EPM corresponding to the formation of both spandrel plastic hinges; $M'_{y,sp,l}$ and $M'_{y,sp,r}$ are the yielding moments of the left and the right spandrels, respectively; $M'_{p,sps}$ is the EPM corresponding to the shear failure of the spandrels; $V_{sp\,1st}$ is the lowest shear strength between that of the left and the right spandrel.*

Table 5.19. Summary of the Equivalent Pier Moment (EPM) formulations for exterior and knee joints.

	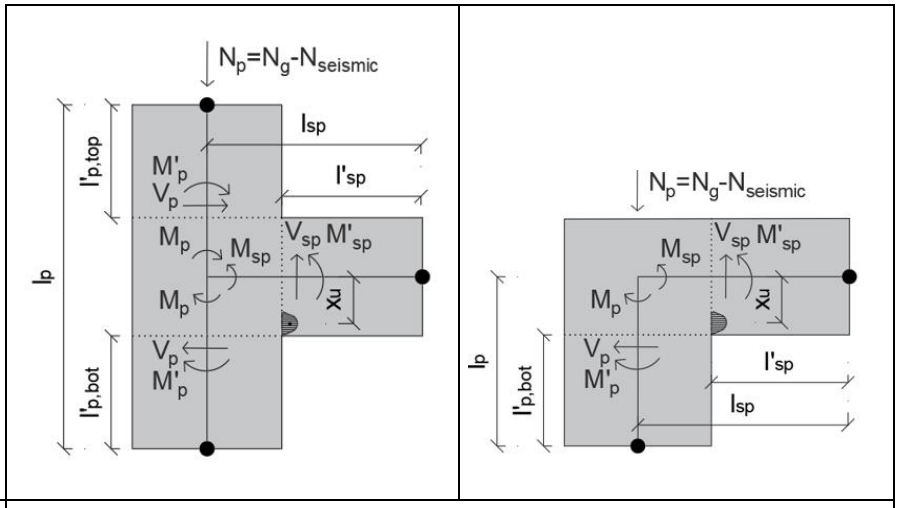
Top pier flexure	$M'_{y,p\ top}$
Bottom pier flexure	$M'_{y,p\ bot}$
Pier shear	$l'_{p,top} V_{p\ top}$ *(or bot)*
Spandrel flexure	$\frac{l'_p l_{sp}}{l_p l'_{sp}} M'_{y,sp}$
Spandrel shear	$l_{sp} \frac{l'_p}{l_p} V_{sp}$
Joint shear	$\frac{V_{jh} l'_p}{\left[\frac{l_p l'_{sp}}{l_{sp} x_u} - 1\right]}$

Table 5.20. Summary of the Equivalent Pier Moment (EPM) formulations for interior and tee joints.

	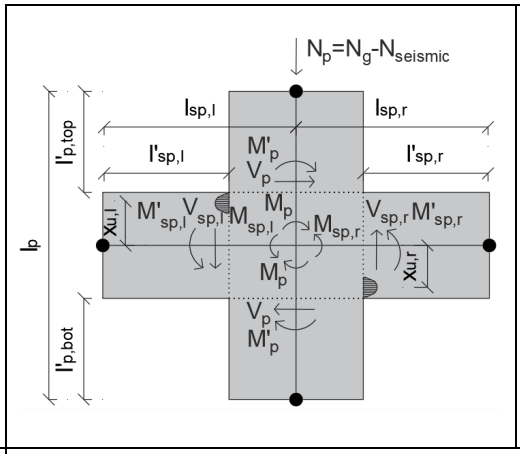	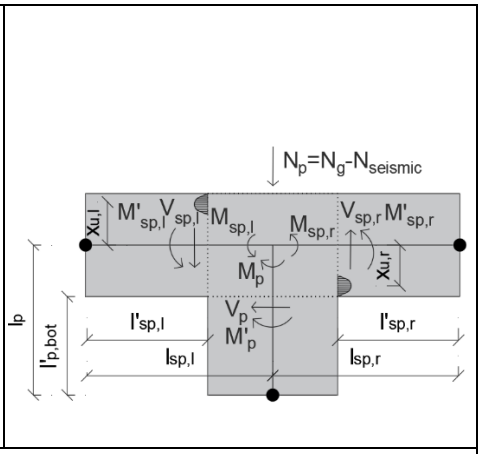
Top pier flexure	$M'_{y,p\ top}$
Bottom pier flexure	$M'_{y,p\ bot}$
Pier shear	$l'_{p,top}V_{p\ top}$ *(or bot)*
Left spandrel flexure	$\frac{l'_p}{l_p}\left(\frac{l_{sp,l}}{l'_{sp,l}}+\frac{l_{sp,r}}{l'_{sp,r}}\right)M'_{y,sp,l}$
Right spandrel flexure	$\frac{l'_p}{l_p}\left(\frac{l_{sp,l}}{l'_{sp,l}}+\frac{l_{sp,r}}{l'_{sp,r}}\right)M'_{y,sp,r}$
Both spandrels flexure	$\frac{l'_p}{l_p}\left(M'_{y,sp,l}\frac{l_{sp,l}}{l'_{sp,l}}+M'_{y,sp,r}\frac{l_{sp,r}}{l'_{sp,r}}\right)$
Spandrel shear	$l_{sp}\frac{l'_p}{l_p}V_{sp\ 1st}$
Joint shear	$\frac{V_{jh}l'_p}{\frac{2l_p}{\left(\frac{l_{sp,l}}{l'_{sp,l}}+\frac{l_{sp,r}}{l'_{sp,r}}\right)x_u}-1}$

Table 5.21. Summary of the Equivalent Spandrel Moment (ESM) formulations for exterior and knee joints.

	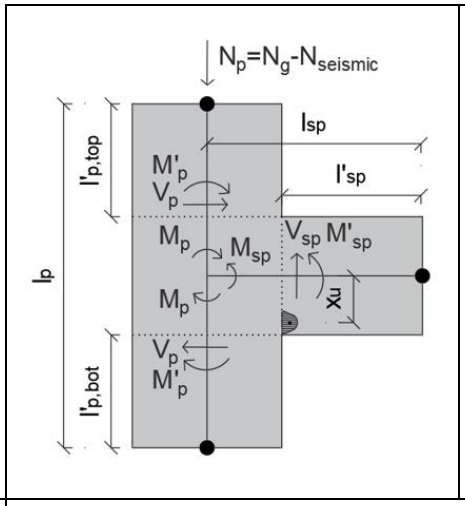	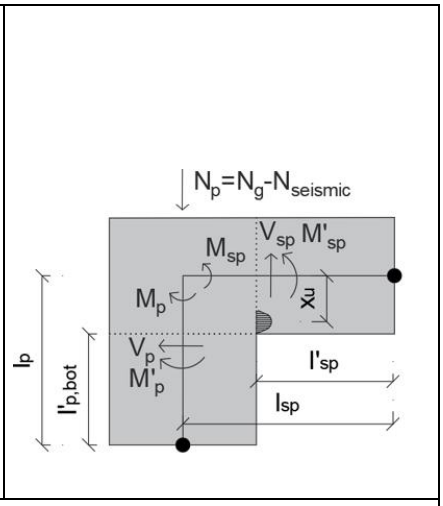
Top pier flexure	$\frac{l_p l'_{sp}}{l'_{p,top} l_{sp}} M_{y,p\ top}$	
Bottom pier flexure	$\frac{l_p l'_{sp}}{l'_{p,bot} l_{sp}} M_{y,p\ bot}$	
Pier shear	$l_{p,top} V_{p\ top}$ *(or bot)*	
Spandrel flexure	$\frac{l_{sp}}{l'_{sp}} M'_{y,sp}$	
Spandrel shear	$l_{sp} V_{sp}$	
Joint shear	$\frac{V_{jh}}{\left[\frac{1}{x_u} - \frac{l_{sp}}{l_p l'_{sp}}\right]}$	

Table 5.22. Summary of the Equivalent Spandrel Moment (ESM) formulations for interior and tee joints.

	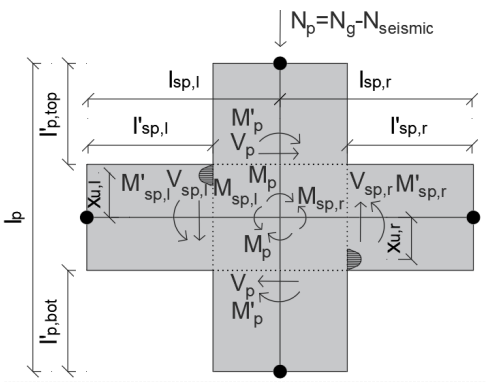	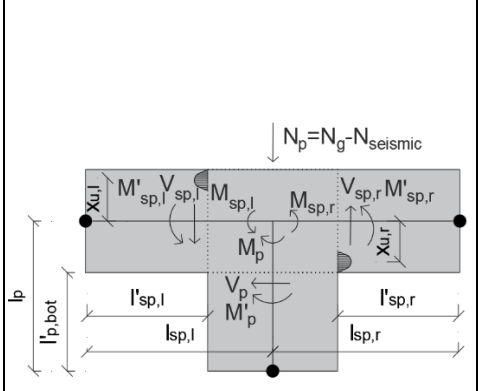
Top pier flexure	$\frac{l_p l'_{sp}}{2l'_{p,top} l_{sp}} M_{y,p\ top}$	
Bottom pier flexure	$\frac{l_p l'_{sp}}{2l'_{p,bot} l_{sp}} M_{y,p\ bot}$	
Pier shear	$\frac{l_p}{2} V_{p\ top}$ *(or bot)*	
Left spandrel flexure	$\frac{l_{sp,l}}{l'_{sp,l}} M'_{y,sp,l}$	
Right spandrel flexure	$\frac{l_{sp,r}}{l'_{sp,r}} M'_{y,sp,r}$	
Both spandrels flexure	$avg\left(M'_{y,sp,l}\frac{l_{sp,l}}{l'_{sp,l}} + M'_{y,sp,r}\frac{l_{sp,r}}{l'_{sp,r}}\right)$	
Spandrel shear	$l_{sp} V_{sp\ 1st}$	
Joint shear	$\frac{V_{jh}}{\frac{2}{x_u} - \frac{1}{l_p\left(\frac{l_{sp,l}}{l'_{sp,l}} + \frac{l_{sp,r}}{l'_{sp,r}}\right) x_u}}$	

5.4.3.3 Seismic demand in terms of axial load variation

In this Section, the axial load variation on the piers, due to the coupling effect of the spandrel during the lateral sway, is taken into account and introduced in the M-N performance domain, adopting a relationship between the axial load and the moment of the top pier at the joint panel interface. Following the formulation suggested in the NZSEE guidelines (NZSEE 2017a) for RC structures, derived from the equilibrium considerations at frame level proposed in Kam (2010), Pampanin *et al*. (2007) and Tasligedik *et al*. (2016), the seismic demand can be adapted to URM buildings, through Equation 5.115:

$$N = N_g \pm \alpha F = N_g \pm \alpha \frac{F}{V_{p,ext}} V_{p,ext} \tag{5.115}$$

where N_g is the gravity axial load acting on the subassembly; α is a coefficient given by $\alpha = 2H_{tot}/3L$, where H_{tot} and L are the height and the length of the frame, respectively; $V_{p,ext}$ is the exterior pier shear that can be defined from the exterior pier moment $M_{p,ext}$ and the exterior pier cantilever height l_p, measured from the contra-flexure point to the joint centroid, as $V_{p,ext} = M_{p,ext}/l_p$; $F/V_{p,ext}$ depends on the column shear distribution and is assumed equal to the number of the piers n_{piers} in the frame; F represents the equivalent seismic load (or global shear strength), assumed to be applied at $2/3$ of H_{tot} (considering a linear force profile).

The NZSEE guidelines (NZSEE 2017a) suggest to use Equation 5.115 for the exterior columns (hence the piers in case of URM buildings), and it is valid for the calculation of the coefficient α for an exterior subassembly on the first floor. For the interior ones, the variation of axial load induced by lateral forces is generally smaller. It can be assumed as zero if the length and the strength of the left and right spandrels are equal. Otherwise, assuming the linear distribution of the axial load variation on the piers, referring to Figure 5.32, the seismic demand in the interior piers can be defined following Equation 5.116.

$$\Delta N_{int,x} = \Delta N \left(1 - \frac{2x}{L}\right) \tag{5.116}$$

where ΔN is the variation of axial load in the exterior piers; x is the distance between the interior and the exterior pier; L is the total length of the frame.

As an approximation for simplifying the procedure, the variation of the axial load in the interior pier-spandrel joints can be neglected or assumed equal to 10-20% of the axial load (NZSEE 2017a).

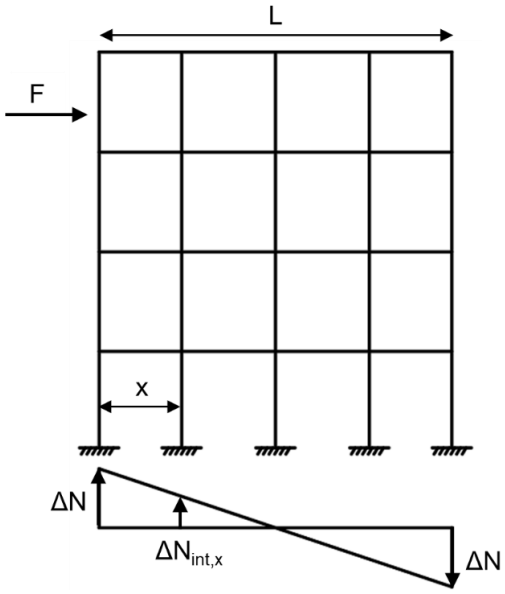

Figure 5.32. Schematization of the linear distribution of the piers axial load variation.

In Equation 5.117 is reported the definition of the OverTurning Moment (OTM), given by the sum of two contributions: i) the moment derived by the rocking mechanism in the piers due to the seismic axial load (ΔNL) and ii) the moments of the piers at the base of the frame ($\sum M_p$). By neglecting the second contribution (generally much lower with respect to the other), the variation of axial load can be expressed as Equation 5.118, thus obtaining $\Delta N = \alpha F$.

$$OTM = \frac{2}{3} H_{tot} F = \sum M_p + \Delta NL \tag{5.117}$$

$$\Delta N = \frac{2H_{tot}}{3L} F \tag{5.118}$$

Regarding the ratio of the equivalent seismic load F to the shear of the exterior pier $V_{p,ext}$, it refers to a simplified equilibrium consideration, related to Figure 5.33. By assuming a pier contra flexure point at $2/3$ of the pier height h_p, the exterior and interior piers moment and the corresponding shear can be calculated according to Equations 5.119 - 5.122.

$$M_{p,ext}^{top} = \frac{2}{3} M_{p,ext}^{bot} \tag{5.119}$$

$$M_{p,int}^{top} = \frac{2}{3} M_{p,int}^{bot} \tag{5.120}$$

$$V_{p,ext} = \frac{M_{p,ext}^{top} + M_{p,ext}^{bot}}{h_p} = \frac{5}{2} \frac{M_{p,ext}^{bot}}{h_p} \tag{5.121}$$

$$V_{p,int} = \frac{M_{p,int}^{top} + M_{p,int}^{bot}}{h_p} = \frac{5}{2} \frac{M_{p,int}^{bot}}{h_p} \tag{5.122}$$

where $M_{p,ext}^{top}$ and $M_{p,ext}^{bot}$ are the moments of the exterior top and bottom base piers, respectively; $M_{p,int}^{top}$ and $M_{p,int}^{bot}$ are the moments of the interior top and bottom base piers, respectively; $V_{p,int}$ is the shear of the interior piers.

Then, according to the procedure proposed by Kam (2010), two different pier shear distributions can be considered, with respect to the possible failure mechanisms expected to occur at the exterior subassemblies: i) an inelastic mechanism as joint shear failure, pier flexural/shear failure or spandrel shear failure, which does not allow the moment redistribution and ii) the interior joint shear failure or the formation of the plastic hinge to the spandrel. In the first case (i), the shear and the moments of the base exterior and interior piers are the same ($V_{p,ext} = V_{p,int}$), and hence the equivalent seismic load F is given by Equation 5.123. From this, the ratio $F/V_{p,ext}$ can be obtained (Equation 5.124).

$$F = \sum V_p = 2V_{p,ext} + (n_{piers} - 2)V_{p,int} = n_{piers} V_{p,ext} \tag{5.123}$$

$$\frac{F}{V_{p,ext}} = \frac{n_{piers} V_{p,ext}}{V_{p,ext}} = n_{piers} \tag{5.124}$$

In the second case (ii), the distribution of the shear of the base pier can be approximated by assuming $V_{c,int} = 2V_{p,ext}$ and hence $M_{p,int}^{top} = 2M_{p,ext}^{bot}$. As a consequence, the equivalent seismic load F and the ratio $F/V_{p,ext}$ can be expressed through Equations 5.125 - 5.126.

$$F = 2V_{p,ext} + (n_{piers} - 2)V_{p,int} = (2n_{piers} - 2)V_{p,ext} \tag{5.125}$$

$$\frac{F}{V_{p,ext}} = \frac{(2n_{piers} - 2)V_{p,ext}}{V_{p,ext}} = 2n_{piers} - 2 \tag{5.126}$$

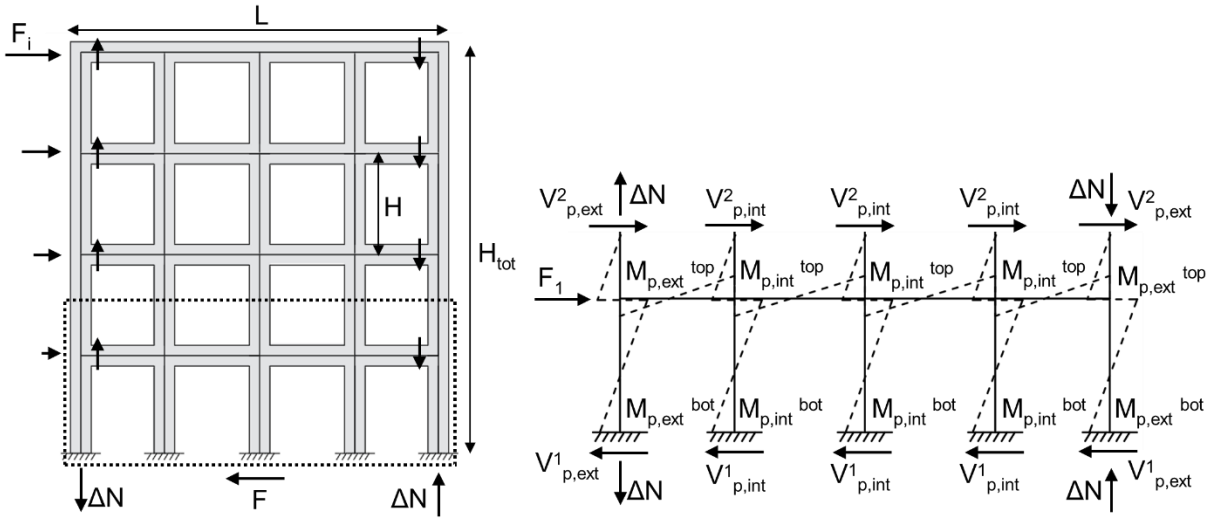

Figure 5.33. Simplified equilibrium of a frame system (adapted from Gentile, 2017).

These formulations can be considered valid only for the subassemblies on the first floor. For those at the upper floors, for which a lower variation of axial load ΔN_i is expected, the procedure proposed in Gentile (2017) can be adopted. It is based on a simplified equilibrium formulation of a portion of the frame from the floor i to the top of the building (Figure 5.34). Assuming a linear inertia force profile, ΔN_i can be expressed through Equation 5.127, adopting the parameter λ_2 (Equation 5.128) that is a function of i th level and the number of the total levels n of the frame.

$$\Delta N_i = \frac{\sum_{j=i}^{n} F_j \left(H_j - H_{i-1}\right)}{L} = \frac{\sum_{j=i}^{n} \frac{2FH_j^2}{H(n+1)n}}{L} = \frac{2FH}{L}\lambda_2 \tag{5.127}$$

$$\lambda_2 = \frac{1}{(n+1)n}\left(\frac{n(n+1)(2n+1) - i(i-1)(2i-1)}{6} - (i-1)\frac{n(n+1) - i(i-1)}{2}\right) \tag{5.128}$$

where H_j and F_j are the height of the j th level (measured from the ground) and the force at the same level; H is the inter-storey height; L is the total length of the frame.

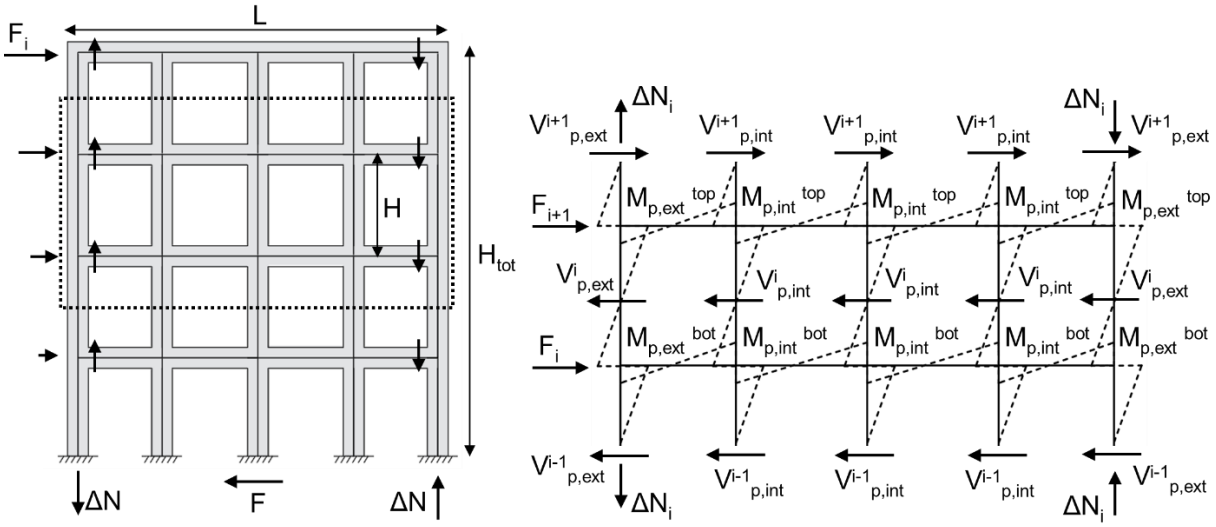

Figure 5.34. Simplified equilibrium of a frame system focusing on the i-storey (adapted from Gentile, 2017).

Alternatively, the variation of the axial load of the exterior piers located at the floors above the first one can be calculated assuming the approximation of linear force profile starting from the considered floor, and not from the ground. It means adopting the same expression for the piers at the first floor (Equation 5.118), but substituting the total height of the frame H_{tot} with the height of the frame from the considered floor $(H_{tot} - H_i)$. The approximated seismic demand in the exterior piers at the upper floors can be calculated by Equation 5.129:

$$\Delta N = \frac{2(H_{tot} - H_i)}{3L} F \tag{5.129}$$

For the interior piers at the same upper levels, Equation 5.116 can be adopted, or eventually, the simplification provided in NZSEE (2017a), i.e. assuming a variation of 10-20% of the axial load.

5.4.3.4 M-N performance domain

From the URM components, strength calculations defined in Section 5.4.3.1 and 5.4.3.2 and the seismic demand calculation outlined in Section 5.4.3.3, the M-N performance domain at each subassembly level can be obtained. In this diagram, the capacity of the failure mechanisms of the structural components are compared, and by the intersection with the

seismic demand, the subassembly sequence of events can be defined. The lower capacity in terms of EPM identifies the crisis mechanism expected to occur and represents the strength of the whole subassembly. An example of the performance domain is shown in Figure 5.35. Detailed calculations are reported in Appendix A.2.

As observed in Figure 5.35, in the push and pull directions (pier axial load decreasing and increasing, respectively), the weakest component mechanism is the spandrel shear failure, hence the strength of the subassembly is related to the EPM corresponding to this mechanism. It is observed that both the flexural and shear capacity of the spandrel can be considered as independent of the axial load applied to the piers, hence the spandrel moment capacity in the M-N performance domain is assumed to be constant.

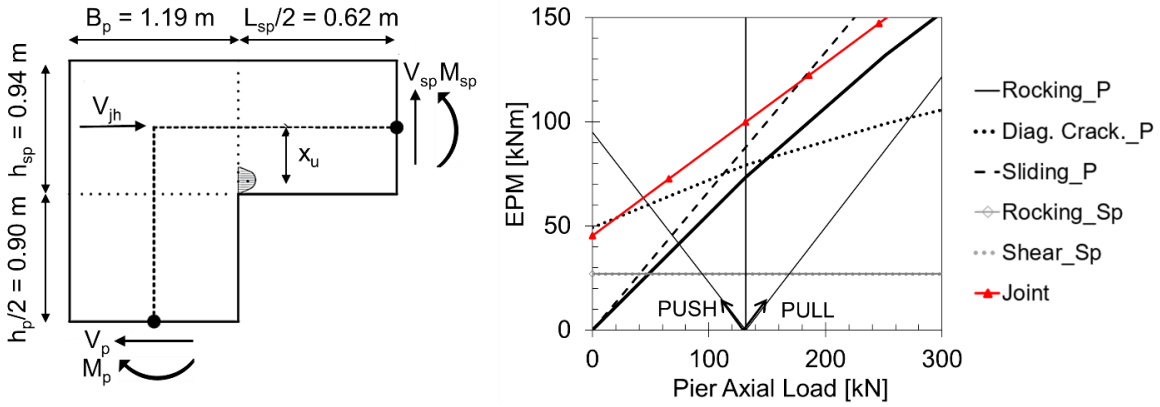

Figure 5.35. M-N performance domains of a knee pier-spandrel joint subassembly.

5.4.4 Analysis at global level

From the strength of each subassembly of the frame, the probable plastic mechanism expected to occur can be defined and the corresponding capacity can be calculated.

Following the suggestion from the SLaMA method in the NZSEE guidelines (NZSEE 2017a), the force-displacement capacity curve of the structure can be defined assuming three different plastic mechanisms, which are the most probable ones that can occur in a frame. In Figure 5.36, the schematization of the capacity curves adapted to the URM cases are shown, with reference to the following plastic mechanisms:

- the *Spandrel-Sway mechanism*. It is assumed the development of the spandrels plastic hinges at each level of the frame and of the piers at the base. It represents the upper bound of the lateral load capacity of the frame and the preferred mechanism in the retrofitting since it respects the capacity design provisions;

- the *Mixed-Sway mechanism*. It can be defined from the hierarchy of strength in each subassembly of the frame and represents the plastic mechanism expected to occur;

- the *Pier-Sway mechanism*. It is assumed the development of a soft-storey mechanism, hence the formation of plastic hinges at the piers located at a given level of the frame. Generally, but not always (i.e. see Del Vecchio *et al*., 2017) for the case of the Column-Sway mechanism), it represents the lower bound of the lateral load capacity of the frame.

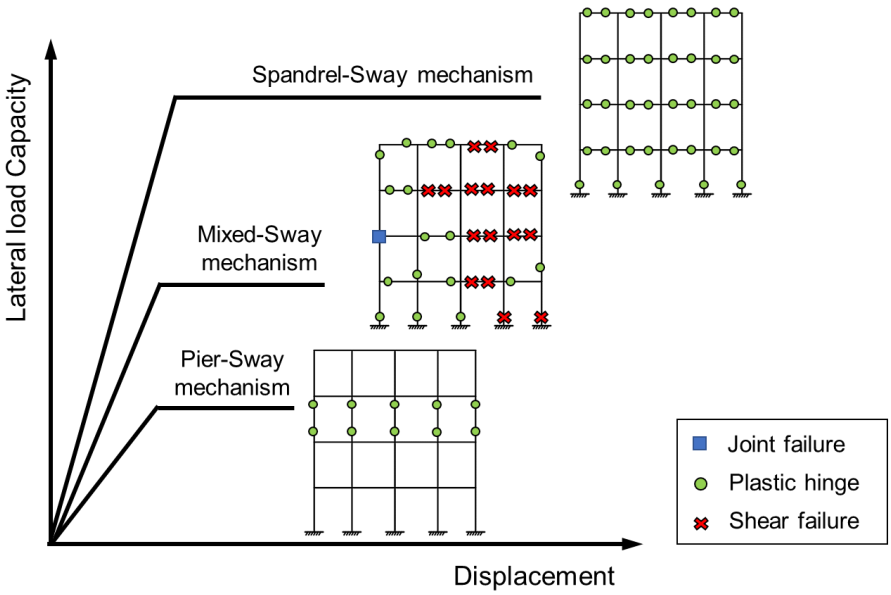

Figure 5.36. Lateral load capacity versus displacement for different global mechanisms: Spandrel-Sway, Mixed-Sway and Pier-Sway.

For these three plastic mechanisms, the base shear V_b can be obtained by the OverTurning Moment (OTM) and an effective height H_{eff} of the frame (to which the seismic force is supposed to be applied), according to a simplified approach based on the global

equilibrium, as suggested in Priestley *et al*. (2007). Furthermore, the displacement capacity can be identified from the rotation capacity of the URM components. The assumed plastic mechanism defines the involved parameters and changes the way to calculate the base shear-displacement bilinear relationships. The Spandrel-Sway, Mixed-Sway and Pier-Sway mechanisms are outlined in Sections 5.4.4.1, 5.4.4.2 and 5.4.4.3, respectively.

5.4.4.1 Spandrel-Sway mechanism

The Spandrel-Sway mechanism corresponds to the situation in which at each subassembly of the frame the spandrel plastic hinge is developed and represents the maximum performance level achieved by the frame in case of retrofitting.

The base shear strength V_b^{SS} of the frame can be derived from the OverTurning Moment OTM^{SS} that can be calculated using a global equilibrium approach by including two contributions (Equations 5.130 - 5.131): (1) the bending moment at the base of the piers and (2) the push-pull overall moment due to the coupling of shear forces at the spandrel-end (a rocking mechanism). It is worth mentioning that in these expressions, it is assumed that the spandrels of the same level are the same such as their moment capacity, hence neglecting the variation of axial load in the interior piers. Moreover, the choice of the left or right exterior spandrels to define the second contribution of OTM^{SS} changes considerably the results. To this aim, the calculation for both cases has to be computed and the average considered.

$$OTM^{SS} = \sum_j M_{p,y\ j} + \left(\sum_i V_{end\ sp,i}\right) L \tag{5.130}$$

$$\sum_i V_{end\ sp,i} = \sum_i \frac{M_{sp,y\ left\ i} + M_{sp,y\ right\ i}}{L_{sp}^{ext}} \tag{5.131}$$

where $M_{p,y\ j}$ is the "yield" moment of the jth pier at the base; $V_{end\ sp,i}$ is the shear force in the exterior spandrel at the ith storey; L is the total length of the frame; $M_{sp,y\ left\ i}$ and $M_{sp,y\ right\ i}$ are the "yield" moments of the left and right exterior spandrel cross-section at the ith storey, respectively; L_{sp}^{ext} is the length of the exterior spandrel.

The OTM^{SS} is then dividing by the effective height of the frame H_{eff}^{SS}, which identifies the point in which the seismic force is supposed to be applied. This parameter depends on the

contribution of the two resisting terms in the OTM^{SS} expression. Following the main steps of the Displacement Based Design approach presented in DBD09 Model Code (Calvi and Sullivan, 2009) and then simplified in Sullivan *et al*. (2012), it is possible to define the spandrels contribution (a rocking mechanism) in the OTM^{SS} through the parameter β_F (Equation 5.132), and the ratio between the effective height H_{eff}^{SS} and the total height H of the frame according to Equation 5.133. Once obtained H_{eff}^{SS}, the base shear can be calculated (Equation 5.134). Alternatively, an approximated and "fixed" effective height H_{eff}^{SS} equal to two-thirds of the total height ($2/3H$) can be considered.

$$\beta_F = \frac{M_{\Delta N}^{SS}}{OTM^{SS}} \tag{5.132}$$

$$\frac{H_{eff}^{SS}}{H} = \frac{\sqrt{9 - 8\beta_F} - 1}{n^{0.25}} \tag{5.133}$$

$$V_b^{SS} = \frac{OTM^{SS}}{H_{eff}^{SS}} \tag{5.134}$$

where $M_{\Delta N}^{SS}$ is the moment resisting contribution due to the coupling of the shear forces at the spandrel-end, or rocking mechanism ($M_{\Delta N}^{SS} = \sum_i V_{end\ sp,i}\, L$); n is the total number of floors.

In Figure 5.37, hypothesizing a push direction of the seismic load (i.e. assuming an increase of the seismic axial load in the right pier and a decrease in the left one), the parameters for the calculation of the OverTurning Moment OTM^{SS} are schematized.

The "yield" Δ_y^{SS} and the ultimate Δ_u^{SS} displacement of the frame at the effective height H_{eff}^{SS} are calculated from the minimum "yield" $\theta_{y,min}^{SS}$ and ultimate $\theta_{u,min}^{SS}$ drift among all the spandrels and the piers at the base, as reported in Equations 5.135 - 5.136.

$$\Delta_y^{SS} = \theta_{y,min}^{SS} H_{eff}^{SS} \tag{5.135}$$

$$\Delta_u^{SS} = \theta_{u,min}^{SS} H_{eff}^{SS} \tag{5.136}$$

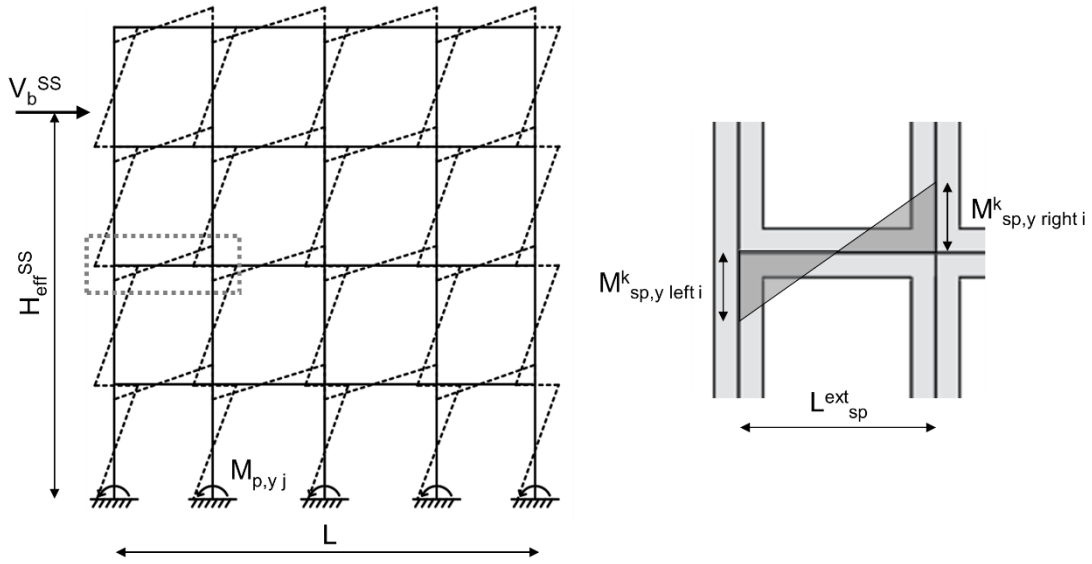

Figure 5.37. OverTurning Moment capacity for the Spandrel-Sway mechanism.

To overcome the approximation of considering only the exterior spandrels, more detailed calculations which take into account also the rocking mechanism formed by the seismic axial load in the interior piers can be considered. More in detail, with regard to Figure 5.38, hypothesizing a push direction of the seismic load, the following expressions to calculate the OTM^{SS} can be adopted (Equations 5.137 - 5.138):

$$OTM^{SS} = \sum_j M_{p,y\ j} + \left(\sum_j \left(V_{sp,j-1} - V_{sp,j} \right) L_j \right) \tag{5.137}$$

$$V_{sp}^k = \sum_i V_{sp,i} = \sum_i \frac{M_{sp,y\ left\ i}^k + M_{sp,y\ right\ i}^k}{L_{sp}^k} \tag{5.138}$$

where $M_{p,y\ j}$ is the "yield" moment of the j[th] pier at the base; $V_{sp,j}$ is the sum over the floors of the spandrels shear forces at the j[th] pier; L_j is the distance of the j[th] pier with respect to the left corner of the frame; V_{sp}^k is the sum over the floors of the spandrels shear forces at the k[th] spandrel span; $M_{sp,y\ left\ i}^k$ and $M_{sp,y\ right\ i}^k$ are the "yield" moments of the left and right k[th] spandrel at the i[th] storey; L_{sp}^k is the length of the k[th] spandrel.

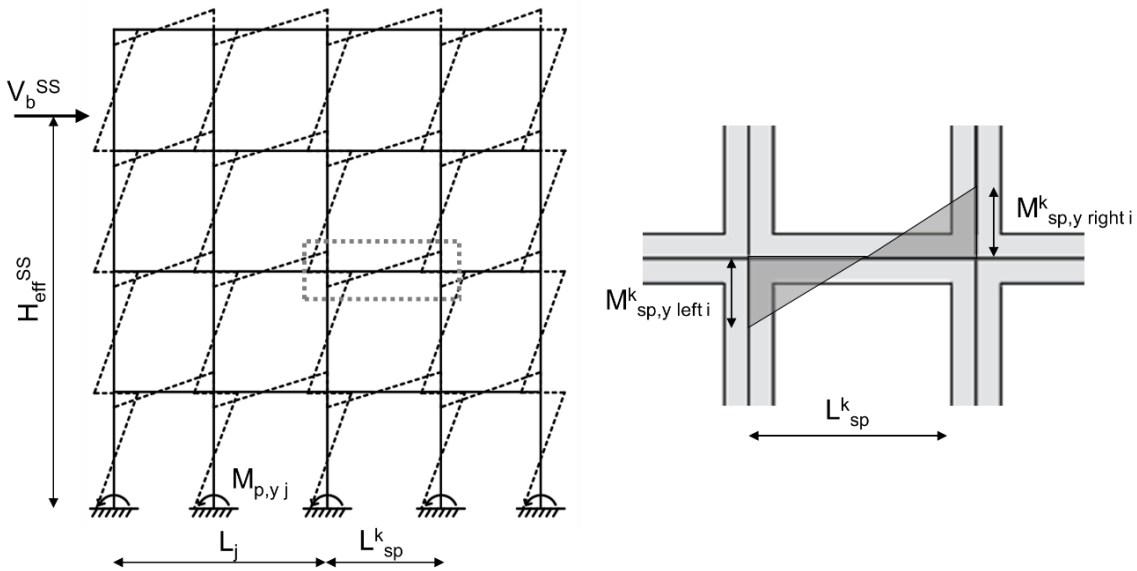

Figure 5.38. OTM^{SS} capacity for the Spandrel-Sway mechanism, considering also the rocking mechanism formed by the seismic axial load in the interior piers.

To consider the pull direction of the seismic load, the two terms representing the total shear forces in the calculation of OTM^{SS} (Equation 5.137) have to be considered in the reverse position, in such a way to assume an increase of the seismic axial load in the left pier of the frame.

To define the effective height and the base shear, Equations 5.133 and 5.134 can be adopted.

5.4.4.2 Mixed-Sway mechanism

The same procedure adopted for the Spandrel-Sway mechanism in Section 5.4.4.1 can be assumed for the Mixed-Sway mechanism, with the important difference that the mechanism of each subassembly of the frame is not assumed a priori (i.e. the formation of plastic hinges at all the spandrels of the frame), but it is based on the hierarchy of strength. The OTM^{MS}, the effective height H_{eff}^{MS} and the base shear V_b^{MS} can be calculated using Equations 5.139 - 5.141.

$$OTM^{MS} = \sum_j M_{p,y\ j} + \sum_i \frac{M_{left\ i}^{sp,eq} + M_{right\ i}^{sp,eq}}{L_{sp}^{ext}} L \tag{5.139}$$

$$H_{eff}^{MS} = \frac{\sqrt{9 - 8\beta_F} - 1}{n^{0.25}} H \tag{5.140}$$

$$V_b^{MS} = \frac{OTM^{MS}}{H_{eff}^{MS}} \tag{5.141}$$

where $M_{p,y\,j}$ is the "yield" moment of the j[th] pier at the base; L is the total length of the frame; $M_{left\,i}^{sp,eq}$ and $M_{right\,i}^{sp,eq}$ are the ESM, calculated in the joint centroid, related to the local failure mechanism at the left and right exterior spandrel cross-sections, at the i[th] storey; L_{sp}^{ext} is the length of the exterior spandrel.

The mechanisms identified in the M-N performance domain let to define the drift capacity of each subassembly from the component failure mechanism that causes the failure of the subassembly. In Figure 5.39, the parameters for the calculation of the OTM^{MS} are schematized, hypothesizing a push direction of the seismic load.

The "yield" Δ_y^{MS} and ultimate Δ_u^{MS} displacements of the bi-linear curve corresponding to the Mixed-Sway mechanism are defined according to the "yield" $\theta_{y,min}^{MS}$ and ultimate $\theta_{u,min}^{MS}$ drifts of the critical structural components (see Equations 5.142 and 5.143), considering all the subassemblies and the base section of the piers.

$$\Delta_y^{MS} = \theta_{y,min}^{MS} H_{eff}^{MS} \tag{5.142}$$

$$\Delta_u^{MS} = \theta_{u,min}^{MS} H_{eff}^{MS} \tag{5.143}$$

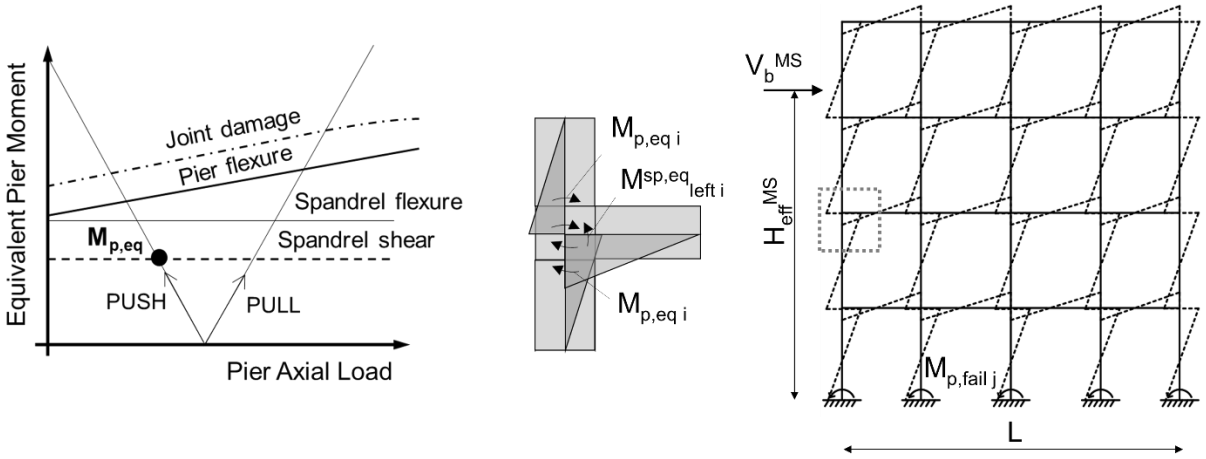

Figure 5.39. OTM^{MS} for the Mixed-Sway mechanism.

As for the Spandrel-Sway mechanism, an approximated effective height of the seismic force equal to two-thirds of the total height of the frame ($H_{eff}^{MS} = 2/3H$) can be adopted.

Moreover, to overcome the approximation of neglecting the contribution of the rocking mechanism given by the interior piers to the definition of the OTM^{MS}, the same approach adopted for the Spandrel-Sway mechanism can be assumed (see Equations 5.137 and 5.138).

5.4.4.3 Pier-Sway mechanism

The Pier-Sway mechanism consists of the assumption of the development of a soft-storey mechanism, hence the formation of the plastic hinges at the piers located at a given level of the frame. In this mechanism, the OTM^{PS} is defined by a single contribution (Equation 5.144): the "yield" moments of the piers that develop plastic hinge. Assuming the formation of soft-storey on the first floor, the inter-storey shear strength and the base shear are the same and they can be calculated by Equation 5.145.

$$OTM^{PS} = \sum_{j} M_{p,y\,j} \tag{5.144}$$

$$V_b^{PS} = \frac{OTM^{PS}}{0.5h_{int}} \tag{5.145}$$

where $M_{p,y\,j}$ is the "yield" moment of the j[th] bottom pier sections at the base; h_{int} is the inter-storey height of the first floor.

In Figure 5.40, hypothesizing a push direction of the seismic load, are schematized the parameters for the calculation of the OTM^{PS}.

To define the "yield" Δ_y^{PS} and ultimate Δ_u^{PS} displacements of the bilinear curve corresponding to the Pier-Sway mechanism, the effective height H_{eff}^{PS} of the frame can be adopted following Equation 5.146 (Priestley, 1997) and the corresponding drifts are defined as the minimum "yield" $\theta_{y,min}^{PS}$ and ultimate $\theta_{u,min}^{PS}$ drifts of the piers, involved in the soft-storey mechanism. The corresponding displacements (Δ_y^{PS} and Δ_u^{PS}) are calculated according to Equations 5.147 and 5.148.

$$H_{eff}^{PS} = 0.5H \tag{5.146}$$

$$\Delta_y^{PS} = \theta_{y,min}^{PS} H_{eff}^{PS} \tag{5.147}$$

$$\Delta_u^{PS} = \theta_{u,min}^{PS} H_{eff}^{PS} \tag{5.148}$$

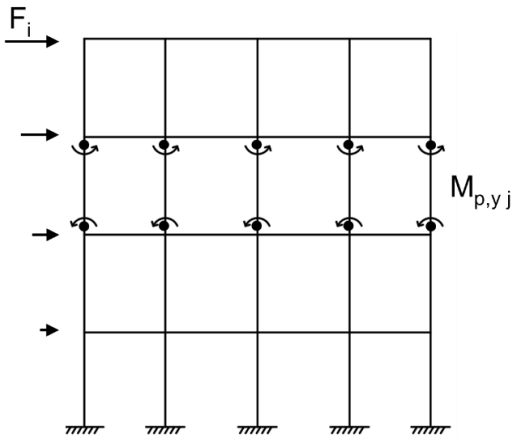

Figure 5.40. OTM^{PS} capacity for the Pier-Sway mechanism.

5.4.5 In-Plane performance level

Once the building capacity curve is obtained, the In-Plane capacity/demand ratio is evaluated. More in details, the intersection between the capacity curve with the ADRS curve identifies the performance point of the structure, allowing to calculate the %NBS of the global In-Plane response.

5.5 Limits and role of the SLaMA-URM method

Speaking about the role of the SLaMA-URM procedure presented so far, it can be said that its simplicity of use and the reasonable results that are capable to achieve, make it a good choice for a preliminary procedure of seismic assessment that can give a fair estimation of the structural behavior. The obtained non-linear pushover curves contain all the uncertainties that reside behind the various assumptions adopted, i.e. unknown exact values of the input parameters, that can act as a starting point for more detailed investigations. The

SLaMA-URM procedure can be used to fast evaluate the effect of the retrofit strategies, in order to have a first screening of the possible retrofitting techniques to be applied to the structure by directly giving an estimation of the %NBS. This can be done also for different seismic intensities by rapidly adapting the pushover curve to the different real earthquakes that can be expected in the area under examination, and then planning the possible combination of different retrofitting techniques. Indeed the SLaMA-URM method deals independently with seismic capacity and demand, i.e. changing the capacity curve does not change the ADRS curve. The low computational needed cost (especially if the procedure is automatized through spreadsheets or coding) makes the SLaMA procedure suitable for performing parametric analysis and sensitivity studies in such a way to evaluate the real uncertainties in the obtained results. This “by-hand” approach is recommended as the first step in any seismic assessment procedure, capable to obtain a fast and reliable estimation of the nonlinear pushover curve of the structure.

However, the simplicity of use of this procedure is counterbalanced by some limitations that need to be considered and fully understood in order to correctly take advantage of the SLaMA-URM capabilities. The principal limitation resides in the adopted assumptions and approximations and they can be identified as:

1) only the first mode of the building is considered active, while the higher modes are neglected. This for taller structures can lead to the wrong estimation since in this configuration, higher mode effects are expected to play a significant role;
2) the torsional aspects are not taken into account, therefore the method is not suitable for cases where a building has significant strength or stiffness eccentricities in plan;
3) little changes in the considered input parameters can lead to step-changes in the exhibited failure mechanisms of the structural components. For example, a small variation in the axial load can induce a change in the failure mode of a pier, i.e. from a rocking one to a brittle shear one, thus resulting in a substantial variation in the ductility capacity of the structure. This issue can be overcome by performing sensitivity analysis with respect to the various input parameters.
4) in the case of crisis due to shear of the masonry components (piers and spandrels), the procedure does not consider the strain-softening in the post-peak range. By assuming the shear failure of URM components brittle, this limitation, however, results in favour of safety.

For how SLaMA method is conceived, given the number of simplified assumptions needed to apply, a degree of error is expected. In Chapter 6 the SLaMA-URM accuracy is addressed starting from simple walls up to multi-storey walls. This is done by comparing the SLaMA-URM to numerical Pushover analyses.

5.6 References

ASCE (2007). Seismic Rehabilitation of Existing Buildings - ASCE/SEI 41-06, American Society of Civil Engineers, Reston, Va.

Asteris, P. G., Antoniou, S. T., Sophianopoulos, D. S. & Chrysostomou, C. Z. (2011). Mathematical Macromodeling of Infilled Frames: State of the Art, Journal of Structural Engineering 137(12), 1508–1517.

Augenti N. (2006). Seismic behaviour of irregular masonry walls. Proceedings of the 1st European Conference on Earthquake Engineering and Seismology, Geneva, paper No. 86.

Augenti, N. and F. Parisi. (2010). Ultimate flexural strength of unreinforced masonry spandrel panels, 8th International masonry conference Dresden, Germany.

Bertoldi, S.H., Decanini, L.D. and Gavarini, C. (1993). Telai tamponati soggetti ad azioni sismiche, un modello semplificato: confronto sperimentale e numerico. In Atti del 6º Convegno Nazionale ANIDIS, 815–824, Perugia: Associazione Nazionale Italiana di Ingegneria Sismica, (in Italian).

Brencich, A. and G. De Felice. (2009). Brickwork under eccentric compression: Experimental results and macroscopic models, Construction and Building Materials, 23(5),1935-1946.

Brencich, A. and U. De Francesco. (2004). Assessment of Multispan Masonry Arch Bridges. 1:Simplified Approach, Journal of Bridge Engineering, ASCE, 9(6),582-590.

Calvi, G., and Sullivan, T. (2009). A model code for the displacement based seismic design of structures. Iuss Press.

Cattari, S. (2007). Modellazione a telaio equivalente di strutture esistenti in muratura e miste muratura-c.a.: formulazione di modelli sintetici, University of Genoa, PhD Dissertation (In Italian), Italy.

Cattari, S. and S. Lagomarsino. (2008). A Strength criterion for the flexural behaviour of spandrels in unreinforced masonry walls, The 14th World Conference on Earthquake Engineering, Beijing, China.

Cavaleri, L., A. Failla, L. La Mendola and M. Papia. (2005). Experimental and analytical response of masonry elements under eccentric vertical loads, Engineering Structures, 27(8),1175-1184.

Cornell, C. A. (1968). Engineering seismic risk analysis. Bulletin of the seismological society of America, 58(5), 1583-1606.

Del Vecchio, C., Gentile, R. & Pampanin, S. (2017). The Simple Lateral Mechanism Analysis (SLaMA) for the seismic performance assessment of a case study building damaged in the 2011 Christchurch earthquake, Research report N. 2016-02, Technical report, Department of Civil and Natural Resources, University of Canterbury, Christchurch (New Zealand).

Dolce, M. (1991). Schematizzazione e modellazione degli edifici in muratura soggetti ad azioni sismiche. L'Industria delle Costruzioni, 25:44-57 (in Italian).

EN 1996 (European Committee for Standardization). (2006). Design of masonry structures - Part 1-1: General rules for reinforced and unreinforced masonry structures. Eurocode 6: EN.

EN 1998 (European Committee for Standardization). (2005). Design of structures for earthquake resistance - Part 3: Assessment and retrofitting of buildings. Eurocode 8, Brussels, Belgium: EN.

FEMA 306 (Federal Emergency Management Agency). (1998). Evaluation of earthquake damaged concrete and masonry wall buildings: Basic procedures manual. Washington DC, US:FEMA.

Flanagan, R. D. & Bennett, R. M. (2001). In-plane analysis of masonry infill materials, Practice Periodical on Structural Design and Construction 6(4), 176–182.

Gentile, R. (2017). Extension, refinement and validation of the simple lateral mechanism analysis (SLaMA) for the seismic assessment of RC structures. Diss. PhD thesis, Department of Civil, Environmental and Landscape, Building Engineering and Chemistry, Polytechnic University of Bari, Bari, Italy.

Gentile, R., Del Vecchio, C., Pampanin, S., Raffaele, D. and Uva, G. (2019). Refinement and validation of the Simple Lateral Mechanism Analysis (SLaMA) procedure for RC frames. J. Earthq. Eng., 1–29.

Holmes, M. (1961). Steel frames with brickwork and concrete infilling, ICE Proceedings 19(4), 473–478.

Kam, W. Y. (2010). Selective weakening and post-tensioning for the seismic retrofit of nonductile RC frames, PhD thesis, University of Canterbury.

Kaushik, H.B., D.C. Rai and S.K. Jain. (2007). Stress-strain characteristics of clay brick masonry under uniaxial compression, Journal of Materials in Civil Engineering, 19(9),728-738.

Kent, D.C. and R. Park. (1971). Flexural members with confined concrete, Journal of Structural Division, ASCE, 97(1),1969-1990.

Knox, C. (2012). Assessment of perforated unreinforced masonry walls responding in-plane (Doctoral dissertation, ResearchSpace@ Auckland).

Knox, C.L., Dizhur, D. and Ingham, J.M. (2017). Experimental cyclic testing of URM pier-spandrel substructures. J. Struct. Eng. 143:04016177.

Lagomarsino, S., Penna, A., Galasco, A. and Cattari, S. (2013). TREMURI program: an equivalent frame model for the nonlinear seismic analysis of masonry buildings. Eng. Struct. 56:1787–1799.

Liuaw, T. C. & Kwan, K. H. (1984). Nonlinear behaviour of non-integral infilled frames, Computers and Structures 18, 551–560.

Lumantarna, R. (2012). Material Characterisation of New Zealand Unreinforced Masonry Buildings, University of Auckland, PhD Thesis, Auckland.

Mainstone, R. J. (1971). On the stiffnesses and strengths of infilled frames, ICE Proceedings 4, 57-90.

Mainstone, R. J. (1974). Supplementary note on the stiffness and strengths of infilled frames, ICE Procedings.

Mann, W. and Müller, H. (1982). Failure of shear-stressed masonry: an enlarged theory, tests and application to shear walls. In Proc. of the British Ceramic Society, 30, 223–235. Stoke-on-Trent: British Ceramic Society.

Ministry Decree n.65 7/3/2017. (2017). Ministerial Decree n.65 of 27 February 2017, integrated with the changes of n.58 of 7 March 2017. Guidelines for the seismic risk classification of constructions. Rome, Italy: Italian Ministry of Infrastructures and Transport. (In Italian).

Moon FL, Yi T, Leon RT, Kahn LF. (2006). Recommendations for seismic evaluation and retrofit of low-rise URM structures. Journal of Structural Engineering, 132 (5), 663-672.

NTC (Norme Tecniche per le Costruzioni). (2018). Aggiornamento delle Norme Tecniche per le Costruzioni. Decreto ministeriale del 17 gennaio 2018. Rome: Ministero delle Infrastrutture e dei Trasporti. (in Italian).

NZSEE (New Zealand Society for Earthquake Engineering). (2006). Assessment and improvement of the structural performance of buildings in earthquakes. Wellington, New Zealand.

NZSEE (New Zealand Society for Earthquake Engineering). (2017a). The Seismic Assessment of Existing Buildings: Part C5, Concrete Buildings, Technical Guidelines for Engineering Assessments. Wellington: NZSEE.

NZSEE (New Zealand Society for Earthquake Engineering). (2017b). The Seismic Assessment of Existing Buildings: Part C8, Unreinforced Masonry Buildings, Technical Guidelines for Engineering Assessments. Wellington: NZSEE.

Pampanin, S., Priestley, M.J.N. and Sritharan, S. (2001). Analytical modelling of the seismic behaviour of precast concrete frames designed with ductile connections. J. Earthq. Eng. 5, 329–367.

Pampanin, S. (2003). Alternative design philosophies and seismic response of precast concrete buildings. Structural Concrete, 4(4), 203–212.

Pampanin, S., Bolognini, D. and Pavese, A. (2007). Performance-based seismic retrofit strategy for existing reinforced concrete frame systems using fiber-reinforced polymer composites, Journal of Composites for Construction 11(2), 211–226. doi:10.1061/(ASCE)1090-0268(2007)11:2(211).

Park, R. (1995). A static force-based procedure for the seismic assessment of existing reinforced concrete moment resisting frames, Bulletin of the New Zealand Society for Earthquake Engineering 30(3), 213–226.

Paulay, T. and Priestley, M. J. N. (1992). Seismic Design of Reinforced Concrete and Masonry Buildings.

Polyakov, S. V. (1960). On the interaction between masonry filler walls and enclosing frame when loading in the plane of the wall, Translation in earthquake engineering, Earthquake Engineering Research Institute (EERI), San Francisco pp. 36–42.

Priestley, M. & Calvi, G. (1991). Towards a capacity-design assessment procedure for reinforced concrete frames, Earthquake Spectra 7(3), 413–437.

Priestley, M. (1997). Displacement-based seismic assessment of reinforced concrete buildings, Journal of Earthquake Engineering 1(1), 157–192.

Priestley, M. J. N., Calvi, G. M. & Kowalsky, M. J. (2007). Displacement-based seismic design of structures, IUSS Press, Pavia, Italy.

Smith, B. S. (1966). Behavior of square infilled frames, Journal of Structural Division 92(1), 381–403.

Sullivan, T.J., Priestley, M.J.N. and Calvi, G.M. (2012). A Model Code for the Displacement-Based Seismic Design of Structures: DBD12. Pavia, IT: IUSS Press.

Tasligedik, A. S., Akguzel, U., Kam, W. Y. and Pampanin, S. (2016). Strength hierarchy at reinforced concrete beam-column joints and global capacity, Journal of Earthquake Engineering, Taylor & Francis 22(3), 1–34.

Turnšek, V. and Čačovič, F. (1971). Some experimental results on the strength of brick masonry walls. In Proc. of the 2nd Int. Brick Masonry Conf., 149–156. Stoke-on-Trent: British Ceramic Research Association.

6. Applications of the SLaMA-URM method: In-Plane performance

6.1 Introduction

In this Chapter, the application of the SLaMA-URM method to some URM cases study from experimental tests, subjected to In-Plane loads, is presented. At first, the well-known Ispra panels (Section 6.2), experimentally tested in the European Laboratory for Structural Assessment (Joint Research Centre) in Ispra (Italy) have been analyzed, as an example of very simple structures. Subsequently, a one-storey substructure, characterized by two piers connected by a spandrel, studied in Knox (2012) and tested at the University of Auckland, has been analyzed (Section 6.3). Finally, the two-storey "Door Wall", which was part of a prototype building tested at the University of Pavia, has been investigated (Section 6.4).

In order to investigate aspects related to the computational burden and hence to the complexity of the analysis, different modelling approaches have been adopted. Indeed, the aforementioned cases study are presented together with the developed numerical simulation based on macro-mechanical Finite Element Model (FEM, by using the software DIANA FEA and ABAQUS), and on Equivalent Frame Model (EFM, by using the software 3MURI).

Once the procedure has been validated for the three cases study mentioned above, further parametric analysis has been conducted on a simple prototype building, by varying the number of bays and the number of levels (Section 6.5). In this context, the SLaMA-URM accuracy is addressed, by comparing the results with those obtained through an EFM.

6.2 Ispra panels

The first analyzed cases study are the Ispra panels, that were tested at European Laboratory for Structural Assessment (Joint Research Centre) in Ispra (Italy), as a part of the experimental campaign carried out by Anthoine *et al*. (1995) (Figure 6.1). They consist of a

slender panel (1.00 m long and 2.00 m high) and a squat panel (1.00 m long and 1.35 m high), both with a thickness equal to 0.25 m, made of solid clay bricks. The panels were tested under controlled boundary conditions, with fixed-fixed conditions (or double-bending conditions), preventing the rotation of the top through a steel beam. These conditions reproduced the real ones experienced by the piers in a building during a seismic event. Both the panels are subjected to a constant vertical distributed load (or vertical stress equal to 0.6 MPa), whose resultant is 150 kN. The horizontal displacements were imposed on the top beam, with cyclic load history. A flexural-rocking behavior was observed in the slender panel, instead, a shear behavior characterized by diagonal cracking was observed in the squat one (Figure 6.2a-b). The same results in terms of failure modes have been observed from the numerical analyses carried out in Anthoine *et al*. (1995), adopting a monotonic loading history. Regarding the numerical curves, it was observed that they overestimate the envelopes of the experimental ones (Figure 6.2c-d). This is due to the fact that the considered monotonic loading is less damaging than the cyclic one, and also to the fact that the masonry was modelled (in a simplified way) as a two-dimensional continuum, subjected to isotropic damage, thus not respecting its actual orthotropic nature.

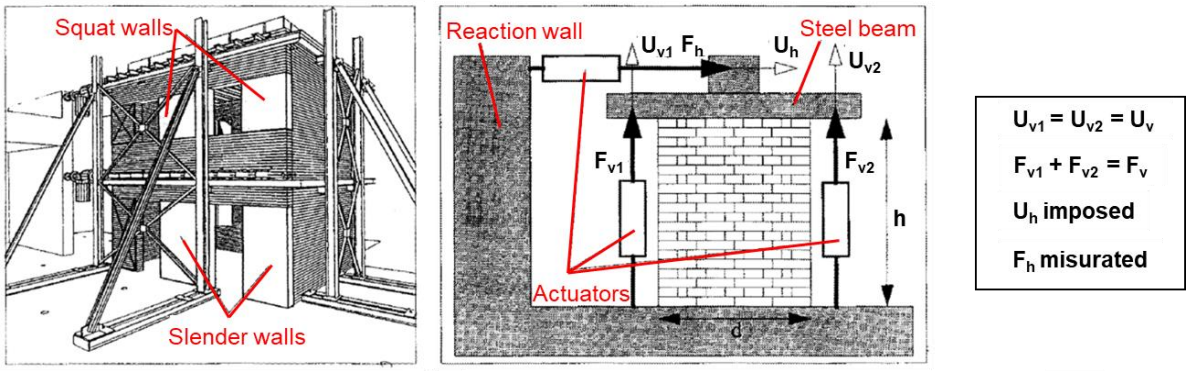

Figure 6.1. Experimental test of Ispra panels: (a) testing set-up; (b) boundary and loading conditions (adapted from Anthoine et al., 1995).

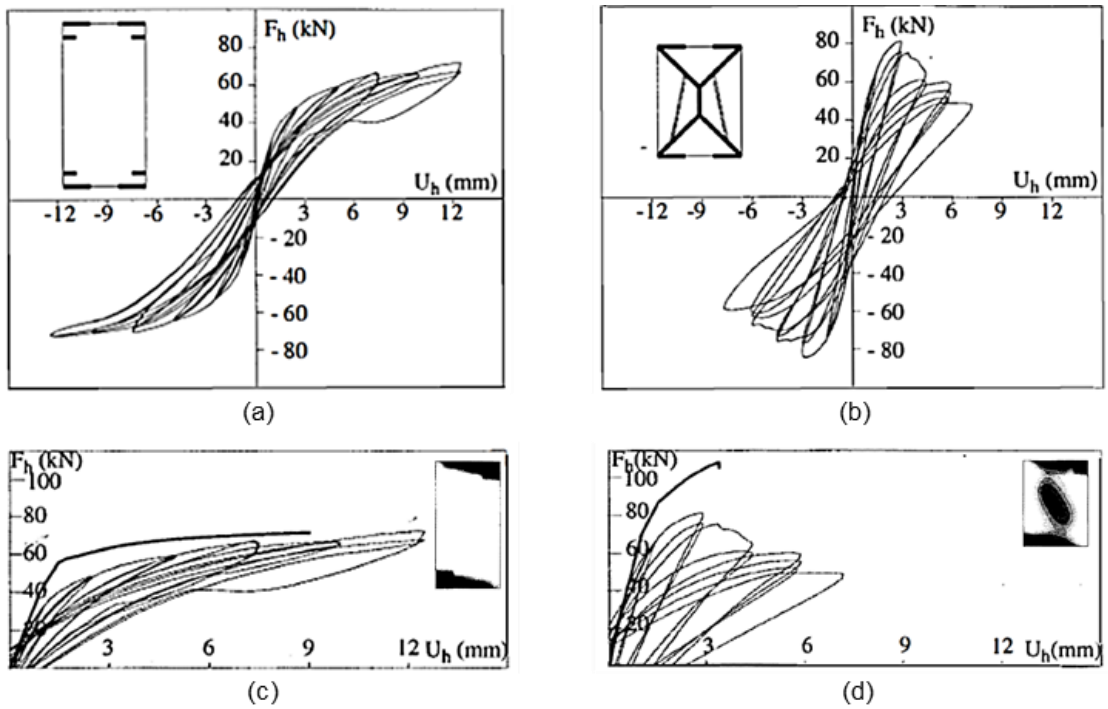

Figure 6.2. Ispra panels: cyclic response and crack pattern from experimental campaign of (a) slender and (b) squat panels; monotonic response and crack pattern from numerical modelling of (c) slender and (d) squat panels (adapted from Anthoine et al., 1995).

The mechanical parameters have been deduced by Magenes and Calvi (1997) from experimental tests on components and small assemblages: Young modulus $E_m = 1700\ \mathrm{N/mm^2}$, Poisson coefficient $\nu = 0.15$, masonry compressive strength $f_{cm} = 6.20\ \mathrm{N/mm^2}$ and initial shear strength at zero compressive stress $f_{v0} = 0.17\ \mathrm{N/mm^2}$. A summary of these values is reported in Table 6.1.

Table 6.1. Mechanical properties of Ispra panels.

E_m (N/mm²)	Young modulus	1700
ν	Poisson ratio	0.15
f_{cm} (N/mm²)	Compressive strength	6.20
f_{v0} (N/mm²)	Initial shear strength (zero compr. stress)	0.17

6.2.1 Numerical modelling: macro-mechanical Finite Element Model (FEM)

FE analyses of Ispra panels have been performed by DIANA (DIANA 2019) and ABAQUS (ABAQUS, 2012) software by adopting a macro-mechanical approach. In DIANA software, the masonry mechanical behaviour has been analyzed using two different isotropic constitutive models: the Total Strain Rotating Crack (TSRC) and the Crack and Plasticity (C&P, with a Drucker-Prager yielding surface). In ABAQUS software, it has been studied using the Concrete Damaged Plasticity (CDP) model.

It is worth noting that the used constitutive laws can be classified into two main categories. The TSRC and C&P models are formulated following the smeared crack approach, in which a crack is considered as a continuum material. The smeared crack concept can be classified into: fixed (C&P) and rotating (TSRC). With the fixed concept the crack orientation is fixed during the computational process. On the contrary, a rotating approach allows the crack orientation to rotate with the principal strain axis. According to the goal of this Thesis, the attention is focused on the modelling and the analysis. For a more detailed description of these constitutive laws refer to Selby (1995), Feenstra (1993), Litton (1974), De Borst and Nauta (1985) and Rots (1988). Moreover, the CDP model is formulated according to the continuum damage theory, which considers the material as a continuum medium. For more details refer to Hillerborg *et al.* (1976), Lee and Fenves (1998) and Lubliner *et al.* (1989).

For all the adopted models, 2D 4-node quadrilateral finite elements in-plane stress have been used for the discretization of the panels and a structured mesh with a size of 100 mm. Static nonlinear analyses have been performed using the iterative Newton-Raphson method. Moreover, for the TSRC and the CDP models, an exponential softening diagram has been assumed in tension and a parabolic one in compression (see Figures 6.3 and 6.5). While for the C&P model an elastic-plastic diagram has been assumed in tension and a linear one in compression (see Figure 6.4).

The optimal dimension of the mesh has been selected by means of sensitivity analysis conducted with the aim of reducing excessive calculation times (which would occur with a too dense mesh) while not reducing the degree of approximation (as in the case of a mesh too loose).

The TSRC model is a damage model, while the C&P and CDP models are characterized by damage and plasticity. The herein reported applications have the aim to show the different results obtained by these three FE models. A brief description of each model is given in the following.

Total Strain Rotating Crack (TSRC) model

The Total Strain Rotating Crack model is a damage constitutive model that follows the smeared crack approach with the fracture energy regularization. The cracking is considered as a distributed effect with directionality and the cracked material can be represented as a continuous medium with anisotropic characteristics. It is based on the modified compression field theory of Vecchio and Collins (1986), further developed by Feenstra *et al*. (1998). It was proposed at first for the concrete material, but successively it was also used to study the behavior of masonry structures. In this context, it can be adopted to model mortar joints, bricks or alternatively the masonry in its complex. In this Thesis, the macro-mechanical modelling approach was assumed, hence the masonry was described as a homogeneous material (see Section 2.4.2).

TSRC assumes a linear elastic isotropic behaviour of the material before the cracking is activated. It happens when the maximum principal stress, evaluated at a Gauss point of the FE, exceeds the tensile strength. The crack directions are updated to rotate with the principal directions during the loading process and the constitutive relations are evaluated in the principal directions of the strain vector. The cracking phenomenon is quantified by the area under the stress-strain diagram, denoted as fracture energy: G_f^I for tension and G_c for compression.

Different compressive and tension softening functions can be found in DIANA 2019. In this Thesis, the compressive behaviour of masonry was defined by a parabolic curve. This accounts for compressive strength f_c, for compressive fracture energy G_c and for crack bandwidth h (Figure 6.3a). The area under the softening part of the stress-strain curve is equal to G_c/h. The compressive fracture energy is a material constant and represents the energy required to create one unit of crack surface. It is difficult to measure because it strongly depends on the testing procedure, but empirical equations proposed by CEB-FIP Model Code (1990) can be considered. The tensile behaviour of masonry was assumed to diminish exponentially (i.e. the exponential softening occurs when the tensile stress exceeds the tensile strength of the material). The tension curve is based on the tensile strength f_t, on

the tensile fracture energy G_f^I and the crack bandwidth h (Figure 6.3b). The area under the softening part of the tensile stress-strain curve is equal to G_f^I/h. If this parameter cannot be directly tested, it can be estimated (in N/mm) through Equation 6.1 (Lourenço, 2010):

$$G_f^I = 0.025(2f_t)^{0.7} \tag{6.1}$$

where f_t is the tensile strength (in N/mm^2).

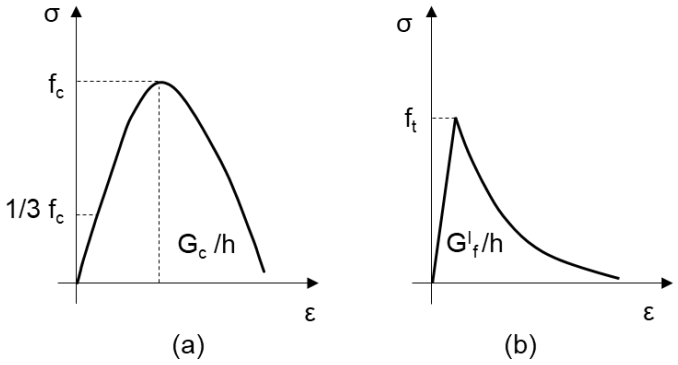

Figure 6.3. Total Strain Rotating Crack (TSRC) model: (a) compressive behaviour and (b) tensile behaviour (adapted from DIANA, 2019).

In conclusion, the TSRC model requires the following inputs: i) elastic properties, such as the Young's modulus and the Poisson's ratio, and ii) parameters related to the tensile, compressive and shear behavior.

This model does not distinguish tensile cracks and shear cracks, thus it fails to simulate the different failure modes of masonry.

Crack and Plasticity (C&P) model

The Crack and Plasticity (C&P) model, although it is based on the smeared crack approach of the TSRC, it differs strongly for its intrinsic nature: it is characterized by damage and plasticity. It is given by the combination of different approaches in compression and tension. By the smeared crack approach the tensile post-cracking behaviour is simulated, while by a plasticity model, such as the Drucker-Prager model (that considers strain hardening and tension cut-off criteria), the compression response is simulated. C&P is a multi-fixed smeared crack model defined by an elastic-plastic constitutive law in

compression. The multi-fixed crack model adopted for representing the tension behaviour is based on the crack concept which keeps its unchanged orientation after its activation. The first crack is formed perpendicular to the direction of the maximum principal stress. The development of other cracks, with a different orientation, but in the same element area, is allowed. This can happen if the tensile strength is again violated by the major principal stress and if the angle between the existing crack and the direction of the major principal stress is greater than the so-called threshold angle, usually set equal to 30°.

The cracking phenomenon is quantified by the area under the tensile stress-strain diagram, denoted as fracture energy G_f^I. For the compression response, as aforementioned, the elastic-plastic constitutive law is considered (Figure 6.4a). For the tension behaviour, it is assumed a linear softening law (Figure 6.4b).

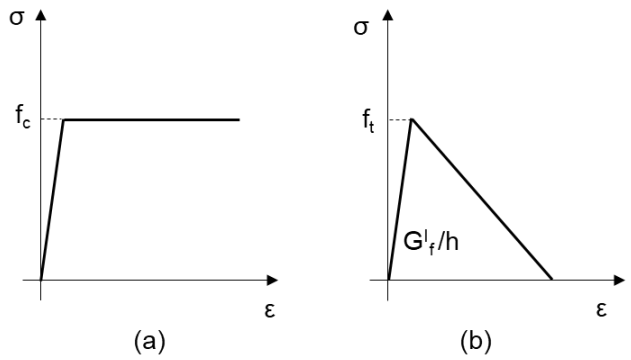

Figure 6.4. Crack and Plasticity (C&P) model: (a) compressive behaviour and (b) tensile behaviour (adapted from DIANA, 2019).

In C&P, the parameters necessary to define the plasticity are: cohesion, friction angle and dilatancy angle. In order to define a cohesion value, Equation 6.2 can be adopted.

$$c = f_c \frac{1 - sin\phi_0}{2cos\phi_0} \tag{6.2}$$

where f_c is the masonry compressive strength and ϕ_0 is the initial angle of internal friction that can be set equal to 30°.

Concrete Damaged Plasticity (CDP) model

The Concrete Damaged Plasticity (CDP) model was originally created to describe the concrete behavior and afterword it was extended to quasi-brittle materials. This constitutive model uses the flow theory of plasticity and damage mechanics to analyse the structures: it allows to capture both the plastic behavior of the material and the reduction of the stiffness caused by the accumulation of damage.

To simulate the tensile and compressive behaviour, a softening trend is provided for the former while for the latter a hardening followed by softening up to failure is assumed. More in detail, under uniaxial tension the stress-strain response follows a linear elastic relationship until the value of the failure stress is reached. This value corresponds to the onset of micro-cracking in the material. This condition leads to a softening stress-strain response, which induces strain localization in the material structure. Under uniaxial compression, the response is linear until the value of initial yield. In the plastic regime, the response is typically characterized by stress hardening followed by strain softening beyond the ultimate stress.

The uniaxial tensile and compressive responses of the material are characterized by damaged plasticity (see Figure 6.5). Two damage mechanisms are taken into account: tensile cracking and compressive crushing. The material is considered isotropic and two damage parameters, separately for compression and tension (d_c and d_t in Figure 6.5) can be adopted to reduce the initial, or undamaged, elastic stiffness of the material (E_0 in Figure 6.5). These variables, assumed to be functions of the plastic strains (ε_c^{pl} and ε_t^{pl} in Figure 6.5) can take values from zero, that represents the undamaged material, to one, which represents the total loss of strength.

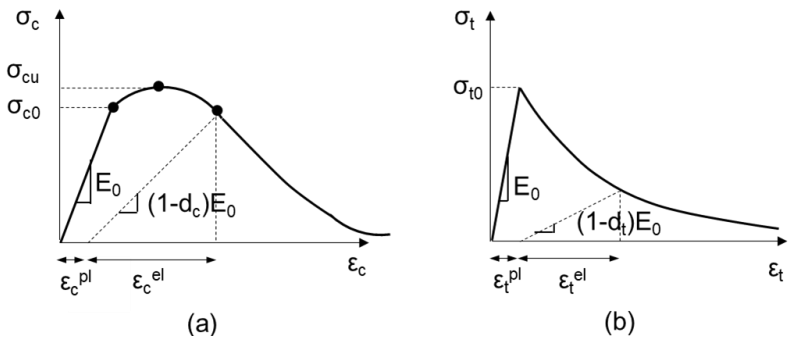

Figure 6.5. Concrete Damaged Plasticity (CDP) model: (a) compressive behaviour and (b) tensile behaviour (adapted from ABAQUS, 2012).

The CDP model, implemented in ABAQUS software, adopts a Drucker-Prager strength criterion with non-associated flow rule to determine the tensile and compressive behaviour of the material. More in detail, the yield surface is a modified Drucker-Prager surface, developed by Lubliner *et al*. (1989) and then by Lee and Fenves (1998). The plasticity parameters that define the modified Drucker-Prager domain are:

- the parameter K, responsible for the shape of the yield surface; it is variable between 0.5 and 1.0: when it assumes this latter value, the deviatoric section of the failure plane becomes a circle;
- the eccentricity parameter ε, that can be used to allow the plastic domain to be smoothed, hence to avoid convergence problems;
- the ratio f_{b0}/f_{c0} of the biaxial compressive yield stress to the uniaxial compressive one;
- the dilation angle ψ, that defines the inclination of the yield surface with respect to the hydrostatic axis in the meridian plane;
- the viscosity parameter, which represents the relaxation time of the visco-plastic system. If it increases, the behavior under static loads changes: as a consequence the damage is widespread over a wider area, altering the results of the analysis.

After these brief descriptions of the models, we move on to describe how the modeling of the panels was done.

Concerning the system boundary conditions, it was defined to: (i) fix the X- and Y-directions at the base of the panels; (ii) adopt a master-slave node strategy to allow the application of a uniform horizontal displacement and, therefore, fix the X-direction on a master node at the top left edge of the panels; (iii) use a tying in the X-direction in the top edge to guarantee the same horizontal displacement on it; (iv) use a tying in Y-direction on the top edge, to consider the double-bending condition. Also a different model has been considered, in which a thin steel plate with elastic behaviour has been modelled on the top edge of the panels (to reproduce the experimental setup conditions), the obtained results in terms of the base shear-displacement curve, perfectly overlapped those derived from the model mentioned above. This last model has been chosen for the lower computational burden requested for the analysis. The numerical model for both panels, with the considered boundary conditions, the applied vertical load, the horizontal displacement and the adopted mesh, are illustrated in Figure 6.6.

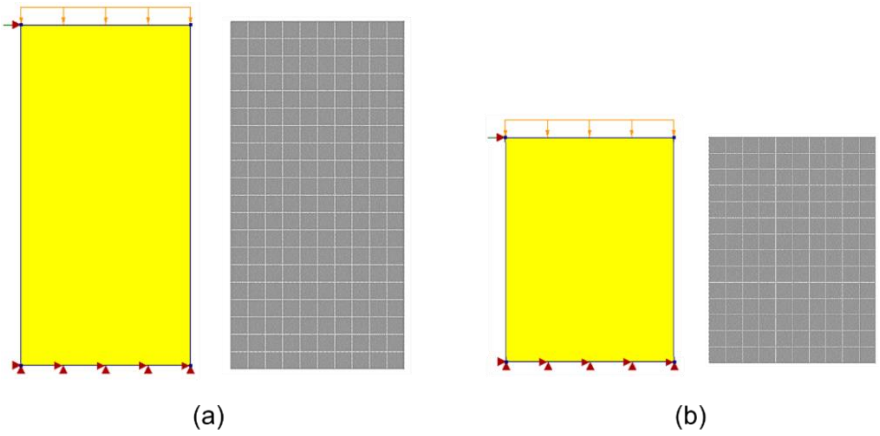

Figure 6.6. Model and mesh of (a) the slender and (b) the squat panels.

The calibration of the FE model has been performed by comparison with experimental results available in the literature, adopting the TSRC model. Then, the obtained mechanical parameters have been used in the FE analysis in C&P and CDP models.

The calibration has been performed on tensile strength and on fracture energies in tension and compression, while elastic parameters and compression strength have been assumed from Magenes and Calvi (1997).

The following mechanical parameters were considered in the three FE models: Young's modulus $E_m = 1700\ \mathrm{N/mm^2}$ and Poisson's coefficient $\nu = 0.15$; for the tensile behavior, a linear-exponential curve with strength $f_t = 0.25\ \mathrm{N/mm^2}$ and fracture energy $G_t = 0.015\ \mathrm{N/mm}$ (sets according to Lourenço (2010), in absence of available experimental data). Concerning the applied loads, the dead weight and the added distributed vertical load corresponding to axial stress, on each panel, of $\sigma = 0.6\ \mathrm{N/mm^2}$, were applied. The horizontal displacement was applied on the right-side edge of the spandrel aiming to properly simulate the first push cycle of the experimental loading.

For the TSRC model were considered, for the compressive behavior, a linear-parabolic curve with a strength equal to $f_{cm} = 6.20\ \mathrm{N/mm^2}$ and fracture energy of $G_c = 1\ \mathrm{N/mm}$. For the C&P model, a cohesion equal to $1.7898\ \mathrm{N/mm^2}$, a friction angle equal to $0.5236\ \mathrm{rad}$ $(30°)$ and a zero dilatancy angle (as suggested in Lourenço and Rots, 1997) were assumed. Finally, for the CDP model, the following parameters were adopted: a dilation angle equal to $30°$; an eccentricity value equal to 0.1, in order to avoid numerical instabilities; the orthotropy ratio f_{b0}/f_{c0} equal to 1.16; the parameter K equal to $2/3$. To catch the more appropriate

value of the viscosity parameter, convergence analyses were performed and a value of 10^{-5} was adopted. The mechanical parameters are resumed in Table 6.2.

Table 6.2. Mechanical parameters for TSRC, C&P and CDP constitutive models.

E_m (N/mm²)	Young modulus		1700	
v	Poisson ratio		0.15	
f_{cm} (N/mm²)	Compressive strength		6.2	
f_t (N/mm²)	Tensile strength		0.25	
G_c (N/mm)	Compressive fracture energy		1	
G^I_f (N/mm)	Tensile fracture energy		0.015	
		TSRC	***C&P***	***CDP***
ϕ (deg)	Internal friction angle	-	30	-
c (N/mm²)	Cohesion	-	1.7898	-
ψ (deg)	Dilatancy angle	-	0	30
ε	Eccentricity	-	-	0.1
f_{b0}/f_{c0}	Orthotropy ratio	-	-	1.16
K		-	-	0.667
	Viscosity parameter	-	-	10^{-5}

The prediction of the envelope curve of the cyclic base shear-horizontal displacement response has been achieved through nonlinear static (pushover) analysis.

The comparison of the corresponding capacity curves for the slender and squat panels are presented in Figures 6.7 and 6.9, respectively.

Base shear-horizontal displacement curves obtained using TSRC, C&P and CDP models are almost coincident in the initial linear branch, for both panels. For the slender one, the TSRC model gives a base shear-horizontal displacement curve closer to the experimental one, while the C&P model shows a higher peak load than the experimental one and gives a

very low ultimate displacement. On the contrary, the CDP model, despite showing a higher curve, catches the experimental trend quite well. Regarding the squat panel, with the CDP model, the curve reaches the same load peak as the experimental one, after which the softening behaviour is shown. After that peak this panel shows a shear failure, hence the peak displacement can be assumed as the ultimate one. The TSRC and C&P models give a higher peak load than the experimental one, but in the former, the experimental ultimate displacement is caught sufficiently well (assuming the peak displacement as the ultimate one), while with the latter it is underestimated.

The experimental and numerical crack patterns are shown in Figures 6.8 and 6.10, for the slender and the squat panel, respectively. As observed, the failure mechanisms of both panels in all the models match the experimental ones, i.e. rocking failure of the slender panel and diagonal cracking failure of the squat one.

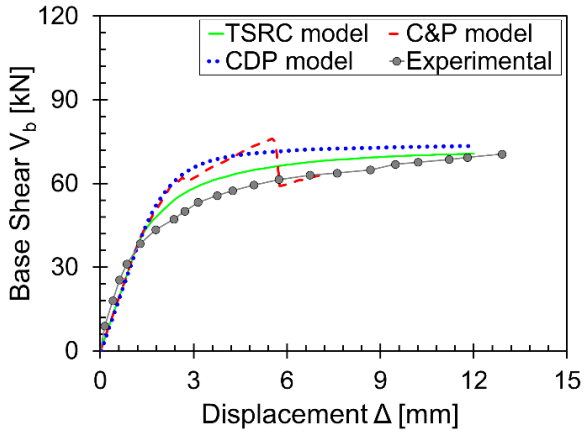

Figure 6.7. Slender panel results: numerical capacity curves against experimental envelope.

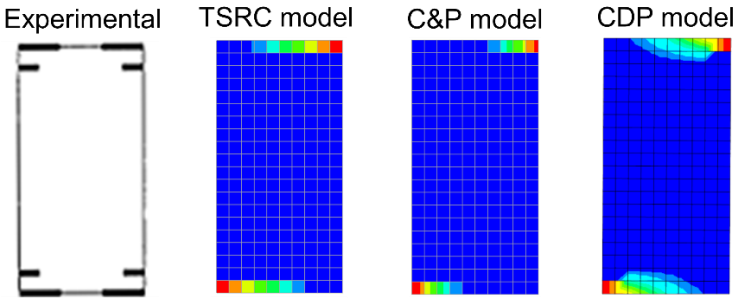

Figure 6.8. Slender panel results: experimental and numerical crack patterns at the ultimate displacement.

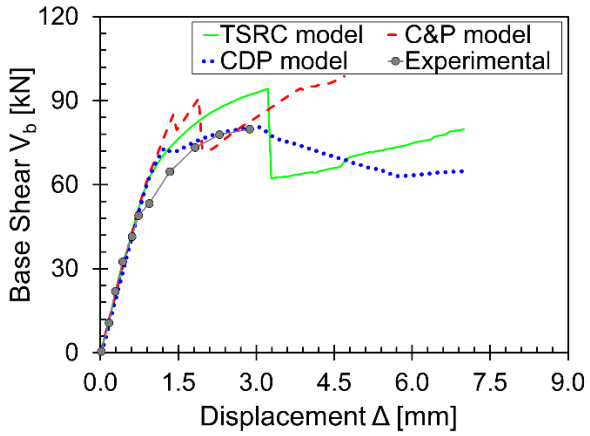

Figure 6.9. Squat panel results: numerical capacity curves against experimental envelope.

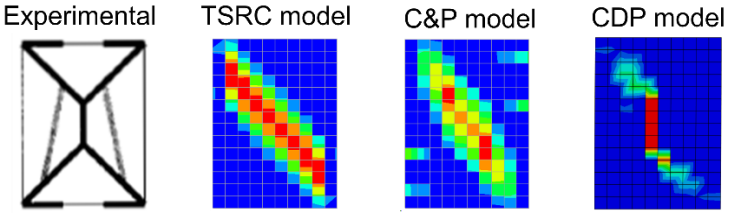

Figure 6.10. Squat panel results: experimental and numerical crack patterns at the ultimate displacement.

The results show clear differences, that are due to the different formulation of the adopted constitutive laws.

6.2.2 Geometric and mechanical data for SLaMA-URM method

The geometry of the Ispra panels was defined according to the Equivalent Frame Model discretization (Figure 6.11) towards the application of the SLaMA-URM method. More in detail, both the panels have a thickness equal to $t_p = 0.25\,\mathrm{m}$ and a length of $B_p = 1\,\mathrm{m}$, the slender panels has height $H_p = 2\,\mathrm{m}$ while the squat one has $H_p = 1.35\,\mathrm{m}$. A concentrated vertical load equal to $N = 150\,\mathrm{kN}$, i.e. axial load ratio $v_r = N/(f_{cm}A_{panel}) = 0.097$ (where A_{panel} is the panel cross-section area), has been applied on each panel. To reproduce the experimental double-bending condition, the rotation restraint at the top node has been considered. Therefore the schematic distribution of the flexural and shear hinges in both panels is shown in Figure 6.11. More in detail, two flexural hinges have been placed at the

base and at the top of the panels, because the maximum moments under lateral load are expected to be at the elements-end. On the contrary, a shear hinge has been placed at the centre of the panels, because the shear can be assumed as constant in the elements.

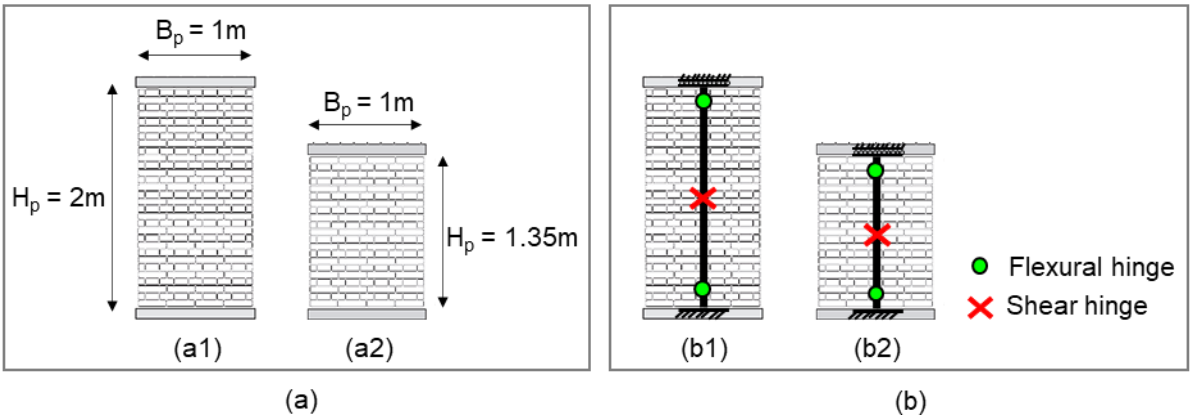

Figure 6.11. Ispra panels: (a) geometry of the slender (a1) and the squat (a2) panels and (b) distribution of the flexural and shear plastic hinges for the slender (b1) and the squat (b2) panels.

The mechanical parameters adopted in the SLaMA-URM method are the same reported in Table 6.1. In addition to those, a friction coefficient equal to $\mu = 0.4$ has been chosen, according to the NTC 2018 suggestions.

6.2.3 Analysis at component level

In Sections 6.2.3.1 and 6.2.3.2, the strength related to the aforementioned flexural and shear hinges has been identified, and subsequently, the failure mode of each panel (characterized by the minimum strength) has been defined. More in detail, the moment-rotation (M-N) curves and the moment axial-load (M-N) domains have been defined, comparing the results obtaining from the adoption of different constitutive laws for masonry. Furthermore, the influence of the axial load applied on the panels has been considered on the M-N diagram as well as on the M-θ one, thus making explicit the dependence of the rotation on the imposed axial load.

6.2.3.1 Moment-rotation curves

The moment-rotation capacity of the slender and squat panels is obtained by hand calculations through the sectional analysis through the MBA approach. Two different constitutive laws to describe the compressive behaviour of the masonry were considered, to catch the variability of the obtained results based on the made choice. Assuming a no-tensile resistant (NTR) behaviour, the elastic-perfectly plastic (EPP) and Kaushik's model (Kaushik *et al.*, 2007) were adopted. The corresponding parameters are reported in Table 6.3. This choice was done in order to evaluate not only a simpler stress-strain relationship (as the EPP model), but also a more complex one, characterized by softening behaviour (as the Kaushik's model), see details in Section 5.4.2.2.

For the EPP model, a compressive peak ε_{yc} and ultimate ε_{uc} strains equal to 1% and 2% were adopted, hence considering a ductility in compression equal to $\mu_{\varepsilon c} = \varepsilon_{uc}/\varepsilon_{yc} = 2$. Regarding the Kaushik's model (Kaushik *et al*., 2007), assuming a mortar without lime, the yield strain ε_{yc} and the ultimate strain ε_{uc}, resulted equal to 0.7% and 1.4%, respectively (with $\mu_{\varepsilon c} = \varepsilon_{uc}/\varepsilon_{yc} = 2$).

Table 6.3. Parameters adopted for the stress-strain relationships in EPP-NTR and Kaushik's models.

Model	ε_{yc} [-]	ε_{uc} [-]	f_{cm} [MPa]
EPP-NTR	0.010	0.020	6.20
Kaushik-NTR	0.007	0.014	6.20

The Monolithic Beam Analogy (MBA) formulation (Pampanin *et al*., 2001) is herein used to define the rotation of the panels (see more details in Section 5.4.2.1) and Equation 6.3 is applied:

$$\theta_i = \frac{\left(\frac{\varepsilon_i}{c_i} - \chi_y\right)\left(L_{cant} - \frac{L_p}{2}\right) L_p}{L_{cant}} \tag{6.3}$$

where ε_i is the strain value at the corresponding neutral axis depth c_i; $\chi_y = 2\,\varepsilon_{yc}/B_p$ is the elastic curvature (where B_p is the length of the panels); L_{cant} is the cantilever length, assumed as half of the height of the panels ($H_p/2$); L_p is the assumed depth of the cracking

and it is taken as $0.1L_{cant}$. To the sectional analysis contribution of the rotation of the panels, the elastic contribution of the element is added from the initial stiffness K_{el} according to Equation 6.4, where n is assumed to equal to 12 (considering fixed-fixed boundary conditions):

$$K_{el} = \left(\frac{{H_p}^3}{nE_m I} + 1.2 \frac{H_p}{B_p t_p G_m} \right)^{-1} \tag{6.4}$$

In Figure 6.12 the moment-rotation curves of both Ispra panels, adopting the EPP-NTR and the Kaushik's models, are reported. From the observation of the experimental capacity curves, it has been chosen to adopt the EPP-NTR model because no-softening behaviour is highlighted.

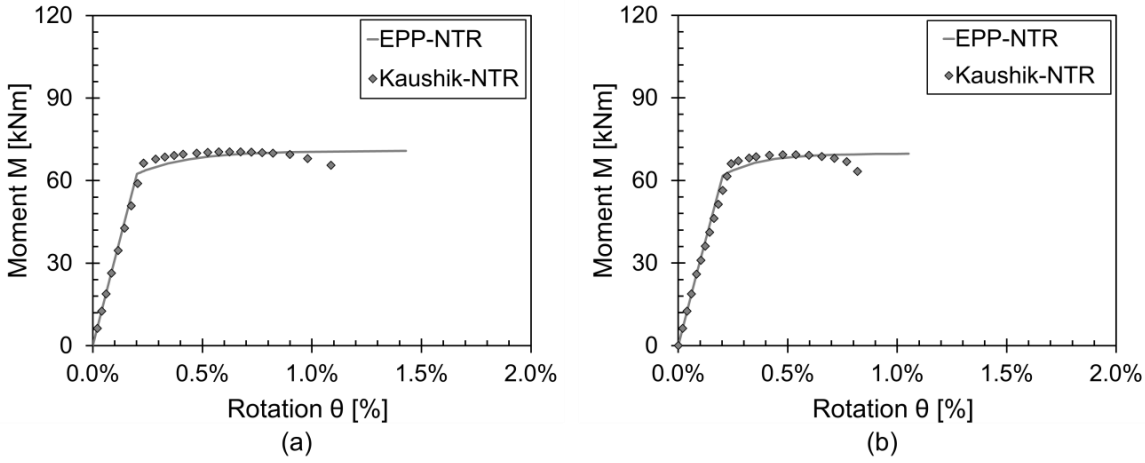

Figure 6.12. Moment-rotation curve of (a) the slender and (b) the squat panel, adopting the elastic-perfectly plastic (EPP) model and the Kaushik's model.

Regarding the shear strength of the panels, the Turnšek and Cačovic (Turnšek and Cačovic, 1971) criterion is adopted for diagonal cracking, and the Mohr-Coulomb (NTC 2018) criterion is assumed for bed-joint sliding (for more detail see Section 5.4.2.2).

The flexural and shear strength thresholds for both panels are shown in Figure 6.13, where the resultant moment-capacity curves are shown in a thick black line. It is observed that the response of the slender panel is governed by a rocking mechanism, while for the squat one a shear failure is expected to occur, as observed from the intersection of the flexural and diagonal cracking strength, marked with a red cross in Figure 6.13b.

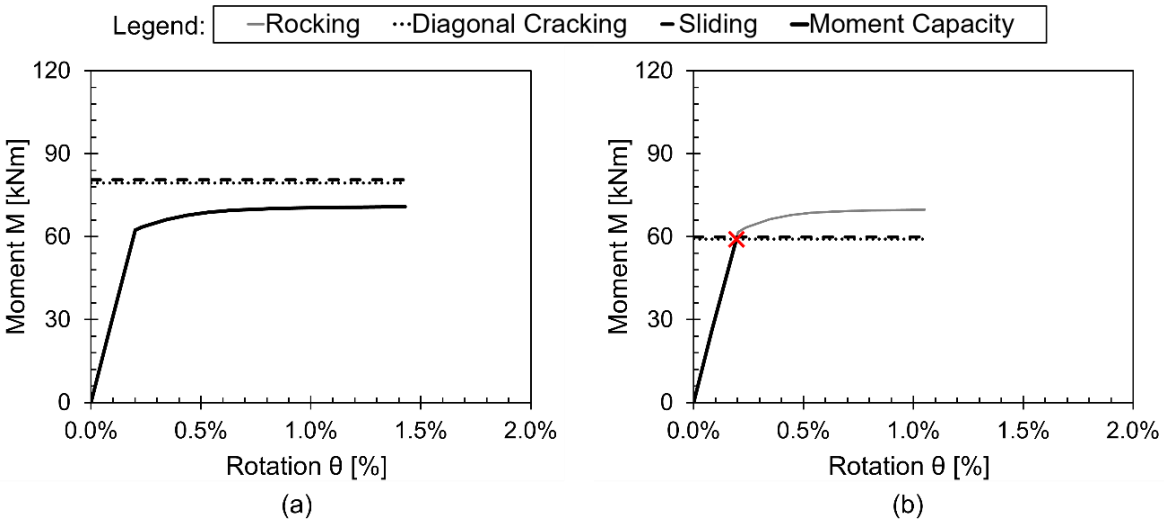

Figure 6.13. Flexural and shear strength thresholds in the moment-rotation diagram for (a) the slender and (b) the squat panel.

6.2.3.2 Moment-axial load (M-N) domains

The M-N domains of the panels were defined by considering the elastic-perfectly plastic (EPP) constitutive law and the Kaushik's one, in compression. The domains obtained for both panels (slender and squat) are the same since they are independent of the height of the elements and depend only on the cross-section dimensions (t_p and B_p).

To emphasize the reliability of the MBA approach (Pampanin *et al*., 2001) (schematized for piers in Figure 6.14), the results obtained by this procedure are compared with those derived from traditional sectional analysis (Figure 6.15a). As observed, the differences among them are negligible.

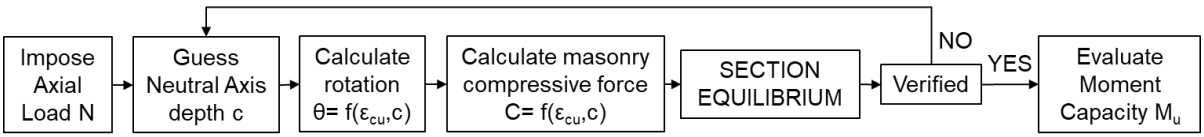

Figure 6.14. Flowchart to calculate the M-N domain of piers through sectional analysis using the MBA approach.

The adoption of different stress-strain models leads to different M-N limit domains. This difference depends especially on the own characteristics of the adopted model. More in

detail, with the Kaushik-NTR stress-strain profile a contracted limit domain is obtained, if compared with the EPP-NTR one (see Figure 6.15a), due to the strength degradation that characterized the model.

Other comparisons are shown in Figure 6.15b: the first consists in describing the moment capacity as a function of the compressive strain ductility $\mu_{\varepsilon c}$, while the second in understanding the over- or under- estimation in the definition of the M-N domains made by Italian code (NTC 2018), or by NZSEE 2017b.

Considering the EPP-NTR, it is shown that when increasing the compressive strain ductility to a value of $\mu_{\varepsilon c} = 2$ (assuming a fixed elastic compressive strain $\varepsilon_{yc} = 1\%$), the M-N domain expands since the neutral axis depth decreases and, consequently, the lever arm of the resultant compression force increases. While, regarding the comparison with the code formulation (from NTC 2018 or NZSEE 2017b), it results that the domain matches perfectly with the EPP-NTR model when $\mu_{\varepsilon c} = 1.2$.

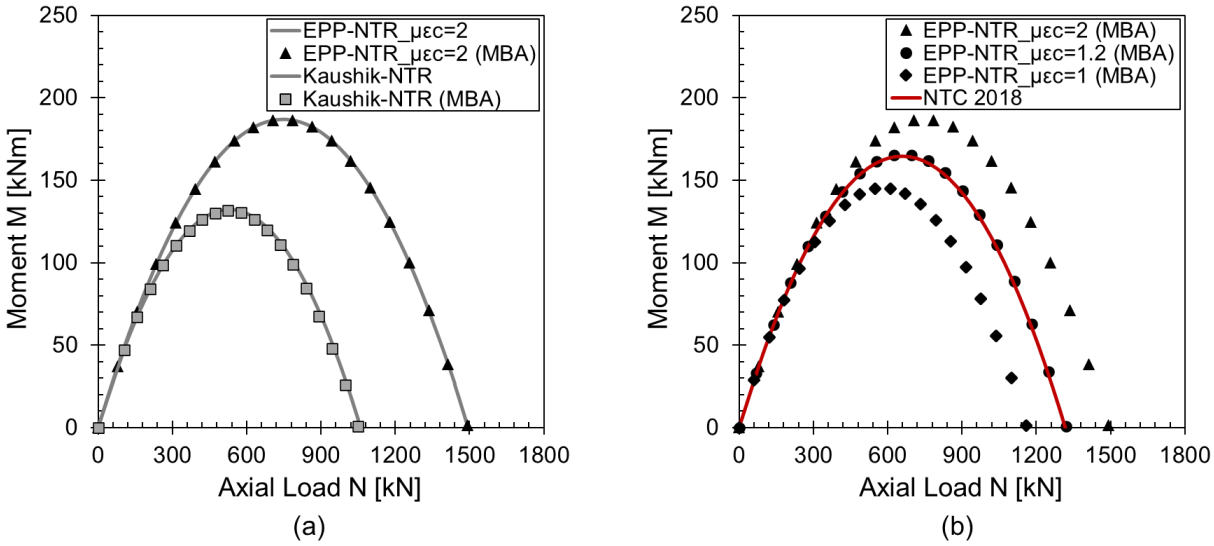

Figure 6.15. Comparison between M-N domains with: (a) EPP and Kaushik's models with traditional sectional analysis and MBA approach; (b) EPP models with different $\mu_{\varepsilon c}$ and the NTC 2018 formulation.

Adopting the EPP-NTR model with a compressive strain ductility of $\mu_{\varepsilon c} = 2$, it is possible to use the M-N domain to represent the strength domain of the elements, by varying the axial load. More in detail, by defining the sliding shear strength with the Mohr-Coulomb

formulation, the diagonal cracking shear strength with the Turnšek and Čačovic (Turnšek and Čačovic, 1971) criterion, and the flexural behaviour, as described above, the strength domain representative of the behaviour of the elements can be defined (Figure 6.16).

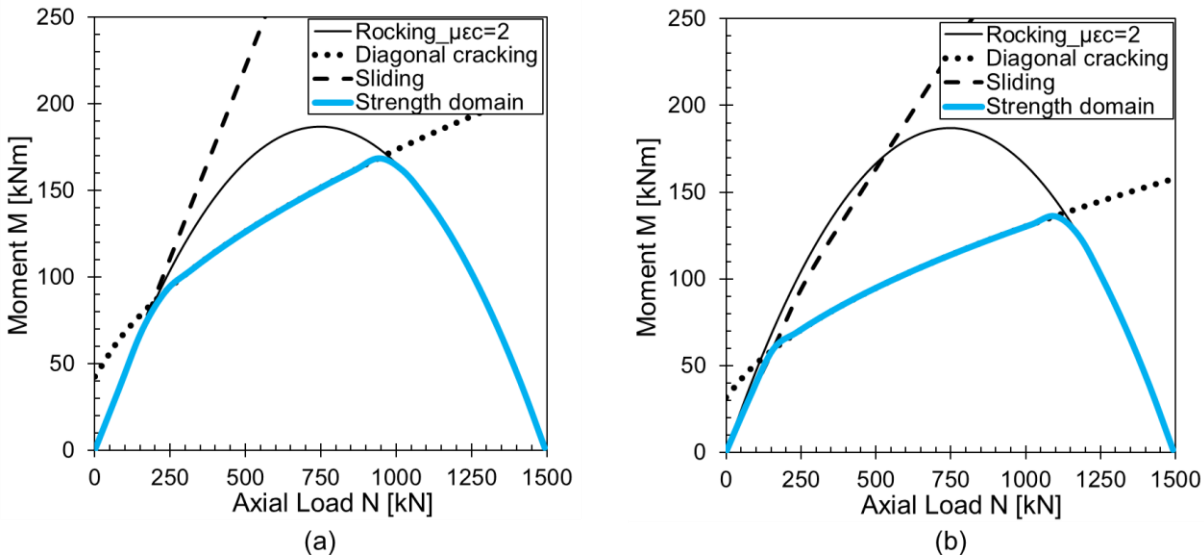

Figure 6.16. Strength criteria and strength domains of (a) the slender and (b) the squat panels.

As observed in Figure 6.16, the slender panel shows a flexural crisis for low and high axial load, while for intermediate values the diagonal cracking failure is expected to occur. For the squat panel, the diagonal cracking behaviour is the crisis for a large part of low and medium level of axial load, while for higher axial load, a rocking behaviour is expected to occur. As highlighted in the moment-rotation diagram (see Section 6.2.3.1), for the gravity axial load of the panels ($N = 150\,\mathrm{kN}$), the rocking failure is observed for the slender panel and the diagonal cracking failure is observed for the squat panel.

It is worth noting that these strength domains are strongly dependent on the boundary conditions of the elements (see Section 6.2.7 for more details).

6.2.4 Analysis at In-Plane global level

From the comparison between the flexural (or rocking) and shear mechanisms in the moment-rotation diagram (Section 6.2.3.1, Figure 6.13) the crisis mechanism of the panels is identified. The SLaMA-URM method ended at the single elements structural level of analysis,

without going through the subassembly analysis. Therefore, the base shear of each panel was determined by dividing the moment capacity by the corresponding cantilever length L_{cant} (already defined as $L_{cant} = H_p/2$). While the displacement was calculated by multiplying the rotation capacity by L_{cant}. With these calculations, the base shear-displacement curves (or capacity curves) were defined and the comparison with the experimental one is shown in Figure 6.17.

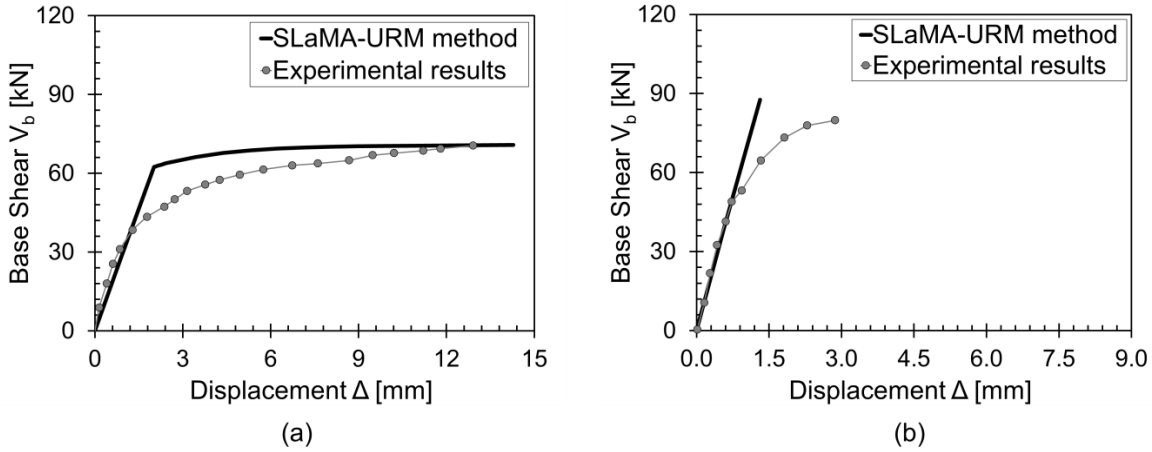

Figure 6.17. Comparison between analytical and experimental capacity curves for (a) the slender and (b) the squat panel.

In Figures 6.18 - 6.21 the comparison in terms of capacity curves and crack patterns between analytical, numerical and experimental results for both panels is shown. It is observed that, for sake of simplicity, in the crack pattern, the only result from the TSRC model is shown, since all other numerical approaches show the same failure crisis (see Figures 6.8 and 6.10).

It can be observed that the proposed analytical procedure allows to obtain a response comparable with the experimental and the numerical one, in terms of pushover curve and expected crisis mechanism: flexural for the slender panel and shear with diagonal cracking for the squat one.

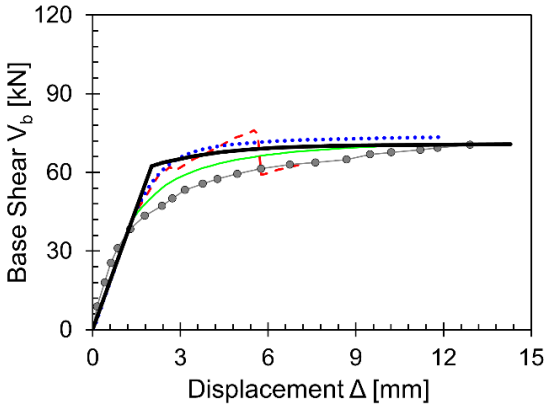

Figure 6.18. Slender panel results: numerical and analytical capacity curves against experimental envelope.

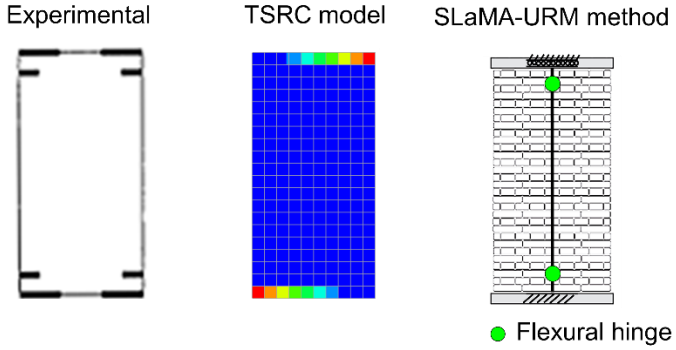

Figure 6.19. Slender panel results: experimental, numerical (TSRC model) and analytical crack patterns at the ultimate displacement.

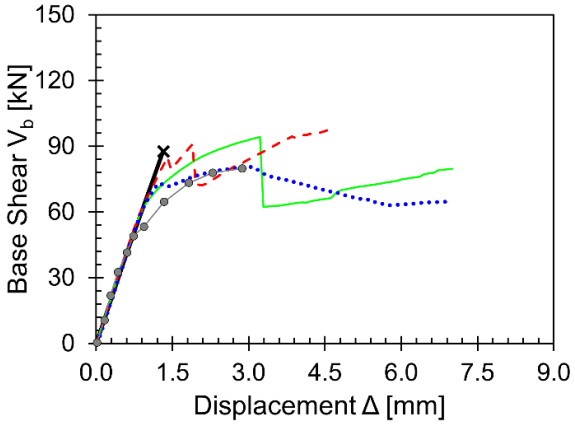

Figure 6.20. Squat panel results: numerical and analytical capacity curves against experimental envelope.

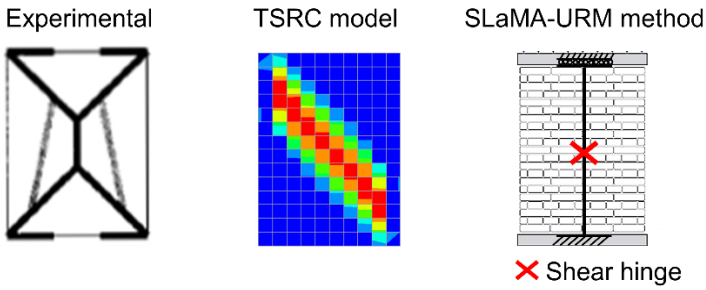

Figure 6.21. Squat panel results: experimental, numerical (TSRC model) and analytical crack patterns at the ultimate displacement.

6.2.5 Effect of the acting axial load

In this Section, the effect of the axial load on the moment-rotation diagram, on the moment-axial load and on the rotation-axial load domains, was investigated. In Figures 6.22 and 6.23 are shown the results for both panels, adopting the EPP-NTR constitutive law, with a compressive strain ductility of $\mu_{\varepsilon c} = 2$.

The results show that by increasing the axial load (from N1 to N4), the moment capacity increases until reaching the top of the M-N limit domain (Figures 6.22a and 6.23a). A further increase of the axial load (up to N5) induces a decrease in the moment capacity (see Figures 6.22a-b and 6.23a-b). This moment behaviour is highlighted also in the moment-rotation curves. The rotation capacity, instead, decreases when the axial load increases (Figures 6.22b-c and 6.23b-c), leading to a reduction of the rotation ductility of the element. The slender panel is characterized by a higher effective height ($h_{eff} = 1\,\mathrm{m}$ against the $h_{eff} = 0.675\,\mathrm{m}$ of the squat one) and the rotation capacity is higher if the same axial load is assumed.

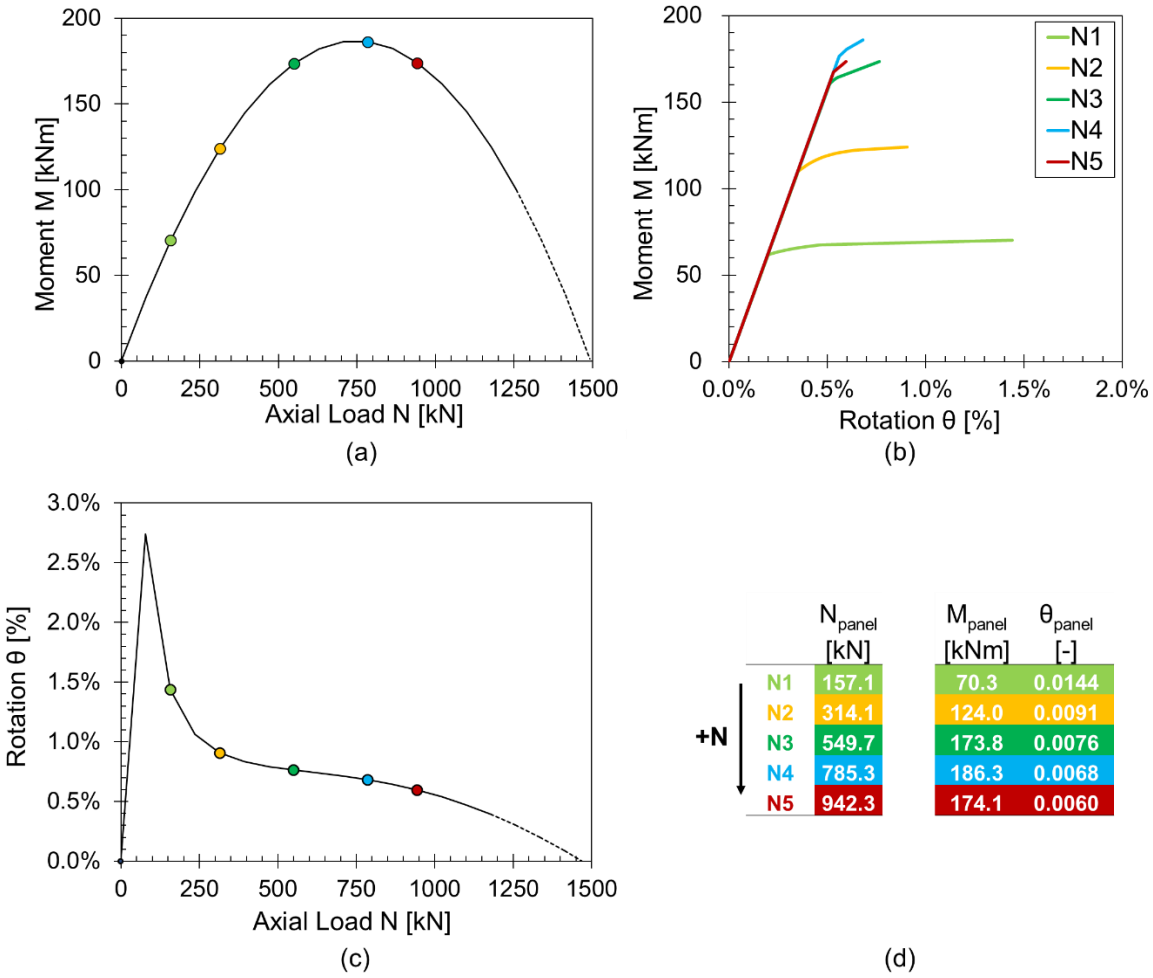

	N_{panel} [kN]	M_{panel} [kNm]	θ_{panel} [-]
N1	157.1	70.3	0.0144
N2	314.1	124.0	0.0091
N3	549.7	173.8	0.0076
N4	785.3	186.3	0.0068
N5	942.3	174.1	0.0060

Figure 6.22. Effect of the axial load for the slender panel: (a) moment-axial load domain; (b) moment-rotation curves; (c) rotation-axial load curves and (d) moment and rotation values at different axial load (from N1 to N5).

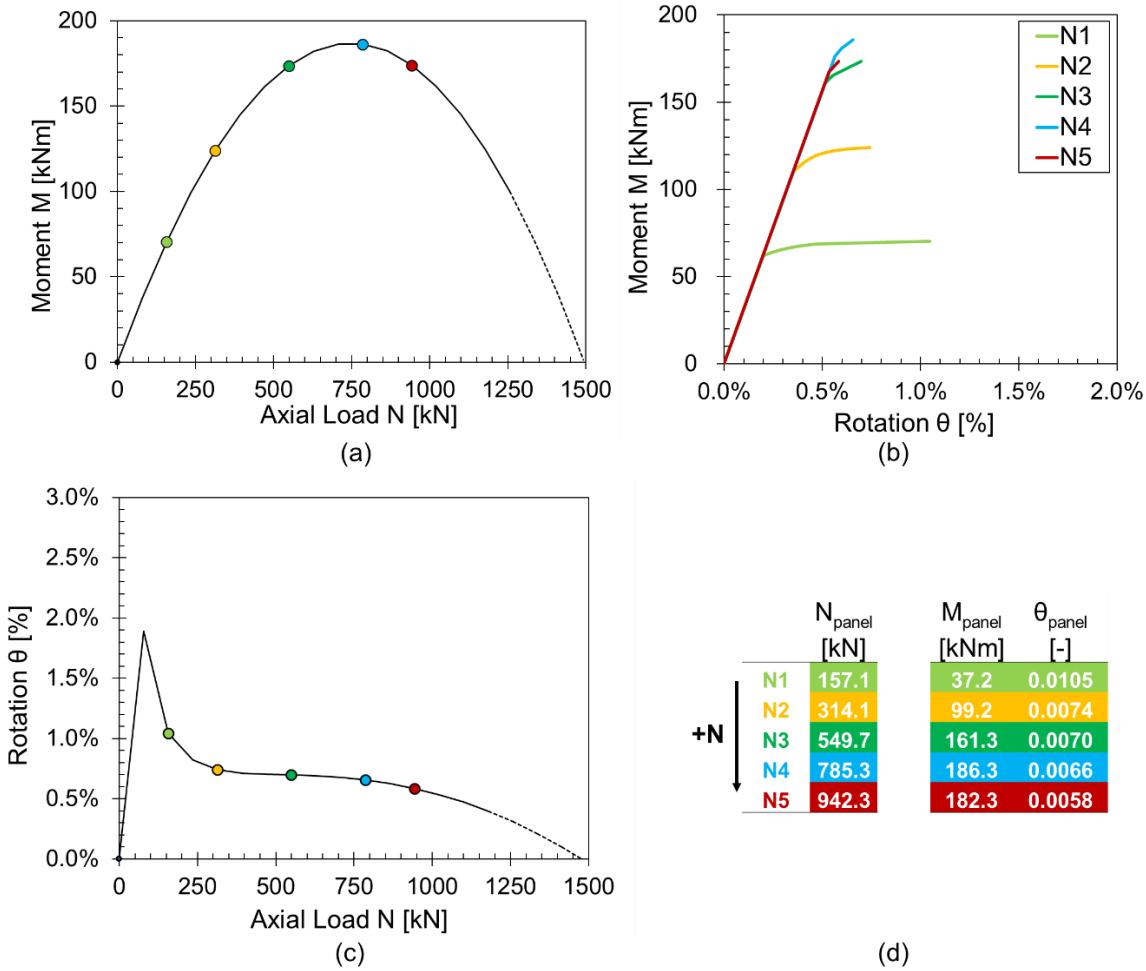

	N_{panel} [kN]	M_{panel} [kNm]	θ_{panel} [-]
N1	157.1	37.2	0.0105
N2	314.1	99.2	0.0074
N3	549.7	161.3	0.0070
N4	785.3	186.3	0.0066
N5	942.3	182.3	0.0058

Figure 6.23. Effect of the axial load for the squat panel: (a) moment-axial load domain; (b) moment-rotation curves; (c) rotation-axial load curves and (d) moment and rotation values at different axial load (from N1 up to N5).

The same analyses were carried out adopting the Kaushik's constitutive law (see Section 6.2.3.1). By comparing these results with the M-N domains obtained with the EPP-NTR model for both panels (Figure 6.24a-c), it can be seen that the Kaushik's model leads to a contraction of the limit strength domain by reducing the maximum axial load. This reduction in moment capacity is mainly due to the presence of strength degradation in the model which reduces the compression force, which in turn reduces the moment capacity (see also Section 6.2.3.2). As a consequence, the axial load-rotation curves are reduced with respect to those obtained with the EPP-NTR model (Figure 6.24b-d).

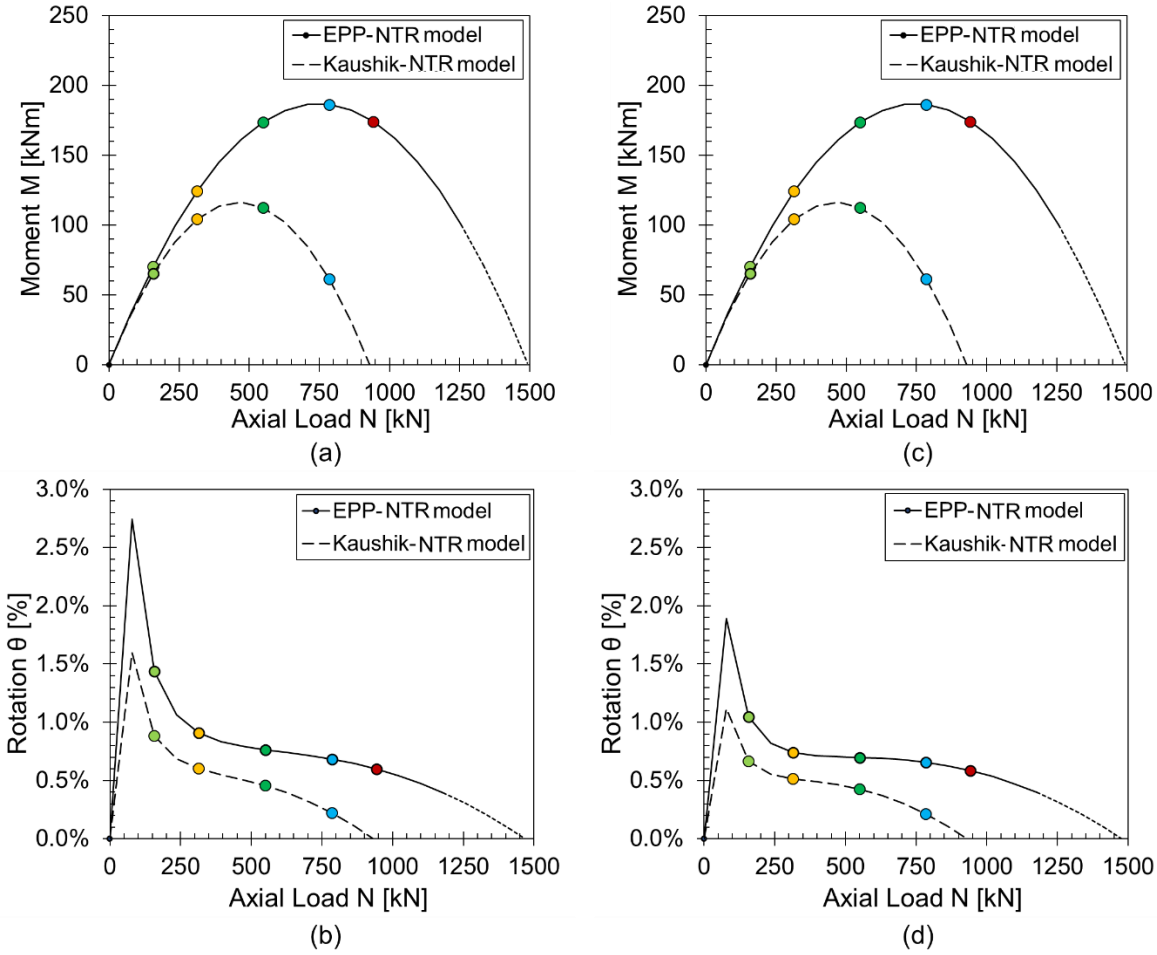

Figure 6.24. Comparisons between EPP-NTR model and Kaushik's-NTR model in moment-axial load (top) domain and rotation-axial load diagram (bottom) for: (a), (b) slender and (c), (d) squat panels.

6.2.6 Influence of the scale effect

Another aspect that was investigated is the influence of the scale effect on the seismic response of the panels. To this aim, assuming the dimensions of the slender and squat panels as a reference, the height (H_p), length (B_p), and thickness (t_p) were increased by a scale factor and hence four specimens for each panel were taken into account. The dead load of each specimen was calculated from its dimensions and added to the imposed axial load of 150 kN, in order to obtain the axial load (N) that was applied.

In Figures 6.25 and 6.26 the schematization of both panels specimens is shown together with the geometrical parameters and the applied axial load.

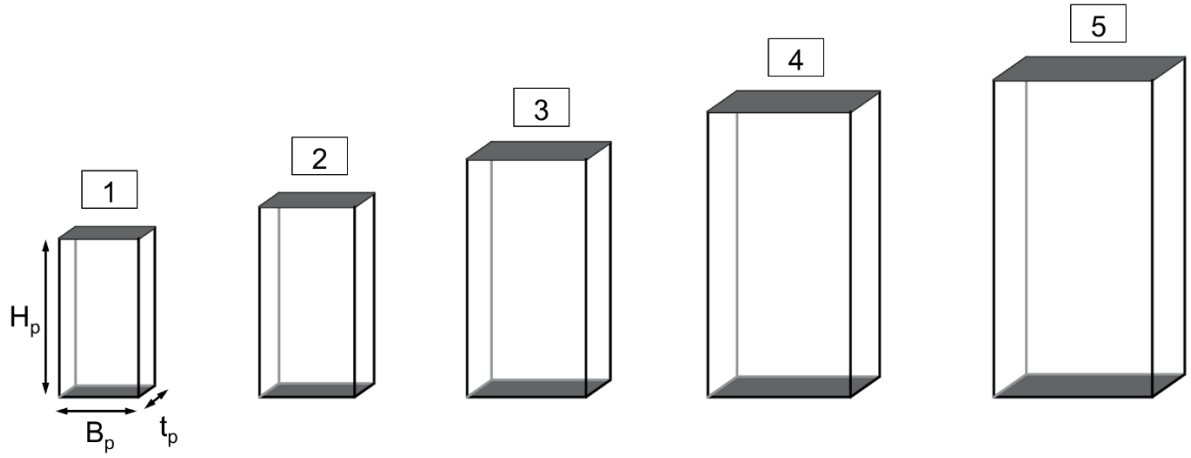

Specimen	*Scale factor*	B_p [m]	h_p [m]	t_p [m]	pp [kN]	N [kN]	σ_0 [kN/m^2]	a.r.=h_p/B_p [-]
1	*1.0*	1.0	2.0	0.250	8.3	158.3	633.0	2
2	*1.2*	1.2	2.4	0.300	14.3	189.9	527.5	2
3	*1.5*	1.5	3.0	0.375	27.9	237.4	422.0	2
4	*1.8*	1.8	3.6	0.450	48.2	284.9	351.7	2
5	*2.0*	2.0	4.0	0.500	66.1	316.5	316.5	2

Figure 6.25. Representations of the specimens derived from slender panel and summary of the geometrical properties and the applied axial load.

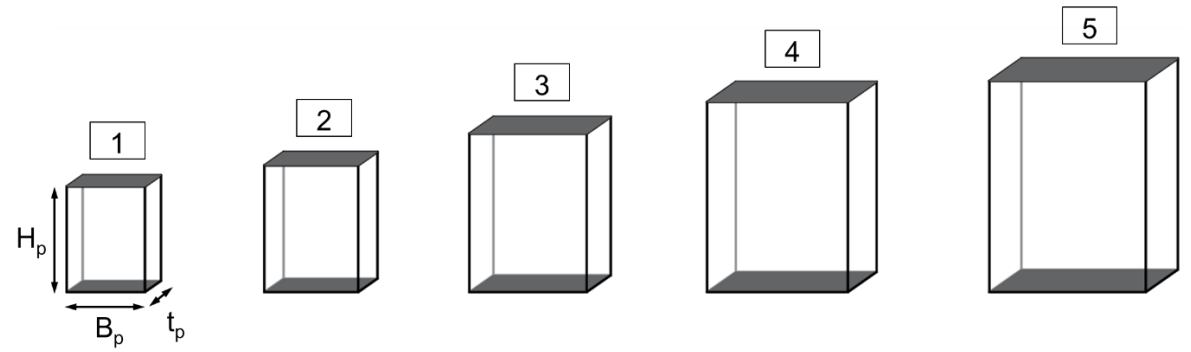

Specimen	*Scale factor*	B_p [m]	h_p [m]	t_p [m]	pp [kN]	N [kN]	σ_0 [kN/m^2]	a.r.=h_p/B_p [-]
1	*1.0*	1.0	1.35	0.250	5.6	155.6	622.3	1.35
2	*1.2*	1.2	1.62	0.300	9.6	186.7	518.6	1.35
3	*1.5*	1.5	2.03	0.375	18.8	233.4	414.9	1.35
4	*1.8*	1.8	2.43	0.450	32.5	280.0	345.7	1.35
5	*2.0*	2.0	2.70	0.500	44.6	311.2	311.2	1.35

Figure 6.26. Representations of the specimens derived from squat panel and summary of the geometrical properties and the applied axial load.

At first, the results for the specimens derived from the slender panel are reported. In Table 6.4 the calculations to define the elastic stiffness (according to Equation 6.4) of each slender panel are reported. By adopting the EPP-NTR model (with $\varepsilon_{yc} = 1\%$ and $\mu_{\varepsilon c} = 2$), the MBA approach was used to define the moment-rotation curves for the five panels.

Table 6.4. Calculations of the elastic stiffness of the five slender panels.

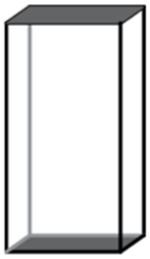

Specimen	I [m^4]	A [m^2]	h_{eff} [m]	K_{el} [kN/m]
1	0.02083	0.250	1.0	31435
2	0.04320	0.360	1.2	37722
3	0.10547	0.563	1.5	47152
4	0.21870	0.810	1.8	56583
5	0.33333	1.000	2.0	62870

As observed in Figure 6.27a, the increase in dimensions leads to an increase of the moment capacity, the initial stiffness and of the rotation capacity. From the moment-rotation curves, the base shear-horizontal displacement was defined by multiplying the rotation values for the effective height ($\Delta = \theta \cdot h_{eff}$) and dividing the moment values with this same value ($V_b = M/h_{eff}$). The so defined capacity curves are represented in Figure 6.27b. These curves follow the same trend as the moment-rotation curves, described above. A comparison between the so calculated capacity curves and those deriving by the NTC 2018 recommendations was performed and it is shown in Figure 6.27b. It should be noted that the flexural failure mechanism is identified as the mechanism expected to occur for all five slender panels.

In Table 6.5 the calculations for the definition of the base shear-horizontal displacement curves of the five slender panels, following the NTC 2018 indications, are reported. More in detail, the flexural and the shear (diagonal cracking and sliding) strength were calculated and the minimum value between these highlights the base shear of the considered panel and hence the corresponding failure mechanism. Regarding the limit elastic displacement, it was calculated by dividing the base shear with the elastic stiffness ($\Delta_{el} = V_b/K_{el}$). The ultimate displacement is calculated by the ultimate drift, that NTC 2018, at ULS, assumes equal to $3/4\,\theta_{u,CLS}$ (where $\theta_{u,CLS}$ is the ultimate drift at CLS and it is assumed as $\theta_{u,CLS} = 0.01$ for the flexural failure mechanism) and the effective height as $\Delta_u = \theta_u \cdot h_{eff}$.

Table 6.5. Calculations of the base shear-displacement capacity curves of the five slender panels, according to the NTC 2018 recommendations.

	FLEXURE		SHEAR						
Specimen	M_u [kNm]	$V_{b,\ flexure}$ [kN]	$V_{b,\ diag.\ crack.}$ [kN]	$V_{b,\ sliding}$ [kN]	$V_{b,\ MIN}$ [kN]	Failure mechanism	Δ_{el} [m]	θ_u [-]	Δ_u [m]
1	69.62	69.62	79.31	80.54	69.62	*FLEXURE*	0.0022	0.0075	0.0075
2	102.54	85.45	107.21	105.84	85.45	*FLEXURE*	0.0023	0.0075	0.0090
3	163.78	109.19	155.81	149.55	109.19	*FLEXURE*	0.0023	0.0075	0.0113
4	239.27	132.93	212.40	200.16	132.93	*FLEXURE*	0.0023	0.0075	0.0135
5	297.51	148.75	254.50	237.74	148.75	*FLEXURE*	0.0024	0.0075	0.0150

The comparison in terms of capacity curves shows that the elastic stiffness and the maximum base shear strength are in good agreement, while the ultimate displacements are different. NTC 2018 imposes the value of the ultimate displacement as a function of the effective height of the considered element only. The MBA approach leads to assume an ultimate rotation from the sectional analysis, calculating the ultimate neutral axis depth from the imposition of the ultimate strain of the masonry. Then the ultimate displacement was identified by the effective height.

In Table 6.6 it is shown the comparison (MBA vs NTC 2018) with respect to the reached ultimate displacements and their relative variation.

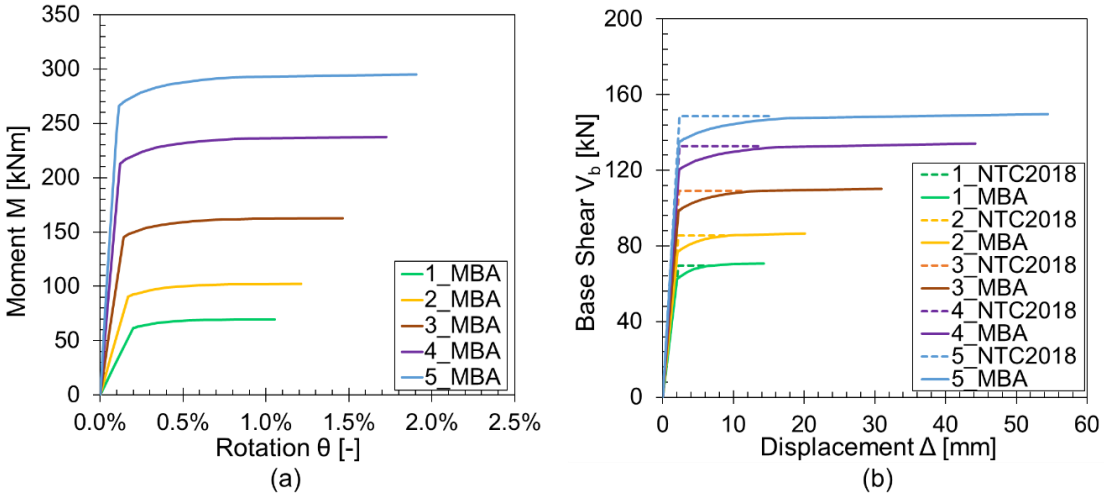

Figure 6.27. Five slender panels results: (a) moment-rotation curves and (b) base shear-displacement curves with the MBA approach and with the NTC 2018 recommendations.

Table 6.6. Ultimate displacements obtained for the five slender panels with the MBA approach and the NTC 2018 recommendations.

	Δ_u [m]		
Specimen	NTC 2018	MBA	Relative variation
1	0.0075	0.0143	1.9
2	0.0090	0.0201	2.2
3	0.0113	0.0309	2.7
4	0.0135	0.0442	3.3
5	0.0150	0.0544	3.6

Regarding the specimens derived from the squat panel, the calculations of the elastic stiffness are reported in Table 6.7. By adopting the EPP-NTR model (with $\varepsilon_{yc} = 1\%$ and $\mu_{\varepsilon c} = 2$), the MBA approach was used to define the moment-rotation curves of the five panels. As observed in Figure 6.28a, the moment and the rotation capacity increase when the dimensions of the panel increase. Moreover, although the aspect ratio is the same (1.35), for panels with scale factor equal to 1 and 1.2 (specimens number 1 and 2) the failure mechanism is the shear one, while in the other cases the flexural crisis is expected to occur. This is due to the increase in the shear strength induced by an increase of thickness and length of the panels.

The calculations according to the NTC 2018 recommendations for the definition of the base shear-displacement curves are reported in Table 6.8. In Figure 6.28b it is shown the comparison between the capacity curves obtained with the MBA approach and with NTC 2018. Also with the NTC 2018 recommendation, specimens 1 and 2 are characterized by the shear failure mechanism.

The ultimate displacements strongly differ assuming the NTC 2018 procedure or the MBA approach. For the first approach, the ultimate displacement is calculated by the ultimate drift that at ULS is assumed equal to $3/4\,\theta_{u,CLS}$ (where $\theta_{u,CLS}$ is the ultimate drift at CLS and it is assumed as $\theta_{u,CLS} = 0.01$ for the flexural failure mechanism and as $\theta_{u,CLS} = 0.005$ for the shear failure mechanism) and the effective height, as $\Delta_u = \theta_u \cdot h_{eff}$. The comparison (MBA vs NTC 2018) in terms of ultimate displacements and their relative variation for the five squat panels is reported in Table 6.9.

Table 6.7. Calculations of the elastic stiffness of the five squat panels.

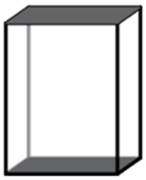

Specimen	I [m^4]	A [m^2]	h_{eff} [m]	K_{el} [kN/m]
1	0.02083	0.250	0.7	68699
2	0.04320	0.360	0.8	82439
3	0.10547	0.563	1.0	103049
4	0.21870	0.810	1.2	123659
5	0.33333	1.000	1.4	137399

Table 6.8. Calculations of the base shear-displacement capacity curves of the five squat panels, according to the NTC 2018 recommendations.

	FLEXURE		SHEAR						
Specimen	M_u [kNm]	$V_{b,\ flexure}$ [kN]	$V_{b,\ diag.\ crack.}$ [kN]	$V_{b,\ sliding}$ [kN]	$V_{b,\ MIN}$ [kN]	Failure mechanism	Δ_{el} [m]	θ_u [-]	Δ_u [m]
1	68.60	101.63	87.59	88.69	87.59	*SHEAR*	0.0013	0.0038	0.0025
2	100.99	124.68	118.44	116.65	116.65	*SHEAR*	0.0014	0.0038	0.0030
3	161.24	159.25	172.21	164.98	159.25	*FLEXURE*	0.0015	0.0075	0.0076
4	235.50	193.83	234.83	220.97	193.83	*FLEXURE*	0.0016	0.0075	0.0091
5	292.78	216.87	281.45	262.56	216.87	*FLEXURE*	0.0016	0.0075	0.0101

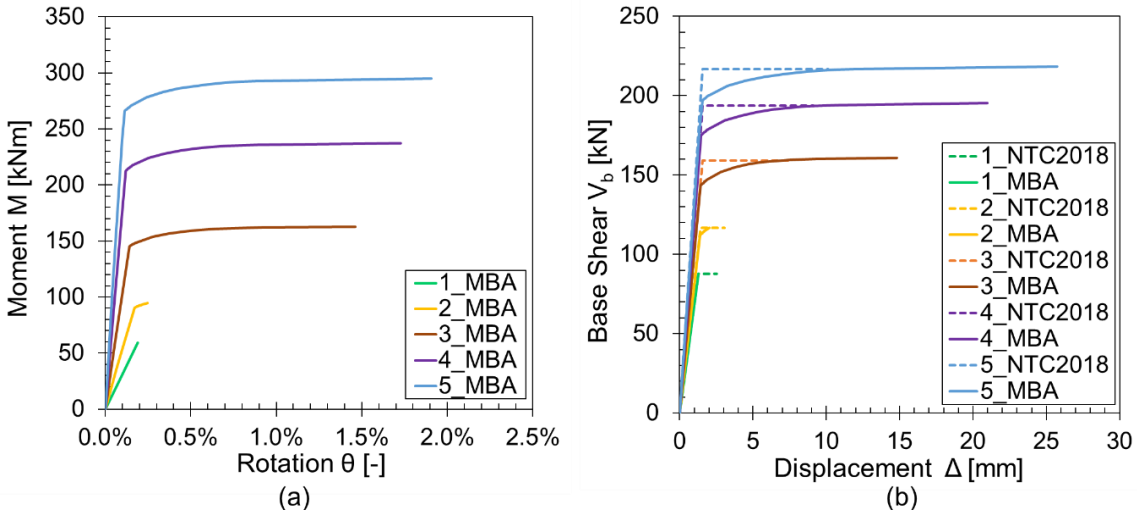

Figure 6.28. Five squat panels results: (a) moment-rotation curves; (b) base shear-displacement curves with the MBA approach and with the NTC 2018 recommendations.

Table 6.9. Ultimate displacement obtained for the five squat panels with the MBA approach and the NTC 2018 recommendations,.

	Δ_u [m]		
Specimen	NTC 2018	MBA	Relative variation
1	0.0025	0.0013	0.5
2	0.0030	0.0020	0.7
3	0.0076	0.0148	2.0
4	0.0091	0.0210	2.3
5	0.0101	0.0257	2.5

6.2.7 Effect of the boundary conditions

The influence of the boundary conditions in the response of the slender and the squat panels is herein investigated. The moment-rotation curves and the base shear-horizontal displacement curves, already defined in Section 6.2.6 for the fixed-fixed condition, were calculated modifying the boundary conditions, hence assuming cantilevered panels. Then, the obtained results were compared with those obtained in the previous Section.

In Figure 6.29 are shown the moment-rotation curves (a) and the base shear-horizontal displacement curves (b) (obtained with the MBA approach and the NTC 2018 recommendations) for the five slender panels illustrated in Section 6.2.6. In Table 6.10 is shown the comparison (MBA vs NTC 2018) in terms of the reached ultimate displacements and their relative variation.

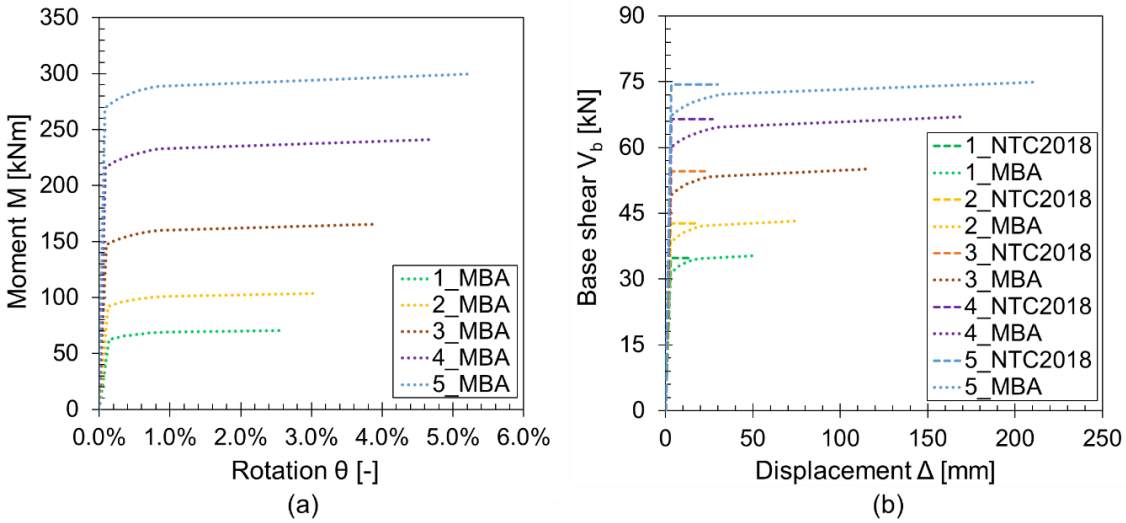

Figure 6.29. Five cantilevered slender panels results: (a) moment-rotation curves; (b) base shear-displacement curves with the MBA approach and with the NTC 2018 recommendations.

Table 6.10. Ultimate displacement obtained for the five slender cantilevered panels with the MBA approach and the NTC 2018 recommendations,.

	Δ_u [m]		
Specimen	NTC 2018	MBA	Relative variation
1	0.0150	0.0513	3.4
2	0.0180	0.0745	4.1
3	0.0225	0.1175	5.2
4	0.0270	0.1705	6.3
5	0.0300	0.2114	7.0

The first main difference in the cantilevered condition with respect to the fixed-fixed one resides in the definition of the elastic stiffness (Equation 6.4) since the parameter n changes from 12 to 3. In Table 6.11 it is reported the comparison between the elastic stiffness calculated in these two conditions. The cantilevered condition leads to a constant reduction of the elastic stiffness equal to 64% for the slender panels and to 46% for the squat ones.

Another important difference resides in the definition of the effective height (see Table 6.11). For the fixed-fixed condition, the moment contra flexure point of the element is expected to be at the mid-height, thus defining the effective height as half height of the element ($h_{eff} = H_p/2$). In the cantilevered condition, instead, the effective height corresponds to the total height of the element ($h_{eff} = H_p$).

Table 6.11. Calculations of the elastic stiffness of the five slender panels obtained with the fixed-fixed and the cantilevered conditions.

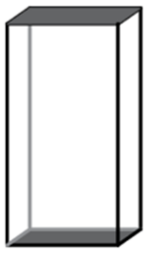

			Fixed-Fixed Condition		Cantilevered Condition	
Specimen	I [m^4]	A [m^2]	h_{eff} [m]	K_{el} [kN/m]	h_{eff} [m]	K_{el} [kN/m]
1	0.02083	0.250	1.0	31435	2.0	11327
2	0.04320	0.360	1.2	37722	2.4	13593
3	0.10547	0.563	1.5	47152	3.0	16991
4	0.21870	0.810	1.8	56583	3.6	20389
5	0.33333	1.000	2.0	62870	4.0	22655

In Figure 6.30 are reported the moment-rotation curves (a) and base shear-displacement curves (b) of the five slender panels, by considering the fixed-fixed condition (“F” in Figure) and the cantilevered one (“C” in Figure).

In the $M-\theta$ diagram, it is shown that the cantilevered panels can reach a higher rotation capacity while maintaining the maximum moment close to the fixed-fixed one. From the $V_b-\Delta$ diagram, it is observed that the cantilevered panels are characterized by a lower strength capacity as well as higher displacement ductility than the fixed-fixed one. For both conditions, the increasing trend of the moment or base shear capacity, as well as of the rotation or displacement capacity, with the increase of the dimensions of the panels, is kept. Moreover, all the combinations show a flexural failure mechanism.

To better elucidate the effect in each panel specimen, the base shear-displacement curves are shown in Figure 6.31 as separate diagrams.

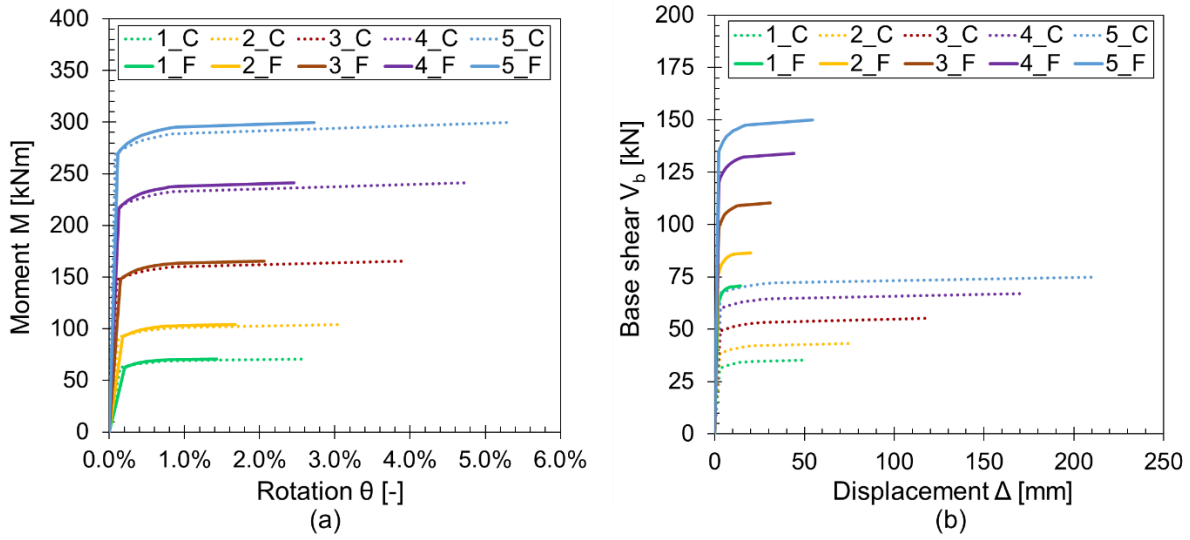

Figure 6.30. Comparison in terms of the (a) moment-rotation curves and (b) base shear-displacement curves between the slender panels in fixed-fixed condition (F) and cantilevered condition (C).

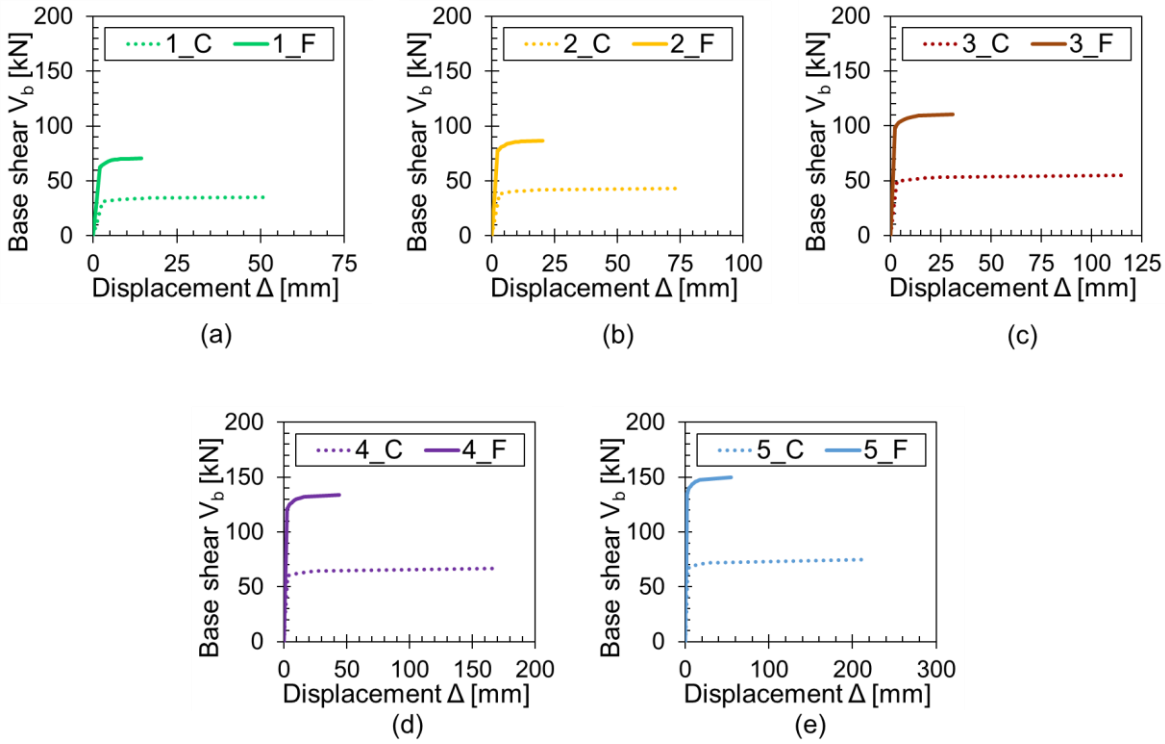

Figure 6.31. Comparison in terms of the base shear-displacement curves of the (a) 1, (b) 2, (c) 3, (d) 4 and (e) 5 slender panels in fixed-fixed condition (F) and cantilevered condition (C).

Regarding the squat panel, in Figure 6.32 are shown the moment rotation curves (a) and the base shear-horizontal displacement curves (obtained with the MBA approach and the NTC 2018 recommendations). In Table 6.12 is shown the comparison (MBA vs NTC 2018) in terms of the reached ultimate displacements and their relative variation.

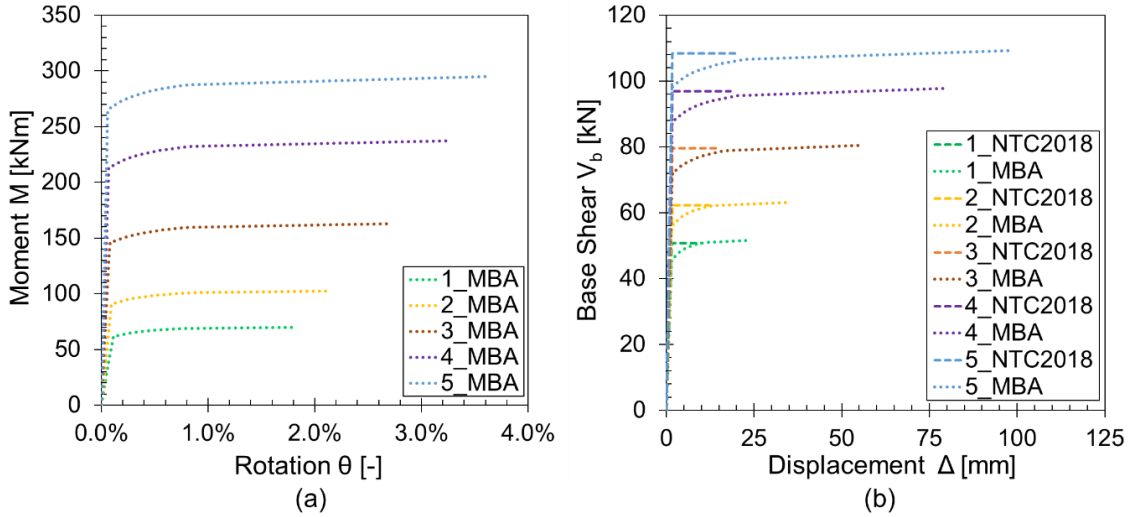

Figure 6.32. Five cantilevered squat panels results: (a) moment-rotation curves and (b) base shear-displacement curves with the MBA approach and with the NTC 2018 recommendations.

Table 6.12. Ultimate displacement obtained for the five squat cantilevered panels with the MBA approach and the NTC 2018 recommendations.

	Δ_u [m]		
Specimen	NTC 2018	MBA	Relative variation
1	0.0101	0.0241	2.4
2	0.0122	0.0348	2.9
3	0.0152	0.0547	3.6
4	0.0182	0.0793	4.4
5	0.0203	0.0983	4.9

As for the slender panels, the comparison between the elastic stiffness in the two boundary conditions is shown in Table 6.13. From the calculations, it results that the cantilevered condition leads to a constant reduction of the elastic stiffness equal to 54% with respect to the fixed-fixed one.

Table 6.13. Calculations of the elastic stiffness of the five squat panels obtained with the fixed-fixed and the cantilevered conditions.

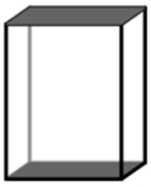

			Fixed-Fixed Condition		Cantilevered Condition	
Specimen	I [m^4]	A [m^2]	h_{eff} [m]	K_{el} [kN/m]	h_{eff} [m]	K_{el} [kN/m]
1	0.02083	0.250	0.7	68699	1.4	31325
2	0.04320	0.360	0.8	82439	1.6	37590
3	0.10547	0.563	1.0	103049	2.0	46987
4	0.21870	0.810	1.2	123659	2.4	56385
5	0.33333	1.000	1.4	137399	2.7	62650

In Figure 6.33 the comparison in terms of the moment-rotation curves (a) and the base shear-displacement curves (b) of the five squat panels, considering the fixed-fixed condition ("F" in Figure) and the cantilevered condition ("C" in Figure) is reported.

From the comparison in the $M-\theta$ diagram, it is shown that the cantilevered panels can reach a higher rotation capacity while maintaining the maximum moment close to the fixed-fixed one. From the $V_b-\Delta$ diagram, it is observed that the cantilevered panels are characterized by a lower strength capacity as well as higher displacement ductility than the fixed-fixed ones. As for the slender panels, also for the squat ones for both conditions, the increasing trend of the moment or base shear capacity, and the rotation or displacement

capacity, with the increase of the dimensions of the panels, is kept. A difference arises when dealing with the failure mechanisms since the two conditions lead to the same failure mechanisms (flexural) only for three panels. The panel specimens, with scale factor equal to 1 and 1.2 (number 1 and 2), in the fixed-fixed condition, lead to the shear failure mechanism, while in the cantilevered condition show a flexural one.

A more clear comparison in terms of base shear-displacement curves for each squat panel is reported in Figure 6.34.

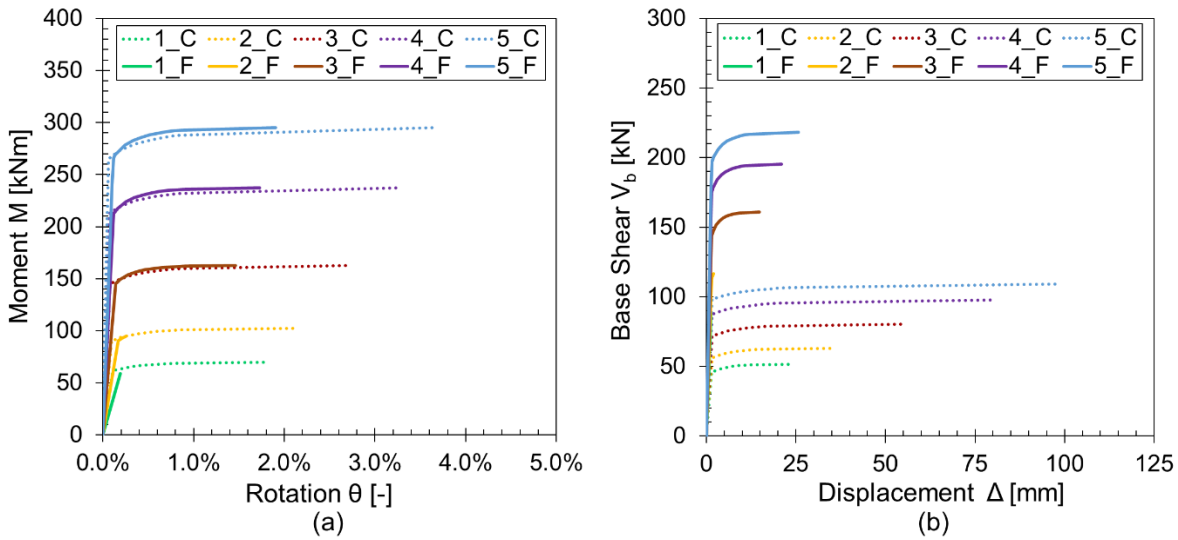

Figure 6.33. Comparison in terms of the (a) moment-rotation curves; (b) base shear-displacement curves between the squat panels fixed-fixed condition (F) and cantilevered condition (C).

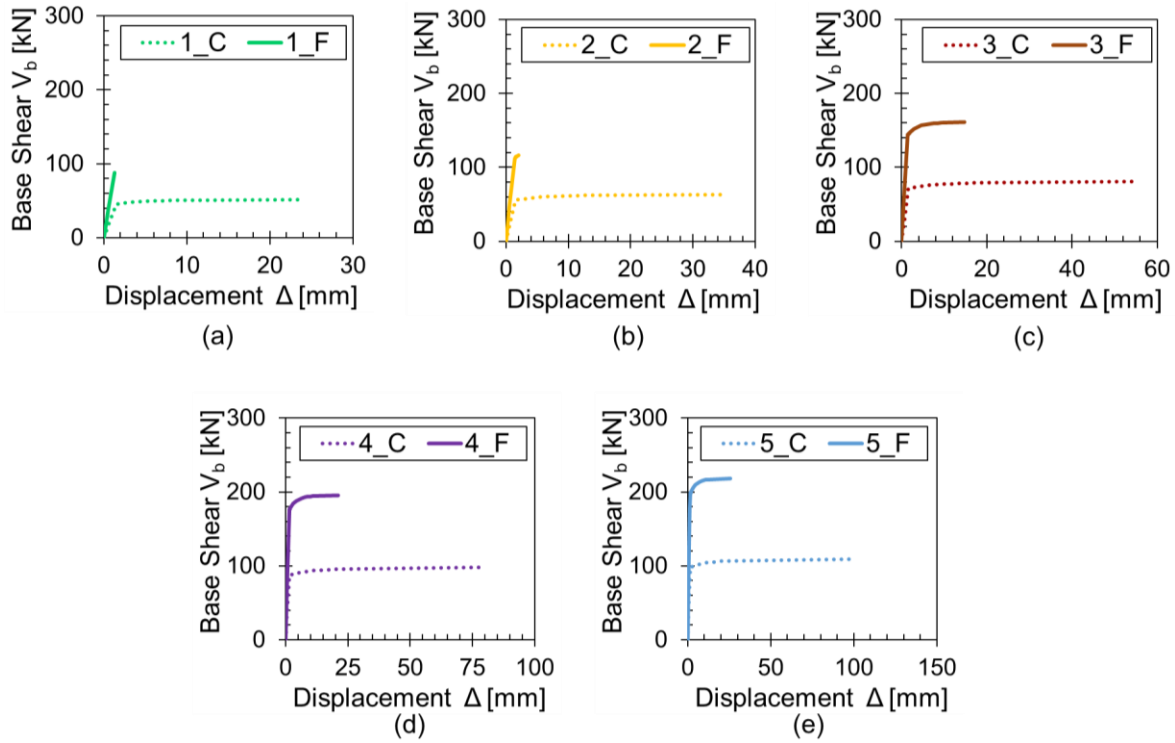

Figure 6.34. Comparison in terms of the base shear-displacement curves of the (a) 1, (b) 2, (c) 3, (d) 4 and (e) 5 squat panels in fixed-fixed condition (F) and cantilevered condition (C).

6.3 One-storey substructure

The analyzed case study is a substructure - designated as PS3 (Figure 6.35) - tested under in-plane lateral cyclic loading by Knox *et al*. (2017). This is a one-storey URM framed substructure with two piers linked by a spandrel. The PS3 specimen presents a total height of $2.74\ \mathrm{m}$ (with piers and spandrel heights of $1.80\ \mathrm{m}$ and $0.94\ \mathrm{m}$, respectively) and a total length of $4.42\ \mathrm{m}$ (with piers and spandrel lengths of $1.19\ \mathrm{m}$ and $1.24\ \mathrm{m}$, respectively). It is a two-wythe (230 mm thick) masonry wall built reusing clay bricks, obtained from a demolished 1930s URM building, and a weak mortar with an average compressive strength of $2.9\ \mathrm{MPa}$, selected to simulate weather-deteriorated mortar typical of old URM buildings.

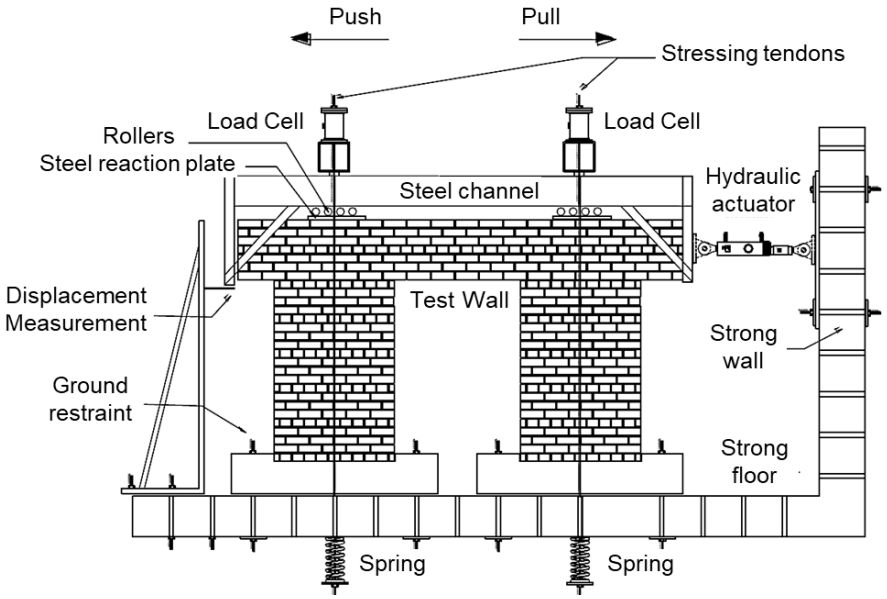

Figure 6.35. Pseudo-static testing setup (adapted from Knox et al., 2017).

The lateral load was applied on the side edges of the spandrel using a hydraulic-powered actuator connected with a reaction wall. The axial load is equal to 0.48 MPa and it is equivalent to the typical weight of two stories of masonry. This load was applied on the top of the spandrel at the centreline of piers. During testing, diagonal tension cracking of the spandrel, characterized by a "X" crack pattern, occurred before any cracking in the piers, but a flexural crack at the interface between the spandrel and the pier-spandrel joints was noted earlier in the test, due to the interlocking effect between the two parts (Cattari and Lagomarsino, 2008). The base shear-displacement response was governed by a rocking mechanism. It was reported that the test was stopped at 1% drift, without failure of the piers and so with a "ductile" flexural-rocking behavior.

6.3.1 Numerical modelling: macro-mechanical Finite Element Model (FEM)

The PS3 substructure was modelled in DIANA software (DIANA 2019) by adopting a FE macro-mechanical approach. The masonry is represented through continuum FEs (Q8MEM, 2D 4-node quadrilateral) using a structured mesh developed with an approximated size of 50 mm. The Total Strain Rotating Crack (TSRC) model and the Crack and Plasticity (C&P) model were assumed to describe the material response. The system boundary conditions

are: (i) fix the X- and Y-directions at the base of the piers; (ii) fix the X-direction at the first bottom masonry course of the piers (according to the direction of the applied displacement) to simulate the concrete grouted base; (iii) adopt a master-slave node strategy to allow the application of a uniform horizontal displacement and, therefore, fix the X-direction on a master node at the mid-height of the right edge of the spandrel. A thin steel plate (10 mm thick) with elastic behavior was modelled at the right side edge of the spandrel in order to apply a uniform displacement. In Figure 6.36 are shown the numerical model with boundary conditions, applied axial load and horizontal displacement, and the adopted mesh.

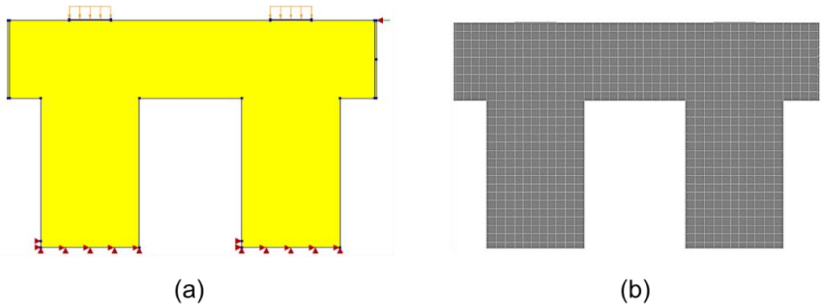

Figure 6.36. PS3 substructure: (a) numerical FE model and (b) adopted mesh.

The following mechanical parameters were considered in the TSRC FE model: Young's modulus $E_m = 1200\,\mathrm{MPa}$ and shear modulus $G_m = 545\,\mathrm{MPa}$; for the tensile behavior, a linear-exponential curve with strength $f_t = 0.3\,\mathrm{MPa}$ and fracture energy $G_t = 0.02\,\mathrm{N/mm}$ (set according to Lourenço (2010), in absence of further experimental data); for the compressive behavior, a linear-parabolic curve with a strength given as $f_{cm} = 9.2\,\mathrm{MPa}$ and fracture energy $G_c = 1\,\mathrm{N/mm}$ (assumed as 1% of f_{cm}). For the C&P model, the same elastic properties selected for the TSRC model were used as well as the same values for compressive and tensile strength. A cohesion equal to $2.656\,\mathrm{N/mm^2}$, a friction angle equal to $0.5236\,\mathrm{rad}$ (30°) and a zero dilatancy angle (as suggested in Lourenço and Rots, 1997) were assumed. The adopted mechanical parameters are resumed in Table 6.14.

Concerning the applied loads, both the dead weight and the added distributed vertical load, corresponding to the axial stress on the piers of $\sigma = 0.48\,\mathrm{MPa}$, were applied. The horizontal displacement was applied on the right-side edge of the spandrel aiming to properly simulate the first push cycle experimental loading.

Table 6.14. Mechanical parameters for the TSRC and C&P constitutive models.

E_m *(N/mm²)*	Young modulus		1200
v	Poisson ratio		0.10
f_{cm} *(N/mm²)*	Compressive strength		9.2
f_t *(N/mm²)*	Tensile strength		0.30
G_c *(N/mm)*	Compressive fracture energy		1
G^I_f *(N/mm)*	Tensile fracture energy		0.020
		TSRC	***C&P***
ϕ *(deg)*	Internal friction angle	-	30
c *(N/mm²)*	Cohesion	-	2.656
ψ *(deg)*	Dilatancy angle	-	0

The prediction of the envelope curve of the cyclic base shear-horizontal displacement response was achieved through a nonlinear static (pushover) analysis. A comparison with the experimental results in terms of crack pattern and corresponding capacity curves is presented in Figures 6.37 and 6.38. As observed, the failure mechanisms of both piers and of the spandrel match the experimental ones, i.e. rocking of piers and diagonal cracking of the spandrel. The obtained FE numerical pushover curves are in good agreement with the experimental envelope one. These results will be used, subsequently, as a reference to evaluate the accuracy of the proposed SLaMA-URM method.

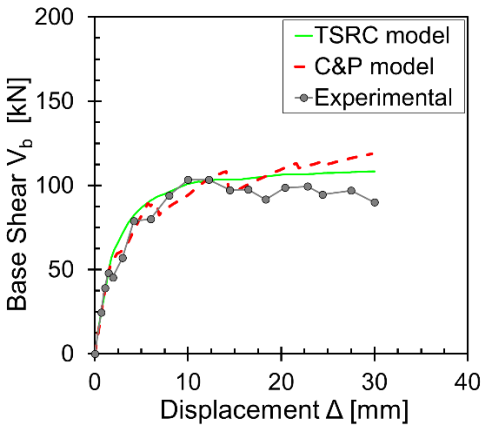

Figure 6.37. PS3 substructure results: numerical capacity curves against experimental envelope.

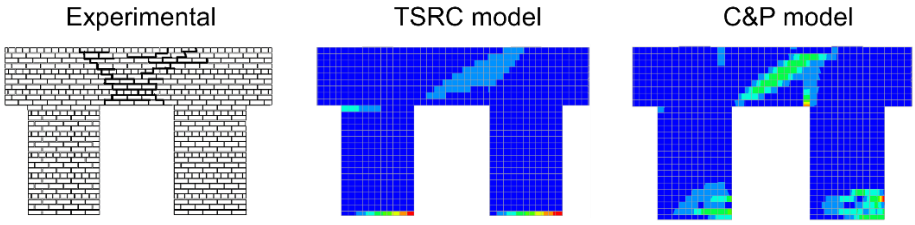

Figure 6.38. PS3 substructure results: experimental and numerical crack patterns at the ultimate displacement.

6.3.2 Geometric and mechanical data for SLaMA-URM method

The SLaMA-URM method is herein validated against the experimental case study and the numerical simulation results described above.

The geometry of the PS3 substructure was defined according to the EF model discretization (Figure 6.39) towards the application of the SLaMA-URM procedure. More in detail: the length and the clear height of both piers were set to $B_p = 1.19\ \mathrm{m}$ and $h_p = 1.80\ \mathrm{m}$, respectively; the height and the length of the spandrel were $h_{sp} = 0.94\ \mathrm{m}$ and $L_{sp} = 1.24\ \mathrm{m}$, respectively; the thickness of both piers and spandrel was $t_p = 0.23\ \mathrm{m}$. The effective height of the piers was $h_{p,eff} = 2.25\ \mathrm{m}$ and it was calculated using the Dolce's rule (Dolce, 1991), while the effective length of the spandrel L_{sp} is its clear span.

The masonry mechanical parameters adopted in the analytical model were those derived from the experimental characterization tests reported in Knox *et al*. (2017): i.e. a masonry compressive strength f_{cm} of $9.2\ \mathrm{MPa}$ while the horizontal compressive strength f_{hm} was assumed equal to f_{cm} as addressed in Beyer and Dazio (2012); a brick tensile strength f_{bt} of $25.4\ \mathrm{MPa}$ and a friction coefficient μ of 0.7. From the calibrated numerical model, a Young's modulus E_m and a shear modulus G_m for the masonry were chosen as $1200\ \mathrm{MPa}$ and $545\ \mathrm{MPa}$, respectively. The tensile strength f_t was considered, as for the FE model, equal to $0.3\ \mathrm{MPa}$, and the initial shear strength at zero compressive stress f_{v0} was estimated as $f_t/1.5$ (NTC 2018), i.e. equal to $0.2\ \mathrm{MPa}$. An equivalent axial load N of $131\ \mathrm{kN}$, i.e. axial load ratio $v_r = N/(f_{cm}A_{pier}) = 0.05$ (where A_{pier} is the pier cross-section area), was applied on each pier.

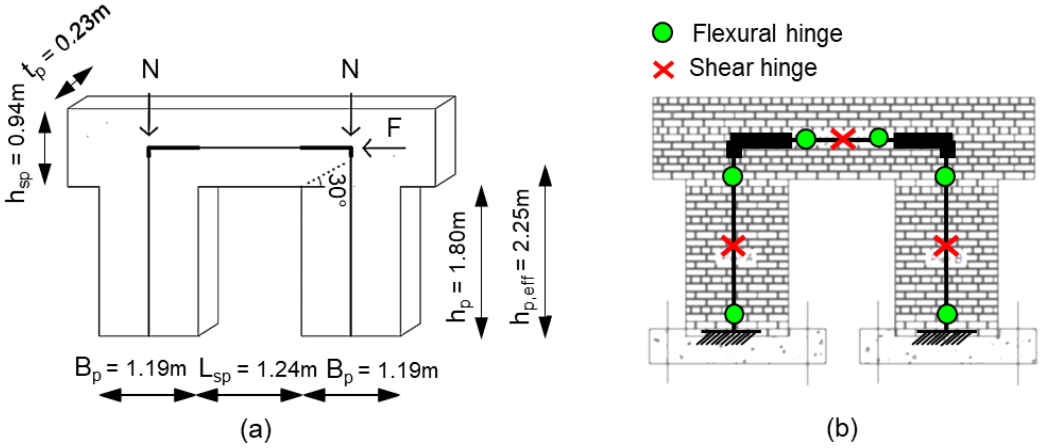

Figure 6.39. Schematic representation and geometry of the PS3 substructure through the EF model: (a) geometry and (b) distribution of the flexural and shear plastic hinges.

6.3.3 Analysis at component level

In Sections 6.3.3.1 and 6.3.3.2, the flexural and shear capacity of the piers and the spandrel are defined at component level, in terms of moment-rotation curves and moment-axial load (M-N) domains.

6.3.3.1 Moment-rotation curves

The flexural capacity of piers is defined from an elastic-perfectly plastic stress-strain relation in compression with no-tensile resistance (EPP-NTR) assumption and the Lumantarna's model in compression with no-tensile resistance (Lumantarna-NTR).

Regarding the spandrel, an elastic-perfectly plastic (EPP) stress-strain, as well as a Lumantarna's model, in compression and resistant in tension (TR) model are considered. More in detail, an equivalent tensile strength f_{tu} related to the interlocking effect (Cattari and Lagomarsino, 2008) is used to calculate the bending moment by performing the sectional analysis. Since the height and the width of the bricks are $\Delta_y = 76\,\mathrm{mm}$ and $\Delta_x = 110\,\mathrm{mm}$, respectively, and the 65% of the mean compressive stress σ is considered as acting on the adjacent pier section (Cattari and Lagomarsino, 2008), the equivalent tensile strength, calculated according to Equation 6.5 (Cattari and Lagomarsino, 2008), results in $f_{tu} = 0.30\,\mathrm{MPa}$.

$$f_{tu} = \frac{\Delta_x}{2\Delta_y} \mu \, 0.65 \, \sigma \tag{6.5}$$

For the EPP model, the compressive yield ε_{yc} and ultimate ε_{uc} strains equal to 1% and 1.2% were adopted, thus considering a ductility in compression equal to $\mu_{\varepsilon c} = \varepsilon_{uc}/\varepsilon_{yc} = 1.2$. In the Lumantarna's model (Lumantarna, 2012), assuming a mortar without lime, the peak ε_{yc} and the ultimate ε_{uc} strains, result equal to 1% and 2.1% respectively (with $\mu_{\varepsilon c} = \varepsilon_{uc}/\varepsilon_{yc} = 2$).

At this first stage, no axial load on the spandrel is considered. The adopted values of compressive and tensile strains used in the sectional analysis for describing the moment-rotation response, elastic (ε_{yc} and ε_{yt}) and ultimate (ε_{uc} and ε_{ut}) strain values, are shown in Figure 6.40 and reported in Table 6.15.

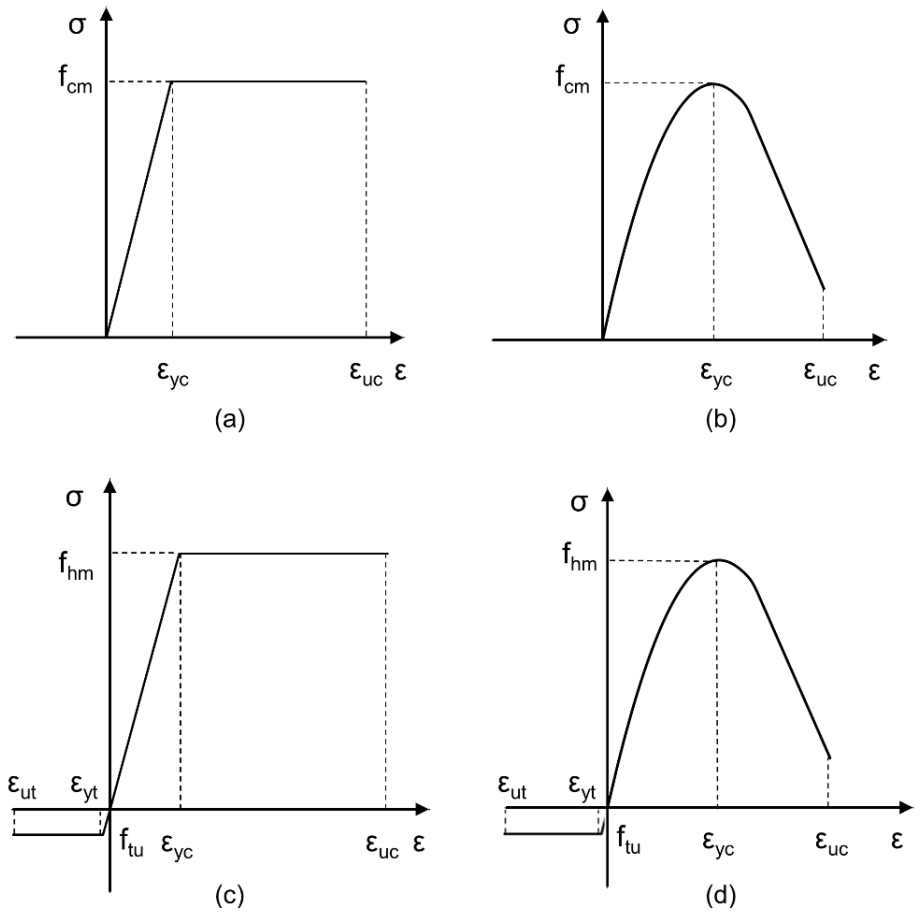

Figure 6.40. Stress-strain relationships: (a) EPP-NTR and (b) Lumantarna-NTR models for the piers and (c) EPP-TR and (c) Lumantarna-TR for the spandrel.

Table 6.15. Parameters adopted for the stress-strain relationships of piers and spandrel.

Structural element	Model	ε_{yc} [-]	ε_{uc} [-]	f_{cm} (=f_{hm}) [MPa]	ε_{yt} [-]	ε_{ut} [-]	f_{tu} [MPa]
PIERS	EPP-NTR	0.010	0.012	9.20	-	-	-
	Lumantarna-NTR	0.010	0.021	9.20	-	-	-
SPANDREL	EPP-TR	0.010	0.012	9.20	0.0004	0.020	0.30
	Lumantarna-TR	0.010	0.021	9.20	0.0004	0.020	0.30

The MBA formulation (Pampanin *et al.*, 2001) discussed for the Ispra panels (Section 6.2.3.1) is herein used to define the rotation of the piers and the spandrel. Therefore, Equation 6.3 is adopted by considering $\chi_y = 2\,\varepsilon_{yc}/B$ with B taken as the length B_p for the piers and the height h_{sp} for the spandrel, and L_{cant} taken as half of the effective height $h_{p,eff}/2$ for piers and as half of the clear span $L_{sp}/2$ for the spandrel. The element elastic contribution is added through Equation 6.4, in which H_p corresponds to the effective height $h_{p,eff}$ derived by the Dolce's rule (Dolce 1991) for the piers and to the clear span L_{sp} for the spandrel.

For the spandrel, the moment-capacity curve is defined in three different ways, according to the EPP-TR model and Lumantarna-TR model, characterized by: 1) limited ductility in tension ($\mu_{\varepsilon t} = \varepsilon_{ut}/\varepsilon_{yt} = 50$), i.e. tension governed failure (EPP-TR-TF), 2) limited ductility in compression ($\mu_{\varepsilon c} = \varepsilon_{uc}/\varepsilon_{yc} = 1.2$) and unlimited ductility in tension, i.e. compression governed failure (EPP-TR-CF) and 3) limited ductility in compression ($\mu_{\varepsilon c} = \varepsilon_{uc}/\varepsilon_{yc} = 2.0$) and unlimited ductility in tension, i.e. compression governed failure (Lumantarna-TR-CF).

The values related to the moment-rotation curves, obtained with the different models for piers and spandrel are reported in Table 6.16, while the corresponding moment-rotation curves are shown in Figure 6.41.

Three different limit state conditions are considered (decompression, peak and ultimate) and a section analysis is performed to define the moment-rotation behavior. More in detail, the decompression condition corresponds to the assumption that the rotation θ_{dec} is equal to the elastic one (obtained from the initial stiffness K_{el}) and consequently the decompression moment M_{dec} is defined. For piers and spandrel (when the EPP (or Lumantarna)-TR-CF model is adopted) from imposing the values of compressive peak ε_{yc} and ultimate ε_{uc}

strains, the peak (M_p) and the ultimate (M_u) moment, together with the corresponding rotations θ_p and θ_u, are defined. On the contrary, when the EPP-TR-TF model is adopted for the spandrel, from imposing the values of tensile peak ε_{yt} and ultimate ε_{ut} strains, the moments M_p and M_u and the corresponding rotations (plastic and ultimate) θ_p and θ_u, are defined.

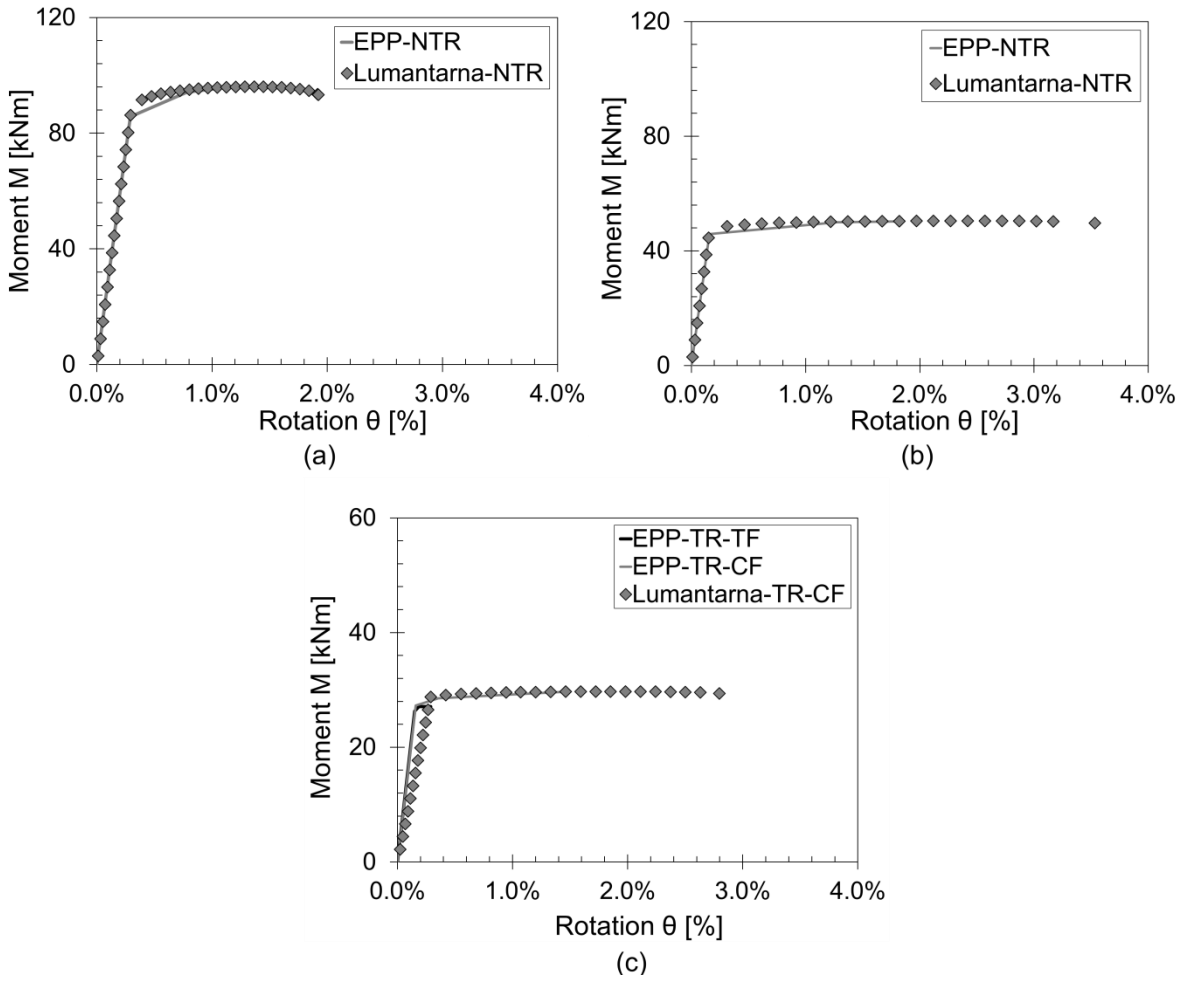

Figure 6.41. Flexural thresholds at the moment-rotation diagram for (a) left pier, (b) right pier and (c) spandrel.

Table 6.16. Rotation and bending moment values obtained for the piers and the spandrel.

Structural component	Model	θ_{dec} [%]	M_{dec} [kNm]	θ_p [%]	M_p [kNm]	θ_u [%]	M_u [kNm]
LEFT PIER	EPP-NTR	0.290	85.67	0.785	94.24	1.046	95.40
	Lumantarna-NRT	0.303	89.51	1.027	95.75	1.921	93.28
RIGHT PIER	EPP-NTR	0.156	45.90	1.272	49.98	1.782	50.28
	Lumantarna-NTR	0.162	47.46	1.749	50.37	3.534	49.74
SPANDREL	EPP-TR-TF	0.149	26.28	0.187	27.08	0.290	27.08
	EPP-TR-CF	0.159	27.29	0.355	28.52	1.442	29.65
	Lumantarna-TR-CF	0.287	28.76	1.982	29.73	2.797	29.37

According to the results obtained so far, for the spandrel, the EPP-TR-TF model is adopted, since it gives lower rotation values, hence the lower flexural ductility. For the piers, instead, the EPP-NTR model is chosen for its precautionary results in terms of the lower rotation values.

Regarding the shear strength of the piers, the Turnšek and Čačovic (Turnšek and Čačovic 1971) criterion is adopted for diagonal cracking, see Section 5.4.2.2 for more details, while for the spandrel, the shear strength is calculated considering the masonry shear strength in absence of axial load (as suggested in NTC 2018), see Section 5.4.2.3 for more details.

The piers and spandrel strength thresholds are expressed in terms of the moment capacity calculated from the pier (or spandrel) shear resistance V_s and the pier (or spandrel) cantilever length L_{cant}, as $M = V_s L_{cant}$.

It should be noted that both PS3 substructure piers are characterized by the same geometry and pre-compression load. Moreover, their capacity and resulting failure mechanism are dependent on the acting axial load, that is given by the sum of the gravity load N and the axial load variation $\pm \Delta N$, due to the coupling effect of the spandrel during the lateral sway (Figure 6.42). The axial load variation ΔN is obtained from the spandrel shear resistance V_{sp} and given as the minimum between flexural and shear strength capacity. Applying the equivalent seismic force from right to left, following the first push cycle load of the experimental test (Knox *et al.*, 2017), the right pier is subjected to a decrease of axial load ($-\Delta N$) and the left pier to an increase of it ($+\Delta N$).

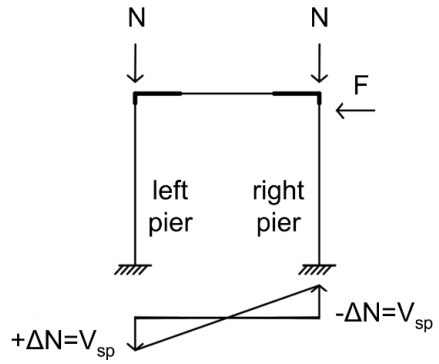

Figure 6.42. Frame subjected to horizontal load and gravity load with axial load variation.

The flexural and shear strength thresholds for the spandrel are shown in Figure 6.43c. It is observed that a flexural-shear mixed failure is expected to occur. Nevertheless, a shear brittle failure mechanism, which disregards the development of flexural failure, may be conservatively assumed. This results in an elastic-brittle response of the spandrel with a failure moment M_p of $26.81\,\mathrm{kNm}$. In order to analyse the piers, the shear strength of the spandrel V_{sp} (equal to the axial load variation ΔN on the piers) is obtained from the spandrel failure moment, according to $V_{sp} = M_p\, L_{sp}/2$, thus resulting $\Delta N = 43.24\,\mathrm{kN}$. Considering the pre-compression load N on each pier, the axial loads applied on the left and right piers are $174.6\,\mathrm{kN}$ and $88.1\,\mathrm{kN}$, respectively.

The thresholds for the flexural and shear strengths of the spandrel and piers are reported in Table 6.17 and shown in Figure 6.43 within moment-rotation diagrams. The response of both piers is governed by a rocking mechanism.

Table 6.17. Moment and rotation values at decompression, peak and ultimate conditions, for spandrel (EPP-TR-TF model) and piers (EPP-NTR model).

Structural component	Model	θ_{dec} [%]	M_{dec} [kNm]	θ_p [%]	M_p [kNm]	θ_u [%]	M_u [kNm]	Failure mechanism
LEFT PIER	EPP-NTR	0.290	85.67	0.785	94.24	1.046	95.40	*ROCKING*
RIGHT PIER	EPP-NTR	0.156	45.90	1.272	49.98	1.782	50.28	*ROCKING*
SPANDREL	EPP-TR-TF	0.149	26.28	0.152	26.81	0.152	26.81	*SHEAR*

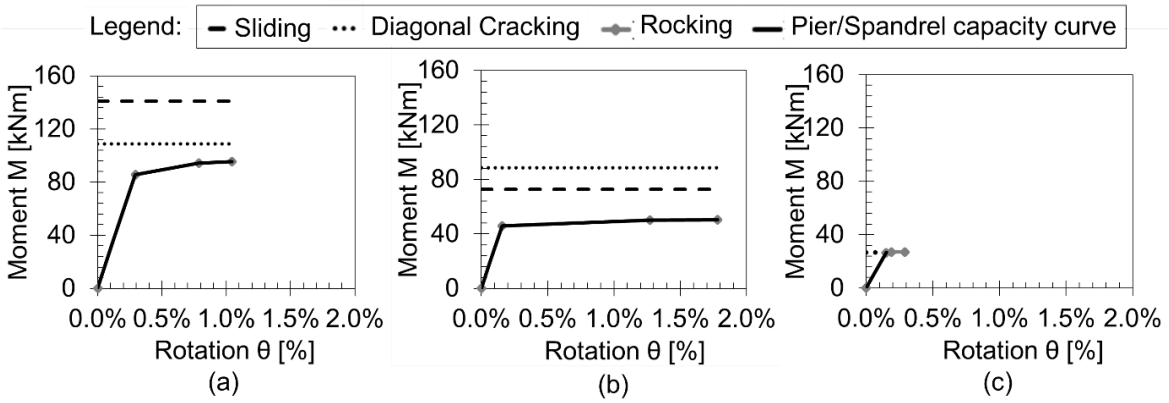

Figure 6.43. Flexural and shear strength thresholds at the moment-rotation diagram for (a) left pier (EPP-NTR model), (b) right pier (EPP-NTR model) and (c) spandrel (EPP-TR-TF model).

6.3.3.2 Moment-axial load (M-N) domains

The flexural capacity of piers is defined through a closed-form equation according to NTC 2018 and NZSEE 2017b, in which the bending moment capacity is defined using an equivalent compressive stress block assumption. Alternatively, the Moment-Axial load (M-N) interaction curve can be obtained through sectional equilibrium equations, in which different constitutive laws can be adopted for masonry.

In such a context, the pier M-N interaction domains are defined by considering the EPP-NTR and the Lumantarna-NTR models. Also in this case, to emphasize the reliability of the MBA approach (Pampanin *et al*., 2001), the results obtained by this procedure are compared next with those derived from traditional sectional analysis.

In Figure 6.44a, the comparison between the M-N domains obtained with the EPP-NTR (with ductility in compression $\mu_{\varepsilon c} = 1.2$) and the Lumantarna-NTR models is shown, adopting the conventional sectional analysis and the MBA approach. It is observed that the results from the two approaches perfectly match each other. Moreover, it is shown that the Lumantarna model gives a more conservative moment capacity with respect to the EPP one. This is due to the presence of strength degradation in the Lumantarna model which reduces the compression force, which in turn reduces the moment capacity.

For the EPP-NTR model, assuming, as an example, a fixed elastic compressive strain of $\varepsilon_{yc} = 1\%$, two different ductility levels in compression ($\mu_{\varepsilon c}$ equal to 1.2 and 3.5) are considered to better understand the influence of the ductility on the M-N strength domain.

The results presented in Figure 6.44b indicate that the domains from EPP-NTR model with $\mu_{\varepsilon c}$ equal to 1.2 converge to those from NTC 2018 or NZSEE 2017b. When increasing the ductility to a value of $\mu_{\varepsilon c} = 3.5$, the M-N domain expands since the neutral axis depth decreases and, consequently, the lever arm of the resultant compression force increases.

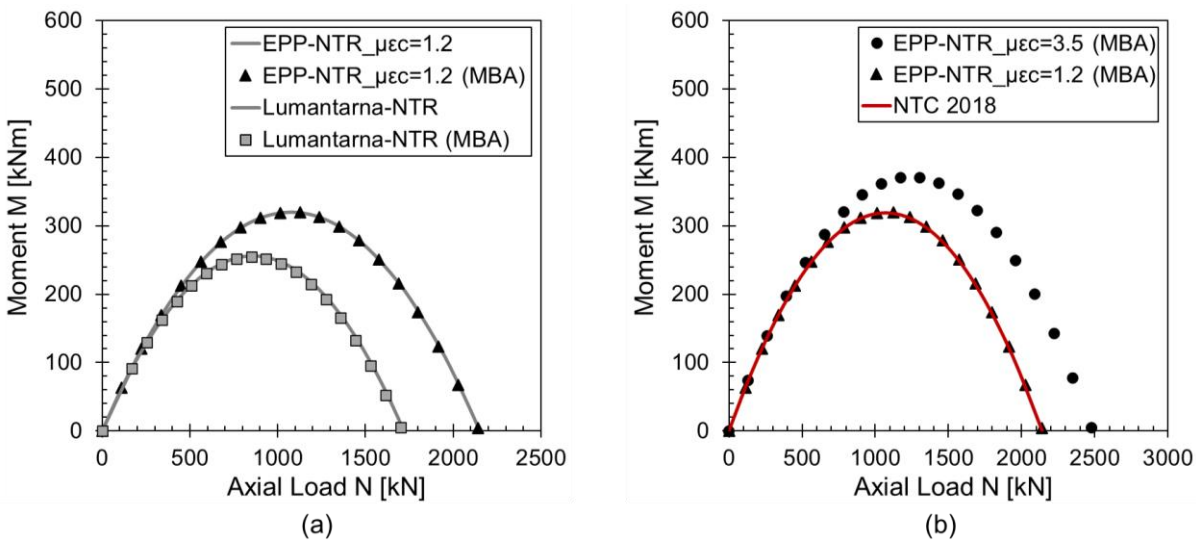

Figure 6.44. Comparison between the piers M-N domains with: (a) EPP and Lumantarna's models with the traditional sectional analysis and the MBA approach; (b) EPP models with different $\mu_{\varepsilon c}$ and the NTC 2018 formulation.

For the spandrels, the elastic-perfectly plastic stress-strain law and tensile resistant (EPP-TR) model is assumed. In Figure 6.45 the M-N domains for the tension governed model with different values of $\mu_{\varepsilon t}$ (a) and η (b) are shown, to elucidate the role of the tension strain ductility ($\mu_{\varepsilon t} = \varepsilon_{ut}/\varepsilon_{yt}$) as well as the ratio between the tensile strength and the compression strength ($\eta = f_{tu}/f_{cm}$).

Reducing the tension strain ductility $\mu_{\varepsilon t}$ (Figure 6.45a), the moment capacity, corresponding to the low axial load, and the peak moment capacity, both decrease. Considering a constant axial load level, as tension strain ductility increases, the depth of the section in tension increases, and the compression and tension forces increase proportionally, and in turn, increases the moment capacity.

By varying the values of η (Figure 6.45b), considering different values of equivalent tensile strength f_{tu}, it can be seen that this latter parameter is important in defining the M-N

domain, since it leads to strongly different results in terms of moment capacity at low values of axial load, while it is not very influent at a high level of it.

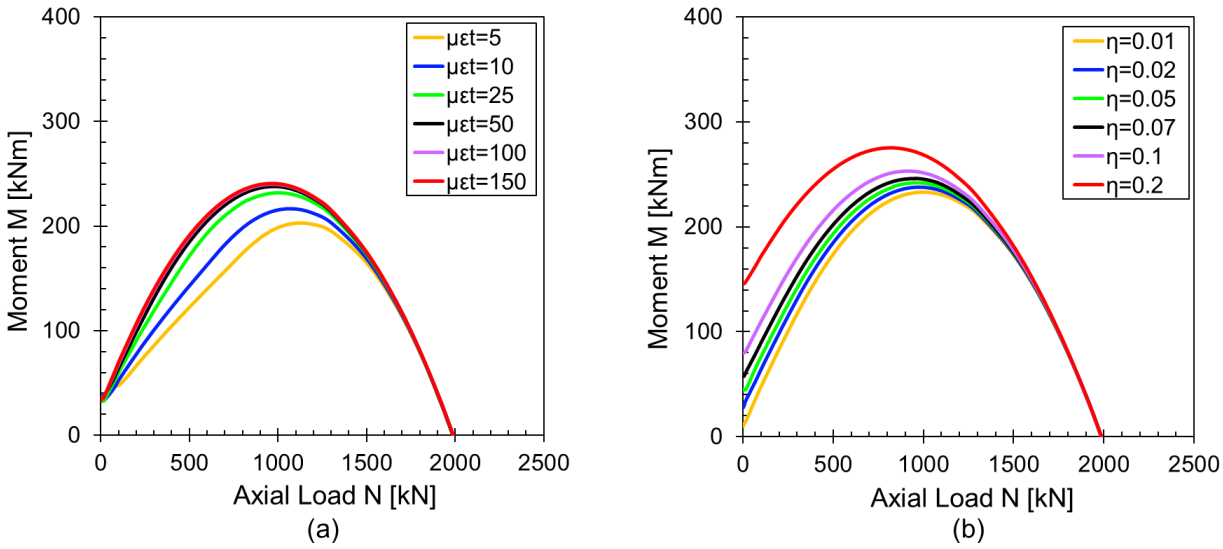

Figure 6.45. Comparison of spandrel M-N domains varying: (a) the tension ductility $\mu_{\varepsilon t}$ values for the tension governed model; (b) the compression strength and tension strength ratio η values for the tension governed model.

In the following, a tension governed (EPP-TR-TF) model with a tension strain ductility of $\mu_{\varepsilon t} = 50$ is considered (with a value of $\varepsilon_{yt} = 0.04\%$ for the yield tensile strain and $\varepsilon_{ut} = 2\%$ for the ultimate tensile strain), as suggested in Knox (2012). Furthermore, a compression governed (EPP-TR-CF) model, with compressive strain ductility values of $\mu_{\varepsilon c} = 1.2$ and $\mu_{\varepsilon c} = 3.5$, is adopted (assuming a value of $\varepsilon_{yc} = 1\%$ for the yield compressive strain).

A comparison of the strength domains of these models is shown in Figure 6.46a. It can be seen that the M-N domain obtained with $\mu_{\varepsilon c} = 3.5$ is strongly similar to that obtained by the tension governed model. Decreasing the compressive ductility to a value of $\mu_{\varepsilon c} = 1.2$, instead, leads to a decrease in moment capacity (as highlighted for the piers in Figure 6.44b). The same M-N domains were defined adopting the conventional sectional analysis and the MBA approach: the obtained results perfectly match each other (Figure 6.46a).

To investigate the effect of the tensile strength, a comparison of the M-N domains, for the EPP and the Lumantarna models, in the case of no-tensile resistance (NTR), and in the case in which an 'equivalent' tensile strength f_{tu} is defined (TR), is shown in Figure 6.46b. It

results clear that the addition of f_{tu} has a strong effect on the moment capacity at low values of axial load, which are typical in the spandrels. With the Lumantarna stress-strain profile a contracted M-N domain with respect to that resulted by the EPP domain was obtained, due to the strength degradation that characterizes this model.

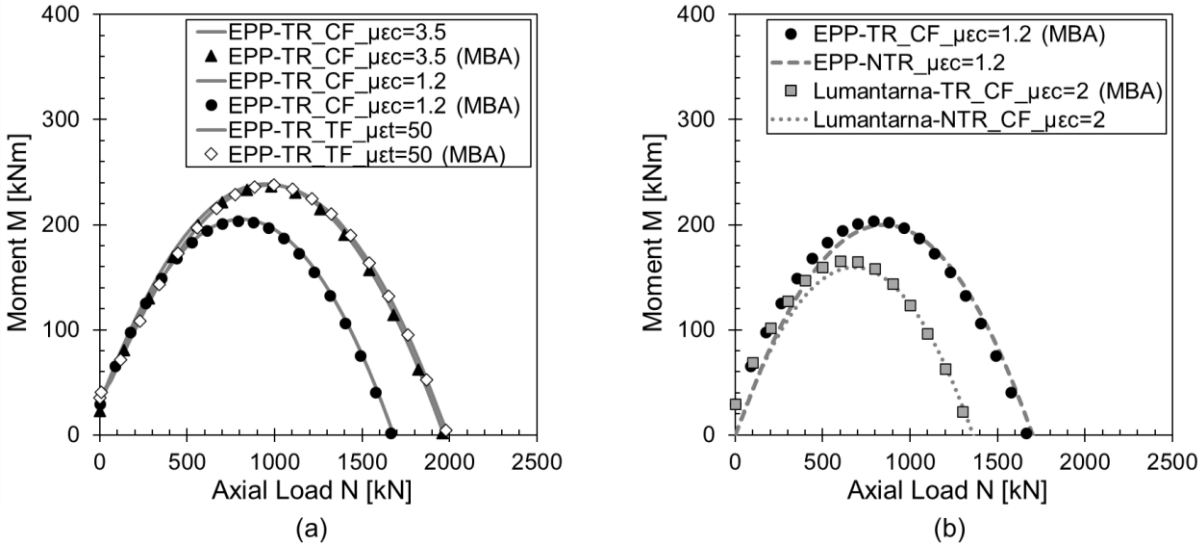

Figure 6.46. Comparison between the spandrel M-N domains with: (a) EPP for tension and compression governed models with both the traditional sectional analysis and the MBA approach; (b) EPP and Lumantarna's models (TR and NTR) for compression governed failure models.

In the following Sections, the spandrel with tensile behavior (TR) is considered, according to the experimental results, that show an interlocking effect of bricks at the spandrel-joint interface region. Moreover, the EPP-TR-TF model is adopted for the flexural response of the spandrel, in which lower values for the rotation, flexural ductility and tensile strain ductility are, conservatively, assumed.

6.3.4 Analysis at subassembly level

The evaluation of the hierarchy of strength between the structural components of a subassembly requires the assessment of the individual capacities having a common parameter as a reference. In this procedure, the taken parameter is the equivalent bending moment in the involved pier, according to Pampanin *et al*. (2007).

Considering that the capacity of the structural components was previously derived as a moment-rotation relation, the pier M-N interaction (or performance) domain is adopted to identify the sequence of failure mechanisms in each pier-spandrel subassembly. In this domain, the demand in terms of axial load variation, due to the lateral load on the frame, is defined. The capacity of the spandrel in terms of the equivalent pier bending moment is identified in correspondence to the type of the considered subassembly, and then referring to a local (rotational) equilibrium between pier and spandrel. In the case under study, both subassemblies are of type “knee corner” (see Section 5.4.3.1 for more details), and therefore are characterized by a “one-to-one” (number of piers vs. spandrels connecting into the joint) moment ratio.

As both the flexural and shear capacities of the spandrel can be considered independent from the axial load applied to the piers, the spandrel moment capacity in the M-N performance domain is assumed to be constant. Under these conditions, the comparison of the strength of structural components is made according to Equation 6.6 (NZSEE 2017a):

$$\Delta N = \pm \frac{2H}{3L} F \tag{6.6}$$

where H and L are the height and the length of the substructure, respectively, and F represents the equivalent seismic load (or global shear strength), assumed to be applied at $2/3$ of H. The intersection of the demand (axial load variation) with the capacity curves determines the sequence of events.

The M-N performance domain of the piers (it is the same for both piers) with the curves corresponding to the potential failure mechanisms of the piers and the spandrel is shown in Figure 6.47.

The sequences of events in the right subassembly, subjected to a decrease of axial load ($-\Delta N$), (squares; numbered from 1 to 2) and in the left subassembly, subjected to an increase of axial load ($+\Delta N$) (triangles; numbered from 1 to 2) are shown in Figure 6.48. In the right subassembly, the onset of failure is given by (i) shear (diagonal cracking) failure of the spandrel, followed by (ii) rocking of the pier. In the left subassembly, instead, it is given by (i) shear (diagonal cracking) failure of the spandrel, followed by (ii) diagonal cracking of the pier.

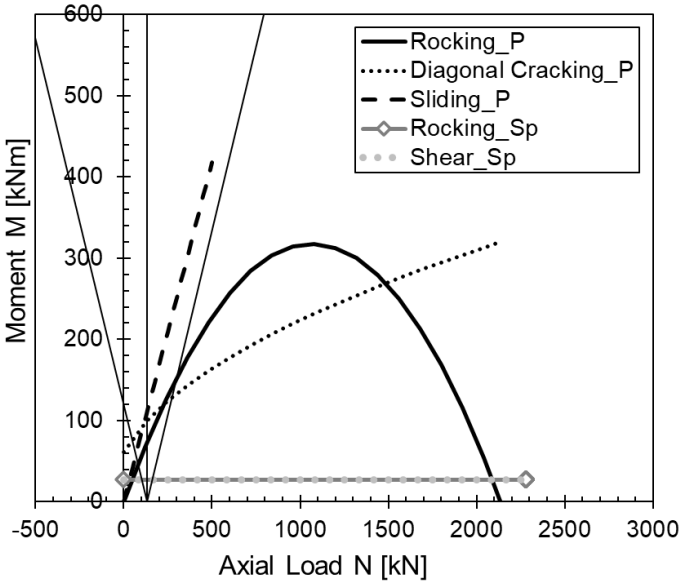

Figure 6.47. M-N performance domain.

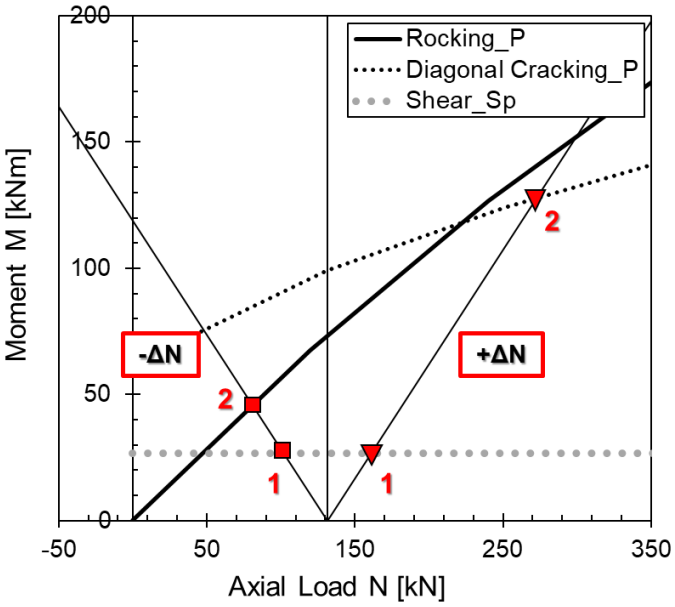

Figure 6.48. Zoom of the M-N performance domain highlighting the sequence of the failure events (■: right subassembly (−ΔN), ▼: left subassembly (+ΔN)).

6.3.5 Analysis at In-Plane global level

The global mechanism of the substructure, i.e. a “mixed sideway” mechanism, can be defined from the hierarchy of strength in each subassembly. The mechanism is characterized

by the shear failure of the spandrel and by the rocking at the base of both piers, as obtained also from experimental test and numerical simulation. Regarding this latter mechanism, the overturning moment (OTM) is calculated using a global equilibrium approach by including two contributions (see Figure 6.49a): (1) the bending moment at the base of the piers $M_{p,i}$, and (2) the push-pull overall moment due to the coupling of shear forces at the spandrel-end V_{sp} (a rocking mechanism). The base shear force V_b is calculated by dividing the OTM by the effective height of the structure H_{eff}, according to Sullivan *et al*. (2012).

More in detail, the spandrel contribution (rocking mechanism) to the OTM is defined through the parameter β_F and results equal to 0.44. The ratio between the effective height H_{eff} and the total height H of the frame is calculated and results equal to 1.335. Due to the fact that this value is greater than the unit, H_{eff} is defined as equal to H. From the value of the OTM (that results equal to $237\ \mathrm{kNm}$), the base shear is given by the ratio of this value to the effective height and results equal to $104.6\ \mathrm{kN}$.

Regarding the "yield" Δ_y and the ultimate Δ_u displacement of the frame at the effective height H_{eff}, they are calculated from the minimum "yield" $\theta_{y,min}$ and ultimate $\theta_{u,min}$ drift. The predicted shear mechanism (brittle failure) of the spandrel occurs first as its drift is the minimum "yield" drift ($\theta_{y,min} = 0.146\%$), and hence the lower displacement ($\Delta_y = 3.3\ \mathrm{mm}$, marked with an "X" in Figure 6.49b). Being a brittle failure mode it would also identify the ultimate drift (or displacement), but by assuming that the structure is still able to withstand lateral load, global rocking occurs up to a drift of $\theta_u = 1.4\%$ (i.e. a displacement of $32\ \mathrm{mm}$).

The SLaMA method, as it is conceived, allows defining a bilinear elastic-perfectly plastic curve as a first approximation to the base shear force-displacement response of the structure. The elastic-limit and ultimate displacements of the bilinear curve are defined according to the elastic-limit and ultimate rotation of the critical structural components. It is worth noting that refinements to this curve are possible by evaluating the aforementioned OTM at earlier stages (e.g. for different limit states). By calculating the OTM at different given states, starting from the elastic-limit condition (identified as the "yield" rotation corresponding to the spandrel shear failure), a "refined" analytical curve is obtained (see Figure 6.49b).

More in detail, considering the "yield" condition, the OTM was recalculated, according to the schematization in Figure 6.49a, at the drift of $\theta_{y,min} = 0.146\%$, obtaining a value of $OTM = 191\ \mathrm{kNm}$ and a base shear equal to $84.5\ \mathrm{kN}$.

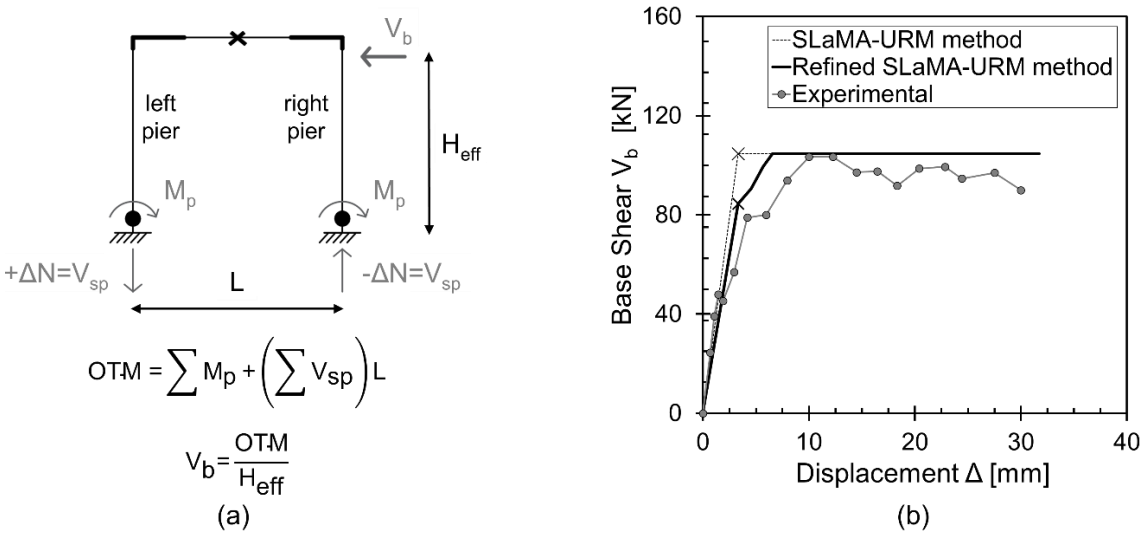

Figure 6.49. PS3 substructure global mechanism analysis: (a) schematization for the calculation of the overturning moment OTM and the base shear V_b; (b) analytical curves from the "standard" and "refined" SLaMA-URM method.

As observed in Figure 6.50, the refined curve is in better agreement with the experimental and numerical responses. The differences in terms of dissipated energy (i.e. the area under the curve) for the standard analytical curve and the refined one are 10% and 8%, respectively, when compared with the experimental curve. In Figure 6.51 it is shown the comparison in terms of the expected crisis mechanism of the substructure from analytical, numerical and experimental approaches.

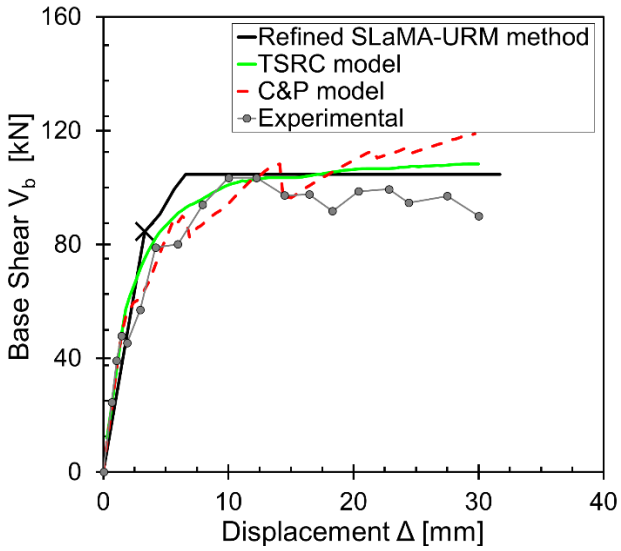

Figure 6.50. Experimental, numerical (TSRC and C&P models) and analytical (refined) responses in terms of capacity curves.

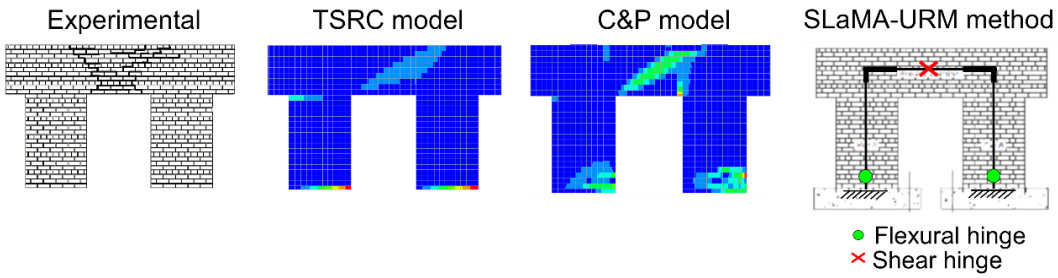

Figure 6.51. Experimental, numerical (TSRC and C&P models) and analytical (refined) responses in terms of crack patterns.

6.3.6 Effect of the geometry

The geometry of the structural components in URM structures plays an important role in its global seismic capacity. By varying the dimensions of the piers and/or of the spandrel, the failure mechanism in each subassembly may be changed. To assess this influence, parametric analyses on the PS3 substructure were carried out, and the M-N performance domains, together with the corresponding pushover curves, were obtained. It is worth noting that, in the following analyses, the PS3 specimen is considered as a benchmark and the shear failure of its spandrel corresponds to the ultimate state of the substructure.

The effective length of the spandrel L_{sp} (clear span of the openings) and its height (or section depth) h_{sp}, as well as the length (or section depth) of the piers B_p and its height (clear, not effective) h_p were varied, individually, in the following ranges: L_{sp} = [1.24 - 2.50 m]; h_{sp} = [0.94 - 2.00 m]; B_p = [0.80 - 1.80 m]; h_p = [1.00 - 3.00 m]. Accordingly, the aspect ratios of the spandrel and piers vary in the range $\lambda_{sp} = L_{sp}/h_{sp}$ = [0.62 - 2.66] and $\lambda_p = h_p/B_p$ = [0.84 - 2.52], respectively.

From the performed analyses, it is highlighted that by increasing the length of the spandrel L_{sp} (for a given height, so increasing the aspect ratio), its failure mechanism changes from shear to flexural type (from λ_{sp} = 1.49), and the resulting capacity curves of the PS3 substructure show an increase in ductility μ (from 1.7 to 2.3), as shown in Figure 6.52. On the contrary, the spandrel capacity increases when its height h_{sp} is increased, and it continues to be governed by a shear failure, i.e. the original failure mechanism of the substructure (Figure 6.53). In this case, there is also an increase of the base shear capacity of the substructure, from 6% to 12%.

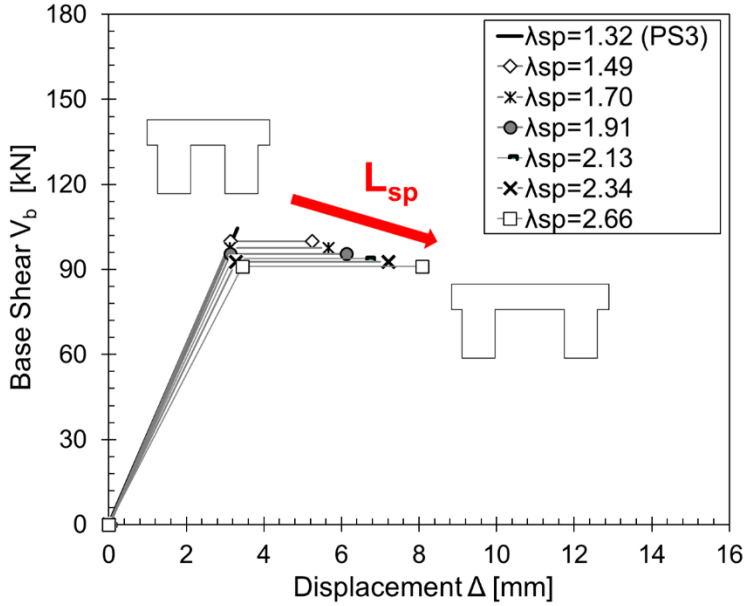

Figure 6.52. Capacity curves of the substructures by varying the spandrel length L_{sp}.

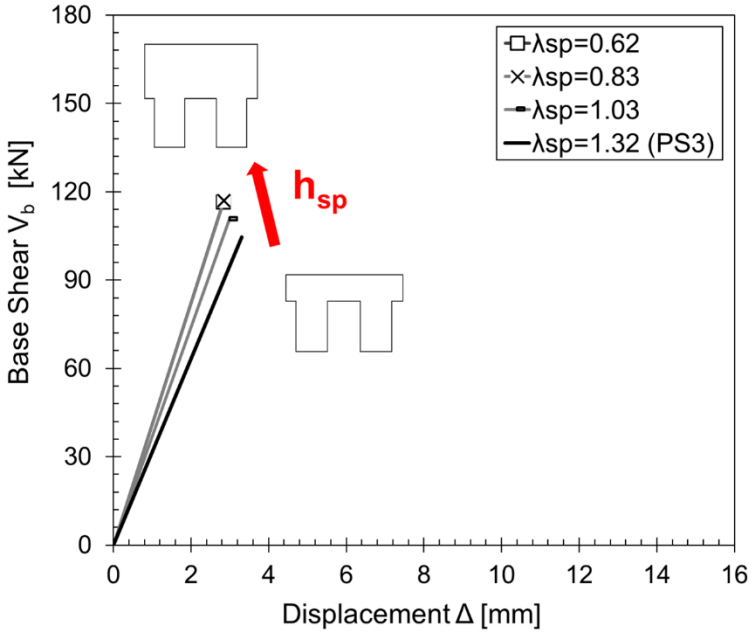

Figure 6.53. Capacity curves of the substructures by varying the spandrel height h_{sp}.

Regarding the piers, the base shear capacity of the substructure increases for larger B_p, within a −27% to +42% variation with respect to the PS3 substructure base shear capacity (black line in Figure 6.54). In this case, the failure mechanism of the spandrel is not changed, i.e. it remains a shear failure. By increasing the pier height h_p, the capacity curves present a lower stiffness and base shear strength (within a +140% to −57% variation and a +54% to

−35% variation, respectively, with respect to the PS3 substructure stiffness and base shear strength, see the black line in Figure 6.55), while the spandrel remains suffering a shear failure. The left pier, subjected to an increase of axial load (+ΔN), is characterized by a rocking mechanism if the ratio λ_p is larger than 1.26, while for lower values it presents a diagonal cracking failure (Figure 6.55).

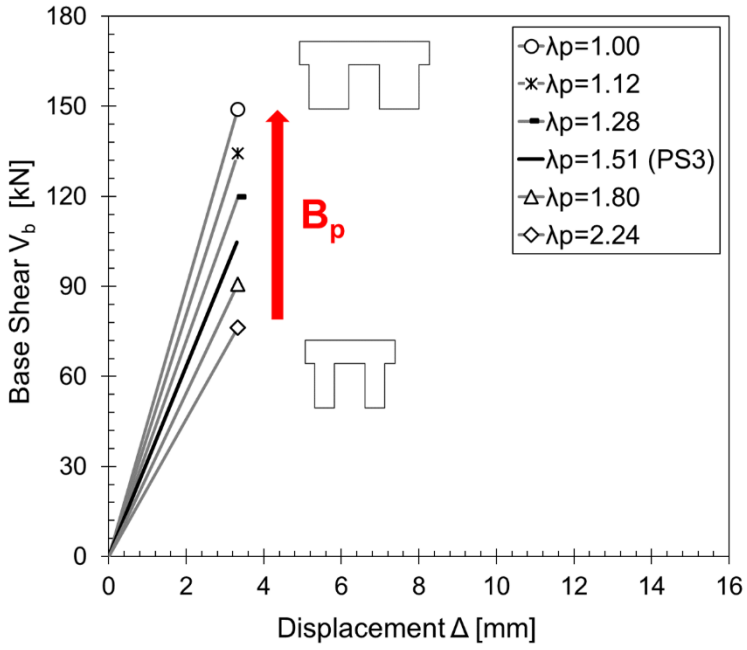

Figure 6.54. Capacity curves of the substructures by varying the piers length B_p.

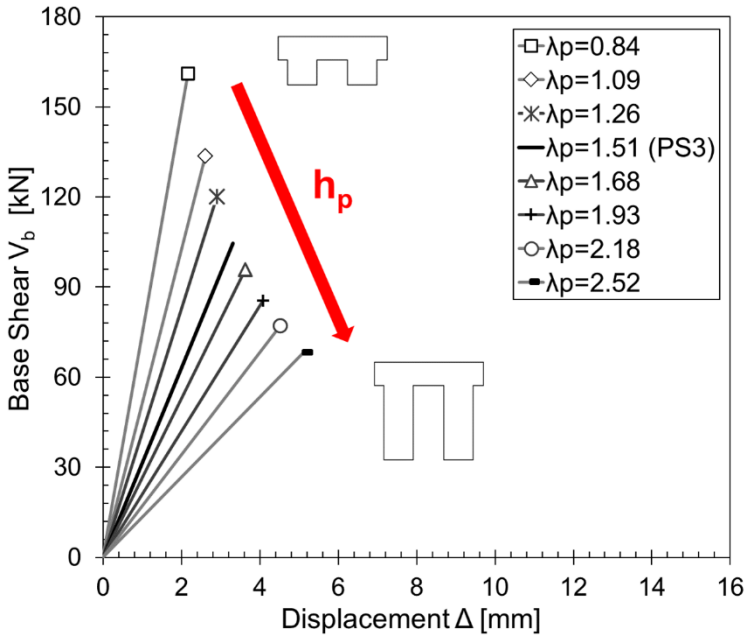

Figure 6.55. Capacity curves of the substructures by varying the piers height h_p.

6.3.7 Effect of the pier-spandrel joints contribution

In all the results presented so far, the influence of the URM pier-spandrel joints on the global capacity of the structure was neglected since these components were assumed as rigid. In this Section, an analytical approach to derive the strength capacity of pier-spandrel joints is considered, with the aim to assess its effect on the pier M-N performance domain. Four potential failure mechanisms of URM pier-spandrel joints are addressed: diagonal compression, toe crushing, sliding shear and diagonal shear (tension). An equivalent diagonal strut mechanism within the pier-spandrel joint is assumed, in analogy with the RC frame-infill wall combined behavior (Bertoldi *et al*., 1993). More details can be found in Section 5.4.2.4.

The procedure is applied to the PS3 substructure. At first, the capacity of the pier-spandrel joints in terms of the equivalent bending moment of the pier needed to be calculated. To this aim, starting from simplified equilibrium equations, the equivalent pier shear force and, consequently, the pier equivalent moment were obtained. The pier equivalent shear force V_p was defined from the lateral resistance of the equivalent strut V_{jh}, based on the geometry of the subassembly, as shown in Figure 6.56. The pier equivalent moment M_p was calculated by multiplying V_p by the half pier height $h_p/2$ (assumed as the pier cantilever length). Then, the hierarchy of strength between the pier, spandrel and joint in the pier M-N performance domain was evaluated.

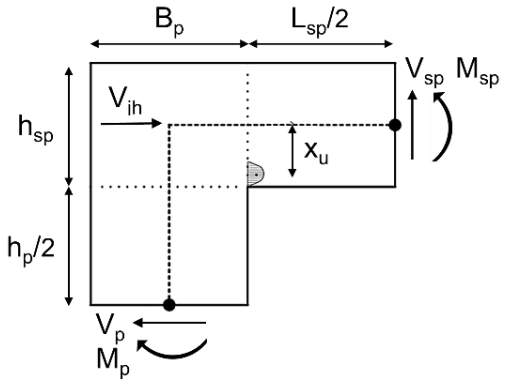

$$V_p = \frac{V_{jh}}{\left[\frac{\left(\frac{h_p + h_{sp}}{2}\right)\frac{L_{sp}}{2}}{\left(\frac{L_{sp} + B_p}{2}\right)x_u} - 1\right]}$$

$$M_p = V_p \frac{h_p}{2}$$

Figure 6.56. Schematization of the parameters to define the strength of a joint at a generic knee subassembly.

For all the investigated cases, the expected failure mechanism of the joints is diagonal cracking. The hierarchy of strength of the given substructures shows that when the spandrel height h_{sp} or the pier length B_p increase, the joint presents a higher capacity, which is enough to exclude its failure in the sequence. On the contrary, the influence of the joint becomes important (i.e. its capacity decreases) when the pier height h_p or the spandrel length L_{sp} increase. To highlight this aspect, some representative domains are presented in Figures 6.58, 6.60, 6.62 and 6.64 corresponding to subassemblies in which the spandrel length L_{sp} (Figures 6.57), the spandrel height h_{sp} (Figures 6.59), the pier length B_p (Figures 6.61) and the pier height h_p (Figures 6.63), were varied respectively. The comprehensive results of all the substructures investigated are reported in Appendix A.3.

Both the spandrel length L_{sp} and the spandrel height h_{sp} influence the joint capacity consistently (see Figures 6.58 and 6.60). For cases with high values of L_{sp} and/or low values of h_{sp}, the capacity of the joint decreases and its influence in the hierarchy of strength could become significant. For example, considering the case with L_{sp} equal to 2.50 m (Figure 6.58c), and taking into account the negative variation of axial load $-\Delta N$, the joint failure follows the rocking failure of the spandrel. It should be noted that disregarding the finite capacity of the joint (as generally done when adopting the hypothesis of a rigid joint), could lead to incorrect predictions of both the local and global failure mechanisms and then to an inappropriate retrofit solution. Indeed, by deciding a priori to disregard the capacity of the pier-spandrel joint, the possible strengthening of the spandrel might not take into account the potential shear failure of the joint.

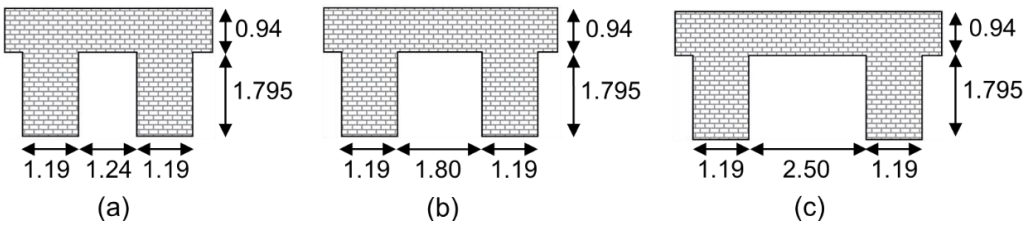

Figure 6.57. Substructures with L_{sp} of (a) 1.24 m, (b) 1.80 m and (c) 2.50 m.

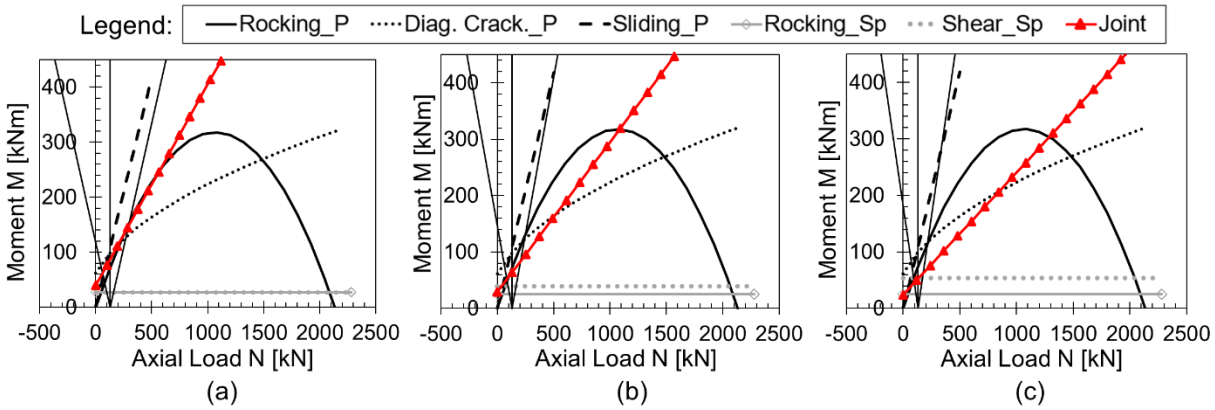

Figure 6.58. Pier M-N performance domains for subassemblies with L_{sp} of (a) 1.24 m, (b) 1.80 m and (c) 2.50 m.

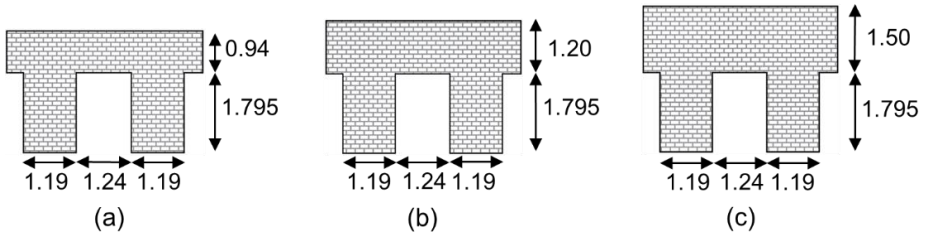

Figure 6.59. Substructures with h_{sp} of (a) 0.94 m, (b) 1.20 m and (c) 1.50 m.

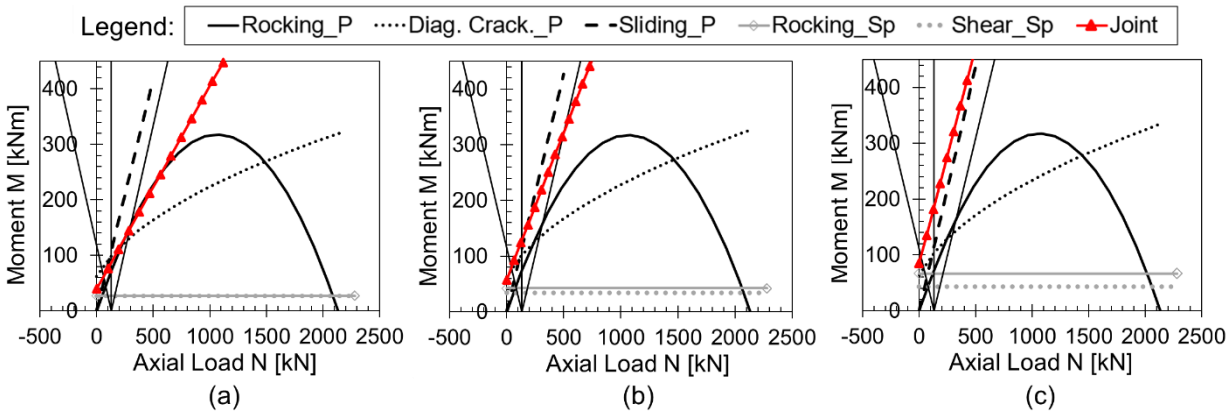

Figure 6.60. Pier M-N performance domains for subassemblies with h_{sp} of (a) 0.94 m, (b) 1.20 m and (c) 1.50 m.

Also the pier length B_p and the pier height h_p influence the capacity of the joint (see Figures 6.62 and 6.64). For cases with low values of B_p and/or high values of h_p, the capacity of the joint decreases. On the contrary, for low values of h_p and/or high values of B_p, for example, when B_p equal to 1.40 m (Figure 6.62c) or h_p is equal to 1.00 m (Figure 6.64a),

the joint capacity is really high and its influence in the hierarchy of strength could be completely neglected.

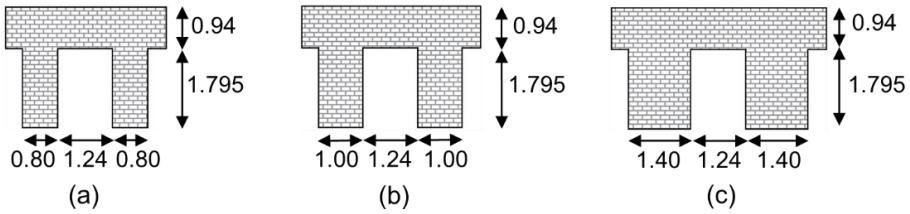

Figure 6.61. Substructures with B_p of (a) 0.80 m, (b) 1.00 m and (c) 1.40 m.

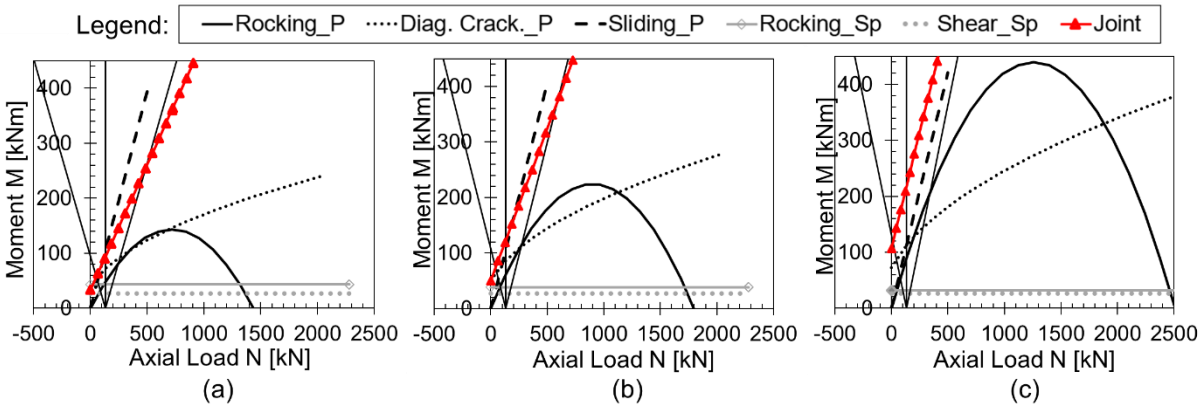

Figure 6.62. Pier M-N performance domains for subassemblies with B_p of (a) 0.80 m, (b) 1.00 m and (c) 1.40 m.

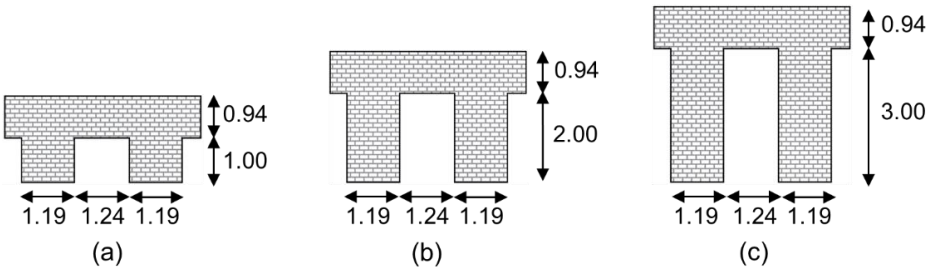

Figure 6.63. Substructures with h_p of (a) 1.00 m, (b) 2.00 m and (c) 3.00 m.

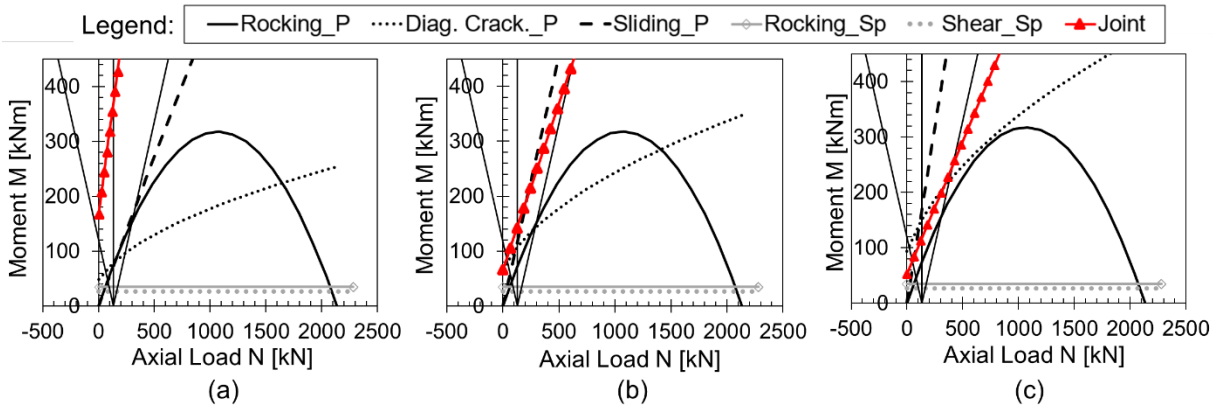

Figure 6.64. Pier M-N performance domains for subassemblies with h_p of (a) 1.00 m, (b) 2.00 m and (c) 3.00 m.

A summary of the performed parametric analyses is presented in Table 6.18, with the identification of the first failure mechanism observed in the substructures. The bold marked values in Table 6.18 refer to variations with respect to the original geometry of the PS3 substructure (in the first row, italicized).

When increasing the spandrel length L_{sp}, the failure mechanism of the substructure is dominated by the flexural behavior of the spandrel. In this case, once the total length of the substructure is increased, the variation of axial load ΔN due to the lateral load tends to decrease. For higher values of L_{sp}, the corresponding shear capacity of the spandrel increases (see Figure 6.58). Regarding the considered variations of h_{sp}, B_p and h_p, instead, the same failure mechanism observed for the PS3 substructure (i.e. starting with the shear failure of the spandrel) is identified.

The increase of h_{sp} leads to a slight increase of shear strength coupled with a large increase of flexural capacity of the spandrel (see Figure 6.60). In this case, as aforementioned, the joint capacity presents a significant increase. When the pier length B_p increases, a decrease of ΔN is observed (due to the increased length of the substructure). As expected, the flexural capacity of the piers increases, while the spandrel flexural capacity decreases (see Figure 6.62). Finally, for higher values of pier height h_p, the shear capacity of the piers (both the sliding and the diagonal cracking) increases and the joint capacity decreases (see Figure 6.64).

Table 6.18. Parametric analyses with respect to the geometry of the PS3 substructure (first row, italicized) and substructures failure mechanism (in bold are the varied parameters).

h_p [m]	B_p [m]	λ_p [-]	L_{sp} [m]	h_{sp} [m]	λ_{sp} [-]	Failure
1.795	*1.19*	*1.51*	*1.24*	*0.94*	*1.32*	*SP Shear*
1.795	1.19	1.51	**1.40**	0.94	**1.49**	*SP Rocking*
1.795	1.19	1.51	**1.60**	0.94	**1.70**	*SP Rocking*
1.795	1.19	1.51	**1.80**	0.94	**1.91**	*SP Rocking*
1.795	1.19	1.51	**2.00**	0.94	**2.13**	*SP Rocking*
1.795	1.19	1.51	**2.20**	0.94	**2.34**	*SP Rocking*
1.795	1.19	1.51	**2.50**	0.94	**2.66**	*SP Rocking*
1.795	1.19	1.51	1.24	**1.20**	**1.03**	*SP Shear*
1.795	1.19	1.51	1.24	**1.50**	**0.83**	*SP Shear*
1.795	1.19	1.51	1.24	**2.00**	**0.62**	*SP Shear*
1.795	**0.80**	**2.24**	1.24	0.94	1.32	*SP Shear*
1.795	**1.00**	**1.80**	1.24	0.94	1.32	*SP Shear*
1.795	**1.40**	**1.28**	1.24	0.94	1.32	*SP Shear*
1.795	**1.60**	**1.12**	1.24	0.94	1.32	*SP Shear*
1.795	**1.80**	**1.00**	1.24	0.94	1.32	*SP Shear*
1.00	1.19	**0.84**	1.24	0.94	1.32	*SP Shear*
1.30	1.19	**1.09**	1.24	0.94	1.32	*SP Shear*
1.50	1.19	**1.26**	1.24	0.94	1.32	*SP Shear*
2.00	1.19	**1.68**	1.24	0.94	1.32	*SP Shear*
2.30	1.19	**1.93**	1.24	0.94	1.32	*SP Shear*
2.60	1.19	**2.18**	1.24	0.94	1.32	*SP Shear*
3.00	1.19	**2.52**	1.24	0.94	1.32	*SP Shear*

SP is for Spandrel.

6.3.8 Effect of different simplified modelling strategies

In this Section the differences in the predicted capacity of the PS3 substructure resulting from the adoption of different simplified modelling strategies are evaluated.

The “strong-spandrel weak-pier” model and the “weak-spandrel strong-pier” model (see Section 3.3.3 for more details) are compared with the results obtained through the equivalent frame schematization (see Section 6.3.5). For the first case, the piers were assumed with the fixed-fixed (FF) boundary condition and two effective heights were considered: the pier height to the axis of the spandrel and the height of the opening. For the second case, the piers were assumed with cantilevered (C) boundary condition and two effective heights were considered: the full height of the substructure to the top of the spandrel and to the axis of the spandrel.

In Figure 6.65, the PS3 substructure idealised as piers and spandrel elements using the two different boundary conditions is shown. In Table 6.19 are reported the effective heights of the piers h_p and the effective heights of the system H_{eff} (identified as the height of the piers up to the contra flexure point) adopted in the simplified models.

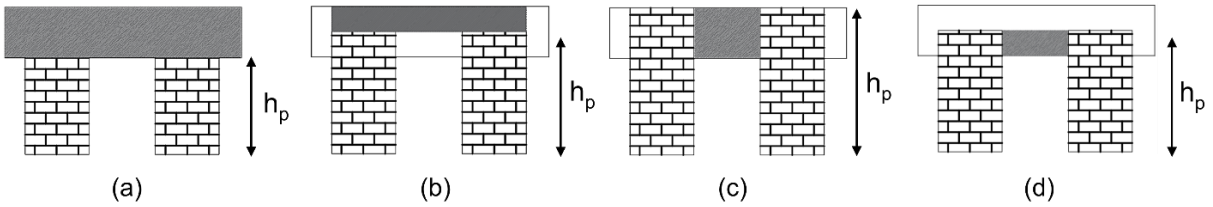

Figure 6.65. Simplified models of PS3 substructure: "strong-spandrel weak-pier" model with effective height equal to (a) the opening height and (b) the pier height to the spandrel axis, and "weak-spandrel strong-pier" model with effective height equal to (c) the full height and (d) the pier height to the spandrel axis.

Table 6.19. Piers height and effective height of the structure adopted in the simplified models.

Simplified models	Boundary conditions	Effective height	h_p [m]	H_{eff} [m]
STRONG-SPANDREL WEAK-PIER	FIXED-FIXED (FF)	Opening height	1.795	0.898
		To spandrel axis	2.265	1.133
WEAK-SPANDREL STRONG-PIER	CANTILEVERED (C)	Full height	2.735	2.735
		To spandrel axis	2.265	2.265

In Table 6.20 are reported the values of the base shear obtained for the "strong-spandrel weak-pier" and the "weak-spandrel strong-pier" models adopting the different aforementioned effective heights. In the same Table, also the ratio V_b/V_{EFM} is reported, to evaluate if the results are representative of the substructure response. In Figure 6.66 the comparison of the pushover curves obtained with the simplified models, the EF model and the experimental one is shown.

In all the configurations, the rocking was found to be the critical failure mode for the piers. The boundary conditions and the effective height of the piers strongly influence the predicted strength value, as shown in Table 6.20.

The fixed-fixed (FF) models overestimate the strength of the expected base shear obtained by the EFM: of 55% when the effective height is equal to the opening height and of 23% when the effective height is assumed to equal to the pier height up to the spandrel axis. It means that more the effective height increases, more this overestimation is reduced. This is due to the fact that the moment associated with the rocking failure has to be divided by a higher effective height, resulting in a lower base shear. Regarding the results obtained by the cantilevered (C) models, the opposite occurs. Due to the fact that the effective height of the system corresponds to the effective height of the piers when it increases the base shear decreases. In these cases, the results underestimate the expected EFM results in terms of the maximum lateral strength by 51% when the effective height is equal to the full height of the substructure and by 61% when the effective height is equal to the pier height up to the spandrel axis.

Table 6.20. Predicted base shear in the simplified models and ratio with respect to the strength obtained by the EFM.

Simplified models	Boundary conditions	Effective height	V_b [kN]	V_b / V_{EFM} [-]
STRONG-SPANDREL WEAK-PIER	FIXED-FIXED (FF)	Opening height	162.0	1.55
		To spandrel axis	128.4	1.23
WEAK-SPANDREL STRONG-PIER	CANTILEVERED (C)	Full height	53.2	0.51
		To spandrel axis	64.2	0.61

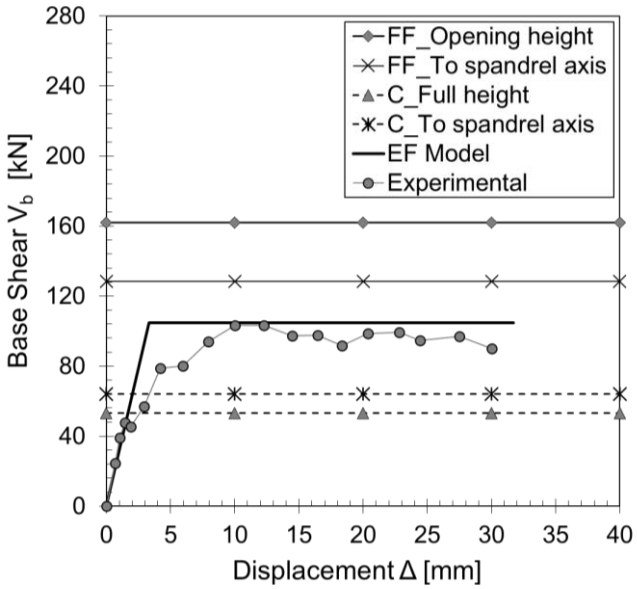

Figure 6.66. Base shear-displacement curves comparing the experimental response of the PS3 substructure with that obtained through simplified modelling strategies.

This comparison shows that although the simplified models are easy to use, they are not enough reliable and competitive with respect to the Equivalent Frame methods. This is due not only to the excessive over, or under, estimation of the global lateral strength but also to the incomplete results given in terms of the crack patterns of the structure (i.e. the spandrel behaviour is not taken into account). This aspect represents an important key point when defining the most adequate retrofit strategy. Designing a retrofit intervention means to plan the most effective solution to avert and prevent brittle failure modes, in favour of the ductile ones. For this reason, a wrong evaluation of the governing failure mode of the structure can lead to a not effective retrofit strategy and hence to significant and unsolvable consequences.

6.4 Two-storey wall

The two-storey URM wall herein analyzed is part of a full-scale building prototype (Figure 6.67a), tested at the University of Pavia, under quasi-static displacements applied to simulate dynamic load/displacement patterns. It is the Door wall (or wall D) (Figure 6.67b), extensively studied in literature (Gambarotta and Lagomarsino 1997b; Magenes and Della Fontana 1998; Grande *et al*., 2011; Sabatino and Rizzano, 2010; Siano *et al*., 2018). It is composed of two-wythe solid fired-clay brick, with a total thickness of $0.25\,\mathrm{m}$. The materials of the structure were chosen to represent the typical old urban construction in Italy. The measured compression strength of masonry was equal to $6.2\,\mathrm{MPa}$. With reference to the entire building, the plan dimensions are $6\,x\,4.4\,\mathrm{m}$ and the height is $6.4\,\mathrm{m}$. The Door wall (wall D) is the longitudinal wall, parallel to the direction of loading and disconnected from the adjacent transverse walls (called A and C), while the window wall B was connected to the transverse walls with an interlocking brick pattern around the corner).

The floors are characterized by a series of isolated steel beams, through which the vertical and horizontal loads are applied. The gravity loads were simulated with concrete blocks reaching a total added vertical load equal to $248.4\,\mathrm{kN}$ and $236.8\,\mathrm{kN}$ at the first and second floor, respectively. The application of the seismic forces was simulated by four concentrated horizontal forces applied at the floor levels, as shown in Figure 6.67a, by means of four displacement-controlled screw jacks.

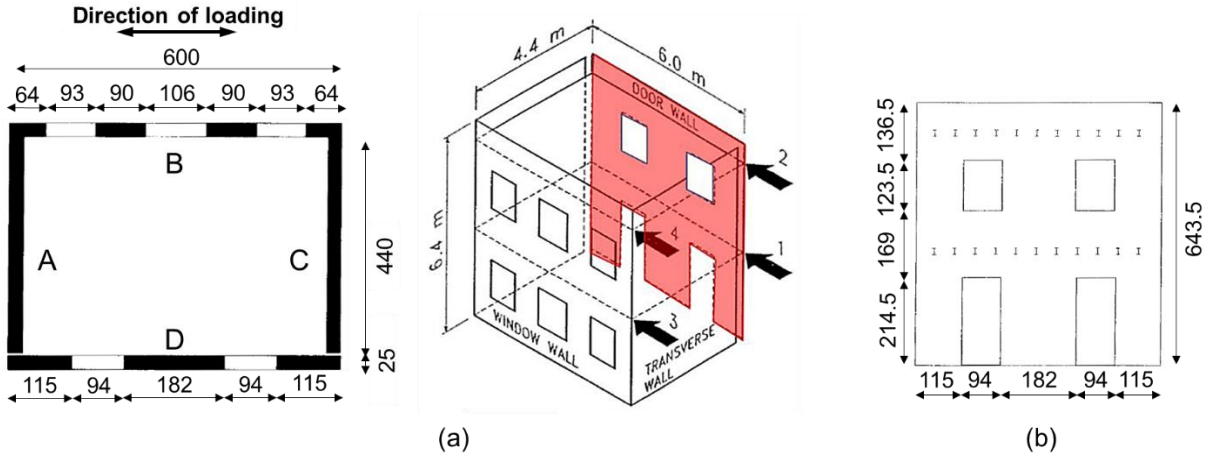

Figure 6.67. (a) Prototype plan and geometry; (b) front view of the Door wall (adapted from Magenes et al., 1995).

Due to the weak coupling of the flexible floor beams, the wall D and walls A+B+C behaved as two independent structural systems. The wall D was subjected to the forces measured in jacks 1 and 2, while the walls A+B+C to those measured in jacks 3 and 4. For this reason, in the following, it is studied only the Door wall, regardless of the rest of the building.

The cracking of the structure started at a drift of approximately 0.1% and the maximum base shear reached was approximately $150\,\mathrm{kN}$. The test was terminated when strong damage was observed in the piers and in the masonry lintels, at a maximum drift of approximately 0.4%. With reference to wall D, initially, the cracking was limited to the spandrels between the openings. This is due to the fact that the spandrels, typically characterized by no axial loads, are generally prone to early shear cracking and also because the region between openings is generally characterized by a lower joint shear strength.

Then, the reduced coupling between the piers leads to the propagation of the cracks and the shear cracking in the central piers became the failure mechanism. Further increasing the displacement leads to the shear failure of the exterior piers.

In Figure 6.68 are shown the experimental results in terms of base shear-top displacement and the crack patterns at different drift levels (Magenes *et al.*, 1995).

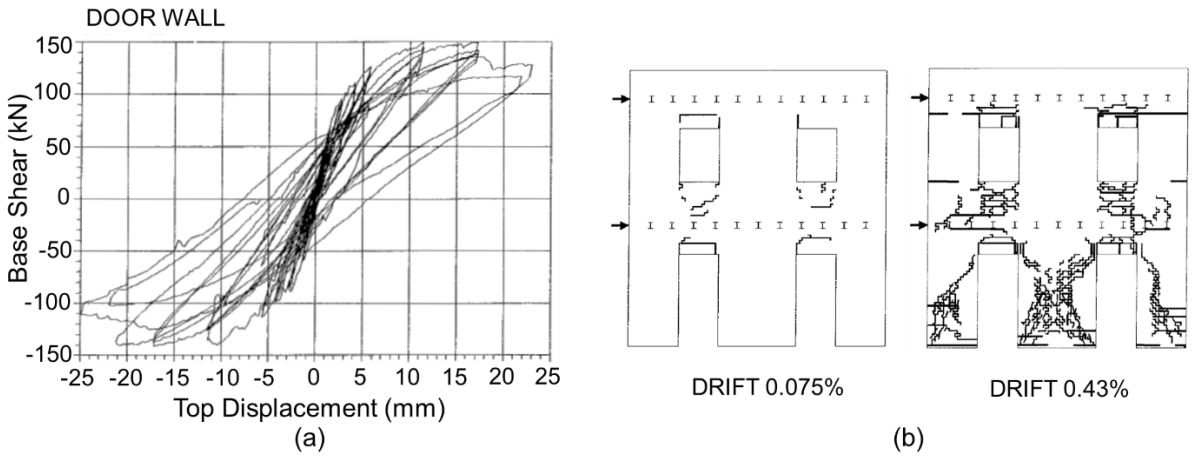

Figure 6.68. Experimental Door wall results: (a) base shear-top displacement curves and (b) crack patterns at different drift levels (adapted from Magenes et al., 1995).

From the experimental results, it was shown that the Door wall behaved as a coupled shear wall. The exterior piers, due to the overturning effect of the horizontal forces, presented diagonal shear cracking only in one direction. Indeed, an increase in the axial load in the pier on the side corresponding to the seismic force direction modifies the rocking or flexural failure mode to a shear-dominated failure.

In Sections 6.4.1 and 6.4.2 the developed Finite Element (FE) and Equivalent Frame (EF) models of the Door wall are shown, and the obtained results in terms of capacity curves and crack patterns are compared with the experimental one.

6.4.1 Numerical modelling: macro-mechanical Finite Element Model (FEM)

The Door wall was modelled in DIANA software (DIANA 2019) by adopting a FE macro-mechanical approach. The masonry is represented through continuum FEs (Q8MEM, 2D 4-node quadrilateral) using a structured mesh developed with an approximated size of 100 mm. The Total Strain Rotating Crack (TSRC) model and the Crack and Plasticity (C&P) model (see Section 6.2.1 for more details) were assumed to describe the material response. The system boundary conditions are defined as: (i) fix the X- and Y-directions at the base of the piers, (ii) adopt a master-slave node strategy to allow the application of uniform horizontal displacements at the floors level (in order to reproduce the rigid plane constraint due to the

presence of stiff steel beams at each floor) and, therefore, fix the X-direction on the master nodes at each floor, to set as equal the horizontal displacements of the nodes at the floors. In Figure 6.69 are shown the numerical model with the selected boundary conditions, the applied axial load and the horizontal displacement as well as the adopted mesh.

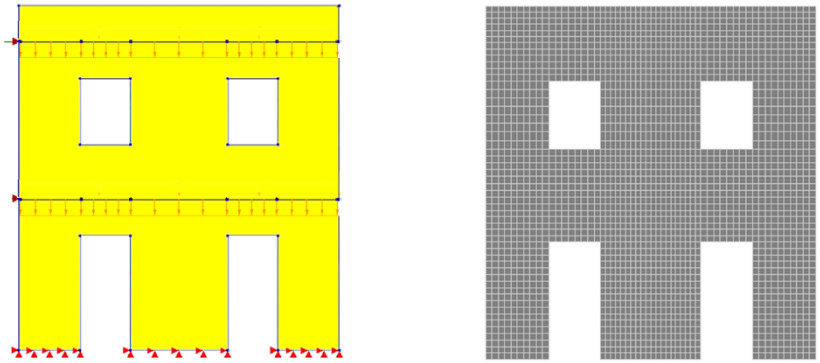

Figure 6.69. Door wall: (a) numerical FE model and (b) mesh adopted.

The adopted mechanical parameters for piers and spandrels were defined according to Sabatino and Rizzano (2010). More in detail, the following mechanical parameters were considered in the Total Strain Rotating Crack (TSRC) FE model: Young's modulus $E_m = 1800\ \mathrm{MPa}$ and shear modulus $G_m = 720\ \mathrm{MPa}$; for the tensile behavior, a linear-exponential curve with strength $f_t = 0.26\ \mathrm{MPa}$ and fracture energy $G_t = 0.015\ \mathrm{N/mm}$ (set according to Lourenço (2010), in absence of further experimental data); for the compressive behavior, a linear-parabolic curve with a strength given as $f_{cm} = 6.2\ \mathrm{MPa}$ and fracture energy $G_c = 1\ \mathrm{N/mm}$. For the Crack and Plasticity (C&P) model the same elastic properties adopted for the TSRC model were used as well as the same values of compressive and tensile strength. A cohesion equal to $1.7898\ \mathrm{N/mm^2}$, a friction angle equal to $0.5236\ \mathrm{rad}$ ($30°$) and a zero dilatancy angle (as suggested in Rots, 1997) were assumed. A detailed list of these mechanical parameters is reported in Table 6.21.

Table 6.21. Mechanical parameters for TSRC and C&P constitutive models.

E_m (N/mm²)	Young modulus		1800
v	Poisson ratio		0.25
f_{cm} (N/mm²)	Compressive strength		6.2
f_t (N/mm²)	Tensile strength		0.26
G_c (N/mm)	Compressive fracture energy		1
G^I_f (N/mm)	Tensile fracture energy		0.015
		TSRC	***C&P***
ϕ (deg)	Internal friction angle	-	30
c (N/mm²)	Cohesion	-	1.7898
ψ (deg)	Dilatancy angle	-	0

Concerning the applied loads, the vertical ones (corresponding to $248.4\,\mathrm{kN}$ at the first floor and $236.8\,\mathrm{kN}$ at the second floor) were applied as distributed forces at each floor level. The horizontal displacements were applied at the left side of the wall at each floor level, following an inverse triangular distribution: displacements of $21\,\mathrm{mm}$ and $10.29\,\mathrm{mm}$ were applied at the first and second floor, respectively.

The prediction of the envelope curve of the cyclic base shear-horizontal displacement response was achieved through nonlinear static (pushover) analysis. The experimental and numerical crack patterns, as well as the comparison of the corresponding global response curves (by depicting the total base shear versus the horizontal displacement measured at the second floor), are presented in Figures 6.70 and 6.71.

It can be observed that the obtained FE numerical pushover curves are in good agreement with the experimental envelope curve. Regarding the failure mechanisms, with the TSRC model, the shear failure of the central pier at the base is not read. The C&P, instead, is able to grasp the shear failure of the central and right piers at the base, as highlighted in Figure 6.71. With reference to the failure mechanisms of the spandrels, both models showed severe cracks in those weak regions. The C&P model is the more suitable to catch the shear failure mechanism that can occur in the structure. This arises from the adoption of a plasticity model that requires specific parameters to define the shear behaviour.

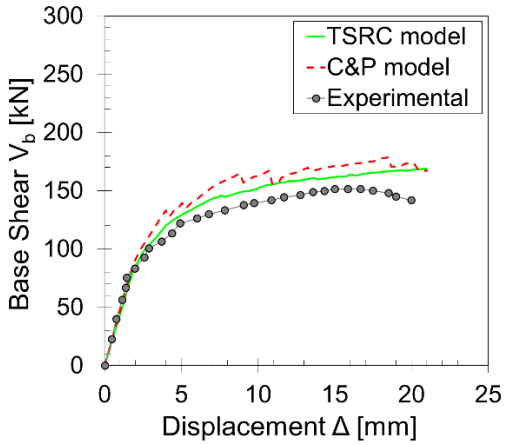

Figure 6.70. Door wall results: FE numerical capacity curves against experimental envelope.

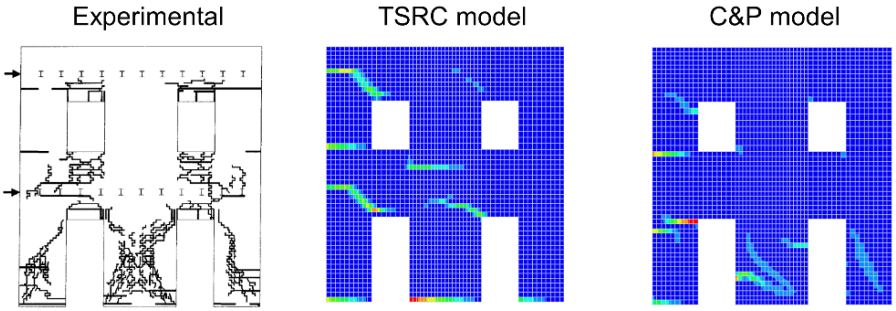

Figure 6.71. Door wall results: experimental and (FE) numerical crack patterns at the ultimate displacement.

6.4.2 Numerical modelling: Equivalent Frame Model (EFM)

The Door wall was modelled in 3MURI software (Lagomarsino *et al*., 2013) by adopting an Equivalent Frame Model (EFM). In this context, the adopted calculation model operates within the framework of the three-dimensional EFM approach, in which the walls are interconnected by horizontal floor diaphragms. It is inspired by a “box-like” conception of the masonry structure according to which the load-bearing structure, with reference to the vertical and horizontal actions, is identified by the walls and the floors. The formers are the load-bearing elements while the latter, in addition to distributing the vertical loads on the walls, are considered as in-plane stiffening elements (modelled as orthotropic membrane elements), on which depend the distribution of the horizontal actions between the walls. The floor elements are characterized by parameters that define the connection that the floor

exerts between nodes in the wall plane, as well as the shear stiffness of the floor itself, which governs the distribution of the horizontal actions between the different walls. The reference finite element considered is the plane element, in a plane stress state.

According to the frame representation, each wall of the building is divided into elements in which is concentrated the deformability and the non-linearity of the response. These elements are the piers and the spandrels, connected by pier-spandrel joints, considered as infinitely rigid portions. The masonry elements are modelled as non-linear beam elements, characterized by six degrees of freedom, by a limited strength and stiffness degradation in the non-linear phase and by an ultimate displacement capacity based on a limited drift. The elastic behavior of the non-linear beam elements, adopted for piers and spandrels, is directly determined starting from the calculation of the shear and bending stiffness contributions, that depend on the mechanical and geometric properties.

The nonlinear behavior is activated when a nodal force reaches its own maximum value defined as the minimum among the following strength criteria: rocking, diagonal cracking-shear and sliding-shear. More in detail, for the piers, are considered: i) the condition of in-plane rocking failure associated with the crushing of the masonry at the compressed edge of the extreme sections; ii) the condition of sliding failure due to the formation of horizontal cracks in the mortar joints that can become sliding planes; iii) the condition of diagonal cracking failure associated to the formation and the development of diagonal cracks in the panel. Regarding the spandrels, the 3MURI software has implemented the indications of CNTC19 (2019). According to these, the spandrels can be considered as piers rotated by 90 degrees if their axial load is known. On the contrary, if the axial load is unknown, an equivalent tensile strength, due to interlocking phenomena, can be calculated to define the rocking response. For the shear strength, it can be calculated by multiplying the thickness and the height of the spandrel section by the masonry initial shear strength at zero compressive stress.

It is important to underline that the non-linear beam element is based on a non-linear correction, starting from the elastic prediction, made by comparing the stresses with the strength limits consequent to the above criteria. Then, if this limit is exceeded, it is carried out an appropriate redistribution of the characteristics of shear stress and bending moment at the ends, in such a way as to ensure the equilibrium of the element itself.

A crucial step in the idealization of the frame wall is represented by the identification of the geometry of the portions that can be schematized as rigid and those in which are concentrated the non-linearity (piers and spandrels). In this regard, neither in the literature nor in the Codes are univocally recognized criteria for carrying out this idealization. The 3MURI software proposes an automatic mesh generation algorithm (defined starting from empirical rules based on the damage observed after seismic events) which, however, can be arbitrarily modified by the user when more appropriate alternative criteria are recognized.

The calculation model allows to carry out linear and non-linear static analyses for the verification of safety against ordinary and seismic actions.

The plan and the mesh of Door wall adopted in the software 3MURI are shown in Figure 6.72. It is observed that the mesh was modified from the automatic one in order to be more similar to the Dolce's rule definition.

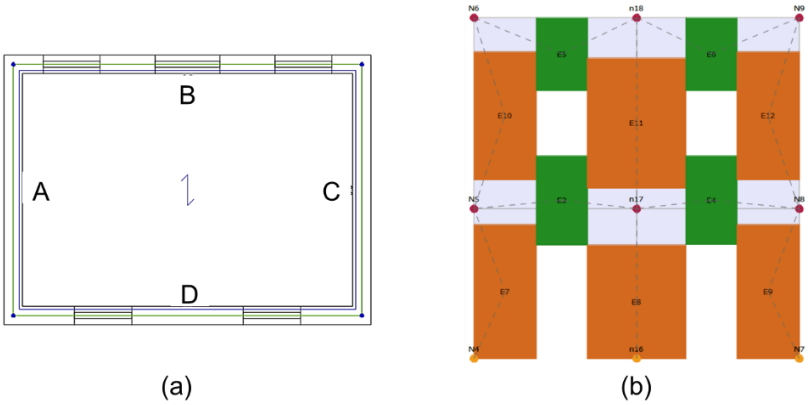

Figure 6.72. Door wall: (a) plan of the structure and (b) mesh adopted according to the EFM.

The adopted mechanical parameters for the piers and the spandrels, according to Sabatino and Rizzano (2010), are: Young modulus $E_m = 1800\ \mathrm{MPa}$ and shear modulus $G_m = 720\ \mathrm{MPa}$; compressive strength $f_{cm} = 6.2\ \mathrm{MPa}$ (the horizontal compressive strength f_{hm} was assumed to equal to f_{cm} as addressed in Beyer and Dazio, 2012); initial shear strength at zero compression $f_{v0} = 0.12\ \mathrm{MPa}$; brick tensile strength $f_{bt} = 1.22\ \mathrm{MPa}$; friction coefficient $\mu = 0.58$. A complete list is reported in Table 6.22.

Table 6.22. Mechanical parameters for EFM model.

E_m (N/mm²)	Young modulus	1800
G_m (N/mm²)	Shear modulus	720
f_{cm} (N/mm²)	Compressive strength	6.2
f_{v0} (N/mm²)	Initial shear strength at zero compressive stress	0.12
f_{bt} (N/mm²)	Brick tensile strength	1.22
μ	Friction coefficient	0.58

For the spandrels, it was considered the tension contribution due to the interlocking phenomena at the spandrels-end. This assumption refers to the Cattari and Lagomarsino (2018) formulation, which leads to define an equivalent tensile strength. To its calculation, an interlocking parameter ($\phi = 2\Delta_y/\Delta_x$, where Δ_y and Δ_x are the height and the length of the bricks, respectively) equal to 0.92 was considered.

Concerning the loads, the axial loads were applied at floors level, as permanent load, to obtain vertical loads equal to $248.4\,\mathrm{kN}$ and $236.8\,\mathrm{kN}$ at the first and at the second floor, respectively. The diaphragms on each floor are assumed as infinitely stiff. Through nonlinear static (pushover) analysis, the base shear-horizontal displacement curve and the prediction of the failure mechanism of the wall were defined and compared with the experimental and the numerical (FE) ones, obtained in Section 6.4.1. These comparisons are presented in Figures 6.73 and 6.74.

It can be shown that the pushover curve obtained through the EFM is in good agreement with the experimental envelope curve, reaching approximately the same maximum base shear. Regarding the failure mechanisms, with the EFM, the shear failure of the spandrels at the first and the second floors are achieved as well as the diagonal cracking shear failure of the piers at the base, as expected by the experimental results.

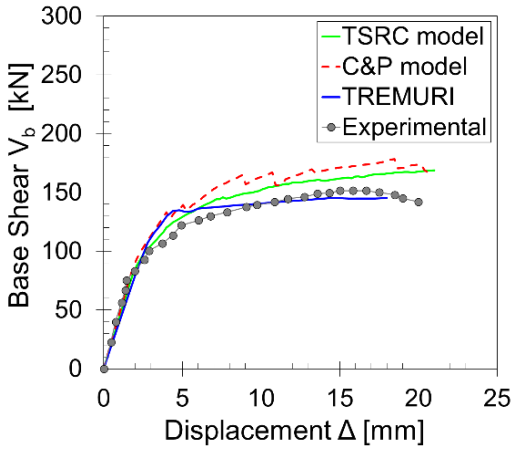

Figure 6.73. Door wall results: FE and EFM numerical capacity curves against experimental envelope.

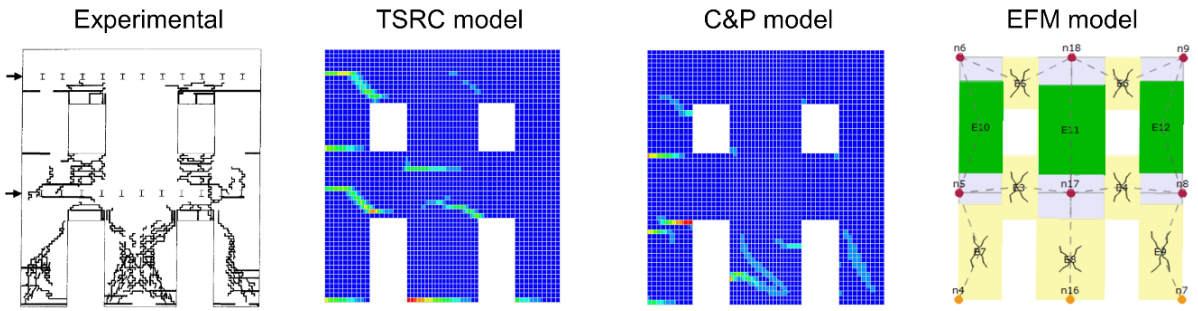

Figure 6.74. Door wall results: experimental and FE and EFM numerical crack patterns at the ultimate displacement.

6.4.3 Geometric and mechanical data for SLaMA-URM method

The SLaMA-URM method is herein validated against the experimental case study and the numerical simulation results, described in Sections 6.4.1 and 6.4.2.

The geometry of the Door wall was defined according to the EF model discretization (Figure 6.75). The rigid offsets are indicated by thick lines, whose lengths were evaluated by the formulation proposed by Dolce (1991) for the piers and considering the clear lengths as the flexible region of the spandrels. Assuming the thickness of both piers and spandrel as $t_p = 0.25$ m, the length and the clear and effective height of the piers (B_p, h_p and $h_{p,eff}$), as well as the length and the height of the spandrels (L_{sp} and h_{sp}), are reported in Table 6.23, with reference to the numbering of piers (P) and spandrels (SP) in Table.

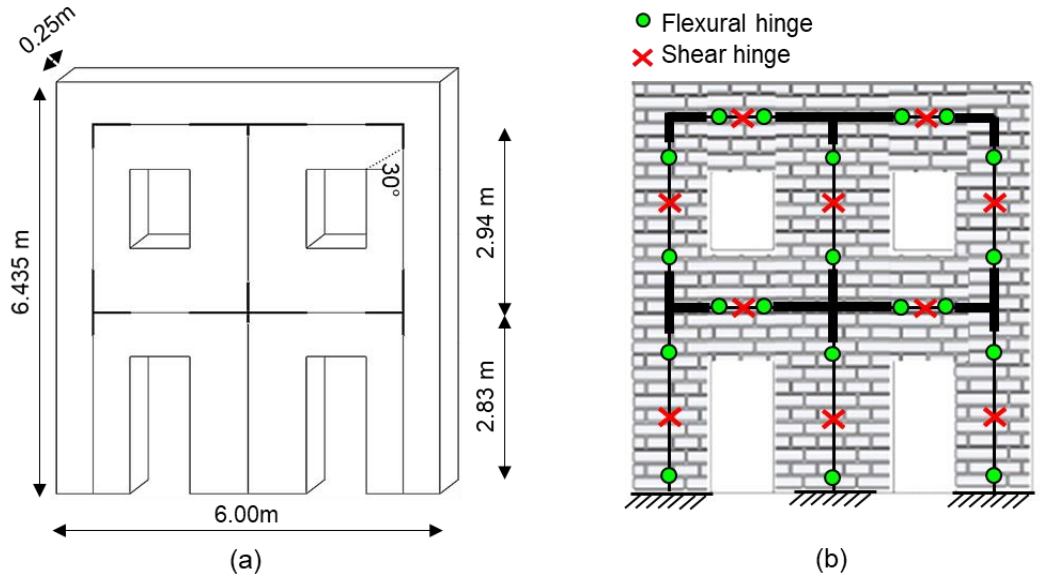

Figure 6.75. Schematic representation and geometry of the Door wall through EF model: (a) geometry and (b) distribution of the flexural and shear plastic hinges.

Table 6.23. Geometric parameters of piers and spandrels of the Door wall.

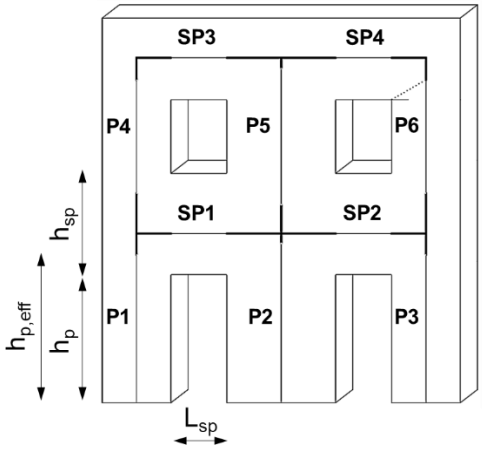

Structural element		B_p [m]	h_p [m]	$h_{p,eff}$ [m]	L_{sp} [m]	h_{sp} [m]
PIERS	**P1**	1.15	2.145	2.532		
	P2	1.82	2.145	2.706		
	P3	1.15	2.145	2.532		
	P4	1.15	1.235	2.109		
	P5	1.82	1.235	2.460		
	P6	1.15	1.235	2.109		
SPANDRELS	**SP1**				0.94	1.69
	SP2				0.94	1.69
	SP3				0.94	1.365
	SP4				0.94	1.365

The masonry mechanical parameters adopted in the analytical model were those reported in Sabatino and Rizzano (2010): i.e. a masonry compressive strength f_{cm} of $6.2\ \mathrm{MPa}$ (the horizontal compressive strength f_{hm} was assumed to equal to f_{cm}, as addressed in Beyer and Dazio, 2012); a brick tensile strength f_{bt} of $1.22\ \mathrm{MPa}$ and a friction coefficient μ of 0.58. Moreover, it was assumed a masonry Young's modulus E_m and shear modulus G_m equal to $1800\ \mathrm{MPa}$ and $720\ \mathrm{MPa}$, respectively. The tensile strength f_t was considered equal to $0.18\ \mathrm{MPa}$, and the initial shear strength at zero compressive stress f_{v0} was estimated as

$f_t/1.5$ (NTC 2018), i.e. equal to $0.12\,\mathrm{MPa}$. The vertical axial loads were applied as concentrated vertical forces on each pier.

6.4.4 Analysis at component level

In the following Sections, are defined the flexural and shear capacity of piers and spandrels at the component level, in terms of moment-rotation curves and moment-axial load (M-N) domains.

6.4.4.1 Moment-rotation curves

The flexural capacity of the piers is defined from an elastic-perfectly plastic stress-strain relation in compression and no-tensile resistance (EPP-NTR) assumption. While for the spandrels, an elastic-perfectly plastic (EPP) stress-strain in compression and resistant in tension (TR) model is considered (adopting an equivalent tensile strength f_{tu} related to the interlocking effect, as suggested in Cattari and Lagomarsino, 2008). Assuming the height and the width of the bricks equal to $\Delta_y = 76\,\mathrm{mm}$ and $\Delta_x = 110\,\mathrm{mm}$, respectively, and considering the 65% of the mean compressive stress σ acting on the adjacent pier section (Cattari and Lagomarsino, 2008), the equivalent tensile strength results in $f_{tu} = 0.22\,\mathrm{MPa}$ for the spandrels at the first floor and in $f_{tu} = 0.13\,\mathrm{MPa}$ for the spandrels at the second floor.

In the EPP model, the compressive peak ε_{yc} and ultimate ε_{uc} strains equal to 0.002 and 0.0035, respectively, were adopted, hence considering a ductility in compression equal to $\mu_{\varepsilon c} = \varepsilon_{uc}/\varepsilon_{yc} = 1.75$. For the spandrels, the tensile peak ε_{yt} and ultimate ε_{ut} strains equal to 0.000018 and 0.0009, respectively, were adopted, considering a ductility in tension equal to $\mu_{\varepsilon t} = \varepsilon_{ut}/\varepsilon_{yt} = 50$. At this first stage, no axial load in the spandrels is considered.

The same MBA formulation (Pampanin *et al*., 2001) used for the PS3 substructure (Section 6.3.3.1) is herein adopted for the piers and spandrels of the Door wall.

For the spandrels, the moment-capacity curve is defined according to the EPP-TR model characterized by limited ductility in compression ($\mu_{\varepsilon c} = 1.75$) and unlimited ductility in tension, i.e. compression governed failure (EPP-TR-CF).

Regarding the shear strength of the piers, the Turnšek and Cačovic (Turnšek and Cačovic 1971) criterion is adopted for diagonal cracking, while for the spandrels, the shear strength is calculated considering the masonry shear strength in absence of axial load (as suggested in NTC 2018).

The piers and the spandrels strength thresholds are expressed in terms of moment capacity calculated from the pier (or spandrel) shear resistance V_s and the pier (or spandrel) cantilever length L_{cant}, as $M = V_s L_{cant}$.

It is worth noting that the capacity and the resulting failure mechanism of the piers are dependent on the acting axial load that results from the gravity load N and the effect of axial load variation $\pm \Delta N$, due to the coupling effect of the spandrels during the lateral sway (Figure 6.76). The variation of the axial load ΔN is obtained by the sum of the spandrels shear resistance V_{sp} at each floors, given as the minimum of their flexural and shear strength capacity. Applying the equivalent seismic force from left to right, means that the right piers (P3 and P6) are subjected to an increase of axial load ($+\Delta N$), while the left piers (P1 and P4) are subjected to a decrease of axial load ($-\Delta N$).

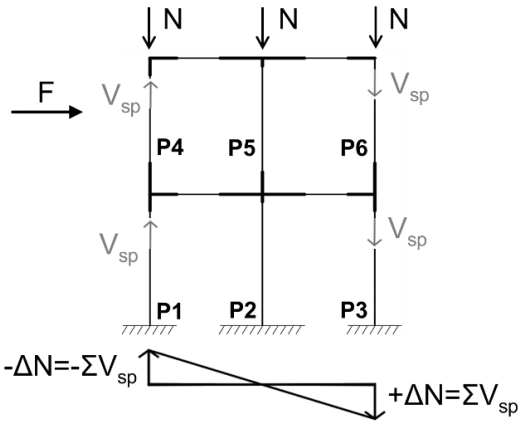

Figure 6.76. Door wall subjected to horizontal and gravity loads with axial load variation.

The flexural and the shear strength thresholds for piers and spandrels are reported in Table 6.24 and shown in Figures 6.77 and 6.78 within moment-rotation diagrams. It is observed that a diagonal cracking shear failure is expected to occur in the piers P2 and P3, due to the higher axial load deriving from the coupling effect of the spandrels. It is observed that the pier P1 shows a flexural-shear mixed failure. Nevertheless, a shear brittle failure

mechanism, which disregards the development of flexural failure, may be conservatively assumed. For the other piers, a rocking or flexural behaviour is expected to occur. In the spandrels on the first and second floor, a shear brittle failure mechanism is obtained.

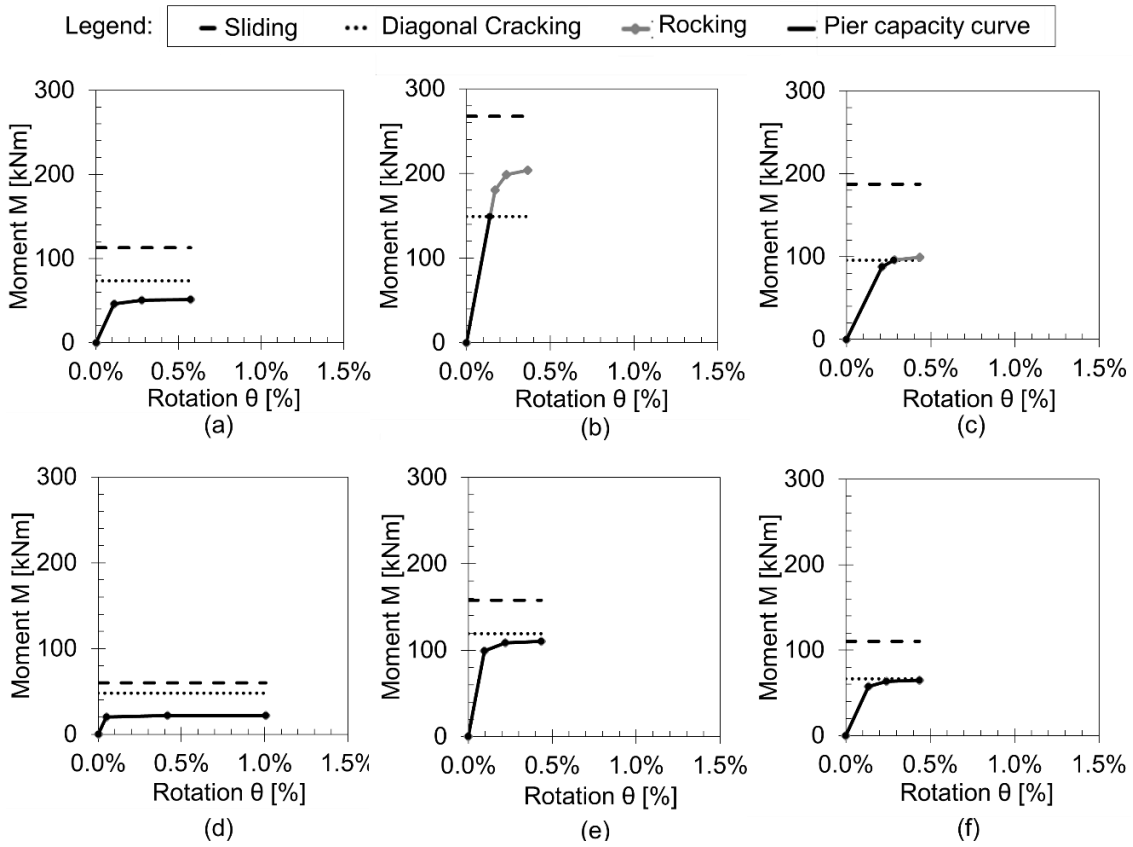

Figure 6.77. Flexural and shear strength thresholds at the moment-rotation diagram for piers: (a) P1, (b) P2, (c) P3, (d) P4, (e) P5 and (f) P6.

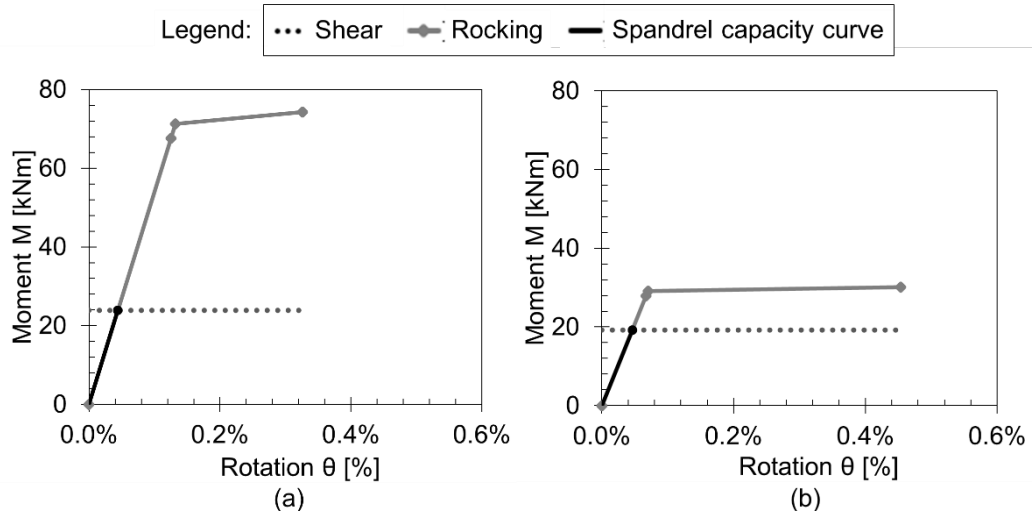

Figure 6.78. Flexural and shear strength thresholds at the moment-rotation diagram for spandrels: (a) SP1 and SP2 and (b) SP3 and SP4.

Table 6.24. Moment and rotation values at decompression, peak and ultimate conditions, for spandrels (EPP-TR-TF model) and piers (EPP-NTR model).

Structural element		θ_{dec} [%]	M_{dec} [kNm]	θ_p [%]	M_p [kNm]	θ_u [%]	M_u [kNm]	Failure mechanism
PIERS	**P1**	0.110	45.87	0.277	50.38	0.574	51.19	*ROCKING*
	P2	0.140	149.35	0.140	149.35	0.140	149.35	*DIAGONAL CRACKING*
	P3	0.210	87.61	0.279	95.49	0.279	95.49	*DIAGONAL CRACKING*
	P4	0.047	20.23	0.414	21.79	1.008	21.93	*ROCKING*
	P5	0.095	99.20	0.221	108.60	0.435	110.06	*ROCKING*
	P6	0.134	57.44	0.241	63.22	0.436	64.55	*ROCKING*
SPANDRELS	**SP1**	0.044	23.84	0.044	23.84	0.044	23.84	*SHEAR*
	SP2	0.044	23.84	0.044	23.84	0.044	23.84	*SHEAR*
	SP3	0.046	19.25	0.046	19.25	0.046	19.25	*SHEAR*
	SP4	0.046	19.25	0.046	19.25	0.046	19.25	*SHEAR*

6.4.4.2 Moment-axial load (M-N) domains

The Moment-Axial load (M-N) interaction curves of piers and spandrels are obtained through sectional equilibrium equations, adopting the EPP-NTR model for the piers and the compression governed (EPP-TR-CF) model for the spandrels, both with ductility in compression equal to $\mu_{\varepsilon c} = 1.75$. In Figure 6.79 the obtained M-N domains are reported.

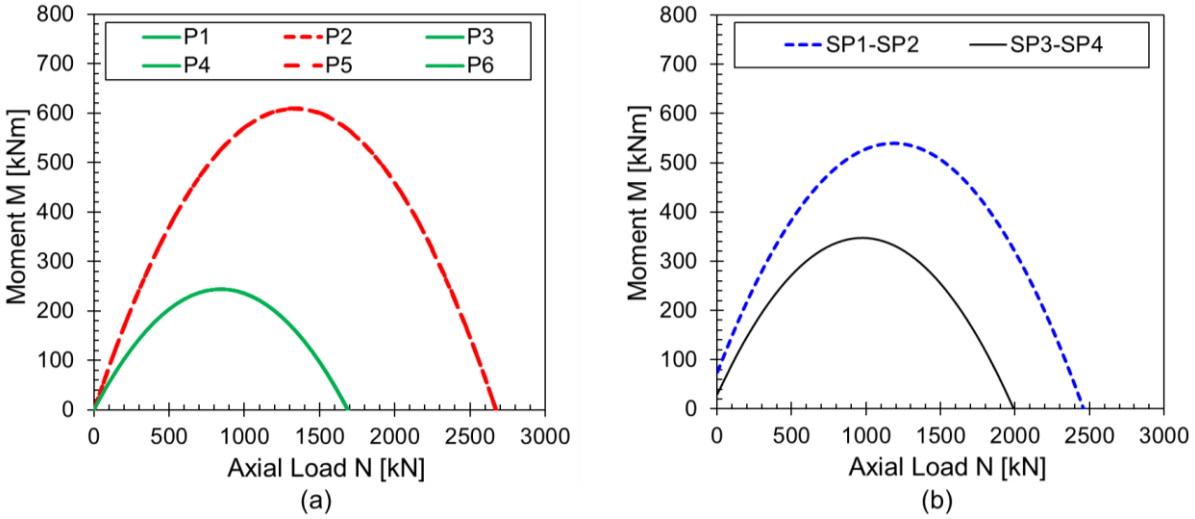

Figure 6.79. M-N domains of: (a) piers (P1-P6) and (b) spandrels (SP1-SP4).

As expected, the piers P1, P3, P4 and P6 (that have the same length B_p) have the same M-N domain. For the same reason, this happens also for the piers P2 and P5. Moreover, from the comparison it can be seen that the P2 and P5 piers have a bigger domain, that is due to their bigger length ($B_p = 1.82$ m, against the $B_p = 1.15$ m of the other piers). Regarding the M-N domains of the spandrels, the SP1 and SP2 have the same domain, as well as the SP3 and SP4. As for the piers, this is due to the same height h_{sp}. The spandrels on the first floor (SP1 and SP2) have a bigger M-N domain, being characterized by a higher height ($h_{sp} = 1.69$ m, against the $h_{sp} = 1.365$ m of the spandrels at the second floor). Due to the fact that the first floor spandrels have a higher axial load stress σ acting on the adjacent pier section, the equivalent tensile strength is higher ($f_{tu} = 0.22$ MPa, against the $f_{tu} = 0.13$ MPa of the spandrels at the second floor), and hence the moment capacity at zero axial load in the M-N domain is higher ($M_{N=0} = 74.19$ kNm, against the $M_{N=0} = 30.14$ kNm of the spandrels at the second floor).

6.4.5 Analysis at subassembly level

At this stage of analysis, the evaluation of the hierarchy of strength between the structural components of a subassembly is defined, comparing the equivalent bending moment in the pier M-N performance domains.

In Figure 6.80 are shown and numbered the subassemblies of the structure. As observed, the subassemblies 1 and 3 are of type “exterior”, and therefore are characterized by a “two-to-one” (number of piers vs. spandrels connecting into the joint) moment ratio; the subassemblies 4 and 6 are of type “knee”, and therefore are characterized by a “one-to-one” moment ratio; the subassembly 2 is of type “interior”, and therefore is characterized by a “two-to-two” moment ratio; the subassembly 5 is of type “tee”, and therefore is characterized by a “one-to-two” moment ratio.

The axial load variation on the piers, due to the coupling effect of the spandrel during the lateral sway, is introduced in the M-N domain, according to NZSEE guidelines (NZSEE 2017a) as: $\Delta N = \pm \frac{2H}{3L} F$, where H and L are the height and the length of the substructure, respectively, and F represents the equivalent seismic load assumed to be applied at $2/3$ of H. It is observed that for the subassemblies at the first floor the variation of the axial load is calculated assuming H equal to the total frame height ($H = 5.77\ \mathrm{m}$), while for those at the second floor, it is calculated assuming H equal to that of the second floor ($H = 2.94\ \mathrm{m}$).

Applying the equivalent seismic force from left to right, the right piers (P3 and P6) are subjected to an increase of axial load ($+\Delta N$) while the left piers (P1 and P4) to a decrease of it ($-\Delta N$). Regarding the central piers (P2 and P5), assuming a linear distribution of the axial load variation, they are subjected only to the gravity axial load, because of $\Delta N = 0$. In the M-N performance domains, the intersection of the axial load variation with the URM components capacity curves determines the sequence of failure events.

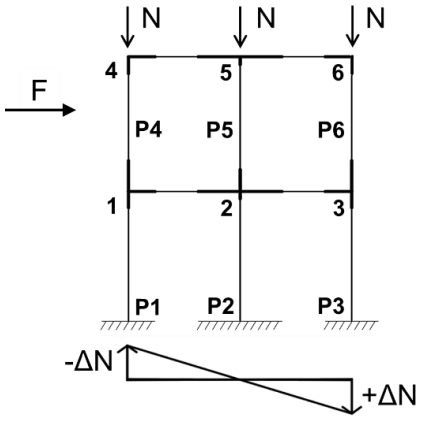

Figure 6.80. Numbering of the Door wall subassemblies.

The M-N performance domains of all the piers are shown in Figure 6.81. The critical failure event in the right, left and central subassemblies are shown in Figure 6.82.

As observed, the failure event that characterized all the subassemblies is the shear (diagonal cracking) failure of the spandrel, at different equivalent pier moment values: $M_{p,eq} = 11.91\ \mathrm{kNm}$ for the subassemblies 1 and 3; $M_{p,eq} = 23.83\ \mathrm{kNm}$ for the subassembly 2; $M_{p,eq} = 19.25\ \mathrm{kNm}$ for the subassembly 4 and 6; $M_{p,eq} = 38.49\ \mathrm{kNm}$ for the subassembly 5.

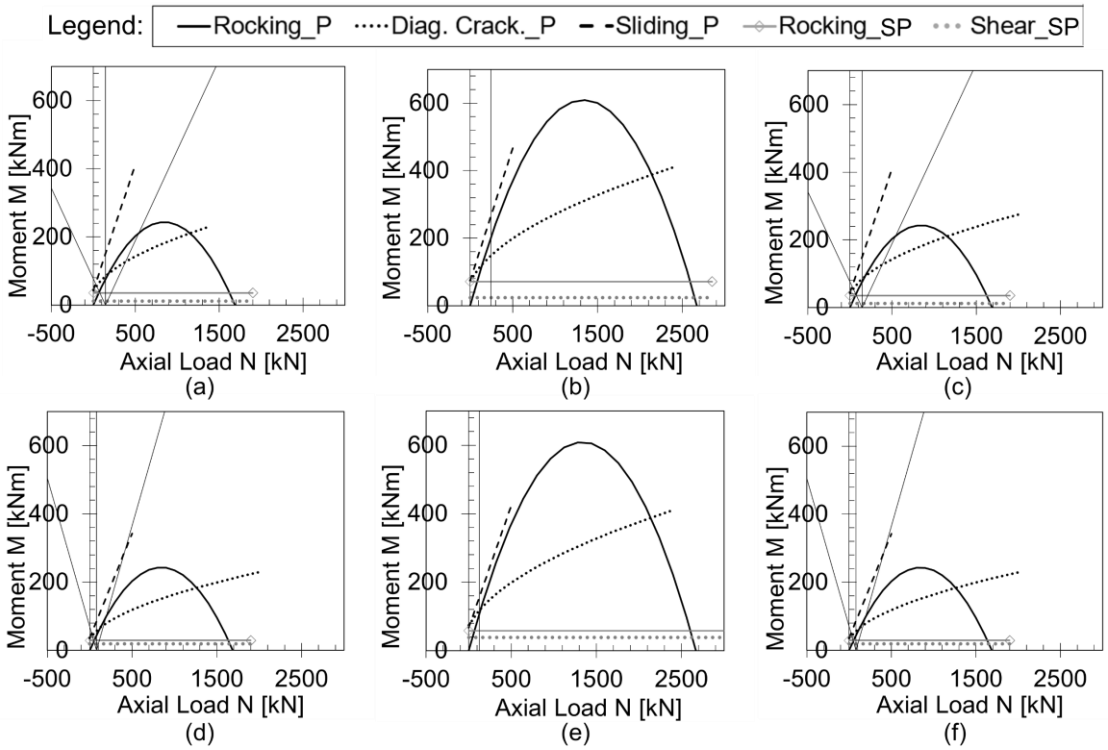

Figure 6.81. M-N performance domain of the subassembly: (a) 1, (b) 2, (c) 3, (d) 4, (e) 5, (f) 6.

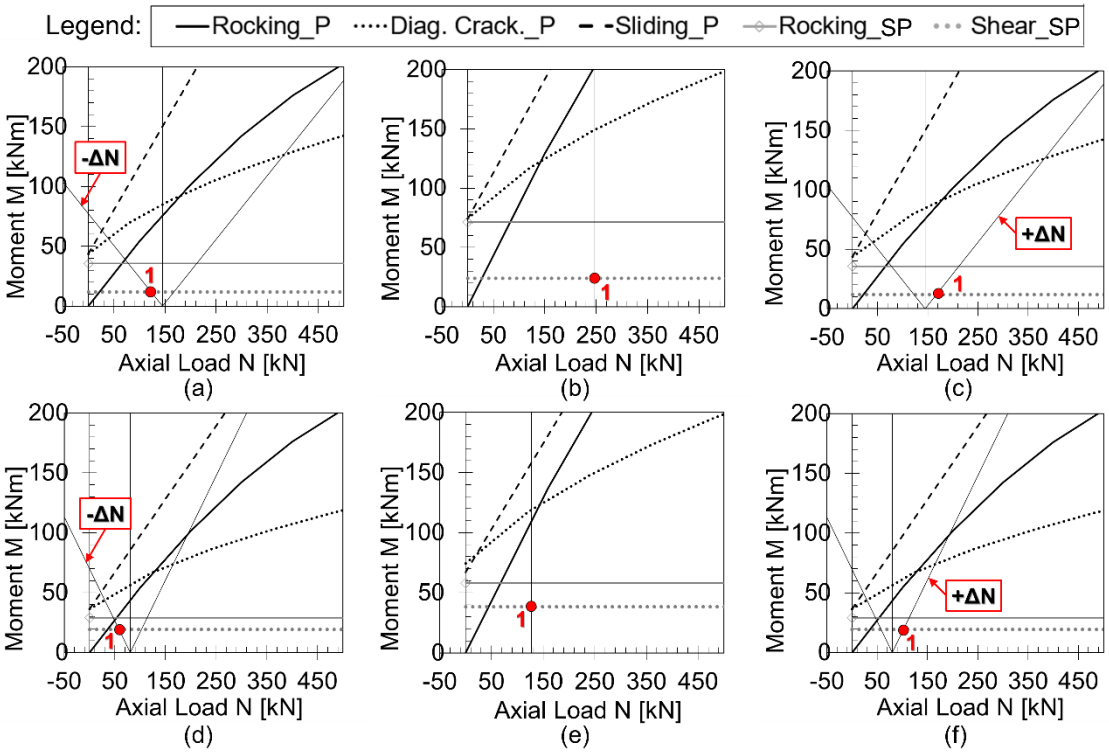

Figure 6.82. Zoom of the M-N performance domains, highlighting the critical failure event (●) according to the push direction load, of the subassembly: (a) 1, (b) 2, (c) 3, (d) 4, (e) 5, (f) 6.

6.4.6 Analysis at In-Plane global level

Starting from the hierarchy of strength in each subassembly highlighted in Section 6.4.5, the "mixed sideway" mechanism was defined. This mechanism is characterized by the shear failure of the spandrels and by the diagonal cracking of the piers P2 and P3 at the base and the rocking of the pier P1 at the base. The overturning moment OTM is calculated using a global equilibrium approach by including two contributions (see Figure 6.83a): (1) the bending moment at the base of the piers ($M_{p1} + M_{p2} + M_{p3}$) and (2) the push-pull overall moment due to the coupling of shear forces at the spandrels-end (V_{sp}) (a rocking mechanism). The base shear force V_b is calculated by dividing the OTM by the effective height of the structure H_{eff}, defined, as assumed in Sullivan *et al*. (2012), through the parameter β_F, that results equal to 0.61 and the ratio $H_{eff}/H = 0.863$. The H_{eff} results equal to $4.98\,\mathrm{m}$, the OTM results equal to $726.4\,\mathrm{kNm}$, and, as a consequence, the base shear (given by the ratio OTM/H_{eff}) is $145.9\,\mathrm{kN}$.

The "yield" Δ_y and ultimate Δ_u displacements of the frame at the effective height H_{eff} are calculated from the minimum "yield" $\theta_{y,min}$ and ultimate $\theta_{u,min}$ drift. The predicted shear mechanism (brittle failure) of the spandrel at the first floor occurs first because its drift is the minimum "yield" drift ($\theta_{y,min} = 0.044\%$), and hence the lower displacement ($\Delta_y = 2.2\ \mathrm{mm}$, marked with an "X" in Figure 6.83b). Since it is a brittle failure mode, it would also identify the ultimate drift (or displacement), but by assuming that the structure is still able to withstand lateral load, the ultimate displacement occurs up to a drift of $\theta_u = 0.27\%$ (or Δ_u of $18.8\ \mathrm{mm}$), that corresponds to the shear failure of the pier P6.

As already discussed for the PS3 substructure, a refined curve can be obtained and it is shown in Figure 6.83b. More in detail, considering the "yield" condition, the OTM was recalculated, according to the schematization in Figure 6.83a, at a drift of $\theta_{y,min} = 0.044\%$. In correspondence with this value, it was found an overturning moment equal to $OTM = 524.4\ \mathrm{kNm}$ and a base shear equal to $105.6\ \mathrm{kN}$.

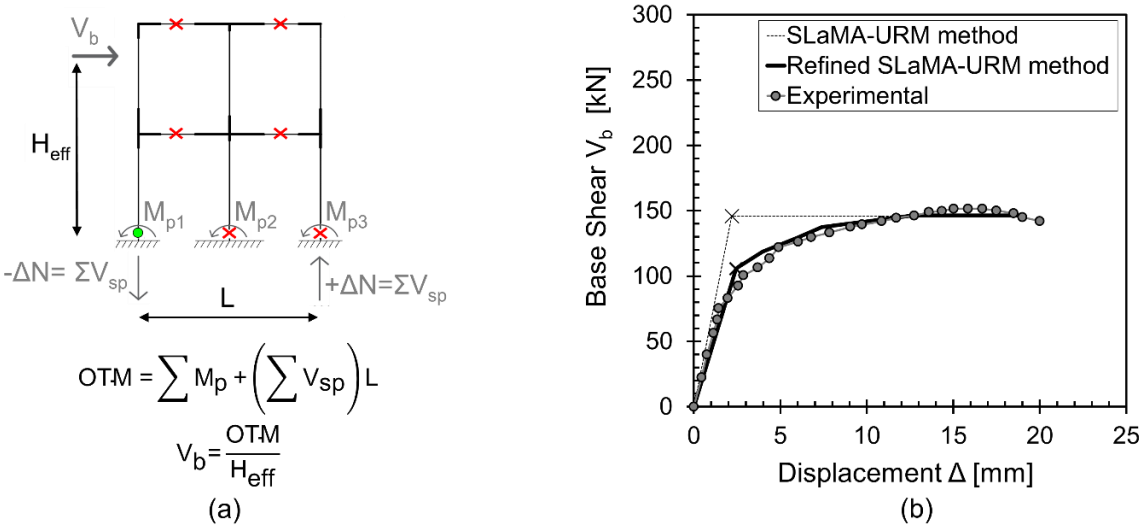

Figure 6.83. Door wall global mechanism analysis: (a) schematization for the calculation of overturning moment OTM and base shear V_b; (b) analytical curves from the "standard" and refined SLaMA-URM method.

As observed in Figure 6.84, the refined curve is in better agreement with the experimental and the numerical ones, since it grasps better the yield displacement. To quantify the refinement with respect to the "standard" curve, differences in terms of dissipated energy (i.e. the area under the curve) for both curves with respect to the

experimental one were calculated. It is obtained that the standard analytical curve and the refined one have differences of 13% and 5%, respectively. In Figure 6.85 is shown the comparison in terms of expected crisis mechanisms of the substructure for the analytical, numerical and experimental approaches. As it is observed, the crack patterns highlighted through the SLaMA-URM method are more suitable than the numerical ones, catching indeed also the shear failure of the spandrels. Hence, this method, even if it is more simplified than a finite element analysis, in this case, can obtain more reliable results.

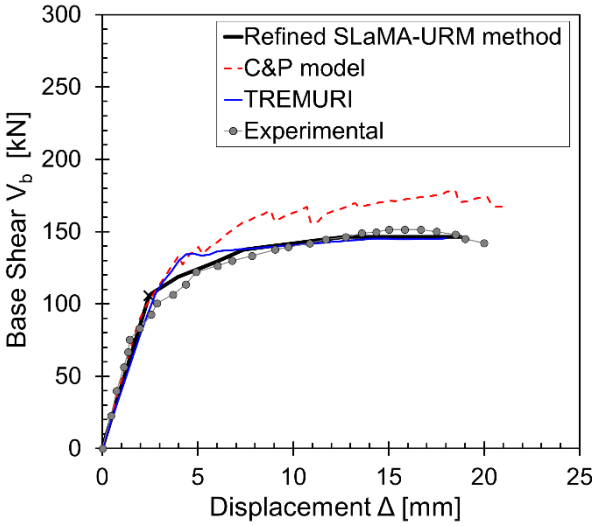

Figure 6.84. Experimental, numerical (with C&P model and EFM model) and analytical (refined) responses in terms of capacity curves.

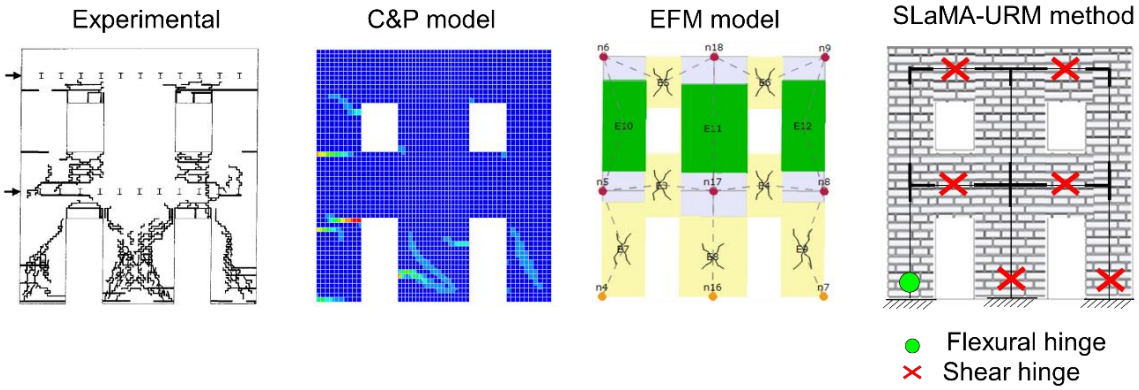

Figure 6.85. Experimental, numerical (with C&P model and EFM model) and analytical (refined) responses in terms of crack patterns.

6.5 Parametric analysis

In this Section, the SLaMA-URM procedure is applied to a set of frame structure case studies derived from the Door wall by varying the number of bays and the number of levels. For each of them, the resulting non-linear capacity curves were compared to the EFM results of the numerical Pushover analyses, performed in 3MURI software, in order to further validate and evaluate the accuracy of the SLaMA-URM method.

The walls considered are characterized by two up to four bays and by two up to four levels (Figure 6.86).

The reference wall (2-bays 2-levels) has the same geometry and mechanical parameters of the Door wall analyzed in Section 6.4. The other frames were modelled starting from this one. More in detail: the height of the first floor is equal to $2.83\ m$, while the upper ones have a height equal to $2.94\ m$; the interior piers have length equal to $B_p = 1.82\ m$ while the exterior ones have $B_p = 1.15\ m$; the effective height of the piers was defined according to Dolce's rule; the height of the spandrels h_{sp} at the upper floor is equal to $1.37\ m$, while for those at the intermediate floors it is equal to $1.69\ m$; the length of all the spandrels is equal to $L_{sp} = 0.94\ m$. Refer to Section 6.4.3 for the adopted mechanical parameters of the piers and the spandrels in the SLaMA-URM method. The characterisation of piers and spandrels and the hierarchy of strength calculations were carried out according to Sections 5.4.2 and 5.4.3.

The walls were modelled in 3MURI software (Lagomarsino *et al*., 2013) by adopting EFM (see Sections 6.4.2 for the reference wall) and Pushover analyses were performed for each case study. The floor slab was considered to be rigid in the plane. The mechanical parameters of the masonry are those already reported in Table 6.22.

Regarding the applied axial loads on the piers, a detailed description is reported in Section 7.2, where the geometry of the entire buildings is shown and described.

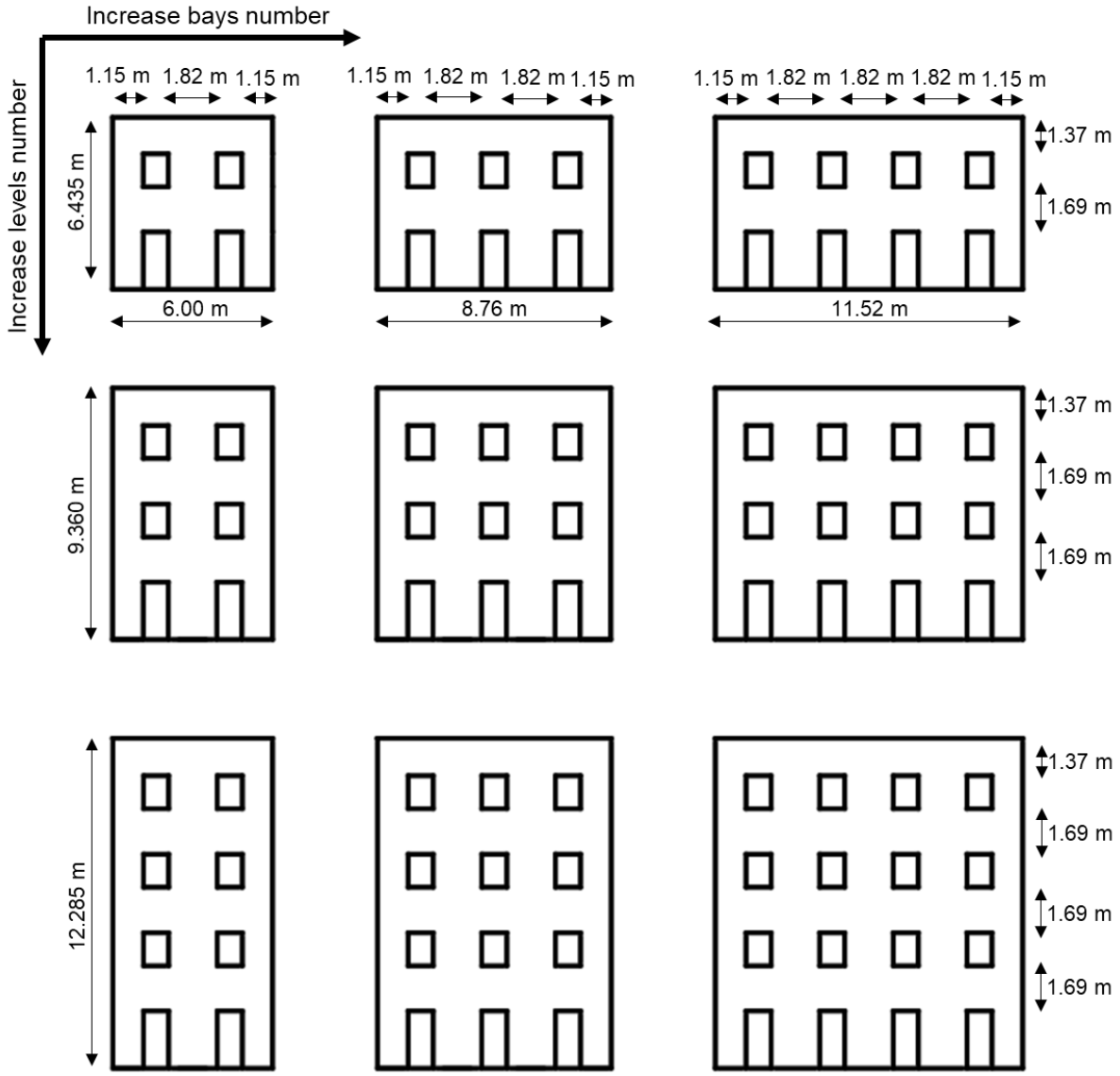

Figure 6.86. Schematization of the parametric analysis.

The comparisons between SLaMA-URM method and EFM numerical simulation in terms of pushover curves and prediction of the failure mechanism of the walls are shown in Figures 6.87 and 6.88.

From the obtained pushover curves, it was shown that by increasing the number of bays the base shear increases, while by increasing the number of levels the initial stiffness decreases. More details on the comparison between the resulted curves by SLaMA-URM method and the EFM numerical simulation are reported in the following.

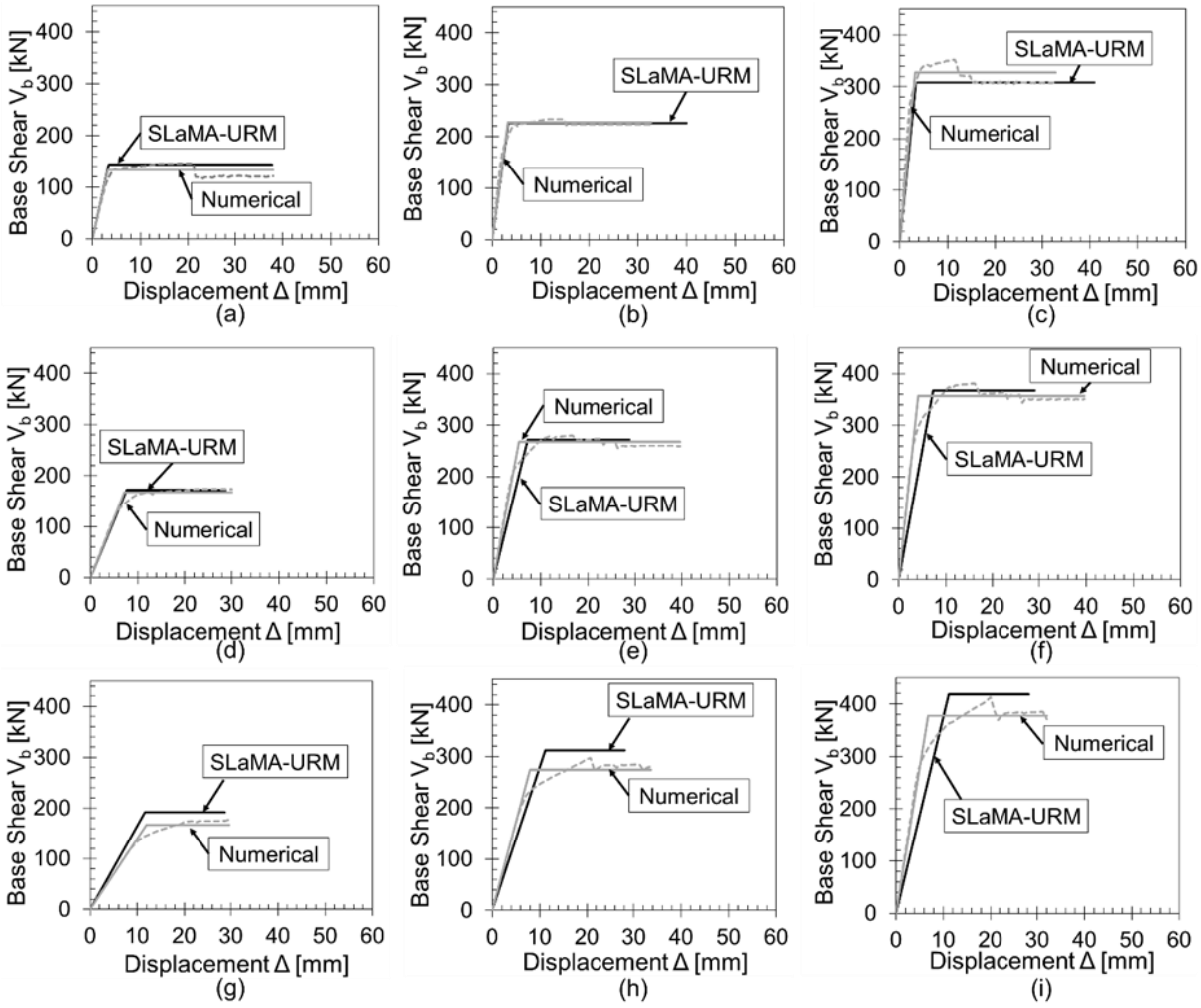

Figure 6.87. Numerical and analytical pushover curves of walls with: (a) 2-bays 2-levels, (b) 3-bays 2-levels, (c) 4-bays 2-levels, (d) 2-bays 3-levels, (e) 3-bays 3-levels, (f) 4-bays 3-levels, (g) 2-bays 4-levels, (h) 3-bays 4-levels, (i) 4-bays 4-levels.

Regarding the results in terms of the expected failure mechanisms in the structures, it can be observed a good agreement between those obtained by the two different approaches. More in detail, the SLaMA-URM method in all the structures identified the shear failure of the spandrels at each level as the most critical mechanism in each subassembly of the structures. Regarding the piers at the base, the central and the right ones fail in shear, while the left one showed a flexural failure, due to the lower axial load to which it is subjected. These failure mechanisms are in good agreement with those obtained by 3MURI software. More in detail, the shear failure of the spandrels is well grasp, as well as of the central and right piers at the base. Different failures are, however, obtained for the left piers at the base that fail in shear instead than in flexure and for the left piers at upper levels in all the

structure, with exception of the 2- and 3-bays 2-levels structures, that show shear failures. However, despite these differences, considering the approximations made in the proposed SLaMA-URM method, the obtained results are quite satisfactory.

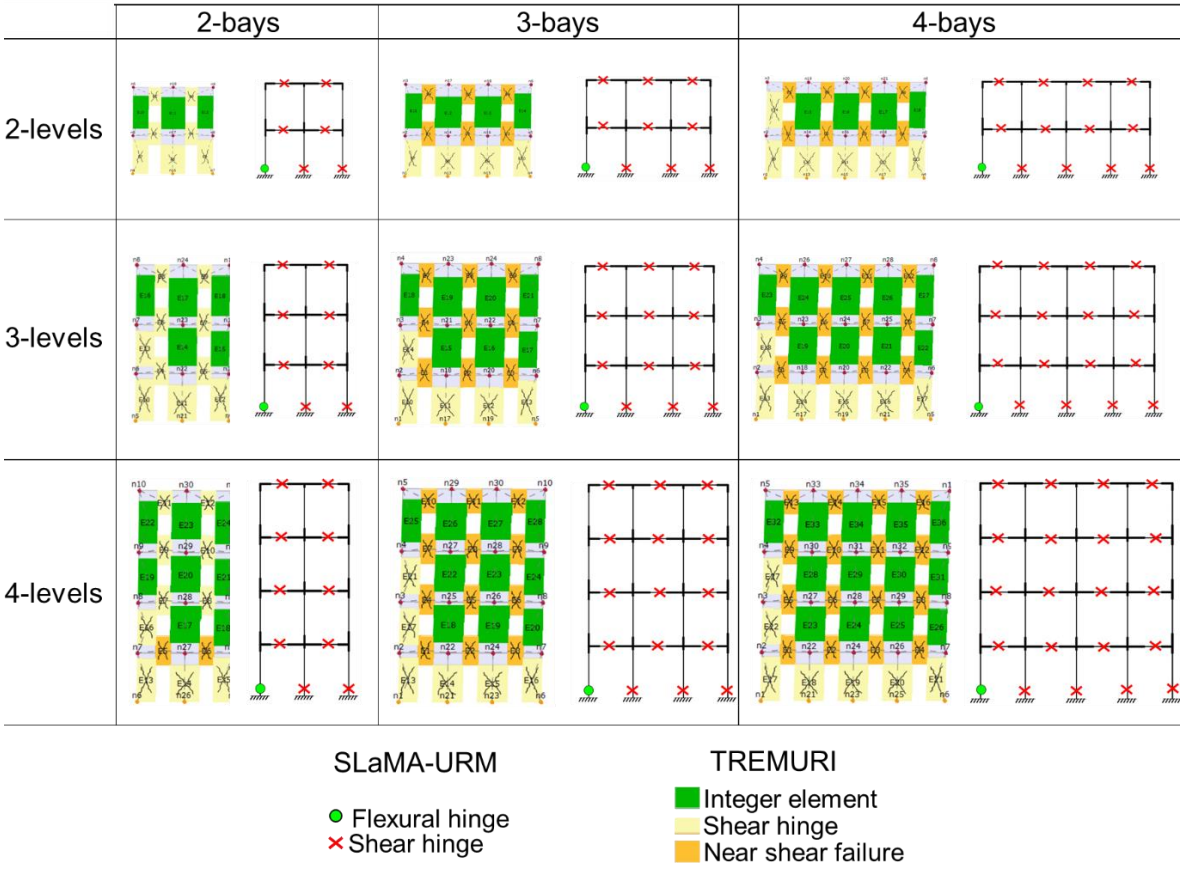

Figure 6.88. Crack pattern results obtained with the EFM model and the SLaMA-URM method.

The main purpose of the SLaMA-URM method is the seismic assessment of existing structures, and hence, the calculated capacity curve is used to perform a capacity/demand check in the Acceleration-Displacement Response Spectrum (or ADRS) domain. Moreover, the ultimate point of the capacity curve represents a fundamental parameter. In Table 6.25, the accuracy of the SLaMA-URM method is judged by comparing the results in terms of the ultimate displacement and base shear, with respect to the bi-linearised numerical curves, for each case, assuming: $Err = (SLaMA - Numerical)/Numerical$.

Table 6.25. Differences between SLaMA-URM and EFM numerical results in terms of ultimate displacement Δ_u and base shear V_b.

Case	Err (Δ_u)	Err (V_b)
2-bays 2-levs	-0.01	+0.07
2-bays 3-levs	-0.04	+0.03
2-bays 4-levs	-0.03	+0.15
3-bays 2-levs	+0.22	-0.01
3-bays 3-levs	-0.27	+0.02
3-bays 4-levs	-0.17	+0.14
4-bays 2-levs	+0.25	-0.06
4-bays 3-levs	-0.27	+0.03
4-bays 4-levs	-0.12	+0.11
average	-0.05	+0.05

It can be seen that the ultimate displacement at the effective height, is reasonably well-predicted, with an average error of around 5%. The same can be said for the comparison in terms of base shear, which shows an average error of 5%. Regarding the yield displacement, in the SLaMA-URM method, even if the spandrels showed a lower rotation capacity, the minimum yield rotation of the piers at the first floor was assumed for the calculation, due to the formation of the soft-storey mechanism. The adoption of the spandrels yield rotation leads to have an elastic stiffness similar to the one obtained adopting the first floor piers minimum yield rotation in the case of 2-levels walls. A higher difference was highlighted increasing the number of levels. Regarding the results obtained in terms of the yield displacement, the average percentage error is 26%, with a wide internal variation of values. A good match was observed for the structures with 2- or 3-levels, while a higher error for the taller frames. It is worth mentioning that small variations of the yield displacement cause high percentage error, even if there is a reasonably good match between the SLaMA-URM and the numerical Pushover curves.

6.6 References

ABAQUS. (2012). Analysis user's manual, Version 6.12.

Anthoine A., G. Magonette, and G. Magenes. (1995). Shear-compression testing and analysis of brick masonry walls, in Tenth European Conference on Earthquake Engineering.

Bertoldi, S.H., Decanini, L.D. and Gavarini, C. (1993). Telai tamponati soggetti ad azioni sismiche, un modello semplificato: confronto sperimentale e numerico. In Atti del 6º Convegno Nazionale ANIDIS, 815–824, Perugia: Associazione Nazionale Italiana di Ingegneria Sismica, (in Italian).

Beyer, K. and Dazio, A. (2012). Quasi-static cyclic tests on masonry spandrels. Earthq. Spectra, 40. 907–929.

Brencich, A. and G. De Felice. (2009). Brickwork under eccentric compression: Experimental results and macroscopic models, Construction and Building Materials, 23(5),1935-1946.

Brencich, A. and U. De Francesco. (2004). Assessment of Multispan Masonry Arch Bridges. 1:Simplified Approach, Journal of Bridge Engineering, ASCE, 9(6),582-590.

Cattari, S. (2007). Modellazione a telaio equivalente di strutture esistenti in muratura e miste muratura-c.a.: formulazione di modelli sintetici. University of Genoa, PhD Dissertation (In Italian), Italy.

Cattari, S. and S. Lagomarsino. (2008). A Strength criterion for the flexural behaviour of spandrels in unreinforced masonry walls. The 14th World Conference on Earthquake Engineering, Beijing, China.

Cavaleri, L., A. Failla, L. La Mendola and M. Papia. (2005). Experimental and analytical response of masonry elements under eccentric vertical loads. Engineering Structures, 27(8),1175-1184.

CEB-FIP Model Code 90. (1993). Thomas Telford Ltd., UK.

CNTC19. (2019). Circolare applicativa delle Norme Tecniche delle Costruzioni di cui al DM 17/01/2018. (NTC 2018). Italy: Gazzetta Ufficiale N.42 del 20/02/218. Ministero delle Infrastrutture e dei Trasporti. (in Italian).

De Borst, R., & Nauta, P. (1985). Non-orthogonal cracks in a smeared finite element model. Engineering Computations 2 (3), 35-46.

DIANA. (2019). User's manual of DIsplacement ANAlyzer finite element software package, release 10.3. DIANA FEA, Delft, https://dianafea.com/manuals/d103/Diana.html.

Dolce, M. (1991). Schematizzazione e modellazione degli edifici in muratura soggetti ad azioni sismiche. L'Industria delle Costruzioni, 25:44-57 (in Italian).

EN 1998 (European Committee for Standardization). (2005). Design of structures for earthquake resistance - Part 3: Assessment and retrofitting of buildings. Eurocode 8, Brussels, Belgium: EN.

Feenstra, P. H. (1993). Computational aspects of biaxial stress in plain and reinforced concrete. PhD thesis, Delft University of Technology.

Feenstra, P., Rots, J., Arnesen, A., Teigen, J., & Hoiseth, K. (1998). A 3d constitutive model for concrete based on a co-rotational concept.

FEMA 306 (Federal Emergency Management Agency). (1998). Evaluation of earthquake damaged concrete and masonry wall buildings: Basic procedures manual. Washington DC, US:FEMA.

Gambarotta, L., and S. Lagomarsino. (1997b). Damage models for the seismic response of brick masonry shear walls-Part II: The continuum model and its application. Earthquake Engineering & Structural Dynamics 26:441–462.

Gentile, R., Del Vecchio, C., Pampanin, S., Raffaele, D. and Uva, G. (2019). Refinement and validation of the Simple Lateral Mechanism Analysis (SLaMA) procedure for RC frames. J. Earthq. Eng., 1-29.

Grande, E., M. Imbimbo, and E. Sacco. (2011). A beam finite element for nonlinear analysis of masonry elements with or without fiber-reinforced plastic (FRP) reinforcements. International Journal of Architectural Heritage 5:693–716.

Graziotti, F., Magenes, G. and Penna, A. (2012). Experimental cyclic behaviour of stone masonry spandrels. In Proc. of the 15th World Conf. on Earthq. Eng., 24–28. Lisbon: International Association for Earthquake Engineering.

Hillerborg, A., Modéer, M., & Petersson, P. E. (1976). Analysis of crack formation and crack growth in concrete by means of fracture mechanics and finite elements. Cement and concrete research, 6(6), 773-781.

Jankowiak T, and Lodygowski T. (2005). Identification of parameters of concrete damage plasticity constitutive model. Found. Civil Environ. Eng. 6: 53–69

Kaushik, H.B., D.C. Rai and S.K. Jain. (2007). Stress-strain characteristics of clay brick masonry under uniaxial compression, Journal of Materials in Civil Engineering, 19(9),728-738.

Kent, D.C. and R. Park. (1971). Flexural members with confined concrete', Journal of Structural Division, ASCE, 97(1),1969-1990.

Knox, C. (2012). Assessment of perforated unreinforced masonry walls responding in-plane (Doctoral dissertation, Research Space@ Auckland).

Knox, C.L., Dizhur, D. and Ingham, J.M. (2017). Experimental cyclic testing of URM pier-spandrel substructures. J. Struct. Eng. 143:04016177.

Lagomarsino, S., Penna, A., Galasco, A. and Cattari, S. (2013). TREMURI program: an equivalent frame model for the nonlinear seismic analysis of masonry buildings. Eng. Struct. 56:1787–1799.

Lee, J., & Fenves, G. L. (1998). Plastic-damage model for cyclic loading of concrete structures. Journal of engineering mechanics, 124(8), 892-900.

Litton, R.W. (1974). A contribution to the analysis of concrete structures under cyclic loading. Ph.D. thesis, University of California, Berkeley.

Lourenço, P. B. (2010). Recent advances in masonry modelling: micromodelling and homogenisation. In Multiscale modeling in solid mechanics: computational approaches (pp. 251-294).

Lourenço, P. B., & Rots, J. G. (1997). Multisurface interface model for analysis of masonry structures. Journal of engineering mechanics, 123(7), 660-668.

Lubliner, J., Oliver, J., Oller, S., & Oñate, E. (1989). A plastic-damage model for concrete. International Journal of solids and structures, 25(3), 299-326.

Lumantarna, R. (2012). Material Characterisation of New Zealand Unreinforced Masonry Buildings, University of Auckland, PhD Thesis, Auckland.

Magenes, G., Kingsley, G. R., & Calvi, G. M. (1995). Seismic testing of a full-scale, two-story masonry building: test procedure and measured experimental response. Consiglio nazionale delle ricerche, Gruppo nazionale per la Difesa dai terremoti.

Magenes, G., & Calvi, G. M. (1997). In-plane seismic response of brick masonry walls. Earthquake engineering & structural dynamics, 26(11), 1091-1112.

Magenes, G., and A. Della Fontana. (1998). Simplified linear seismic analysis of masonry buildings. Proceedings of the British Masonry Society 8:190–195.

Mann, W. and Muller, H. (1982). Failure of shear-stressed masonry: an enlarged theory, tests and application to shear walls. In Proc. of the British Ceramic Society, 30, 223–235. Stoke-on-Trent: British Ceramic Society.

NTC (Norme Tecniche per le Costruzioni). (2008). delle Norme Tecniche per le Costruzioni. Decreto ministeriale del 14 gennaio 2008. Rome: Ministero delle Infrastrutture e dei Trasporti (in Italian).

NTC (Norme Tecniche per le Costruzioni). (2018). Aggiornamento delle Norme Tecniche per le Costruzioni. Decreto ministeriale del 17 gennaio 2018. Rome: Ministero delle Infrastrutture e dei Trasporti (in Italian).

NZSEE (New Zealand Society for Earthquake Engineering). (2017a). The Seismic Assessment of Existing Buildings: Part C5, Concrete Buildings, Technical Guidelines for Engineering Assessments. Wellington: NZSEE.

NZSEE (New Zealand Society for Earthquake Engineering). (2017b). The Seismic Assessment of Existing Buildings: Part C8, Unreinforced Masonry Buildings, Technical Guidelines for Engineering Assessments. Wellington: NZSEE.

Pampanin, S., Priestley, M.J.N. and Sritharan, S. (2001). Analytical modelling of the seismic behaviour of precast concrete frames designed with ductile connections. J. Earthq. Eng. 5, 329–367.

Pampanin, S., Bolognini, D. and Pavese, A. (2007). Performance-based seismic retrofit strategy for existing reinforced concrete frame systems using fiber-reinforced polymer composites. J. Compos. Constr. 11, 211–226.

Parisi, F., Augenti, N. and Prota, A. (2014). Implications of the spandrel type on the lateral behavior of unreinforced masonry walls. Earthq. Eng. Struct. Dyn.,43. 1867–1887.

Paulay, T. and Priestley, M. J. N. (1992). Seismic Design of Reinforced Concrete and Masonry Buildings.

Rots, J. G. (1988). Computational modeling of concrete fracture.

Sabatino, R., and G. Rizzano. (2010). Non-linear Static Analysis of Masonry Structures. Simplified Equivalent Frames and accurate models. Proc. of 14th European Conference on Earthquake Engineering.

Selby, R. G. (1995). Three-dimensional constitutive relations for reinforced concrete.

Siano, R., Roca, P., Camata, G., Pelà, L., Sepe, V., Spacone, E., & Petracca, M. (2018). Numerical investigation of non-linear equivalent-frame models for regular masonry walls. Engineering Structures, 173, 512-529.

Sullivan, T.J., Priestley, M.J.N. and Calvi, G.M. (2012). A Model Code for the Displacement-Based Seismic Design of Structures: DBD12. Pavia, IT: IUSS Press.

Turnšek, V. and Čačovič, F. (1971). Some experimental results on the strength of brick masonry walls. In Proc. of the 2nd Int. Brick Masonry Conf., 149–156. Stoke-on-Trent: British Ceramic Research Association.

Vecchio, F. J., and Collins, M. P. (1986). The modified compression field theory for reinforced concrete elements subjected to shear. ACI Journal 83, 22, 219–231.

7. Seismic assessment and retrofit of URM prototype structures through the SLaMA-URM method

7.1 Introduction

In this Chapter, the application of the SLaMA-URM method to a set of URM cases study buildings with rigid diaphragms and subjected to In-Plane (IP) and Out-Of-Plane (OOP) loads is presented. The global capacity curve of each structure is then derived and the global performance level is identified (Sections 7.3 - 7.6). A further evaluation is carried out (Section 7.7) with respect to different seismic intensities of the construction site (medium and high seismicity, MS and HS). Some retrofit strategies are proposed with the aim to achieve a higher capacity, both in terms of the ultimate performance (%NBS) and the expected damage (EAL), see Section 7.8. The comparison of the results from unreinforced and reinforced structures is carried out in Section 7.9 with respect also to MS and HS construction sites. In the end, a cost-benefit analysis is carried out and the best retrofit solution is identified (Section 7.10).

7.2 Cases study buildings

The proposed procedure, described in Chapter 5, was applied to a set of ideal cases study buildings. The considered structures are nine and differ for the number of levels (from two up to four) and the number of bays (from two up to four) of the longitudinal frames (see Figure 7.1). The structures are composed of two parallel frames that resist lateral forces in the longitudinal direction and two walls in the transversal one. The specific direction of the seismic force was assumed to consider both the IP mechanisms of the frames parallel to this and the OOP mechanisms of the walls orthogonal to this. The orientation of the horizontal diaphragms (assumed as rigid) is considered orthogonal to the frames. The frames to floor connections are assumed to be adequate to transfer all diaphragm forces. On the contrary, poor connections are assumed between the transversal walls and the diaphragms. The wall-

to-wall connections are assumed to be inadequate. The assessment of the walls and frames capacity curves is considered in the SLaMA-URM method.

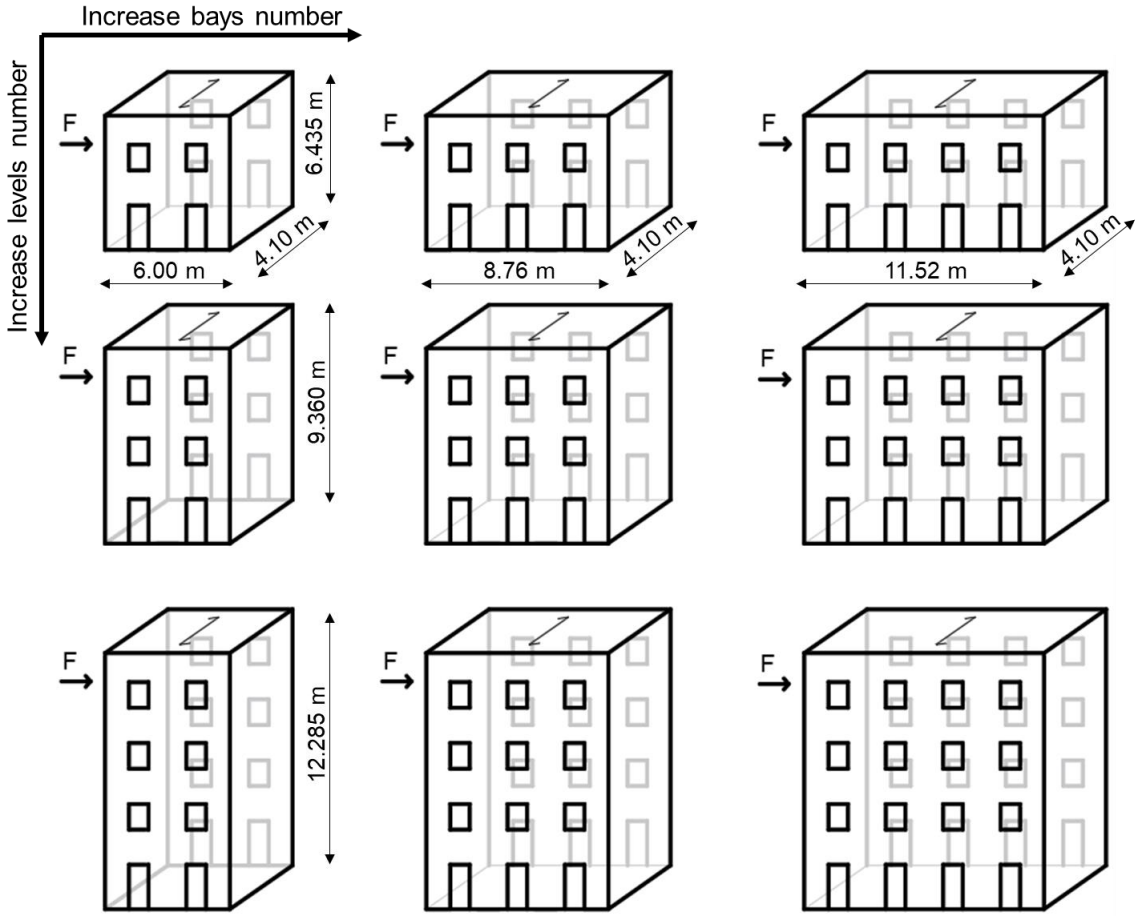

Figure 7.1. Schematization of the cases study structures.

The layout of the structures is regular and the geometry, as well as the material properties of the frames in the longitudinal direction, refer to the frames analyzed in Section 6.5. Due to the fact that the masonry is assumed of good quality (solid bricks and lime mortar), the crumbling of the masonry is considered prevented.

The seismic weights of the buildings are reported in Table 7.1 and, as observed in Figure 7.1, the gross plan area is equal to $24.6\ m^2$ for the 2-bays structures, $35.9\ m^2$ for the 3-bays structures and $47.2\ m^2$ for the 4-bays structures. It was considered a masonry density equal to $\rho = 18\ kN/m^3$, a superimposed dead load equal to $G = 8.5\ kN/m^2$ and a live load equal

to $Q = 2\,kN/m^2$, reduced by a factor of $\psi_e = 0.3$. The axial load on the piers was calculated according to the tributary areas.

Table 7.1. Seismic weights of the analyzed structures.

	2-bays 2-levs	2-bays 3-levs	2-bays 4-levs	3-bays 2-levs	3-bays 3-levs	3-bays 4-levs	4-bays 2-levs	4-bays 3-levs	4-bays 4-levs
Seismic weight (kN)	870	1350	1800	1300	2000	2710	1720	2670	3620

The seismic demand is represented by a displacement spectrum compliant with the Italian Code (NTC 2018), related to a medium seismic intensity (PGA = 0.21g). The adopted class of use is the II ($C_u = 1$) and the characteristics of the construction soil referred to a subsoil category C and a topographic class T1.

The following scenario was considered: the floors are supported by the longitudinal frames and the connections between them and the transversal walls are neglected. In this configuration, the assessment is focused on the most dangerous mechanism that is the overturning of the transversal walls (see Figure 7.2).

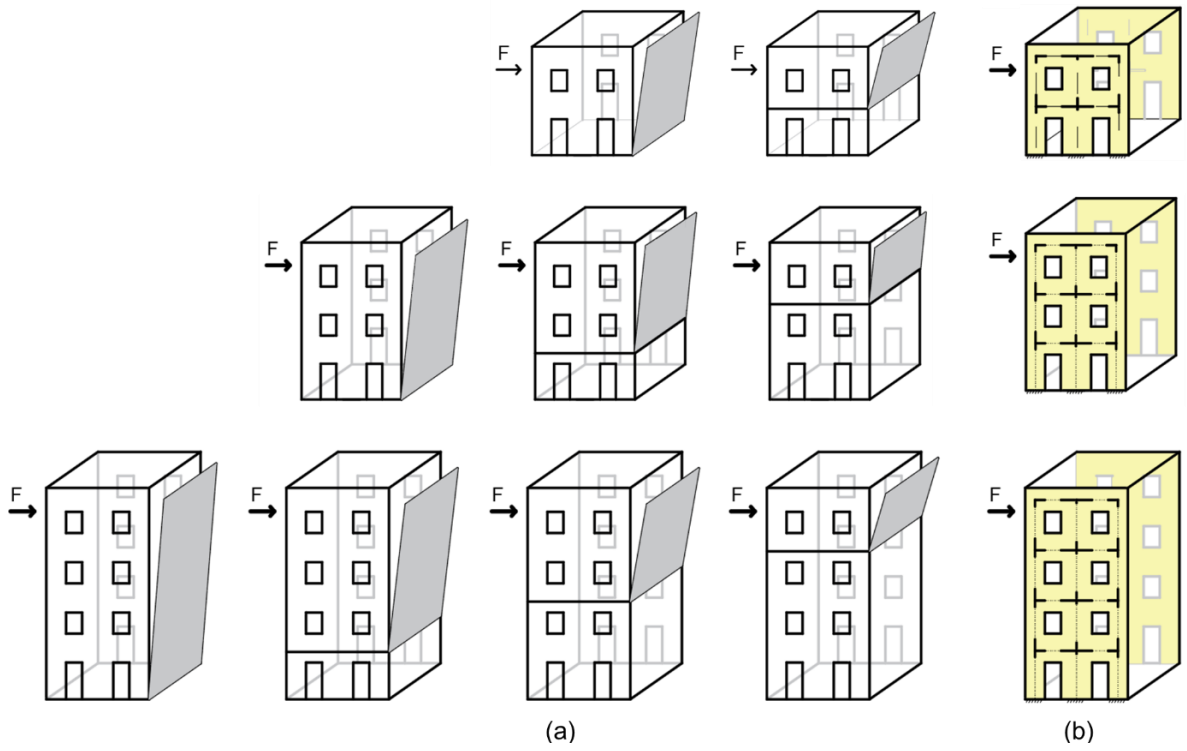

Figure 7.2. Schematization of (a) the probable OOP mechanisms and (b) the EF model of the longitudinal frames of the 2-bays structures with 2-, 3- and 4-levels.

7.3 Out-Of-Plane mechanisms performance level

In the examined cases study buildings, the most vulnerable walls to the Out-Of-Plane response are the transversal ones, since these walls are not loaded by floors and thus they are subjected to low stabilizing actions. Different possible mechanisms were analyzed for each wall, that imply its global or partial overturning (see Figure 7.3).

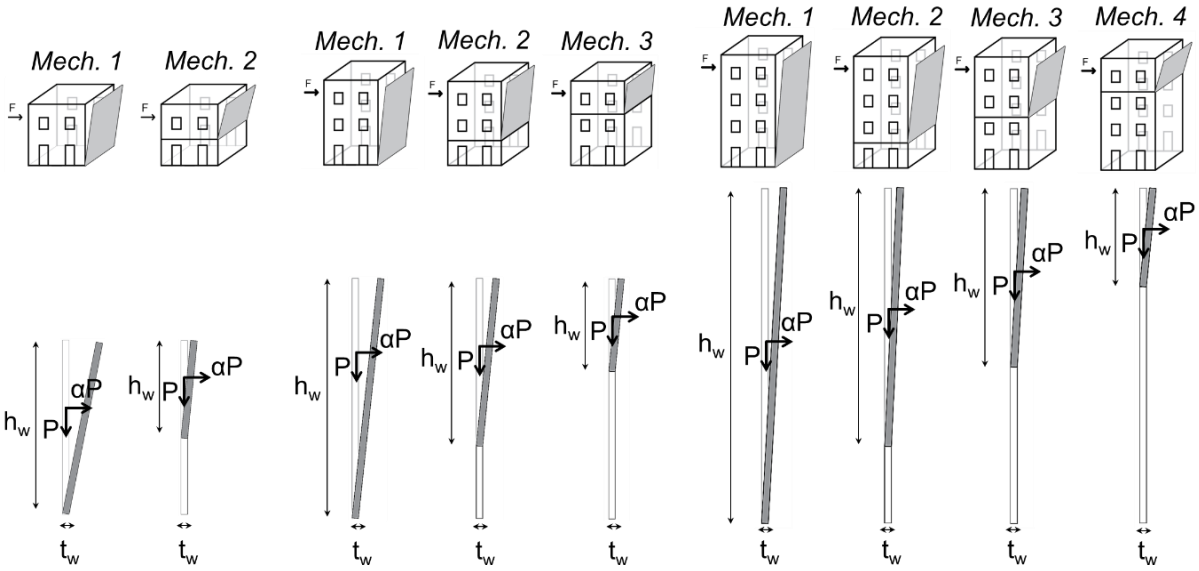

Figure 7.3. Schematization of the analyzed OOP mechanisms for the 2-bays structures with 2-, 3- and 4-levels.

More in detail, the different mechanisms are identified according to the position in which the cylindrical hinge is expected to be activated. When it happens at the base of the building, the mechanism is called “Mechanism 1” in the following. Subsequently, when it happens at the base of the first floor it is named “Mechanism 2”, at the second floor it is named “Mechanism 3” while at the third floor it is named “Mechanism 4”. The assumed mechanisms are the ones potentially feasible by considering the structural details that characterize the structures. For the Out-Of-Plane response, kinematic non-linear analyses were performed. More in detail, the systems expected to overturn are subjected to their dead load as well as the horizontal inertial actions, proportional to them, through a load seismic multiplier. The load static multiplier α_0 is obtained by the Theorem of Virtual Works. Following the DBA, the seismic multiplier α is defined under an incremental kinematic analysis, by increasing step-by-step the rotation of the macro-blocks, till the condition of loss of static equilibrium is

reached. The obtained curves (load multiplier versus displacement of a control point) are then transformed into capacity curves (spectral acceleration versus spectral displacement) of the substitute structures (nonlinear equivalent SDOF).

The walls reported in Figure 7.3 refer to the only three structures, since increasing the number of bays had no influence in the mechanisms.

Assuming the height of the walls (or portion of these) that is involved in the mechanism as equal to h_w (see Table 7.2), and considering common walls thickness and length equal to $t_w = 0.25\,m$ and $L_w = 4.1\,m$, respectively, the dead loads P of the walls were calculated (Table 7.2). Due to the fact that the walls are subjected only to their dead load, the load multiplier α_0 is given by $\alpha_0 = t_w/h_w$ (Table 7.2).

Table 7.2. Height, dead load and load multiplier α_0 associated to each OOP mechanism.

	Mech.1			Mech.2			Mech.3			Mech.4		
Case	**h_w (m)**	**P (kN)**	**α_0 (-)**	**h_w (m)**	**P (kN)**	**α_0 (-)**	**h_w (m)**	**P (kN)**	**α_0 (-)**	**h_w (m)**	**P (kN)**	**α_0 (-)**
2-levs	6.435	119	0.039	3.605	67	0.069	-	-	-	-	-	-
3-levs	9.360	173	0.027	6.530	120	0.038	3.590	66	0.070	-	-	-
4-levs	12.285	227	0.020	9.455	174	0.026	6.515	120	0.038	3.575	66	0.070

The load multiplier-displacement of a control point curve was obtained following Equation 7.1, assuming that the centroid of the walls is the control point and considering that the displacement d_0 that cancels the load multiplier is obtained as $d_0 = t_w/2 = 0.125\,m$.

$$\alpha = \alpha_0 \left(1 - \frac{d_k}{d_0}\right) \tag{7.1}$$

From this last, the capacity curve of the corresponding equivalent SDOF was defined. More in detail, the parameters that define this equivalent SDOF (i.e. the participating mass M^* and the participating mass fraction e^* in the kinematics) were calculated according to Equations 7.2 and 7.3. Through Equation 7.4 the spectral seismic acceleration a^* was obtained. Regarding the spectral displacement d^*, it coincides with the virtual displacement d_k of the control point ($d^* = d_k$), since the application point of P coincides with the control one.

$$M^* = \frac{P}{g} \tag{7.2}$$

$$e^* = \frac{gM^*}{P} \tag{7.3}$$

$$a^* = \frac{g}{e^* FC}\alpha \tag{7.4}$$

where g is the gravity acceleration and FC is the confidence factor that was assumed equal to 1.35 (level of knowledge LC1), as suggested by CNTC19 (2019).

In order to evaluate the displacement capacity and demand, the Italian Code (NTC 2018) was followed. The ultimate displacement capacity d_u (that represents a cautionary displacement for which the dynamic instability under rocking does not occur) was assumed as a fraction of the displacement d_0 ($d_u = 0.4d_0$). For all the structures, the ultimate displacement results equal to $d_u = 0.4 \cdot 0.125 = 0.50\ m$.

Regarding the evaluation of the displacement demand, the definition of the reference period and the seismic input spectrum is required. For the first aspect, NTC 2018 adopts a secant period T_s, by considering a displacement d_s^* which is a fraction of d_u (i.e. $0.4d_u$). For all the structures, resulted in $d_s^* = 0.4 \cdot 0.50 = 0.20\ m$. The secant period can be calculated as $T_s = 2\pi\sqrt{d_s^*/a_s^*}$. For the seismic input, it is considered the elastic spectrum at 5% of viscous damping. For mechanisms expected at different height with respect to the base, the floor spectrum amplified around the fundamental period of the building was defined, according to Degli Abbati *et al*. (2018). If the spectrum at the base was more limiting than the amplified one, it was used in the demand-capacity ratio comparison. The displacement demand $\Delta_d(T_s)$ was calculated as the intersection displacement between the ADRS and the curve at the secant period T_s, as $a_s^* = (2\pi/T_s)^2 d_s^*$.

The $\%NBS_{OOP}$ was evaluated for the possible OOP mechanisms by the displacement capacity-demand ratio ($\%NBS_{OOP} = d_u/\Delta_d(T_s)$). These values are reported in Table 7.3.

Table 7.3. %NBS$_{OOP}$ of each possible OOP mechanism of the analyzed walls.

	%NBS$_{OOP}$			
Case	**Mech.1**	**Mech.2**	**Mech.3**	**Mech.4**
2-levs	35	46	-	-
3-levs	29	28	46	-
4-levs	29	19	28	47

In Figures 7.4 - 7.6 are shown the assessments of the overturning mechanisms with the comparison between the ADRS and the capacity curves of the analyzed structures.

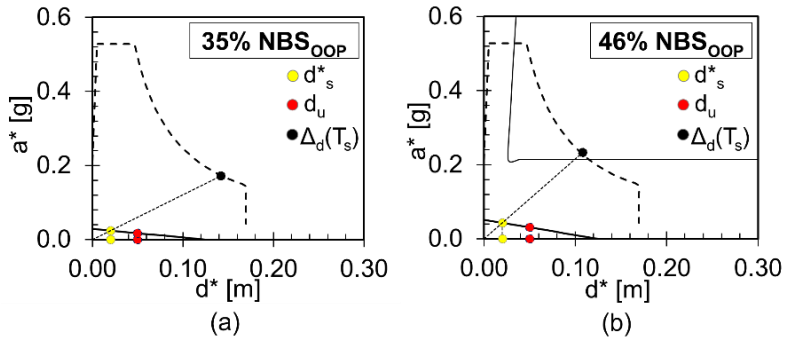

Figure 7.4. %NBS$_{OOP}$ of the (a) Mech. 1 and (b) Mech. 2 of the 2-levels structures.

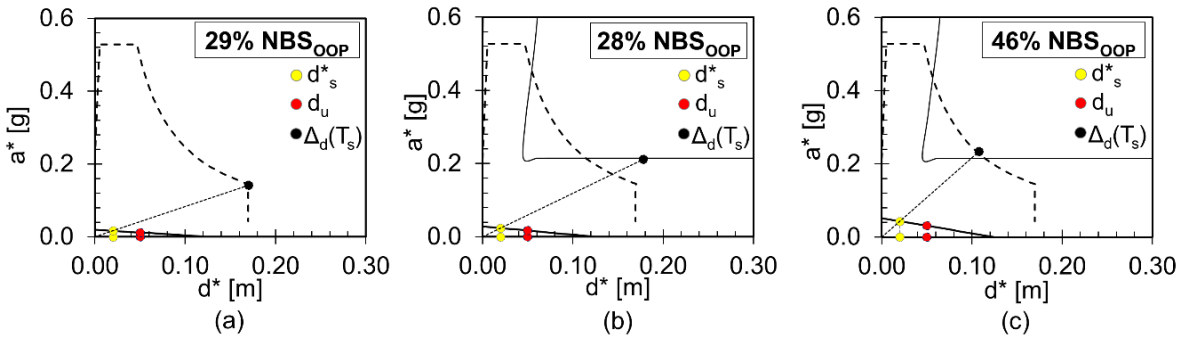

Figure 7.5. %NBS$_{OOP}$ of the (a) Mech. 1, (b) Mech. 2 and (c) Mech. 3 of the 3-levels structures.

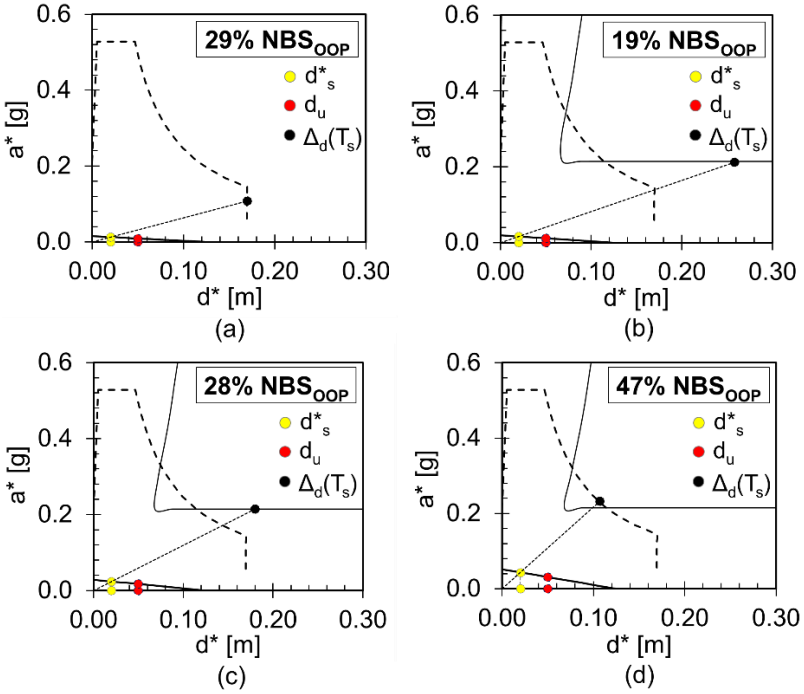

Figure 7.6. %NBS$_{OOP}$ of the (a) Mech. 1, (b) Mech. 2, (c) Mech. 3 and (d) Mech. 4 of the 4-levels structures.

The critical OOP mechanism for each structure is the one with the lower %NBS$_{OOP}$. The 2-levels structures showed that the overturning of the whole walls is the most critical OOP mechanism, with %NBS$_{OOP}$ = 35%. While the 3- and 4-levels structures have a limited performance level due to the overturning of the walls around a cylindric hinge placed at the base of the first floor (%NBS$_{OOP}$ = 28% and %NBS$_{OOP}$ = 19%, respectively).

From these results, it can be observed that the overturning mechanism of the transversal walls is more vulnerable when the cylindric hinge is located at higher levels with respect to the base. Moreover, it is clear that the height of the kinematics plays an important role. Indeed, for higher height of the overturning transversal walls (i.e. Mech. 2 in Figures 7.5 - 7.6) the expected performance is lower, with respect to the lower walls (i.e. Mech. 3 and Mech. 4 in Figures 7.5 - 7.6). This aspect can be observed also in Figure 7.7, where the capacity curves of overturning walls, by varying their height (h_w, Figure 7.7a), the length (L_w, Figure 7.7b) and the thickness (t_w, Figure 7.7c) are shown. As expected, lower height values lead to higher capacities. Moreover, there are no differences in capacity by varying the length of the walls. While an increase of the capacity curves can be achieved in the case of thicker walls.

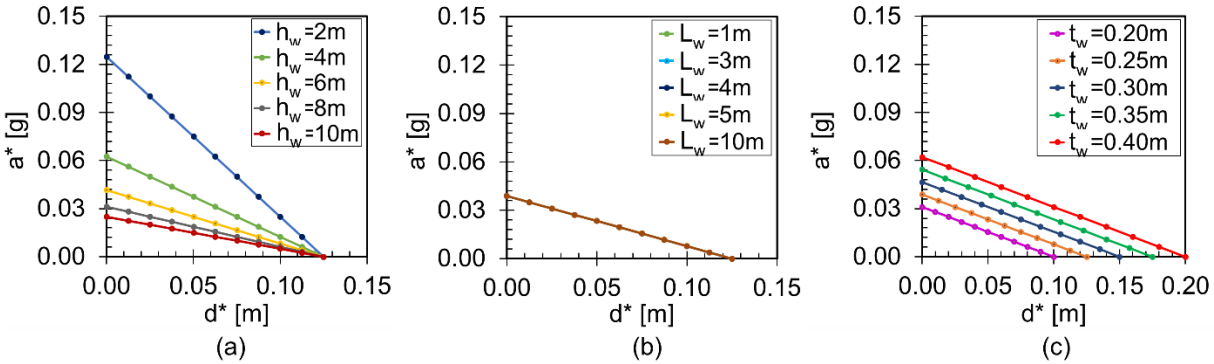

Figure 7.7. Capacity curves of overturning walls by varying: (a) the height h_w, (b) the length L_w and (c) the thickness t_w.

7.4 In-Plane mechanisms performance level

The In-Plane capacity curves of the structures are given by the capacity of the two parallel frames with the same geometric and mechanical characteristics. Hence, starting from the single frame curve already discussed in Section 6.5, was then calculated the longitudinal global one, in such a way as to define the IP seismic performance. For sake of synthesis, the seismic force was supposed applied in the longitudinal push direction (from left to right). In these cases study, due to the symmetry of the structures, the analysis in the pull direction of the seismic force (from right to left) would lead to the same results.

The performance of the structures was identified in the Acceleration-Displacement Response Spectrum (ADRS) by adopting the DBA method (see Section 4.3).

For the $\%NBS_{IP}$ calculation, with reference to CNTC19 (2019), the conversion of the structures (and therefore their capacity curves) in the equivalent SDOF was performed. The SLaMA-URM method, as it is conceived, provides directly both the base shear of this system and the displacement at the effective height of the structure, which corresponds to the displacement d^* of the equivalent SDOF system. The conversion of the In-Plane capacity curve in the Spectral Acceleration - Spectral Displacement curve is obtained by dividing the base shear for the participating mass. In order to consider the regularity of the structures, a participating mass under seismic actions equal to 80% of the seismic mass (see Table 7.1) was assumed.

To determine the $\%NBS_{IP}$, the procedure requires to define the performance point, by identifying the ratio between the maximum acceleration tolerable by the existing structure and the acceleration that would be used for the design of a new structure. If this ratio is lower than one, the structure would be vulnerable to seismic actions.

In Table 7.4 and Figure 7.8, are reported the values and the curves related to the In-Plane capacity of the structures, together with the achieved $\%NBS_{IP}$.

Table 7.4. Drift, spectral displacement, spectral acceleration and $\%NBS_{IP}$ of the analyzed structures.

Case	$Drift_y$ (%)	$Drift_u$ (%)	$S_{d,y}$ (m)	$S_{d,u}$ (m)	S_a (g)	$\%NBS_{IP}$
2-bays 2-levs (a)	0.072	0.793	0.003	0.038	0.41	80
3-bays 2-levs (b)	0.070	0.846	0.003	0.040	0.43	83
4-bays 2-levs (c)	0.070	0.846	0.003	0.041	0.45	87
2-bays 3-levs (d)	0.134	0.505	0.008	0.029	0.32	61
3-bays 3-levs (e)	0.130	0.514	0.007	0.029	0.34	64
4-bays 3-levs (f)	0.130	0.514	0.007	0.029	0.34	65
2-bays 4-levs (g)	0.179	0.440	0.012	0.029	0.27	55
3-bays 4-levs (h)	0.177	0.443	0.011	0.028	0.29	58
4-bays 4-levs (i)	0.176	0.444	0.011	0.028	0.29	58

From these results, it was shown that the structures with 2-levels are characterized by a strongly higher value of $\%NBS_{IP}$, with respect to the 3- and 4-levels ones. Moreover, among those, the performance increases by increasing the number of bays. The same trend was observed in the other “groups” of structures (such as 3- and 4-levels structures), but with a slower increase, settling approximately on a constant value from the structures with 3- and 4-bays. By increasing the number of bays, there is a slight variation in performance. This is due to the fact that in masonry, the spandrels couple less than would happen if the structures were in reinforced concrete. On the other hand, when increasing the number of levels, it can be seen that the performance stabilizes in structures with a number of levels equal and higher than three. This last aspect was already discussed by Priestley and Kowalsky (2000). Other considerations can be derived from the results: i) lower ductility in the 3- and 4-levels structures with respect to the 2-levels structures; ii) no-evident differences in ductility in the structures with the same number of levels but a different number of bays; iii) lower initial stiffness from 2- to 4-levels structures; iv) slight increase of the initial stiffness from 2- to 4-bays in structures with the same number of levels.

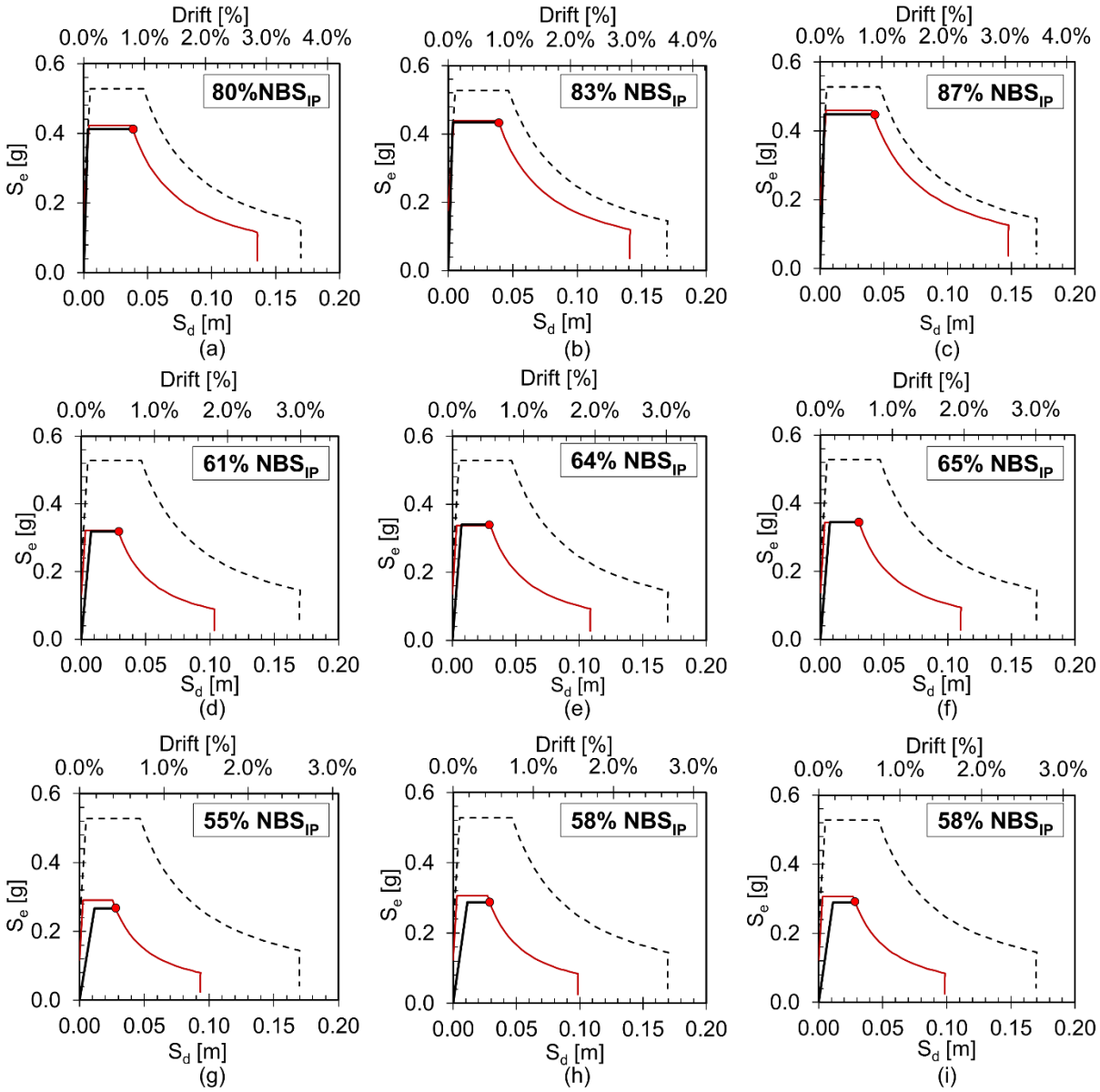

Figure 7.8. In-Plane performance levels in terms of %NBS$_{IP}$ of: (a) 2-bays 2-levels, (b) 3-bays 2-levels, (c) 4-bays 2-levels, (d) 2-bays 3-levels, (e) 3-bays 3-levels, (f) 4-bays 3-levels, (g) 2-bays 4-levels, (h) 3-bays 4-levels, (i) 4-bays 4-levels structures.

These considerations can be easily observed in Figure 7.9, where a complete comparison of the capacities of the analyzed structures, with the elastic spectrum, is shown. The curves are separated into three “groups”, essentially distinguished by the number of levels.

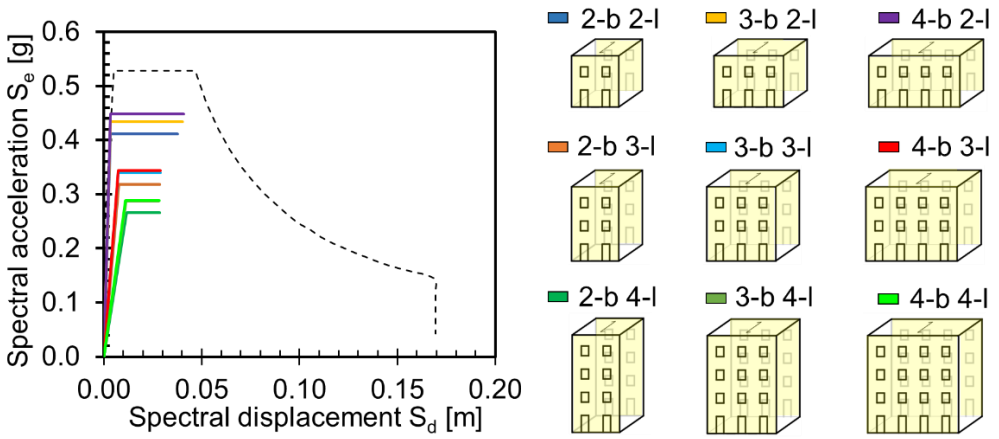

Figure 7.9. In-Plane performance levels of the structures ("b" is for bays and "l" is for levels).

7.5 Global performance level

The global performance of the structures is the lowest one between the OOP and the IP seismic performance (e.g. $\%NBS_{OOP}$ and $\%NBS_{IP}$). The comparison between the OOP and the IP performances was directly made in the ADRS. In Figure 7.10 are shown the results of the analyzed structures and, to easily compare the performances, the values of the $\%NBS_{IP}$ and $\%NBS_{OOP}$ are reported in Table 7.5. In bold are shown the critical values of each structure. In all cases, is the $\%NBS_{OOP}$ that limits the global performance. Moreover, it is worth noting that the mechanisms that follow the critical one are all the other OOP mechanisms that each structure can develop (see Table 7.5).

Table 7.5. $\%NBS_{OOP}$, $\%NBS_{IP}$ and in bold the critical one for each structure.

	$\%NBS_{OOP}$				$\%NBS_{IP}$
Case	**Mech.1**	**Mech.2**	**Mech.3**	**Mech.4**	
2-bays 2-levs (a)	**35**	46	-	-	80
3-bays 2-levs (b)	**35**	46	-	-	83
4-bays 2-levs (c)	**35**	46	-	-	87
2-bays 3-levs (d)	29	**28**	46	-	61
3-bays 3-levs (e)	29	**28**	46	-	64
4-bays 3-levs (f)	29	**28**	46	-	65
2-bays 4-levs (g)	29	**19**	28	47	55
3-bays 4-levs (h)	29	**19**	28	47	58
4-bays 4-levs (i)	29	**19**	28	47	58

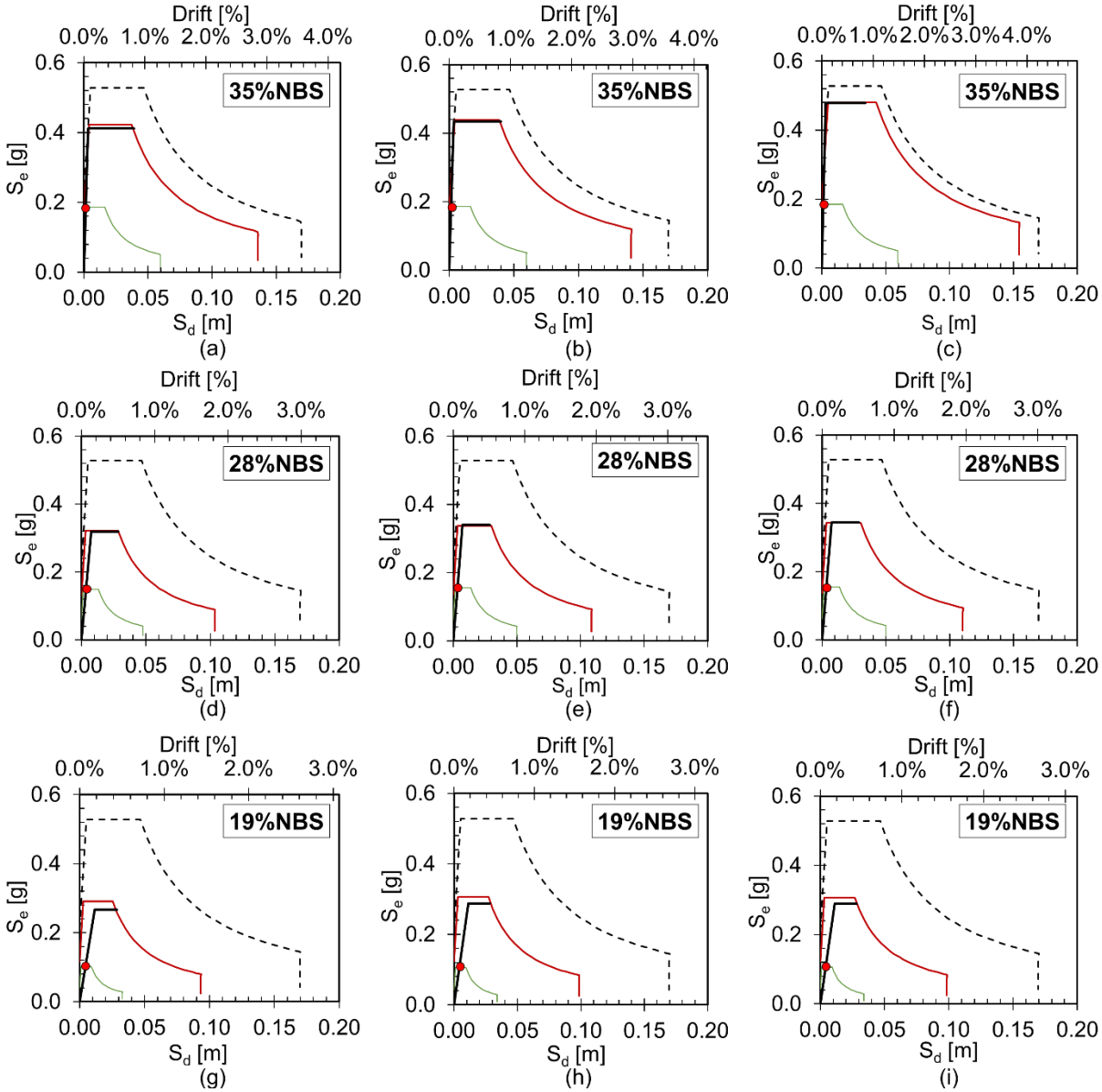

Figure 7.10. Minimum performance levels in terms of %NBS of: (a) 2-bays 2-levels, (b) 3-bays 2-levels, (c) 4-bays 2-levels, (d) 2-bays 3-levels, (e) 3-bays 3-levels, (f) 4-bays 3-levels, (g) 2-bays 4-levels, (h) 3-bays 4-levels, (i) 4-bays 4-levels structures.

7.6 Losses evaluation

As highlighted in Section 4.4, the evaluation of the direct economic losses of the building damaged by the earthquakes represents an important aspect to transit toward a Performance-Based approach in economic terms. In this Thesis, the procedure presented in Ministry Decree n.65 7/03/2017 was adopted to evaluate the EAL (or PAM in Italian). It was

estimated by computing the performance of the structures to different earthquake intensities/return periods T_r, in the reference life of the construction, expressed in terms of the mean annual frequency of exceedance ($\lambda = 1/T_r$) and the relevant repair costs (%RC). By connecting the points (λ, %RC) representative of each limit state, the EAL curve was obtained. The area under the curve represents the EAL.

In the procedure, the repair cost (%RC) is associated to different limit states by comparing the actual costs monitored in the reconstruction process of private residential buildings outside the historical center, damaged by the L'Aquila earthquake of 2009 (Dolce and Manfredi, 2015; Di Ludovico *et al*., 2017a-b). More in detail, the repair costs (%RC) associated with the Starting Damage Limit State (SDLS) and the total loss or reconstruction Limit State (RLS), conventionally related to a fixed $\lambda = 10\%$ and $\lambda = 0$, respectively, are assumed equal to 0% and 100%, respectively. Moreover, the %RC for OLS and CLS is set equal to %RC = 7% and %RC = 80%, respectively, while the %RC associated with DLS and VLS is set equal to %RC = 15% and %RC = 50%, respectively.

According to this definition of the EAL, it should result that, for example, the overturning of the two transversal walls that strongly limits the performance of the structures, leads to a direct loss at VLS equal to %RC = 50%. However, this result is highly questionable, i.e. the collapse of the two transversal walls would lead to an excessive loss in terms of the reconstruction cost since they are smaller than the longitudinal ones. In order to obtain a more reliable result, a new proposal is herein made. It is intended as a "qualitative" suggestion, that should be validated on the basis of evidence of earthquakes damage, with the aim to have disaggregated costs and losses, associated with damage due to the structural components involved in the IP or the OOP mechanisms.

This new proposal consists of considering the masonry volume actually involved in the OOP mechanisms (named V_{OOP}) with respect to the total masonry volume (V_{TOT}) of the structure. More in detail, it is considered that the %RC associated with each limit state is equal to $\%RC_{LS,OOP} = (V_{OOP}/V_{TOT}) \cdot \%RC$. In this way, the two contributions, EAL_{IP} and EAL_{OOP}, are disaggregated, even if only the OOP contribution is herein considered since these are the mechanisms that limit the global performances of all the structures.

In Figure 7.11 it is shown the comparison of the EAL_{OOP} curve of the 2-bays 2-levels structure, obtained by the proposed procedure and the one presented in Ministry Decree n.65 7/03/2017. In Table 7.6 are reported the corresponding values of %RC and λ.

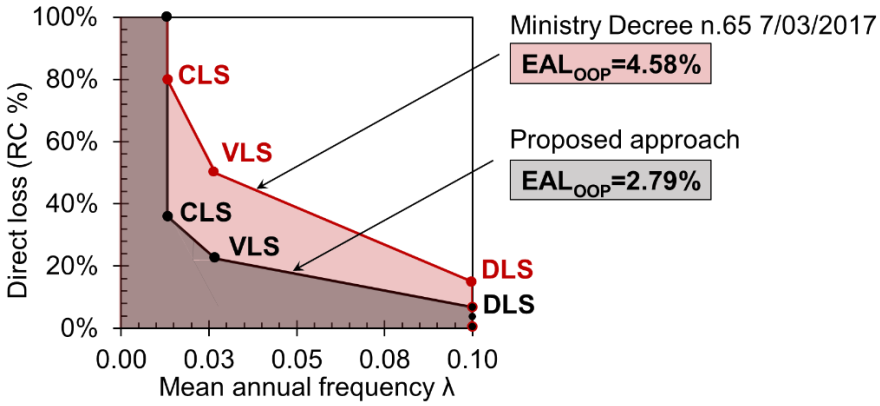

Figure 7.11. EAL_{OOP} curves comparison: Ministry Decree n.65 7/03/2017 approach vs proposed one.

Table 7.6. Values of the EAL_{OOP} curves obtained by the Ministry Decree n.65 7/03/2017 approach and the proposed one.

	2-bays 2-levels			
	Ministry Decree n.65 7/03/2017		***Proposed approach***	
LS	**%RC**	**λ (-)**	**%RC**	**λ (-)**
RLS	100	0.0132	100	0.0132
CLS	80	0.0132	36	0.0132
VLS	50	0.0269	22	0.0269
DLS	15	0.1	7	0.1
OLS	7	0.1	3	0.1
SDLS	0	0.1	0	0.1
EAL $_{OOP}$(%)	**4.58**		**2.79**	

From this comparison, it can be observed that the EAL_{OOP} resulting from the proposed approach is strongly lower (-1.79) than the one obtained using the Ministry Decree n.65 7/03/2017. The results obtained by the proposed approach seem to be more realistic, leading to an expected loss at VLS and CLS, less than half of what would have been obtained using the Ministry Decree approach. With reference to the value of mean frequency of exceedance at DLS, OLS and SDLS in both the curves, it is worth noting that, according to Cosenza *et al*. (2018), a lower bound of $\lambda = 10\%$ (i.e. return period $T_r = 10$ years) was set.

The calculation of the volume ratio $\beta = (V_{OOP}/V_{TOT})$ was performed for all the structures, and the values are reported in Table 7.7. From these results, it can be observed that the structures with the same number of bays but a different number of levels show the same weighted contribution of OOP mechanisms. This is due to the fact that by varying the number

of levels, the volume ratio between the longitudinal frames and the transversal walls remains constant. Moreover, by increasing the number of bays, the OOP contribution to the total volume decreases, because the longitudinal frames are characterized by a higher length.

Table 7.7. OOP volume contribution V_{OOP} and corresponding volume ratio β for each structure.

	V_{OOP}	V_{TOT}	β
Case	(m^3)	(m^3)	(-)
2-bays 2-levs	13.2	19.3	0.45
3-bays 2-levs	13.2	36.6	0.36
4-bays 2-levs	13.2	43.9	0.30
2-bays 3-levs	19.2	42.9	0.45
3-bays 3-levs	19.2	53.7	0.36
4-bays 3-levs	19.2	64.4	0.30
2-bays 4-levs	25.2	56.5	0.45
3-bays 4-levs	25.2	70.7	0.36
4-bays 4-levs	25.2	84.9	0.30

From the disaggregated contributions, the EAL_{OOP} curves and the EAL_{OOP} of the structures were defined and they are reported in in Table 7.8 and shown in Figure 7.12.

From these results, according to the previous considerations, it can be observed that by increasing the number of bays, the losses associated with the OOP mechanisms decreases. Moreover, EAL_{OOP} increases when the number of levels increases.

Table 7.8. EAL_{OOP} obtained from the analyzed structures.

	2-bays				**3-bays**				**4-bays**			
		2-levs	**3-levs**	**4-levs**		**2-levs**	**3-levs**	**4-levs**		**2-levs**	**3-levs**	**4-levs**
LS	**%RC**	**λ (-)**	**λ (-)**	**λ (-)**	**%RC**	**λ (-)**	**λ (-)**	**λ (-)**	**%RC**	**λ (-)**	**λ (-)**	**λ (-)**
RLS	100	0.013	0.023	0.049	100	0.013	0.020	0.049	100	0.013	0.020	0.049
CLS	36	0.013	0.023	0.049	29	0.013	0.020	0.049	24	0.013	0.020	0.049
VLS	22	0.027	0.047	0.1	18	0.027	0.042	0.1	15	0.027	0.042	0.1
DLS	7	0.1	0.1	0.1	5	0.1	0.1	0.1	5	0.1	0.1	0.1
OLS	3	0.1	0.1	0.1	3	0.1	0.1	0.1	2	0.1	0.1	0.1
SDLS	0	0.1	0.1	0.1	0	0.1	0.1	0.1	0	0.1	0.1	0.1
EAL_{OOP} (%)		**2.79**	**3.75**	**6.38**		**2.49**	**3.21**	**6.08**		**2.32**	**3.02**	**5.88**

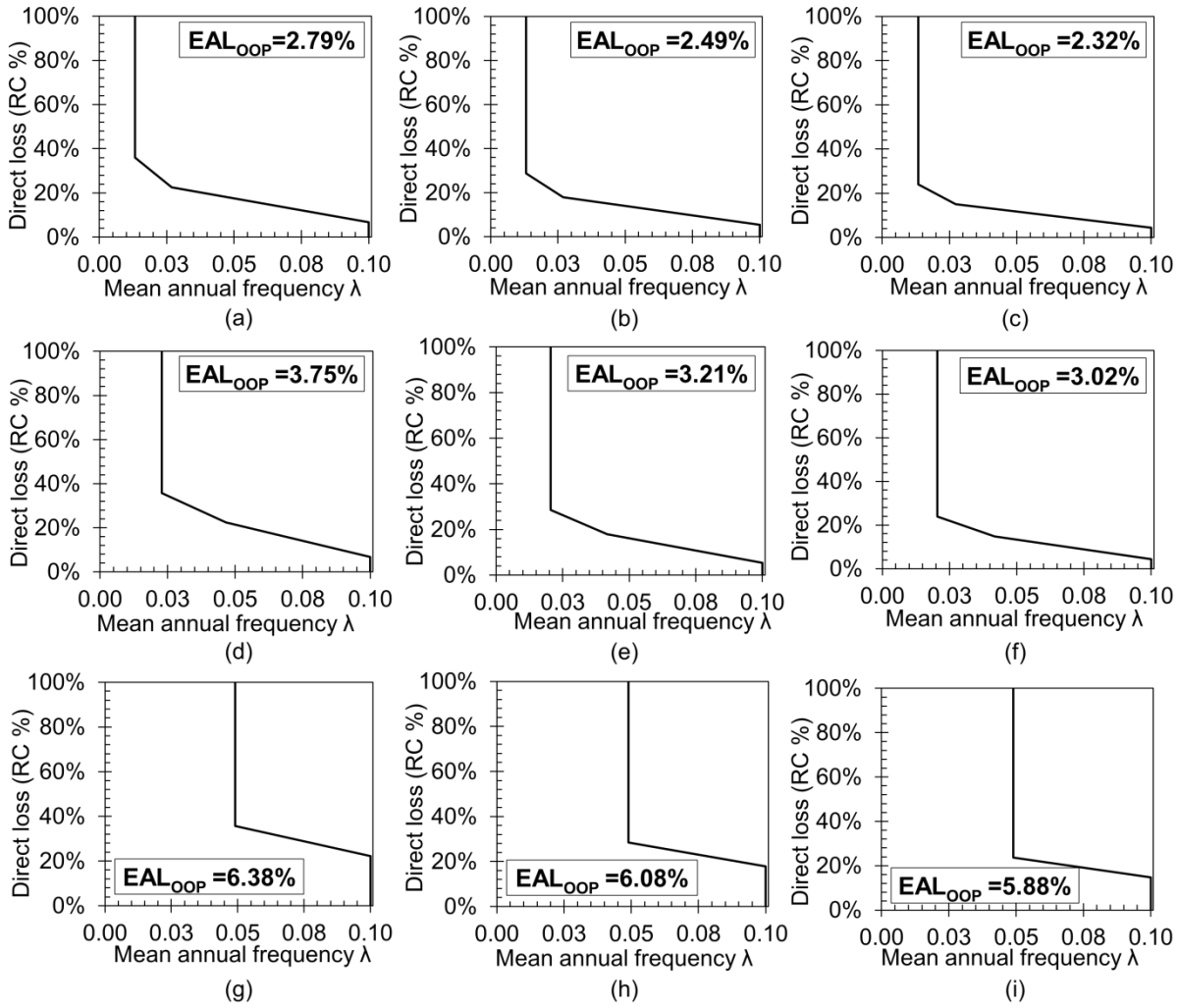

Figure 7.12. Performance levels in terms of EAL_{OOP} of: (a) 2-bays 2-levels, (b) 3-bays 2-levels, (c) 4-bays 2-levels, (d) 2-bays 3-levels, (e) 3-bays 3-levels, (f) 4-bays 3-levels, (g) 2-bays 4-levels, (h) 3-bays 4-levels, (i) 4-bays 4-levels structures.

In Figure 7.13 it is shown the direct comparison of all the EAL_{OOP} curves. From this, it can be observed that three “groups” of curves can be distinguished, i.e. those related to the i) 2-levels structures, ii) 3-levels structures and iii) 4-levels structures. From this comparison, it is clear that the increase of the number of levels affects the results by strongly increasing the area under the curve (or EAL_{OOP}). Moreover, also the increase in the number of bays influences the results, leading to a small decrease in EAL_{OOP}.

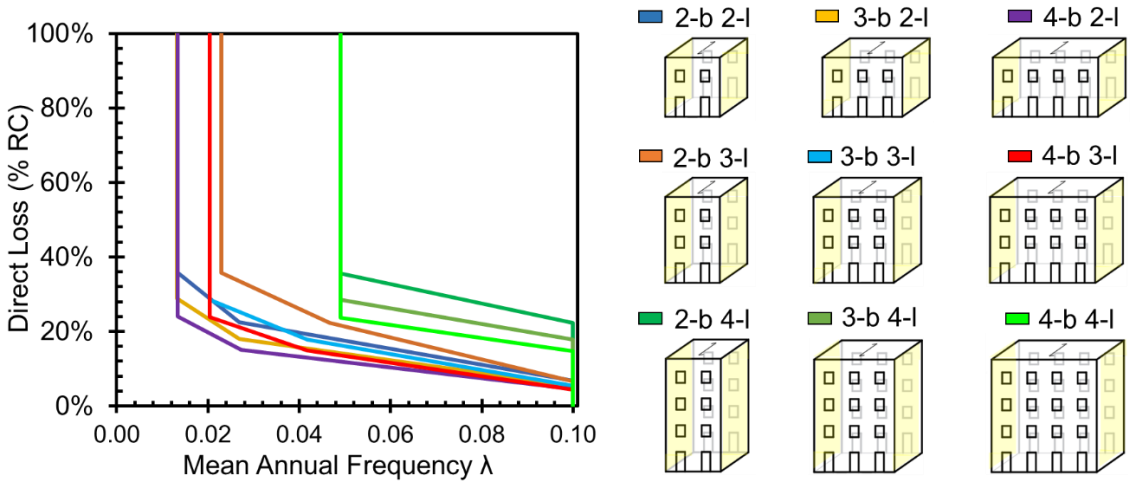

Figure 7.13. EAL_{OOP} curves of the structures ("b" is for bays and "l" is for levels).

As aforementioned, to prevent the development of the premature OOP mechanisms in all the analyzed structures, seismic intervention strategies should be provided. Once the probable activation of the overturning of the transversal walls is protect, some interventions to increase the global strength capacity can be considered.

7.7 Performances and losses comparison: medium vs high seismicity

In order to further investigate the response of the structures (in terms of performance and economic losses), these were analyzed also by varying the seismicity of the construction site. More in detail, the results obtained for the medium seismicity (PGA = 0.21g), reported in the previous Sections, are herein compared with those for high seismicity (PGA = 0.34g).

At first, the performance and the EAL curves were defined for high seismicity sites. In Table 7.9 are reported the %NBS of both OOP and IP mechanisms. As for the medium seismicity case, the OOP performance strongly limits the global performance.

Table 7.9. High Seismicity: $\%NBS_{OOP}$ and $\%NBS_{IP}$, highlighting in bold the critical one for each structure.

	$\%NBS_{OOP}$				$\%NBS_{IP}$
Case	**Mech.1**	**Mech.2**	**Mech.3**	**Mech.4**	
2-bays 2-levs (a)	**26**	27	-	-	60
3-bays 2-levs (b)	**26**	27	-	-	60
4-bays 2-levs (c)	**26**	27	-	-	62
2-bays 3-levs (d)	22	**15**	28	-	45
3-bays 3-levs (e)	22	**15**	28	-	47
4-bays 3-levs (f)	22	**15**	28	-	47
2-bays 4-levs (g)	19	**10**	16	28	40
3-bays 4-levs (h)	19	**10**	16	28	42
4-bays 4-levs (i)	19	**10**	16	28	42

Regarding the losses evaluation, the same approach proposed in Section 7.6 was applied to disaggregate the OOP and the IP EAL contributions. In Figure 7.14 are reported the EAL_{OOP} curves of the analyzed structures. From these, it can be observed that the 3- and 4-levels structures are almost completely overlapped. This is due to the fact that these cases achieve the maximum losses possible, calculated by assuming a maximum mean annual frequency equal to $\lambda = 10\%$ at VLS, DLS, OLS and SDLS. As for the medium seismicity case, it is observed that, by increasing the number of levels, EAL_{OOP} increases, while it decreases by increasing the number of bays.

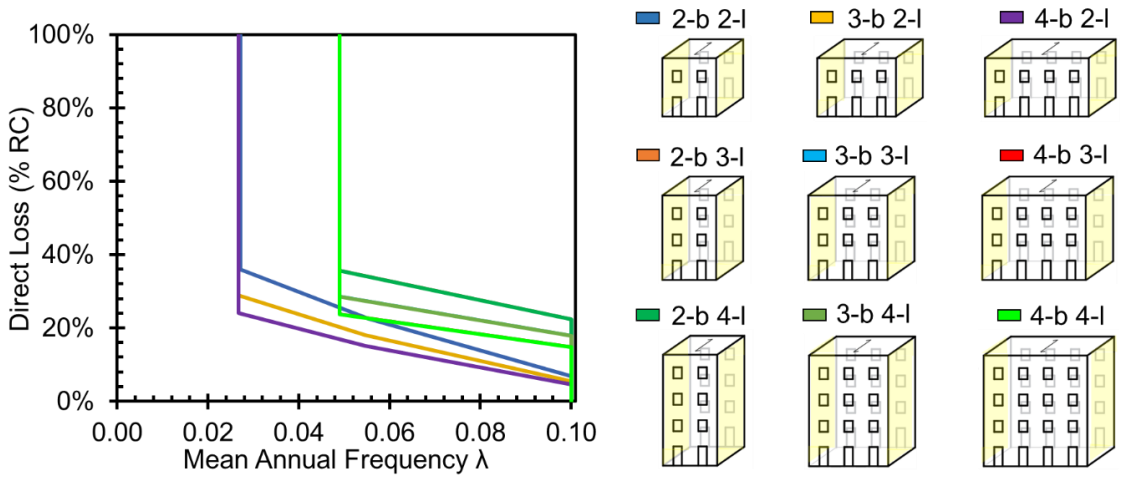

Figure 7.14. High seismicity: EAL_{OOP} curves of the structures ("b" is for bays and "l" is for levels).

In Figures 7.15 and 7.16 and in Table 7.10 are shown the direct comparisons in terms of $\%NBS_{OOP}$ and EAL_{OOP}, respectively for the medium seismicity (MS) case and the high seismicity (HS) one. It can be observed that when moving from medium to high seismicity, the OOP performance in the 2- and 4-levels structures decreases of 9%, obtaining $26\%NBS_{OOP}$ for the 2-levels and $10\%NBS_{OOP}$ for the 4-levels. While in the 3-levels structures the performance decreases of 13%, achieving a $\%NBS_{OOP}$ equal to 15%. Regarding the obtained EAL_{OOP}, for the 2-levels structures, an average increase of 1.4% was observed (ranging from 3.67% to 4.19%), while an average of 2.8% was obtained for the 3-levels structures (ranging from 5.89% to 6.38%). No-differences, instead, were observed for the 4-levels structures: the values that range from 5.88% of the 4-bays structure to 6.38% of the 2-bays one, remained unchanged between MS and HS. This is due to the fact that in both cases the maximum EAL_{OOP} was obtained (by setting a maximum mean annual frequency equal to $\lambda = 10\%$).

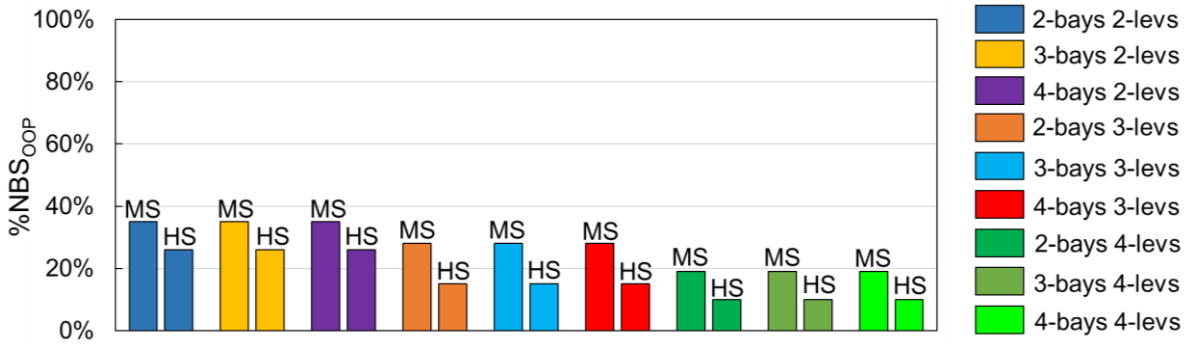

Figure 7.15. $\%NBS_{OOP}$: Medium Seismicity (MS) and High Seismicity (HS) comparison.

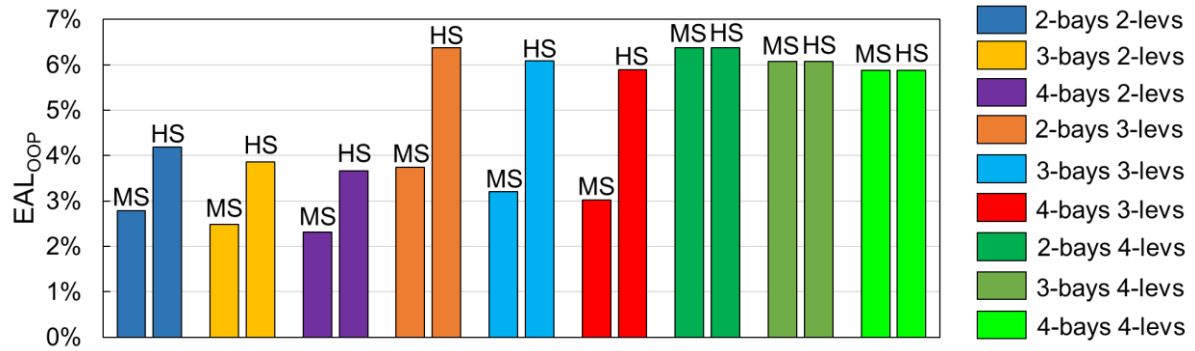

Figure 7.16. EAL_{OOP}: Medium Seismicity (MS) and High Seismicity (HS) comparison.

Table 7.10. Comparison of $\%NBS_{OOP}$ and EAL_{OOP} obtained in Medium Seismicity (MS) and High Seismicity (HS) zones.

	$\%NBS_{OOP}$		EAL_{OOP} (%)	
Case	**MS**	**HS**	**MS**	**HS**
2-bays 2-levs (a)	35	26	2.79	4.19
3-bays 2-levs (b)	35	26	2.49	3.86
4-bays 2-levs (c)	35	26	2.32	3.67
2-bays 3-levs (d)	28	15	3.75	6.38
3-bays 3-levs (e)	28	15	3.21	6.09
4-bays 3-levs (f)	28	15	3.02	5.89
2-bays 4-levs (g)	19	10	6.38	6.38
3-bays 4-levs (h)	19	10	6.08	6.08
4-bays 4-levs (i)	19	10	5.88	5.88

7.8 Seismic retrofit

With reference to the results obtained in medium seismicity (MS), see Section 7.5, the Out-Of-Plane mechanisms strongly limit the global response and the ductility of all the considered URM structures (as shown by the achieved %NBS = $\%NBS_{OOP}$).

To allow the structures to show their global In-Plane ductility, the first seismic retrofit interventions have to impair the activation of the expected OOP mechanisms of the walls orthogonal to the seismic action. Once this issue was solved, the seismic retrofit strategies to increase the IP response can be taken into account.

In the following Sections, some retrofit solutions are applied to the analyzed structures to increase the global strength capacity. Moreover, it is evaluated how the different intervention techniques influence the outcomes of the structural response for both the OOP and the IP mechanisms, in terms of the displacement capacity-demand ratio and economic losses.

It is worth noting that the implementation of the retrofit interventions was performed through the herein proposed SLaMA-URM method, which is capable to analyze both the existing as well as the reinforced masonry buildings.

7.8.1 Retrofit interventions for Out-Of-Plane mechanisms

The chosen seismic retrofit intervention to avoid expected OOP mechanisms was the adoption of tie rods, which represents one of the oldest and most effective techniques for this purpose (see Section 4.5.2 for more details). These elements increase the connection between orthogonal walls and reduce the possibility of the walls to overturn out of the plane.

Taking into consideration the transversal walls subjected to their own weight (stabilizing force) and to the inertial force due to this (destabilizing force), by balancing the rotation around the cylindrical hinge, the lever arm of the stabilizing force is much smaller than the lever arm of the destabilizing ones, so the walls are not verified (see Section 7.3). If the contribution of the tie rods is added to the stabilizing force, this contributes considerably to stabilize the walls because the lever arm of the force is comparable to that of the unstable inertial force. Hence, to obtain satisfactory verifications, it is necessary to design the tie rods in such a way that they have sufficient strength to obtain the positive outcome of the verification.

Taking into account the tie rods length L equal to the longitudinal length of the frames, it was assumed the tie rods failure deformation equal to 10‰ of this length. Consequently, the ultimate displacement of the application point of the tie rods was assumed to equal to $0.01L$. The corresponding displacement of the control point (centroid of the walls) was calculated. For the reinforced system, the displacement capacity was assumed as the minimum between the displacement capacity of the unreinforced system and this last calculated value.

To define the axial load that the tie rods should sustain to satisfy the verification, at first the mechanism activation load multiplier α_{0C} of the reinforced structure was calculated, by imposing the equality between the capacity and the demand in terms of the spectral acceleration. From this value, through the rotational balance around the cylindrical hinge, the stabilizing contribution due to the tie rods was made explicit, through Equation 7.5:

$$T = \frac{\alpha_{0C} P y_G - P x_G}{n y_T} \tag{7.5}$$

where P is the dead load of the walls; y_G and x_G are the lever arms of P and $\alpha_{0C}P$, respectively, with respect to the position of the hinge; n is the number of the tie rods and y_T is the height at which they are placed.

At this stage, the design of the tie rods was carried out, by considering four failure mechanisms: the failure of the metal tie, the masonry punching, the failure due to the contact pressure under the external anchor and the failure of the external anchor. More in detail, are assumed two round-shaped metal ties with a diameter of $\phi = 12$ mm at each level of the 2- and 3-levels structures and of $\phi = 14$ mm at each level of the 4-levels structures. The design tensile strength of the steel is equal to $f_{yd} = 223.8$ MPa (S235 Steel) and the strength of each metal tie was defined as $T_t = f_{yd}(\pi \cdot \phi^2/4)$. The external anchor was assumed as square-shaped, with dimensions 30 x 30 cm and a thickness of 2 cm. To define the masonry punching strength T_p (Equation 7.6), the contact pressure T_c (Equation 7.7) and the external anchor strength T_a (Equation 7.8), the formulations reported in Podestà and Scandolo (2019) were assumed.

$$T_p = 2t_w\sqrt{1 + tan^2\alpha}(a + b + 2t_w tan\alpha)\tau_d \tag{7.6}$$

$$T_c = \sqrt{\frac{(2t_w + a)(2t_w + b)}{ab}}ab\sigma_r \tag{7.7}$$

$$T_a = \frac{t^2 ab f_{da}}{3l^2} \tag{7.8}$$

where f_{ct} is the masonry tensile strength; t_w is the thickness of the walls; a and b are the planar dimensions of the external anchor; τ_d is the design shear strength of the masonry, that can be calculated from $\tau_k = \tau_0 + \mu\sigma_0$, where τ_0 is the masonry shear strength in absence of axial compression, μ is the friction coefficient assumed equal to 0.577 (as suggested by CNTC19, 2019) and σ_0 is the mean axial stress on the detachment surface due to the vertical loads (in absence of floor loads, it can be defined as $\sigma_0 = (H - y_R)w$, where H is the masonry height at the external anchor from the hinge, y_R is the external anchor height from the hinge and w is the density of the masonry); α is the diffusion load angle, generally assumed equal to 45 degrees; σ_r is the design masonry compression strength; l is the half diagonal of the external anchor plate and f_{da} is the design tensile strength of the steel of the external anchor.

The minimum strength between that of the metal tie strength and those calculated by Equations 7.6 - 7.8 identifies the tie rods strength. It is important to say that the choice of the geometry of the eternal anchor was defined in order to avoid the premature crisis of the masonry and hence to guarantee the crisis of the tie rods due to the yield of the metal tie.

Whit this choice in the design, resulted that T_p, T_c, T_a were higher than T_t, in such a way that higher deformation capacities of the system can be obtained.

By inverting Equation 7.5, the new load multiplier was defined and hence the capacity curve of the reinforced walls was defined. From the comparison between the displacement capacity and demand, the seismic performance of the reinforced walls with tie rods was calculated for each structure.

In Table 7.11 are reported the values of the new achieved %NBS_{OOP}. It is observed that all the structures satisfy the seismic verification, guaranteeing a capacity higher than the demand. Moreover, the variation of the bays does not influence the results (for more details see Section 7.3), hence the same results were achieved for structures characterized by a different number of bays and the same number of levels. In Figure 7.17 an example of the application of the tie rods on the 3-bays 3-levels structure is reported with the detail of the adopted square-shaped external anchor.

Table 7.11. %NBS_{OOP} of OOP mechanisms of the structures reinforced with tie rods.

	%NBS_{OOP}			
Case	**Mech.1**	**Mech.2**	**Mech.3**	**Mech.4**
2-levs	375	132	-	-
3-levs	329	106	122	-
4-levs	424	135	115	161

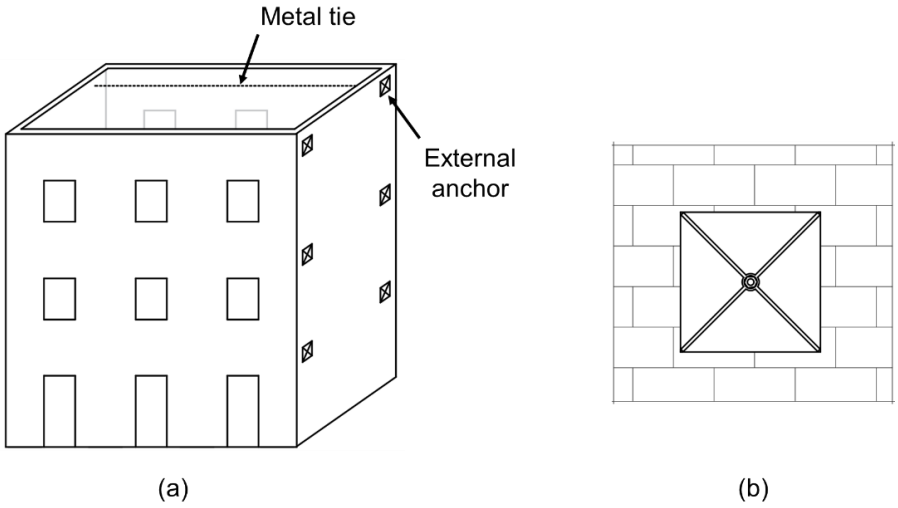

Figure 7.17. (a) Intervention with tie rods on the 3-bays 3-levels structure and (b) the detail of the adopted square-shaped external anchor.

Once the OOP mechanisms are prevented, the %NBS of the structures corresponds to that calculated and reported in Section 7.4. While the EAL were calculated according to Ministry Decree n.65 7/03/2017. The results for all the analyzed structures are reported in Table 7.12 and shown in Figure 7.18.

From these results, it can be observed that the expected losses increase when the number of levels of the structures increases. More in detail, for the 2-bays structures the EAL increases from 0.65% to 1.16%, when moving from 2- to 4-levels, while for the 3-bays structures it increases from 0.62% to 1.04% and for the 4-bays structures it increases from 0.60% to 1.03%. Moreover, a slight decrease of EAL can be observed in structures with the same number of levels while an increasing number of bays. More in detail, for the 2-levels structures, it is equal to 0.65% in the 2-bays structure, while it is equal to 0.60% in the 4-bays one. For the 3-levels structures, it is equal to 0.93% in the 2-bays structure, while it is equal to 0.83% in the 4-bays one. Finally, it is equal to 1.16% in the 2-bays 4-levels structure, while it is equal to 1.03% in the 4-bays 4-levels.

Table 7.12. Losses curve and EAL of the analyzed structures after the tie rods application.

		2-bays 2-levs (a)	3-bays 2-levs (b)	4-bays 2-levs (c)	2-bays 3-levs (d)	3-bays 3-levs (e)	4-bays 3-levs (f)	2-bays 4-levs (g)	3-bays 4-levs (h)	4-bays 4-levs (i)
LS	**%RC**	**λ (-)**	**λ (-)**	**λ (-)**	**λ (-)**	**λ (-)**	**λ (-)**	**λ (-)**	**λ (-)**	**λ (-)**
RLS	100	0.002	0.002	0.001	0.003	0.003	0.003	0.004	0.004	0.004
CLS	80	0.002	0.002	0.001	0.003	0.003	0.003	0.004	0.004	0.004
VLS	50	0.004	0.003	0.003	0.007	0.006	0.006	0.009	0.008	0.008
DLS	15	0.004	0.003	0.003	0.007	0.006	0.005	0.010	0.009	0.008
OLS	7	0.006	0.005	0.005	0.011	0.010	0.009	0.018	0.015	0.014
SDLS	0	0.100	0.100	0.100	0.100	0.100	0.100	0.100	0.100	0.100
EAL (%)		**0.65**	**0.62**	**0.60**	**0.93**	**0.86**	**0.83**	**1.16**	**1.04**	**1.03**

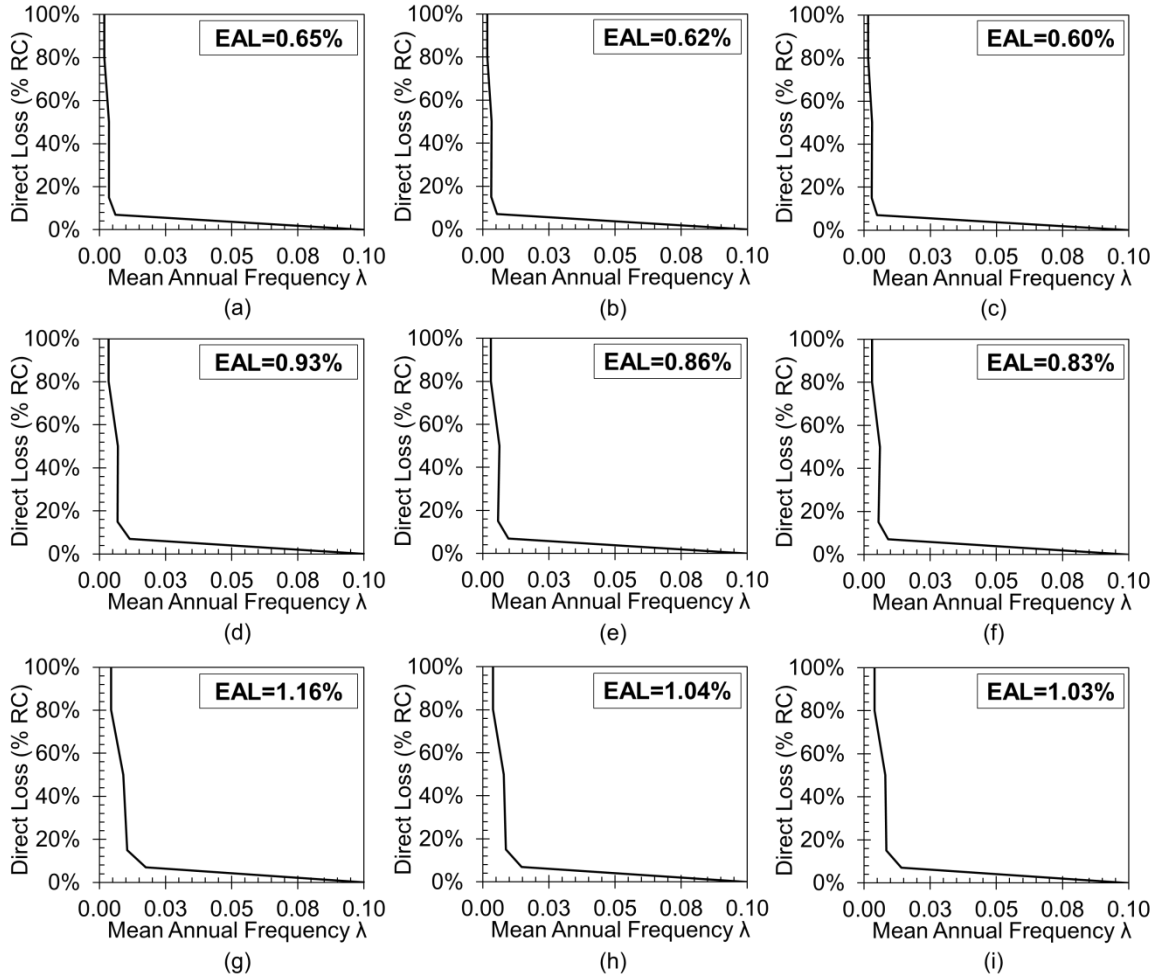

Figure 7.18. Performance levels in terms of EAL, after the tie rods applications, of: (a) 2-bays 2-levels, (b) 3-bays 2-levels, (c) 4-bays 2-levels, (d) 2-bays 3-levels, (e) 3-bays 3-levels, (f) 4-bays 3-levels, (g) 2-bays 4-levels, (h) 3-bays 4-levels, (i) 4-bays 4-levels structures.

In Figure 7.19 it is shown the comparison of the EAL curves of all the analyzed structures. The curves seem to be separated into three “groups”, distinguished by structures with the same number of levels. On the contrary, by varying the number of bays, a small variation can be observed in the 2-levels structures while a higher variation is obtained when moving from 2- to the 3-bays, in the structures with 3- and 4-levels.

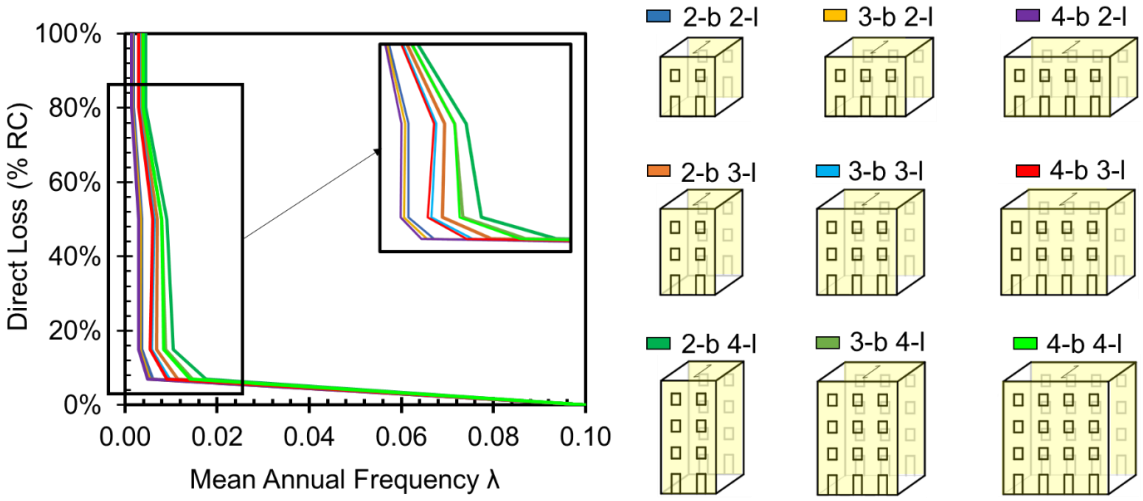

Figure 7.19. EAL curves of the analyzed structures after the intervention with tie rods.

7.8.2 Retrofit interventions for In-Plane mechanisms

To strengthen the walls subjected to the In-Plane seismic forces, different intervention strategies were considered and, as a consequence, different intervention techniques were adopted (a detailed list is reported in Section 4.5.2).

They should be aimed essentially at solving the main structural deficiencies. According to the results obtained by the SLaMA-URM method (see Sections 6.5 and 7.4), both in terms of capacity curves and expected (or more probable) crisis mechanisms, it is needed to proceed to the strengthening of the first level, that is constituted by a weak system. In addition, it is needed to intervene on the brittle shear failures of the spandrels that strongly reduce the global capacity of all the structures.

The following two strategies were considered: i) increase the global ductility and ii) increase the global stiffness and strength of the structures. Regarding the adopted techniques, were taken into account the more widely used in the reconstruction period after the L'Aquila earthquake (Dolce and Manfredi, 2015), such as the grout injections to increase the global ductility and the reinforced plaster and FRP strips to increase the global stiffness and strength of the structures. It was decided to set the target %NBS equal to 80% since in Ministry Decree n.65 7/03/2017 this represents the threshold value to access the first risk class, that corresponds to that in which the least vulnerable structures are grouped.

In the following is reported a brief description of how the adopted techniques were implemented in the SLaMA-URM method. Then, the results obtained by the analyzed structures in terms of performance (%NBS) and economic losses (EAL) are shown.

Grout injection

The grout injections represent a traditional technique adopted to increase the strength of the existing structures, generally in combination with other interventions. It was a widely studied technique (Binda *et al*., 1997; Mazzon, 2010; Oliveira *et al*., 2012; Silva *et al.,* 2014; Vintzileou *et al*., 2015) and its effectiveness depends on the characteristics of the used mortar and on the presence and interconnection of voids in the masonry.

By the indications deriving from research studies and experimental campaigns, CNTC19 (2019) provides a table of the corrective coefficients to quantify the achieved improvement of the retrofit. These coefficients, that change according to the type of masonry, have to be applied to both strength parameters (compressive and shear) as well as to the elastic modules (Young's and shear one).

In this Thesis the indications provided by CNTC19 (2019) were adopted. For the masonry characterized by solid bricks and lime mortar, a corrective coefficient equal to 1.2 was used. It is worth noting that the injections of grout are applied to all the piers in the structures. For the spandrels, instead, in order to have precautionary results, this intervention was not considered.

In Table 7.13 are resumed the main mechanical parameters of the masonry reinforced with the grout injections and adopted in the following applications.

Table 7.13. Mechanical parameters of the masonry reinforced with grout injections.

E_m [MPa]	G_m [MPa]	f_{cm} [MPa]	f_{v0} [MPa]
2160	864	7.4	0.14

Reinforced plaster

The reinforced plaster is a technique that is applied at both sides of the considered walls and it can increase their strength as well as the flexural capacity of the spandrels. Indeed,

the presence of tensile resistant elements (i.e. the electro-welded meshes), if well anchored, leads to consider a tensile strength in the spandrels. Moreover, the effect of this intervention is more evident when applied at the lower levels of the structure, since the walls flexural strength strongly increases for high values of axial loads, while the shear strength increases also for lower axial loads.

As observed from several studies (Ghiassi *et al*., 2012; Churilov e Dumova-Jovanoska, 2013), it was possible to quantify the increase of strength by means of corrective coefficients to apply to mechanical parameters and to the elastic modules of the masonry. In order to well grasp the increase of strength according to the different typology of existing masonry, different coefficients can be adopted. The proposal of these coefficients by CNTC19 (2019) was herein adopted and, according to the typology of the selected masonry, this corrective coefficient is set equal to 1.5.

In Table 7.14 are resumed the main mechanical parameters of the masonry reinforced with the reinforced plaster and adopted in the following applications.

Table 7.14. Mechanical parameters of the masonry reinforced with reinforced plaster.

E_m [MPa]	G_m [MPa]	f_{cm} [MPa]	f_{v0} [MPa]
2700	1080	9.3	0.18

The intervention is realized by means of two (one on each wall side) 3 cm thick concrete sheets with electro-welded mesh, with mesh size 15 x 15 cm and diameter $\phi = 6$ mm (B450C Steel, $f_{yd} = 391.3$ MPa). In order to provide their effective anchorage, transversal connections (injected bars) were considered.

With this intervention it was improved the coupling effect of the spandrels, increasing both the compression and the shear strength. Moreover, in addition to the shear strength, also the flexural strength of the masonry spandrels was further increased. More in detail, the tensile strength of the spandrels can be calculated by the minimum between the masonry and the tensile elements contributions, following Equation 7.9 (CNTC19, 2019):

$$H_p = min\left[(0.4 f_{hd} ht); 2n f_{yd} \frac{\pi \phi^2}{4}\right] \tag{7.9}$$

where f_{hd} is the horizontal masonry compression strength; h and t are the height and the thickness of the spandrel, respectively; f_{yd} is the design tensile strength of the steel and n is the number of the reinforcement bars per side.

Due to the fact that the aim of the retrofit strategy was to achieve a seismic performance higher than 80%NBS, the application of the reinforced plaster was limited on a number of levels such that this threshold was reached. More in detail, for the 2-levels structures it was applied only on the first floor, while for the 3- and 4-levels structures to all the floors.

FRP

The application of the FRP strips is the third intervention technique herein considered. FRP material is used to enhance the flexural and shear capacity of piers and spandrels.

The increase of the shear strength was achieved through the arrangement of the FRP strips parallel to the direction of the shear. This can be obtained when an ideal isostatic truss system is defined. Hence, in addition to the reinforcement parallel to the direction of the shear, it was needed to provide also the arrangement of two strips, parallel to the axis of the piers (or spandrels), to let the development of the truss model.

The intervention with FRP was adopted to increase the shear strength of the piers at the base and to prevent the expected shear failure of the spandrels. For these reasons, the design of the flexural strengthening was considered. More in detail, it was supposed to apply two symmetrically disposed of FRP strips, parallel to the axes of the elements (vertically in the piers and horizontally in the spandrels).

Following the instructions in CNR DT200 (2004), the characteristics of the composite material were defined. More in detail, adopting the CFRP type, it was assumed the FRP tensile elastic modulus equal to $E_f = 230\ \mathrm{GPa}$, the characteristic FRP tensile strength as $f_{fk} = 1500\ \mathrm{MPa}$ and the design FRP tensile strength as $f_{fRd} = 1295.5\ \mathrm{MPa}$ (assuming a conversion factor equal to $\eta = 0.95$ and a safety partial coefficient for the failure mode collapse equal to $\gamma_f = 1.1$). In order to consider the linear behaviour of the material, the design strain was calculated as $\varepsilon_{fRd} = f_{fRd}/E_f = 0.0056$. Also, the possible delamination failure, that can occur in the intervention with FRP, was taken into account. More in detail, the ultimate strain due to the delamination failure ε_{fdd} as well as the tensile strength f_{fdd} were identified, following Equations 7.10 and 7.11:

$$\varepsilon_{fdd} = \frac{1}{\gamma_{fd}} \sqrt{\frac{2\Gamma_{Fd}}{t_f E_f}} \tag{7.10}$$

$$f_{fdd} = \frac{1}{\gamma_{fd}} \sqrt{\frac{2\Gamma_{Fd} E_f}{t_f}} \tag{7.11}$$

where γ_{fd} is the safety partial coefficient for the delamination failure mode, set equal to 1.2; t_f is the thickness of the strips, equal to $t_f = 0.189\ \mathrm{mm}$ (defined from a fibres weight per unit area of $\rho_f = 350\ \mathrm{g/m^2}$ and a fibres specific weight of $\rho_f = 1.85\ \mathrm{g/cm^3}$); Γ_{Fd} is the design fracture energy, defined by the area under the tangential stress-sliding curve that represents the needed work to produce the failure of an interface area. Following the CNR DT200 (2004) instructions, this last parameter is considered equal to $\Gamma_{Fd} = \Gamma_{Fk}/\gamma_m$, where Γ_{Fk} is the characteristic value, defined in Equation 7.12, and γ_m is the safety coefficient of the masonry (assumed equal to 2):

$$\Gamma_{Fk} = c_1 \sqrt{f_{mk} f_{mkm}} \tag{7.12}$$

where c_1 is a coefficient equal to 0.015; f_{mk} and f_{mkm} are the characteristic compression and tensile strength of the masonry. In absence of experimental data it was assumed $f_{mkm} = 0.1 f_{mk}$.

The FRP ultimate strain is the minimum value between ε_{fRd} and ε_{fdd}, and consequently, the FRP tensile strength is obtained multiplying it by the tensile elastic modulus. To avoid delamination issues, mechanical connectors were introduced to increase ε_{fdd}. These devices are generally made with FRP material and are placed inside the wall in order to connect the reinforcing elements on both sides of the element. With the use of the connectors, the ultimate strain was set equal to 3‰ (Vinci, 2019).

The flexural strength of the components (pier and spandrel) reinforced with FRP was calculated by sectional analysis through the MBA approach (presented in Section 5.4.2.1). In the pier (or spandrel)-FRP system the compression strength is given by the masonry contribution (FRP shows a very low compression stiffness), while the tensile strength is provided by the composite material. The shear capacity of the strengthened element is given by the equilibrium of the shear forces in the activated truss mechanism. More in detail, this capacity was defined by the sum of the masonry contribution $V_{Rd,m}$ and the FRP contribution

$V_{Rd,f}$, up to the maximum value $V_{Rd,max}$ that induces the failure of the compressed strut of the truss (CNR DT200, 2004). Assuming a shear strengthening parallel to the mortar joints, the following formulations were adopted (Equations 7.13 and 7.14):

$$V_{Rd,m} = \frac{1}{\gamma_{Rd}} dt f_{vd} \tag{7.13}$$

$$V_{Rd,fm} = \frac{1}{\gamma_{Rd}} \frac{0.6 d A_{fw} f_{fd}}{\rho_f} \tag{7.14}$$

where d is the lever arm of the FRP force with respect to the masonry compression force; t is the component thickness; f_{vd} is the design shear strength of the masonry; A_{fw} is the area of the FRP shear strengthening; ρ_f is the center-to-center spacing of FRP and f_{fd} is the design strength of FRP reinforcement (defined as the lower value between FRP tensile failure strength and the delamination one). The partial factor γ_{Rd} was assumed to equal to 1.

Regarding the maximum shear capacity, Equation 7.15 was adopted:

$$V_{Rd,max} = 0.3 f_{mh} t d \tag{7.15}$$

where f_{mh} is the masonry compressive strength parallel to the mortar joints.

The FRP applications, in order to achieve the aforementioned purpose to reach the minimum performance of 80%NBS, was applied as follows:

- in the 2-levels structures, the FRP strips were applied to increase the flexural and shear capacity of the three piers at the base and of the two spandrels at the second floor;
- in the 3-levels structures, the intervention with FRP is performed on the four piers at the base and on the spandrels at the first and second floor;
- in the 4-levels structures, the FRP was applied on the five piers at the base and on all the spandrels of the structures.

It is worth noting that the reinforced structural components, after the intervention with FRP, changed their failure mechanism, from shear type to flexural one.

In Table 7.15 are reported the geometric arrangements (i.e. the width b_f and the spacing of the shear strips ρ_f) of the applied FRP on each structural component of the analyzed structures.

Generally speaking, the same dimensions were assumed for the exterior piers at the base of all the structures ($b_f = 100\,\text{mm}$ and $\rho_f = 500\,\text{mm}$), while for the interior ones, different values of ρ_f were used, in order to guarantee that the shear strength was higher than the flexural one. More in detail, for the 2-levels structures the same geometry of the exterior piers was adopted, while for the 3- and 4-levels structures a lower value of ρ_f of the strips was required ($\rho_f = 300\,\text{mm}$ for the 3-levels structures and $\rho_f = 200\,\text{mm}$ for the 4-levels structures).

Table 7.15. Geometric characteristics of the FRP strips on the exterior and interior piers of the 2-, 3- and 4-levels structures.

	EXTERIOR		INTERIOR	
	b_f (mm)	ρ_f (mm)	b_f (mm)	ρ_f (mm)
2-levs	100	500	100	500
3-levs	100	500	100	300
4-levs	100	500	100	200

Regarding the FRP arrangements on the spandrels, the following values were assumed: $b_f = 100\,\text{mm}$ and $\rho_f = 300\,\text{mm}$.

In Figure 7.20 are reported the results in terms of the performance and the economic losses by adopting the aforementioned retrofit interventions for the 2-bays 2-levels structure. The results of the retrofit interventions for all the other structures are reported in Appendix A.4.

In Figure 7.20a, it is observed that the application of the grout injections (green line) leads to an increase of the displacement capacity. An increase of the global performance (+20%) was obtained, achieving the target %NBS, which however is not sufficient to achieve the safety check (%NBS = 88% < 100%) yet. On the contrary, a significant increase of the strength capacity is observed when the reinforced plaster is applied at the first level of the structure (red line) and when the FRP strips are arranged on the piers at the base and on the

spandrels at the second floor (blue line). This is essentially due to the increase of the spandrels strength. Indeed, these components strongly limit the unreinforced structure as well as the one reinforced with injections of grout, hence by intervening on the spandrels, and by increasing their coupling effect, the global capacity of the structure increases. In the case of application of reinforced plaster, a performance equal to %NBS = 108% is achieved (+28% with respect to the unreinforced case), satisfying the safety check. As observed by the corresponding capacity curve, an increase of the displacement capacity is obtained (+35% with respect to the unreinforced case), thanks to the increase of the displacement capacity of the left pier at the base. It is important to highlight that by adopting this intervention, the failure mechanisms of the components are unchanged with respect to the unreinforced structure, hence it is still expected the shear failure of the spandrels and the shear failure of the central and right piers at the base. Adopting the FRP strips to strengthen the piers at the base and the spandrels at the second floor, the %NBS = 100% is achieved and the failure mechanisms of the strengthened components are changed from the shear type to the flexural one.

In terms of EAL curves (Figure 7.20b), a slight reduction in the curve, with respect to the unreinforced case, is achieved by using injections of grout. More in detail, a decrease of losses can be observed at the ultimate limit state, leading to EAL = 0.62% (-0.03% with respect to the unreinforced case). A higher decrease of EAL is observed for reinforced plaster (-0.15%, leading to EAL = 0.50%) and FRP strips (-0.13%, leading to EAL = 0.52%).

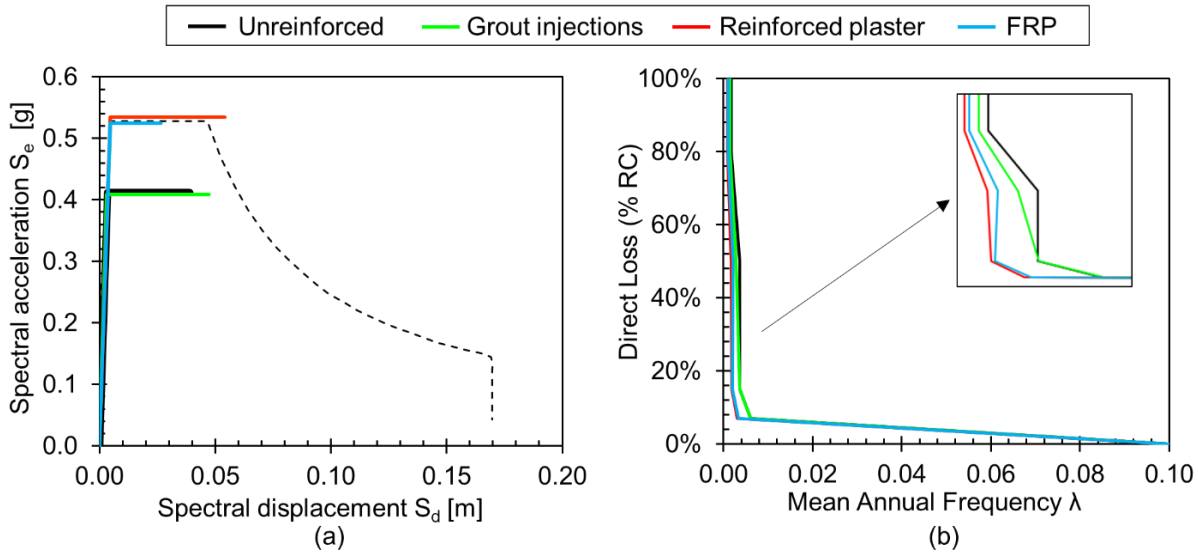

Figure 7.20. Retrofit interventions results of the 2-bays 2-levels structure: (a) seismic performances and (b) expected annual losses curves.

In Figure 7.21 is shown the comparison of the achieved %NBS and the expected EAL for the 2-bays 2-levels structure through the retrofit interventions described above.

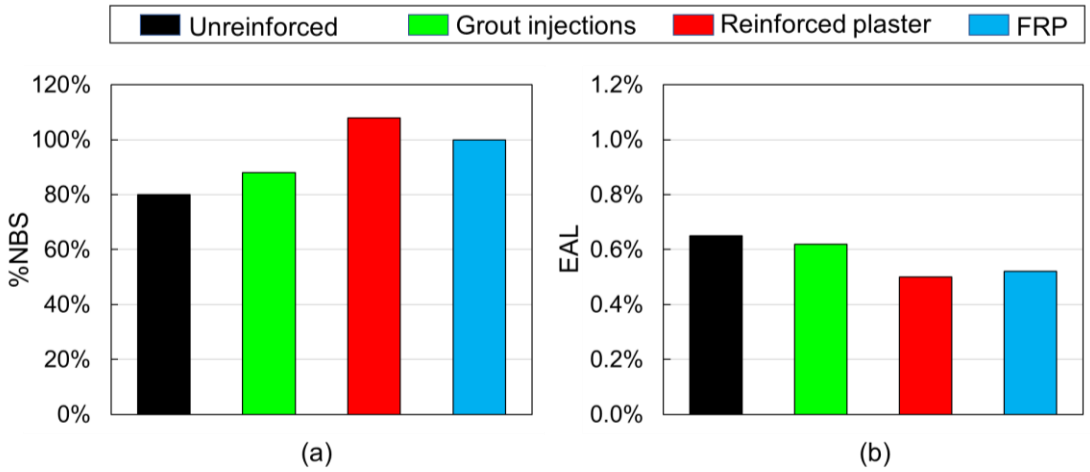

Figure 7.21. Retrofit interventions results of the 2-bays 2-levels structure: (a) %NBS and (b) EAL.

The same considerations made for the 2-bays 2-levels structure can be made for the other 2-levels structures (see Figure 7.22). More in detail, it is possible to observe that all the structures, having already good performance in the unreinforced case, can achieve a low increase in terms of the %NBS with the grout injections (approximately +10%), while a strong increase is observed when FRP (+15% in the case of 3- and 4-bays) and reinforced plaster (+24% in the case of 3- and 4-bays) are used. Generally speaking, no clear differences emerge when varying the number of bays in the 2-levels structures. The best performance is achieved by adopting reinforced plaster on the first floor, but with this intervention, unlike using FRP, the expected brittle failures of piers and spandrels do not change to a ductile one.

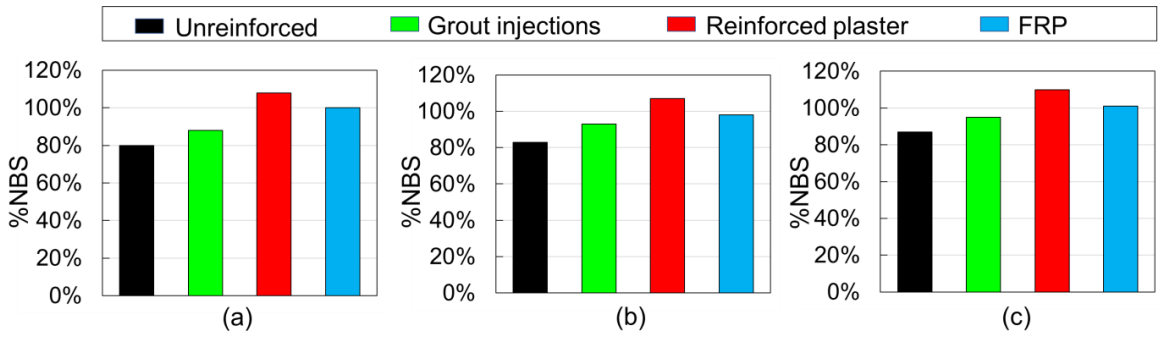

Figure 7.22. %NBS achieved with different retrofit interventions for: (a) 2-bays 2-levels structure, (b) 3-bays 2-levels structure and (c) 4-bays 2-levels structure.

Regarding the 3-levels structures, the performance achieved in terms of the %NBS by adopting different retrofit interventions are shown in Figure 7.23. From these results, it can be highlighted that the influence of the retrofit by grout injections is definitively lower than in the 2-levels structures. More in detail, an increase of 4% is obtained for all the structures, i.e. half of the one obtained in the 2-levels structures. The strengthening by FRP and reinforced plaster allows achieving approximately the same increase with respect to the unreinforced structure. This variation ranges from 33% to 39%. Both these techniques can achieve the maximum performance (equal or higher than 100%NBS) in the 3- and 4-bays structures. While, in the 2-bays structure, the intervention with the reinforced plaster reaches 94%NBS and that with FRP 98%NBS.

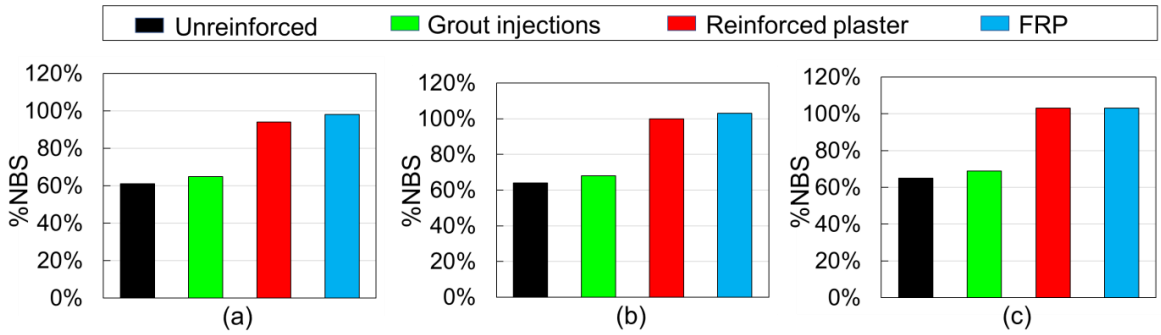

Figure 7.23. %NBS achieved with different retrofit interventions for: (a) 2-bays 3-levels structure, (b) 3-bays 3-levels structure and (c) 4-bays 3-levels structure.

Regarding the 4-levels structures, as shown in Figure 7.24, the grout injections almost do not affect the performance achieved in terms of %NBS (increases of 2% with respect to the unreinforced case). For the intervention with FRP, the increase is around 42% (similar to what obtained for the 3-levels structures), achieving %NBS values that range from 98% to 100%. A lower increase of %NBS is observed by adopting reinforced plaster, which leads to an increase of around 28% (approximately 10% less than what obtained for the 3-levels structures).

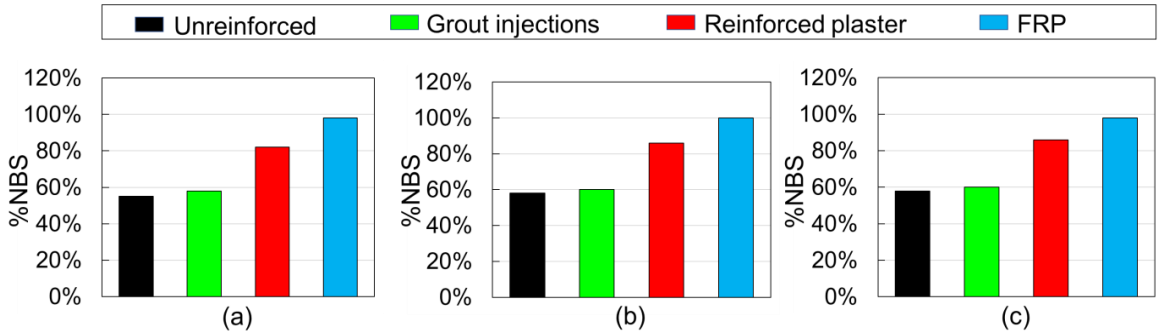

Figure 7.24. %NBS achieved with different retrofit interventions for: (a) 2-bays 4-levels structure, (b) 3-bays 4-levels structure and (c) 4-bays 4-levels structure.

About the EAL results, for the 2-levels structures (see Figure 7.25) it was observed that, by varying the number of bays, no clear differences with respect to the 2-bays structure (Figure 7.21b) are observed. The grout injections lead to a slight decrease of EAL (around 0.03% with respect to the unreinforced case), leading to values that range from 0.62% to 0.57%. With the reinforced plaster and the FRP, a lower decrease of EAL is obtained by increasing the number of bays. More in detail, in the 2-bays structure a variation of 0.15% and 0.13% is obtained for each intervention (obtaining EAL = 0.50% and EAL = 0.52%, respectively), while in the 4-bays structure a variation of 0.11% and 0.08% (obtaining EAL = 0.49% and EAL = 0.52%, respectively) is observed.

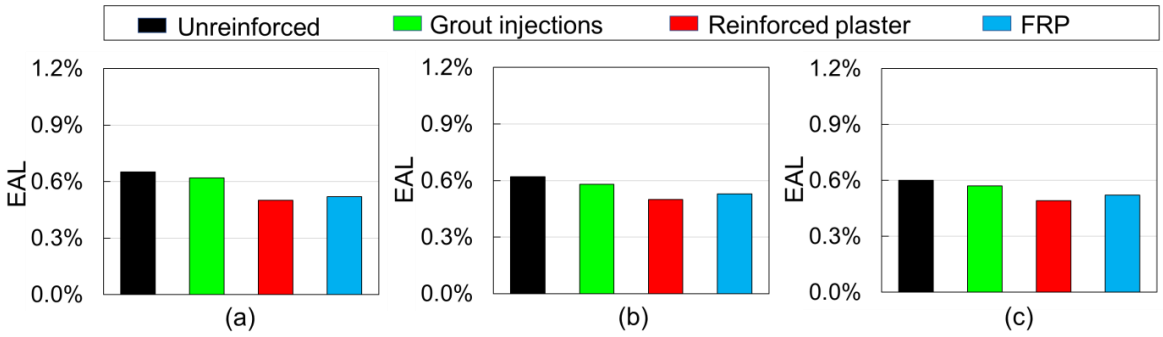

Figure 7.25. EAL obtained with different retrofit interventions for: (a) 2-bays 2-levels structure, (b) 3-bays 2-levels structure and (c) 4-bays 2-levels structure.

For the 3-levels structures, the results shown in Figure 7.26 highlight that the grout injections give a similar improvement obtained for the 2-levels structures, while by adopting the reinforced plaster and FRP a great decrease of EAL (around 0.35% with respect to the unreinforced case) is obtained. More in detail, the intervention with grout injections leads to

EAL values that range from 0.89% to 0.81%. The reinforced plaster application allows obtaining EAL values that range from 0.55% to 0.51%, while the intervention with FRP from 0.53% to 51%. By varying the number of bays no significant differences are highlighted in the trend.

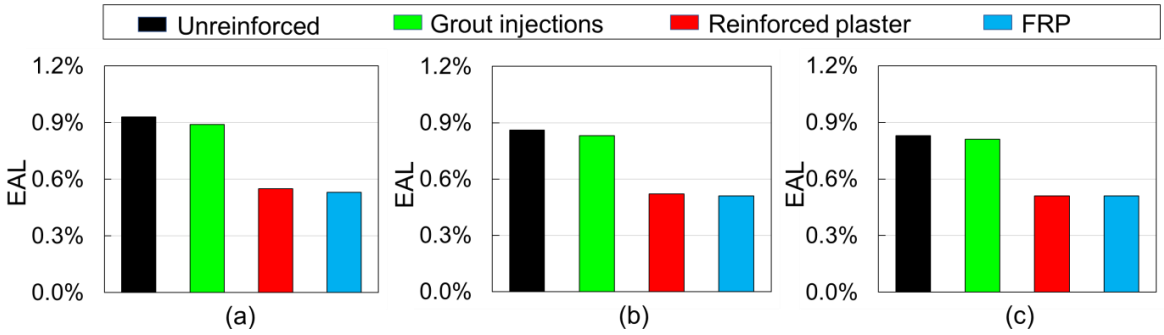

Figure 7.26. EAL obtained with different retrofit interventions for: (a) 2-bays 3-levels structure, (b) 3-bays 3-levels structure and (c) 4-bays 3-levels structure.

Regarding the 4-levels structures, the results are shown in Figure 7.27. The differences with the structures discussed above reside in the EAL values obtained by considering the FRP and the reinforced plaster interventions. Indeed, the former grants a lower value of EAL (around 0.53%) with respect to the unreinforced structure (with a decrease that ranges from 63% to 52%). While the latter intervention gives EAL values that range from 0.63% to 0.60%. Moreover, it is worth noting that the trend that considers an improvement of EAL values, starting from the 2-levels up to the 4-levels, is herein again confirmed. Also in these cases, by varying the number of bays no significant differences can be observed in the results.

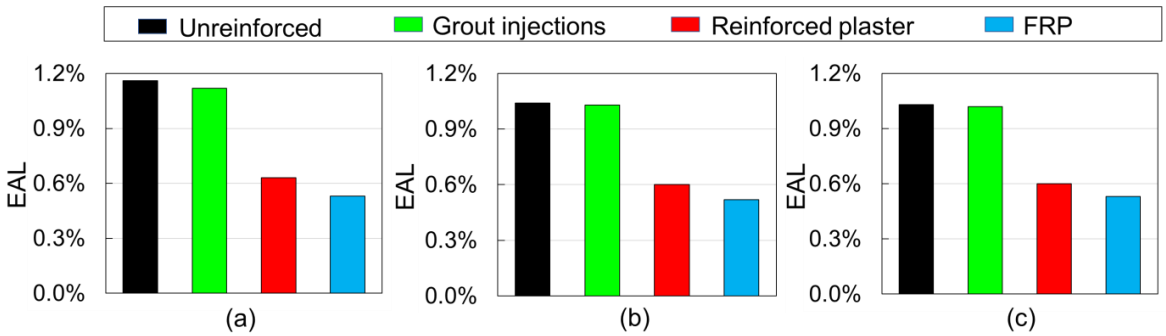

Figure 7.27. EAL obtained with different retrofit interventions for: (a) 2-bays 4-levels structure, (b) 3-bays 4-levels structure and (c) 4-bays 4-levels structure.

A summary of all the achieved %NBS values and the obtained EAL by adopting the different retrofit interventions is reported in Tables 7.16 and 7.17, respectively.

Table 7.16. %NBS achieved with different retrofit interventions for the analyzed structures.

	2-bays				3-bays				4-bays			
2-levs	80	88	108	100	83	93	107	98	87	95	110	101
3-levs	61	65	94	98	64	68	100	103	65	69	103	103
4-levs	55	58	82	98	58	60	86	100	58	60	86	98

Unreinforced Grout injections Reinforced plaster FRP

Table 7.17. EAL obtained with different retrofit interventions for the analyzed structures.

	2-bays				3-bays				4-bays			
2-levs	0.65	0.62	0.50	0.52	0.62	0.58	0.50	0.53	0.60	0.57	0.49	0.52
3-levs	0.93	0.89	0.55	0.53	0.86	0.83	0.52	0.51	0.83	0.81	0.51	0.51
4-levs	1.16	1.12	0.63	0.53	1.04	1.03	0.60	0.52	1.03	1.02	0.60	0.53

Unreinforced Grout injections Reinforced plaster FRP

In summary, it can be said that varying the number of bays has no significant effects on the %NBS and EAL, for all the different retrofit interventions. While, by increasing the number of levels, the achieved performance of the reinforced structures decreases and, at the same time, the expected economic losses increase.

Although the FRP and the reinforced plaster interventions lead to similar results both in terms of %NBS and EAL, by adopting the former intervention, the failure mechanisms of the structural components do not change, while by applying FRP, the brittle shear failure of the spandrels and of the piers at the base changes in the flexural one.

7.9 Retrofit interventions comparison: medium vs high seismicity

In order to highlight the differences obtained by applying retrofit interventions on structures located in different seismicity zones, the results obtained in Section 7.8 for the medium seismicity (MS) are herein compared with those obtained in conditions of high seismicity (HS, PGA = 0.34g). It should be noted that this change, in the SLaMA-URM method, consists of considering different seismic demands.

Regarding the OOP performance, the results of the unreinforced structures are reported in Section 7.5. By supposing to intervene with tie rods to prevent the activation of these mechanisms, as for the MS case, the results in terms of $\%NBS_{OOP}$ are reported in Table 7.18. The same design procedure described in Section 7.8.1 was considered, with the difference that, to satisfy the safety verifications, it was needed to consider thicker round-shaped metal ties, i.e. a diameter of $\phi = 14$ mm at each floor of the 2-levels structures, and of $\phi = 16$ mm at each floor of the 3- and 4-levels structures. Due to the fact that the variation of bays does not influence the results, the same outcomes are expected for structures with the same number of levels. All the structures, after the retrofit intervention with tie rods, show the overturn around the cylindric hinge at the base of the first floor as the critical mechanism expected to occur (Mechanism 2).

Table 7.18. High seismicity results: $\%NBS_{OOP}$ of the structures reinforced through tie rods.

	$\%NBS_{OOP}$			
Case	**Mech.1**	**Mech.2**	**Mech.3**	**Mech.4**
2-levs	313	106	-	-
3-levs	370	115	132	-
4-levs	357	109	114	143

Once the OOP mechanisms were prevented, attention was given to the global performance achieved by the structures placed in the HS zone. In Figure 7.28 are shown the capacity curves compared with the elastic spectrum and the EAL curves.

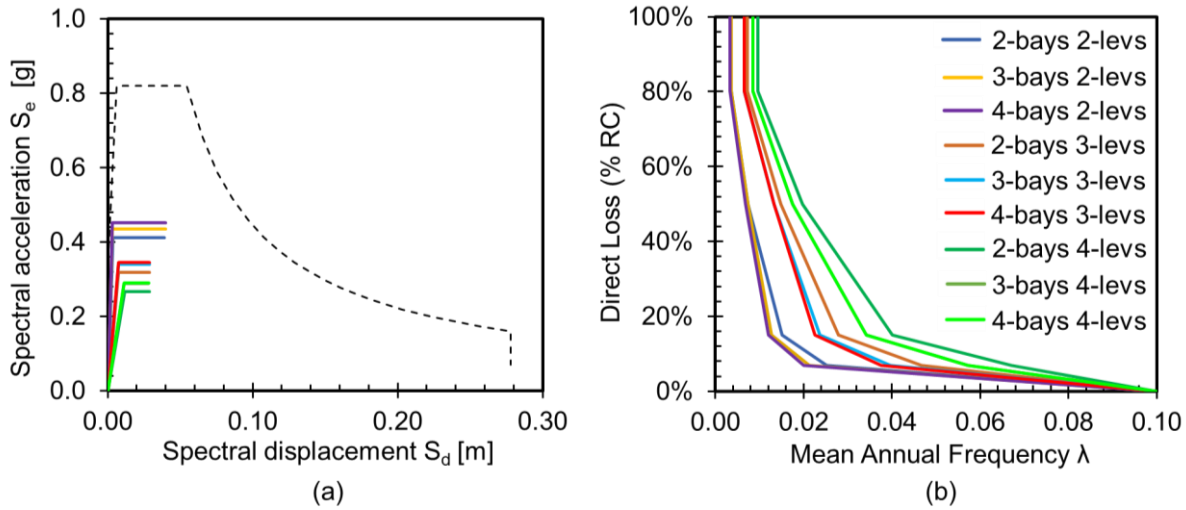

Figure 7.28. High seismicity: (a) In-Plane performance levels and (b) EAL curves of the structures.

In Figures 7.29 and 7.30 are shown the comparisons between the results obtained in MS and in HS zones, in terms of %NBS and EAL values, respectively.

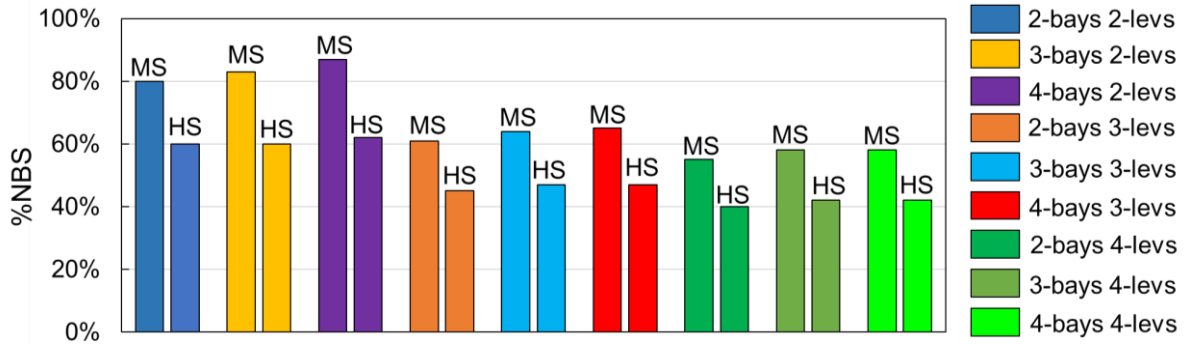

Figure 7.29. %NBS after the intervention with tie rods: MS and HS comparison.

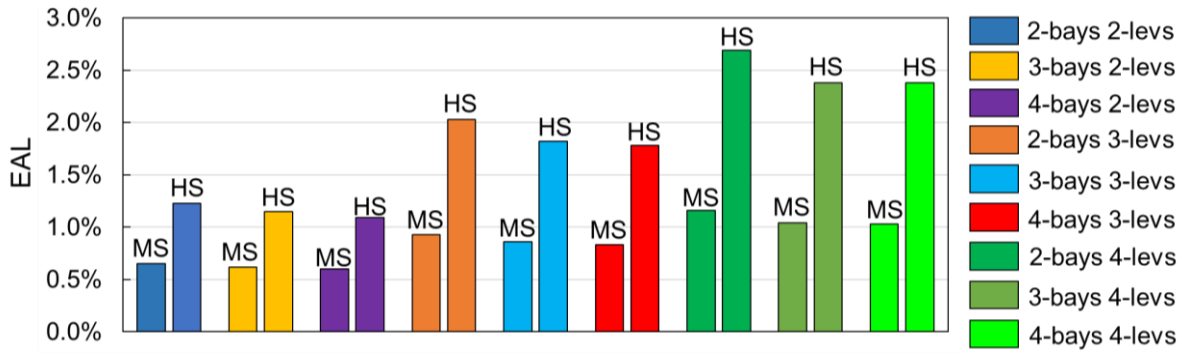

Figure 7.30. EAL after the intervention with tie rods: MS and HS comparison.

From the results, it can be observed that the variation of the performance ranges from 15% to 25% when moving from MS to HS zones. More in detail, the HS leads to a strong decrease of %NBS in the 2-levels structures (e.g. 20-25%), obtaining a value of 60% in the 2- and 3-bays structures and of 62% in the 4-bays structure. While a lower decrease is observed in the 3- and 4-levels structures (e.g. 15-18%), where are achieved values of 45% in the 2-bays 3-levels structure, of 47% in the 3- and 4-bays 3-levels structures, of 40% in the 2-bays 4-levels structure and of 42% in the 3- and 4-bays 4-levels structures.

The higher variation of the %NBS in the 2-levels structures can be motivated by their higher ductility capacity. In MS, the capacity curves are close to the plateau of the elastic spectrum, as a consequence, a lower damping value is needed in order to achieve the performance point. In HS, instead, the curves are more distant from the elastic spectrum, hence a higher damping value is necessary.

Regarding the EAL values, the HS leads to an increase of the expected economic losses that range from 0.49% to 1.53%, with respect to the MS case. More in detail, a drastic increase is observed in the 4-levels structures (variations of 1.34 - 1.53%), leading to EAL = 2.69% for the 2-bays structure and EAL = 2.38% for the 3- and 4-bays structures. Also in the 3-levels structures, an increase is observed (from 0.95% to 1.10%), obtaining EAL values of 2.03% for the 2-bays structure, 1.82% for the 3-bays and 1.78% for the 4-bays. A lower variation is observed in the 2-levels structures (from 0.49% to 0.58%), in which the EAL values obtained are: 1.23% for the 2-bays, 1.15% for the 3-bays and 1.09% for the 4-bays structure.

The difference observed in the 2-levels structures with respect to the 3- and 4-levels structures can be explained by the higher losses expected at serviceability limit states (DLS and OLS) in these latter with respect to those requested for the 2-levels ones. Higher values of the mean frequency of exceedance at these limit states, increase the area under the EAL curves and consequently lead to higher EAL values.

Once the performance of the existing structures was defined, the retrofit solutions (grout injections, reinforced plaster and FRP) were considered. Since the results obtained in MS zones, showed that the number of bays does not affect the trend of %NBS and EAL, for sake of brevity, for the HS case the retrofit analyses were carried out only on the three structures with 2-bays, i.e. 2-levels, 3-levels and 4-levels.

More in detail, the grout injections were applied to all the piers of the structures and with the same modality described in the MS condition.

The reinforced plaster was applied with the same details described in the MS condition but by varying the number of floors subjected to this retrofit interventions.

The FRP, in order to achieve the target %NBS (i.e. 80%) was applied to the second floor spandrels of the 2-levels structure and to all the spandrels of the 3- and 4-levels structures. The arrangements of the strips in the spandrels consisted of setting $\rho_f = 300\ \mathrm{mm}$ in all the cases and $b_f = 100\ \mathrm{mm}$ for the 2-levels structure, while $b_f = 150\ \mathrm{mm}$ for the 3- and 4-levels structures. Moreover, the FRP was applied also to all the piers at the base of the analyzed structures. For the geometric arrangements on the piers at the base refer to Table 7.19.

To satisfy the safety check in HS, it was needed to increase the width of the strips of the interior and the exterior piers at the base (from $b_f = 100\ \mathrm{mm}$ to $b_f = 200\ \mathrm{mm}$) in the 3- and 4-levels structures, with respect to those applied in MS. Once increased b_f, it was possible to increase the spacing of the FRP strips on the interior piers (passing from $\rho_f = 300\ \mathrm{mm}$ to $\rho_f = 500\ \mathrm{mm}$ in the 3-levels structure and from $\rho_f = 200\ \mathrm{mm}$ to $\rho_f = 300\ \mathrm{mm}$ in the 4-levels structure), because the shear failure was no longer the limiting factor once that the width of the strips was increased. On the contrary, these modifications were not necessary in the 2-levels structure, i.e. the same FRP arrangement of the MS case was maintained.

Table 7.19. Geometric characteristics of the FRP strips on exterior and interior piers of the 2-, 3- and 4-levels structures in HS zones.

	EXTERIOR		INTERIOR	
	b_f (mm)	ρ_f (mm)	b_f (mm)	ρ_f (mm)
2-levs	100	500	100	500
3-levs	200	500	200	500
4-levs	200	500	200	300

In Figure 7.31 are shown the results obtained for the 2-bays 2-levels structure. The retrofit interventions that were applied consist in: i) grout injections, ii) application of reinforced plaster at the first floor (I, in Figure) and at the first and second floor (I+II, in

Figure), iii) application of the FRP strips on the piers at the base and on the spandrels at the second floor (FRP (1), in Figure) or on the piers at the base and on the spandrels at the first and second floor (FRP (2), in Figure).

From Figure 7.31a it can be observed that the application of the grout injections on all the piers of the structures gives a small increase (+6%) of the %NBS, but it is still not sufficient to achieve the target %NBS (e.g. 80%). The application of the reinforced plaster at the first floor (I, in Figure) leads to an important increase in the performance (+21%), achieving a %NBS equal to 81%, close to the target value. In order to further improve its effect, the reinforced plaster is applied also to the second floor, reaching %NBS = 84%. Regarding the FRP application, the configuration (1) is not able to give the minimum required %NBS (arrives at %NBS = 64%). By using the configuration (2), instead, the achieved %NBS is 94%, with a significant increase (+34%) with respect to the unreinforced case.

In Figure 7.31b it can be observed that the best results in terms of EAL were obtained by adopting the configuration (2) of the intervention with FRP, which shows a great reduction of EAL (-0.65% with respect to the unreinforced case). Regarding the grout injections, a very small decrease of 0.08% is obtained, while in the case of the reinforced plaster to the first and the second floor (I+II, in Figure) a reduction of 0.53% is obtained.

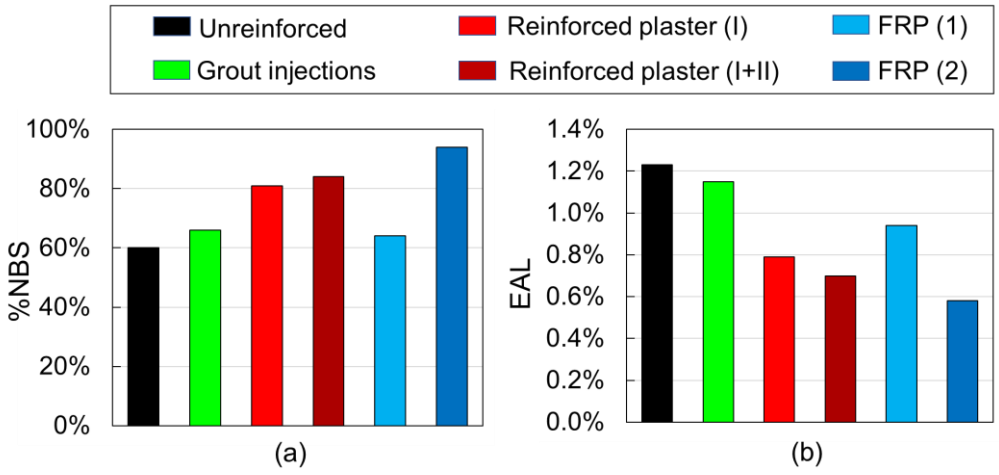

Figure 7.31. Retrofit interventions results in HS zones for the 2-bays 2-levels structure: (a) %NBS and (b) EAL.

By increasing the number of levels (see Figure 7.32), the adoption of the reinforced plaster to all the floors of the structures does not allow to reach the target %NBS. More in

detail, for the 3-levels structure is obtained %NBS = 68%, while for the 4-levels %NBS = 56%. The intervention with grout injections, as happened for the 2-levels structure, does not allow to give the required performance (grants a %NBS = 48% in the 3-levels structure and %NBS = 44% in the 4-levels structure). On the contrary, by using the FRP strips, with the modified geometric configuration previously discussed (that justifies the different colour used in Figure), the target %NBS is achieved. More in detail, the FRP is applied on the piers at the base and on the spandrels at each level. The achieved %NBS is equal to 108% in the 3-levels structure and to 102% in the 4-levels structure.

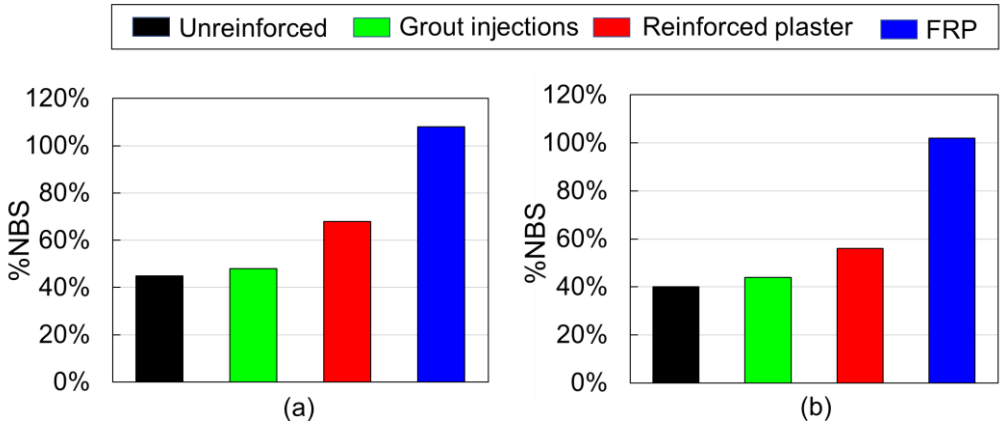

Figure 7.32. %NBS achieved in HS zones with different retrofit interventions for: (a) 2-bays 3-levels structure and (b) 2-bays 4-levels structure.

In Figure 7.33 are shown the results in terms of EAL for the 3- and 4-levels structures. Although the application of the reinforced plaster to all the floors of the 3- and 4-levels structures does not allow to achieve the desired %NBS, it allows to obtain a good reduction of EAL (-1.09% in the 3-levels structure and -1.47% in the 4-levels structure). More evident is the EAL improvement obtained through FRP (-1.51% in the 3-levels structure and -2.15% in the 4-levels structure), while with the grout injections intervention a slight reduction is observed (-0.05% in the 3-levels structure and -0.06% in the 4-levels structure).

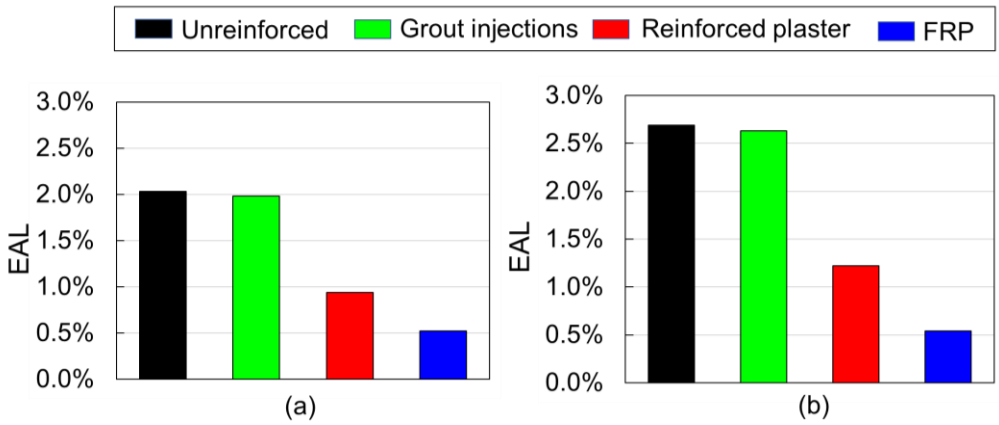

Figure 7.33. EAL obtained in HS zones with different retrofit interventions for: (a) 2-bays 3-levels structure and (b) 2-bays 4-levels structure.

A summary of the %NBS values achieved and the EAL obtained by adopting the different retrofit interventions in HS zones for the 2-, 3- and 4-levels structures are reported in Tables 7.20 and 7.21, respectively.

In summary, these results showed that the 2-levels structure is not characterized by a critical condition, since it achieves the target %NBS with both the reinforced plaster and the FRP interventions. While regarding the 3- and 4-levels structures the adoption of the reinforced plaster does not allow to improve the performance as required. In all the analyzed cases, the intervention with FRP represents the best retrofit solution, since it achieves the higher performance and the lower expected economic losses. Moreover, it should be evidenced that the structures located in HS zones are not only more vulnerable in their unreinforced condition but also the choice of their retrofit strategy represents a not-so-trivial aspect.

Table 7.20. %NBS achieved in HS zones with different retrofit interventions for: (a) the 2-levels structure and (b) the 3- and 4-levels structures.

	2-levs
Unreinforced	60
Grout injections	66
Reinforced plaster (I)	81
Reinforced plaster (I+II)	84
FRP (1)	64
FRP (2)	94

(a)

	3-levs	4-levs
Unreinforced	45	40
Grout injections	48	44
Reinforced plaster	68	56
FRP	108	102

(b)

Table 7.21. EAL obtained in HS zones with different retrofit interventions for: (a) the 2-levels structure and (b) the 3- and 4-levels structures.

	2-levs
Unreinforced	1.23
Grout injections	1.15
Reinforced plaster (I)	0.79
Reinforced plaster (I+II)	0.70
FRP (1)	0.94
FRP (2)	0.58

(a)

	3-levs	4-levs
Unreinforced	2.03	2.69
Grout injections	1.98	2.63
Reinforced plaster	0.94	1.22
FRP	0.52	0.54

(b)

In Figures 7.34 and 7.35 are shown the comparisons between the results obtained in MS and HS zones, in terms of %NBS and EAL values, respectively, for the 2-bays structures, after the retrofit interventions. It is worth noting that, although the arrangements of the interventions are different in HS zone with respect to the MS one, as observed above, the colours of the histograms were homogenised according to the considered interventions, for a more clear comparison.

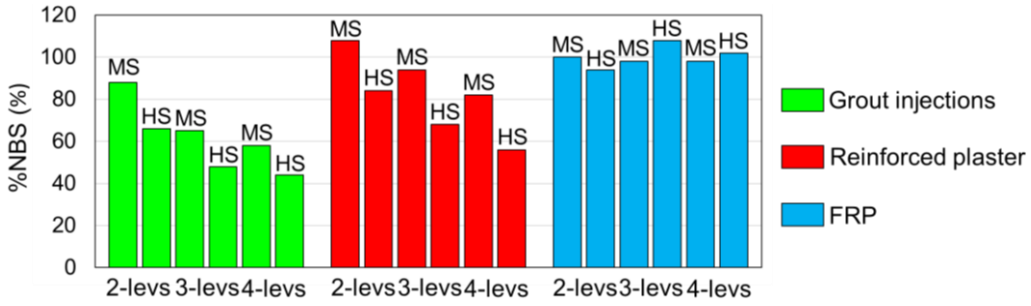

Figure 7.34. %NBS achieved after IP retrofit interventions for 2-bays structures: MS vs HS comparison.

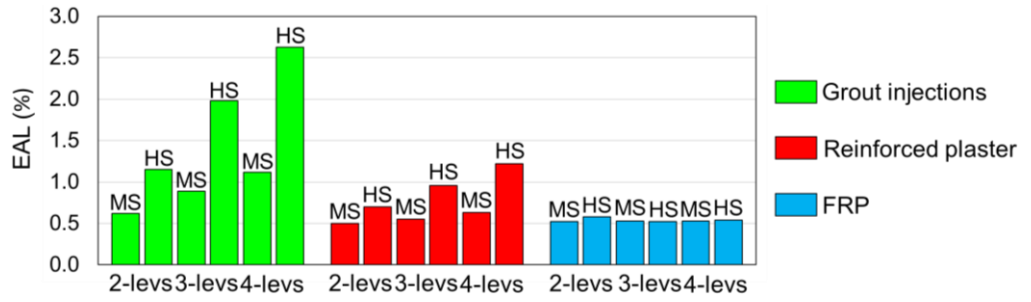

Figure 7.35. EAL obtained after IP retrofit interventions for 2-bays structures: MS vs HS comparison.

From these results, it can be seen that the grout injections achieve the target %NBS only in the 2-levels structure placed in MS zones (88%), while in all the other cases they reach values lower than 66%NBS. Regarding the reinforced plaster intervention, it leads to the target %NBS in all the structures, except for the 3- and 4-levels structures in HS zones, that achieve 68% and 56%NBS, respectively. In all of the three cases study, the %NBS obtained in MS zones is higher of around 25% than that achieved in HS zones. Concerning the intervention with FRP, little differences can be observed in terms of %NBS, since in all cases it exceeds 94%.

The results in terms of EAL obtained with the grout injections and the reinforced plaster suggest that higher economic losses are expected in all the structures placed in HS zones. While in the intervention with FRP no evident differences can be observed in the EAL results obtained in both seismic conditions. More in detail, for the grout injections an increase of around 0.5% is observed in the 2-levels structure, of around 1% in the 3-levels structure and of 1.5% in the 4-levels one, when moving from MS to HS zones. For the intervention with reinforced plaster, a lower variation is obtained when moving from MS to HS zones: an increase of around 0.2% in the 2-levels structure, 0.4% in the 3-levels structure and 0.6% in the 4-levels one. Finally, regarding the intervention with FRP there are almost no differences in terms of EAL when moving from MS to HS zone, for all the 2-bays structures.

It is worth noting that the analyses proposed above are not intended as a complete and all-inclusive study of all the possible retrofit interventions, but they want to give an idea of how the SLaMA-URM method can also be used to study the behaviour and the response of reinforced structures and to design the different retrofit interventions according to the highlighted weaknesses of the analyzed structure. Hence, the interest was focused on the investigation of the behavior of the masonry structures before and after the different interventions, in order to quantify the comparison in terms of %NBS and EAL.

7.10 Retrofit interventions costs

In this Section, a comparison between the improvement in performance and the investment required for the different retrofit interventions is provided. More in detail, an immediate analysis between costs and benefits of the different retrofit strategies described in the previous sections is carried out.

At first, are evaluated the costs of the interventions and in order to do this, the regional price lists of public works in retrofit interventions (Genio Civile, 2018) were considered. The unit prices described in the following include all the charges concerning the design, construction and implementation of the intervention. More in detail, the specialized labor and the charges of safety were also taken into account. Moreover, in order to provide a useful criterion for comparing the different intervention strategies, the corresponding cost of each percentage point of NBS (1%NBS), defined as the ratio between the intervention cost and the variation of %NBS ($\%NBS_{post\ operam}$ - $\%NBS_{ante\ operam}$) of the considered intervention, is considered.

For the application of the tie rods, necessary to prevent the OOP mechanisms, with reference to Genio Civile (2018), was assumed a unit cost that ranges from 300€ up to 590€ based on the length of the adopted metal tie as well as its diameter.

Regarding the retrofit interventions to increase the In-Plane performance of the frames parallel to the seismic action, Genio Civile (2018) was considered to identify the intervention costs. More in detail, for the intervention with grout injections, the cost per square meter equal to 50 €/m^2 was considered, and by defining the area of the strengthened piers, the total cost of the intervention was defined. For the reinforced plaster application, a cost per square meter equal to 130 €/m^2 was assumed. By considering the net area of the intervention, the corresponding cost was defined. Finally, for the intervention with FRP, a cost per square meter of FRP strips equal to 430 €/m^2 was considered and, calculating the area of the applied strengthening material, the cost of the intervention was defined.

For sake of brevity, in the following Sections, the only 2-bays structures costs are reported, considering both the MS and HS case. The complete set of costs for the structures located in MS zones is reported in Appendix A.5.

7.10.1 Medium seismicity

At first, the OOP mechanisms need to be impaired by means of tie rods. The unit costs associated with each structure and the corresponding cost of 1%NBS are resumed in Table 7.22.

Table 7.22. Tie rods intervention costs in MS zones of all the analyzed structures.

Case	Number (-)	Diameter (mm)	Length (m)	Cost (€/cad)	Cost (€)	%NBS$_{a.o.}$ (%)	%NBS$_{p.o.}$ (%)	1%NBS Cost (€)
2-bays 2-levs	4	12	6.00	300	1200	35	132	12
3-bays 2-levs	4	12	8.76	350	1400	35	132	14
4-bays 2-levs	4	12	11.52	400	1600	35	132	16
2-bays 3-levs	6	12	6.00	300	1800	28	106	23
3-bays 3-levs	6	12	8.76	350	2100	28	106	27
4-bays 3-levs	6	12	11.52	400	2400	28	106	31
2-bays 4-levs	8	14	6.00	340	2720	19	115	28
3-bays 4-levs	8	14	8.76	410	3280	19	115	34
4-bays 4-levs	8	14	11.52	480	3840	19	115	40

These costs are needed to consider the global behaviour of the structures, hence they are necessary to introduce the following retrofit intervention costs.

To strengthen the frames subjected to the IP seismic forces, different interventions were considered: i) grout injections, ii) reinforced plaster and iii) FRP. In order to calculate the costs of these retrofit interventions, the details of the application described in Section 7.8.2 were considered. In Tables 7.23 - 7.25 the intervention costs and the corresponding 1%NBS costs of the 2-bays structures are reported.

Table 7.23. Grout injections costs of the 2-bays structures in MS zones.

Case	Area (m²)	Cost (€/m²)	Cost (€)	%NBS$_{a.o.}$ (%)	%NBS$_{p.o.}$ (%)	1%NBS Cost (€)
2-bays 2-levs	27.8	50	1391	80	88	174
2-bays 3-levs	38.0	50	1899	61	65	475
2-bays 4-levs	48.2	50	2408	55	58	803

Table 7.24. Reinforced plaster costs of the 2-bays structures in MS zones.

Case	Area (m²)	Cost (€/m²)	Cost (€)	%NBS$_{a.o.}$ (%)	%NBS$_{p.o.}$ (%)	1%NBS Cost (€)
2-bays 2-levs	25.9	130	3362	80	108	120
2-bays 3-levs	95.5	130	12418	61	94	376
2-bays 4-levs	126.2	130	16406	55	82	608

Table 7.25. FRP costs of the 2-bays structures in MS zones.

Case	Area (m^2)	Cost (€/m^2)	Cost (€)	%$NBS_{a.o.}$ (%)	%$NBS_{p.o.}$ (%)	1%NBS Cost (€)
2-bays 2-levs	19.5	430	8385	80	100	419
2-bays 3-levs	31.3	430	13464	61	98	364
2-bays 4-levs	50.4	430	21667	55	98	504

The total intervention costs and the 1%NBS costs for the 2-bays 2-levels structure are shown in Figure 7.36. As it can be observed in Figure 7.36a, the intervention with grout injections is the cheapest one (it costs 1391€ against the 3362€ of the reinforced plaster and the 8385€ of the FRP). While in terms of 1%NBS cost (see Figure 7.36b) it is less convenient with respect to the reinforced plaster one, while the FRP remains the less convenient. More in detail, the grout injections require 174€ to increase the performance of 1%NBS, instead, the reinforced plaster requires 120€ and the FRP requires 419€. For these reasons in the 2-bays 2-levels structure, the intervention with reinforced plaster represents the more convenient one, since it allows to reach the maximum seismic performance with the minimum financial investment.

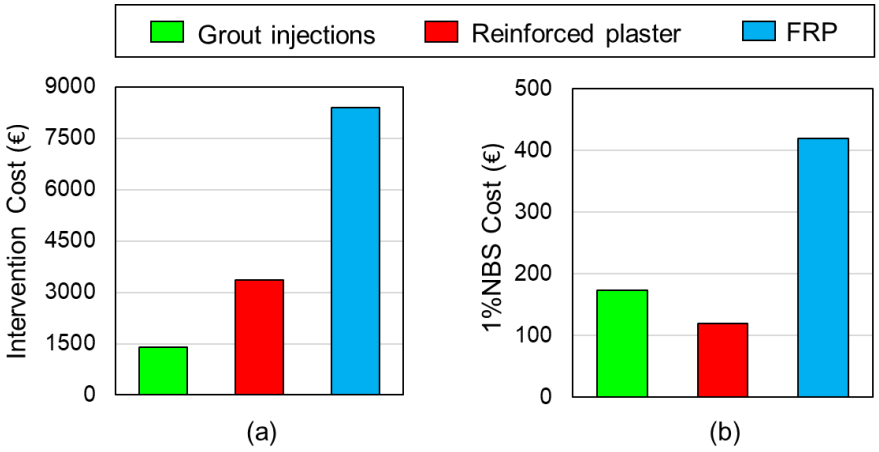

Figure 7.36. Retrofit costs of the 2-bays 2-levels structure in MS zones: (a) intervention costs and (b) 1%NBS cost.

In Figure 7.37 are reported the retrofit costs related to the 2-bays 3-levels structure. As it can be observed in Figure 7.37a, the intervention with grout injections is again the cheapest one (it costs 1899€ against the 12418€ of the reinforced plaster and the 13464€ of the FRP),

but it does not allow to reach the target %NBS. In terms of 1%NBS cost (see Figure 7.37b) it is less convenient with respect to the other two interventions. More in detail, the grout injections require 475€ to increase the performance of 1%NBS, while the reinforced plaster requires 376€ and the FRP application requires 364€. From these considerations, it results that, in the 2-bays 3-levels structure, the reinforced plaster is the best choice in terms of intervention cost, while the FRP one is the more suitable in terms of 1%NBS cost.

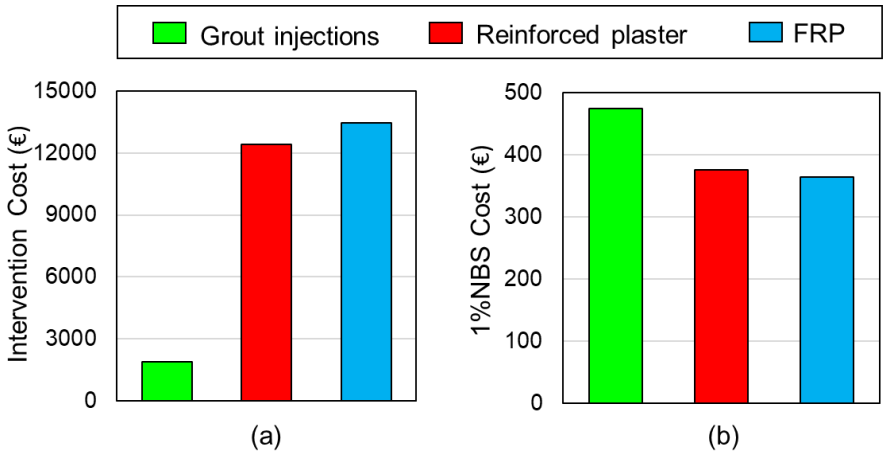

Figure 7.37. Retrofit costs of the 2-bays 3-levels structure in MS zones: (a) intervention costs and (b) 1%NBS cost.

In Figure 7.38 the retrofit costs related to the 2-bays 4-levels structure are reported. As it can be observed in Figure 7.38a, the cheapest intervention remains the grout injections (they cost 2408€ against the 16406€ of the reinforced plaster and the 21667€ of the FRP). In terms of 1%NBS cost (see Figure 7.38b), however, they are less convenient with respect to both the reinforced plaster and the FRP one. More in detail, the grout injections require 803€ to increase the performance of 1%NBS, while the reinforced plaster requires 608€ and the FRP application requires 504€. As for the 2-bays 3-levels structure, it resulted that in the 2-bays 4-levels structure, the reinforced plaster is the best choice in terms of intervention cost, while the FRP one is the more suitable in terms of the 1%NBS cost.

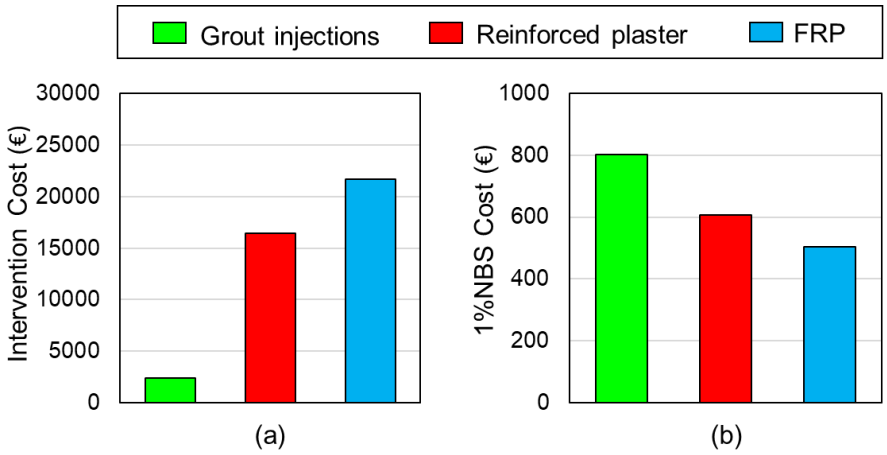

Figure 7.38. Retrofit costs of the 2-bays 4-levels structure in MS zones: (a) intervention costs and (b) 1%NBS cost.

From these comparisons, it can be highlighted that for the 2-levels structure the intervention with FRP is not convenient, because it is the most expensive one and by adopting this, a higher cost is needed to increase the performance of 1%NBS. Contrarily, for the 3- and 4-levels structures, the intervention with FRP, although it remains the most expensive one against the reinforced plaster in terms of the 1%NBS cost, however, it represents the best retrofit solution.

7.10.2 High seismicity

As described for the MS case (see Section 7.10.1), also in HS at first the OOP mechanisms need to be impaired by means of tie rods. The costs are resumed in Table 7.26.

As discussed above, these costs are needed to consider the global behaviour of the structures, hence they are necessary to introduce the following retrofit intervention costs.

Table 7.26. Tie rods intervention costs in HS zones of all the analyzed structures.

Case	Number (-)	Diameter (mm)	Length (m)	Cost (€/cad)	Cost (€)	%NBS$_{a.o.}$ (%)	%NBS$_{p.o.}$ (%)	1%NBS Cost (€)
2-bays 2-levs	4	14	6.00	340	1360	26	106	17
3-bays 2-levs	4	14	8.76	410	1640	26	106	21
4-bays 2-levs	4	14	11.52	480	1920	26	106	24
2-bays 3-levs	6	16	6.00	390	2340	15	115	23
3-bays 3-levs	6	16	8.76	490	2940	15	115	29
4-bays 3-levs	6	16	11.52	590	3540	15	115	35
2-bays 4-levs	8	16	6.00	390	3120	10	109	32
3-bays 4-levs	8	16	8.76	490	3920	10	109	40
4-bays 4-levs	8	16	11.52	590	4720	10	109	48

To strengthen the frames subjected to the IP seismic forces, the different retrofit interventions described in Section 7.9 are considered. The costs related to these interventions on the 2-bays structures located in HS zones were calculated and are reported in Tables 7.27 - 7.29, in terms of the intervention costs and the corresponding 1%NBS costs.

Table 7.27. Grout injections costs of the 2-bays structures in HS zones.

Case	Area (m²)	Cost (€/m²)	Cost (€)	%NBS$_{a.o.}$ (%)	%NBS$_{p.o.}$ (%)	1%NBS Cost (€)
2-bays 2-levs	27.8	50	1391	60	66	232
2-bays 3-levs	38.0	50	1899	45	48	633
2-bays 4-levs	48.2	50	2408	40	44	602

Table 7.28. Reinforced plaster costs of the 2-bays structures in HS zones.

Case	Area (m²)	Cost (€/m²)	Cost (€)	%NBS$_{a.o.}$ (%)	%NBS$_{p.o.}$ (%)	1%NBS Cost (€)
2-bays 2-levs	65.0	130	8447	60	84	352
2-bays 3-levs	95.5	130	12418	45	68	540
2-bays 4-levs	126.2	130	16406	40	56	1025

Table 7.29. FRP costs of the 2-bays structures in HS zones.

Case	Area (m^2)	Cost (€/m^2)	Cost (€)	%$NBS_{a.o.}$ (%)	%$NBS_{p.o.}$ (%)	1%NBS Cost (€)
2-bays 2-levs	28.2	430	12105	60	94	356
2-bays 3-levs	61.0	430	26221	45	108	416
2-bays 4-levs	78.9	430	33920	40	102	547

In Figure 7.39 the retrofit costs related to the 2-bays 2-levels structure are reported. It is observed that the colors associated with the retrofit interventions correspond to those already described in Section 7.9. More in detail, the reinforced plaster is considered applied at the first and second floor (I+II, in Figure) and the FRP strips are considered applied on the piers at the base and on the spandrels at the first and second floor (FRP (2), in Figure).

As observed in Figure 7.39a, the intervention with grout injections is the cheapest one (it costs 1391€ against the 8447€ of the reinforced plaster and the 12105€ of the FRP), but it does not allow to reach the target %NBS. In terms of 1%NBS cost (see Figure 7.39b) the grout injections require 232€ to increase the performance of 1%NBS, while the reinforced plaster requires 352€ and the FRP application requires 356€. Although the FRP and the reinforced plaster interventions show a small difference in terms of 1%NBS cost, in the 2-bays 2-levels structure, the latter one represents the more convenient intervention, since it allows to reach the required seismic performance with the minimum financial investment.

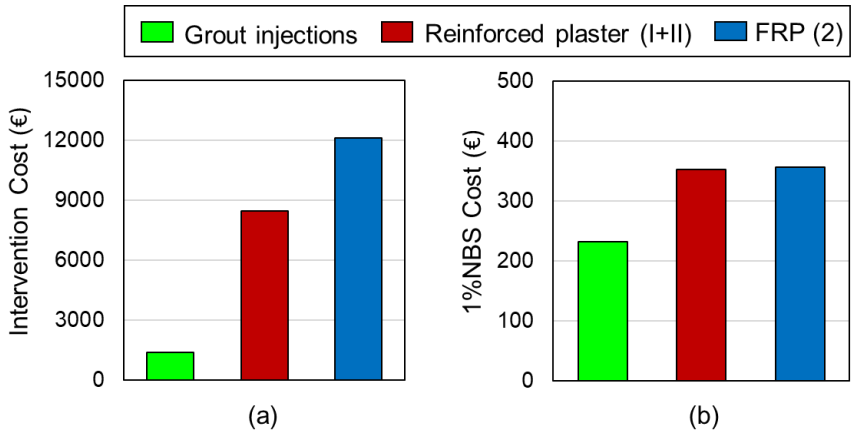

Figure 7.39. Retrofit costs of the 2-bays 2-levels structure in HS zones: (a) intervention costs and (b) 1%NBS cost.

In Figure 7.40 are reported the retrofit costs of the 2-bays 3-levels structure. It is observed that due to the fact that the FRP arrangement differs from that adopted in the MS case, a different color was used in the graph, see Section 7.9 for more details. As it can be observed in Figure 7.40a, the intervention with grout injections is still the cheapest one (it costs 1899€ against the 12418€ of the reinforced plaster and the 26221€ of the FRP), but it does not allow to reach the target %NBS. In terms of 1%NBS cost (see Figure 7.40b) the grout injections require 633€ to increase the performance of 1%NBS, while the reinforced plaster requires 540€ and the FRP application requires 416€. From these considerations it results that, in the 2-bays 3-levels structure, the FRP, even if is the more expensive intervention, is the best retrofit solution in terms of the lower 1%NBS cost, allowing also to reach a higher %NBS with respect to the reinforced plaster.

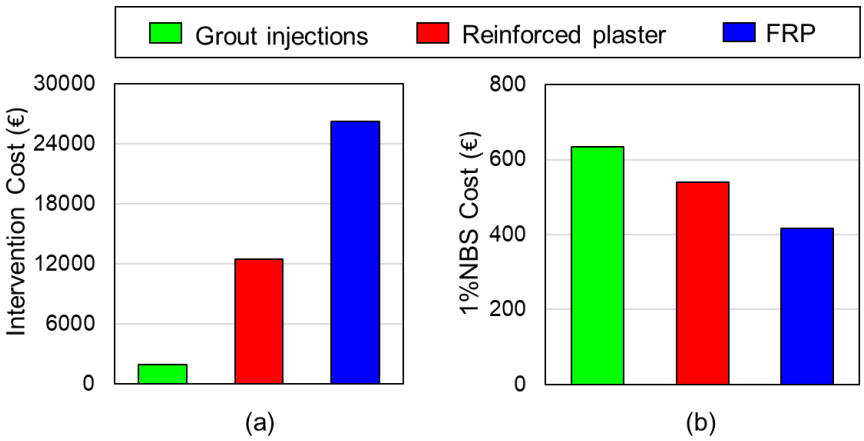

Figure 7.40. Retrofit costs of the 2-bays 3-levels structure in HS zones: (a) intervention costs and (b) 1%NBS cost.

In Figure 7.41 are reported the retrofit costs related to the 2-bays 4-levels structure. As it can be observed in Figure 7.41a, the cheapest intervention remains the grout injections (they cost 2408€ against the 16406€ of the reinforced plaster and the 33920€ of the FRP) but again they do not allow to achieve the target %NBS. In terms of 1%NBS cost (see Figure 7.41b) the grout injections require 602€ to increase the performance of 1%NBS, while the reinforced plaster requires 1025€ and the FRP requires 547€. From these comparisons, it results that in the 2-bays 4-levels structure, although the intervention with FRP is the most expensive one, it represents the best choice in terms of the obtained 1%NBS cost.

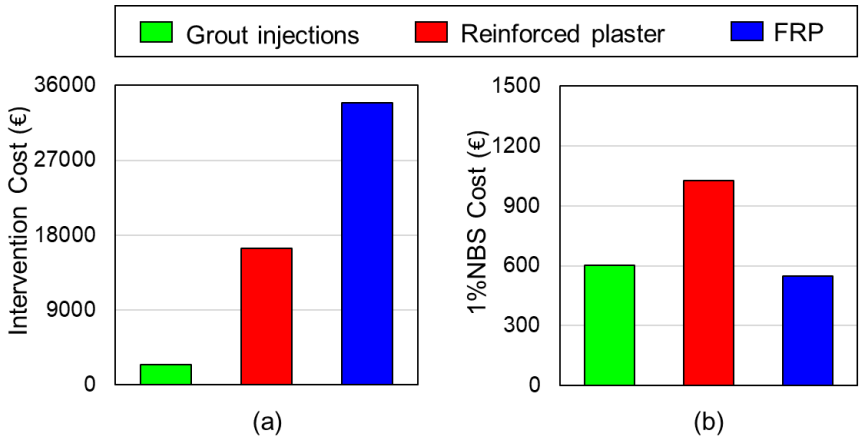

Figure 7.41. Retrofit costs of the 2-bays 4-levels structure in HS zones: (a) intervention costs and (b) 1%NBS cost.

From these comparisons, it can be highlighted that for the 2-levels structure the intervention with FRP is the more expensive one but also the best solution in terms of 1%NBS cost. Indeed, excluding the intervention with grout injections that does not allow to achieve the target %NBS in all the 2-bays structures, by adopting FRP, a lower cost is needed to increase the performance of 1%NBS, with respect to the intervention with reinforced plaster. The only case of 2-levels structure shows compatible 1%NBS cost between the FRP and the reinforced plaster interventions, which, only in this case, grants the target %NBS.

7.10.3 Medium vs high seismicity comparison

In this Section, a comparison between the retrofit costs obtained for structures in MS and HS zones is reported and some considerations about the most convenient retrofit interventions, in terms of total and 1%NBS costs for all the structures, are made.

From the interventions with tie rods, it can be briefly observed that, as expected, the intervention costs, as well as the 1%NBS cost related to the structures in HS zones, are higher than those in MS ones, since higher diameters of tie rods are required in these zones.

In Figures 7.42 and 7.43 are reported the comparisons in terms of intervention costs and 1%NBS cost associated with each retrofit technique applied to the 2-bays structures, in MS and HS zones.

The intervention costs related to the grout injections (green, in Figure 7.42) are the same in MS and HS zones since the intervention is conducted on the same elements. This consideration is valid also for the reinforced plaster (red, in Figure 7.42), applied to the 3- and 4-levels structures. The intervention with reinforced plaster for the 2-levels structure, instead, is cheaper of about 2.5 times in the MS zones than in the HS ones. This is due to the fact that in the first case it is applied only to the first floor, while in the second case it is applied to both floors. Regarding the intervention with FRP (blue, in Figure 7.42), its costs in HS zones are always higher than in MS ones. More in detail, in the 2-levels structure it is 1.5 times more expensive, 2 times in the 3-levels structure and 1.8 times in the 4-levels structure. These differences arise from the different arrangements of FRP strips that are needed to obtain the target %NBS in the structures in MS and HS zones: in HS zones more strengthening material is required, hence higher costs are obtained.

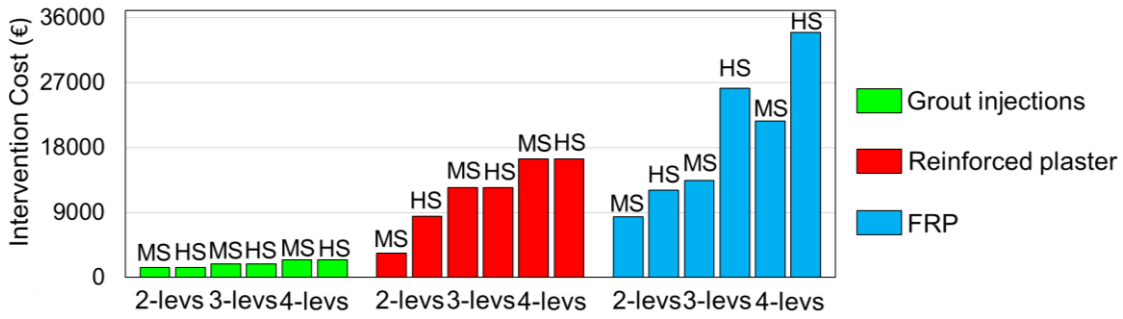

Figure 7.42. Retrofit intervention costs of the analyzed structures in MS and HS zones.

Regarding the 1%NBS costs, the results are shown in Figure 7.43. In all cases, the obtained values differ between MS and HS zones, since this parameter takes into account also the %NBS variation and not only the intervention costs. For the grout injections, the intervention in MS zones has around 1.3 times lower 1%NBS values than those in HS ones for the 2- and 3-levels structures. For the 4-levels structure, instead, the intervention in HS zones results 1.3 times more convenient than that in the MS zone. This is due to the fact that, for the same intervention cost (2408€), the achieved variation of the %NBS is equal to the 3% in the MS zones while it was equal to the 4% in the HS zones. Regarding the intervention with reinforced plaster, higher values of 1%NBS cost are always observed in structures placed in HS zones: more in detail, for the 2-levels structure it is 2.9 times higher, for the 3-levels structure 1.4 times and for the 4-levels structure 1.7 times. The higher difference observed in the 2-levels structure arises from the different configuration of the

intervention in the two cases: in MS zones it is needed to apply reinforced plaster only to the first floor, while in HS zones it is required also to the second floor. Moreover, the high variation observed in the 4-levels structure is due to the lower variation of %NBS obtained in HS zones (16%), with respect to that obtained in MS zones (27%). Regarding the intervention with FRP, it is observed that in the 2-levels structure the cost of 1%NBS is higher in MS zones (of 1.2 times). This is due to the lower increase in the achieved %NBS (20%), with respect to what happens in the HS zones (34%). On the contrary, in the 3- and 4-levels structures, the 1%NBS cost is slightly higher in the HS case (around 1.1 times).

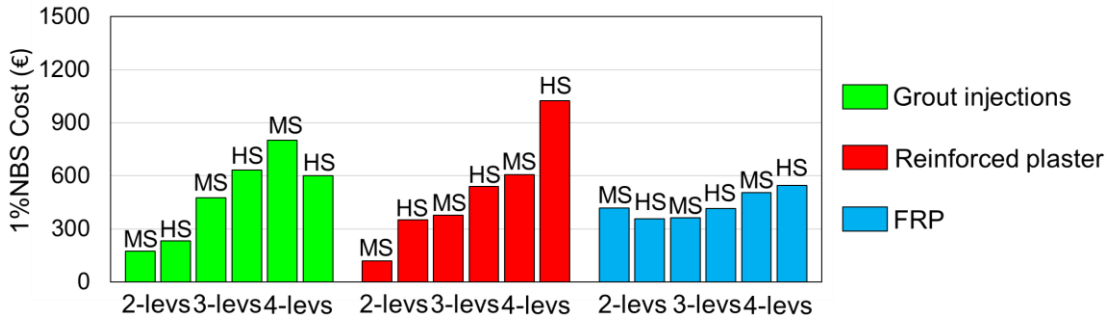

Figure 7.43. 1%NBS cost of the retrofit interventions of the analyzed structures in MS and HS zones.

In summary, it is observed that the grout injections are the cheapest intervention (see Figure 7.42), but they are not the most convenient one, for two main reasons: they do not allow to reach the target %NBS and, especially for the 3- and 4-levels structures, the costs in terms of 1%NBS are really high. Regarding the intervention with reinforced plaster, it shows competitive costs, both in terms of intervention and 1%NBS costs, except for the 4-levels structure in HS zones (see Figure 7.43). The intervention with FRP is the most expensive one, for all the structures and the considered seismic zones, as observed in Figure 7.42. These high costs can initially deter the use of this intervention, but by evaluating the 1%NBS costs, the intervention with FRP represents the most suitable among the three. Moreover, it is worth noting that it is the cheapest for the higher structures (such as the 3- and the 4-levels one), while for the 2-levels structure the reinforced plaster results the best choice.

7.11 References

Binda, L., Modena, C., Baronio, G., & Abbaneo, S. (1997). Repair and investigation techniques for stone masonry walls. Construction and Building Materials, 11(3), 133-142.

Churilov, S., & Dumova-Jovanoska, E. (2013). In-plane shear behaviour of unreinforced and jacketed brick masonry walls. Soil Dynamics and Earthquake Engineering, 50, 85-105.

CNR DT200. (2004). Guide for the design and construction of an externally bonded FRP system for strengthening existing structures. Technical document, (200).

CNTC19. (2019). Circolare applicativa delle Norme Tecniche delle Costruzioni di cui al DM 17/01/2018. (NTC 2018). Italy: Gazzetta Ufficiale N.42 del 20/02/218. Ministero delle Infrastrutture e dei Trasporti. (in Italian).

Cosenza, E., Del Vecchio, C., Di Ludovico, M., Dolce, M., Moroni, C., Prota, A., & Renzi, E. (2018). The Italian guidelines for seismic risk classification of constructions: technical principles and validation. Bulletin of Earthquake Engineering, 16(12), 5905-5935.

Degli Abbati, S., S. Cattari, and S. Lagomarsino. (2018). Theoretically-based and practice-oriented formulations for the floor spectra evaluation. Earthquake and Structures 5: 565–81. doi: 10.12989/ eas.2018.15.5.565.

Di Ludovico M, Prota A, Moroni C, Manfredi G, Dolce M. (2017a). Reconstruction process of damaged residential buildings outside the historical centres after L'Aquila earthquake—Part I: light Reconstruction. Bull Earthq Eng 15(2):667–692. https ://doi.org/10.1007/s1051 8-016-9877-8

Di Ludovico M, Prota A, Moroni C, Manfredi G, Dolce M. (2017b). Reconstruction process of damaged residential buildings outside the historical centres after L'Aquila earthquake—Part II: heavy Reconstruction. Bull Earthq Eng 15(2):693–729. https ://doi.org/10.1007/s1051 8-016-9979-3

Dolce M, Manfredi G. (2015). Libro Bianco sulla ricostruzione privata fuori dai centri storici nei comuni colpiti dal sisma dell'Abruzzo del 6 Aprile 2009. (in Italian) Doppiavoce: 210. ISBN 978-88-89972-50-2.

Fajfar, P. (1999). Capacity spectrum method based on inelastic demand spectra. Earthquake Engineering and Structural Dynamics 28, pp. 979-993: John Wiley & Son, Ltd.

Genio Civile. (2018). Prezziario Unico del Cratere. Centro Italia [Construction price Book, Central Italy]. Rome: DEI.

Ghiassi, B., Soltani, M., & Tasnimi, A. A. (2012). Seismic evaluation of masonry structures strengthened with reinforced concrete layers. Journal of Structural Engineering, 138(6), 729-743.

Mazzon, N. (2010). Influence of Grout Injection on the Dynamic Behaviour of Stone Masonry Buildings.

Ministry Decree n.65 7/3/2017. (2017). Ministerial Decree n.65 of 27 February 2017, integrated with the changes of n.58 of 7 March 2017. Guidelines for the seismic risk classification of constructions. Rome, Italy: Italian Ministry of Infrastructures and Transport. (In Italian).

NTC (Norme Tecniche per le Costruzioni). (2018). Aggiornamento delle Norme Tecniche per le Costruzioni. Decreto ministeriale del 17 gennaio 2018. Rome: Ministero delle Infrastrutture e dei Trasporti. (in Italian).

Oliveira, D. V., Silva, R. A., Garbin, E., & Lourenço, P. B. (2012). Strengthening of three-leaf stone masonry walls: an experimental research. Materials and structures, 45(8), 1259-1276.

Podestà, S., and Scandolo, L. (2019). Earthquakes and Tie-Rods: Assessment, Design, and Ductility Issues. International Journal of Architectural Heritage, 13(3), 329–339.

Priestley, M. J. N., & Kowalsky, M. J. (2000). Direct displacement-based seismic design of concrete buildings. Bulletin of the New Zealand Society for Earthquake Engineering, 33(4), 421-444.

Silva, B., Pigouni, A. E., Valluzzi, M. R., & Modena, C. (2014). Calibration of analytical formulations predicting compressive strength in consolidated three-leaf masonry walls. Construction and Building Materials, 64, 28-38.

Vinci, M. (2019). Metodi di calcolo e tecniche di consolidamento per edifici in muratura (in Italian). Dario Flaccovio.

Vintzileou, E., Mouzakis, C., Adami, C. E., & Karapitta, L. (2015). Seismic behavior of three-leaf stone masonry buildings before and after interventions: Shaking table tests on a two-storey masonry model. Bulletin of Earthquake Engineering, 13(10), 3107-3133.

8. Conclusions and future developments

This Thesis successfully develops and validates the SLaMA-URM method, adapting the SLaMA method for reinforced concrete buildings to masonry ones. This is a mechanism-based analytical procedure that aims to provide an estimation, through by-hand calculations, of the global seismic capacity of URM structures from the analysis at sub-system level. It consists at first in defining the structural deficiencies of the building, highlighting the possible Out-Of-Plane (OOP) mechanisms that can compromise the “box behaviour” of the structure. Once these are prevented, the In-Plane (IP) mechanisms performance level can be evaluated.

In this Thesis, an extensive validation of the procedure is presented. This is conducted on some structures, starting from simple panels to multi-storey prototype frames, against numerical modelling (e.g. finite element and equivalent frame) herein performed and experimental results, available from literature. More in detail, from the numerical simulations, it is observed that the SLaMA-URM method is able to well grasp the expected failure mechanisms as well as the capacity curves of the analyzed structures. Indeed, even if it is a simplified approach, the proposed procedure, in some cases, showed more reliable results than the numerical ones, when compared to the experimental data.

The SLaMA-URM method defines the In-Plane performance by: (i) the evaluation of moment-rotation capacity curves of URM components (pier and spandrel); (ii) the assessment of the hierarchy of strength in each subassembly; (iii) the definition of the structural capacity curve according to the expected failure mechanism. An important innovative aspect introduced in this Thesis concerns the adoption, at component level, of the Monolithic Beam Analogy: a peculiar sectional analysis in which the masonry components are assumed as rigid and all the inelastic behaviour is assumed concentrated at the end of the elements, where a gap is expected to open.

The evidence of no (or limited) damage to pier-spandrel joints in URM walls during earthquakes has led to assume them as rigid nodes in the Equivalent Frame modelling (EFM) approach. In this Thesis, in order to investigate this aspect, is proposed a new

analytical approach to derive the strength capacity of pier-spandrel joints, with the aim to assess its effect in the pier M-N performance domain.

Moreover, post-earthquake damage evidences in masonry structures highlighted the importance of the Out-Of-Plane mechanisms. For this reason, in this Thesis, the interaction between the In-Plane and the Out-Of-Plane mechanisms performance levels is taken into account and studied in prototype structures. The SLaMA-URM method is used to evaluate the seismic performance of these prototype buildings, thus identifying the expected failure mechanisms of the structural components. Moreover, the procedure is used to quantify the effect of different retrofit interventions, evaluating the performance of the reinforced structures.

In this Thesis, several analyses are performed to emphasize the main potentialities and advantages of the proposed SLaMA-URM method. These can be summarized as follows:

- **Through the Monolithic Beam Analogy, the procedure is able to catch the actual masonry behaviour.** Through the MBA approach, it is possible to consider different constitutive laws for masonry, from simpler to more sophisticated and realistic ones, thus obtaining more reliable moment-rotation curves and M-N domains of the structural components. Moreover, the proposed approach is able to capture their expected failure mechanism. Through a comparison with the capacity curves obtained by using codes indications, it is shown that the MBA approach catches the actual element ultimate displacement, while the codes define it as “a priori”.

- **It is possible to study the response of the elements by varying their geometry, applied axial load and boundary conditions**. By studying the scale effect on the Ispra panels, it is observed that the increasing dimensions lead to an increase of the moment capacity, the initial stiffness and the rotation capacity. When varying the axial load, it results that, by increasing its value, the moment capacity increases until reaching the top of the M-N limit domain. A further increase of the axial load induces a decrease in the moment capacity. Moreover, the rotation capacity decreases when the axial load increases, leading to a reduction of the rotation ductility of the element. When varying the boundary conditions, it is clear how the procedure can identify the possible crisis mechanisms of the element, which, according to the different configurations (in terms of geometry and applied axial load), can change from flexural to shear type.

- **It is quick to implement different geometric configurations to investigate the global response of framed structures.** The masonry structures behaviour is strongly influenced by the global geometry and/or by that of their components. Hence, in the one-storey substructure, the variation of piers and spandrels dimensions was considered and the corresponding pushover curves were obtained, highlighting different failure mechanisms. More in detail, by increasing the length of the spandrel, the substructure shows an increase in ductility, while by increasing its height, the base shear capacity increases. Moreover, the substructure capacity increases for higher piers length, while by increasing their height, it shows a lower stiffness and base shear capacity. Different geometric configurations were also investigated through a set of framed structures that vary the number of bays and the number of levels. The procedure shows that by increasing the number of bays the base shear increases while by increasing the number of levels the initial stiffness decreases.

- **The procedure gives important improvements with respect to simplified modelling strategies available in literature.** The capacity curves obtained through the SLaMA-URM method were compared with those resulting from the adoption of the “strong-spandrel weak-pier” model and the “weak-spandrel strong-pier” model. This comparison shows that these simplified models are not enough reliable and competitive with respect to the Equivalent Frame Method, showing the high potentiality of the SLaMA-URM method. These differences are mainly due to the excessive over, or under, estimation of the global lateral strength and to the incomplete results in terms of crack patterns. This last aspect represents an important key point when defining the most adequate retrofit strategy since a wrong evaluation of the governing failure mode of the structure can lead to significant and unsolvable consequences when the seismic retrofitting is performed.

- **It is possible to consider the influence of the pier-spandrel joints in the hierarchy of strength.** In analogy with the RC frame-infill wall combined behavior, in this Thesis, an equivalent diagonal strut mechanism within the masonry pier-spandrel joint was proposed. By varying the geometry of the structural components, the pier-spandrel joint capacity was computed. The hierarchy of strength shows that when the spandrel height or the pier length increase or when the pier height decreases, the joint presents a high capacity, which is enough to exclude its failure in the sequence. On the contrary, the influence of the joint becomes important when the pier height or the spandrel length increase. These findings indicate that disregarding the finite capacity of the joint (as generally done when adopting the hypothesis of a rigid joint) could lead to incorrect predictions of local and global failure mechanisms and then to an inappropriate retrofit solution.

- **It is possible to obtain the global performance of URM structures from the interaction of the In-Plane and Out-Of-Plane performance.** The SLaMA-URM procedure was applied to prototype buildings, obtaining the OOP and the IP capacity curves. By their intersection in the ADRS domain, the global seismic performance of each structure was evaluated in terms of %NBS. The capacity curves of the OOP mechanisms were calculated according to well-known literature approaches. The IP mechanisms were investigated through the proposed procedure, highlighting that the performance increases when increasing the number of bays, while decreases when increasing the number of levels. Moreover, it is obtained: i) lower ductility in higher structures; ii) no-evident differences in ductility when varying the number of bays; iii) lower initial stiffness when increasing the number of levels; iv) slight increase of the initial stiffness when increasing the number of bays. In all the cases, the OOP performance resulted to be the limiting one, thus confirming the hierarchy of the failure modes in masonry structures.

- **It is able to point out the expected failure mechanisms of structural components, hence easily identify the more suitable retrofit strategy and evaluate its effect.** In the prototype buildings, the SLaMA-URM method identified the most vulnerable structural components to be strengthened. In the ADRS domain, the retrofit strategy (i.e. increase in ductility and/or increase in strength/stiffness) can be easily assessed, with respect to the required effect. In all the analyzed cases, the spandrels and the piers at the base showed brittle shear failure, that should be prevented through retrofit interventions, by modifying them in a ductile one. More in detail, this, in addition to a high increase of strength, was obtained through the application of FRP. The adoption of reinforced plaster allowed to increase the strength and the stiffness of the structures without modifying the crisis mechanisms of the components. The grout injections granted a slight increase in structural ductility.

- **It is possible to easily consider different seismic intensities of the construction site.** Since in the SLaMA-URM method the seismic intensity is represented by the seismic demand in the ADRS domain, it can be easily modified, allowing to quickly analyse structures located in different seismic zones. This was demonstrated by performing these analyses on the prototype buildings. More in detail, the “ante operam” structural performances obtained in high seismicity (HS) zones were lower than the ones achieved in medium seismicity (MS), as expected. Regarding the retrofitting, in order to reach the target performance level, more massive interventions were required in HS with respect to MS zones.

In order to evaluate the accuracy of the SLaMA-URM method, the Pushover curves and failure mechanisms obtained on framed prototype structures, by varying the number of bays and levels, were compared with those derived from EFM. The expected failure mechanisms were in good agreement, while the results in terms of the ultimate displacement and the base shear were reasonably well-predicted, with an average error of around 5%. Regarding the yield displacements, the average percentage error was around 26%, with a wide internal variation of values. It is worth mentioning that small variations of the yield displacement cause high percentage error, even if there is a reasonably good match between the SLaMA-URM and the numerical Pushover curves.

To exploit the capabilities of the SLaMA-URM procedure, in the strengthening of masonry structures, some retrofit techniques were applied to the prototype buildings (tie-rods, grout injection, reinforced plaster and FRP) and their effect was quantified. In order to select the best retrofit strategy, not only the increase in %NBS was considered, but also the Expected Annual Losses (EAL) as well as the total cost of each intervention. By introducing 1%NBS cost as a comparison parameter, it is shown how the SLaMA-URM method can rapidly give an idea of the best retrofit solution to adopt, according to the available investment, the “ante-operam” performance and the desired performance to achieve (“post operam” performance).

In conclusion, this Thesis introduces, validates and demonstrates the capabilities of the SLaMA-URM method. The presented applications are intended to show the potentialities of the proposed methodology that can represent an alternative and useful tool that can help researchers and practitioners engineers in the seismic assessment studies and in the decision-making process of the best retrofit intervention.

The research developed within this Thesis suggests the following studies, herein recommended as main future works:

- *Introduce flexible diaphragms in the procedure*. In this Thesis, the diaphragms, as a first approximation, are assumed as rigid. A further development of the procedure would consist of the introduction of their in-plane flexibility. This is the first suggestion in order to consider in the analyses the wooden, metallic or vaulted diaphragms that are commonly found in existing URM buildings. Indeed, the post-earthquake damage evidences show that their stiffness (or vice versa flexibility) plays an important role in the global response of URM structures. The horizontal diaphragms have the task of redistributing the seismic force

between the vertical resistant elements and this capacity depends greatly on their typology. More in detail, a flexible diaphragm does not guarantee the global response of the structure to the seismic action, causing often out-of-plane local mechanisms.

- *Numerical and experimental validation of the proposed analytical approach to obtain the pier-spandrel joint capacity*. In this Thesis is proposed a new analytical approach to derive the strength capacity of pier-spandrel joints. It is foreseen the validation of this approach with numerical simulation and/or experimental campaign. Further investigations in this context are expected, to define the actual strength and deformability of URM joints, thus allowing us to understand their real behaviour in masonry structures. Parametric analyses to identify the response of these elements by varying the masonry properties as well as their geometry, would be suggested, pointed towards the understanding of the limitations of the EF modelling.

- *Disaggregation of the costs (and EAL) associated with the Out-Of-Plane and In-Plane mechanisms*. The Ministry Decree n.65 7/03/2017, generally adopted for the simplified EAL definition, refers to the costs of the entire buildings monitored in the reconstruction process after the L'Aquila earthquake of 2009. When dealing with the OOP mechanisms, that limit the global performance of the buildings, this adoption would give highly questionable results (i.e. overestimation). In this Thesis, in order to obtain a more reliable result, a "qualitative" suggestion is made, with the aim to have disaggregated costs and losses, associated with the damage due to the structural components actually involved in the IP or OOP mechanisms. As a future perspective, it is suggested to further develop and validate this proposed approach, on the basis of earthquakes damage evidences.

- *Application of the SLaMA-URM method to real URM buildings.* In this Thesis the SLaMA-URM method is applied to prototype buildings that are characterized by regular plan and height. It would be interesting to apply this procedure to real buildings, that can present irregular configuration, different masonry quality and peculiar structural details. In these cases, the key point is to achieve the correct schematization of the structure in the EF model, to be analyzed in the procedure.

- *Extend the application of the SLaMA-URM method to territorial scale.* The final goal of the SLaMA-URM method, generally speaking, intends to be extending the seismic assessment and retrofit analyses to a territorial scale. As a future development, it aims to provide an analytical framework able to support the planning of policies to reduce the seismic

risk of existing masonry buildings. With this tool, the local authorities can plan an appropriate campaign of seismic prevention, which takes into account not only the safety but also the economy, the speed and reliability of the interventions, as well as the invasiveness and the inactivity time of the structure. Hence, it is foreseeable a proposal for an economic and financial strategy/plan to support the practical implementation of such an integrated intervention plan at national level.

A.1 Appendix

In this Appendix are reported the equations to define the Moment-Axial load (M-N) domains for rectangular cross-sectioned URM piers and spandrels, with the EPP and the Lumantarna stress-strain relationships, according to the traditional sectional analysis (i.e. in Cattari, 2007 and Knox, 2012).

PIERS. Elastic-perfectly plastic stress-strain model

For the piers, the elastic-perfectly plastic (EPP) stress-strain model is assumed for the masonry with a no-tensile resistant (NTR) behaviour. For the compressive behaviour, it is assumed the yield strain ε_{yc} and the ultimate strain as $\varepsilon_{uc} = \mu_{\varepsilon c}\varepsilon_{yc}$, where $\mu_{\varepsilon c}$ is the compression strain ductility.

Considering a rectangular cross-section with depth H and width b and assuming that the plane sections remain plane after bending, the strains are linearly proportional to the distance from the neutral axis x (Figure A.1.1). From this, Equations A.1.1 and A.1.2 can be defined:

$$\frac{x}{\varepsilon_{uc}} = \frac{(x-y)}{\varepsilon_{yc}} \qquad (A.1.1)$$

$$y = x\left(1 - \frac{1}{\mu_{\varepsilon c}}\right) \qquad (A.1.2)$$

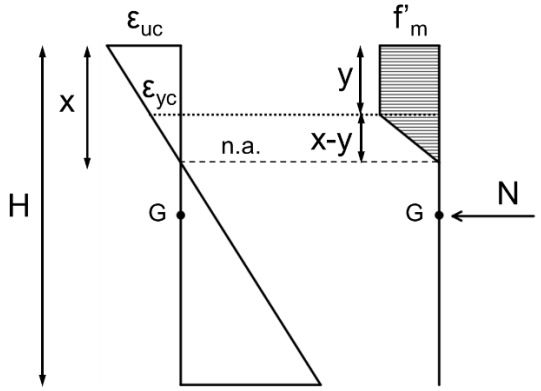

Figure A.1.1. Strain and stress profiles for the Elastic-Perfectly Plastic (EPP) model for piers.

With this consideration, the axial Load N and the corresponding moment M are defined from the equilibrium of the translational and rotational (around centre of gravity G) forces in the section, as follows (Equations A.1.3 and A.1.4):

$$N = (x-y)\frac{1}{2}f'_m b + bf'_m y = f'_m bx - \frac{f'_m bx}{2\mu_{\varepsilon c}} \qquad (A.1.3)$$

$$M_G = \frac{1}{2}\left[f'_m b(x-y)\left(\frac{H}{2} - \frac{1}{3}(x-y) - y\right)\right] + \left[f'_m by\left(\frac{H}{2} - \frac{y}{2}\right)\right] = \\ = \frac{f'_m b}{2}\left[Hx - \frac{Hx}{2\mu_{\varepsilon c}} - x^2 + \frac{x^2}{\mu_{\varepsilon c}} - \frac{x^2}{3{\mu_{\varepsilon c}}^2}\right] \qquad (A.1.4)$$

PIERS. Strain softening model NTR: Lumantarna stress-strain relationship

The more reliable and realistic stress-strain relationship to represent the behaviour of the unreinforced masonry is a strain-softening model. The Lumantarna model is a modification of the one reported in Kaushik *et al*. (2007), after some experimental tests on New Zealand prism samples. It is characterized by an initial parabolic trend and, after a post-peak softening trend (from stress as $0.9f'_m$). It is assumed a linear decreasing variation until a constant stress ($0.2f'_m$) is reached. The model proposes two different final linear slopes, according to the strength of the mortar f'_j . The ultimate compressive strain is a multiple of peak strain ε_{yc}.

The representation of the strain and stress profile for a rectangular cross-section (with depth H and width b) is shown in Figure A.1.2.

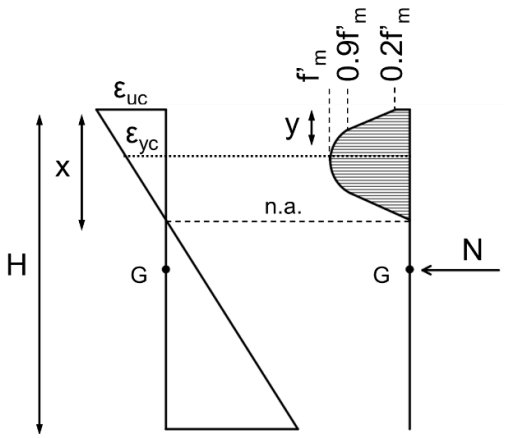

Figure A.1.2. Strain and stress profiles for Lumantarna model for piers.

To define the Moment-Axial load (M-N) limit domain deriving from the Lumantarna stress-strain model, at first the strain $\varepsilon(0.9f'_m)$, corresponding to the stress $f_m = 0.9f'_m$, is defined. Then for the definition of the axial load N, the area under the stress-strain model is divided into simple geometric elements, while the area under the parabolic variation is derived by integrating the expression of the stress in the range $\varepsilon_m = [0;\ \varepsilon(0.9f'_m)]$. Assuming the Euler-Bernoulli hypothesis, and considering a low mortar strength f'_j (lower than 5 MPa), the ultimate strain is equal to $\mu_{\varepsilon c}\varepsilon_{yc} = 2\varepsilon_{yc}$ (where $\mu_{\varepsilon c}$ is the compression strain ductility), then the peak strain ε_{yc} corresponds to half of the neutral axis depth ($x/2$). From the translational and rotational force equilibrium, the axial load and moment, respectively, are defined. The formulation is presented in the following:

- Stress-strain model equation: $\frac{f_m}{f'_m} = 2\frac{\varepsilon_m}{\varepsilon_{yc}} - \left(\frac{\varepsilon_m}{\varepsilon_{yc}}\right)^2$
- Strain corresponding to the stress $f_m = 0.9f'_m$: $\varepsilon_{(0.9f'_m)} = 1.32\varepsilon_{yc}$
- Area under the parabolic variation: $\int_0^{1.32} f_m(\varepsilon) = 0.97\varepsilon_{yc}f'_m$
- With Euler-Bernoulli hypothesis: $\frac{x}{\varepsilon_{uc}} = \frac{(x-y)}{\varepsilon_{(0.9f'_m)}} \Rightarrow \frac{x}{\mu_{\varepsilon c}\varepsilon_{yc}} = \frac{(x-y)}{1.32\varepsilon_{yc}}$

  $\Rightarrow \quad y = x\left[1 - \frac{1.32}{\mu_{\varepsilon c}}\right]$

- Axial Load: $N = 0.97\frac{x}{2}f'_m b + \frac{1}{2}0.7f'_m yb + 0.2f'_m yb$
- Moment: $M_G = 0.97\frac{x}{2}f'_m b\left(\frac{H}{2} - 0.60x\right) + \frac{1}{2}0.7f'_m yb\left(\frac{H}{2} - \frac{2}{3}y\right) + 0.2f'_m yb\left(\frac{H}{2} - \frac{y}{2}\right)$

SPANDRELS. Elastic-perfectly plastic stress-strain model

For the spandrels, the elastic-perfectly plastic (EPP) stress-strain model is assumed for the masonry with a tensile resistant (TR) behaviour.

Regarding the analysis of the URM spandrels, characterized by a compression stress-strain relationship and a resistant in tension (TR) model, the moment-capacity curves can be defined in two different ways that are characterized by: 1) limited ductility in compression

($\mu_{\varepsilon c} = \varepsilon_{uc}/\varepsilon_{yc}$) and unlimited ductility in tension, i.e. compression governed failure (TR-CF) or 2) limited ductility in tension ($\mu_{\varepsilon t} = \varepsilon_{ut}/\varepsilon_{yt}$), i.e. tension governed failure (TR-TF).

Regarding the compression governed failure (TR-CF) the moment capacity is reached when the extreme compression fibre reaches the ultimate compression strain ε_{uc}.

Considering a rectangular cross-section with depth H and width b and assuming that the plane sections remain plane after bending, the strains are linearly proportional to the distance from the neutral axis x (Figure A.1.3). From this, Equations A.1.5 and A.1.6 can be defined:

$$\frac{x}{\varepsilon_{uc}} = \frac{(x-y)}{\varepsilon_{yc}} \qquad (A.1.5)$$

$$y = x\left(1 - \frac{1}{\mu_{\varepsilon c}}\right) \qquad (A.1.6)$$

Moreover, defining the ratio between the tensile and compressive strength as $\eta = f_{tu}/f'_{mh}$, the distance z (see Figure A.1.3) can be defined as (Equation A.1.7):

$$z = x\frac{\eta}{\mu_{\varepsilon c}} \qquad (A.1.7)$$

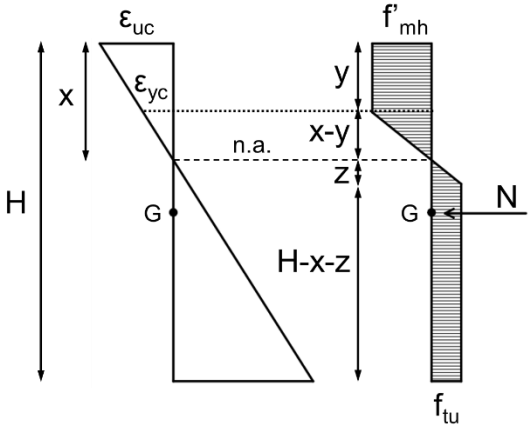

Figure A.1.3. Strain and stress profile for the Elastic-Perfectly Plastic model with tension capacity (EPP-TR-CF) for spandrels.

The axial load N and the corresponding moment M are defined from the equilibrium of the translational and rotational (around centre of gravity G) forces in the section, following Equations A.1.8 and A.1.9:

$$N = yf'_m b + \frac{1}{2}(x-y)bf'_m - (H-z-x)bf_{tu} - \frac{1}{2}zf_{tu}b \qquad (A.1.8)$$

$$M_G = \left[\left(yf'_m b\right)\left(\frac{H}{2}-\frac{y}{2}\right)\right] + \left[\left(\frac{1}{2}(x-y)bf'_m\right)\left(\frac{H}{2}-\frac{1}{3}(x-y)-y\right)\right] + \\ + \left[\left((H-z-x)bf_{tu}\right)\left(\frac{H}{2}-\frac{H-x-z}{2}\right)\right] + \left[\left(\frac{1}{2}zf_{tu}b\right)\left(\frac{H}{2}-x-\frac{2}{3}z\right)\right] \qquad (A.1.9)$$

Regarding the tension governed failure (TR-TF), the moment capacity is reached when the extreme tension fibre reaches the ultimate tension strain ε_{ut}. The moment-axial load domains can be obtained by translational and rotational equilibrium of the section. More in detail, two different cases can be distinguished according to the maximum compression strain. When it is lower than the yield compression strain, which corresponds to a normalised neutral axis depth $\hat{h}$ greater than $\frac{1}{\frac{\varepsilon_{yc}}{\varepsilon_{uc}}+1}$, it is possible to refer to the schematization reported in Figure A.1.4. The axial force and corresponding moment can be obtained through Equations A.1.10 and A.1.11.

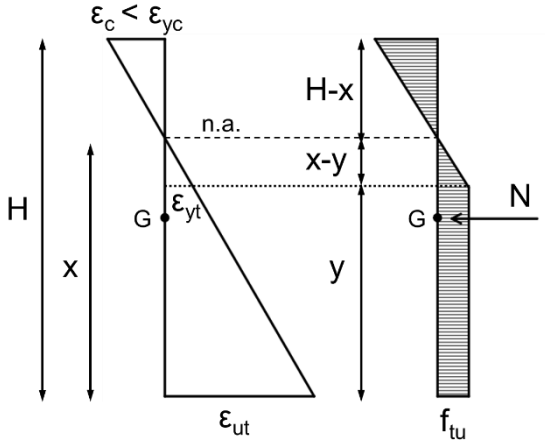

Figure A.1.4. Strain and stress profiles for tension governed failure EPP-TR-TF for $\hat{h} > \frac{1}{\frac{\varepsilon_{yc}}{\varepsilon_{uc}}+1}$.

$$N = \frac{H-x}{z}f'_m\frac{1}{2}b(H-x) - \frac{1}{2}(x-y)f_{tu}b - yf_{tu}b \qquad (A.1.10)$$

$$M_G = \left[\left(\frac{H-x}{z} f'_m \frac{1}{2} b(H-x)\right)\left(\frac{H}{2} - \frac{H-x}{3}\right)\right] + \left[\left(\frac{1}{2}(x-y) f_{tu} b\right)\left(\frac{H}{2} - \frac{1}{3}(x-y) - y\right)\right] + \\ + \left[(y f_{tu} b)\left(\frac{H}{2} - \frac{y}{2}\right)\right] \qquad (A.1.11)$$

When the maximum compression strain is higher than the yield compression strain, which corresponds to a normalised neutral axis depth $\hat{h}$ lower than $\frac{1}{\frac{\varepsilon_{yc}}{\varepsilon_{uc}}+1}$, it is possible to refer to the schematization reported in Figure A.1.5. The axial force and corresponding moment can be obtained through Equations A.1.12 and A.1.13.

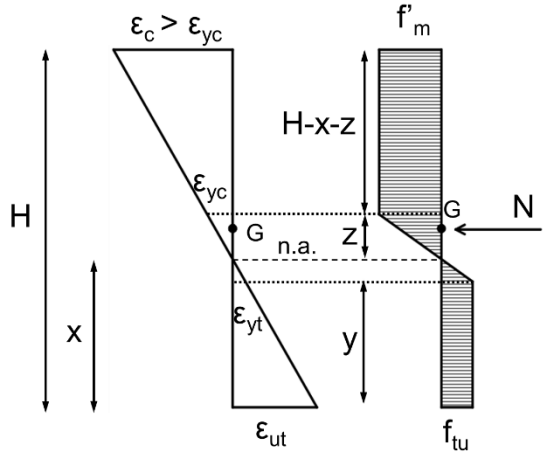

Figure A.1.5. Strain and stress profiles for tension governed failure EPP-TR-TF for $\hat{h} < \frac{1}{\frac{\varepsilon_{yc}}{\varepsilon_{uc}}+1}$.

$$N = (H - z - x) f'_m b + \frac{1}{2} z b f'_m - \frac{1}{2}(x-y) b f_{tu} - y f_{tu} b \qquad (A.1.12)$$

$$M_G = \left[\left((H-z-x) f'_m b + \frac{1}{2} z b f'_m\right)\left(\frac{H}{2} - (H-x)\right)\right] + \\ + \left[\left(\frac{1}{2}(x-y) b f_{tu}\right)\left(\frac{H}{2} - \frac{1}{3}(x-y) - y\right)\right] + \left[(y f_{tu} b)\left(\frac{H}{2} - \frac{y}{2}\right)\right] \qquad (A.1.13)$$

SPANDRELS. Strain softening model TR: Lumantarna stress-strain relationship

The formulations for defining the M-N domains of the spandrels, adopting the Lumantarna model, are herein reported. For sake of simplicity, it is referred only to the resistant in tension

(TR) model with limited ductility in compression ($\mu_{\varepsilon c} = \varepsilon_{uc}/\varepsilon_{yc}$) and unlimited ductility in tension, i.e. compression governed failure (TR-CF).

The representation of the strain and stress profile for a rectangular cross-section (with depth H and width b) is shown in Figure A.1.6.

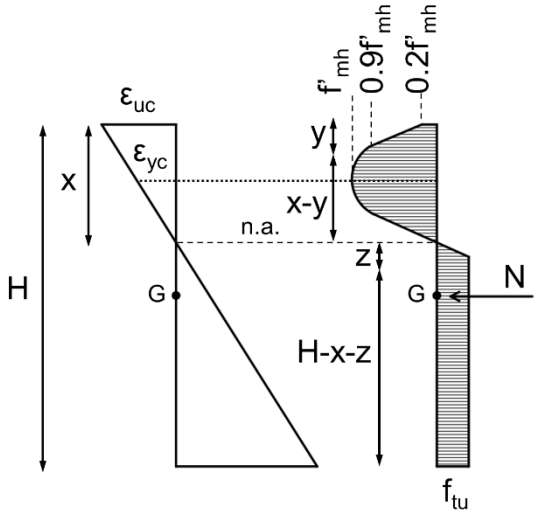

Figure A.1.6. Strain and stress profiles for Lumantarna model with tension capacity (TR-CF) for spandrels.

The axial Load N and the corresponding moment M are defined from the equilibrium of the translational and rotational (around centre of gravity G) forces in the section, following Equations A.1.14 and A.1.15:

$$N = 0.97\frac{x}{2}f'_m b + \frac{1}{2}0.7f'_m yb + 0.2f'_m yb + \frac{1}{2}zbf_{tu} - (H - x - z)bf_{tu} \qquad (A.1.14)$$

$$M_G = \left[\left(0.97\frac{x}{2}f'_m b\right)\left(\frac{H}{2} - 0.60x\right)\right] + \left[\left(\frac{1}{2}0.7f'_m yb\right)\left(\frac{H}{2} - \frac{2}{3}y\right)\right] + \\ + \left[\left(0.2f'_m yb\right)\left(\frac{H}{2} - \frac{y}{2}\right)\right] + \left[\left(\frac{1}{2}zbf_{tu}\right)\left(\frac{H}{2} - (H - x - z) + \frac{z}{3}\right)\right] + \\ + \left[\left((H - x - z)bf_{tu}\right)\left(\frac{H}{2} - \frac{(H - x - z)}{2}\right)\right] \qquad (A.1.15)$$

A.2 Appendix

In this Appendix are reported the step-by-step calculations of the hierarchy of strength between pier, spandrel and pier-spandrel joint for a knee subassembly, shown in Figure A.2.1, that refers to the substructure analyzed in Section 6.3. The needed geometrical characteristics are listed in Table A.2.1, while the masonry mechanical parameters are reported in Table A.2.2.

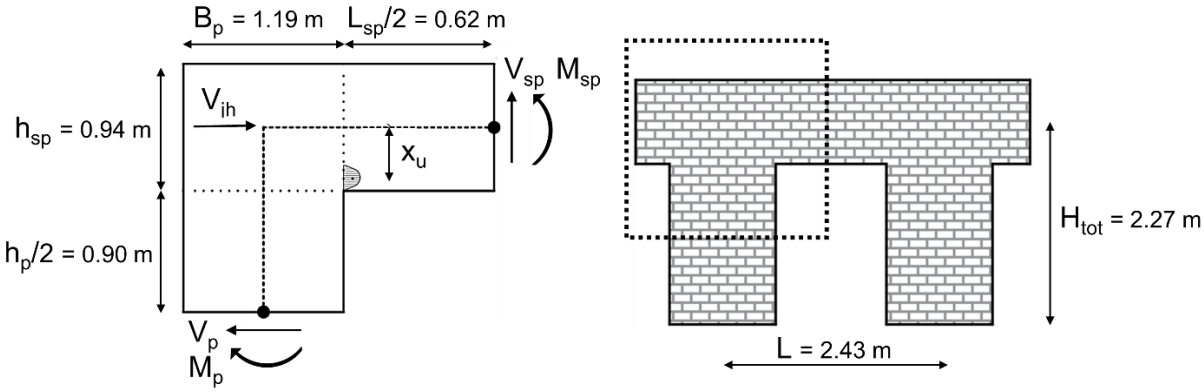

Figure A.2.1. Geometric characteristics of the knee subassembly.

Table A.2.1. Main geometrical parameters of the knee subassembly and the frame.

	Symbol	Value
Spandrel height	h_{sp}	0.940 m
Spandrel length	L_{sp}	1.240 m
Thickness	t_p	0.230 m
Pier height	h_p	1.795 m
Pier length	B_p	1.190 m
Pier axial load	N_g	131.4 kN
Pier axial stress	σ	480 kN/m^2
Joint height	h_j	0.940 m
Joint width	b_j	1.190 m
Strut diagonal length	d_w	1.516 m
Diagonal strut slope	θ	0.669 rad
Building length	L	2.430 m
Building height	H_{tot}	2.265 m

Table A.2.2. Main mechanical parameters of the masonry of the knee subassembly.

	Symbol	Value
Compression strength	f_m (or f'_w)	9200 kN/m^2
Tensile strength	f_t	300 kN/m^2
Initial shear strength at zero compressive stress	f_{v0}	200 kN/m^2
Shear strength of the diagonal compression	f_{ws}	200 kN/m^2
Friction coefficient	μ	0.7

Spandrel capacity

The moment-rotation curve of the spandrel is defined and its flexural yield capacity can be identified. To this aim, at first, the equivalent tensile strength f_{tu} is defined according to Equation A.2.1, where Δ_x and Δ_y are the height and the width of the bricks, respectively, and σ is the mean compressive stress acting on the adjacent pier section (assumed as twice the pier gravity axial load).

$$f_{tu} = \frac{\Delta_x}{2\Delta_y}\mu\ 0.65\ \sigma = \frac{110}{2 \cdot 76} 0.7 \cdot 0.65 \cdot\ 915 = 0.30\ \mathrm{kN/m^2} \qquad (A.2.1)$$

By assuming this value, the MBA approach is applied, with an elastic-perfectly plastic (EPP) stress-strain relationship with tension governed failure (TR-TF). A tensile “yielding” strain equal to $\varepsilon_{yt} = 0.0004$ is assumed and consequently the corresponding “yielding” curvature is defined through Equation A.2.2, while the cantilever length is assumed to equal to $L_{cant} = L_{sp}/2 = 0.620$ m and the plastic length equal to $L_p = 0.1 L_{cant} = 0.062$ m.

$$\phi_y = \frac{2\varepsilon_{yt}}{h_{sp}} = \frac{2 \cdot 0.0004}{0.940} = 0.0009\ \mathrm{m^{-1}} \qquad (A.2.2)$$

From the equilibrium of the compression and tension forces contributions, by varying the rotation values, the moment capacity is defined. From that curve, the “yielding” point is identified and the corresponding moment results equal to $M_{y,sp} = 26.96$ kNm. The Equivalent Pier Moment (EPM) is defined according to Equation A.2.3:

$$M_{p\ spf} = \frac{\frac{h_p}{2}\left(\frac{L_{sp} + B_p}{2}\right)}{\left(\frac{h_p + h_{sp}}{2}\right)\frac{L_{sp}}{2}} M_{y,sp} = \frac{0.90\left(\frac{1.24 + 1.19}{2}\right)}{\left(\frac{1.795 + 0.94}{2}\right)0.62} 26.96 = 34.68\ \mathrm{kNm} \qquad (A.2.3)$$

Regarding the shear strength Equation A.2.4 is used, while to define the EPM value Equation A.2.5 is taken into account.

$$V_{sp} = h_{sp} t_p f_{v0} = 0.94 \cdot 0.23 \cdot 200 = 43.24 \text{ kN} \quad (A.2.4)$$

$$M_{p\,sps} = \left(\frac{L_{sp} + B_p}{2}\right) \frac{\frac{h_p}{2}}{\left(\frac{h_p + h_{sp}}{2}\right)} V_{sp} = \left(\frac{1.24 + 1.19}{2}\right) \frac{\frac{1.795}{2}}{\left(\frac{1.795 + 0.94}{2}\right)} 43.24 = 34.48 \text{ kNm} \quad (A.2.5)$$

Pier capacity

The flexural capacity of the pier is evaluated through the calculation of the moment capacity value at the fixed ultimate strain. By assuming the MBA formulations and adopting the elastic-perfectly plastic (EPP-NTR) stress-strain relationship, the following parameters are considered (Equations A.2.6 - A.2.8):

$$\phi_y = \frac{2\varepsilon_y}{B_p} = \frac{2 \cdot 0.01}{1.19} = 0.017 \text{ m}^{-1} \quad (A.2.6)$$

$$L_{cant} = h_p/2 = 0.90 \text{ m} \quad (A.2.7)$$

$$L_p = 0.1 L_{cant} = 0.09 \text{ m} \quad (A.2.8)$$

From the equilibrium of the compression forces with the applied axial load (i.e. $N_g = 131.4$ kN), an ultimate neutral axis depth of $c_u = 0.107$ m is obtained and hence the ultimate rotation results equal to $\theta_u = 0.0082$ rad (Equation A.2.9), while the ultimate moment capacity, equivalent to the EPM, is equal to $M_{p\,f} = 73.36$ kNm.

$$\theta_u = \left[\frac{\left(\frac{\varepsilon_u}{c_u} - \phi_y\right)\left(L_{cant} - \frac{L_p}{2}\right) L_p}{L_{cant}}\right] = \left[\frac{\left(\frac{0.012}{0.107} - 0.017\right)\left(0.90 - \frac{0.09}{2}\right)(0.09)}{0.90}\right] = 0.0082 \text{ rad} \quad (A.2.9)$$

Regarding the shear strength, Equations A.2.10 and A.2.11 are adopted to define the diagonal cracking strength and the corresponding EPM, while Equations A.2.12 and A.2.13 are used for the bed-joint sliding strength and the corresponding EPM.

$$V_{p\,s,dc} = \frac{B_p t_p f_t}{b}\sqrt{1+\frac{\sigma}{f_t}} = \frac{1.19 \cdot 0.23 \cdot 300}{1.5}\sqrt{1+\frac{480}{300}} = 88.27\ \text{kN} \qquad (A.2.10)$$

$$M_{p\,s,dc} = V_{p\,s,dc} L_{cant} = 88.27 \cdot 0.90 = 79.22\ \text{kNm} \qquad (A.2.11)$$

$$V_{p\,s,bdj} = l' t_p (f_{v0} + \mu\sigma) = 0.12 \cdot 0.23(200 + 0.7 \cdot 480) = 97.68\ \text{kN} \qquad (A.2.12)$$

$$M_{p\,s,bdj} = V_{p\,s,bdj} L_{cant} = 97.68 \cdot 0.90 = 87.66\ \text{kNm} \qquad (A.2.13)$$

Pier-spandrel joint capacity

To define the joint capacity at first the characteristics of the equivalent diagonal strut have to be defined.

From the geometric parameters of the joint reported in Table A.2.1, the joint moment of inertia can be defined as: $I_j = t_j b_j^3/12 = 0.23 \cdot 1.19^3/12 = 0.032\ \text{m}^4$. The parameter λh is defined through Equation A.2.14:

$$\lambda h = \sqrt[4]{\frac{t_j sen(2\theta)}{4 I_j h_j}}\, h = \sqrt[4]{\frac{0.23 \cdot sen(2 \cdot 0.669)}{4 \cdot 0.032 \cdot 0.94}}\, 0.94 = 1.20 \qquad (A.2.14)$$

From this value ($\lambda h < 3.14$), it is possible to define the parameters $K1$ and $K2$ that result equal to 1.3 and -0.178, respectively. From these, the width of the equivalent diagonal strut b_w can be defined according to Equation A.2.15:

$$b_w = \left(\frac{K_1}{\lambda h} + K_2\right) d_w = \left(\frac{1.3}{1.20} - 0.178\right) 1.516 = 1.373\ \text{m} \qquad (A.2.15)$$

Once all the strut parameters are defined, the strength associated with the possible failure mechanisms can be calculated. The compression failure at the centre of the panel, the compression failure at the corner edges, the sliding shear failure and the diagonal tension failure can be referred to Equations A.2.16 - A.2.19, respectively:

$$\sigma_{w,cfcp} = \frac{1.16 f'_w tan\theta}{K_1 + K_2 \lambda h} = \frac{1.16 \cdot 9200 \cdot tan 0.669}{1.3 + (-0.178) \cdot 1.20} = 7759.9\ \text{kN/m}^2 \qquad (A.2.16)$$

$$\sigma_{w,cfce} = \frac{1.12 f'_w \, sin\theta \, cos\theta}{K_1(\lambda h)^{-0.12} + K_2(\lambda h)^{0.88}} = \frac{1.12 \cdot 9200 \cdot sin0.669 \cdot cos0.669}{1.3(1.20)^{-0.12} + (-0.178)(1.20)^{0.88}} = 4715.8 \frac{\text{kN}}{\text{m}^2} \quad (A.2.17)$$

$$\sigma_{w,ssf} = \frac{(1.2sin\theta + 0.45cos\theta) f_{wu} + 0.3\sigma}{b_w/d_w} = \\ = \frac{(1.2sin0.669 + 0.45cos0.669)536 + 0.3 \cdot 480}{1.373/1.516} = 808.7 \text{ kN/m}^2 \quad (A.2.18)$$

$$\sigma_{w,dtf} = \frac{0.6 f_{ws} + 0.3\sigma}{b_w/d_w} = \frac{0.6 \cdot 200 + 0.3 \cdot 480}{1.373/1.516} = 291.7 \text{ kN/m}^2 \quad (A.2.19)$$

where $f_{wu} = f_{v0} + \mu\sigma$ is the shear sliding strength in the joint.

The minimum strength corresponds to that of the tension diagonal shear failure mechanism $\sigma_{w,dtf}$, that hence represents the first one expected. The corresponding horizontal shear force V_{jh} can be calculated through Equation A.2.20.

$$V_{jh} = \sigma_{w,dtf} b_w t_j cos\theta = 291.7 \cdot 1.373 \cdot 0.23 \cdot cos0.669 = 72.3 \text{ kN} \quad (A.2.20)$$

The corresponding pier shear capacity and the EPM can be calculated according to Equations A.2.21 and A.2.22, respectively:

$$V_{p\,j} = \frac{V_{jh}}{\left[\frac{\left(\frac{h_p + h_{sp}}{2}\right)\frac{L_{sp}}{2}}{\left(\frac{L_{sp} + B_p}{2}\right)x_u} - 1\right]} = \frac{72.3}{\left[\frac{\left(\frac{1.795 + 0.94}{2}\right)\frac{1.24}{2}}{\left(\frac{1.24 + 1.19}{2}\right)0.423} - 1\right]} = 111.2 \text{ kN} \quad (A.2.21)$$

$$M_{p\,j} = V_{p\,j} \frac{h_p}{2} = 111.2 \cdot \frac{1.795}{2} = 99.8 \text{ kNm} \quad (A.2.22)$$

where $x_u = 0.423$ m is defined from the spandrel moment-rotation curve analysis.

Seismic demand

To define the seismic demand, Equations A.2.23 and A.24 are used, where the equivalent seismic load (or global shear strength) F can be defined through Equation A.2.25.

$$\Delta N = \frac{2H_{tot}}{3L} F \quad (A.2.23)$$

$$N = N_g \pm \Delta N \tag{A.2.24}$$

$$F = n_{col} V_p = n_{col} \frac{M}{\frac{h_p}{2}} = 2 \frac{M}{\frac{1.795}{2}} \tag{A.2.25}$$

Hierarchy of strength

The EPM calculated for spandrel, pier and joint can be represented in the same M-N performance domain and the hierarchy of strength can be defined by comparing these capacities with the seismic demand. The same procedure, herein presented for the case of fixed axial load N_g, can be adopted varying it, thus obtaining the M-N curves.

In Figure A.2.2, the capacities of all the considered components failure mechanisms are represented. The moment capacity values determined in this Appendix, at gravity axial load N_g, are highlighted in green. To define the correct sequence of events, according to the direction of the seismic action, it is needed to consider the intersection points of the capacity with the seismic demand.

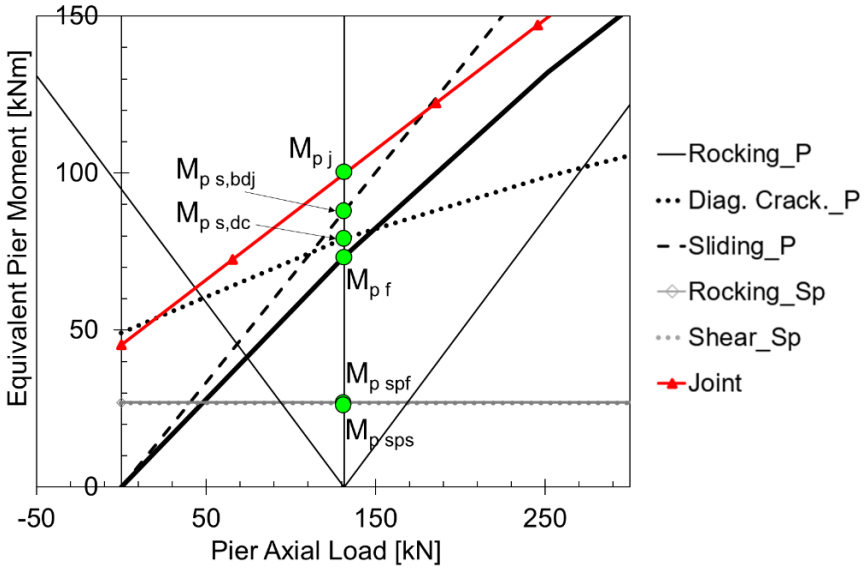

Figure A.2.2. M-N performance domain of the analyzed knee subassembly.

In case the pier-spandrel joints are assumed as rigid, according to the Equivalent Frame Model, the same procedure herein developed can be adopted by modifying the height of the pier in the effective one.

A.3 Appendix

In this Appendix are reported the results in terms of the M-N performance domains of the substructures presented in Section 6.3.7. In the following graphs, the influence of the pier-spandrel joints is highlighted in red. A summary of the performed parametric analyses is reported in Table A.3.1, while the geometric parameters are shown in Figure A.3.1. Bold marked values in Table A.3.1 refer to the variations with respect to the original geometry of the PS3 substructure (in the first row, italicized), which was taken as reference. Each structure model is numbered (first column in Table A.3.1) and this number is reported in each Figures caption (Figures A.3.2 - A.3.23), in order to organize the results. See Section 6.3.7 for more details.

Table A.3.1. Parametric analyses with respect to the PS3 substructure geometry (first row, italicized) and identified substructure failure mechanism.

Model number	h_p [m]	B_p [m]	λ_p [-]	L_{sp} [m]	h_{sp} [m]	λ_{sp} [-]	Failure mechanism
PS3	*1.795*	*1.19*	*1.51*	*1.24*	*0.94*	*1.32*	*SP Shear*
1	1.795	1.19	1.51	**1.40**	0.94	**1.49**	*SP Rocking*
2	1.795	1.19	1.51	**1.60**	0.94	**1.70**	*SP Rocking*
3	1.795	1.19	1.51	**1.80**	0.94	**1.91**	*SP Rocking*
4	1.795	1.19	1.51	**2.00**	0.94	**2.13**	*SP Rocking*
5	1.795	1.19	1.51	**2.20**	0.94	**2.34**	*SP Rocking*
6	1.795	1.19	1.51	**2.50**	0.94	**2.66**	*SP Rocking*
7	1.795	1.19	1.51	1.24	**1.20**	**1.03**	*SP Shear*
8	1.795	1.19	1.51	1.24	**1.50**	**0.83**	*SP Shear*
9	1.795	1.19	1.51	1.24	**2.00**	**0.62**	*SP Shear*
10	1.795	**0.80**	**2.24**	1.24	0.94	1.32	*SP Shear*
11	1.795	**1.00**	**1.80**	1.24	0.94	1.32	*SP Shear*
12	1.795	**1.40**	**1.28**	1.24	0.94	1.32	*SP Shear*
13	1.795	**1.60**	**1.12**	1.24	0.94	1.32	*SP Shear*
14	1.795	**1.80**	**1.00**	1.24	0.94	1.32	*SP Shear*
15	**1.00**	1.19	**0.84**	1.24	0.94	1.32	*SP Shear*
16	**1.30**	1.19	**1.09**	1.24	0.94	1.32	*SP Shear*
17	**1.50**	1.19	**1.26**	1.24	0.94	1.32	*SP Shear*
18	**2.00**	1.19	**1.68**	1.24	0.94	1.32	*SP Shear*
19	**2.30**	1.19	**1.93**	1.24	0.94	1.32	*SP Shear*
20	**2.60**	1.19	**2.18**	1.24	0.94	1.32	*SP Shear*
21	**3.00**	1.19	**2.52**	1.24	0.94	1.32	*SP Shear*

SP is for Spandrel.

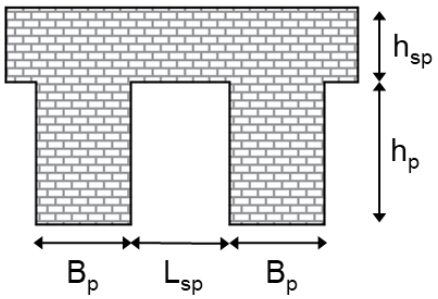

Figure A.3.1. Geometric parameters of the substructures.

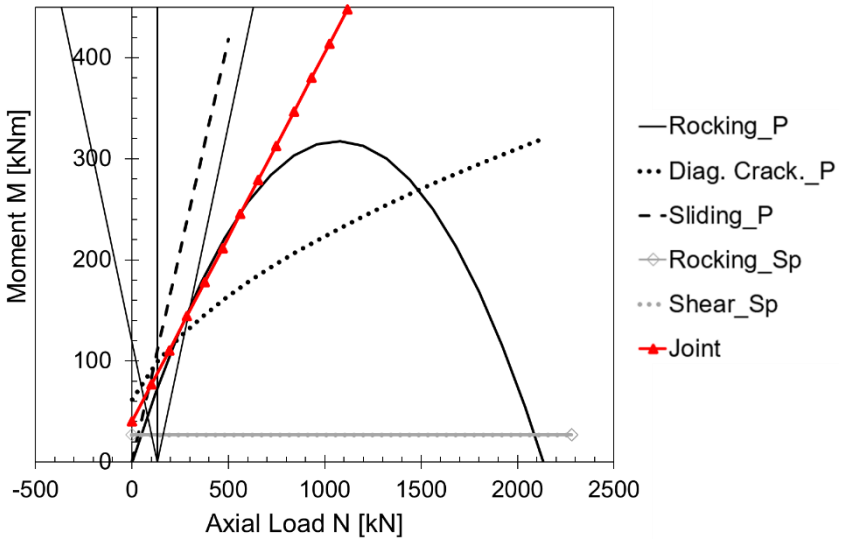

Figure A.3.2. Pier M-N performance domain of the subassembly PS3.

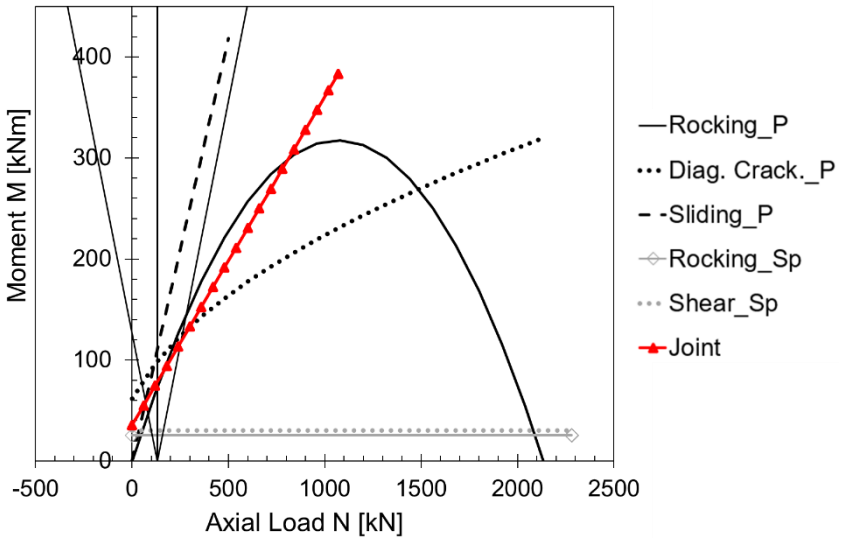

Figure A.3.3. Pier M-N performance domain of the model 1.

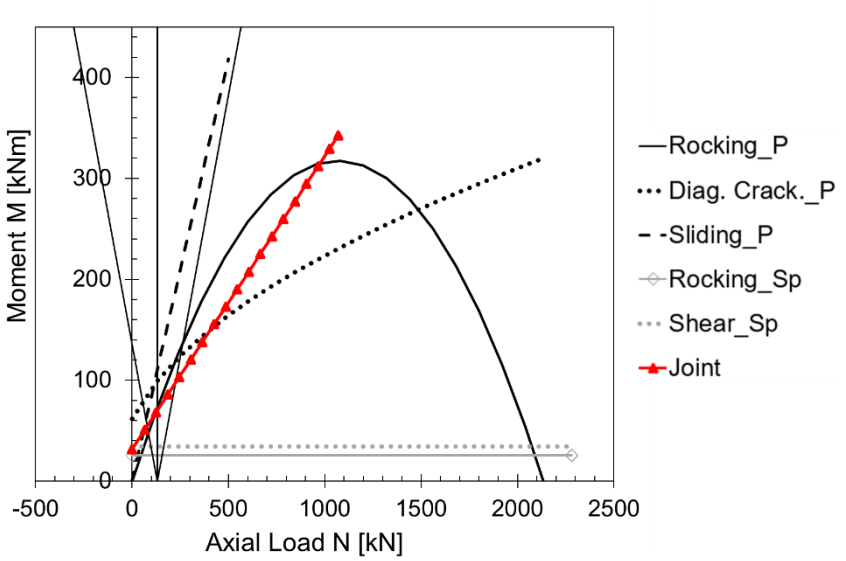

Figure A.3.4. Pier M-N performance domain of the model 2.

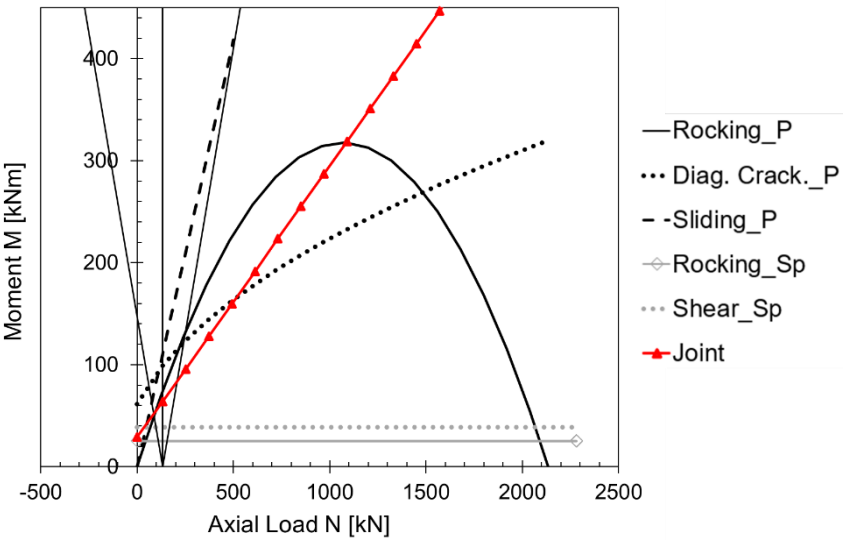

Figure A.3.5. Pier M-N performance domain of the model 3.

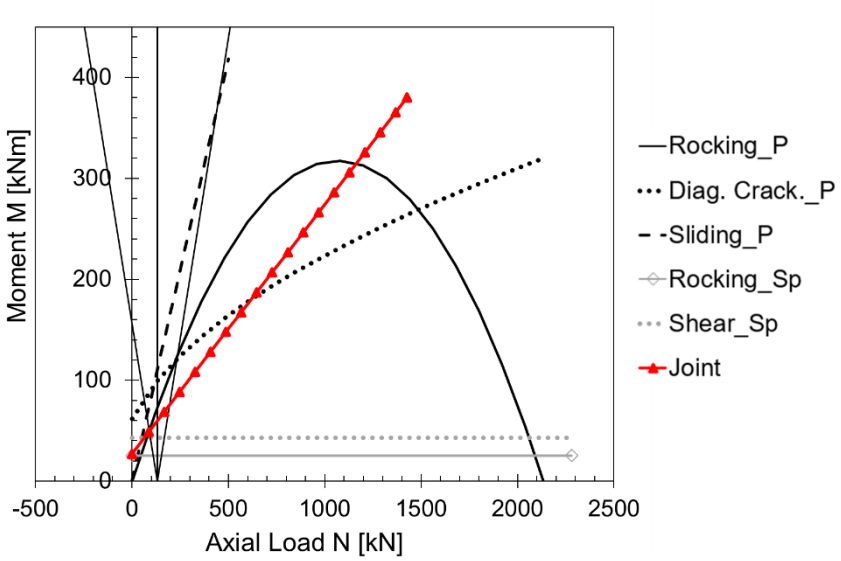

Figure A.3.6. Pier M-N performance domain of the model 4.

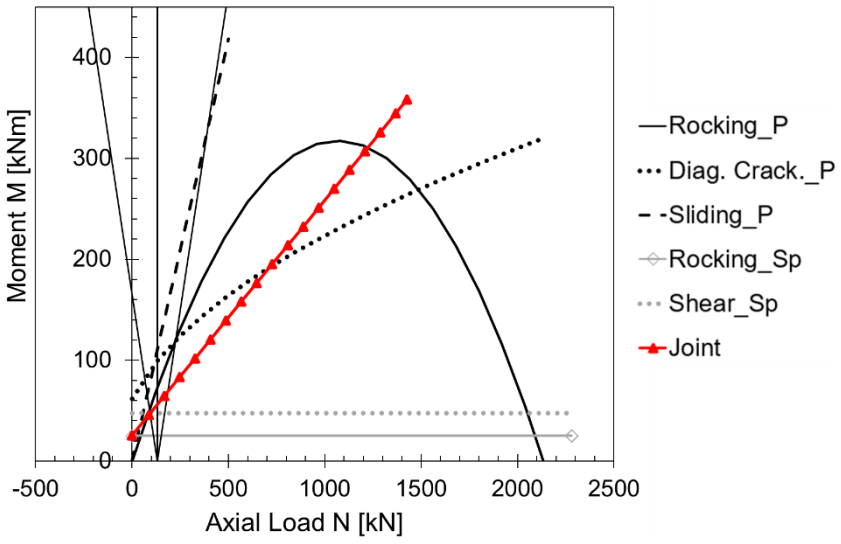

Figure A.3.7. Pier M-N performance domain of the model 5.

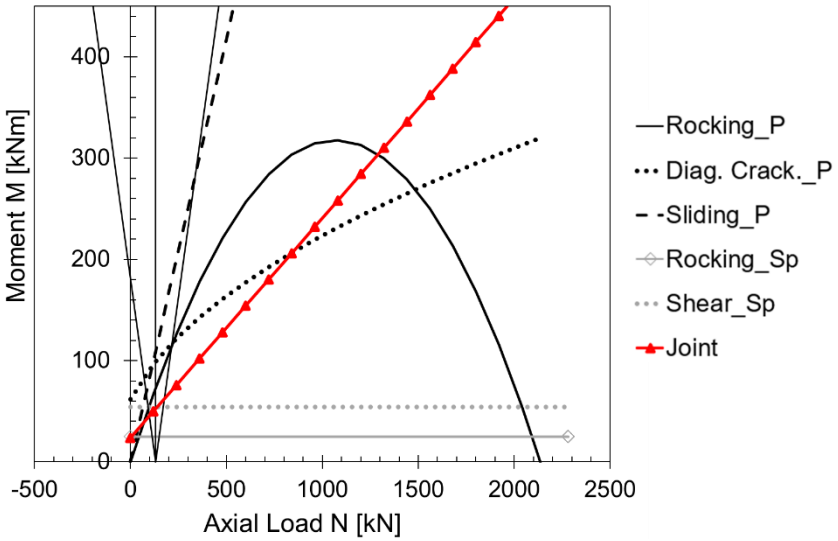

Figure A.3.8. Pier M-N performance domain of the model 6.

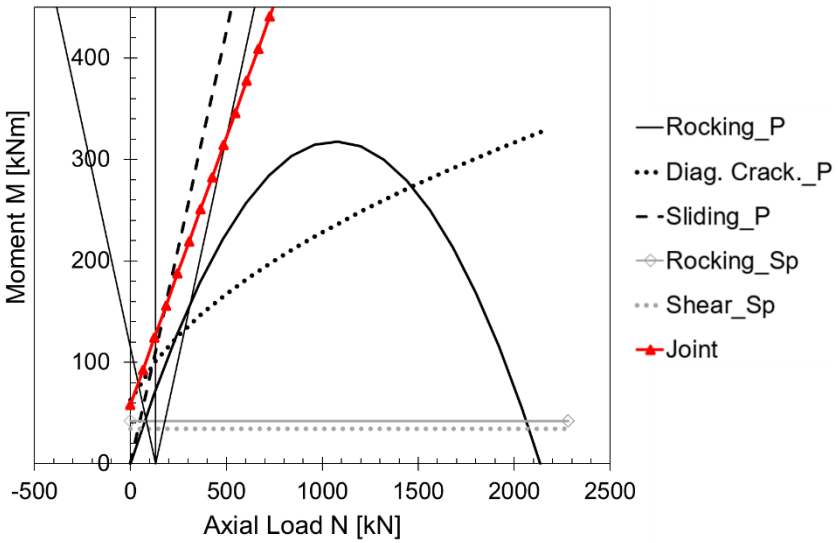

Figure A.3.9. Pier M-N performance domain of the model 7.

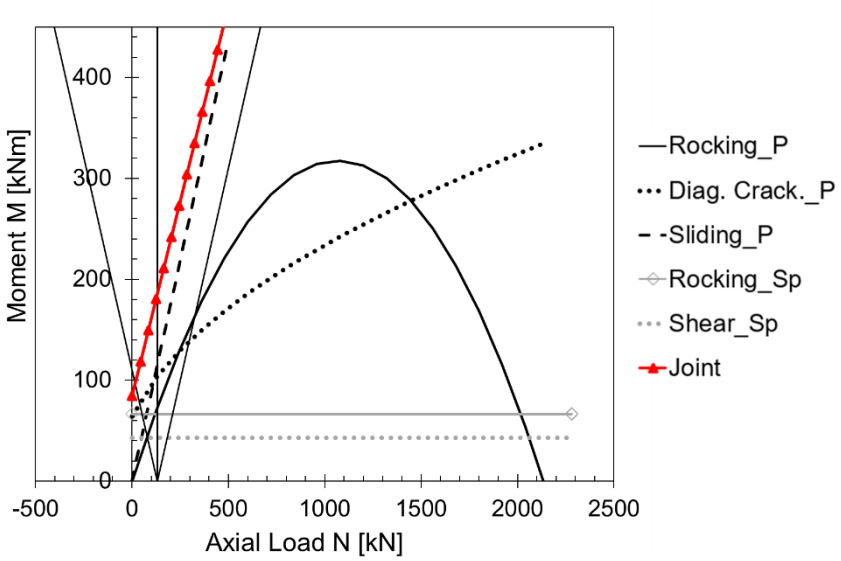

Figure A.3.10. Pier M-N performance domain of the model 8.

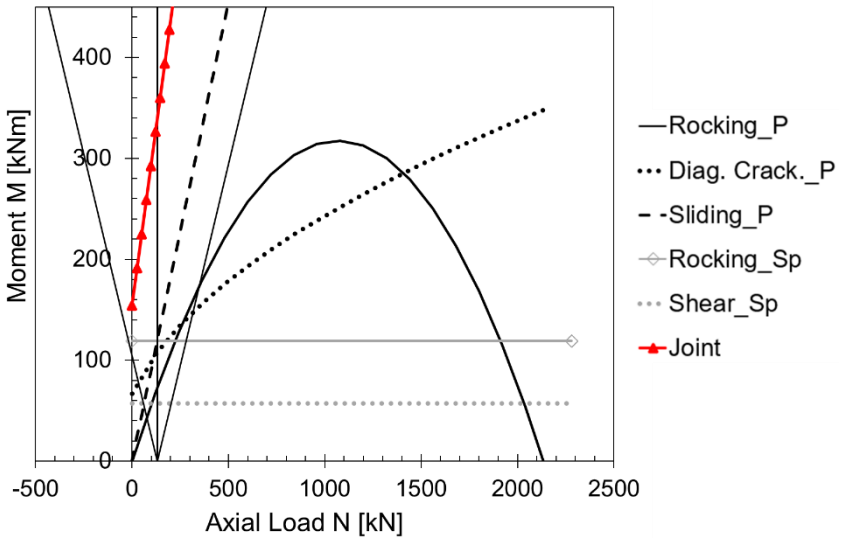

Figure A.3.11. Pier M-N performance domain of the model 9.

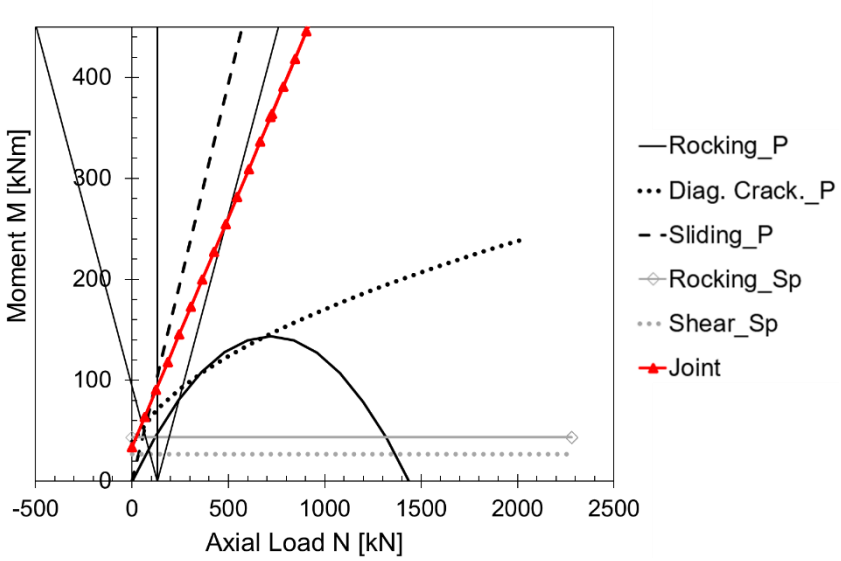

Figure A.3.12. Pier M-N performance domain of the model 10.

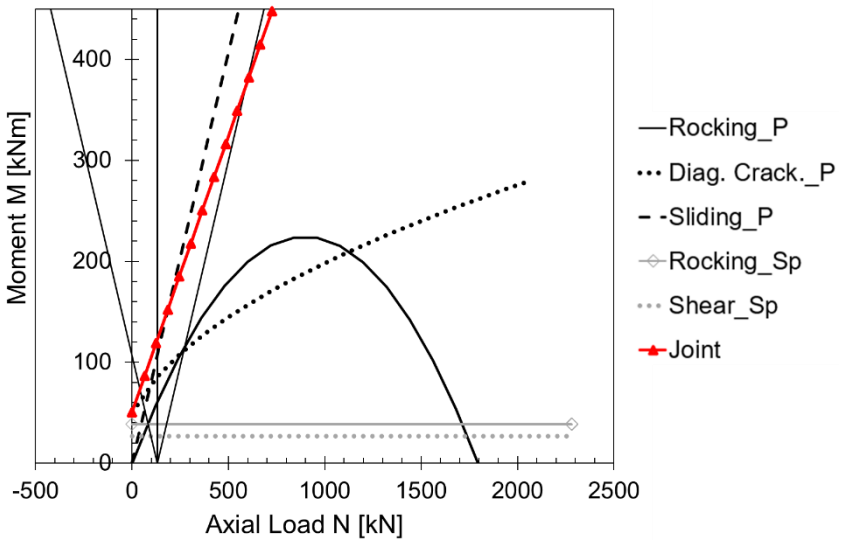

Figure A.3.13. Pier M-N performance domain of the model 11.

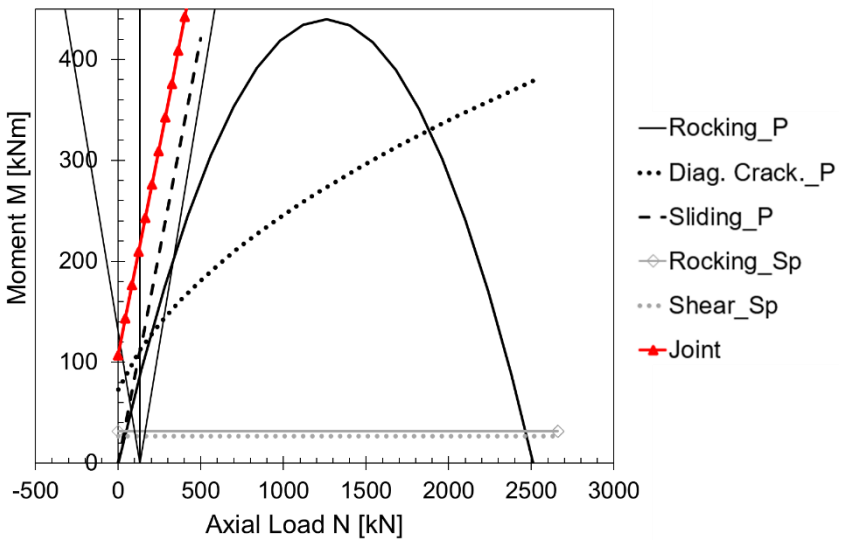

Figure A.3.14. Pier M-N performance domain of the model 12.

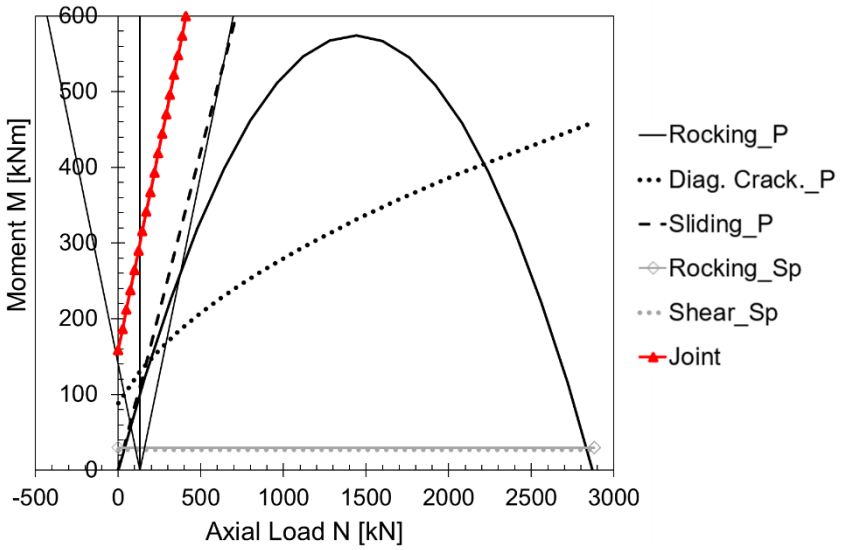

Figure A.3.15. Pier M-N performance domain of the model 13.

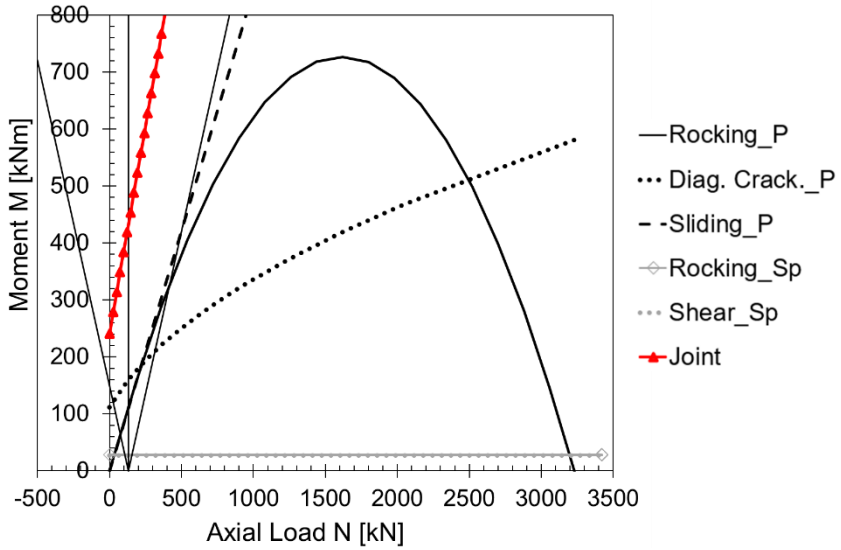

Figure A.3.16. Pier M-N performance domain of the model 14.

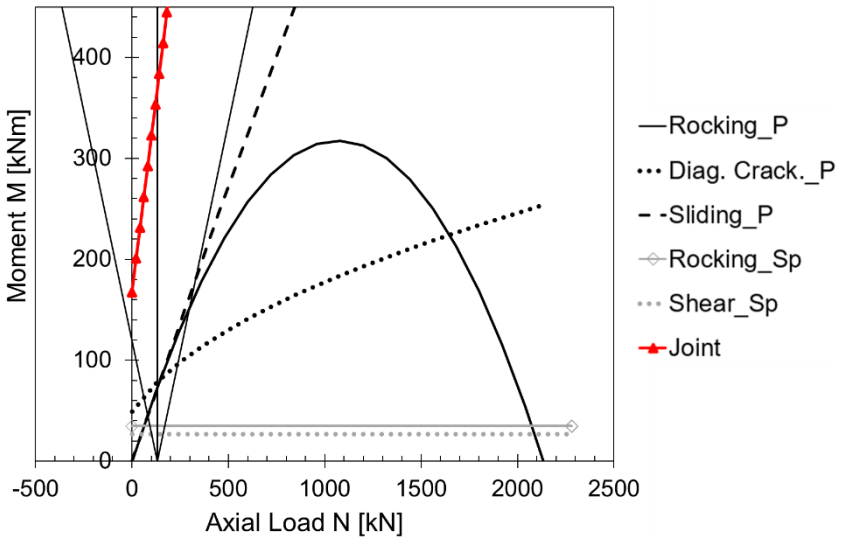

Figure A.3.17. Pier M-N performance domain of the model 15.

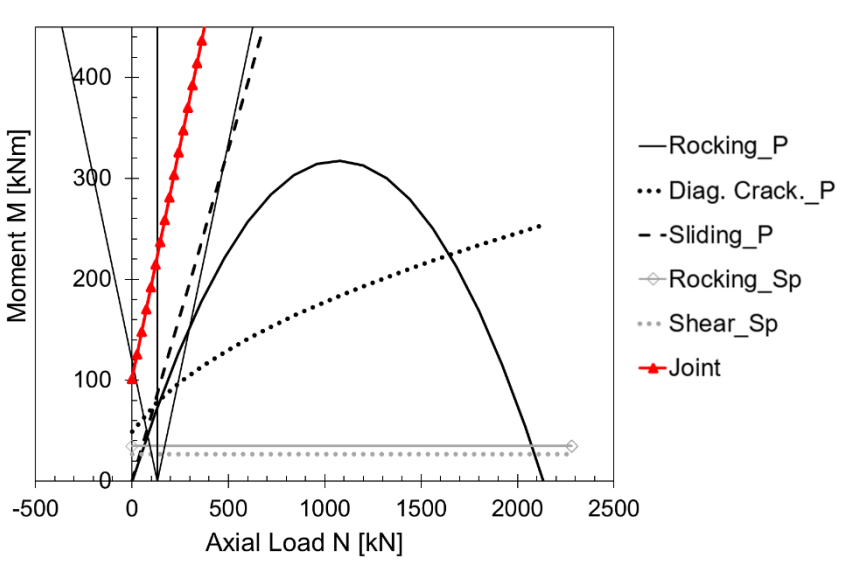

Figure A.3.18. Pier M-N performance domain of the model 16.

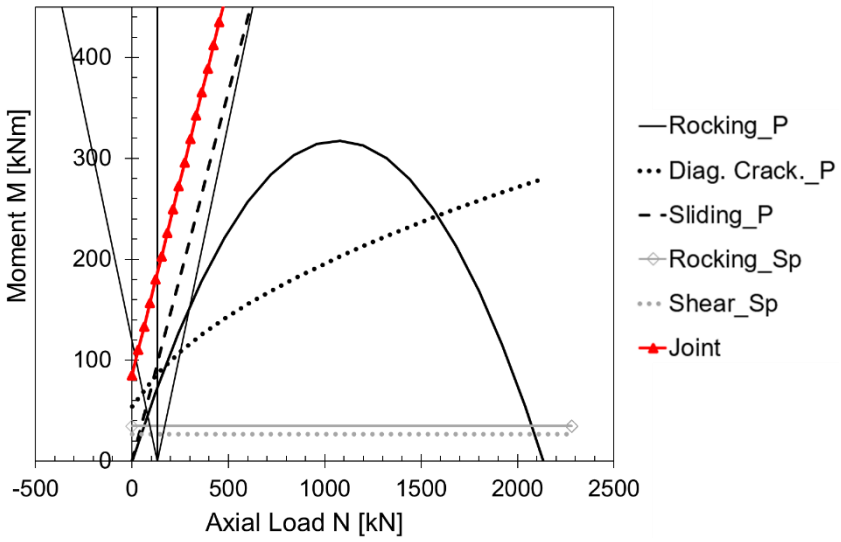

Figure A.3.19. Pier M-N performance domain of the model 17.

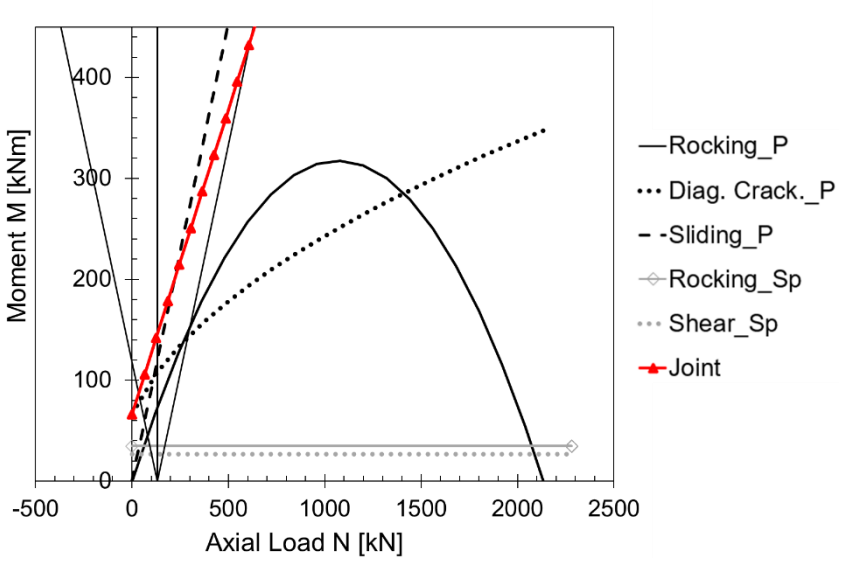

Figure A.3.20. Pier M-N performance domain of the model 18.

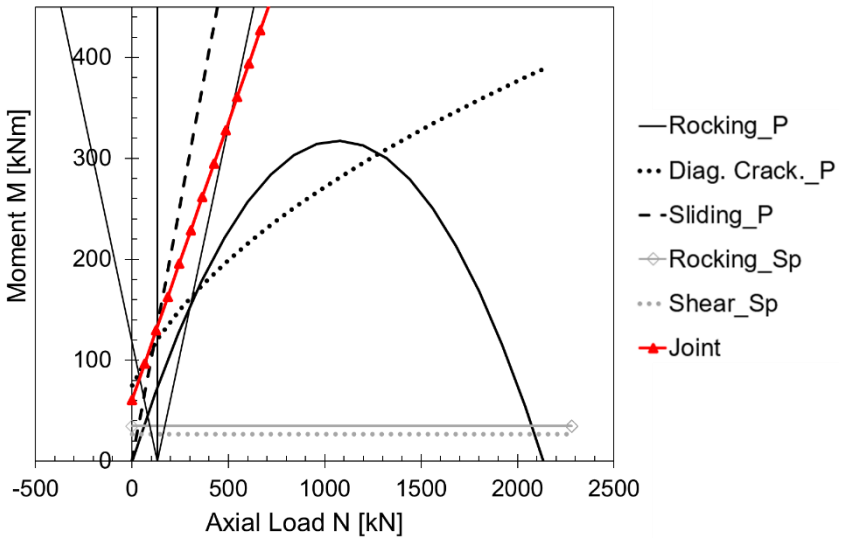

Figure A.3.21. Pier M-N performance domain of the model 19.

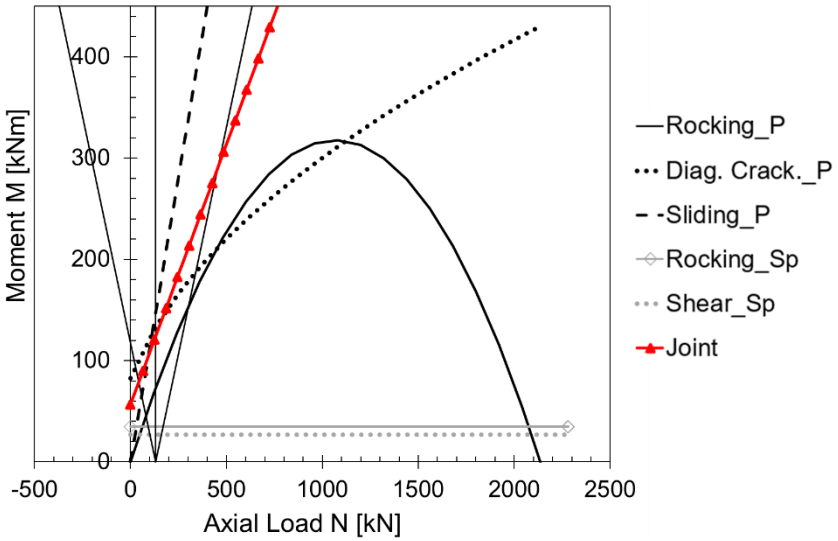

Figure A.3.22. Pier M-N performance domain of the model 20.

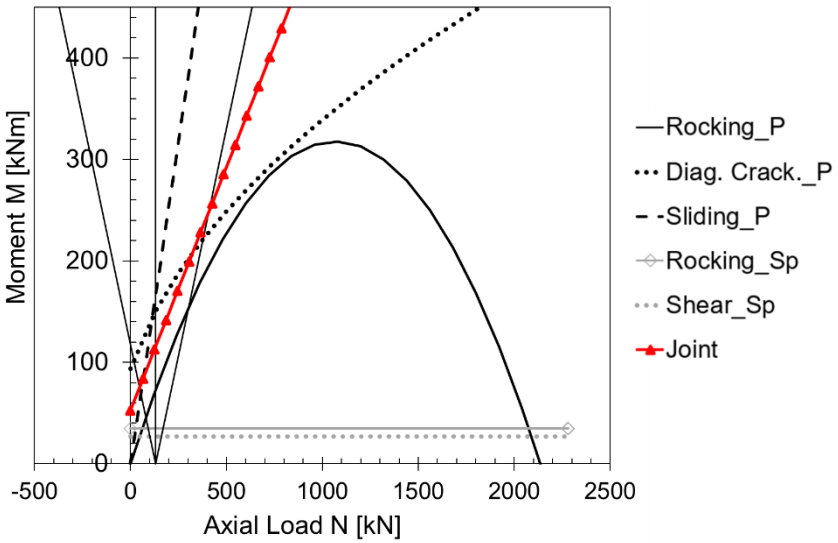

Figure A.3.23. Pier M-N performance domain of the model 21.

A.4 Appendix

In this Appendix are reported the results obtained in terms of the performance and the economic losses by adopting the retrofit interventions described in Section 7.8.2. More in detail, the results of the 2-levels structures are shown in Figures A.4.1 and A.4.2, while in Figures A.4.3 - A.4.5 are reported those of the 3-levels structures and in Figures A.4.6 - A.4.8 those of the 4-levels structures. See Section 7.8.2 for more details.

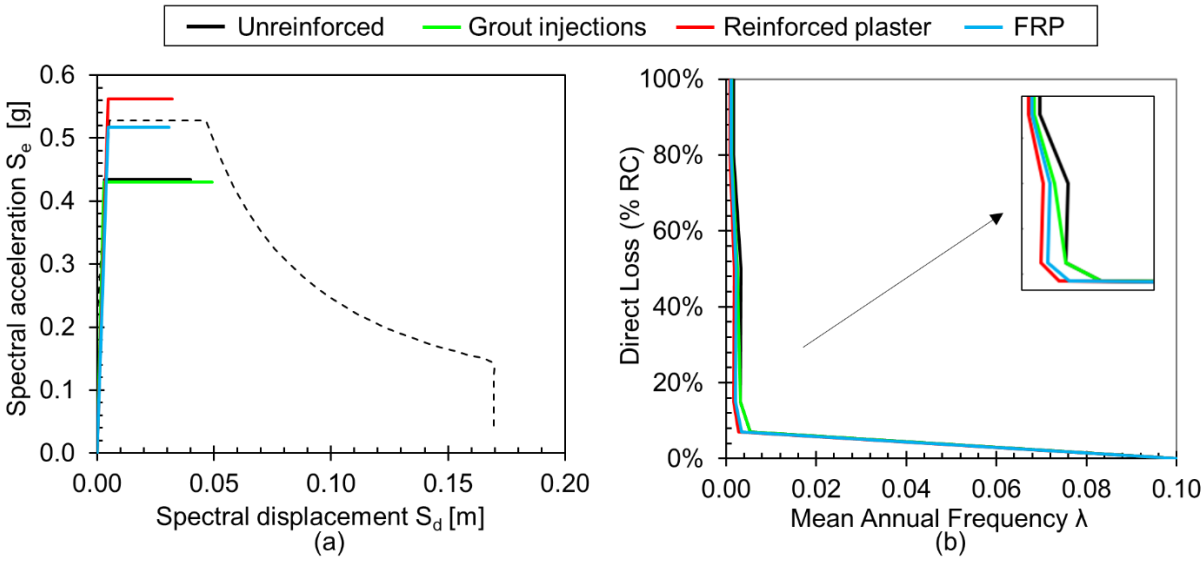

Figure A.4.1. Retrofit interventions results of the 3-bays 2-levels structure: (a) seismic performances and (b) expected annual losses curves.

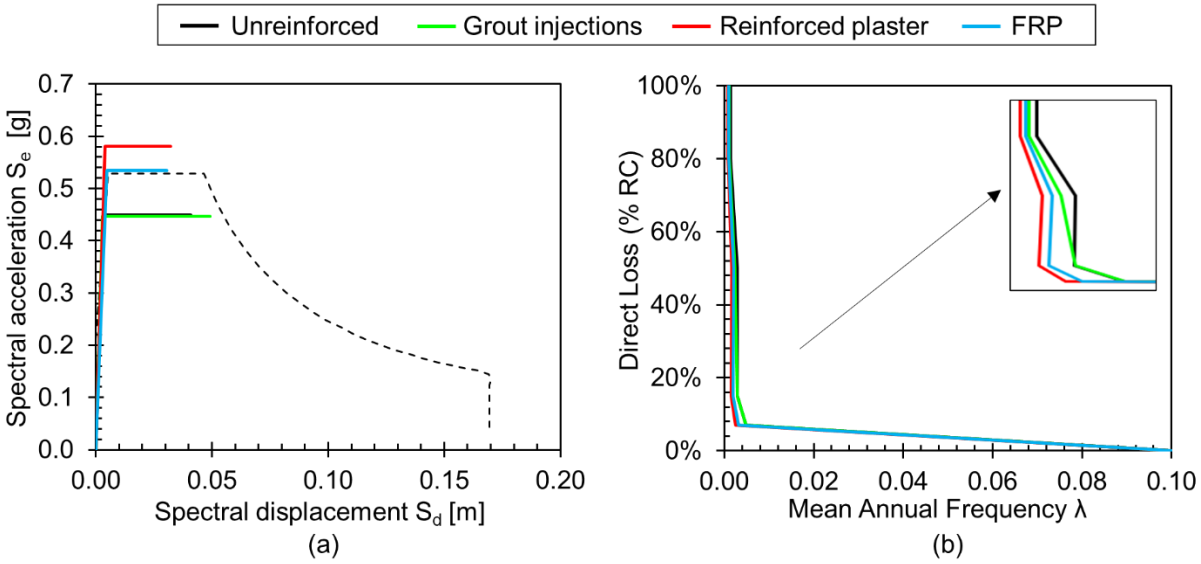

Figure A.4.2. Retrofit interventions results of the 4-bays 2-levels structure: (a) seismic performances and (b) expected annual losses curves.

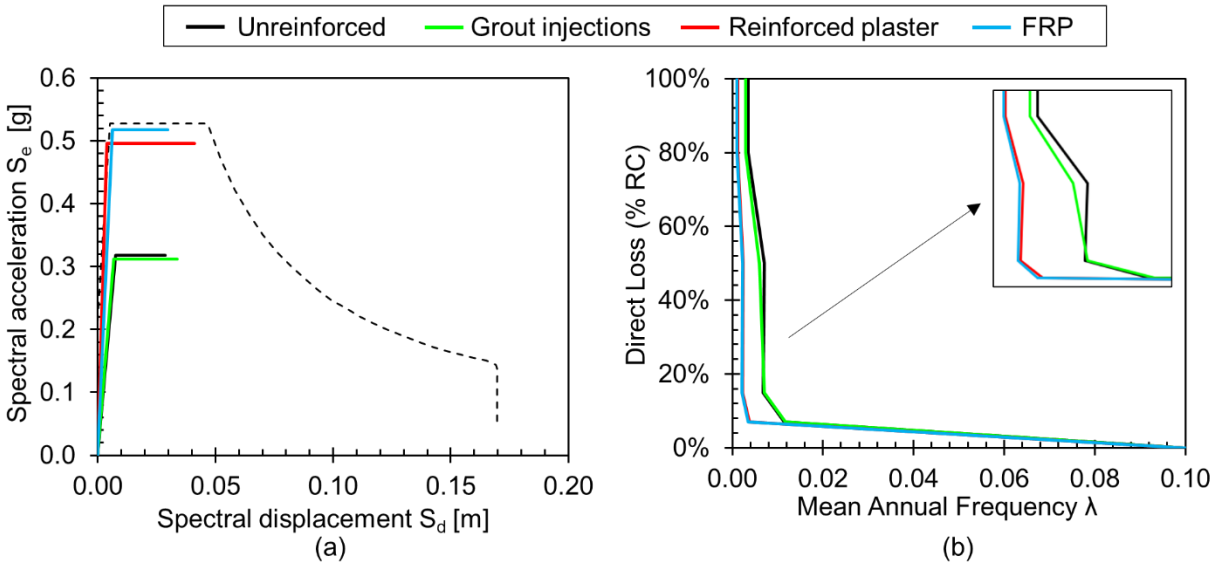

Figure A.4.3. Retrofit interventions results of the 2-bays 3-levels structure: (a) seismic performances and (b) expected annual losses curves.

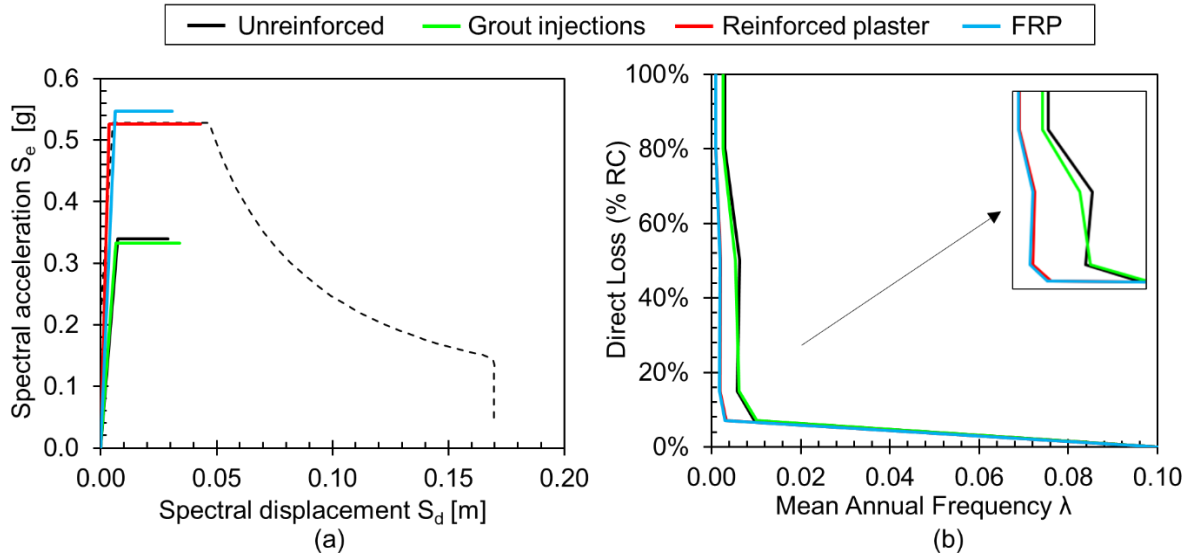

Figure A.4.4. Retrofit interventions results of the 3-bays 3-levels structure: (a) seismic performances and (b) expected annual losses curves.

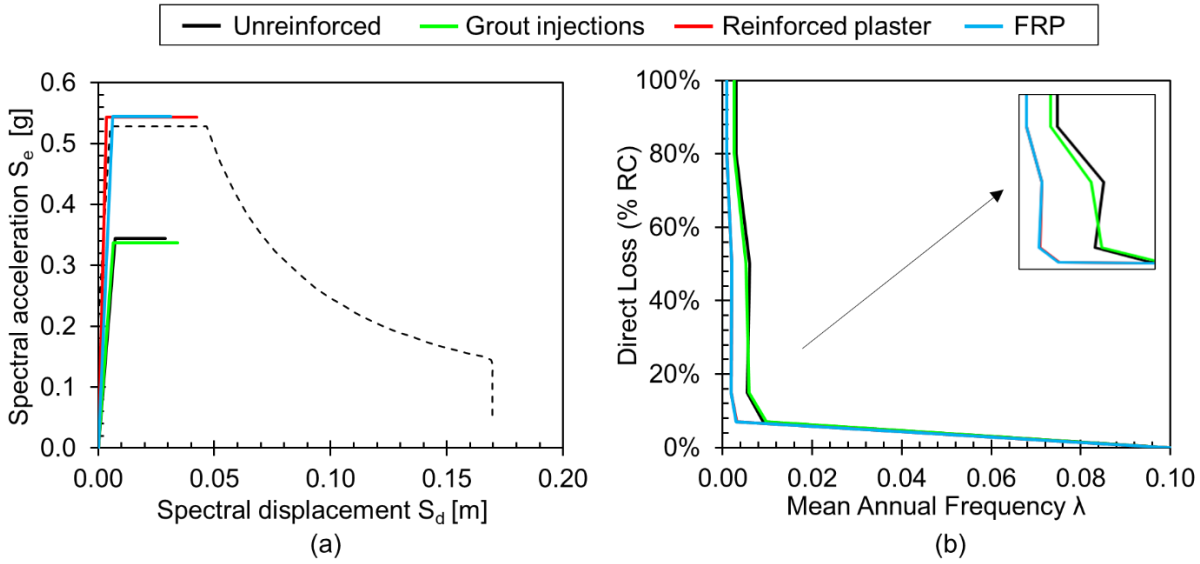

Figure A.4.5. Retrofit interventions results of the 4-bays 3-levels structure: (a) seismic performances and (b) expected annual losses curves.

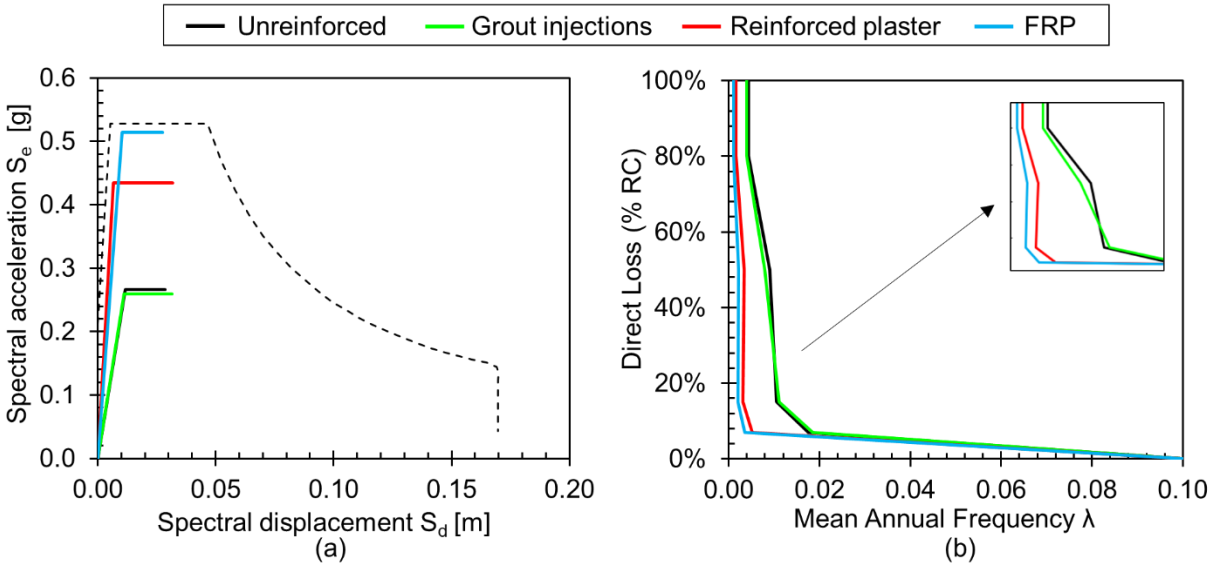

Figure A.4.6. Retrofit interventions results of the 2-bays 4-levels structure: (a) seismic performances and (b) expected annual losses curves.

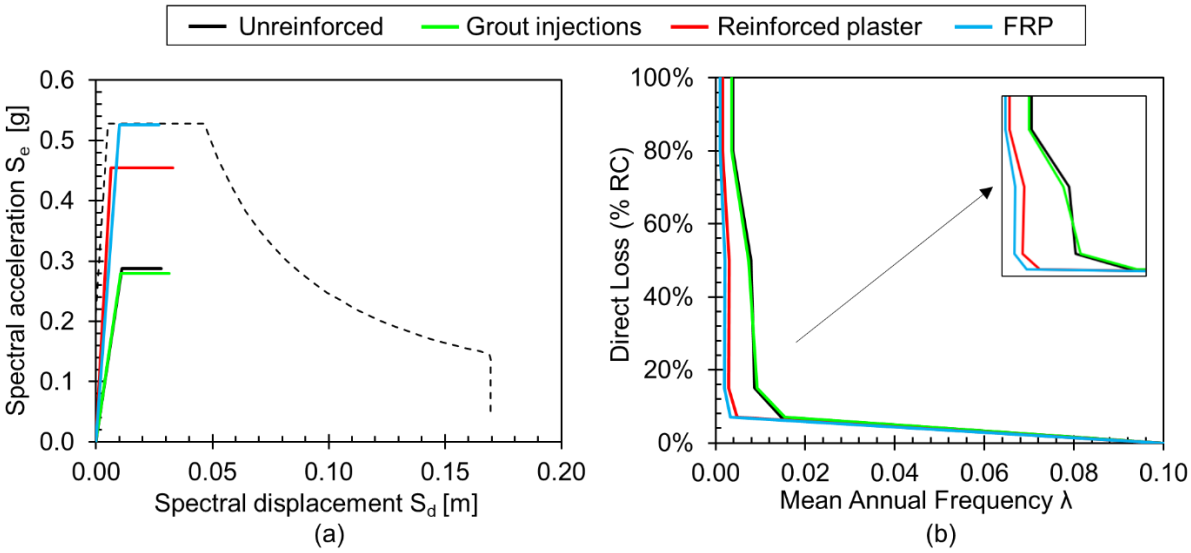

Figure A.4.7. Retrofit interventions results of the 3-bays 4-levels structure: (a) seismic performances and (b) expected annual losses curves.

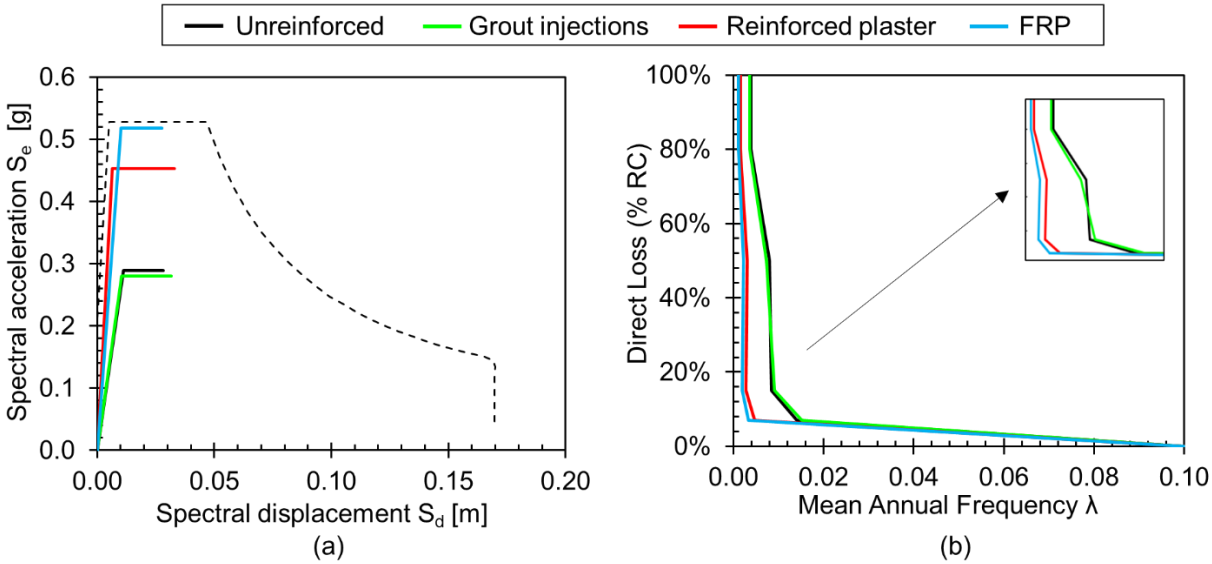

Figure A.4.8. Retrofit interventions results of the 4-bays 4-levels structure: (a) seismic performances and (b) expected annual losses curves.

A.5 Appendix

In this Appendix are reported the results obtained in terms of the costs related to the retrofit interventions adopted to increase the In-Plane performance of the 3- and 4-bays structures, located in MS zones and partially discussed in Section 7.10.1. To strengthen the frames, the following interventions were considered: i) the grout injections, ii) the reinforced plaster and iii) the FRP. For sake of brevity, in Section 7.10.1 are shown only the costs related to 2-bays structures. Hence, in Tables A.5.1 - A.5.3 the intervention costs and the 1%NBS costs of the 3- and 4-bays structures are reported, for each typology of intervention. In Figures A.5.1 - A.5.6 the values are represented in histograms.

Table A.5.1. Grout injections costs of the 3- and 4-bays structures in MS zones.

Case	Area (m^2)	Cost (€/m^2)	Cost (€)	$\%NBS_{a.o.}$ (%)	$\%NBS_{p.o.}$ (%)	1%NBS Cost (€)
3-bays 2-levs	40.1	50	2005	83	93	200
3-bays 3-levs	54.8	50	2738	64	68	685
3-bays 4-levs	69.4	50	3472	58	60	1736
4-bays 2-levs	52.4	50	2619	87	95	327
4-bays 3-levs	71.5	50	3577	65	69	894
4-bays 4-levs	90.7	50	4536	58	60	2268

Table A.5.2. Reinforced plaster costs of the 3- and 4-bays structures in MS zones.

Case	Area (m^2)	Cost (€/m^2)	Cost (€)	$\%NBS_{a.o.}$ (%)	$\%NBS_{p.o.}$ (%)	1%NBS Cost (€)
3-bays 2-levs	37.4	130	4867	83	107	203
3-bays 3-levs	138.9	130	18052	64	100	501
3-bays 4-levs	183.4	130	23839	58	86	851
4-bays 2-levs	49.0	130	6373	87	110	277
4-bays 3-levs	182.1	130	23678	65	103	623
4-bays 4-levs	240.6	130	31273	58	86	1117

Table A.5.3. FRP costs of the 3- and 4-bays structures in MS zones.

Case	Area (m^2)	Cost (€/m^2)	Cost (€)	$\%NBS_{a.o.}$ (%)	$\%NBS_{p.o.}$ (%)	1%NBS Cost (€)
3-bays 2-levs	27.5	430	11835	83	98	789
3-bays 3-levs	46.4	430	19943	64	103	511
3-bays 4-levs	73.8	430	31748	58	100	756
4-bays 2-levs	35.5	430	15286	87	101	1092
4-bays 3-levs	61.4	430	26423	65	103	695
4-bays 4-levs	97.3	430	41829	58	98	1046

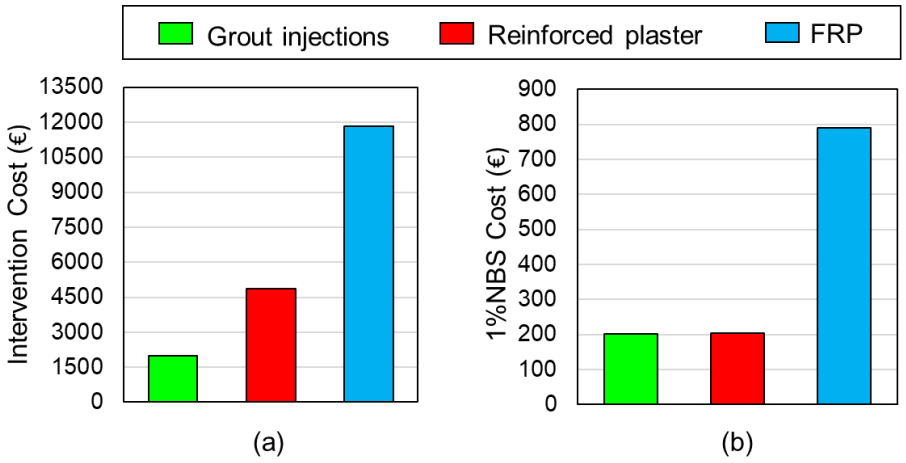

Figure A.5.1. Retrofit costs of the 3-bays 2-levels structure in MS zones: (a) interventions costs and (b) 1%NBS cost.

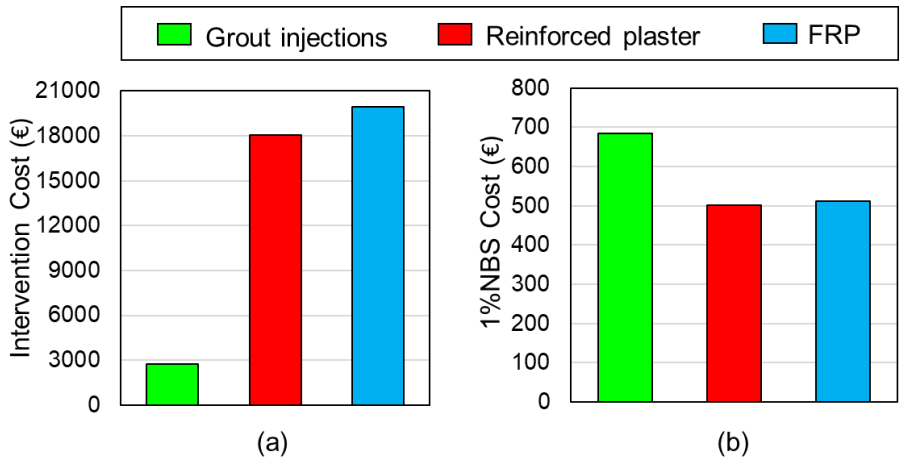

Figure A.5.2. Retrofit costs of the 3-bays 3-levels structure in MS zones: (a) interventions costs and (b) 1%NBS cost.

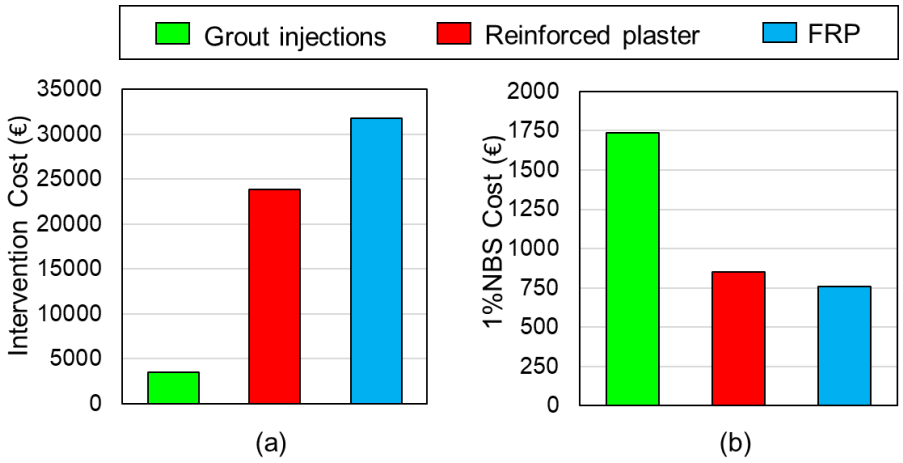

Figure A.5.3. Retrofit costs of the 3-bays 4-levels structure in MS zones: (a) interventions costs and (b) 1%NBS cost.

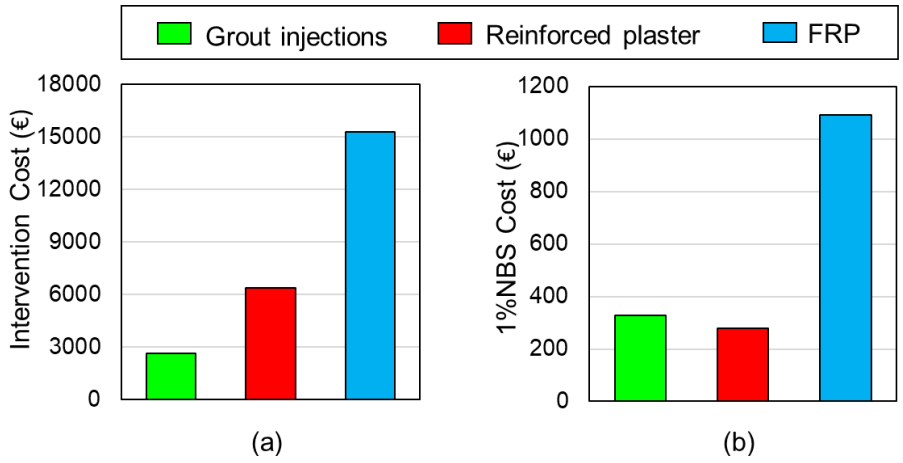

Figure A.5.4. Retrofit costs of the 4-bays 2-levels structure in MS zones: (a) interventions costs and (b) 1%NBS cost.

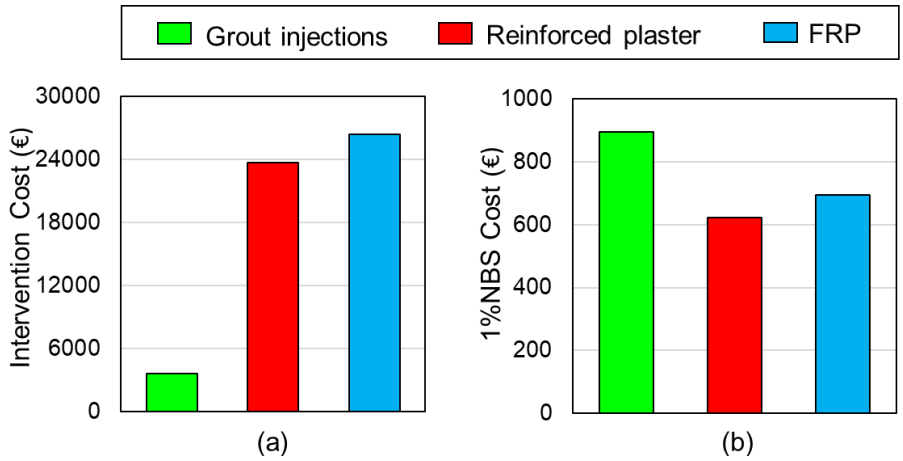

Figure A.5.5. Retrofit costs of the 4-bays 3-levels structure in MS zones: (a) interventions costs and (b) 1%NBS cost.

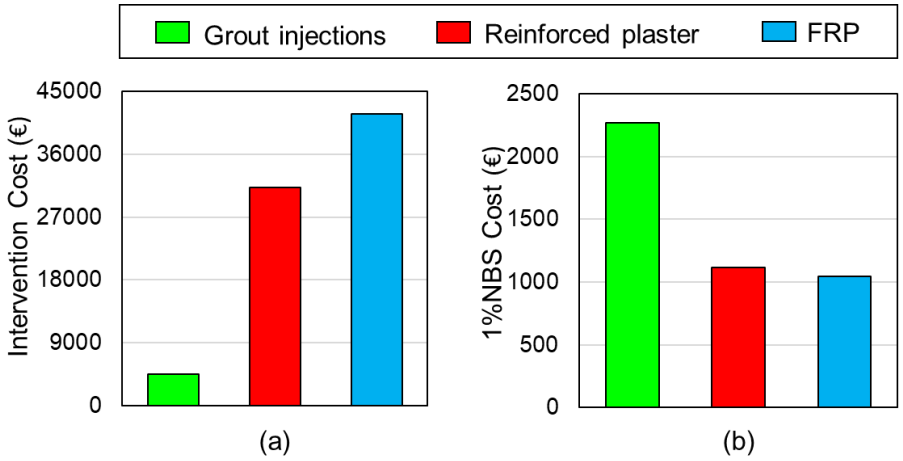

Figure A.5.6. Retrofit costs of the 4-bays 4-levels structure in MS zones: (a) interventions costs and (b) 1%NBS cost.